

NASA Contractor Report 3656

NASA
TP
3656
c.1

Refinement and Application of Acoustic Impulse Technique To Study Nozzle Transmission Characteristics

0062427



TECH LIBRARY KAFB, NM

LOAN COPY: RETURN TO
AFWL TECHNICAL LIBRARY
KIRTLAND AFB, N.M.

M. Salikuddin, W. H. Brown,
R. Ramakrishnan, and H. K. Tanna

CONTRACT NAS3-20797
FEBRUARY 1983

NASA



NASA Contractor Report 3656

Refinement and Application of Acoustic Impulse Technique To Study Nozzle Transmission Characteristics

M. Salikuddin, W. H. Brown,
R. Ramakrishnan, and H. K. Tanna
Lockheed-Georgia Company
Marietta, Georgia

Prepared for
Lewis Research Center
under Contract NAS3-20797



National Aeronautics
and Space Administration

Scientific and Technical
Information Branch

1983

SUMMARY

The work described in this report presents an improved acoustic impulse technique and its application to study the acoustic transmission characteristics of duct/nozzle systems.

The objective of this program was to investigate the various problems associated with the spark-discharge impulse technique used in the first two phases of the present contract and to determine the means to overcome those problems. In addition, the refined impulse technique was to be used to obtain an improved understanding of the acoustic transmission properties of selected nozzle geometries.

To accomplish these objectives, various problems associated with the spark-discharge impulse technique were first studied. These included (1) the nonlinear behavior of high intensity pulses, (2) the contamination of the signal with flow noise, (3) low signal-to-noise ratio at high exhaust velocities, and (4) the inability to control or shape the signal generated by the source, especially when multiple spark points were used as the source.

The first step to resolve these problems was the replacement of the spark-discharge source with electroacoustic driver(s). Following this, several processes to improve the impulse technique were studied and implemented. These included (1) synthesizing an acoustic impulse with acoustic driver(s) to control and shape the output signal, (2) time-domain signal averaging to remove the flow noise from the contaminated signal, (3) signal editing to remove unwanted portions of the time history, (4) spectral averaging, and (5) numerical smoothing.

The acoustic power measurement technique was improved by taking multiple induct measurements and by utilizing a modal decomposition process to account for the contribution of higher order modes in the power computation. The improved acoustic impulse technique was then validated by comparing the results derived by an impedance tube method.

The mechanism of acoustic power loss, that occurs when sound is transmitted through nozzle terminations, was investigated first by visual means. In addition, the amount of power loss was evaluated experimentally and by a theoretical prediction method. The important phenomena observed in flow-visualization results was the formation of a vortex ring at the nozzle termination when a sound wave was transmitted out. The intensity of the vortex ring was increased with increased intensity of the sound wave at the termination. The quantitative results indicated that the acoustic power loss was proportional to the intensity of the sound. Therefore, it can be concluded that the acoustic power loss was due to the formation of vortex ring at the nozzle termination and the cause of vortex ring was the conversion of acoustic energy into vortical energy.

Finally, the refined impulse technique was applied to obtain more accurate results for the acoustic transmission characteristics of a conical nozzle and a multi-lobe multi-tube suppressor nozzle, both of which were tested earlier in phase II of this contract.

CONTENTS

	Page
1.0 INTRODUCTION	1
2.0 BACKGROUND	4
2.1 THE ACOUSTIC IMPULSE TECHNIQUE WITH SPARK DISCHARGE SOURCE. .	4
2.2 TEST CONFIGURATIONS AND PROCEDURES.	4
2.2.1 Test Facility for Single Stream Nozzles.	4
2.2.2 Test Facility for Coannular Nozzles.	5
2.3 EXPERIMENTAL PROCEDURE, DATA ANALYSIS AND DATA PRESENTATION .	12
2.3.1 Data Aquisition.	12
2.3.2 Data Analysis.	12
2.3.3 Presentation of Transmission Data.	12
2.4 TYPICAL RESULTS AND POSSIBLE ERRORS ASSOCIATED WITH THEM. . .	14
2.4.1 Reflection Coefficients for Duct and Conical Nozzles .	15
2.4.2 Induct Reflection Time Histories and Reflection	
Coefficient Spectra for Nozzles.	18
2.4.3 Far-Field Time Histories	23
2.4.4 Far-Field Power.	23
2.4.5 Power Balance.	28
2.4.6 Time Histories Due to Multi-Point Source in Annular	
Region for the Multi-Chute Suppressor.	28
2.5 CONCLUSIONS	32
3.0 EXPERIMENTAL SETUP	33
3.1 SINGLE STREAM FLOW FACILITY	33
3.2 ANNULAR FLOW FACILITY	37
3.3 DATA ACQUISITION AND ANALYSIS.	41
3.3.1 Experimental Procedure	41
3.3.2 Calibration of In-duct and Far-field Microphones . . .	41
3.3.3 Presentation of Transmission Data.	43
4.0 ACOUSTIC IMPULSE TECHNIQUE IMPROVEMENT	45
4.1 SYNTHESIZING ON ACOUSTIC IMPULSE WITH ACOUSTIC DRIVER	45
4.1.1 Characteristics of Electroacoustic Driver and Objective	
of Signal Syntheseis	46
4.1.2 Summary of Previous Work	46
4.1.3 Principle and the Mathematical Background.	46
4.1.4 Test Facilities and Operational Procedure.	49
4.1.5 Experimental Results	53
4.1.6 Limitations of Signal Synthesis.	65
4.2 SIGNAL AVERAGING.	65
4.2.1 Principle of Signal Averaging.	65
4.2.2 Signal Averaging Procedure	67
4.2.3 Effect of Signal Averaging	67

4.3	SIGNAL EDITING.	71
4.4	SPECTRAL AVERAGING.	78
4.4.1	Objective and Procedure of Spectral Averaging.	78
4.4.2	Effect of Spectral Averaging	78
4.5	NUMERICAL SMOOTHING	78
4.5.1	Objective and Procedure of Numerical Smoothing	78
4.5.2	Effect of Numerical Smoothing	81
4.6	LIMITATIONS AND GUIDELINES FOR SIGNAL AVERAGING	81
4.6.1	Limitations for Signal Averaging	81
4.6.2	Guidelines for Signal Averaging.	81
4.7	CONCLUSIONS	91
5.0	IN-DUCT ACOUSTIC POWER MEASUREMENTS.	94
5.1	EXPERIMENTAL PROCEDURES AND DATA ANALYSIS	95
5.2	RADIAL AND AZIMUTHAL VARIATION OF IN-DUCT PRESSURE FIELD.	98
5.2.1	Radial Variation of Induct Pressure Field for Single Stream Duct and Validity of Single Point Measurement	101
5.2.2	Radial and Azimuthal Variation of Induct Pressure Field for Annular Duct and Validity of Single Point Measurement.	129
5.3	MODAL DECOMPOSITION OF IN-DUCT ACOUSTIC POWER	144
5.3.1	Expression for Acoustic Pressure Field	145
5.3.2	Derivation of Acoustic Power in Modal Form	161
5.3.3	Derivation of Reflection Coefficient in Modal Form	164
5.3.4	Experimental Results for Single Stream Duct.	165
5.3.5	Experimental Results for Annular Duct.	172
5.4	CONCLUSIONS	182
5.4.1	Single Stream Duct/Nozzle System	182
5.4.2	Annular Stream Duct/Nozzle System.	185
6.0	VALIDATION OF ACOUSTIC IMPULSE TECHNIQUE	186
6.1	IMPLICATIONS OF FLOW IN IMPEDANCE TUBE MEASUREMENTS	186
6.2	EXPERIMENTAL CONFIGURATION.	187
6.3	EXPERIMENTAL PROCEDURE.	187
6.4	MATHEMATICAL APPROACH OF MODIFIED IMPEDANCE TUBE TECHNIQUE.	190
6.5	CALIBRATION OF THE PROBE MICROPHONE	196
6.6	COMPARISON OF EXPERIMENTAL RESULTS FOR SINGLE STREAM DUCT	196
6.7	COMPARISON OF EXPERIMENTAL RESULTS FOR ANNULAR DUCT	198
6.8	CONCLUSION.	204
7.0	ACOUSTIC ENERGY LOSS MECHANISM	206
7.1	FLOW VISUALIZATION.	206
7.1.1	Test Set-up and Experimental Procedure	207
7.1.2	Experimental Results	211
7.2	QUANTITATIVE EVALUATION OF POWER LOSS	226
7.2.1	Effect of Acoustic Intensity on Power Loss	232

7.2.2	Effect of Nozzle Exit Area on Power Loss	237
7.2.3	Effect of Nozzle Geometry on Power Loss.	237
7.2.4	Effect of Mean Flow on Power Loss.	237
7.3	CONCLUSIONS	242
8.0	APPLICATION OF IMPROVED ACOUSTIC IMPULSE TECHNIQUE	245
8.1	TEST CONFIGURATIONS AND EXPERIMENTAL PROCEDURE.	245
8.1.1	Nozzle Description	245
8.1.2	Test Plan.	247
8.1.3	Instrumentation.	250
8.1.4	Experimental Procedure and Data Analysis Scheme.	250
8.2	EXPERIMENTAL RESULTS.	253
8.2.1	Effects of Jet Mach Number	282
8.2.2	Flight Effects	298
8.3	CONCLUSIONS	298
9.0	CONCLUDING REMARKS	304
9.1	IMPROVEMENT OF THE QUALITY OF RESULTS USING THE REFINED IMPULSE TECHNIQUE	304
9.2	GENERAL COMMENTS ON THE APPLICATION OF THE ACOUSTIC IMPULSE TECHNIQUE	308
APPENDIX A	NOMENCLATURE.	312
APPENDIX B	DATA REDUCTION COMPUTER PROGRAMS.	314
B.1	SIGNAL SYNTHESIS.	314
B.2	MODAL DECOMPOSITION	321
B.2.1	Radial Modal Decomposition for Single Stream Duct/Nozzle System	321
B.2.2	Radial and Azimuthal Modal Decomposition for Annular Stream Duct/Nozzle System.	339
B.3	NONLINEAR REGRESSION TECHNIQUE FOR MODIFIED IMPEDANCE TUBE DATA ANALYSIS.	362
B.4	COMPUTATION OF INDUCT AND FAR-FIELD ACOUSTIC PARAMETERS	374
REFERENCES.	396

1. INTRODUCTION

During the past several years, research on the transmission of sound through aircraft engine nozzles has been ongoing at the Lockheed-Georgia Company, and as part of this work, several conical, co-annular (ref. 1) and suppressor nozzles (ref. 2) have been tested for a variety of operating conditions. At the beginning of this program, as a result of many important considerations, an impulsive acoustic source was chosen for the input to determine the nozzle acoustic transmission characteristics. The impulse makes it possible to isolate the incident and reflected internal acoustic fields. Moreover, unlike a discrete-frequency experiment, the impulse test technique allows the determination of transmission characteristics over a range of frequencies at one time (ref. 3).

As a result of the first two phases of this contract (NAS3-20797), some very positive accomplishments have been made. These include (i) a limited understanding of the influence of nozzle shape and flow velocity (and velocity profile) on the transmission of internal sound to the far field, (ii) the identification of two different physical mechanisms related to nozzle radiation efficiency, associated with the open termination and the solid part of the nozzle, (iii) the experimental determination of the influence of suppressor nozzles on internal noise radiation efficiency, and (iv) the development of the acoustic impulse technique as an automated and rapid method for obtaining the spectral characteristics of the nozzle transfer coefficients (refs. 1,2,3).

During the course of the above-mentioned work, however, many problems were faced which either made some of the acquired data unreliable (e.g., due to the low signal-to-noise ratio at high jet velocities) or made the interpretation of the data difficult (e.g., due to the measured imbalance between the transmitted and the far-field acoustic powers). It became apparent that before the impulse technique can be universally accepted as a standard acoustic test technique, certain characteristics and problems must be thoroughly investigated and understood.

Some of the more important problems and possible solutions are summarized below:

(1) Inherent Operational Problems With the Spark Source

A spark discharge was used in the work described in references 1 and 2. The spark discharge led to numerous instrumentation and equipment problems resulting from the electro magnetic fields. Furthermore, the spark time signature was not precisely repeatable and also several minutes were required between discharges to recharge the capacitor bank.

These problems could be solved with an electroacoustic source, provided other practical problems associated with the electroacoustic source could be resolved.

(2) Low Signal-to-Noise Ratio at High Jet Exhaust Velocities

All data acquired in the first two phases of this contract (refs. 1 and 2) were based on a single pulse analysis scheme. However, the presence of jet mixing noise, superimposed as a background on the impulse received in the far field, inevitably produced spectral contamination. This condition became aggravated at high flow velocities due to higher jet mixing noise, and it was particularly severe at small polar angles where the refraction effect reduced the pulse amplitude while the convective amplification increased the jet mixing noise.

The traditional solution in this situation is to use the technique of signal averaging. If a sufficient number of individual records are averaged, the stochastic contribution from the jet mixing noise will average to zero and thus the pulse time history will be recovered cleanly.

(3) Imbalance Between Transmitted and Far-Field Acoustic Power

A comparison between the transmitted acoustic power (calculated from the in-duct measurements) and the measured far-field acoustic power indicated a low-frequency power loss and a high-frequency power gain even when there was no flow through the nozzle system.

This observation could be due to one or more of the following three factors: (1) inadequacy of the single-point intensity measurement inside the duct, (2) nonlinear propagation of high-intensity spark discharge pulses, and (3) conversion of acoustic energy to flow energy.

The major objective of the work described in this report was to investigate the above problems associated with the acoustic impulsive test technique and to determine the means to overcome these problems. In addition, with the resolution of some or all of these problems, selected nozzle transmission tests were to be repeated to improve the existing data base.

The work conducted in the earlier two phases under this contract is briefly described in the next section, where typical results indicating the above mentioned problems are included.

The facility used in the present study and the data analysis procedure are described in section 3.

The various processes used to improve the acoustic impulse technique are described in section 4. These include signal synthesis of acoustic pulses from electroacoustic drivers, signal averaging, signal editing, spectral averaging, and numerical smoothing.

Section 5 describes the acoustic power measurement technique for single and annular stream flow systems. This includes the modal power calculation using modal decomposition techniques.

The improved acoustic impulse technique was validated by comparing the results derived using this technique with similar results derived from other established methods, namely, the impedance tube technique. This validation is presented in section 6.

The acoustic power loss mechanisms was investigated qualitatively by visual means. Also, the acoustic power loss was quantitatively evaluated using a theoretical model. These results are presented in section 7.

Finally, the refined acoustic impulse technique was applied to study the acoustic transmission characteristics of a 6.2 cm diameter conical nozzle and a multi-lobe multi-tube suppressor nozzle with an equivalent exit diameter of 6.2 cm, both of which were tested earlier in Phase II of the present contract. The new results are described in section 8.

Important conclusions drawn from the present study are outlined in section 9. In addition specific improvements achieved due to the refined impulse technique and the limitations of this technique are also described in this section.

The important symbols used in this report are listed in Appendix A. The major computer programs used for data analysis are listed in Appendix B of this report.

2. BACKGROUND

During the past five years, experimental research on the transmission of sound through aircraft engine exhaust nozzles has been conducted at the Lockheed-Georgia Company under NASA Contract NAS3-20797. In the initial part of this contract (Phase I), the major emphasis was placed on (1) developing the acoustic impulse technique, using a spark discharge source, as a method for measuring the acoustic transmission characteristics of nozzles, and (2) using this technique to determine the internal noise radiation efficiency of coaxial nozzles with inverted flow velocity profiles (ref. 1). In Phase II of this contract, the work conducted in Phase I was extended to cover the internal noise radiation from various suppressor nozzle configurations, both single-stream and dual-stream (ref. 2).

2.1 THE ACOUSTIC IMPULSE TECHNIQUE WITH SPARK DISCHARGE SOURCE

In many of the experiments to study the transmission of internally generated sound through aircraft engine exhaust nozzles, a knowledge of the behavior of the incident and the reflected signals by themselves is required but has been difficult to obtain because of the inability of isolating these two signals. As a result of this extreme difficulty in experimentally separating the incident and reflected acoustic waves for either periodic or continuous broadband excitation, a transient test technique, using a high voltage spark discharge as the impulsive sound source, was developed (ref. 3). Use of the impulse source makes this separation very simple by ensuring that each component (i.e., incident and reflected) of the pulse wave train is adequately separated in time. Another desirable feature of the impulse technique is that each of the incident, the reflected and the transmitted pulse contains the spectral information over a wider band necessary for computing the desired transmission and reflection characteristics in a single test. Therefore, the test time is dramatically reduced. This technique has been successfully used at Lockheed to study the transmission characteristics of various duct terminations including suppressor nozzles, orifices, and perforated plates (refs. 1, 2 and 4 through 6).

2.2 TEST CONFIGURATIONS AND PROCEDURES

The acoustic measurements for determining the transmission coefficients of various nozzle terminations were carried out in two separate facilities. The single-stream conical nozzles and the daisy lobe suppressor nozzle were tested in the anechoic free jet facility. The coannular round nozzles and the multi-chute suppressor nozzle, for which no flight simulation data were acquired, were tested in the anechoic static jet facility.

2.2.1 Test Facility for Single Stream Nozzles

The anechoic free-jet wind tunnel facility is powered by a jet ejector and is capable of providing continuous free-jet velocities up to 95 m/s with a circular test section of diameter 0.71 m. For minimum blockage in the working section, the air-supply ducting for the primary jet is installed axially in the intake/contraction section.

Various conical nozzles of different exit diameters with a fixed convergence angle (about 6 degrees) were tested in this facility. These nozzles were connected to the 10 cm diameter flow duct. In addition, a multi-lobe multi-tube suppressor with an equivalent round nozzle exit diameter of 6.2 cm was also tested in this facility. A photographic view of the suppressor nozzle is shown in figure 2.1. The results derived for the suppressor nozzle were compared to those derived for the reference conical nozzle of 6.2 cm exit diameter.

The experimental configuration in its basic form is shown in figure 2.2. It contains the spark source placed on the center line of the 10 cm diameter supply duct, about 6 meters upstream of the nozzle exit. Internal noise is generated by inducing sparks across two graphite electrodes separated by a small air gap.

2.2.2 Test Facility for Coannular Nozzles

The acoustic measurements to determine the nozzle transmission coefficients for the dual stream round nozzles and multi-chute nozzle were made in the anechoic static jet facility. The anechoic chamber used for these studies provides a free-field environment for all frequencies above 200 Hz, and incorporates a specially-designed exhaust collector/muffler which provides adequate quantities of jet entrainment air, distributes this entrainment air symmetrically around the jet axis, and keeps the air flow circulation velocities in the room to a minimum.

The conical nozzles tested in the co-annular facility are shown in figure 2.3. In all, six secondary nozzles were used in conjunction with one fixed primary nozzle of diameter 7.62 cm and conical half-angle of 15 degrees. Three outer nozzles had conical half angle of 20 degrees, and the remaining three had 40 degrees. Each set of these nozzles were distinguished by their L/h ratios, where, L is the protrusion of primary exit beyond the fan exit and h is the annulus width, which were 1, 3 and 5, respectively. Figure 2.4 shows a co-annular nozzle mounted in the co-axial jet facility.

The multi-chute suppressor was a co-axial 36-chute nozzle, shown in figure 2.5. This suppressor is fitted with a 6.7 cm diameter plug.

For the dual-stream nozzles, six spark sources, equispaced in the secondary plenum, were used. A schematic view of the source section is shown in figure 2.6. The source section for the primary plenum is also shown here.

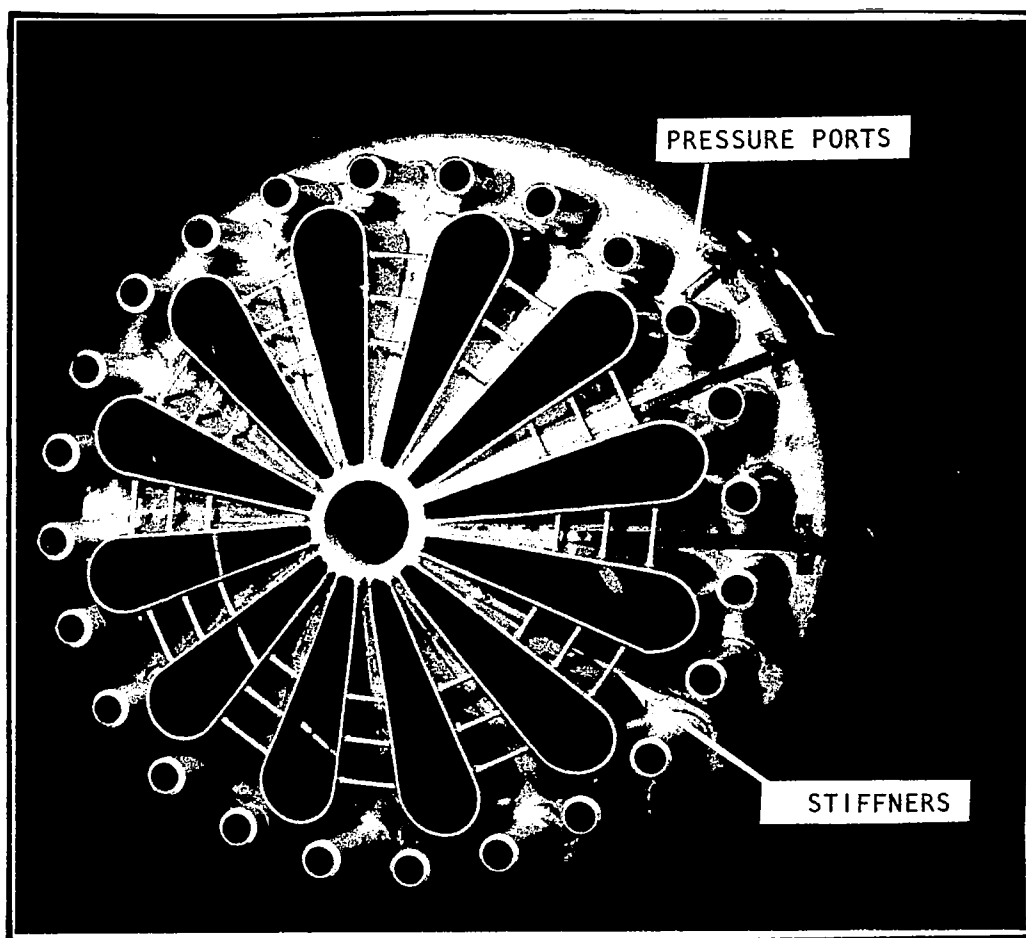


Figure 2.1 A close-up view of the daisy lobe suppressor with the plug removed.

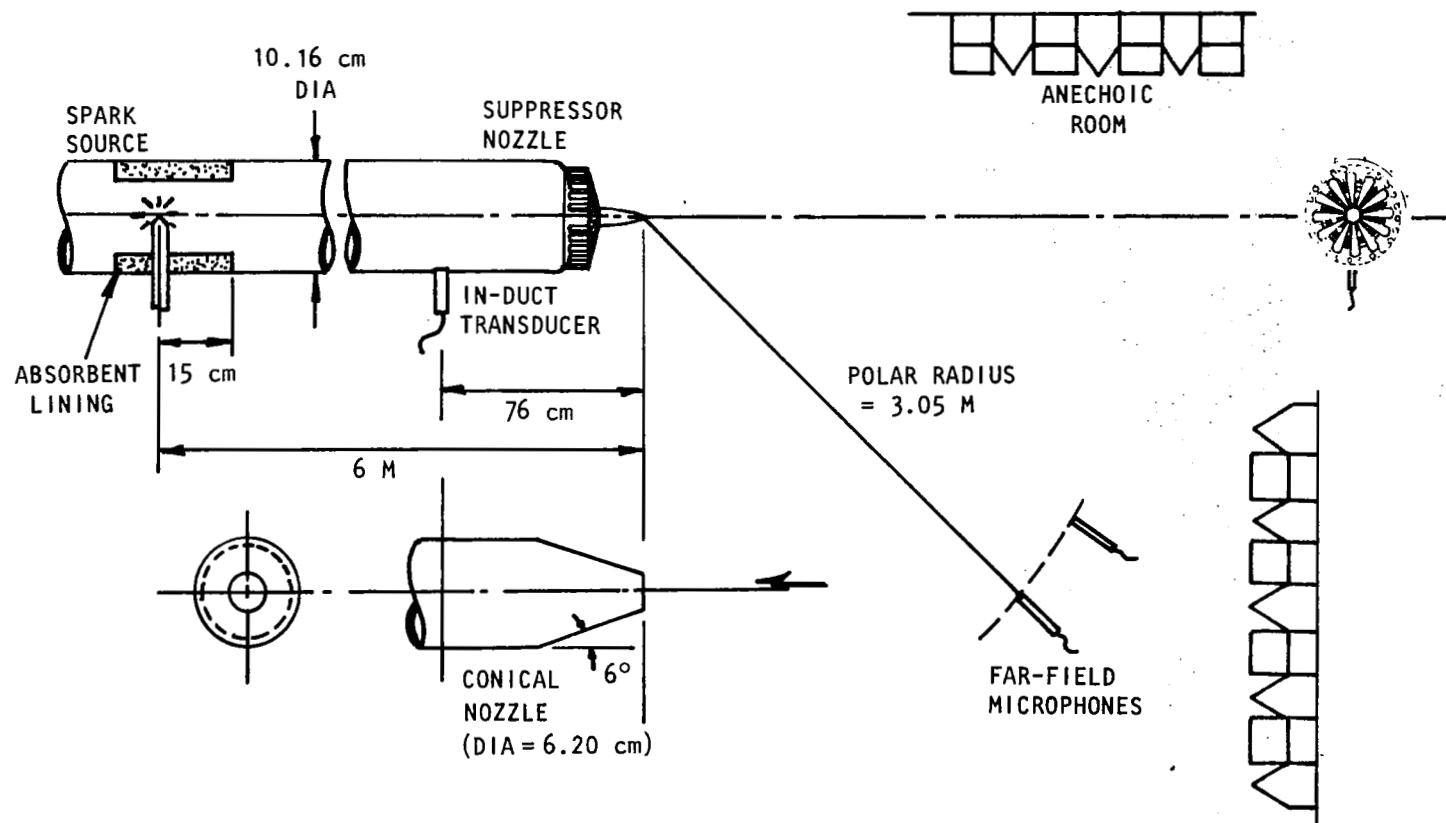


Figure 2.2 The source section for the daisy lobe and the reference conical nozzle and the measurement configuration

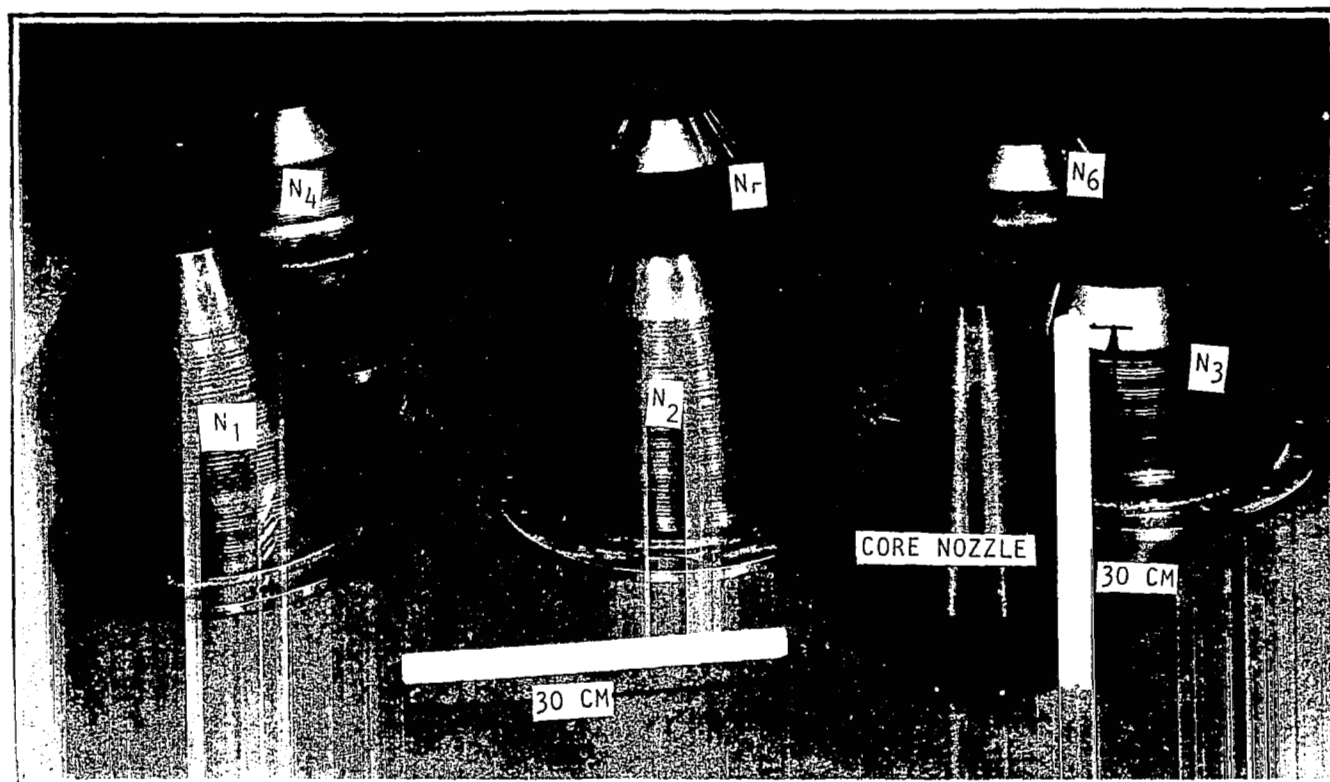


Figure 2.3 Illustration of core and fan nozzles N_1 to N_6 .

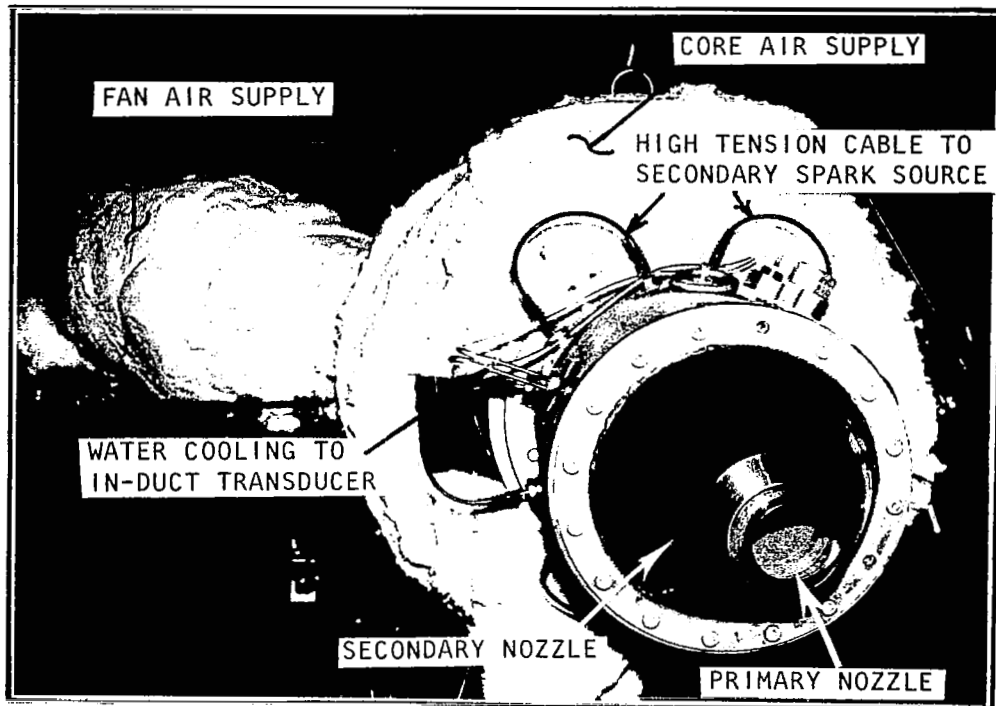


Figure 2.4 The coaxial jet facility.

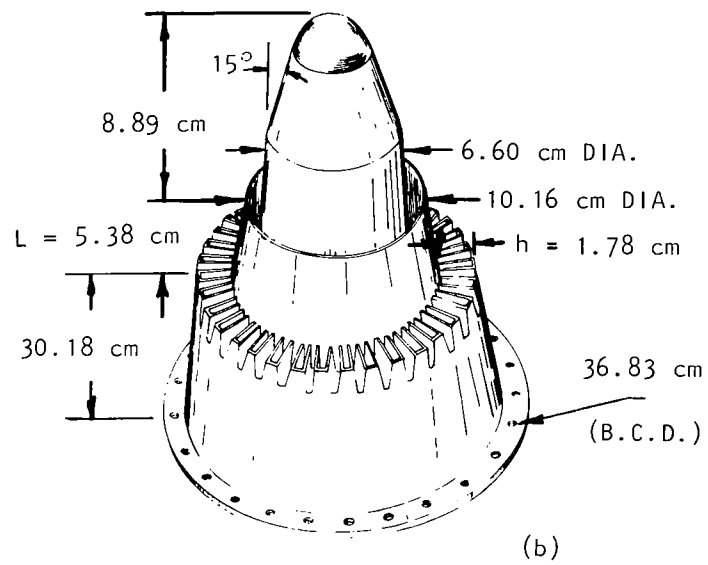
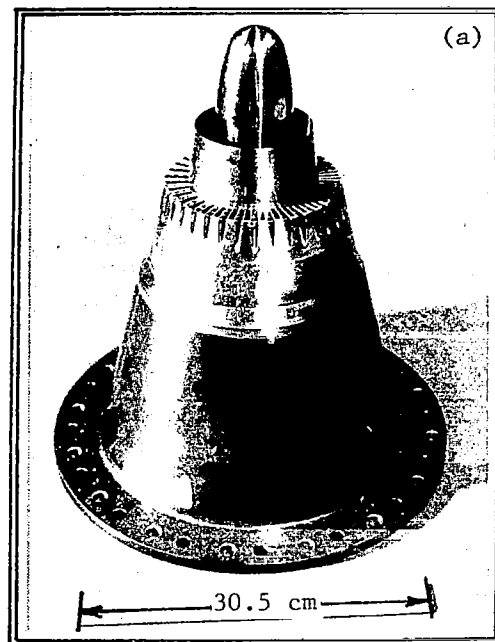


Figure 2.5 The 36-chute dual stream suppressor nozzle
($L/h = 3$)

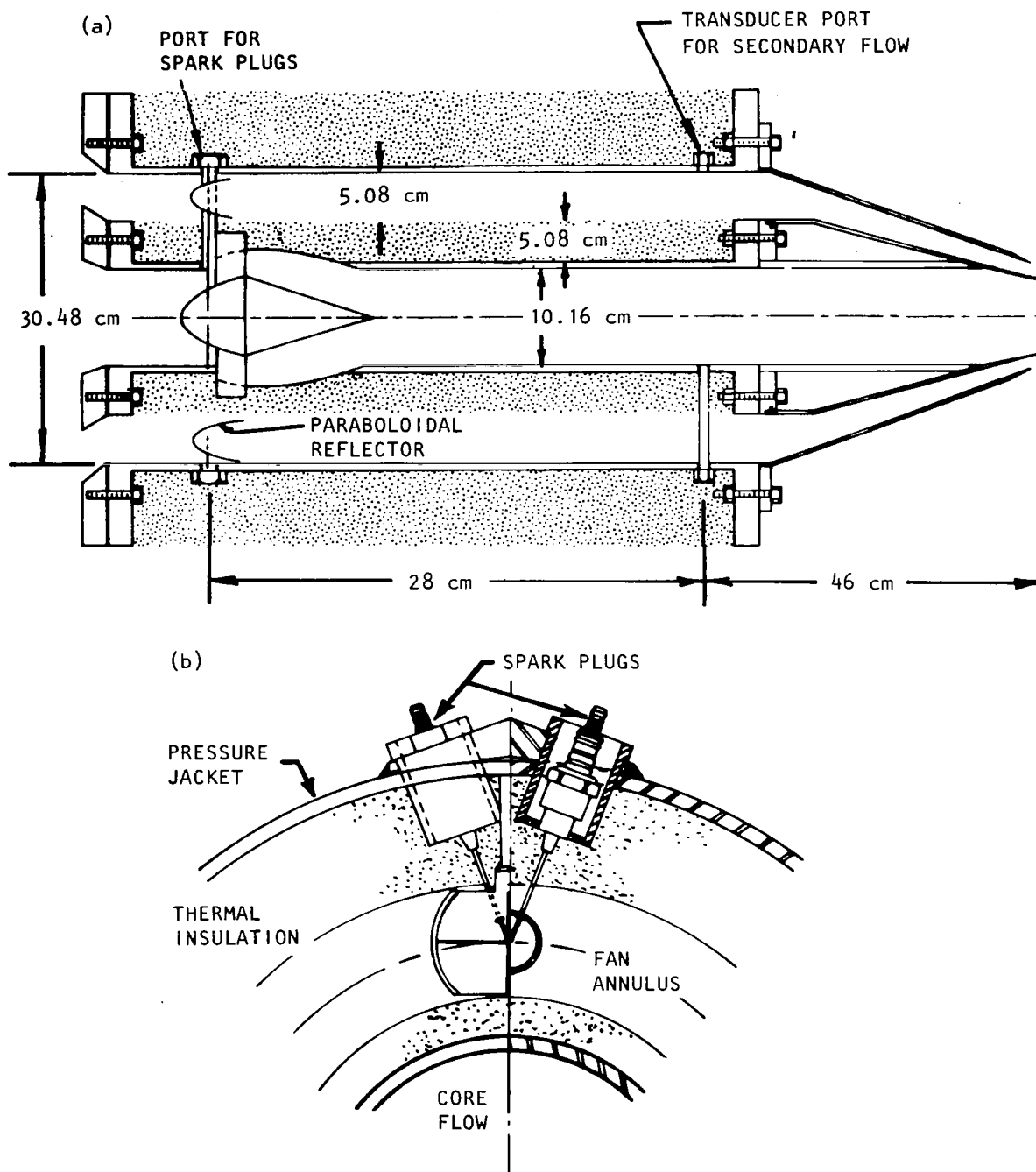


Figure 2.6 Source section for the multichute and the reference coaxial nozzle.
(Not to Scale)

It is to be noted that unlike the configuration for the single-stream nozzle, where the spark source was placed a considerable distance away from the nozzle exit, the source in the dual-nozzle configuration was located only 74 cm upstream of the nozzle exit plane. A larger travelling distance is desirable so that the spherical wave fronts of an impulsive point source will have such a large radius of curvature that it will appear essentially as a plane wave, which is the desired in-duct condition (ref. 2). However, a very long secondary plenum was not practical with the existing facility. Hence, as shown in figure 2.6, the spark source (electrode gap) was used in conjunction with a paraboloidal reflector. The effect of the paraboloidal reflector was to increase the impulse energy traveling in the axial direction and to modify the wave front from spherical to essentially plane in nature.

Each of the spark gaps in this configuration was connected in series through high voltage cables such that all of them fired simultaneously. Unlike the electrodes for the single-nozzle configuration where the two electrodes actually faced each other, the secondary plenum electrodes in this case had an included angle of 20 degrees as shown in figure 2.6(b). A photograph of the electrodes placed at the focus of the paraboloid, in the core plenum, is shown in figure 2.7.

2.3 EXPERIMENTAL PROCEDURE, DATA ANALYSIS AND DATA PRESENTATION

2.3.1 Data Acquisition

The in-duct measurements were made by a Sundstrand transducer located at a suitable distance upstream of the nozzle exit (=76 cm) so that it was possible to isolate the incident and reflected parts of the time history. The far-field signals were measured by 0.635 cm B&K microphones on a polar arc of radius 3.5 m at every 10 degrees in the range 0 degree to 120 degrees with the jet axis.

2.3.2 Data Analysis

The data analysis for internal noise was carried out using the transient capture mode of the real time SD-360 analyzer. In this mode it was possible to capture the in-duct and far-field time histories and to edit out the unwanted parts of the signals. This made it possible to retain only the incident part of the in-duct transient signal (A) and only the transient (impulse) component of the far-field signal (B). Signals A and B were then Fourier transformed to obtain their respective spectra. Following this, appropriate corrections for microphone frequency response and atmospheric absorption were applied, and the resulting spectra were utilized to calculate various transmission parameters described below.

2.3.3 Presentation of Transmission Data

Three basic parameters of interest were calculated from the

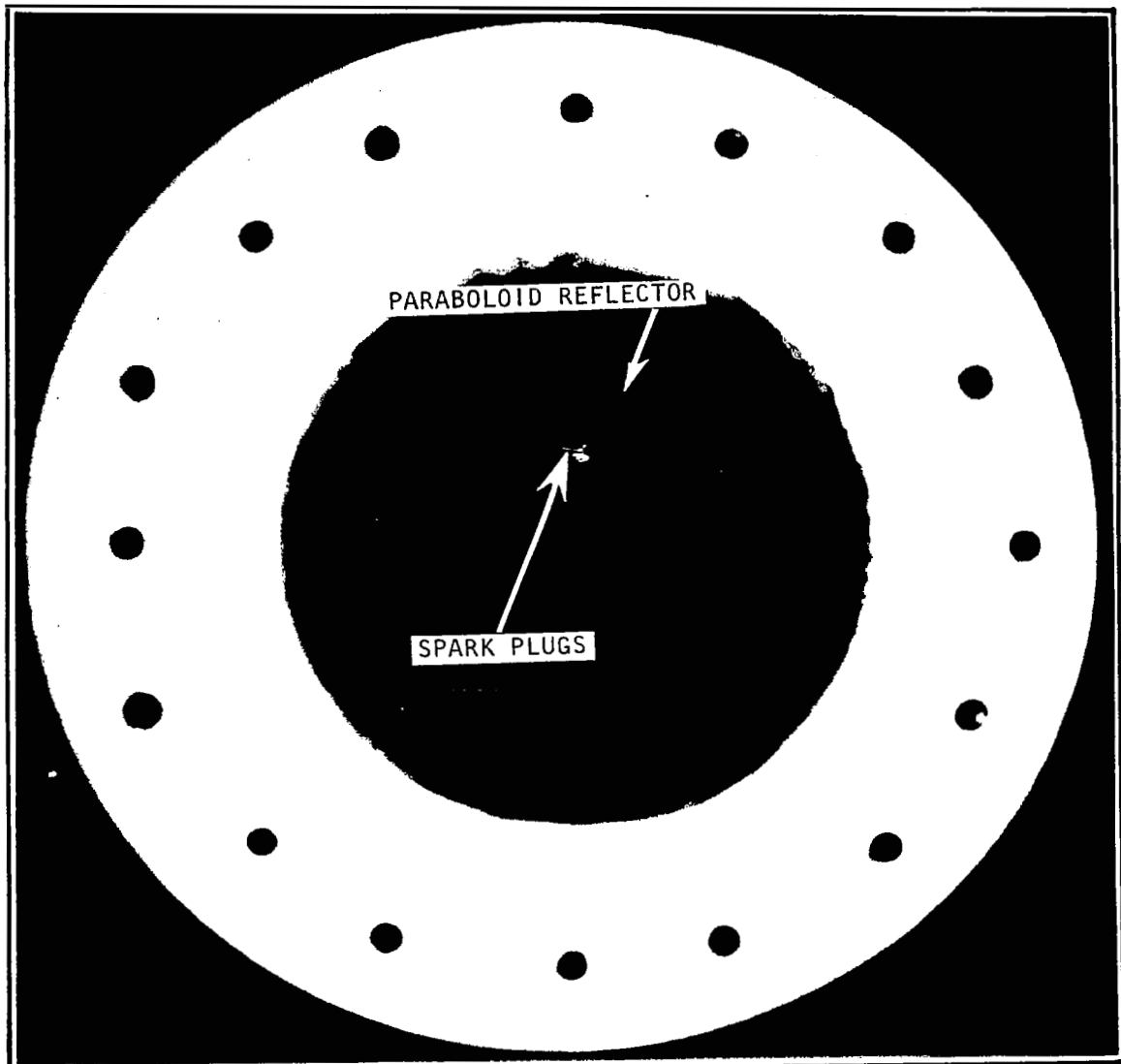


Figure 2.7 Source section of core nozzle plenum.

measurements made in the far-field and inside the duct. These were the Reflection Coefficients (σ), Normalized Transmission Coefficients (NTC), and Power Transfer Functions (PTF). The expressions for these parameters are given below (ref. 2). If p_i , p_r , and p_f are the amplitudes of the incident, reflected and far-field acoustic pressures, respectively, then

Reflection Coefficient	σ	(dB) = $10 \log_{10} (p_r^2/p_i^2)$
Normalized Transmission Coefficient	NTC(θ)	(dB) = $10 \log_{10} (I_f(\theta)/I_p)$
Power Transfer Function Normalized to Incident Power	PTF _i	(dB) = $10 \log_{10} (W_f/W_i)$
Power Transfer Function Normalized to Transmitted Power (Power Imbalance)	PTF _t	(dB) = $10 \log_{10} (W_f/W_t)$

where,

Far-field Intensity	$I_f(\theta) = \frac{p_f^2(\theta)}{\rho_o c_o}$
Incident Intensity for an Equivalent Point Source	$I_p = \frac{W_i}{4\pi R_m^2}$
Incident Power	$W_i = \frac{A_D p_i^2}{\rho_D c_D} (1+M_D)^2$
Reflected Power	$W_r = \frac{A_D p_r^2}{\rho_D c_D} (1-M_D)^2$
Transmitted Power	$W_t = W_i - W_r$
Far-field Power	$W_f = \int \frac{p_f^2(\theta)}{\rho_o c_o} dA$

NTC is thus the ratio of the far-field intensity measured at a given point to that produced at the same point by a point source of total power W_i located at the nozzle exit center. Similarly, PTF_i and PTF_t are the far field acoustic powers normalized with respect to the incident power and the transmitted power, respectively.

2.4 TYPICAL RESULTS AND POSSIBLE ERRORS ASSOCIATED WITH THEM

Most of the results, presented in references 1 and 2, derived using the spark discharge sound source (under the first two phases of the present contract), are considered to be accurate. The accuracy of some of these results was validated by suitable comparisons. However, a

small amount of data were judged to be unreliable, either due to low signal-to-noise ratio at high jet velocities or due to nonlinear propagation effects associated with high intensity pulses used in these tests. Some of those unreliable results are discussed in this section. The objective of these discussions is to establish the need for further improvement of the impulse technique, so that, this technique can be used in future for transmission tests without having any doubt about the accuracy of the results.

2.4.1 Reflection Coefficients for Duct and Conical Nozzles

Levine and Schwinger (ref. 7) developed an exact mathematical analysis of the sound field within and outside an unflanged circular pipe for a plane wave mode incident on the pipe termination from within the pipe. This analytical solution is applicable for comparison with similar results experimentally derived using the spark discharge sound source. The reflection coefficient amplitudes obtained experimentally using high intensity pulses (about 150 dB) are compared with predicted values in figure 2.8. The experimental data are contaminated by cut-on of the first radial mode. However, even below this cut-on frequency ($kR_D = 3.83$) the comparison is not quite as good, with the measured value decreasing more rapidly with increasing frequency than that predicted by Levine and Schwinger (ref. 7).

To establish whether or not this discrepancy is due to the nonlinear propagation of high intensity pulse, similar results were derived using very low intensity pulse (about 100 dB) and also using the impedance tube technique where only low intensity, discrete frequency, pressure waves were used (ref. 5). These results are also plotted in figure 2.8. The reflection coefficient amplitude results derived by the impulse technique using the low intensity pulse, and by the impedance tube method, and by the Levine & Schwinger's solution agree very well with one another at least up to $kR_D = 2.5$. The reflection coefficient amplitudes derived using the impulse technique with high intensity pulse do not agree with the results obtained by low intensity pulse. The deviation between the two can be attributed to the nonlinear behavior of the high intensity pulse. Therefore, a low intensity impulsive source is desirable for the impulse technique. At this stage it appears that a low intensity spark discharge impulsive source would serve the purpose. However, it will be shown in this section that such a source would not be adequate for transmission study in the presence of mean flow.

To demonstrate further the effect of nonlinear behavior of high intensity pulses, the reflection coefficient amplitudes for a straight duct and two conical nozzles, evaluated using low intensity pulses, are compared with the corresponding coefficient amplitudes for high intensity pulses in figure 2.9 (ref. 5). The reflection coefficient amplitudes for the low intensity pulses are considerably higher compared to those for the high intensity pulses. Again, these significant differences occur due to nonlinear propagation effects associated with high intensity pulses.

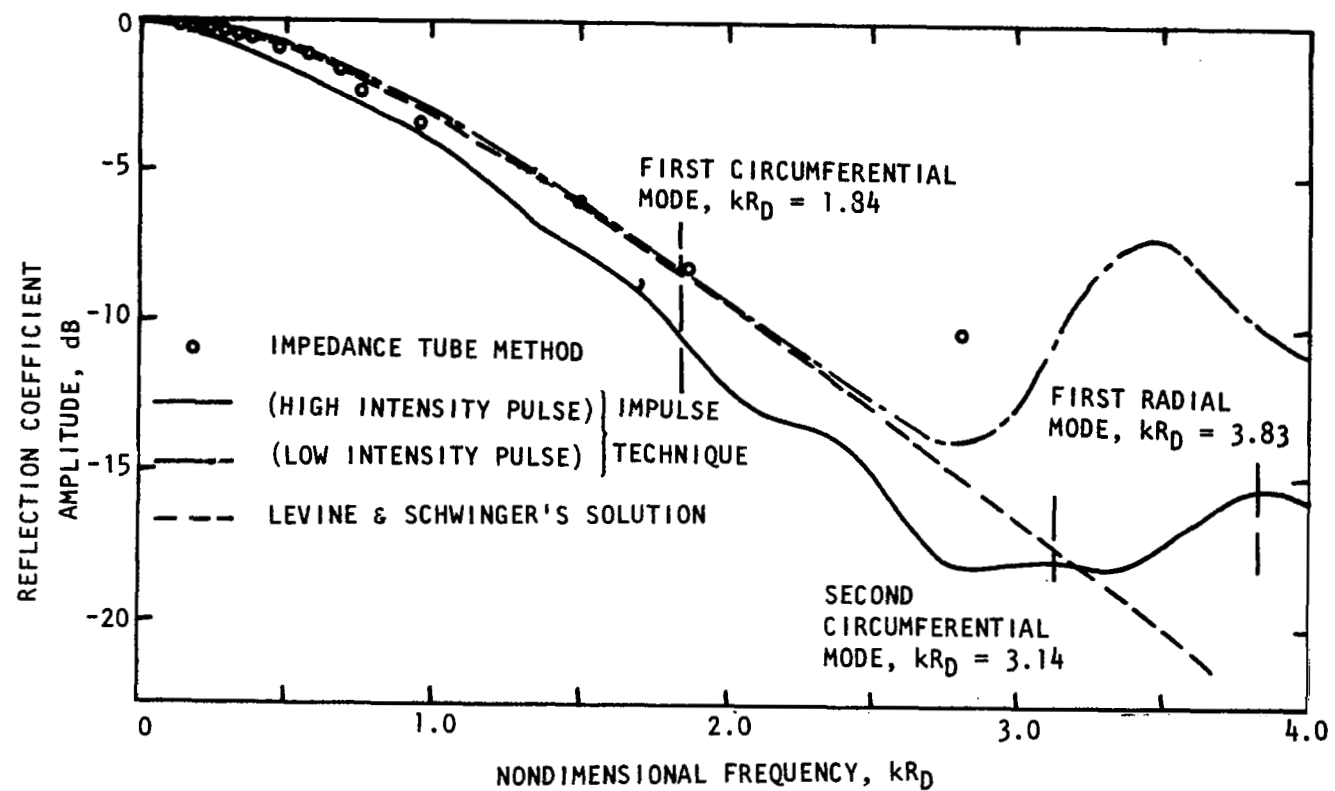


Figure 2.8 Reflection coefficient comparisons between impulse method with high intensity (about 148 dB) and low intensity (about 100 dB) pulses, impedance tube method and Levine-Schwinger's theory for a 10 cm diameter duct termination.

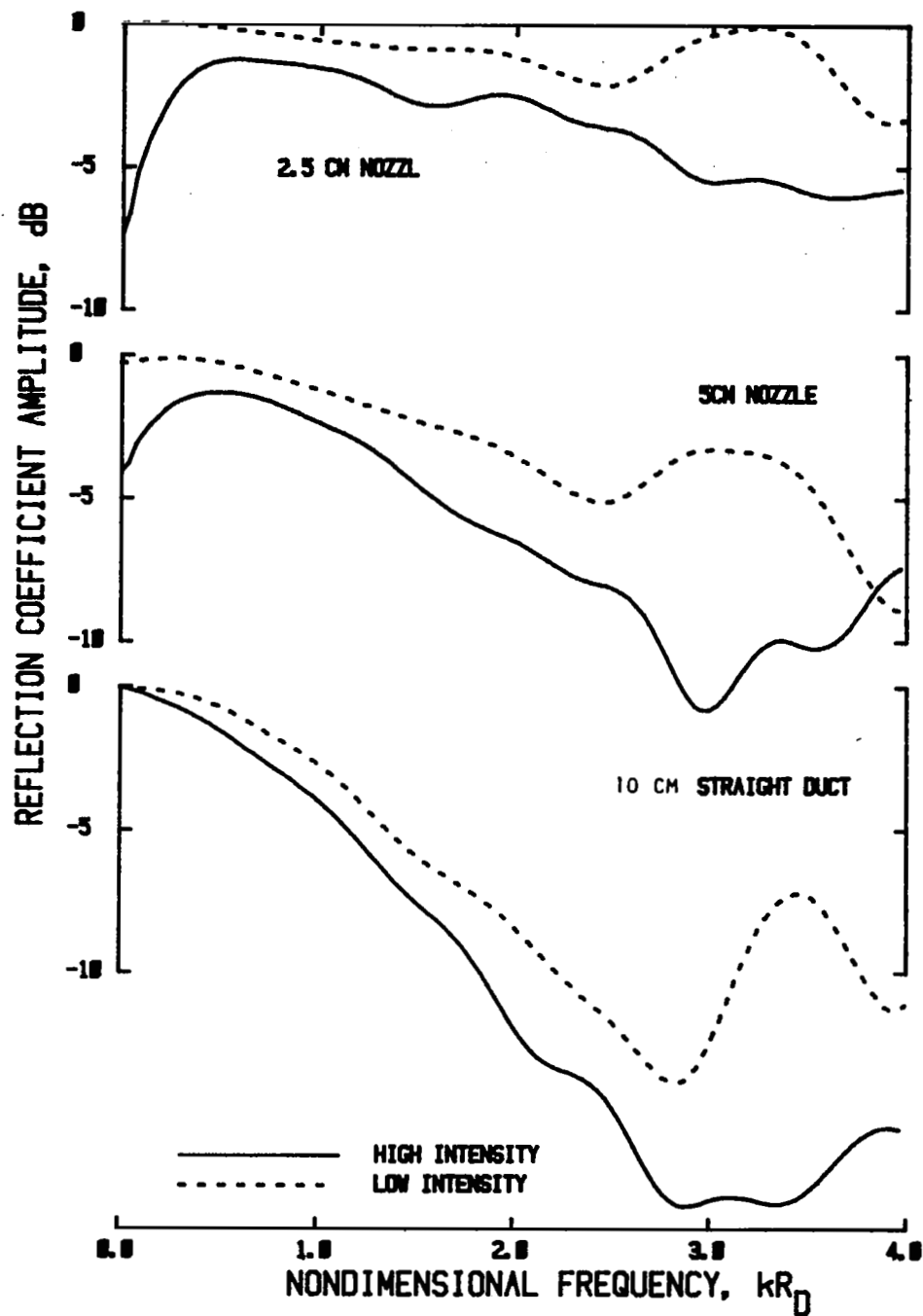


Figure 2.9 Comparison between reflection coefficients evaluated using high intensity pulses (about 148 dB) and low intensity pulses (about 100 dB) for a duct and two nozzle terminations.

2.4.2 Induct Reflection Time Histories and Reflection Coefficient Spectra for Nozzles.

Figure 2.10 shows the effect of jet Mach number on the relative levels of the incident and the reflected components of the in-duct signal for the daisy lobe nozzle (ref. 2). Clearly, the reflection from the open end decreases with increasing Mach number. A dramatic change in the time histories is noticed as the jet Mach number is increased beyond 0.4. There is little sign of reflection from the open end but that from the hard (or solid) part of the nozzle termination increases considerably as the jet Mach number increases. At $M_J = 1.2$ the incident and the reflected signals appear to be of the same amplitude. The implication of these results is that if there was considerable internal noise generated upstream of the suppressor nozzle exit, much of it should be reflected back at higher Mach numbers. Similar qualitative results were also obtained for the 6.20 cm diameter conical nozzle (ref. 2), and these are shown in figure 2.11.

The behavior depicted in figures 2.10 and 2.11 can be better seen when the results are plotted in the form of reflection coefficients as shown in figure 2.12. Here, the reflection coefficients for the daisy lobe nozzle (σ_{DL}) for four jet Mach numbers ($M_J = 0, 0.4, 0.8$ and 1.2) are presented in Figure 2.12 as a function of 1/3-octave frequency. For comparison, the data for the reference conical nozzle (σ_C) are also superimposed in this figure. These results are further cross-plotted in figure 2.13, where the reflection coefficients at various frequencies are plotted as a function of the duct Mach number at the measurement location.

As the jet Mach number (and so the duct Mach number) is increased, the reflection coefficients for the conical nozzle decrease while those for the daisy lobe suppressor nozzle increase at all frequencies. At supersonic jet Mach numbers, σ_{DL} appears to approach 0 dB (i.e., complete rigid termination). This is also observed from the time history plot in figure 2.10. If actually a complete rigid reflection is taking place, then, it would appear that there will be no transmission of acoustic energy out to the far field. However, it will be shown later on, both from far field time history and from far field power spectra, that a considerable amount of energy has in fact been transmitted out.

Further, the trends in the variation of reflection coefficient with frequency are exactly the opposite for the two nozzles. The daisy lobe reflection coefficients increase with frequency while those for the conical nozzle decrease with frequency at almost all Mach numbers. It will be shown later that this behavior is in complete contradiction to the far field power measurements.

The behavior of σ_{DL} is difficult to explain without considerable theoretical and further experimental work. This is certainly related to the complicated geometry and the flow conditions encountered by the

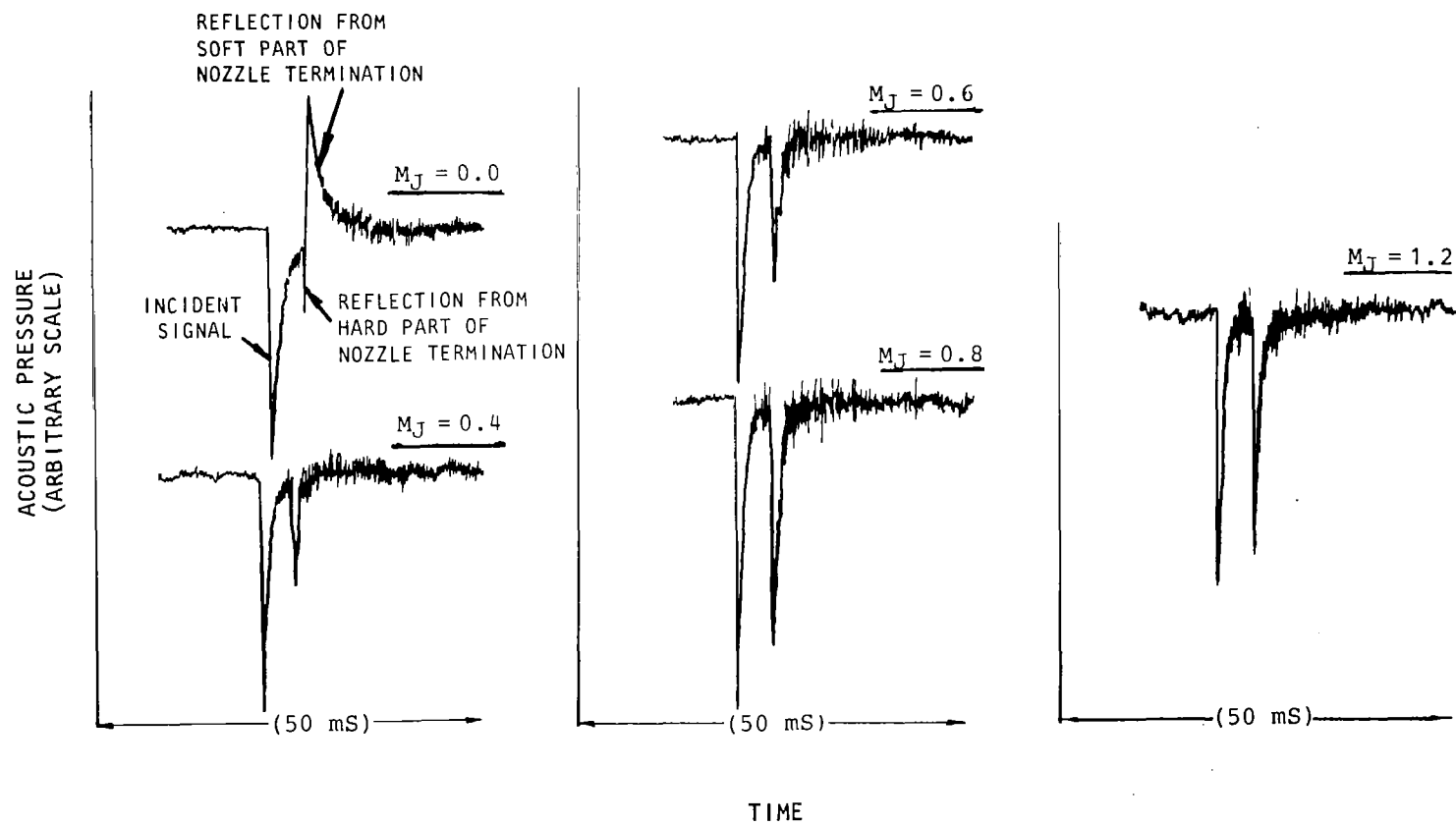


Figure 2.10 In-duct time histories for the daisy lobe nozzle at various jet Mach numbers.

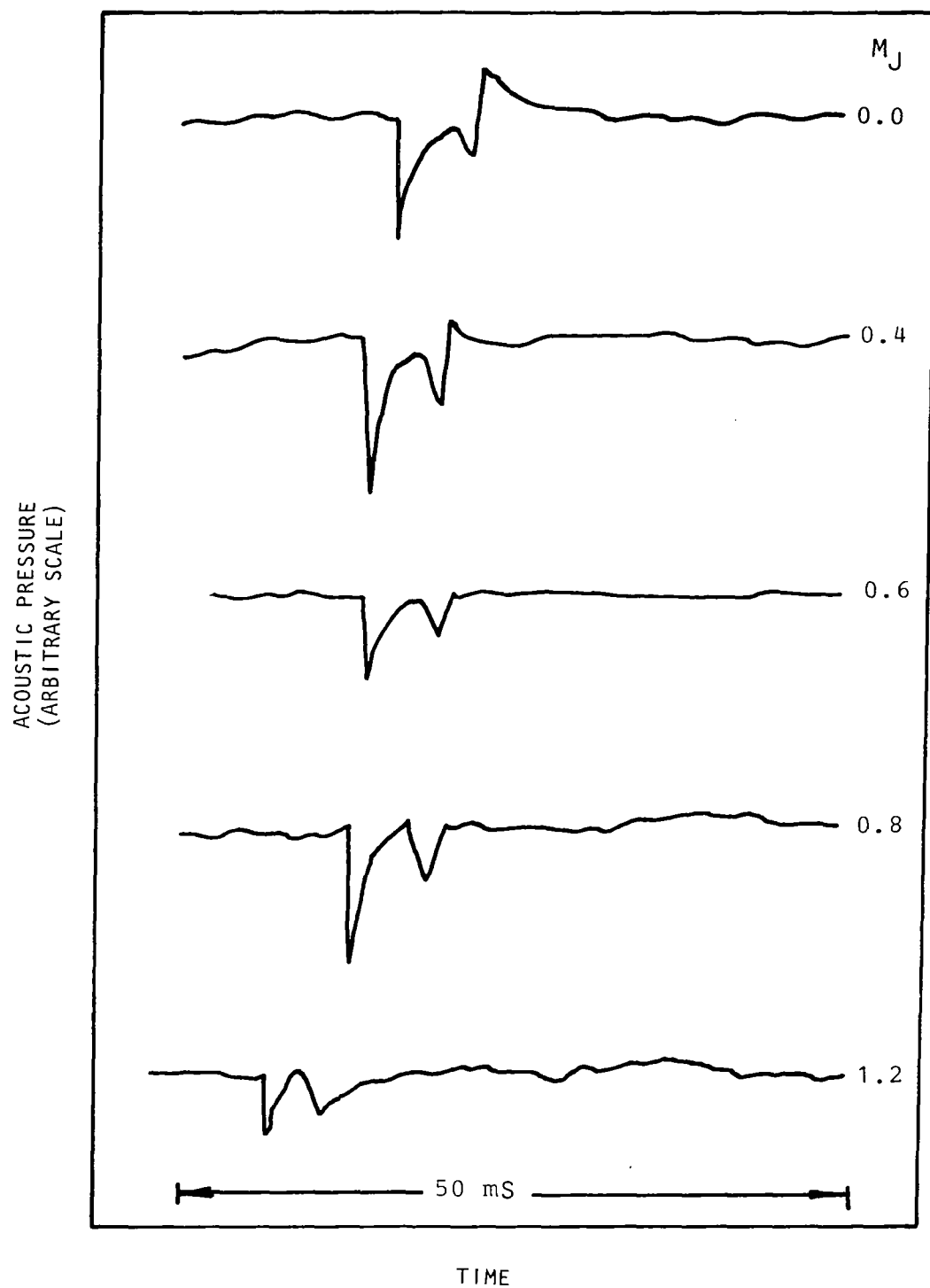


Figure 2.11 In-duct time histories for the 6.20 cm diameter reference conical nozzle at various jet Mach numbers (unheated).

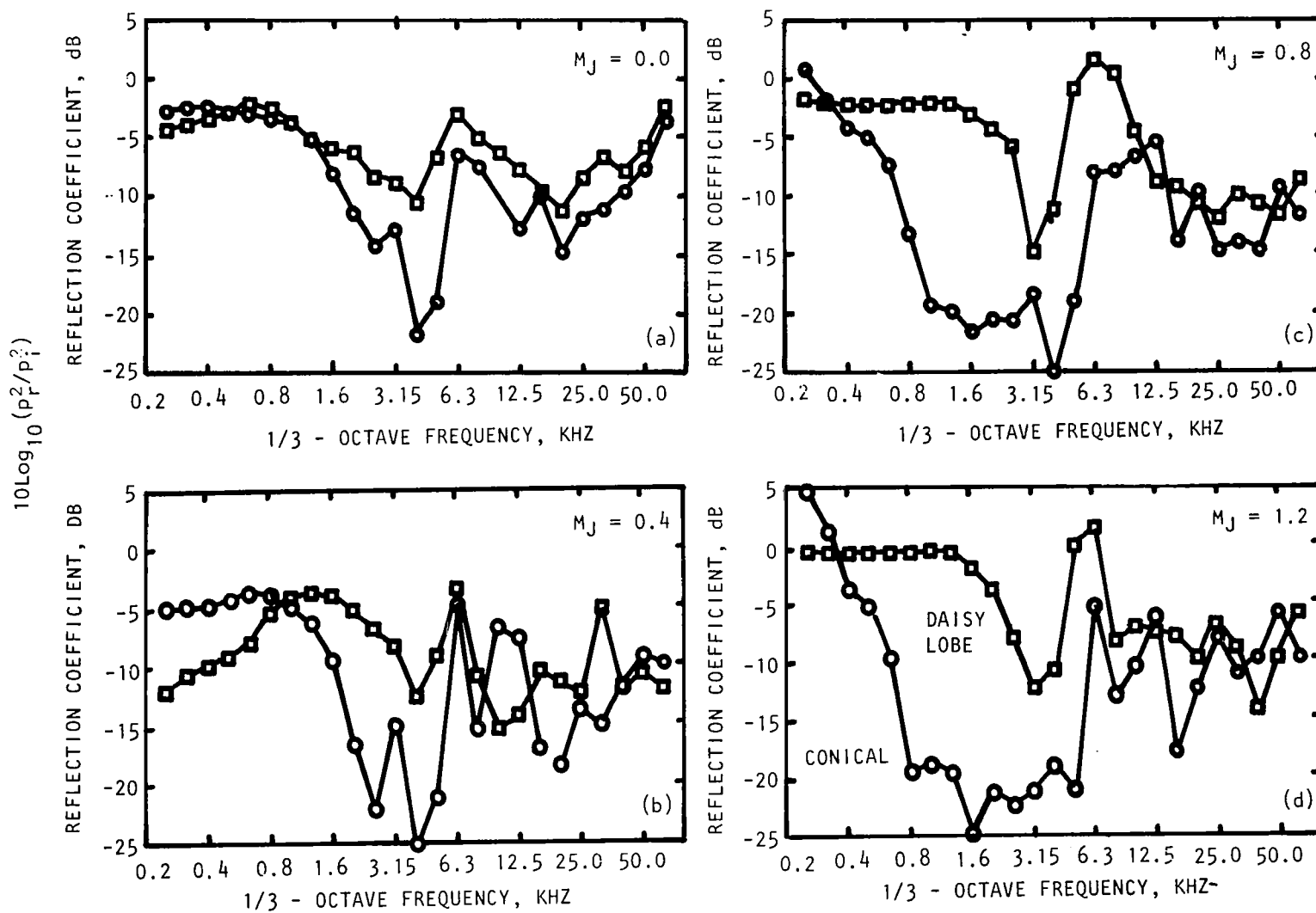


Figure 2.12 Effect of nozzle geometry on reflection coefficient spectra for various jet exit Mach numbers (unheated). \square daisy lobe nozzle; \circ reference conical nozzle

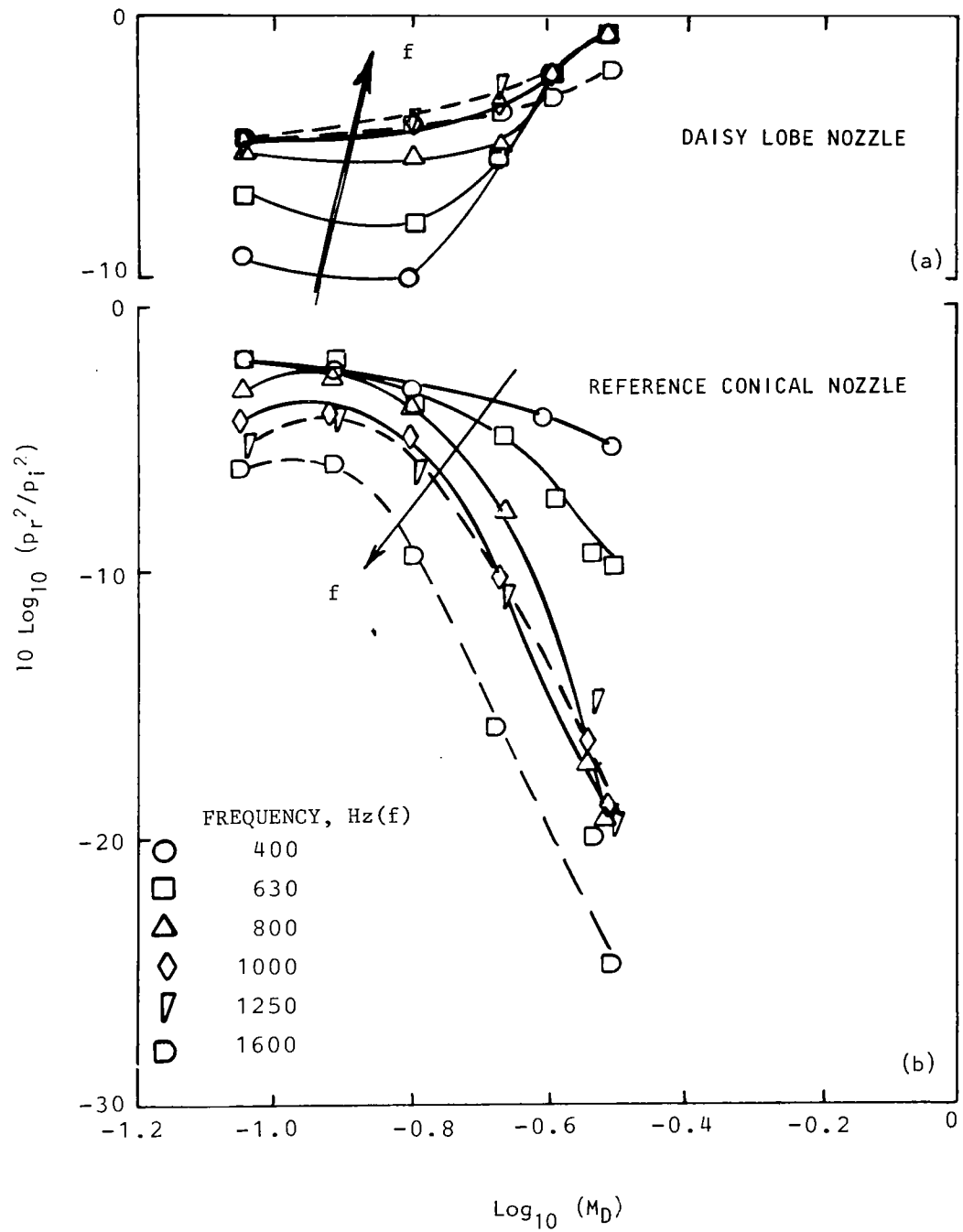


Figure 2.13 Effect of duct Mach number on the reflection coefficients of (a) daisy lobe nozzle and (b) conical nozzle at various frequencies.

incident wave in travelling from upstream to the multi-jet exits and back. For example, the daisy lobe nozzle has a sharp shoulder with convergence angle of 50 degrees (see fig. 2.1). The tubes and the daisy lobes are attached to this shoulder, the inlets of which do not all lie in the same plane. The tubes are straight while the lobes are convergent and have different widths at different radial locations. The exits of all tubes lie in the same plane (which is also normal to the nozzle axis) while those for the lobes lie in a conic. This also means that for a given axial location the flow Mach numbers will be different at various radial positions. Therefore, to derive a more accurate reflection coefficient, measurements at various radial locations may be necessary.

2.4.3 Far-Field Time Histories

Typical far-field time histories for the daisy lobe nozzle and the reference conical nozzle are shown in figures 2.14 and 2.15, respectively (ref. 2). Data for zero, subsonic ($M_J = 0.6$) and supersonic ($M_J = 1.2$) jet Mach numbers are shown at $\theta = 30^\circ, 60^\circ, 90^\circ$ and 120° . The time histories shown here have fixed time scale but have arbitrary amplitude scale. The pulses shown in these figures get contaminated with jet mixing noise with increasing Mach number. This contamination also seems to be worse for larger polar angles. In fact for Mach number 1.2, the far-field pulses are completely buried in the jet mixing and shock associated noise at larger polar angles. Therefore, it is not possible to get any information on the pulses at these angles. This problem, however, can be overcome if a signal averaging process can be incorporated by generating the incident pulse from the source repeatedly. This is possible if an acoustic driver can be used instead of the spark discharge as the source.

2.4.4 Far-Field Power

Figure 2.16 shows the comparison of far-field acoustic power spectra, normalized with respect to the incident power spectra, for the daisy lobe and the reference conical nozzles for Mach numbers of 0, 0.4, 0.6 and 0.8 (ref. 2). For almost all flow conditions the results show little difference in the radiated acoustic power levels for the two nozzles. This observation does not agree with the reflection coefficient results (see figures 2.12 and 2.13) where the reflection coefficient spectra for the daisy lobe nozzle were higher compared to those for the conical nozzle. Based on the earlier results, the far-field power for the daisy lobe nozzle should have been much lower compared to that for the reference conical nozzle.

This contradiction further implies single-point induct measurements may have been inadequate to obtain the reflection correctly.

A similar conclusion can also be made from figure 2.17 where the far-field spectra for the daisy lobe nozzle and the reference conical nozzle are plotted for various jet Mach numbers (ref. 2). Data for the

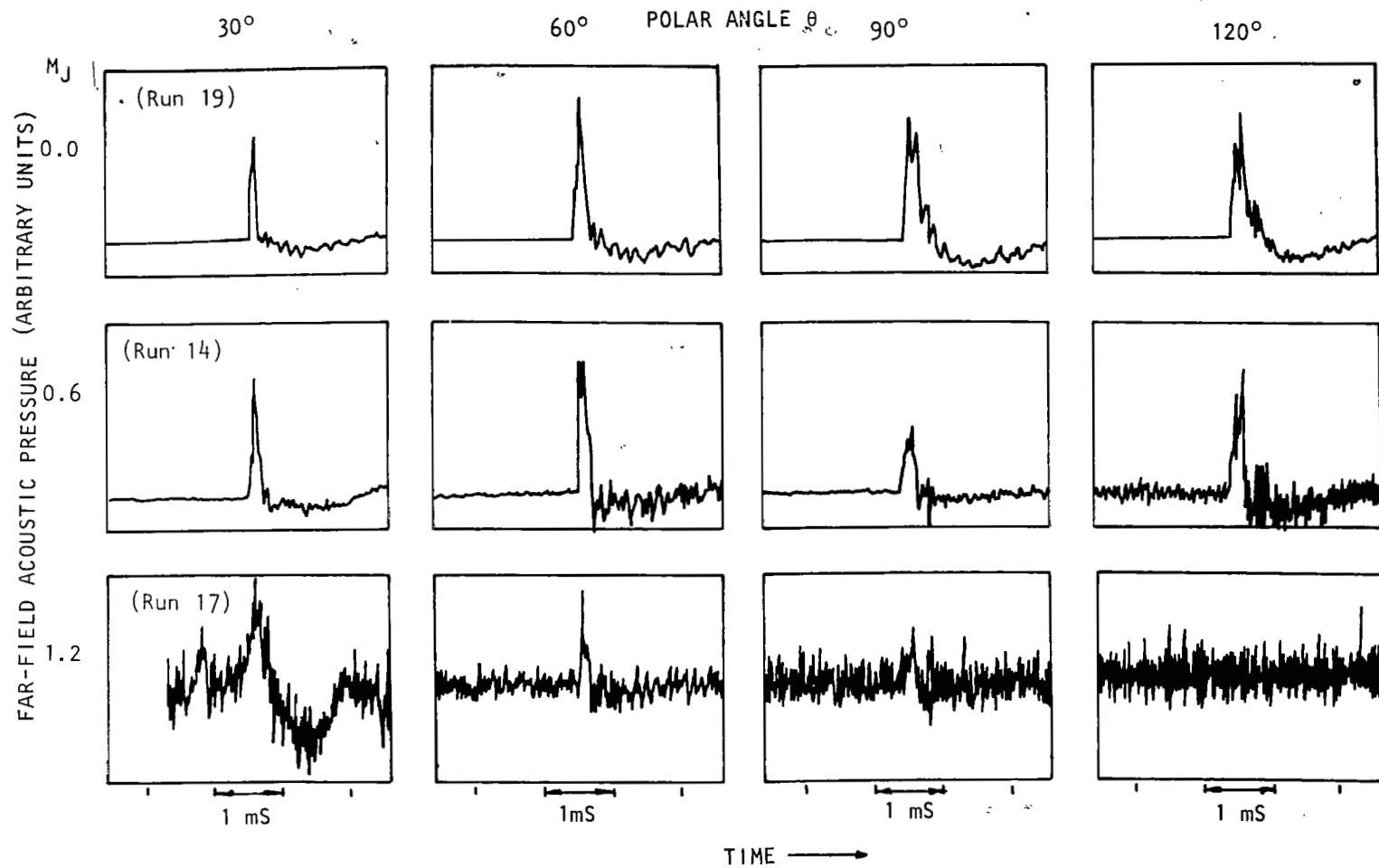


Figure 2.14 Far-field time histories for the daisy lobe nozzle as a function of jet Mach number and measurement angle (jet unheated)

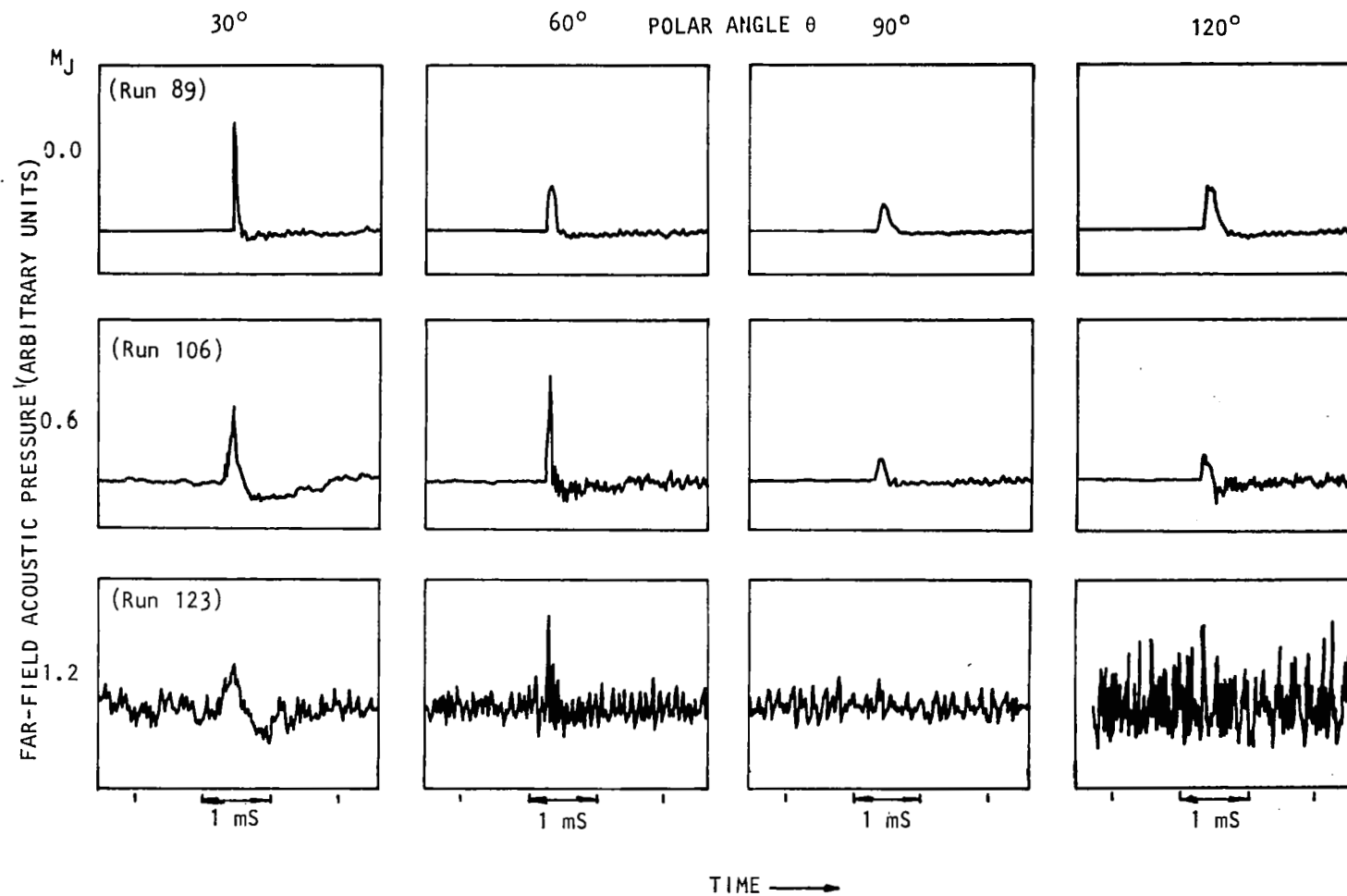


Figure 2.15 Far-field time histories for the reference conical nozzle as a function of jet Mach number and measurement angle.

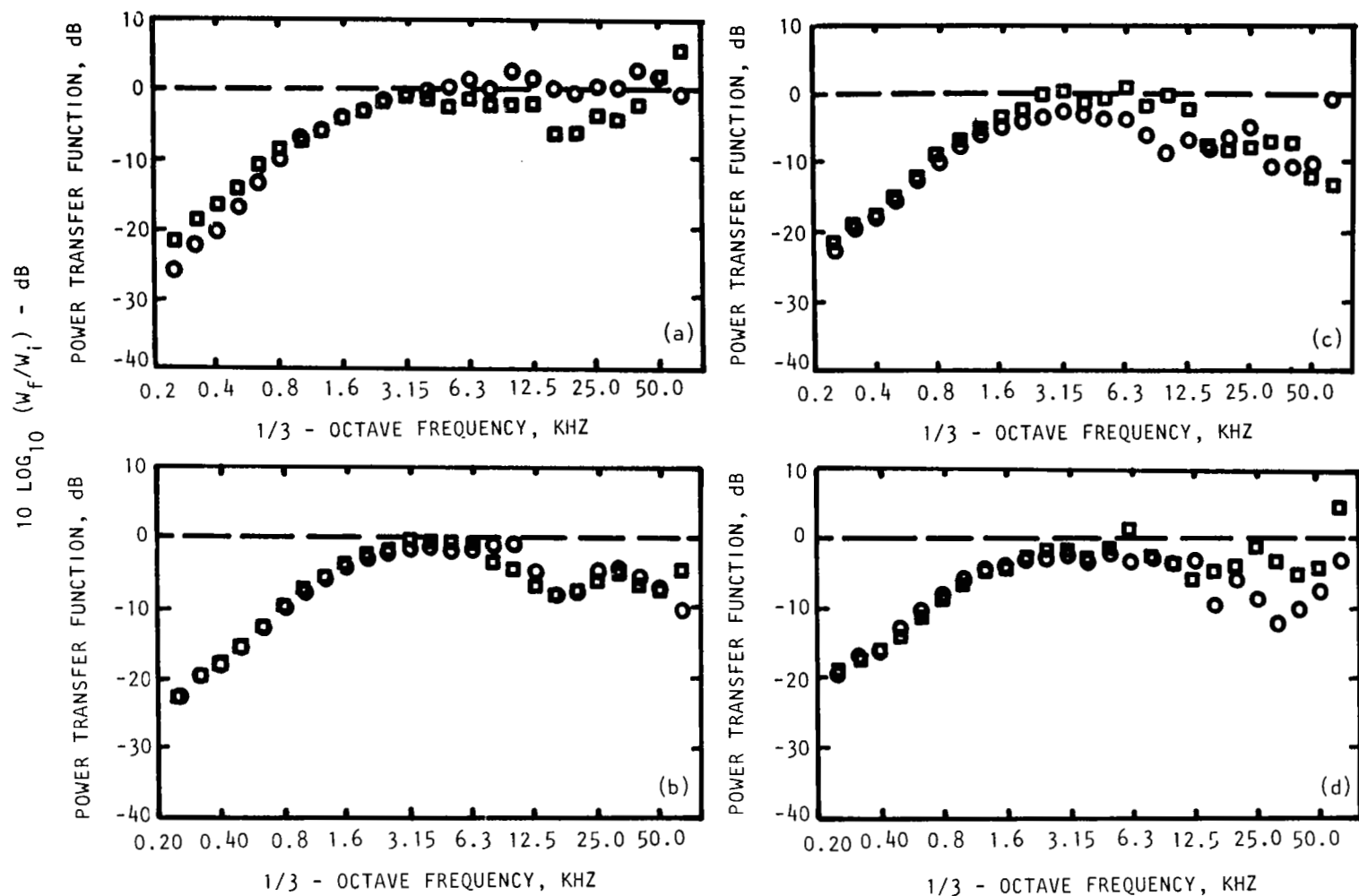


Figure 2.16 Effect of nozzle geometry on far-field acoustic power normalized with respect to incident power. M_J = (a) 0.0, (b) 0.4, (c) 0.6 and (d) 0.8
 Legend: \square daisy lobe nozzle; \circ conical nozzle

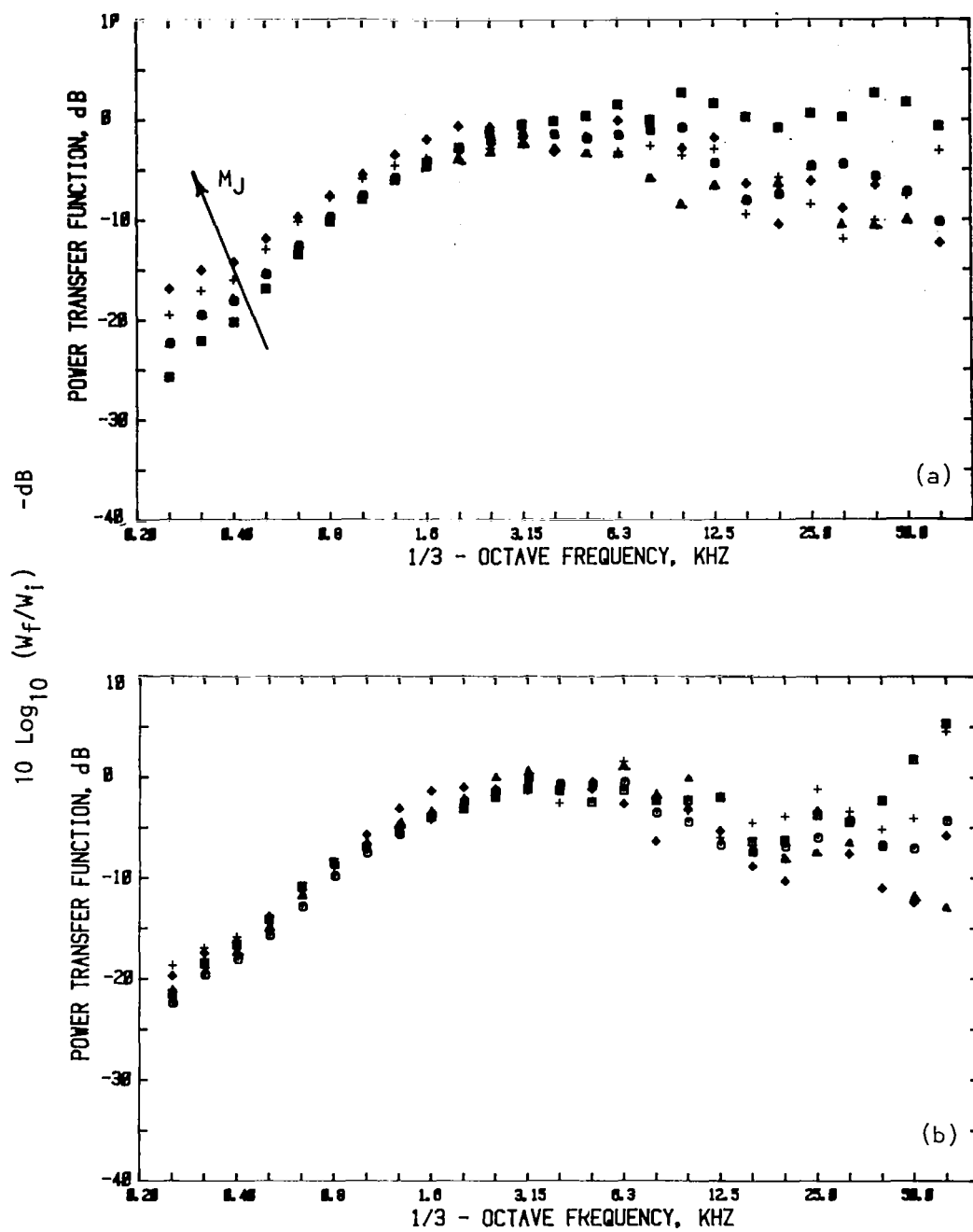


Figure 2.17 Effect of jet Mach number on far-field acoustic power spectra for (a) conical nozzle and (b) the daisy lobe nozzle.
 Legend for M_J : \square , 0.0; \odot , 0.4; \triangle , 0.6; $+$, 0.8; \diamond , 1.2

conical nozzle (figure 2.17 (a)) clearly indicate that more and more of the low frequency incident energy is radiated to the far-field as the jet Mach number is increased, with opposite effect at high frequencies. Acoustic powers for the daisy lobe nozzle (figure 2.17(b)), however, first decrease and then start increasing with increasing jet Mach number. This behavior certainly does not correlate with the reflection coefficient data, where, with increasing jet Mach number, higher reflection coefficients were obtained for the daisy lobe nozzle, thus implying a reduction in far-field acoustic power with increasing Mach number.

2.4.5 Power Balance

The far-field power normalized to the transmitted power for the daisy lobe nozzle and the reference conical nozzle are compared in figure 2.18 at various jet Mach numbers (ref. 2). A considerable amount of low frequency power loss is observed for both the nozzles at all Mach numbers, including $M_J = 0$ for which a power balance was expected. However, the nonlinear effect of the high intensity pulses, used in this study, is responsible for such a high amount of low frequency power absorption.

2.4.6 Time Histories Due to Multi-Point Source in Annular Region for the Multi-Chute Suppressor

As described in section 2.2.2 the source section for the dual-stream multi-chute nozzle was different from that used for the single-stream daisy lobe nozzle. First, instead of a single spark plug, six spark plugs with their gaps located at the foci of paraboloidal reflectors were used as the impulsive sound source, and were equi-spaced circumferentially within the annular plenum chamber upstream of the nozzle exit. Second, the source section was located only 74 cm upstream of the exit instead of 6 m as for the daisy lobe nozzle. For these reasons, both the in-duct and the far-field time histories for the multi-chute coaxial nozzle, shown in figures 2.19 and 2.20, have different shapes compared with those for the daisy lobe suppressor nozzle tested in a different facility (ref. 2). For example, the incident wave, instead of being a single pulse, now consists of four sharp pulses followed by other fluctuations of lower amplitude. The reflected signal, however, is not defined well enough due to the complex shape of the incident signal. Similar to the in-duct signal, the far-field signal also has multiple pulses. Due to the complex shape of the induct and far-field signals, it was difficult to accurately carry out the editing process necessary to isolate the incident, the reflected and the far-field signals. Therefore, it is desirable to generate a single sharp pulse at the induct measurement location. This can be feasible by using acoustic drivers as the sound sources and applying a signal synthesis which would control the combined output of the drivers.

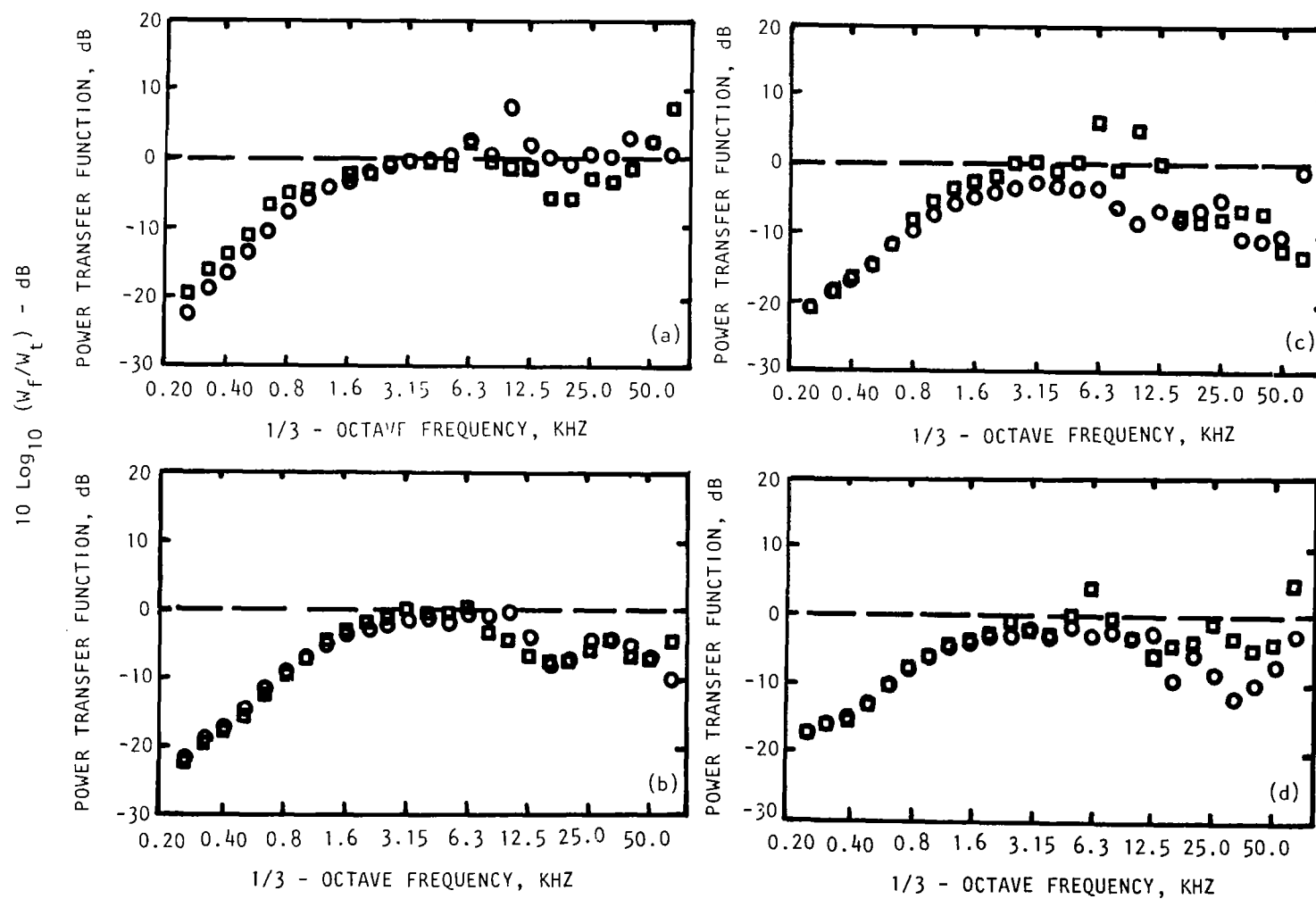


Figure 2.18 Effect of nozzle geometry on far-field acoustic power normalized w.r.t. transmitted power M_j : (a) 0.0, (b) 0.4, (c) 0.6 and (d) 0.8
 □ daisy lobe nozzle, ○ conical nozzle

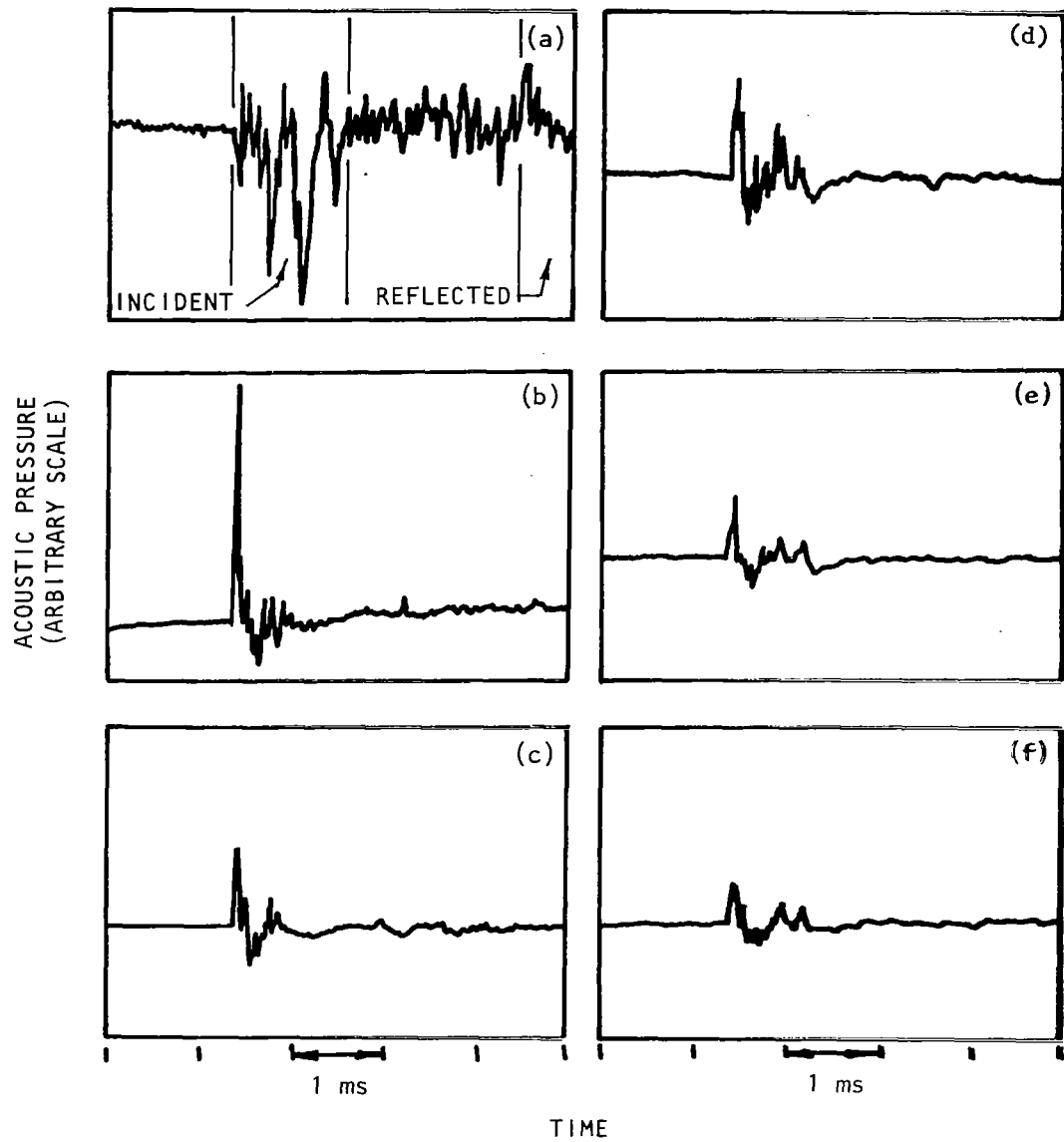


Figure 2.19 In-duct and far-field pressure time histories for the multi-chute suppressor nozzle at $M_{J1} = M_{J2} = 0$
 (a) In-duct, (b) $\theta = 10^\circ$, (c) $\theta = 30^\circ$, (d) $\theta = 50^\circ$
 (e) $\theta = 90^\circ$ and (f) $\theta = 120^\circ$.

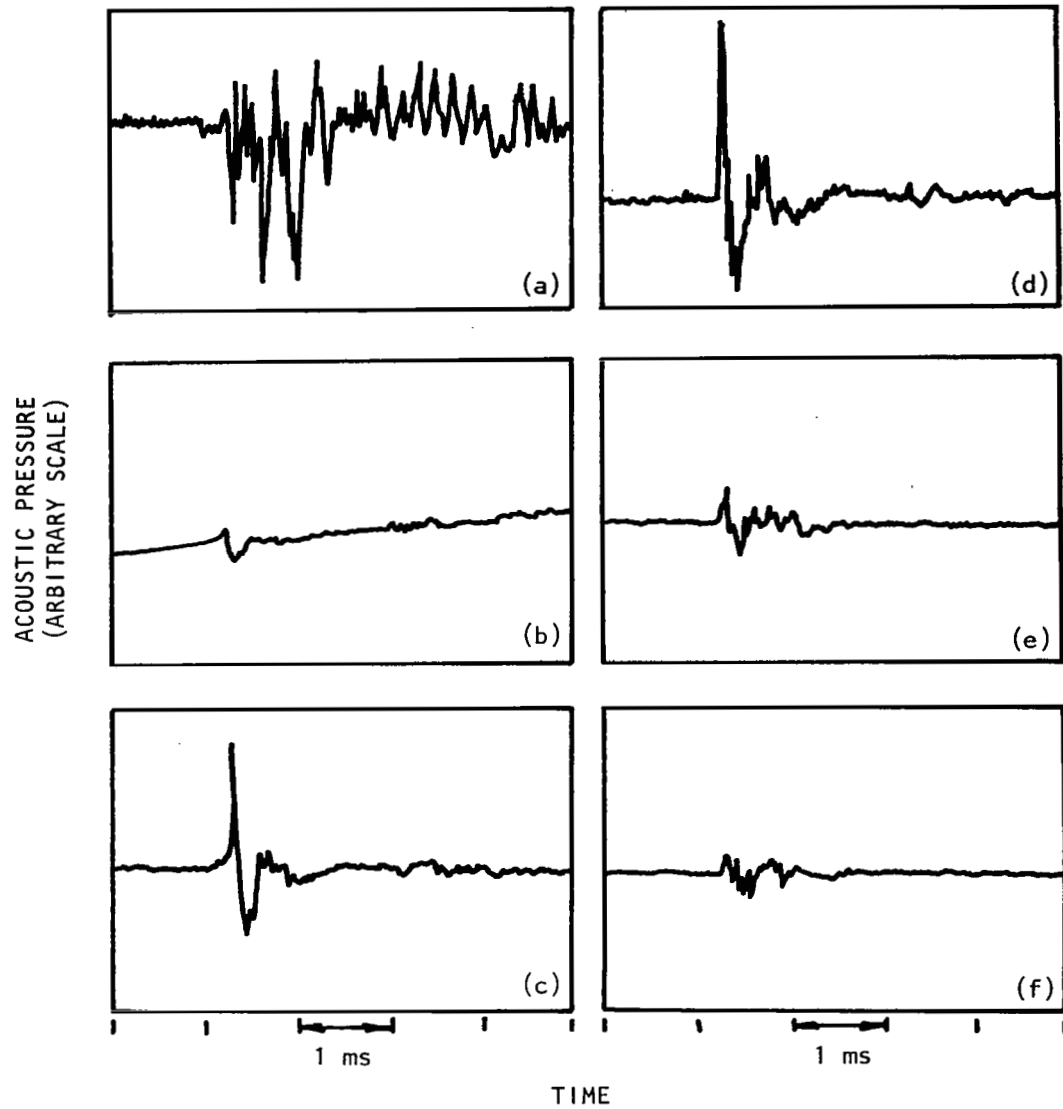


Figure 2.20 Pressure time histories for the multi-chute suppressor nozzle at $M_{J1} = 0.4$ and $M_{J2} = 0.6$ (unheated)
 (a) In-duct, (b) $\theta = 10^\circ$, (c) $\theta = 30^\circ$, (d) $\theta = 50^\circ$
 (e) $\theta = 90^\circ$ and (f) $\theta = 120^\circ$

2.5 CONCLUSIONS

The following conclusions can be drawn from the results presented in this section.

(1) The nonlinearity associated with the high intensity pulses used in these studies gives erroneous reflection coefficients (see figures 2.8 and 2.9). Also a considerable amount of low frequency power loss occurs due to nonlinear propagation of high intensity pulses.

(2) The contamination of the pulses with jet mixing noise either gives erroneous results or makes it impossible to identify the internal signal.

(3) The inconsistencies between the reflection results and the far-field power results indicate that a single point induct measurement may not be adequate to account for the reflected sound field, especially for complicated terminations.

(4) Since there is no control on the pulse shape, for multi-point source system it is difficult to generate a single pulse using spark discharge sources.

The above conclusions clearly put some severe limitations on the use of the spark discharge impulsive source for transmission studies. Therefore, it is desirable to develop an alternate impulsive source which overcomes the limitations described above and which can be used universally. The work conducted in Phase 3 of this contract, and which is described in the remainder of this report, clearly establishes that acoustic drivers can be used for this purpose to meet all the requirements.

3.0 EXPERIMENTAL SETUP

The acoustic measurements for the present investigation were carried out in the Lockheed anechoic free jet facility. This facility is powered by a jet ejector and is capable of providing free-jet velocities of up to 95 m/s through a 71 cm exit diameter free jet test section to simulate flight effects. The exhaust air to the duct-nozzle system is supplied by a 10 cm diameter duct located along the centerline of the free jet. This acoustic test facility was modified to an annular facility to carry out the studies for an annular flow stream.

A brief description of the facilities is given in this section, and includes both the single-stream and the annular-stream flow systems. The layout of the source section to generate the acoustic pulses using loudspeaker drivers (i.e., electroacoustic drivers) is also presented. Finally, the general procedure for data acquisition and data analysis, including facility instrumentation, microphone calibrations, and definition of various transmission parameters, are described.

3.1 SINGLE STREAM FLOW FACILITY

The source section and the induct and the far-field acoustic measurement systems for the single-stream flow system are shown in figure 3.1. The figure shows a single electroacoustic driver noise source located about 6 meters from the duct termination, which is surrounded by an anechoic room. A photographic view of the single driver source section is shown in figure 3.2. For severe flow conditions multiple drivers were used in the source section to generate more intense acoustic pulses. The source section in figure 3.3 shows the layout of a multiple driver source system section where four 100 watt acoustic drivers are arranged around the circumference of the 10 cm diameter duct connecting the test nozzles. This source section was physically located at the same position in the supply duct where the single driver source section was located.

A microphone probe was mounted through the duct wall 76.5 cm upstream of the termination. This probe could be a single microphone or piezoelectric transducer or a multiple point measuring probe. While a single microphone or transducer measures the induct acoustic field at one radial location, the multiple point measuring probe can simultaneously measure the induct acoustic field at various radial locations.

For the preliminary investigation to improve the impulse test technique, a single piezoelectric transducer was flush mounted through the duct wall for induct measurements. However, to measure the radial variation of the induct pressure field, two different traverse systems were fabricated. Finally, for the nozzle transmission study, a six-point probe was fabricated. The details of these probes are described in the

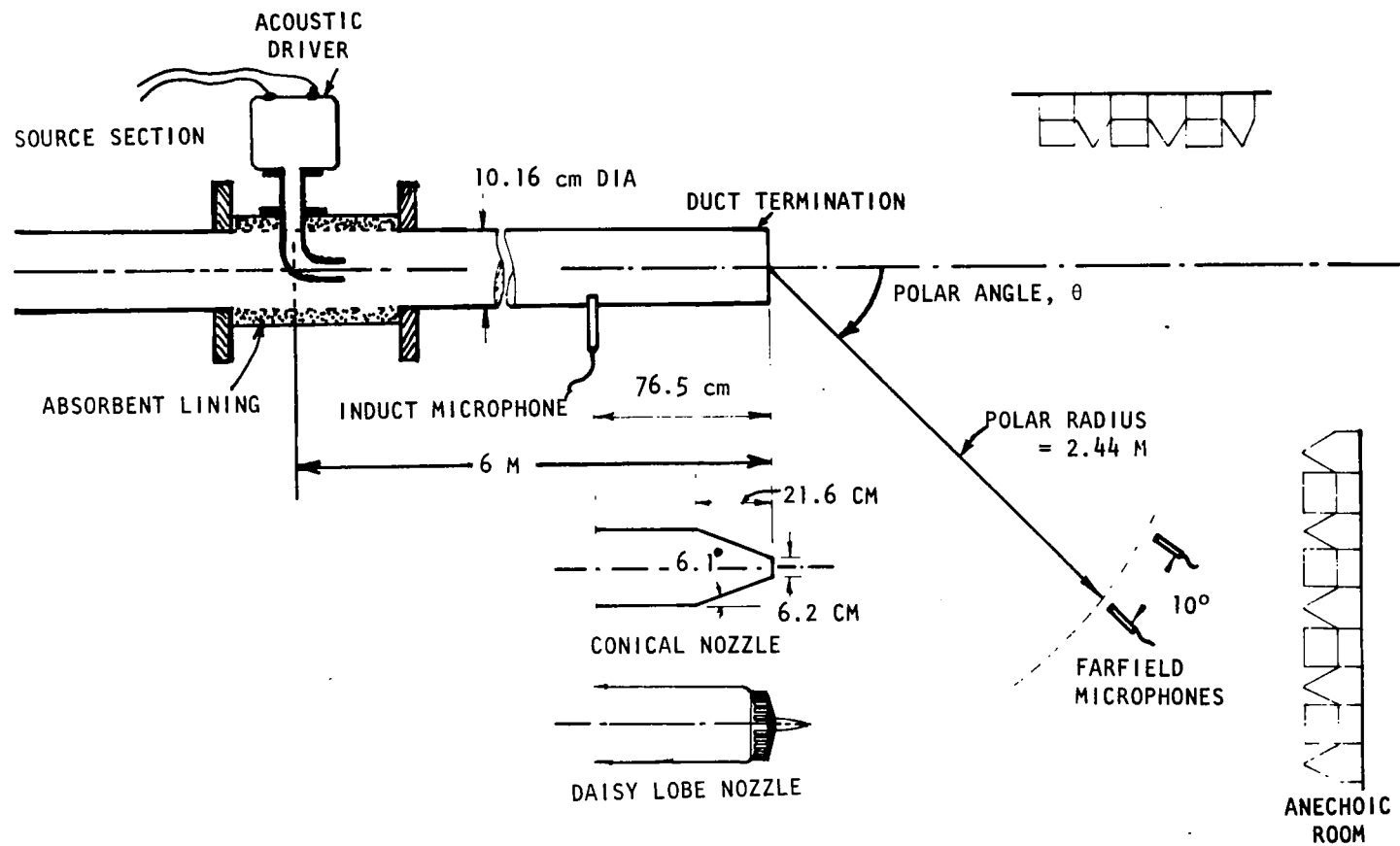


Figure 3.1 Schematic showing the source section and the induct and far-field acoustic measurement system.

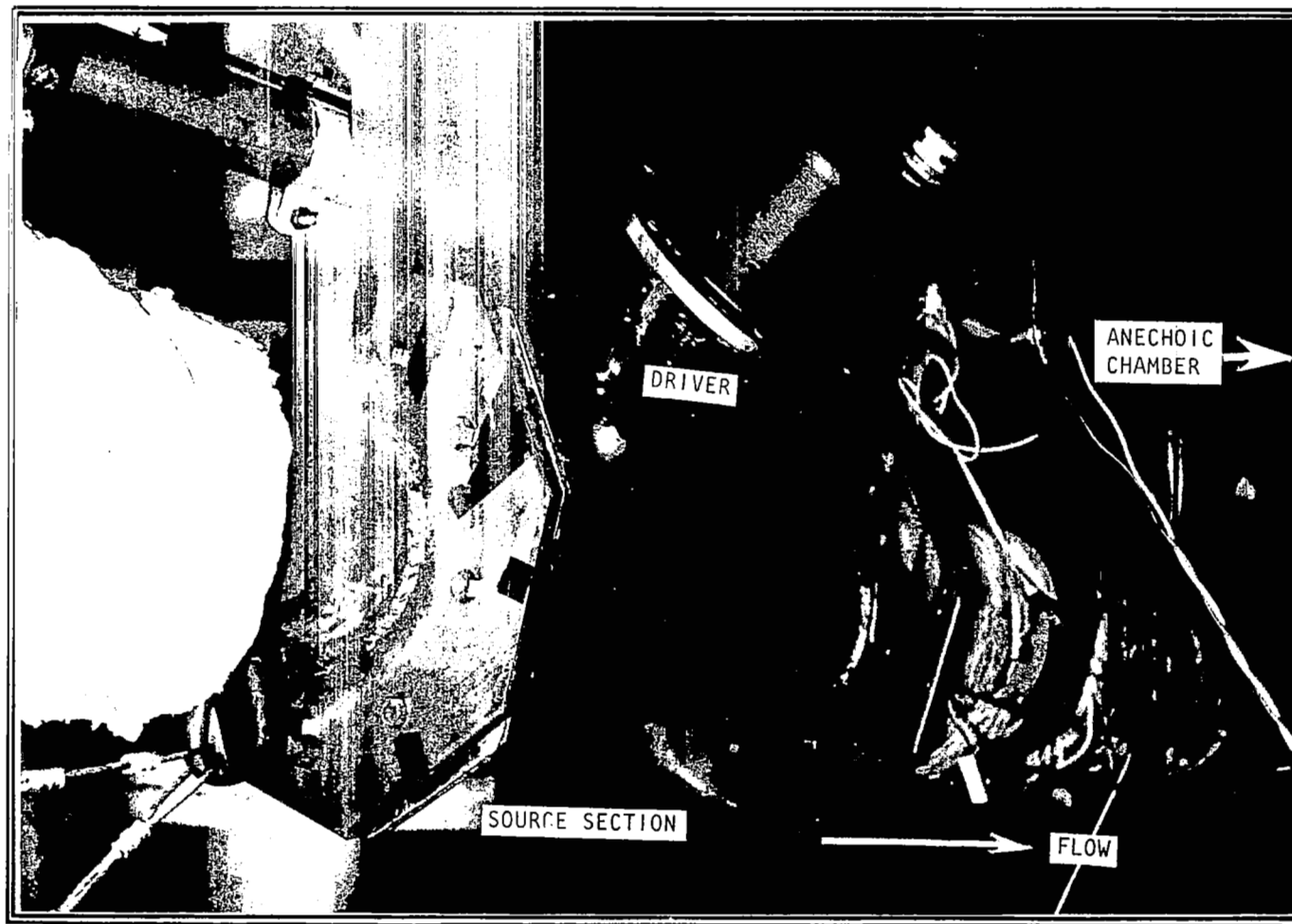
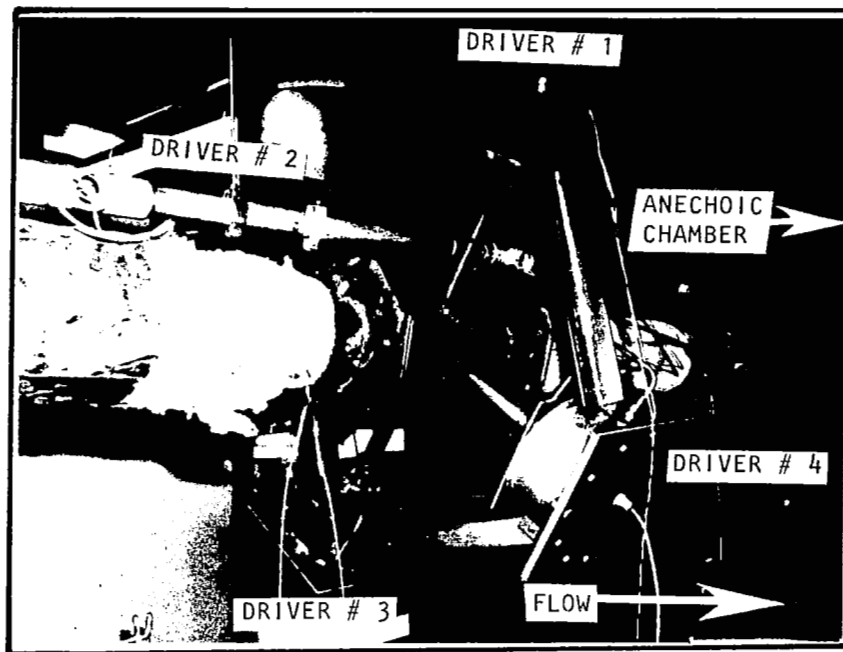
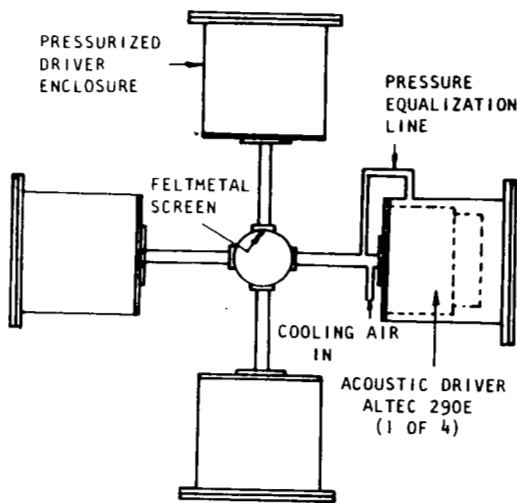


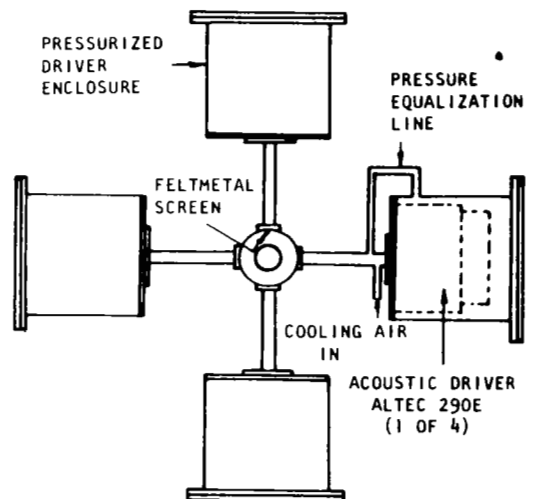
Figure 3.2 Photographic view of an acoustic loudspeaker driver mounted on the source section for a single stream flow duct.



(a) PHOTOGRAPHIC VIEW OF FOUR DRIVER SYSTEM



(b) SOURCE SECTION FOR SINGLE STREAM DUCT



(c) SOURCE SECTION FOR COANNULAR DUCT

Figure 3.3 Source section with four acoustic loudspeaker drivers for single stream or annular flow duct system

appropriate sections of this report.

In addition to the 10 cm diameter straight duct termination, a conical nozzle termination with 6.2 cm exit diameter and a multi-lobe multi-tube suppressor with equivalent exit diameter of 6.2 cm could be fitted to the 10 cm diameter flow duct. A photographic view of the suppressor nozzle mounted in the flight simulation facility is shown in figure 3.4.

Far-field microphones were placed (see figure 3.1) at 10 degree intervals on a polar arc of 2.44 meter radius, extending from 0 to 120 degrees with respect to the jet axis.

3.2 ANNULAR FLOW FACILITY

The acoustic test facility for the single-stream flow tests (i.e., for the single nozzle tests) was modified to an annular facility (see figure 3.5) by installing a 10.3 m long, 3.34 cm O.D. inner duct at the center of the outer 10.16 cm I.D. air supply duct. The upstream end of the inner duct was blocked with a suitably designed fairing to minimize flow separation. The inner duct was supported at four axial positions. Each axial support consisted of three 3.43 cm long airfoil-shaped struts, placed in the annular cross-section at 120° intervals. Three fine rods, threaded at one end, were provided at 36 cm upstream of the termination for finer adjustment of the concentricity of the two ducts. The facility was designed such that the 6.2 cm diameter conical nozzle could also be used.

The inner duct was blocked at its faired upstream end. Therefore, there was no flow in the inner duct during the experimentation. The faired end of the inner duct was placed at about 3.6 m upstream of the source section to eliminate any possible interference of the reflections from that end.

The source section, shown in figure 3.3, consisted of four 100 watt electro-acoustic drivers arranged around the circumference of the outer duct connecting the test nozzles. This source section was physically located at the same position in the supply duct where the single driver source was originally located. The output of each driver was fed into the annular section through a tube connecting the driver and the outer duct.

A special six-microphone probe was fabricated for induct measurements. In this probe (see figure 3.6), six miniature Knowles microphones were used. The length of the probe which remains inside the annular cross-section was about 3.25 cm. This was covering the entire width of the annular cross-section with six radial measurement locations 0.65 cm apart. The microphones were placed inside a supporting tube which remained outside the annular section during measurements. The individual microphones were connected to thin (about 0.16 cm) stainless steel tubes and these tubes, with miniature nose cones at the sensing

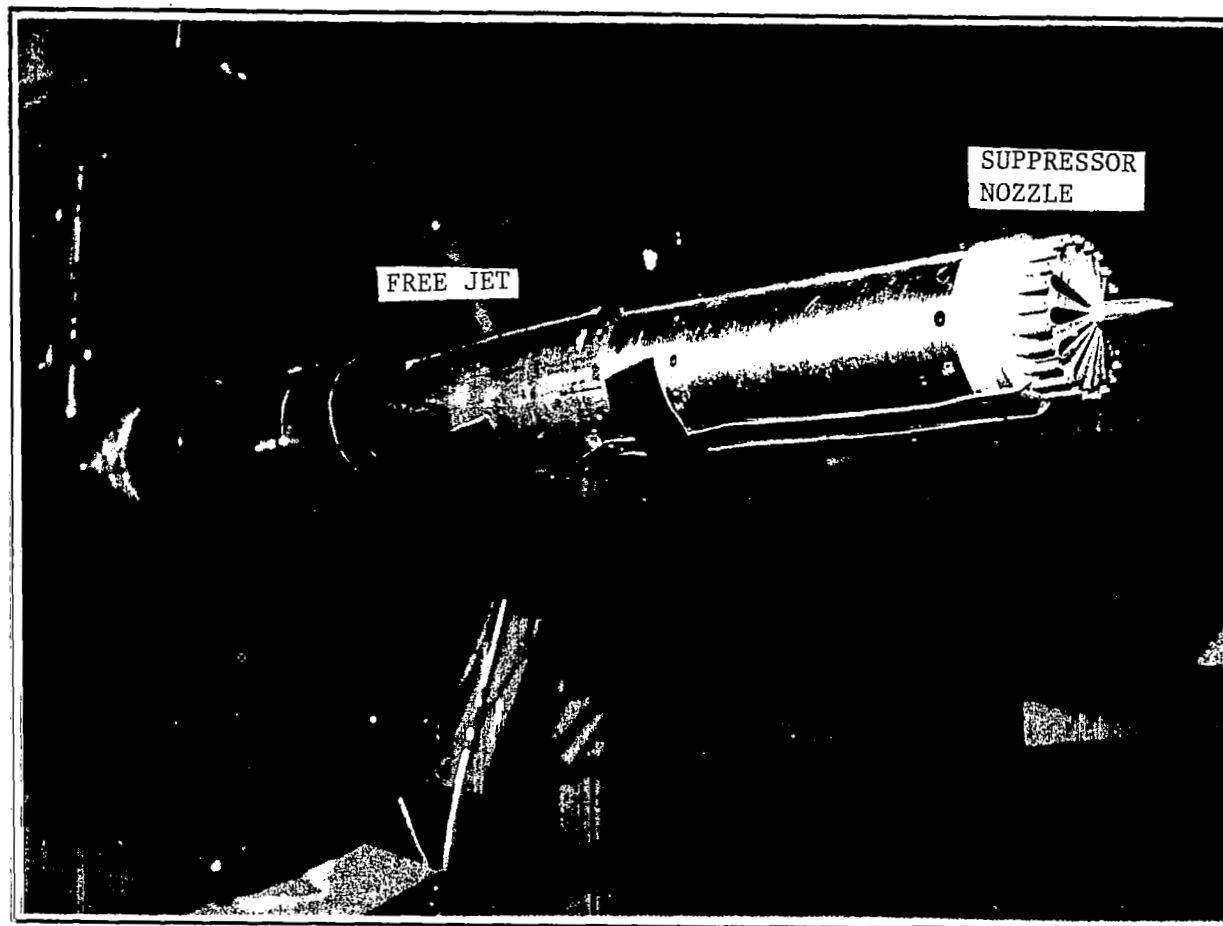


Figure 3.4 A photographic view of the 12-lobe, 24-tube nozzle suppressor mounted in the flight simulation facility.

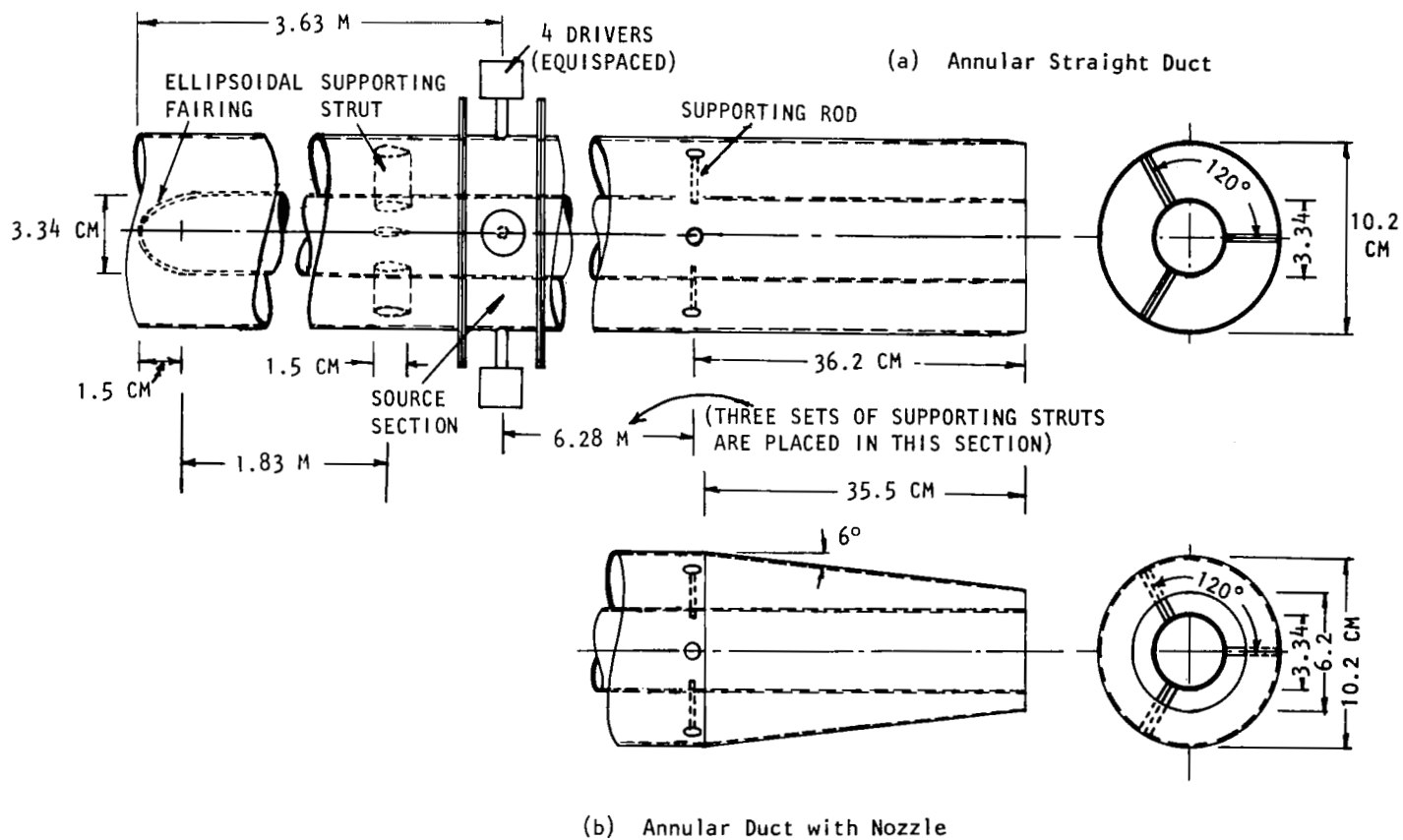


Figure 3.5 Modified annular facility

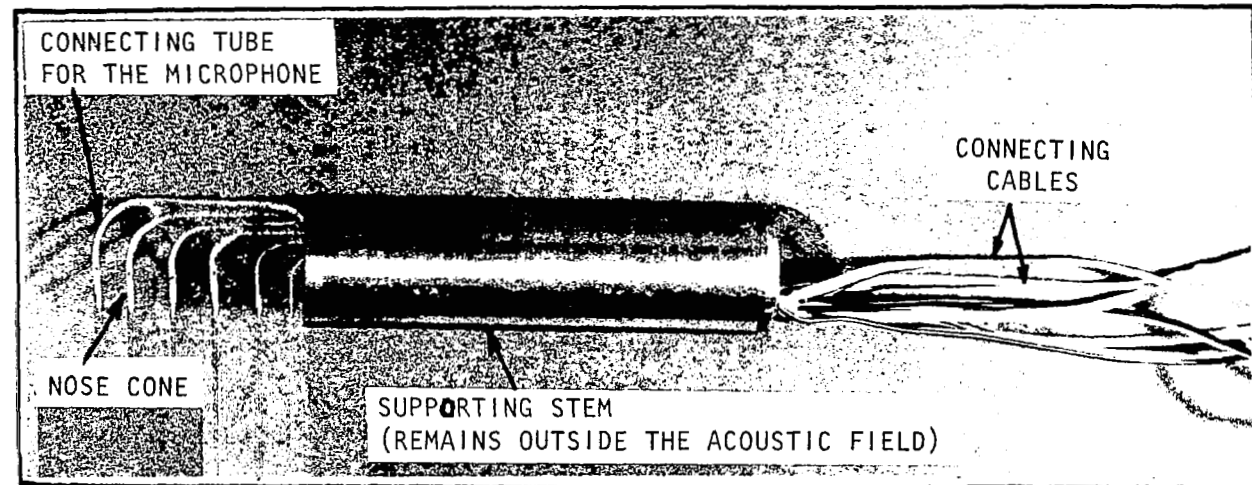


Figure 3.6 Six-microphone probe for simultaneous radial measurement.

ends, were terminated inside the annular section at the measurement locations (i.e., about 76 cm upstream of the termination). The lengths of these tubes were kept constant to minimize the phase differences in the measured data. All six tubes were bent by 90° to face the direction of the flow inside the annular section. The radial measurements for a given azimuthal angle, therefore, were achieved simultaneously without traversing a single microphone. Moreover, all the six measurements were obtained exactly at the same flow condition which would not be feasible if a single microphone had been used to acquire these data. Measurements at different azimuthal positions were obtained by rotating the outer tube at a location just upstream of the induct measurement location, keeping the inner duct fixed. In the present investigation six azimuthal positions were covered at 60° intervals.

The far field measurements were made by 1.27 cm (1/2 inch) diameter B&K microphones mounted on a 2.44 m radius polar arc, between the jet axis and 120° to the jet axis at 10° intervals (see figure 3.7).

3.3 DATA ACQUISITION AND ANALYSIS

3.3.1 Experimental Procedure

The basic test procedure consisted of generating a repeated pulse train from a single or multiple acoustic driver system at the desired operating flow conditions, and simultaneously recording the signals, both in-duct and far-field, on a 28-channel tape recorder. Subsequent analysis of the data recorded from each microphone channel was achieved on a dual-channel FFT analyzer. The multipoint induct measurements were analyzed to determine the complex pressure spectra for incident and reflected fields at each spatial location. The far-field measurements were analyzed to determine the sound pressure level (amplitude) spectra at each polar angle. These data were used to evaluate all the acoustic transmission parameters.

3.3.2 Calibration of In-duct and Far-field Microphones

In order to obtain an absolute measure of the sound pressure level and the phase relationship between the microphones of the multipoint in-duct probe, it was essential to account for the frequency response of each microphone. This was accomplished by mounting a reference microphone, whose frequency response was known, next to each of the far-field microphones (one at a time) and also the induct probe (single or multipoint), and measuring the response to white noise generated by an acoustic driver mounted at a location directly in front of the reference and the calibrating microphones. Since the signal recorded by the calibrating microphone and the reference microphone were the same, a transfer function between the two was used to derive the calibration for the microphone. For the multipoint induct probe, the simultaneously recorded data by each microphone were used to derive the amplitude and phase calibration for the probe. The calibration for each microphone

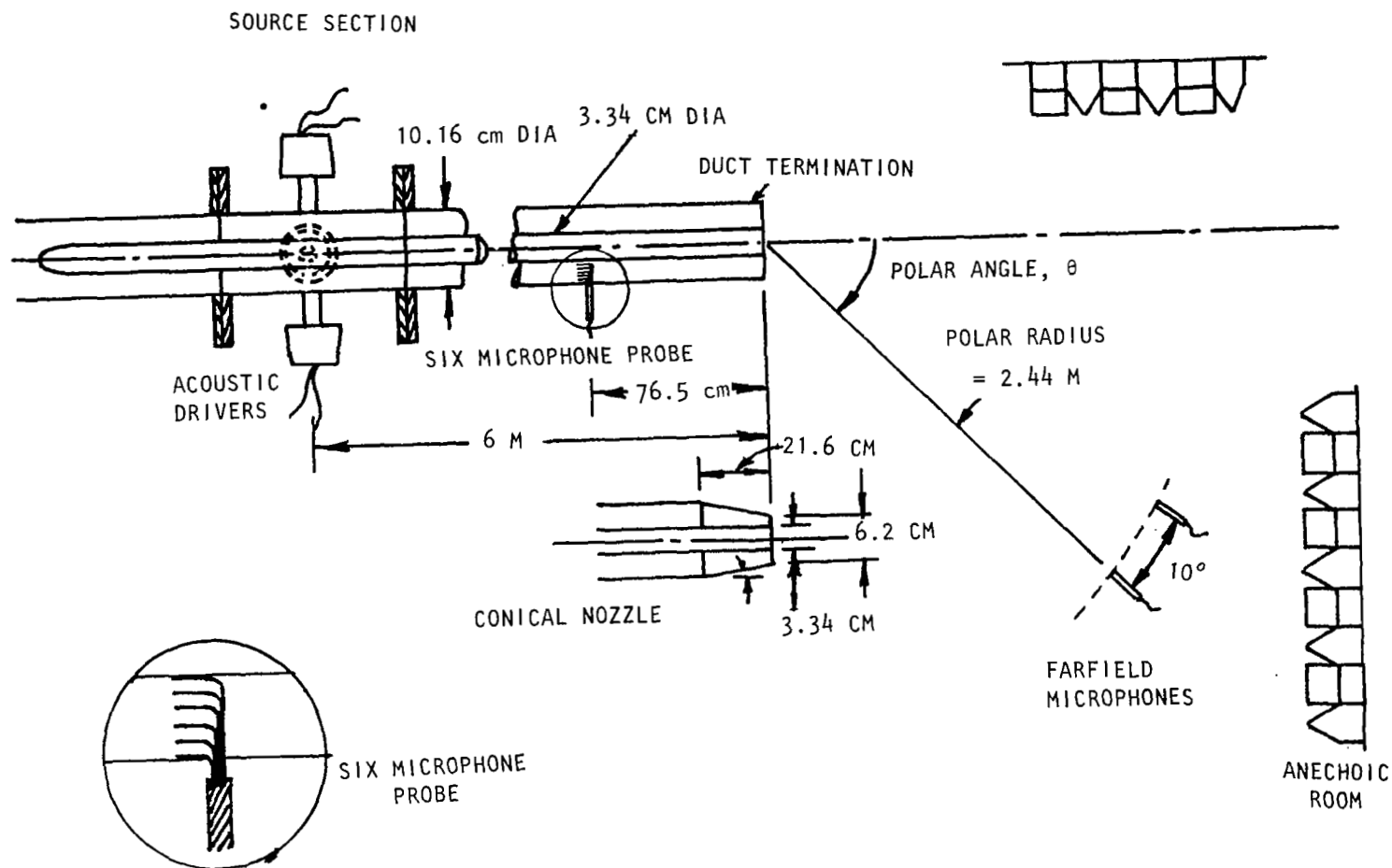


Figure 3.7 Schematic showing the source section and the induct and far-field acoustic measurement system for an annular duct/nozzle arrangement.

thus obtained was incorporated as a frequency response correction in the data reduction procedure.

3.3.3 Presentation of Transmission Data

Three basic parameters of interest were calculated from the measurements made in the far-field and inside the duct. These were the Reflection Coefficient (σ), the Normalized Transfer Function or Coefficient (NTF or NTC), and the Power Transfer Function (PTF). Expressions for these parameters for the plane wave mode are given below:

$$\text{Reflection Coefficient, } \sigma = 10 \text{ LOG}_{10} \left(\frac{p_r^2}{p_i^2} \right), \text{ dB} \quad (3.1)$$

$$\text{Incident Power, } W_i = \frac{A_D}{\rho_D c_D} [p_i^2 (1 + M_D)^2] \quad (3.2)$$

$$\text{Reflected Power, } W_r = \frac{A_D}{\rho_D c_D} [p_r^2 (1 - M_D)^2] \quad (3.3)$$

$$\text{Transmitted Power, } W_t = \frac{A_D}{\rho_D c_D} [p_f^2 (1 + M_D)^2 - p_r^2 (1 - M_D)^2] \quad (3.4)$$

$$\text{Far-field Power, } W_f = \frac{1}{\rho_o c_o} \int p_f^2(\theta) \Delta s(\theta) \quad (3.5)$$

If a point source of power equal to W is assumed to be radiating in the far-field from the nozzle exit, the intensity at the measurement location at a distance R from the nozzle exit due to this source will be

$$I_p = W_i / 4\pi R_m^2 \quad (3.6)$$

The measured far-field intensity is given by

$$I_f(\theta) = \frac{p_f^2(\theta)}{\rho_o c_o} \quad (3.7)$$

The Normalized Transmission Coefficient or Normalized Transfer Function is simply the ratio of $I_f(\theta)$ and I_p and can be expressed in the following form:

$$\text{NTC}(\theta) \text{ or } \text{NTF}(\theta) = \frac{4\pi R_m^2}{\rho_o c_o} \cdot \frac{p_f^2(\theta)}{W_i} \quad (3.8)$$

Using equation (3.2) and the equation of state, the above expression can be rewritten as follows:

Normalized Transfer Function,

$$\text{NTC}(\theta) \text{ or } \text{NTF}(\theta) = 10 \text{ LOG}_{10} \left\{ \frac{p_f^2(\theta)}{p_i^2} \right\} + 10 \text{ LOG}_{10} \left\{ \frac{4\pi R_m^2}{A_D} \cdot \frac{P_D}{P_o} \cdot \frac{1}{(1+M_D)^2} \sqrt{\frac{T_o}{T_D}} \right\}, \text{ dB} \quad (3.9)$$

Using equations (3.3) through (3.5) the Power Transfer Function (PTF) can be expressed as follows:

Power Transfer Function with Respect to Incident Power,

$$\text{PTF}_i = 10 \text{ LOG}_{10} (W_f/W_i), \text{ dB} \quad (3.10)$$

Power Transfer Function with Respect to Transmitted Power,

$$\text{PTF}_t = 10 \text{ LOG}_{10} (W_f/W_t), \text{ dB} \quad (3.11)$$

When multipoint induct measurements are made for the purpose of evaluating the induct power (i.e. incident, reflected and transmitted) more accurately by accounting for the contributions of higher order modes, the expressions for induct powers are different. The proper expressions are derived and presented in section 5. The modal reflection coefficients and the overall reflection coefficients for such cases are also discussed in section 5. However, the expression for the far-field power (equation (3.5)) remains the same whether the induct powers are estimated using equations (3.2) through (3.4) for the plane wave mode or the expressions derived in section 5.

4.0 ACOUSTIC IMPULSE TECHNIQUE IMPROVEMENT

During the past four years, extensive experimental research on the transmission of sound through nozzles has been conducted at Lockheed using an acoustic impulse technique. In this technique, pulses generated by high voltage spark discharge were used as the internal sound sources. The main problems associated with the spark discharge impulse technique are (1) low signal-to-noise ratio at high jet velocities, and (2) nonlinear characteristics of the high intensity spark pulses

The spark discharge impulse technique was based on a single pulse analysis scheme. Therefore, the presence of flow noise, superimposed as a background on the impulse received by the microphones, inevitably produces spectral contamination. This condition becomes aggravated at high flow velocities. The traditional solution to this problem is to use the technique of signal averaging. If a sufficient number of individual records are averaged, the stochastic contribution is averaged to zero so that the pulse time-history is recovered. Implicit in this technique is the assumption that the pulse waveforms from sample to sample are identical. However, it is very difficult to generate identical pulses using the spark discharge, because the discharge intensity varies from one spark to another. Moreover, the rate of pulse generation is very much limited with respect to time.

These problems are eliminated by the use of an acoustic driver instead of a spark discharge source to generate the pulses. Also, the nonlinearities associated with high intensity pulses, generated for the purpose of increasing the signal-to-noise ratio, can be avoided by using repetitive low intensity pulses from an acoustic driver. In this case the signal-to-noise ratio is increased by signal averaging. To generate a single pulse of desired frequency content, a convolution technique can be used to synthesize the acoustic impulse.

The various techniques studied to improve the acoustic impulse technique are described in this section. The process of signal synthesis to generate a desired single pulse from loudspeaker driver(s) and the method of signal averaging to minimize the background noise are described in sections 4.1 and 4.2, respectively. In addition, the method of signal editing to remove unwanted portions of a time-domain signal and the method of spectral averaging to improve the statistical accuracy of the spectral results are described in sections 4.3 and 4.4, respectively. A numerical smoothing procedure is illustrated in section 4.5 to obtain smoother spectral distribution such that the data for different flow conditions or configurations can be compared on an overall basis. Finally, the limitations and the guidelines for signal averaging are discussed in section 4.6.

4.1 SYNTHESIZING ON ACOUSTIC IMPULSE WITH ACOUSTIC DRIVER

4.1.1 Characteristics of Electroacoustic Driver and Objective of Signal Synthesis

The objective is to use electroacoustic driver(s) as the impulsive sound source for the nozzle transmission studies. The output signal of the driver(s) should be a single sharp pulse of very short duration, so that it will not be appreciably contaminated with reflections from the nozzle exit and other distant objects. The spectral characteristics are not very critical as long as the pulse contains reasonably high intensity levels throughout the desired frequency range. However, it is not simple to generate such a desired pulse. In reality, the drivers do not have a flat frequency response. In addition, the driver's response is very much influenced by the impedance match of the driver with its surrounding. Therefore, when an impulsive electronic signal (with almost a flat frequency spectrum) is fed into the driver, it does not necessarily provide an acoustic signal with a similar pulse shape or spectrum characteristics. On the contrary, the output signal contains a series of pulses, trailing for a long time after the passage of the initial pulse. Therefore, the output signal becomes contaminated by reflections from the exit and other distant objects. Moreover, such a pulse results in a multilobe spectrum, instead of the desired flat spectrum.

In principle, however, there must be a signal of some shape which, when fed to the driver, will produce a sharp pulse. Such an electronic input can be derived by using the response of the acoustic driver and its surrounding. The procedure to create the distorted input to the driver to obtain a clean pulse is defined as signal synthesis.

4.1.2 Summary of Previous Work

Signal synthesis has been tried by others in the past with limited success. Favour et al (ref. 8) presented a simple algorithm and applied it successfully to shock testing equipment. As per their requirement the waveform that was produced had a small bandwidth. However, the fundamental concept behind the synthesis procedure was the same. Niedzwiecki and Ribner (ref. 9) applied signal synthesis in their sonic boom experiments to produce a particular N-wave. Singh and Katra (ref. 10) in their study of muffler characteristics with the aid of an impulsive source also attempted to synthesize the impulsive signal. In a subsequent note (ref. 11) they reported that they were unable to apply signal synthesis and resorted to a time-consuming trial and error method. Recently, Aioshima (ref. 12) used wave form compression techniques to study the response characteristics of acoustic systems subject to impulses. But the author did not use the system response directly in the signal synthesis. Davies et al (ref. 13) used signal synthesis to produce short duration signals from a loudspeaker. They were able to produce different target functions and their work is very similar to that reported in reference 8.

4.1.3 Principle and the Mathematical Background

The signal synthesis is defined as the procedure to obtain a distorted waveform from the response of the driver system. The calculated distorted waveform, when fed back to the driver system (i.e., the driver(s) with surroundings), completes a feed-back loop and the output of the driver system is the desired signal. This is illustrated in figure 4.1. A similar predistorsion procedure is outlined by Niedzwiecki and Ribner (ref. 9). The analytical details of this process are described in reference 14 by Ramakrishnan et al. However, the basic signal synthesis procedure is outlined below.

Let $x(t)$ be the electronic analog signal input to the driver system which can be provided in any arbitrary fashion, t being the time. If $y(t)$ is the output of the driver system, then the cumulative response of the driver system, $h(t)$, can be determined. The Fourier transforms of the various functions are defined as follows (ref. 15).

$$\begin{aligned} X(\omega) &= \int x(t)e^{-i\omega t} dt \\ Y(\omega) &= \int y(t)e^{-i\omega t} dt \\ H(\omega) &= \int h(t)e^{-i\omega t} dt \end{aligned} \quad (4.1)$$

Where, $\omega = 2\pi f$

All the integrands in equation (4.1) are transient causal functions. Hence, they satisfy all the necessary convergent conditions for the Fourier transforms to exist. The driver system is assumed to be a linear response system. For linear systems the following relationship holds (ref. 15):

$$Y(\omega) = H(\omega) \cdot X(\omega) \quad (4.2)$$

The response function is then,

$$H(\omega) = Y(\omega)/X(\omega) \quad (4.3)$$

Let $z(t)$ be the desired transient output and $Z(\omega)$ be its Fourier transform. Then, the synthesized input signal $s(t)$ can be determined as,

$$s(t) = \frac{1}{2\pi} \int S(\omega) e^{i\omega t} d\omega$$

where,

$$S(\omega) = Z(\omega)/H(\omega) \quad (4.4)$$

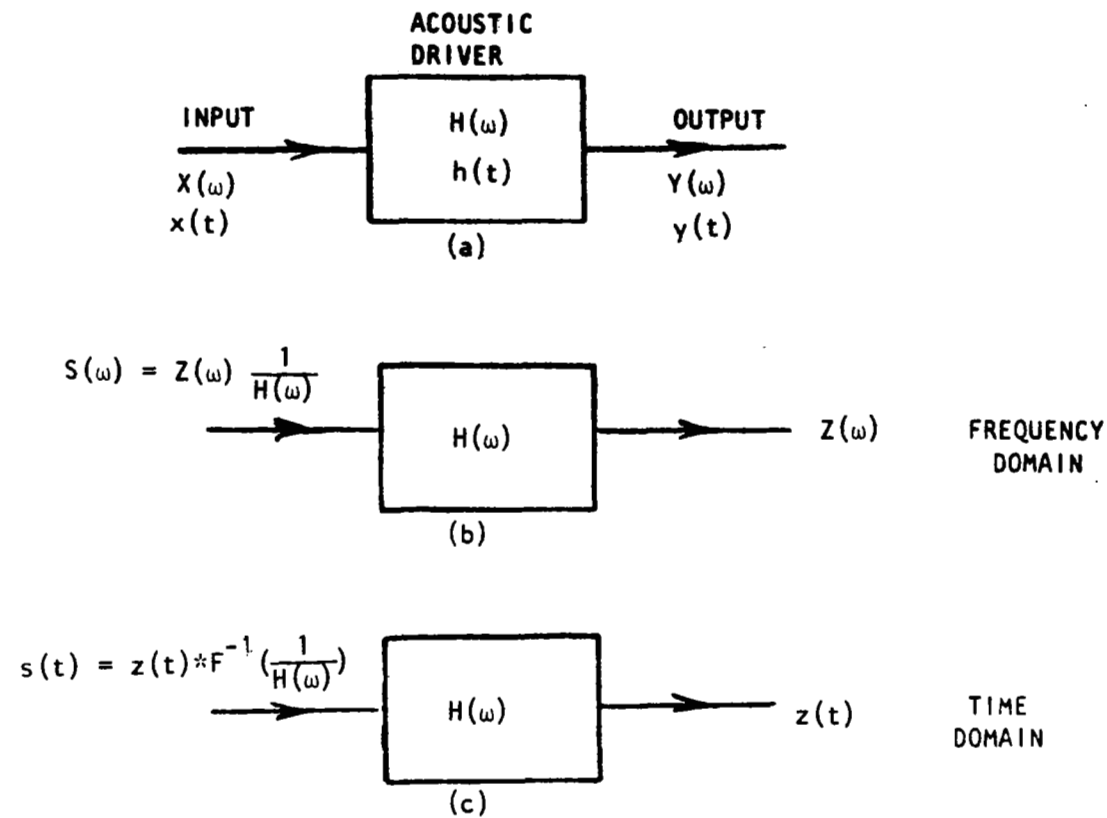


Figure 4.1 Schematic of obtaining a desired pressure pulse $x(t)$ from an acoustic driver with transfer function $H(\omega)$

If $s(t)$ is fed into the driver system the output would be as follows:

$$\int_0^t s(t-\tau) h(\tau) d\tau = z(t) \quad (4.5)$$

which is the desired signal. Equation (4.5) can also be written as follows:

$$s(t) * F^{-1} \left(\frac{1}{H(\omega)} \right) = z(t) \quad (4.6)$$

In most of the cases the desired output $z(t)$ is the same as $x(t)$. Thus, if the frequency response or transfer function of the driver system is represented by $H(\omega)$, then for a given input $X(\omega)$, the output will be $X(\omega) \cdot H(\omega)$. Similarly, if the product of $X(\omega)$ and $1/H(\omega)$ is fed to the driver, the output would be exactly equal to $X(\omega)$ itself. In the time domain, this is equivalent to feeding the convolution of $x(t)$ and the inverse Fourier transform of $1/H(\omega)$ (i.e., $x(t) * F^{-1}(1/H(\omega))$).

4.1.4 Test Facilities and Operational Procedure

To carry out the signal synthesis procedure two specific driver configurations were used in the source section: (1) a single driver configuration as shown in figure 4.2 where a single acoustic driver noise source was used for the single stream duct; and (2) a four driver configuration as shown in figure 4.3 where four acoustic drivers were used for both single stream and annular flow duct systems.

In the single driver source section, the impulsive sound was injected through a small tube opening located at the centerline of the duct. The tube was connected to the driver through another tube which was bent by 90°. In the four driver configuration the drivers were equiangularly arranged around the circumference of the flow duct connecting the test nozzles. In either of the configurations, an induct measuring probe was located in the duct about 76.5 cm upstream of the termination as described in section 3. For the coannular duct, the probe was placed in the annular space of the duct. For this study Altec 290E loudspeaker drivers were used. These drivers can produce an overall sound pressure level of 134 dB at 1.2 meters in the frequency range of 500 Hz to 3 KHz and have a frequency response of 300 Hz to 8 KHz.

The signal synthesizing procedure is carried out in four steps as illustrated in figure 4.4.

(a) An arbitrary sharp pulse is created in the digital FFT analyzer (SD360). Then the pulse is rotated at a fixed frequency to generate a train of identical pulses. This periodic impulsive signal, $x(t)$, is recorded on an analog tape recorder.

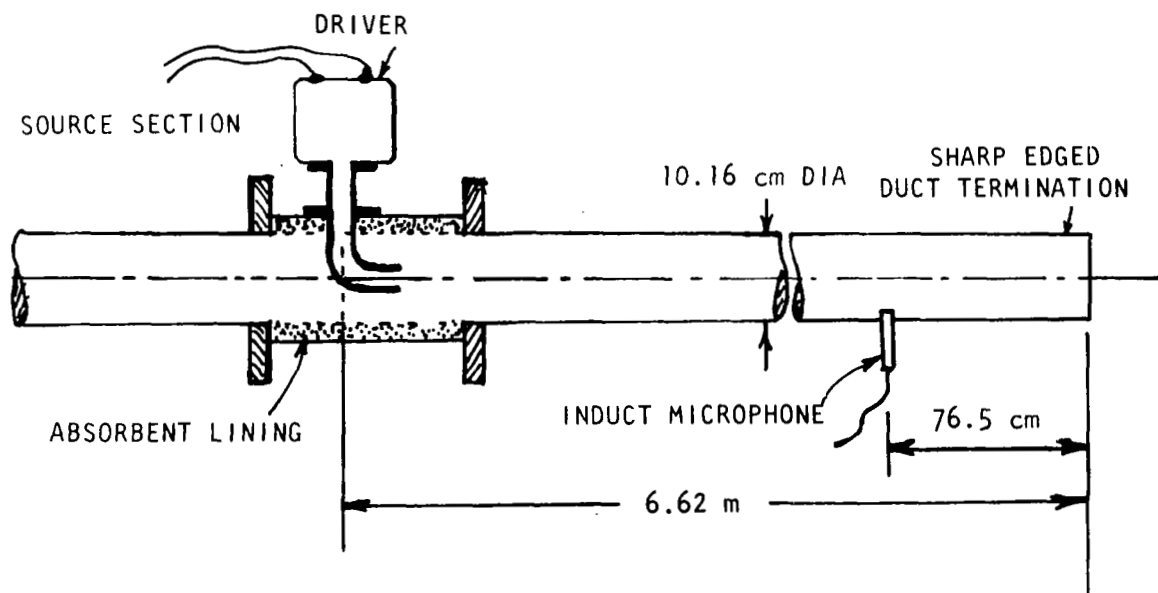


Figure 4.2 Schematic showing the source section and the induct measurement system.

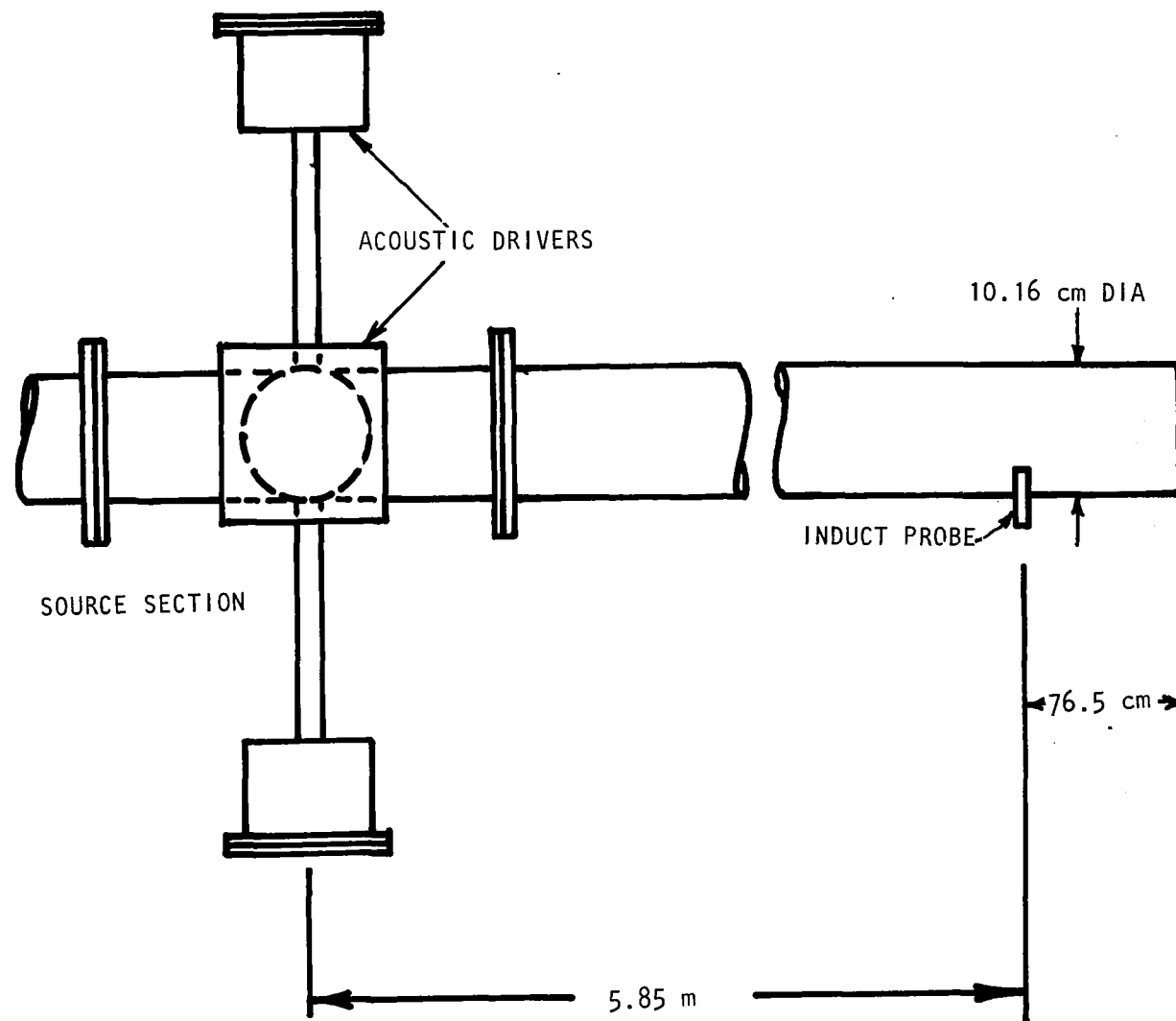


Figure 4.3 Schematic showing the source section with four acoustic drivers.

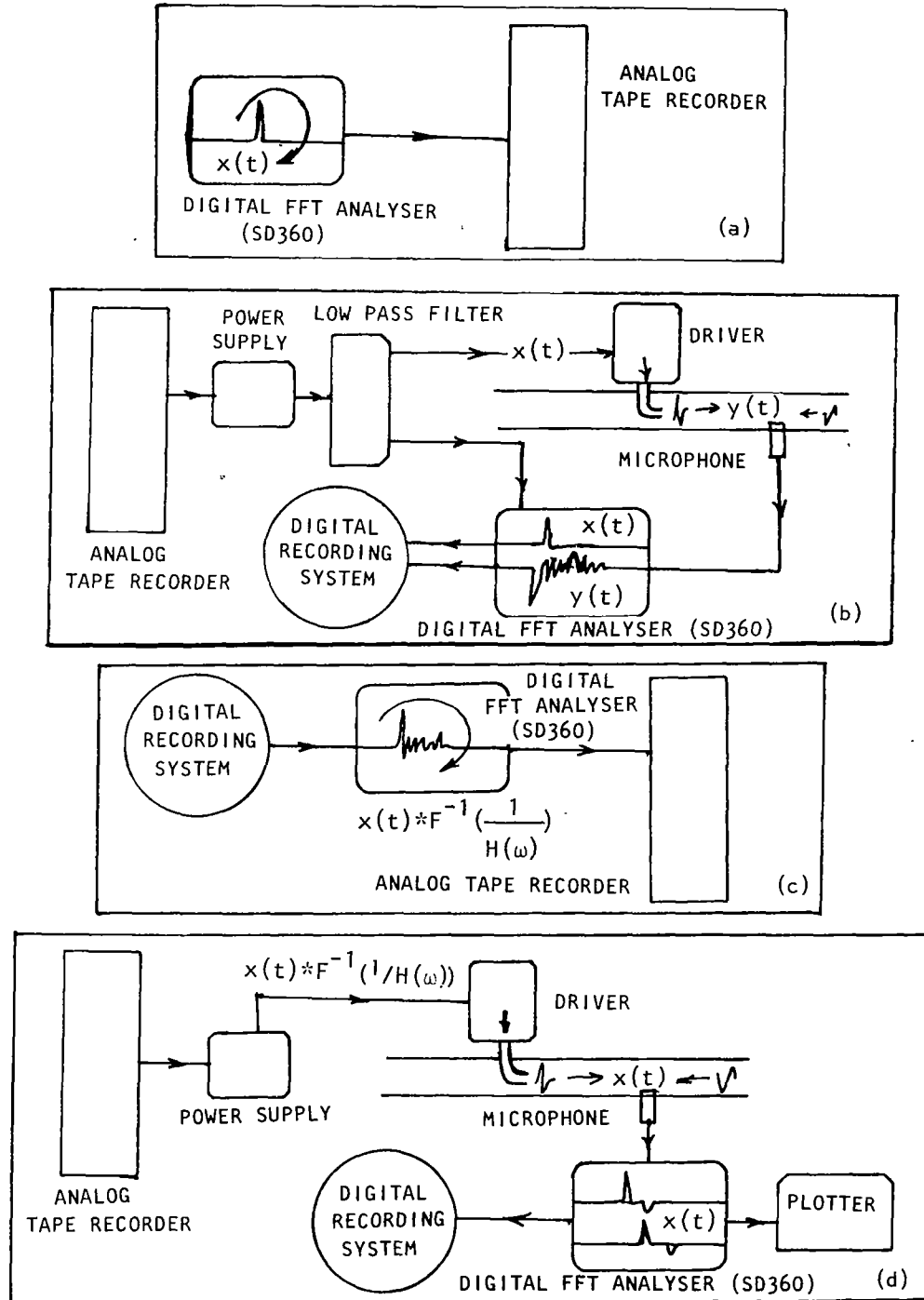


Figure 4.4 Block diagram showing the synthesizing procedure for an acoustic impulse with a loudspeaker driver.

(b) The recorded signal is played back and fed to the driver(s), located in the facility source section, through a power supply. A lowpass filter is used to filter out the high frequency content of the driving signal when desired. The driving signal, $x(t)$, and the output signal of the driver are captured in the FFT analyzer. The reflected part of the output signal is edited out to isolate the output of the driver, $y(t)$. The driving signal, $x(t)$, and the output signal, $y(t)$, are recorded on a magnetic tape. This procedure is illustrated in figure 4.4(b). Then $x(t)$ and $y(t)$ are used to compute the response of the driver, $H(\omega)$, using equation (4.3). Following this, the desired driving signal, $x(t)*F^{-1}(1/H(\omega))$ is computed and recorded on a magnetic tape.

(c) The driving signal is then fed into the FFT analyzer and is rotated with a fixed frequency. The periodic output (i.e., a series of equally-spaced pulses) from the FFT analyzer is recorded on an analog tape recorder.

(d) The recorded signal, $[x(t)*F^{-1}(1/H(\omega))]$, is played back and fed to the driver(s), located in the facility source-section, through a power supply. The output signal of the driver(s) including the reflection of the duct termination is captured in the FFT analyzer. This is illustrated in figure 4.4(d).

4.1.5 Experimental Results

(1) Single Driver in a Single Stream Duct:

Tests were conducted in the test facility shown in figure 4.2 in which an acoustic impulse was synthesized using an arbitrary triangular pulse, $x_1(t)$. The pulse $x_1(t)$ and the corresponding output signal from the driver $y_1(t)$ were used to derive the response of the driver, $H(\omega)$, as follows:

$$H(\omega) = Y_1(\omega)/X_1(\omega) \quad (4.7)$$

A synthesized input signal, $x_2(t)$, was then derived using the response function $H(\omega)$ and the arbitrary triangular signal $x_1(t)$:

$$x_2(t) = x_1(t)*F^{-1}(1/H(\omega)) \quad (4.8)$$

The input signals, $x_1(t)$ and $x_2(t)$, and their corresponding output signals from the driver, $y_1(t)$ and $y_2(t)$, are plotted in figure 4.5. The termination reflections are also present in $y_1(t)$ and $y_2(t)$. Signal $y_1(t)$ contains multiple pulses and is contaminated by reflections from the duct termination. Therefore, the editing process needed to isolate the output signal of the driver from the termination reflection would

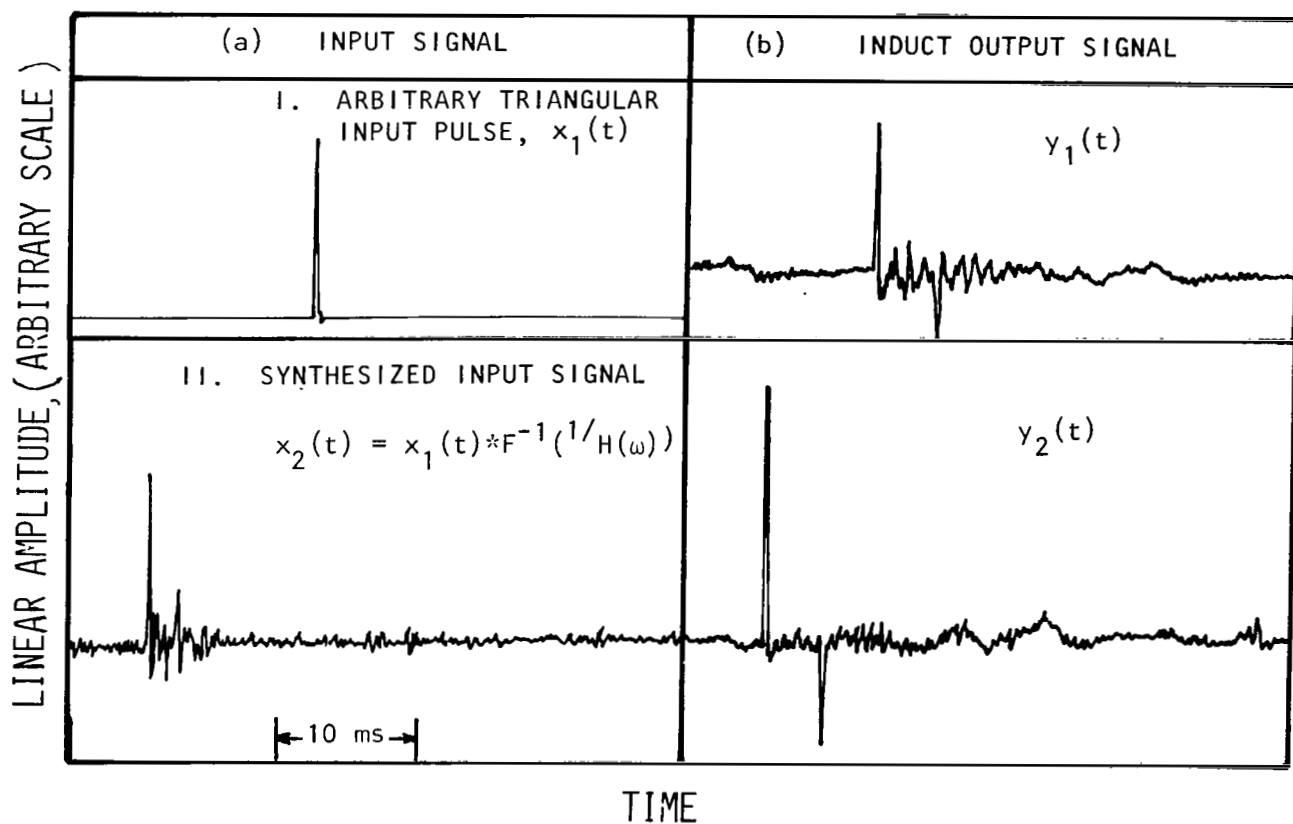


Figure 4.5 Time histories of (a) the input signals to the driver and (b) the corresponding output signals from the driver, including the termination reflections, measured inside the duct.

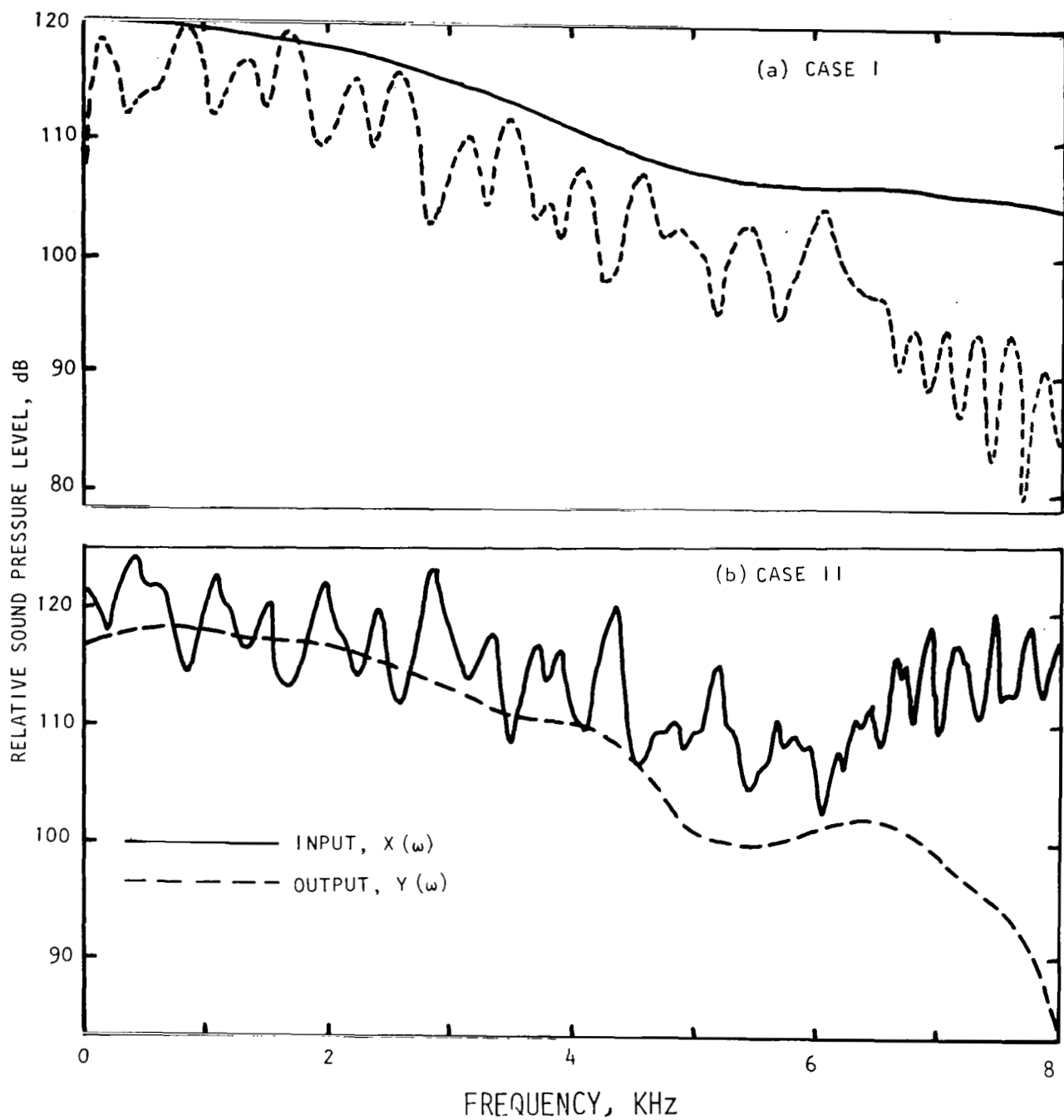


Figure 4.6 Spectra of the driver input and output signals shown in figure 4.5.

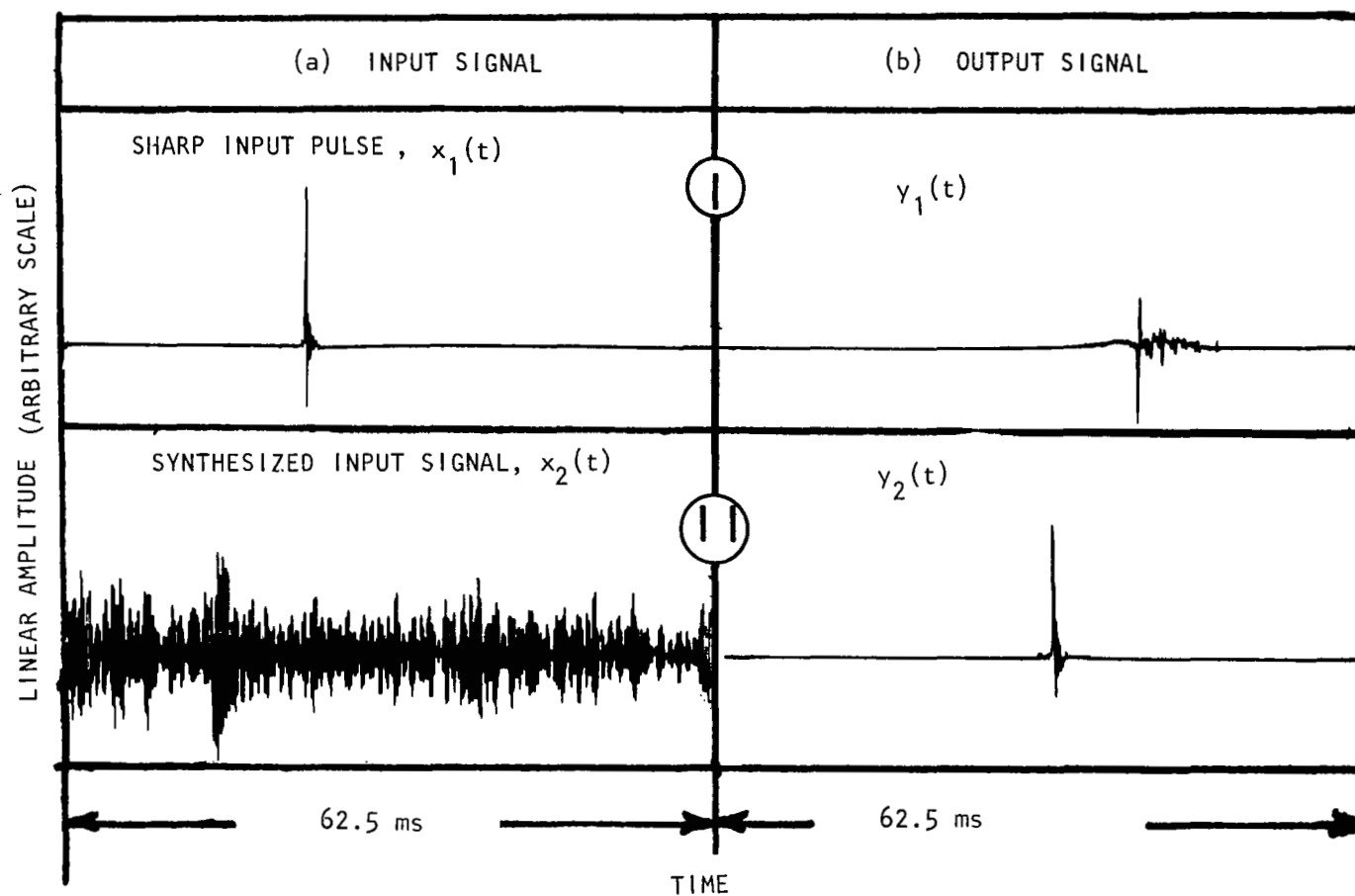


Figure 4.7 Time histories of (a) the input signals to the driver and (b) the corresponding output signals from the driver measured inside the duct.

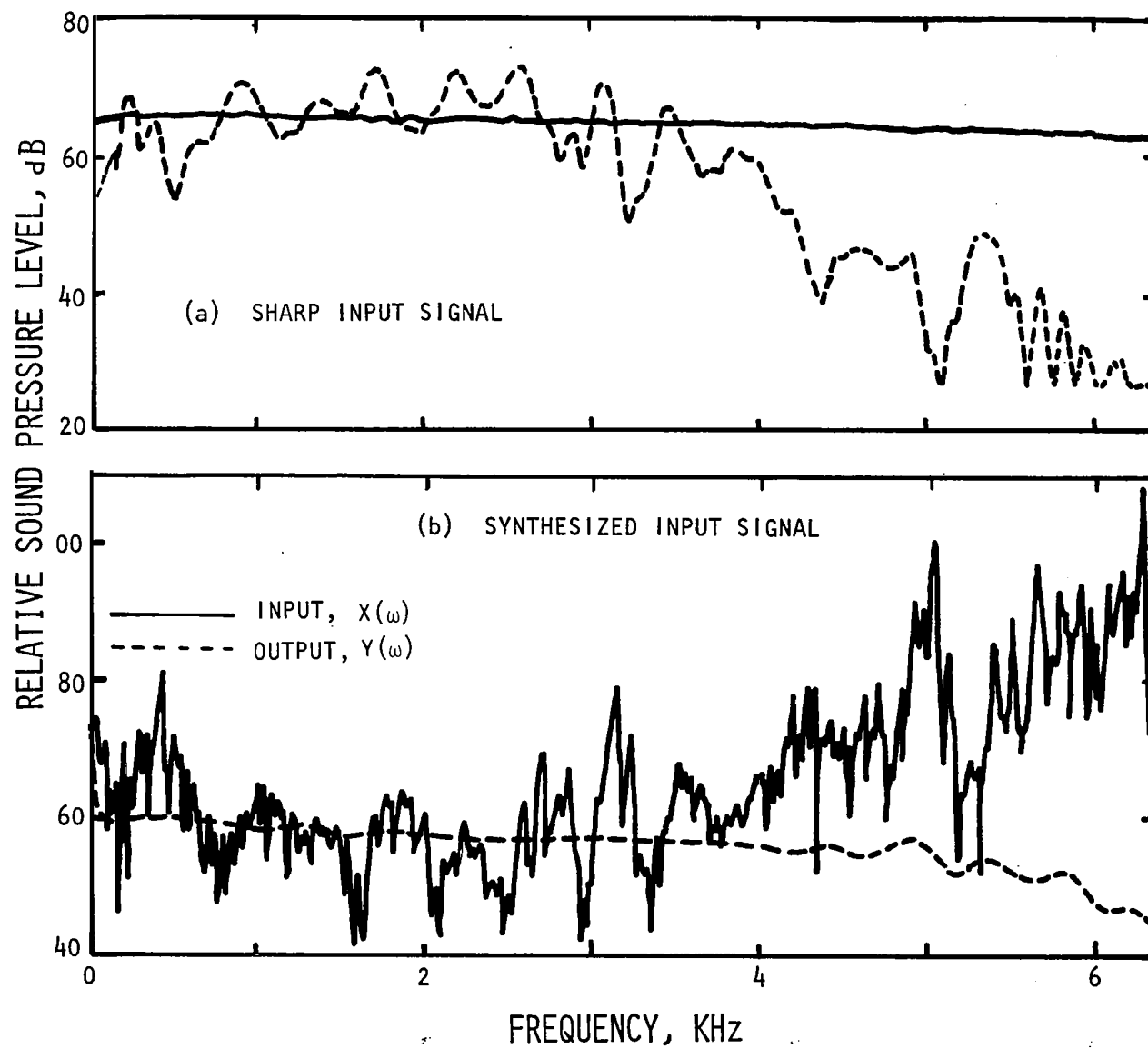


Figure 4.8 Spectra of the driver input and output signals shown in figure 4.7

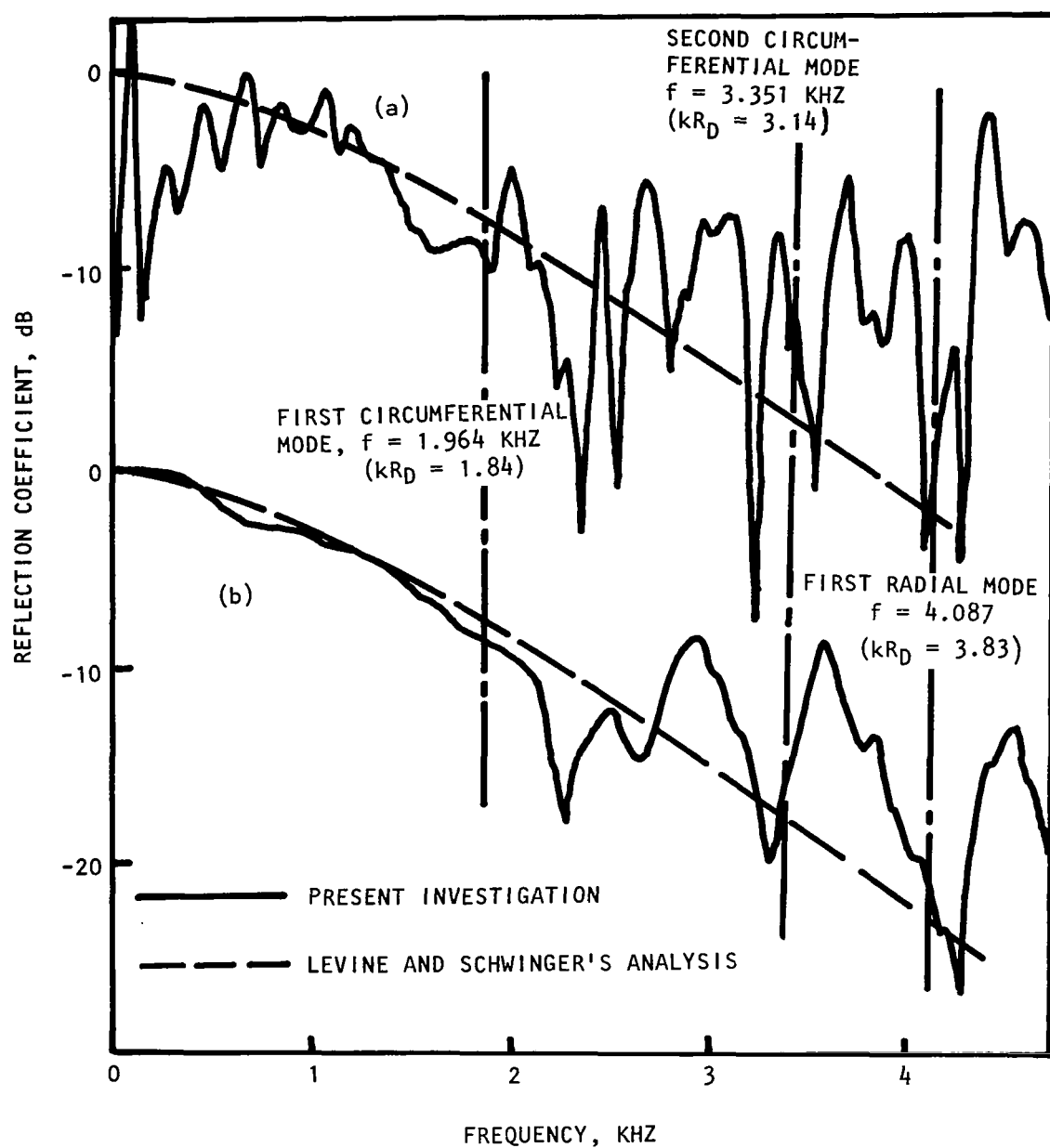


Figure 4.9 Effect of signal synthesis on the reflection coefficient of a straight duct; the induct sound field generated using (a) an arbitrary triangular signal as input to the driver, (b) a synthesized signal as input to the driver.

cause an error in the resulting data. In contrast, an examination of the output signal $y_2(t)$, which is obtained by synthesizing, indicates that the incident pulse (output of the driver) is well separated from the reflected signal. Therefore, the signal can be edited unambiguously.

The spectra of each of the input signals, $x(t)$, and the corresponding output signals from the driver (after editing out the reflections) are plotted in figure 4.6. In spite of the flat characteristics of the input signal spectrum, as seen in figure 4.6(a), the output signal spectrum is not flat, which was expected due to the inherent non-flat frequency response of the driver. However, when the synthesized signal is used as input, the output spectrum is reasonably flat, as seen in figure 4.6(b).

A similar exercise was also carried out to demonstrate that the acoustic driver is also capable of generating a sharp pulse with a flat frequency spectrum by the use of signal synthesis process. In this exercise, a sharp pulse, $x_1(t)$, (i.e., delta function) in place of the triangular pulse was used for the synthesis. The input signals, $x_1(t)$ and $x_2(t)$, and their corresponding output signals from the driver, $y_1(t)$ and $y_2(t)$, similar to those shown in figure 4.5 are plotted in figure 4.7. Unlike the output signals shown in figure 4.5, the termination reflections are removed from the output time histories in figure 4.7. The spectra of each of the input signals, $x(t)$, and the corresponding output signals, $y(t)$, from the driver are plotted in figure 4.8. It can be seen that the spectrum of the final output signal, $y_2(t)$, is almost as flat as the spectrum of the initial input signal, $x_1(t)$. This further established the capability of signal synthesis to generate any desired signal including a sharp pulse (i.e., a delta function) with specific frequency content.

To demonstrate the usefulness of the signal synthesis process, the reflection coefficients of the duct determination were derived by using the induct time histories $y_1(t)$ and $y_2(t)$ of figure 4.5. The reflection coefficients thus obtained from each of the induct signals are presented in figure 4.9 and are compared with the analytical solution of Levine and Schwinger (Ref. 7). Figure 4.9 clearly demonstrates the usefulness of the signal synthesizing procedure by showing good agreement between the results derived using the synthesized signal and the Levine-Schwinger analysis.

(2) Four Drivers in a Single Stream Ducts:

The synthesized signal for a single duct with a single acoustic driver cannot be used where multiple drivers are placed around the flow duct. If the synthesized signal for a single driver system is used to drive the four driver system, the output at the measurement location will not be a single pulse. This is because the response of the four driver system is not the same as that for the single driver system.

Therefore, to obtain a desired single sharp pulse from the four

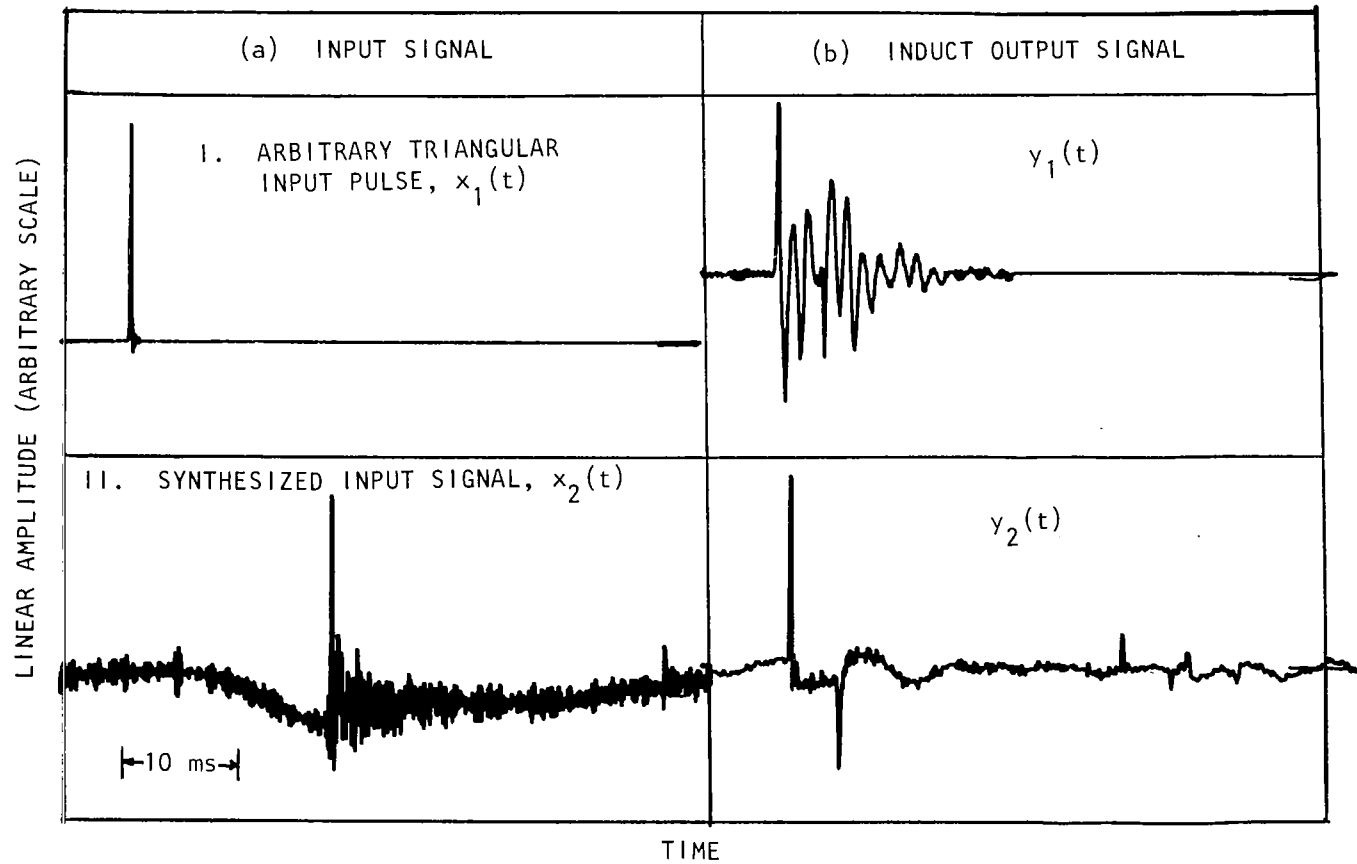


Figure 4.10 Time histories of (a) the input signals to the four driver system used in single stream duct and (b) the corresponding output signals from the driver, including the termination reflections, measured inside the duct.

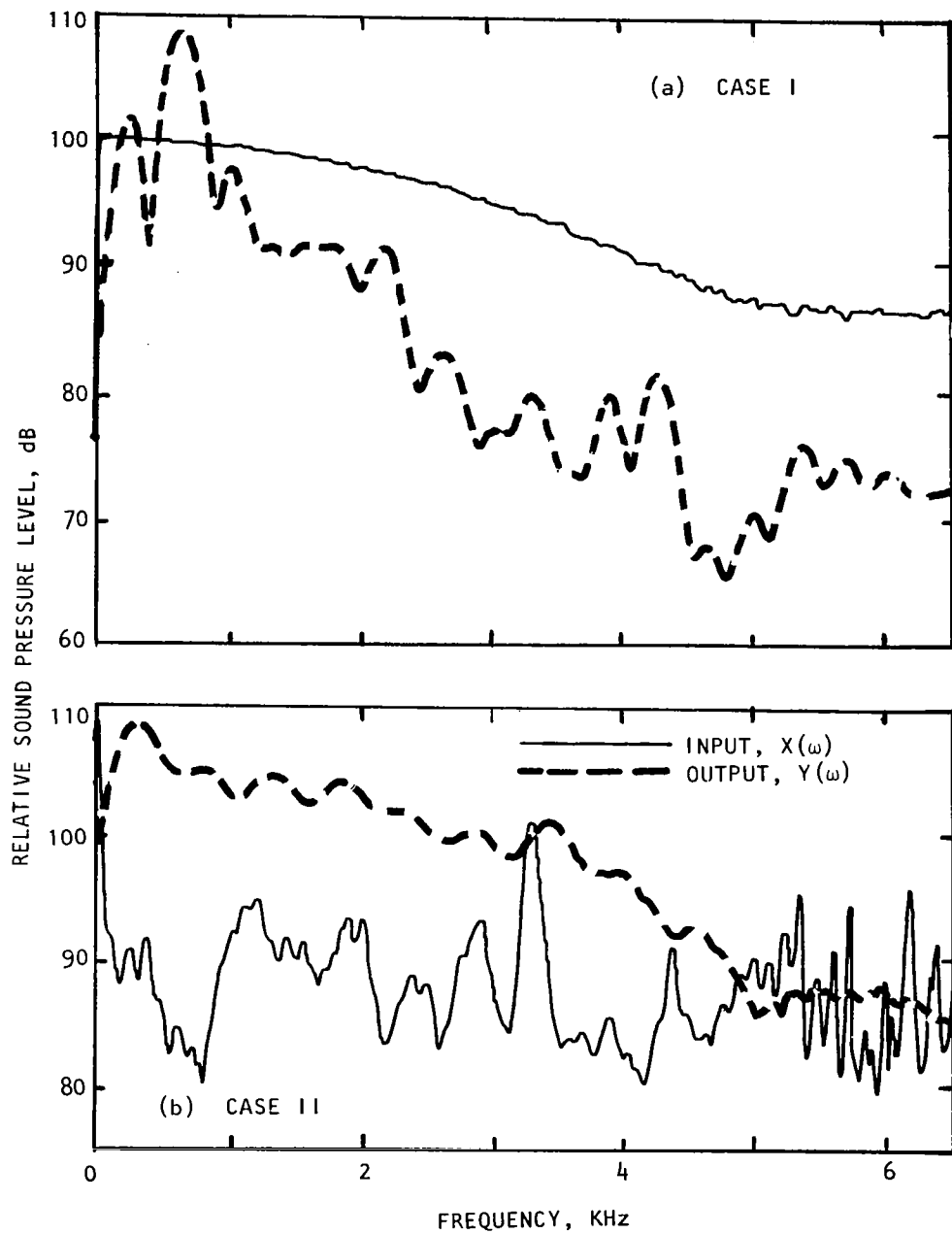


Figure 4.11 Spectra of the driver input and output signals, shown in Figure 4.10, for the four driver system in the single flow duct.

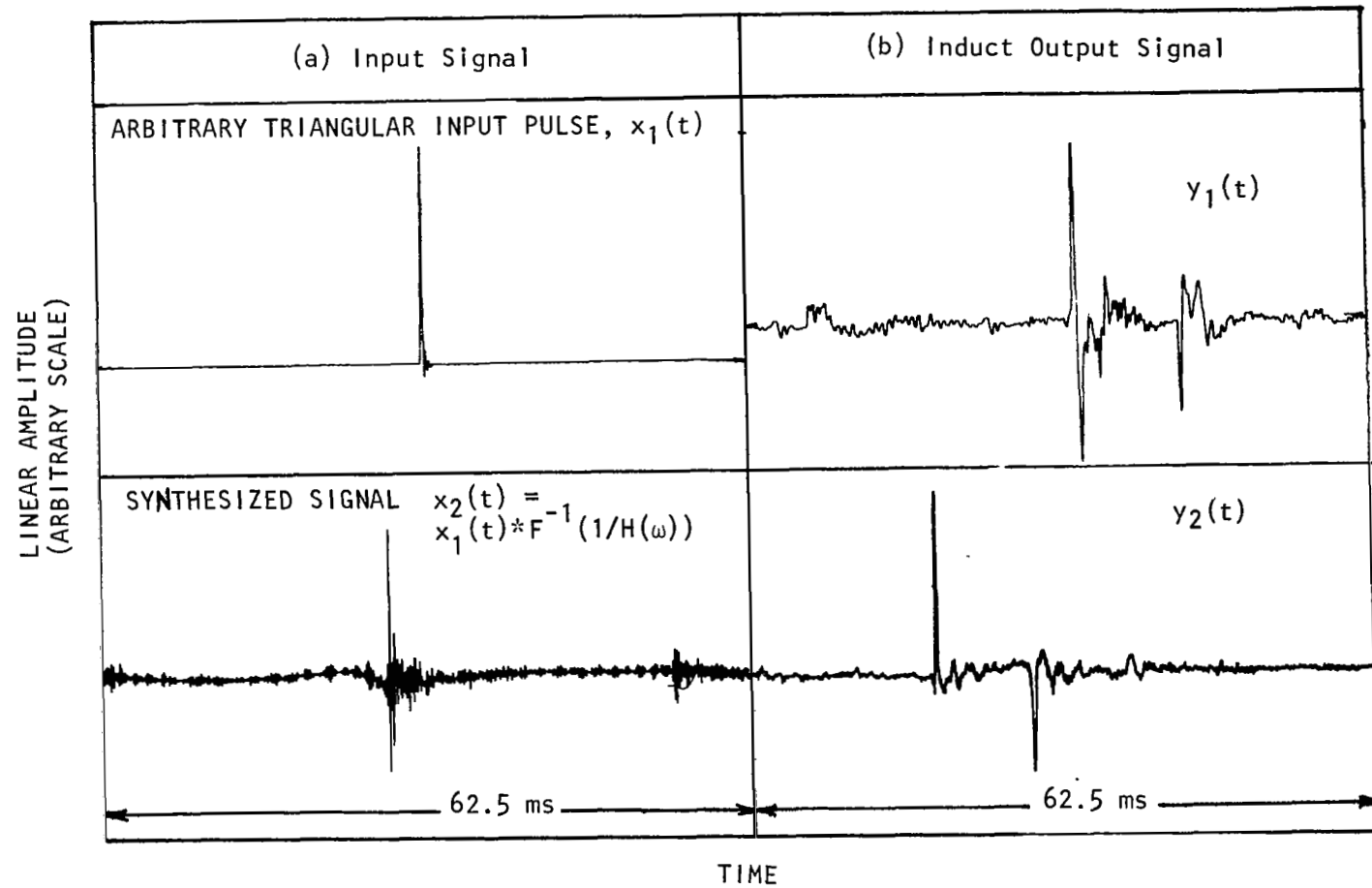


Figure 4.12 Time histories of (a) the input signals to the driver and (b) the corresponding output signals from the driver, including the termination reflections, measured inside the annular cross section of the duct.

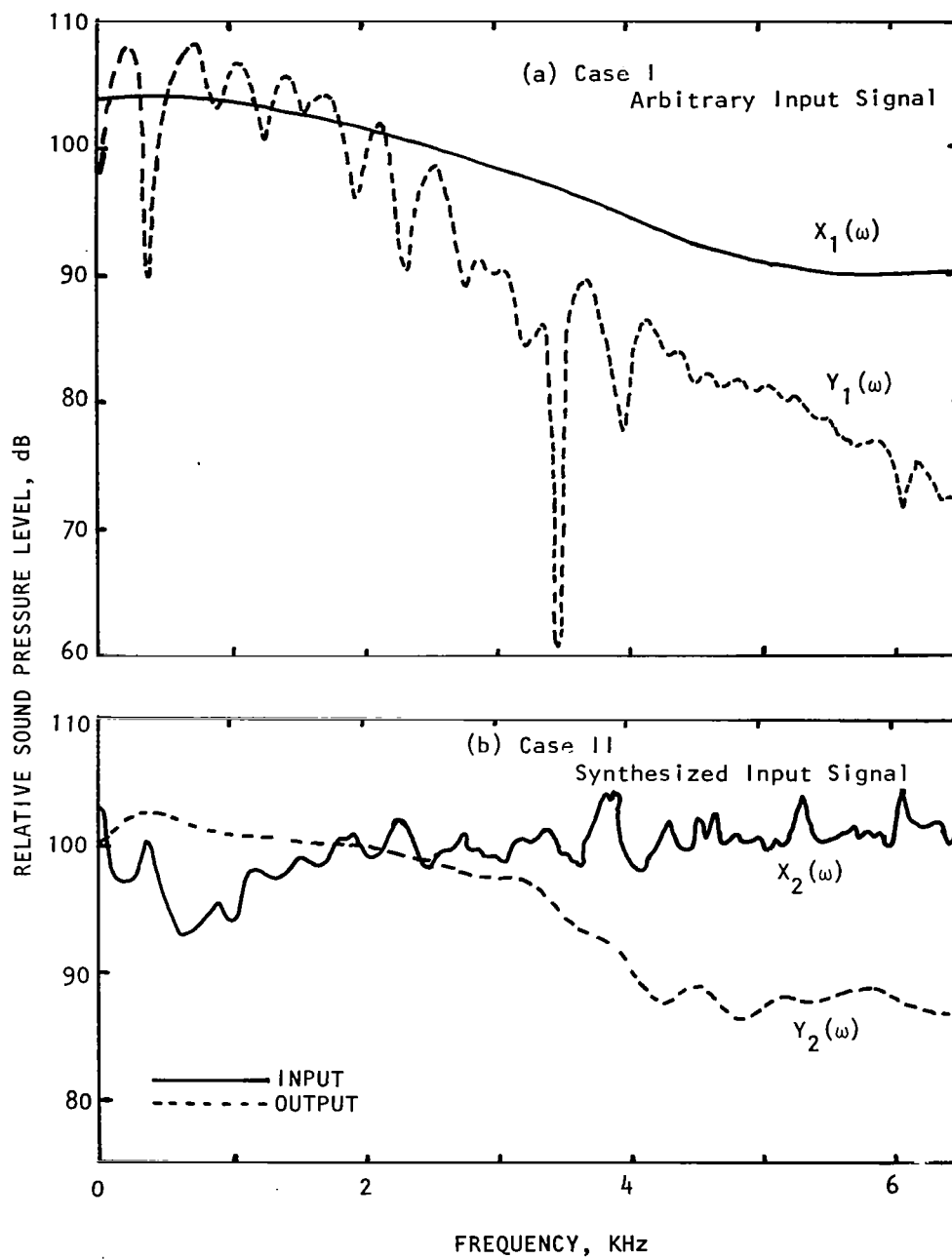


Figure 4.13 Spectra of the input signals to the drivers and the output signals from the drivers for the annular facility (the time histories are shown in figure 4.12)

driver system, the signal synthesis was carried out collectively for the whole system. An arbitrary pulse $x_1(t)$ was used to drive each of the four drivers together. The pulse $x_1(t)$ and the corresponding output signal from the driver system $y_1(t)$ were used to derive the response of the driver system $H(\omega)$. A synthesized input signal, $x_2(t)$, was then derived using the response function $H(\omega)$ and the signal $x_1(t)$.

The input signals, $x_1(t)$ and $x_2(t)$, and the corresponding output signals from the driver system, $y_1(t)$ and $y_2(t)$, are plotted in figure 4.10. The termination reflections are also present in $y_1(t)$ and $y_2(t)$. Signal $y_1(t)$ contains multiple pulses and is contaminated by reflections from the duct termination. However, the incident pulse of the output signal $y_2(t)$, which was obtained by synthesizing the signal; is quite similar to the input signal $x_1(t)$, and is well separated from the termination reflection.

The spectra of each of the input signals and the corresponding output signals (after editing out the reflections) are plotted in figure 4.11. In contrast to the non-flat characteristics of the spectrum of $y_1(t)$, the spectrum of $y_2(t)$ is reasonably flat.

(3) Four Drivers in an Annular Duct:

The signal synthesis process was finally carried out for the annular duct system (see figure 3.3(b)) with four acoustic drivers using an initial arbitrary pulse $x_1(t)$. The input signals, $x_1(t)$ and $x_2(t)$, and the corresponding output signals from the driver system, $y_1(t)$ and $y_2(t)$, are plotted in figure 4.12. The spectra of each of the input signals and the corresponding output signals (after editing out the reflections) are plotted in figure 4.13.

In general, it was observed that the synthesized signals for the four driver systems are not as perfect as the synthesized signal obtained previously for the single driver system. In these situations, the main pulse is followed by other small amplitude pulses. The main reason for this effect is that the assumption of a linear system response is no more valid in the multiple driver case. In other words, the response of one acoustic driver is influenced by the acoustic field generated by another driver. For the single driver case, such a problem was not present. Since the acoustic field was different when the drivers were excited by $x_1(t)$ compared to the acoustic field due to $x_2(t)$, the response of the driver system was different in the two cases. Therefore, the synthesized signal $x_2(t)$, which was evaluated on the basis of a response function, derived using $x_1(t)$ as the input, was not capable of generating the desired signal exactly (i.e., $x_1(t)$) when fed into the drivers. This effect was more apparent for the annular system which was relatively more complex compared to the single duct system.

In spite of the above effects, the shape of the output signal, $y_2(t)$, is reasonably similar to the desired signal $x_1(t)$, and the incident pulse of $y_2(t)$ is clearly separated from the termination reflections.

Therefore, no further attempt was made to improve the synthesis process.

4.1.6 Limitations of Signal Synthesis

(1) The major limitation of the signal synthesis technique arises due to the frequency bandwidth of the acoustic driver. The acoustic driver is incapable of generating sufficient signal levels at frequencies outside its frequency band limits. Therefore, if the signal synthesis is used to generate a signal with a frequency content beyond the driver's frequency band limits, the synthesis procedure fails. This limitation is quite important for zero frequency. From the physics of the acoustic driver it is apparent that the response of the driver at zero frequency is identically zero (i.e. $H(0) = 0$). However, during the process of signal synthesis, due to the residual signal contributions from various electronic equipment used for the purpose, the values of $X_1(0)$ and $Y_1(0)$ come out to be finite (instead of zero). Therefore, if $H(0)$ is not forced to zero in this process, a dominant $X_2(0)$ would be the result and this would completely dominate the synthesized input signal, $x_2(t)$.

(2) Since the response of the driver as well as the response of the duct between the driver and the measurement location change with test condition, a synthesized signal derived for a given test condition to generate a specific signal cannot be used for another test condition. Therefore, for each test condition a separate synthesis is required. However, this limitation is not severe as long as the change in the flow condition is not drastic.

4.2 SIGNAL AVERAGING

4.2.1 Principle of Signal Averaging

Signal averaging is a powerful means of minimizing background noise. In this technique, the signals are sampled at fixed time intervals, converted to digital form and stored at separate locations in a memory. Each memory location corresponds to a definite sample time. The sampling process is continued for a preset number of repetitions. At each repetition the new sampled values are added algebraically to the values already accumulated at the corresponding memory locations. After a given number of repetitions the sum stored in each memory location is equal to the number of repetitions times the average of the samples taken at that point on the desired waveform. A synchronizing signal is used to find the start of each repetition. Such a simple summation process tends to increase the signal-to-noise ratio. The signal portion of the input is a constant for any sample point, and so its contribution to the stored sum is multiplied by the number of repetitions. On the other hand, the noise, which is random and not time-locked to the signal, makes both positive and negative contributions at any point during successive repetitions. Therefore, the noise portion of the stored sum grows slowly as compared to the signal portion.

This qualitative description of the signal averaging technique can also be demonstrated quantitatively by expressing the improvement in the signal-to-noise ratio (S/N) as a function of the number of averages (ref. 15). Let the input be $f(t)$, composed of a repetitive signal portion $s(t)$ and a noise portion $n(t)$. Then

$$f(t) = s(t) + n(t) \quad (4.9)$$

Let the k^{th} repetition of $s(t)$ begin at time t_k (and let $t_1 = 0$). If in each repetition, the samples are taken every T second, then

$$\begin{aligned} f(t_k + iT) &= s(t_k + iT) + n(t_k + iT) \\ &= s(iT) + n(t_k + iT) \end{aligned} \quad (4.10)$$

For a given i and k , $n(t_k + iT)$ is a random variable and can in most practical cases be assumed to have a mean value of zero and an r.m.s. value of say β . And for different k 's the noise samples are usually statistically independent.

Now the signal-to-noise ratio (S/N) for the i^{th} point on any particular repetition can be given by

$$S/N = \frac{s(iT)}{\beta} \quad (4.11)$$

After m repetitions, the value stored in the i^{th} memory location is

$$\begin{aligned} \sum_{k=1}^m f(t_k + iT) &= \sum_{k=1}^m s(iT) + \sum_{k=1}^m n(t_k + iT) \\ &= m s(iT) + \sum_{k=1}^m n(t_k + iT) \end{aligned} \quad (4.12)$$

Since the noise is random and the m samples are independent, the mean square value of the sum of the m noise samples is $m\beta^2$, and the r.m.s. value is $\beta\sqrt{m}$. Therefore, the signal-to-noise ratio after summation is

$$(S/N)_m = \frac{ms(iT)}{\beta\sqrt{m}} = \sqrt{m} (S/N) \quad (4.13)$$

Thus summing m repetitions improves the signal-to-noise ratio by a factor of \sqrt{m} . Thus an enhancement of signal-to-noise ratio by 20 dB (a factor of 10) will require 100 separate repetitions. However, if signal-to-noise ratio is defined in terms of r.m.s. quantities, and not squared quantities, then an enhancement of signal-to-noise ratio by 10 dB (a factor of 10) will require 100 separate repetitions.

4.2.2 Signal Averaging Procedure

The signal averaging experiments were conducted in the anechoic free jet facility using the single stream flow system with a single acoustic driver at the source section (see figure 3.1).

The signal averaging procedure, illustrated in figure 4.14, is carried out in the following manner. A synthesized periodic signal to drive the loudspeaker driver is recorded on an analog tape recorder. The recorded periodic signal is played back and fed to the acoustic driver. The same electronic signal from the tape recorder, that excites the driver, is also used as the triggering (or the synchronizing) signal, which is fed to the real time analyzer (SD-360) along with the actual signal measured in the far-field which is contaminated with jet-mixing noise. Typical time histories of (1) the electronic signal fed to the driver and also used as the triggering signal, (2) the output of the driver, (3) the pure jet mixing noise signal in the far-field, and (4) the impulse signal in the far-field, before and after signal averaging, are shown in figure 4.14.

4.2.3 Effect of Signal Averaging

The following experiments (see Table 4.1) were conducted using three different configurations and various jet Mach numbers.

Table 4.1 Test conditions for signal averaging experiments

CONFIGURATION	JET MACH NUMBERS
1. Straight Duct	0.0, 0.2
2. 6.2 cm Diameter Conical Nozzle	0.0, 0.2, 0.4, 0.6, 0.8, 1.2
3. Daisy Lobe Nozzle with Equivalent Diameter of 6.2 cm	0.0, 0.2, 0.4, 0.6, 0.8, 1.2

Figure 4.15 shows the time histories of the transmitted signal contaminated with jet noise for Mach numbers of 0.6 and 1.2 at various polar angles for the daisy lobe nozzle termination. It is impossible to identify the presence of the transmitted impulsive signal in these plots. However, after signal averaging, the pulses stand out clearly, as shown superimposed in a darker shade over the contaminated signal in figure 4.15. To quantify the effect of signal averaging the following results are presented.

The time histories of far-field signal at the polar angle of 120° , with and without averaging, for the straight duct termination, without any flow, are plotted in figure 4.16(a). The effect of averaging with no flow condition is insignificant. This is to be expected, since the random noise level in the absence of flow is very low. This is further demonstrated in figure 4.16(b), where the sound pressure level spectra

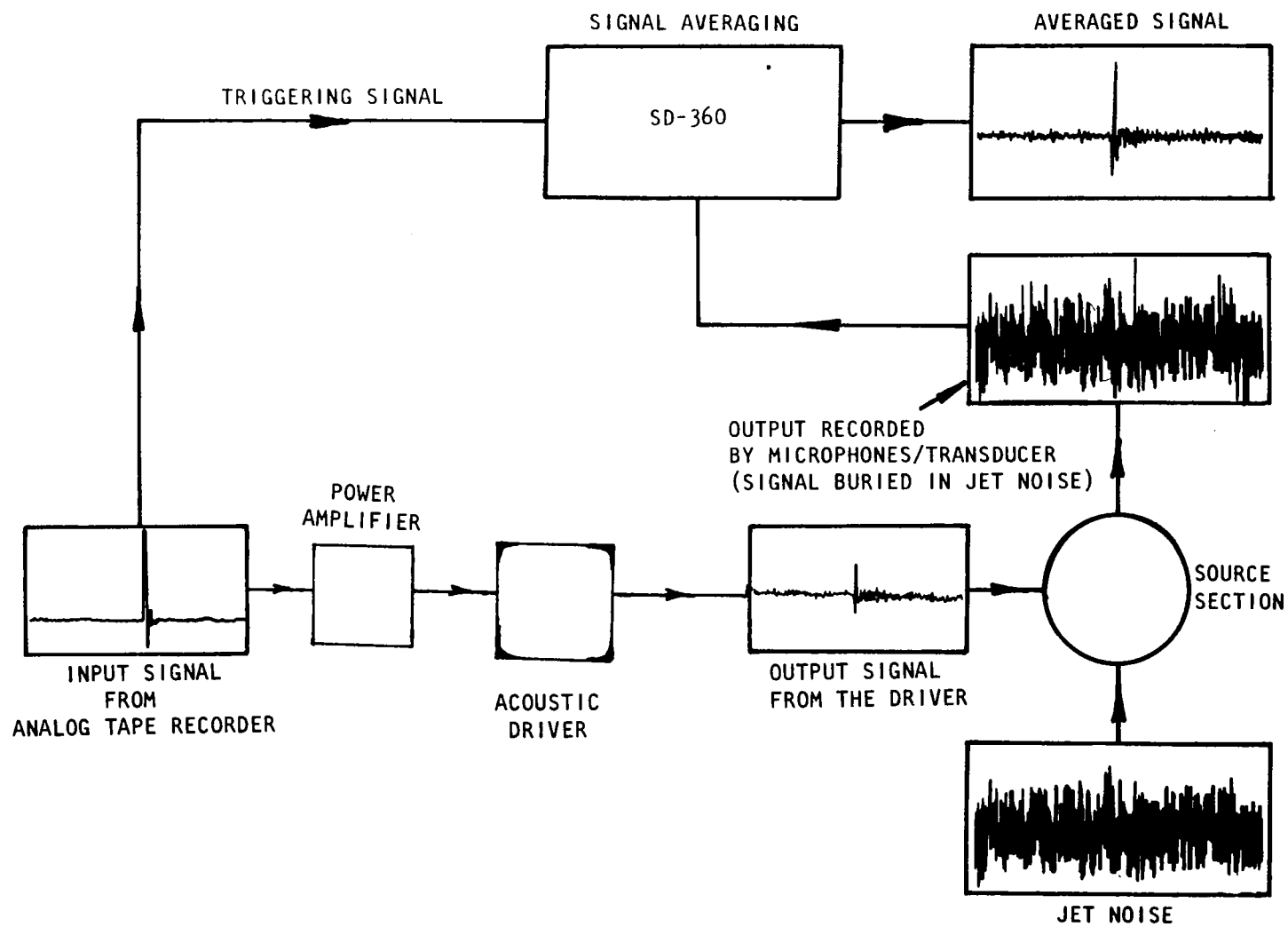


Figure 4.14 Schematic to show the signal averaging procedure.

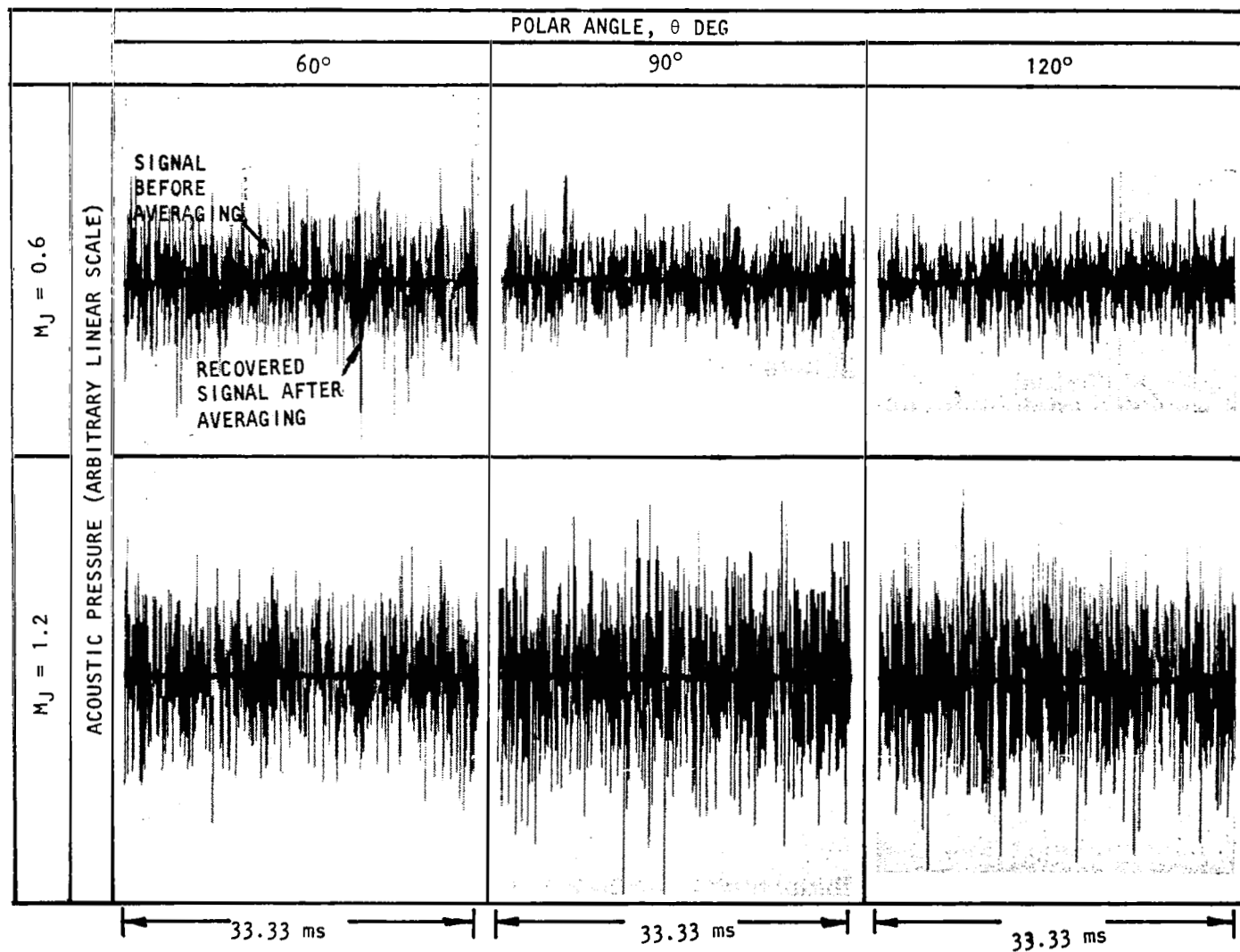


Figure 4.15 Recovery of the pulse from the jet noise by signal averaging process for the daisy lobe nozzle.

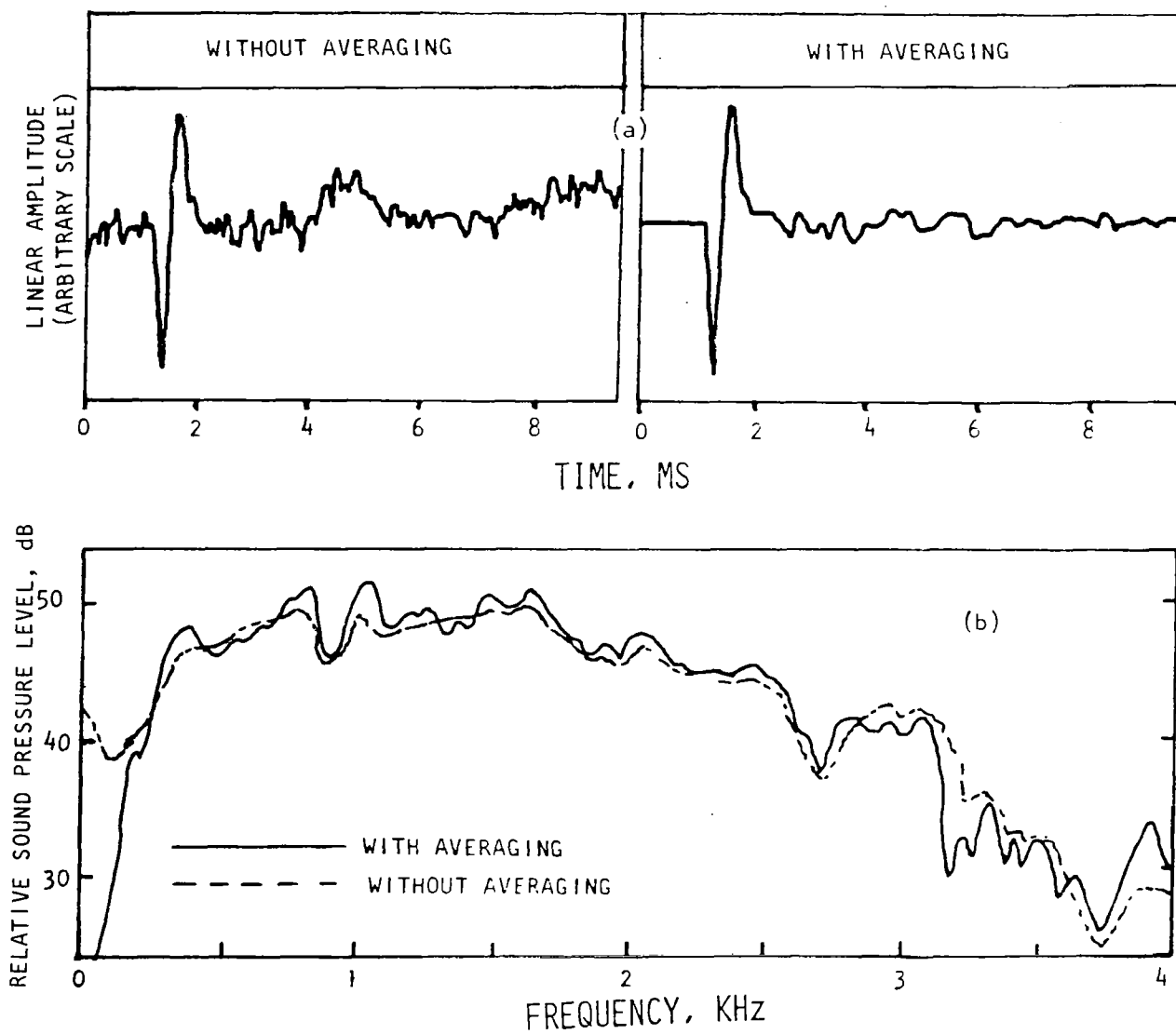


Figure 4.16 The effect of signal averaging on (a) the far-field signal at a polar angle of 120° and (b) its sound pressure level spectrum, for a duct at $M_j = 0$.

of the pulses with and without signal averaging are compared. Figure 4.16(b) shows that the spectra with and without signal averaging are nearly identical. The major difference occurs at very low frequencies where the signal averaging process reduces the random ambient or background noise levels considerably.

The time histories of the far-field signal at the polar angle of 120° , for the straight duct with a flow Mach number of $M_j = 0.2$, are plotted in figure 4.17(a). The effect of signal averaging is very clearly demonstrated in this figure. The signal, though identifiable before signal averaging, was severely contaminated with jet mixing noise. Signal averaging removed most of the jet mixing noise from the contaminated signal. In figure 4.17(b) the corresponding sound pressure level spectra of the pulses with and without signal averaging are compared. The spectrum obtained without signal averaging is considerably different from that obtained with signal averaging. The signal averaging process is shown to reduce the random noise level and to make the spectrum smoother.

4.3 SIGNAL EDITING

The main purpose of signal editing is to remove the unwanted portions of the signals from the total signal time history.

In the sound transmission studies conducted so far using the impulse technique, the transient signals generated by spark discharges were edited in a consistent manner. To explain the editing process applied to the transient signals, it is necessary to describe typical pulses measured inside the duct and in the far field. A typical induct time history, as measured sufficiently upstream of the duct exit, consists of a single sharp incident pulse (compression wave) and a reflected pulse, separated from the incident pulse (see figure 4.18). Before the initiation of the incident pulse and after the completion of the reflected pulse, the transient time history contains nothing but the background noise superimposed on the zero level extensions. As the incident pulse propagates out from the duct to the far field, the pulse shape changes. A typical far-field pulse contains a main compression pulse (similar to the incident pulse) followed by a low amplitude rarefaction pulse. The rest of the far-field time history contains nothing but the background noise (see figure 4.18). In the absence of any background noise, both the induct and the far-field pulses would contain only zero level signals in place of the uniform background noise. These regions of the transient pulse tails are conveniently termed as the "zero level extensions" of the impulsive signals.

The transient signal, either induct or far-field, after being captured in the FFT analyzer, was edited in such a way that only that part of the signal which was of interest could be retained. Also, the low amplitude background noise superimposed on the signal was edited out mostly from the zero level extensions of the impulsive signal. The

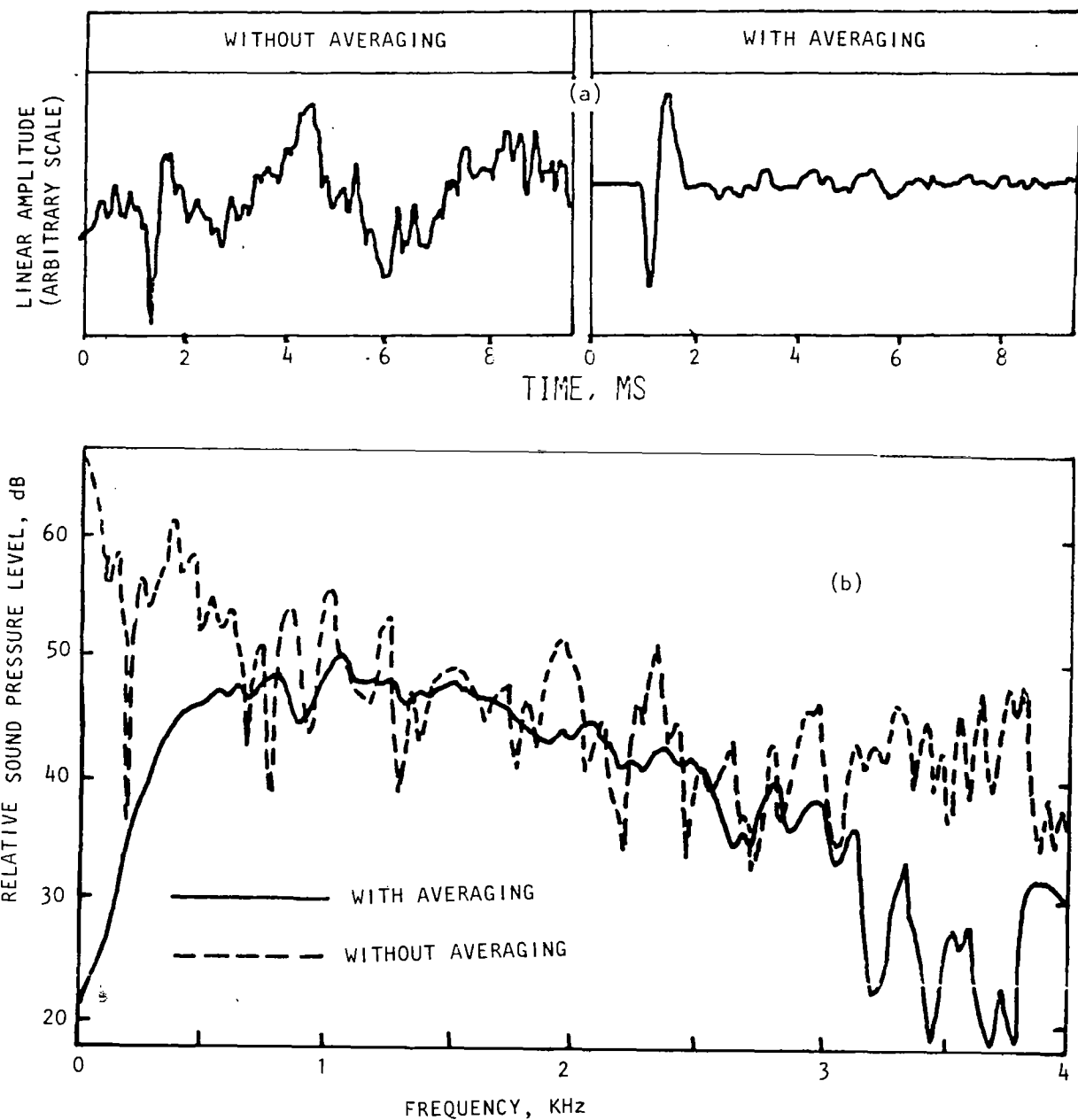


Figure 4.17 The effect of signal averaging on (a) the far-field signal at a polar angle of 120° and (b) its sound pressure level spectrum for a duct at $M_j = 0.2$.

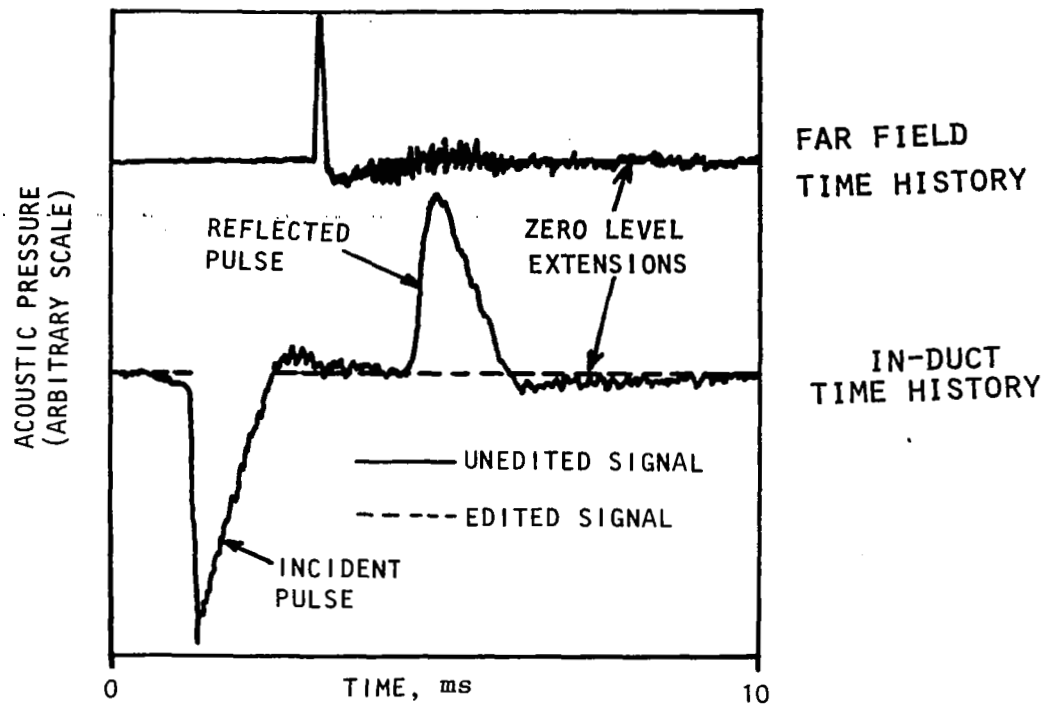


Figure 4.18 Typical induct and far-field time histories generated by spark discharge and an example of editing process used to evaluate the spectral distribution of the incident and the far-field pulses.

effect of such editing was not significant on the spectral distribution of the pulse, since the impulsive sound generated by a spark discharge was very intense compared to the background noise.

On the other hand, when the pulses are generated by an acoustic driver, their intensities are relatively low, and therefore, the editing process could severely influence the spectral distribution of the pulse, especially when the background noise contamination is edited out arbitrarily. Although this problem is mostly eliminated by the signal averaging process, which removes or minimizes the random background noise without affecting the pulse, experiments were conducted for completeness to evaluate the effect of editing on the spectral content of the signal.

In one of these tests, a clean pulse, representative of a typical far-field pulses [shown in figure 4.19(a)], was constructed and its spectral content was evaluated [see figure 4.19(b)]. Then a random noise sample, as shown in figure 4.19(a), was superimposed on the clean pulse. The spectrum of the contaminated pulse is compared with that of the clean signal in figure 4.19(b). It can be seen that, except in the low frequency range where the spectral content of the clean signal is higher than that for the random noise, the spectrum of the pulse at higher frequencies is completely buried in the random noise spectrum.

Attempts were made to remove the background noise from the contaminated signal by various editing procedures. Three distinct editing stages are illustrated in figure 4.20(a). In the first stage, the main pulse was left as it was and the rest of the signal was cleaned. In the second stage, the low amplitude rarefaction wave of the signal was partially edited, and finally, in the third stage, the low amplitude rarefaction wave was completely removed.

The spectral contents of each of these edited signals are compared with those of the clean signal in figure 4.20(b). At higher frequencies the spectra from each of the edited signals are considerably different from that of the clean signal. This indicates that the contamination of the main pulse itself contributes considerably to the spectral contents of the signal at higher frequencies. The removal of rarefaction pulse, affects the spectral content only in the very low frequency range.

This exercise indicates that, in general, editing of single (as opposed to averaged) pulses is not a suitable means to recover the signal from the background noise when the signal-to-noise ratio is low. Instead, it is better to use the signal averaging process, which is a very powerful means to eliminate the background noise successfully. This is illustrated again in figure 4.21. The clean pulse and the recovered pulse after signal averaging are shown in figure 4.21(a). The comparison between the spectral content of the clean pulse and the recovered pulse is shown in figure 4.21(b), which shows a very good agreement between the two. In some cases, even after many averages, the zero level extensions of the pulse may still be slightly contaminated

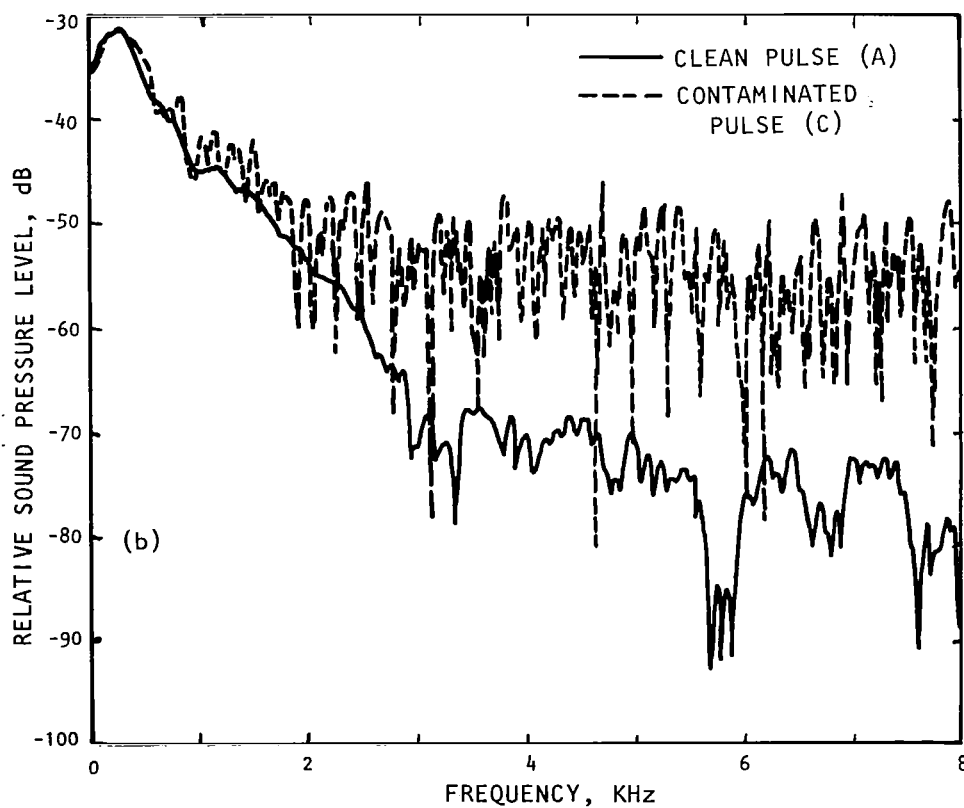
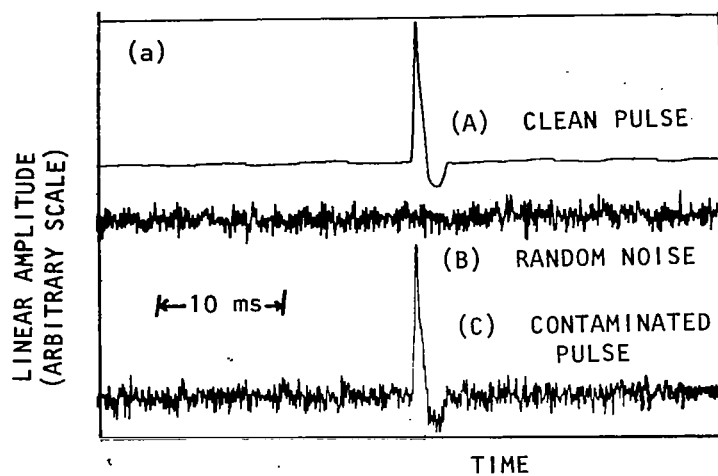


Figure 4.19 Effect of random noise contamination; (a) on the time history of a clean pulse, and (b) on its sound pressure level spectrum.

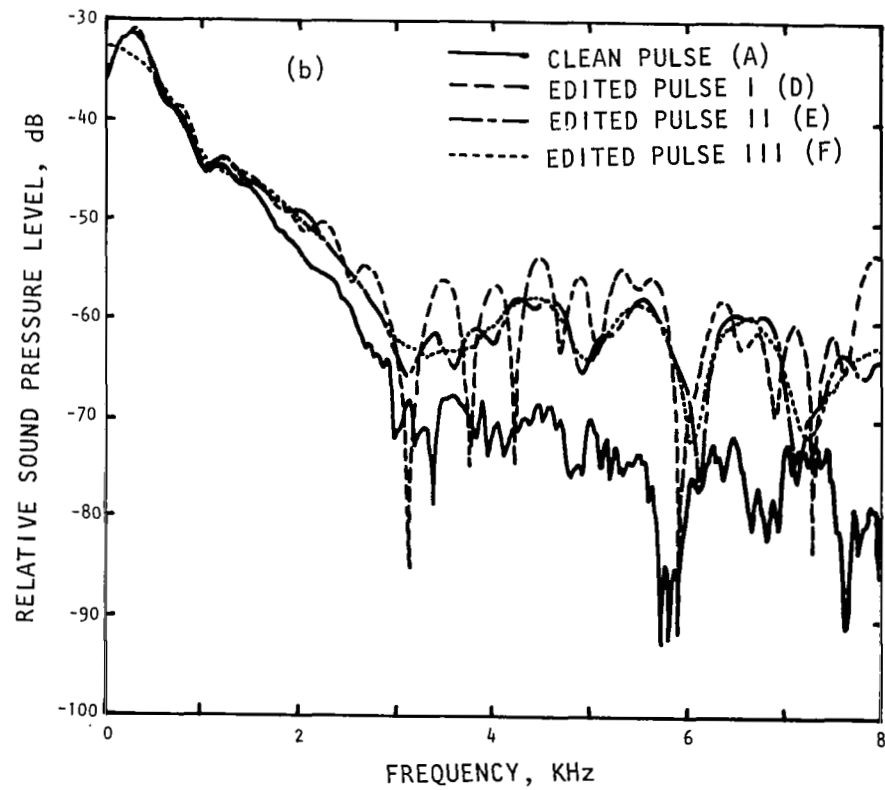
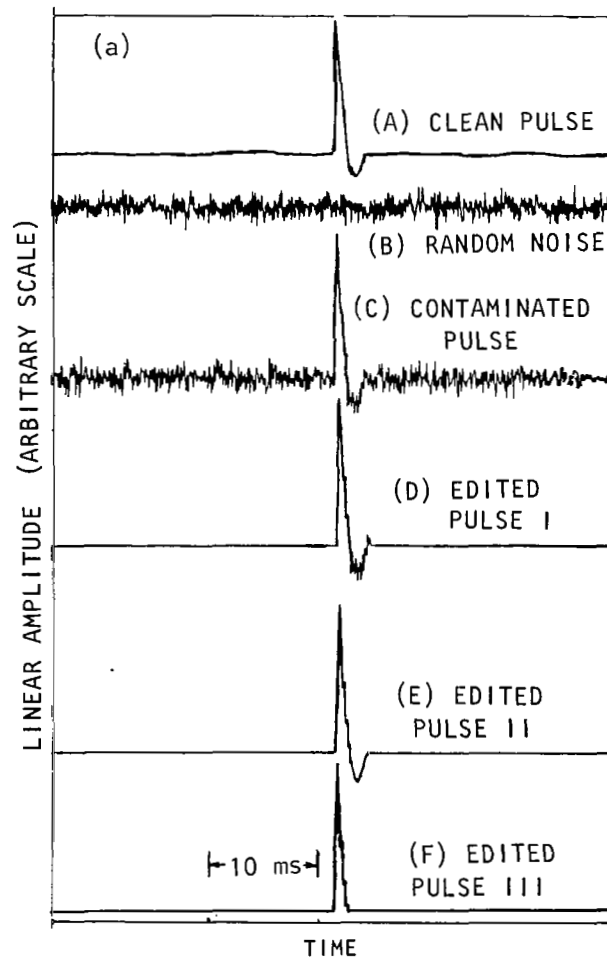


Figure 4.20 Effect of signal editing process; (a) on the pulse time history and (b) on the sound pressure level spectrum of the pulse.

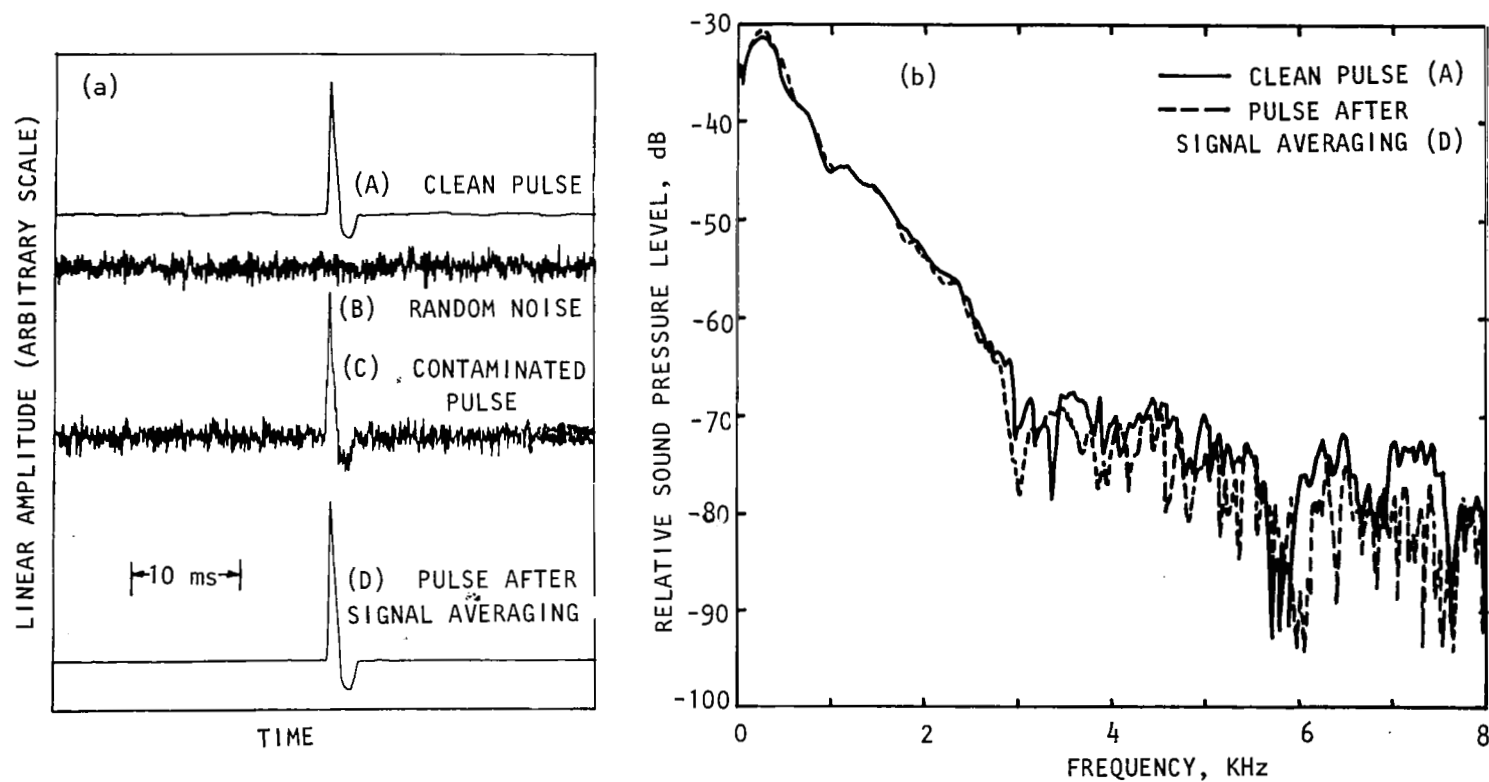


Figure 4.21 Effect of signal averaging; (a) on the pulse time history and (b) on the sound pressure level spectrum of the pulse.

with jet mixing noise or electronic system noise. In such situations, to get a smooth spectral distribution, the editing process is simply used to zero out the extensions of the pulse. This editing process does not affect the spectral content of the pulse.

4.4 SPECTRAL AVERAGING

4.4.1 Objective and Procedure of Spectral Averaging

Whereas signal averaging is required to eliminate or minimize background noise, it is quite possible that multiple spectral averaging for a single test configuration would improve the statistical accuracy and would smooth the spectral results. This aspect has been studied by conducting a series of experiments with different jet Mach numbers for a 6.2 cm diameter conical nozzle connected to a 10 cm diameter duct. In this study, the spectral data of several averaged signals for a fixed flow condition were evaluated. Then these data were utilized in spectral averaging, using a computer.

The spectral averaging procedure is quite simple. The spectral data for a test condition are evaluated several times using different analog time domain data. These spectra are arithmetically summed for each frequency point and an average spectrum is thus computed. Mathematically, this is represented by

$$\bar{F}(f) = \frac{1}{N} \sum_{i=1}^N F_i(f) \quad (4.14)$$

where $F_i(f)$ are the spectral levels in linear scale (not in dB) at frequency f for $i=1,2,---,N$, and $\bar{F}(f)$ is the averaged value at frequency f , evaluated using N number of individual spectral data. Therefore, any random variation in $F_i(f)$ would be smoothed out due to this summation procedure.

4.4.2 Effect of Spectral Averaging

Figure 4.22 illustrates the effect of spectral averaging on far field sound pressure level spectra at polar angle of 90 degrees for a 6.2 cm diameter conical nozzle with jet flow Mach numbers of 0.6 and 0.8. The effect of spectral averaging on these spectra seems to be very small, even after six averages. From this studies it can be concluded that spectral averaging is no more necessary to improve the statistical accuracy of the spectral results when identical pulses are generated (as in the present study) and are averaged in the time domain to remove the random noise.

4.5 NUMERICAL SMOOTHING

4.5.1 Objective and Procedure of Numerical Smoothing

The spectral distribution of the various transmission parameters,

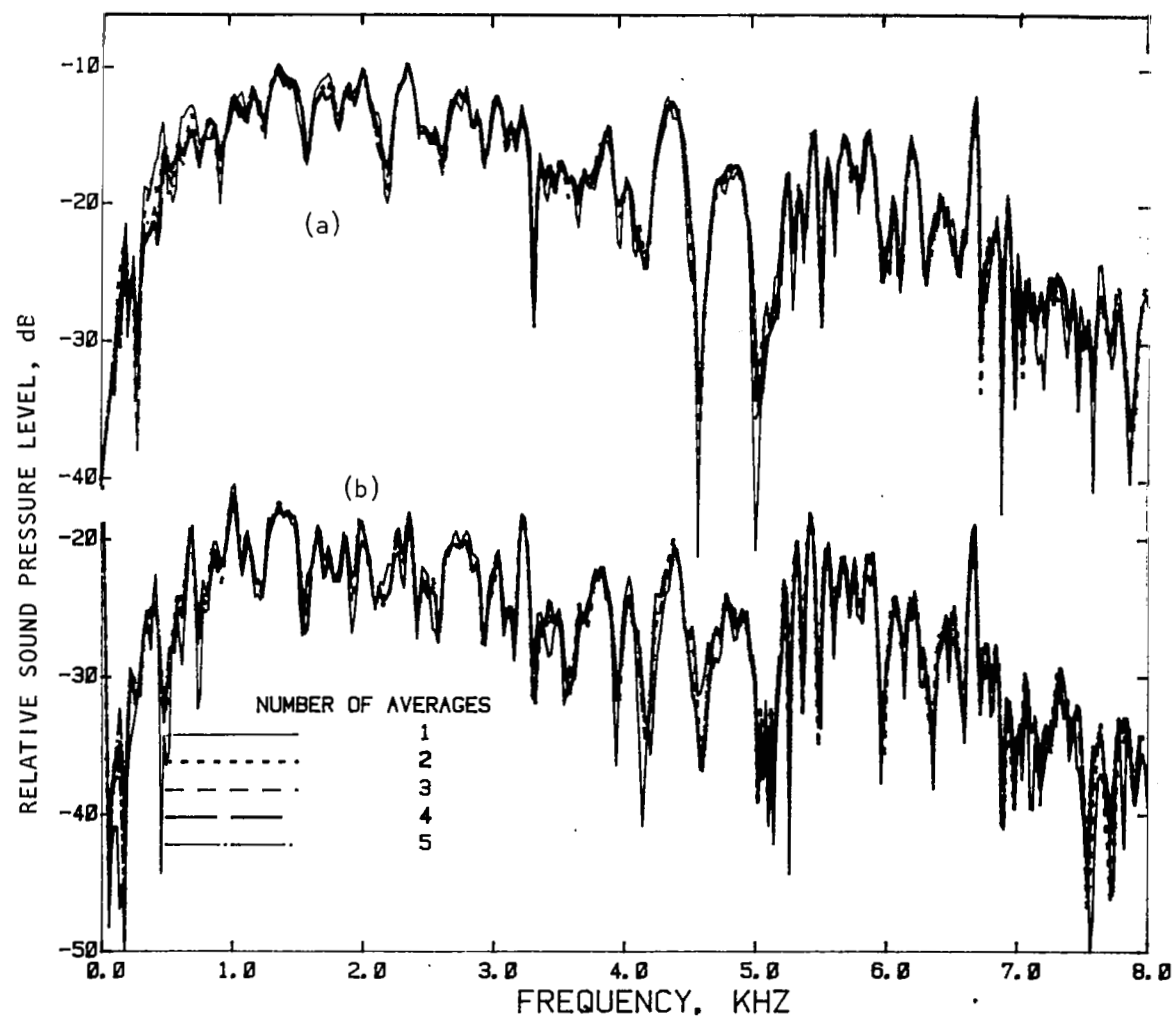


Figure 4.22 Effect of spectral averaging on sound pressure level spectrum for a 6.2 cm diameter conical nozzle at polar angle of 90 degree, and with jet Mach numbers of (a) $M_J = 0.6$; (b) $M_J = 0.8$.

for example, the reflection coefficient and the far field sound pressure levels, as derived from the induct and far field signals, are "noisy" in nature and this behavior is particularly dominant in the higher frequency range, instead of being smooth throughout the frequency range. With this situation it is difficult to distinguish between the effects of various parameters, such as flow velocity and nozzle shape, on the corresponding sound pressure level spectra. Therefore, instead of using the "noisy" sound pressure level spectra as derived, it is quite possible to utilize some type of numerical averaging procedure to smooth the spectral results. This aspect has been discussed in reference 6. However, the basic procedure is outlined in this section.

The numerical averaging (or smoothing) technique used in this study is illustrated as follows. The smoothed value of the function (power spectra or reflection coefficient spectra) F , at the I^{th} frequency point is given by

$$\bar{F}(I) = \frac{F_1(I)}{X_{I+m} - X_{I-m}} \quad (4.15)$$

where

$$F_1(I) = \frac{H}{3} \{F(I-m) + 4F(I-m+1) + 2F(I-m+2) + 4F(I-m+3) + \dots + 2F(I+m-2) + 4F(I+m-1) + F(I+m)\} \quad (4.16)$$

X_I = coordinate of I^{th} frequency point,

H = difference between the coordinates of two successive points

$2m+1$ = number of points used for averaging

Let

$$n = 2m+1$$

The smoothing procedure can be repeated several times and the number of data points n , used for averaging can also be altered. By increasing the number of data points n , and/or increasing the number of averages keeping the number of data points fixed in this smoothing process, the spectrum becomes smoother. However, by using a large number of points in the smoothing technique, minor details of the spectral distribution are lost. Therefore, depending on the type of information needed, the number of data points to be used in smoothing should be selected accordingly. One also reaches a similar conclusion when the number of averages is increased keeping the number of data points fixed.

4.5.2 Effect of Numerical Smoothing

The number of points n , for the numerical smoothing utilized in the present study, has been taken to be 11 and the process is repeated three times (three averages). In this study the difference between two successive frequency points is 20 Hz (bandwidth).

Figure 4.23 illustrates the effect of numerical smoothing on far field sound pressure level spectra for a 6.2 cm diameter conical nozzle at polar angle of 90 degrees with jet flow Mach numbers of 0.6 and 0.8. It can be clearly seen that the numerically smoothed spectral data represent an overall distribution of the spectral behavior. Since larger fluctuations in the spectral distribution are eliminated by numerical smoothing such a representation is useful when the data for different flow conditions or configurations are to be compared.

4.6 LIMITATIONS AND GUIDELINES FOR SIGNAL AVERAGING

4.6.1 Limitations for Signal Averaging

Implicit in signal averaging technique is the assumption that the pulse waveforms from sample to sample are identical, or nearly so, and that the time reference for signal averaging is constant, thus ensuring proper pulse enhancement. So far as the pulse waveforms are concerned, they are very much alike since the driver is periodically excited by the same signal. So far as the propagation time of the pulse is concerned, the pulse propagates through the turbulent jet flow medium before reaching the far-field microphones. Thus, small variations in the propagation speed are possible and pulse times of arrival with respect to the reference signal may exhibit some "jitter". However, within the frequency range (i.e. 8 KHz) of the present experiments, the small variation in the propagation time of successive pulses was found to be insignificant to cause any jitter problem. On the other hand, when the study requires a higher frequency range, the jitter problem may be significant.

4.6.2 Guidelines for Signal Averaging

The guidelines for the signal averaging technique can be established by determining the number of averages needed to acquire accurate data since the signal-to-noise ratio improvement is proportional to the square root of the number of impulse samples averaged. For completeness this theory has been experimentally verified. In this experiment, white noise of a certain r.m.s value was averaged in the time domain by different number of averages using a periodic pulse as the triggering signal. The plot between Log_{10} (r.m.s value of the white noise) and Log_{10} (number of averages) is a straight line with a slope of $-1/2$ (see figure 4.24) which agrees with the above theory, (i.e., for example, 100 averages reduce the noise level by 10 dB). For different samples of white noise with different initial r.m.s values, similar plots can be generated with the same slope.

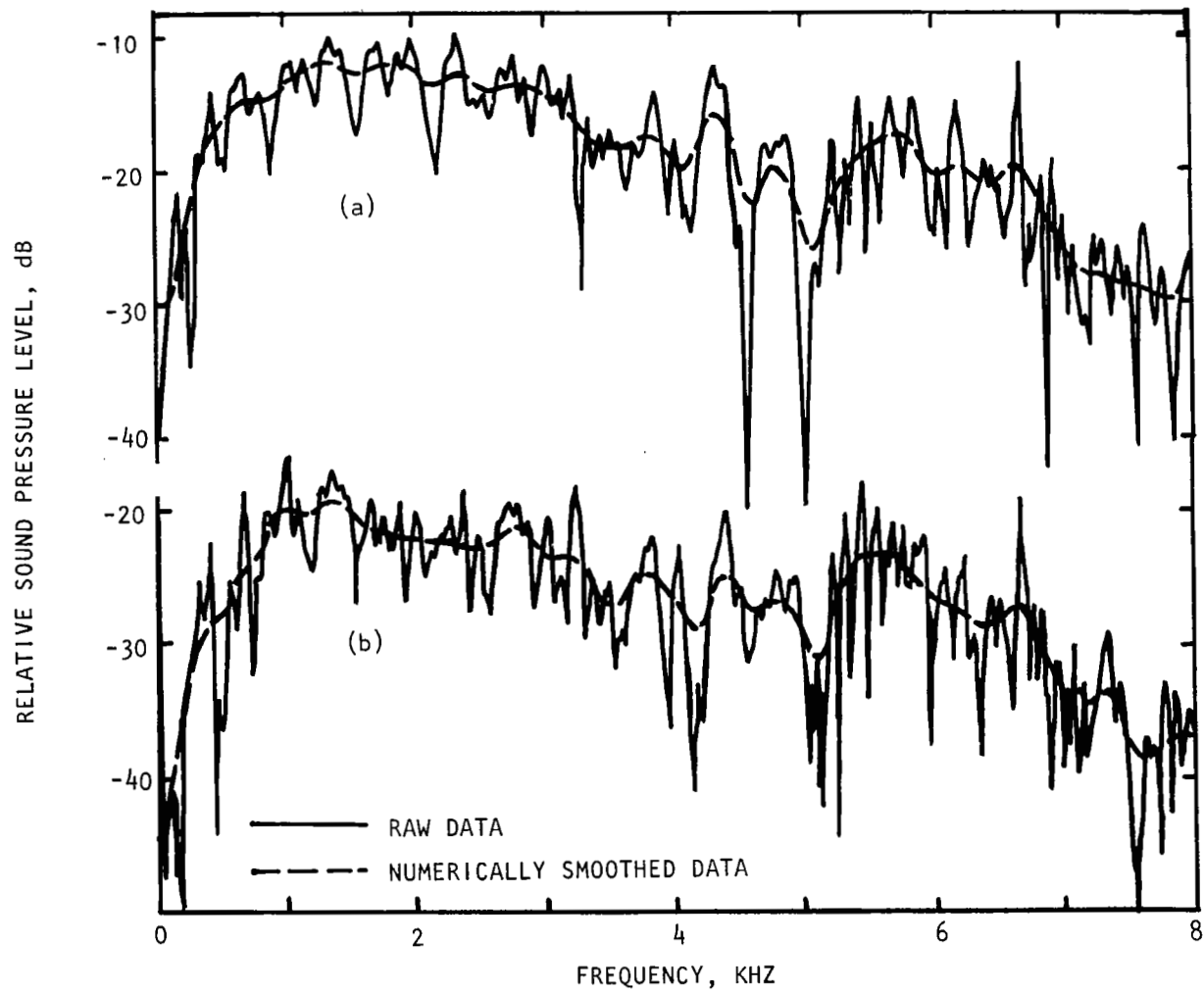


Figure 4.23 Effect of numerical smoothing on sound pressure level spectrum for a 6.2 cm diameter conical nozzle at polar angle of 90 degree, and with jet Mach numbers of (a) $M_J = 0.6$, (b) $M_J = 0.8$.

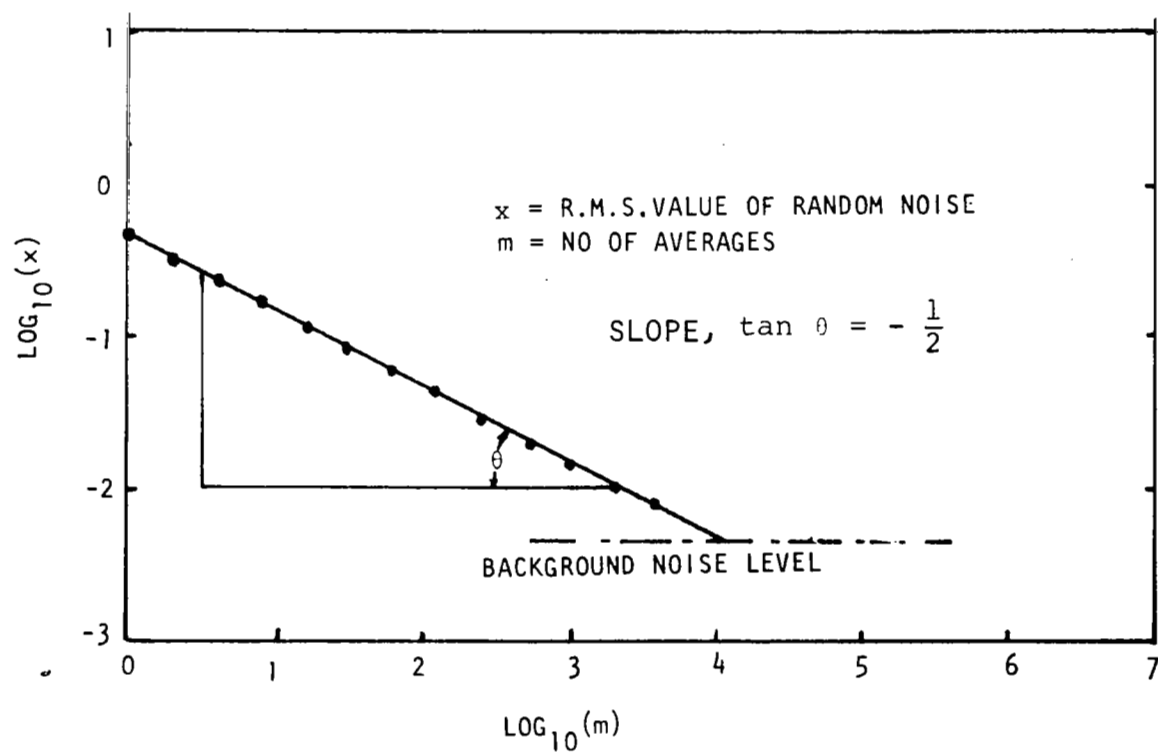


Figure 4.24 Effect of number of signal averages on the r.m.s. value of random noise with an initial fixed r.m.s. level.

Therefore, to determine the number of averages needed for a particular flow condition, it is necessary to find out the r.m.s level of the flow noise in the absence of internal signal (i.e. impulse in this case) and the r.m.s. value of the background noise. Using these two r.m.s. values the number of averages needed to recover the signal up to the level of background noise can be determined either from the plot shown in figure 4.24 or by using the following relationship.

$$\sqrt{m} = \frac{\text{r.m.s value of the flow noise}}{\text{r.m.s value of the background noise}} \quad (4.17)$$

where m is the required number of averages. The background noise in this case is referred to the instrumentation noise inherent with the system. In some situations, the internal signal may be an integral part of the flow noise. For example, in an actual aircraft engine the internal noise is generated due to various components of the running engine. In this case the r.m.s. value of the mixed noise can be used in equation (4.17) instead of flow noise. The number of averages thus determined will be higher than the required number of averages.

The equation (4.17) provides the number of signal averages required to recover a signal to the maximum possible extent from the contaminating noise. However, in practice, one may not use that many averages for the signal recovery. Most of the noise is eliminated by using a very few averages, since the signal recovery is very rapid during the initial signal averaging process and then the recovery process slows down considerably. Therefore, it is possible to recover the signal with insignificant amount of contamination by applying a smaller number of signal averages than that predicted by equation (4.17).

This behavior is demonstrated below by applying different number of averages to a signal generated by superimposing white noise on a train of sharp pulses repeated with a fixed time interval. In this example, the spectral content of the white noise was much higher than that of the pulse (see figure 4.25). Since the spectral distribution of the white noise sample was not smooth, the spectra for both the white noise and the pulse were numerically smoothed and are presented in figure 4.26 for a better visual display. Then the highly contaminated signal was averaged by different number of averages. The corresponding spectral distributions (numerically smoothed) are shown in figure 4.27. It is remarkable that after 64 averages the spectral distribution of the signal is quite close to that of the clean signal. However, the final recovery is achieved after averaging the contaminated signal by 4096 times.

The guidelines for signal averaging, as established above for hypothetical conditions, were then followed to recover the induct and

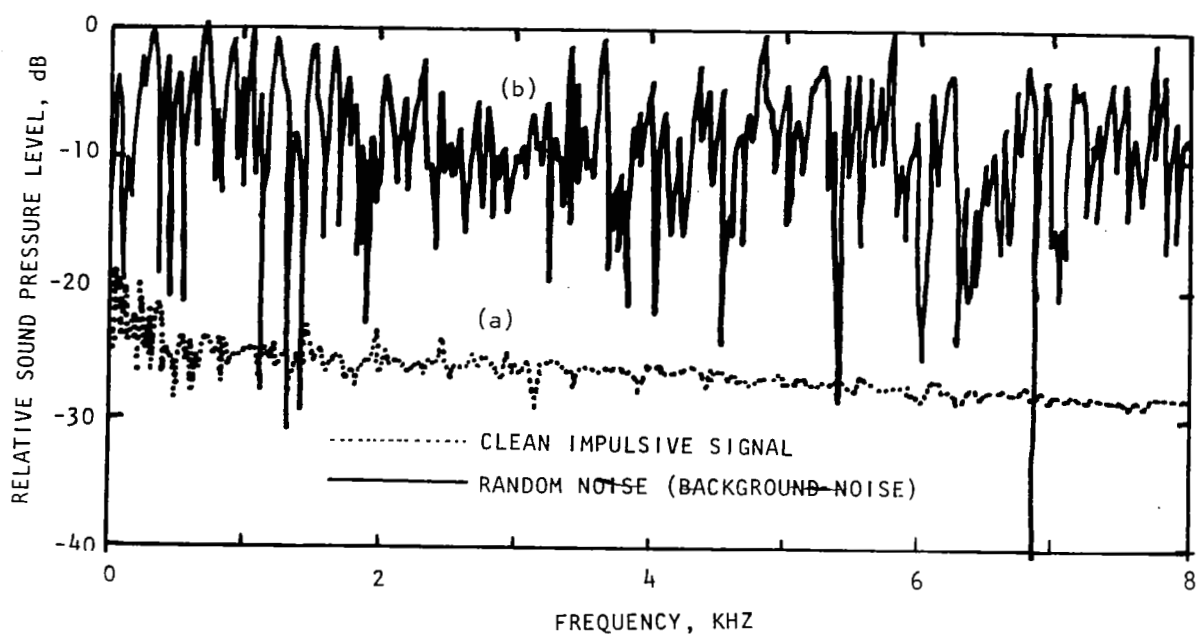


Figure 4.25 Sound pressure level spectra of (a) a clean impulsive signal and (b) a random noise sample.

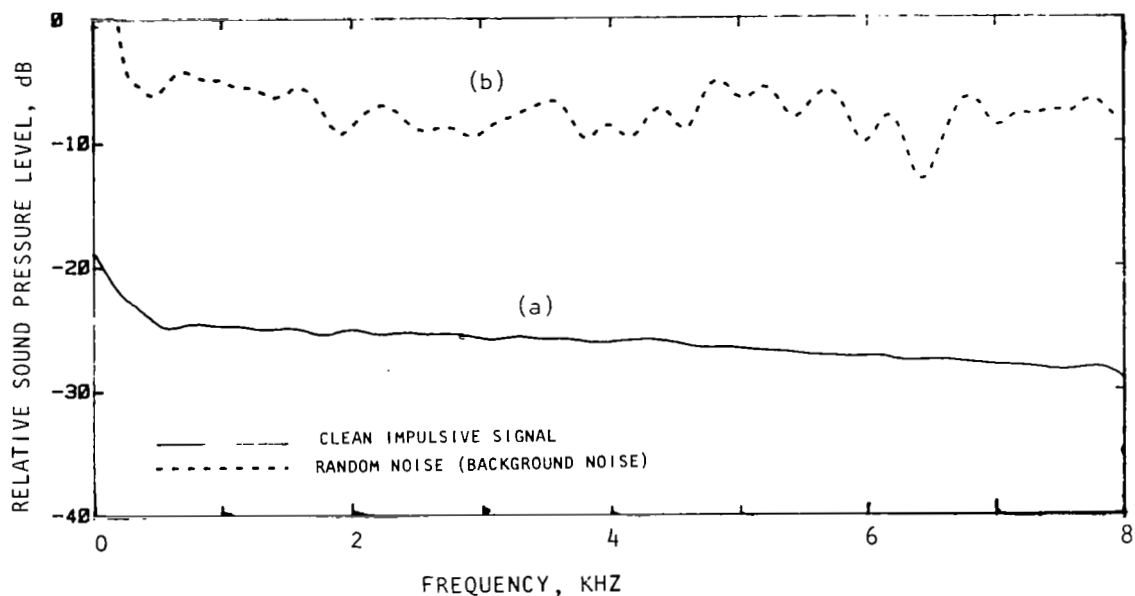


Figure 4.26 Sound pressure level spectra of (a) a clean impulsive signal and (b) a random noise sample (numerically smoothed.)

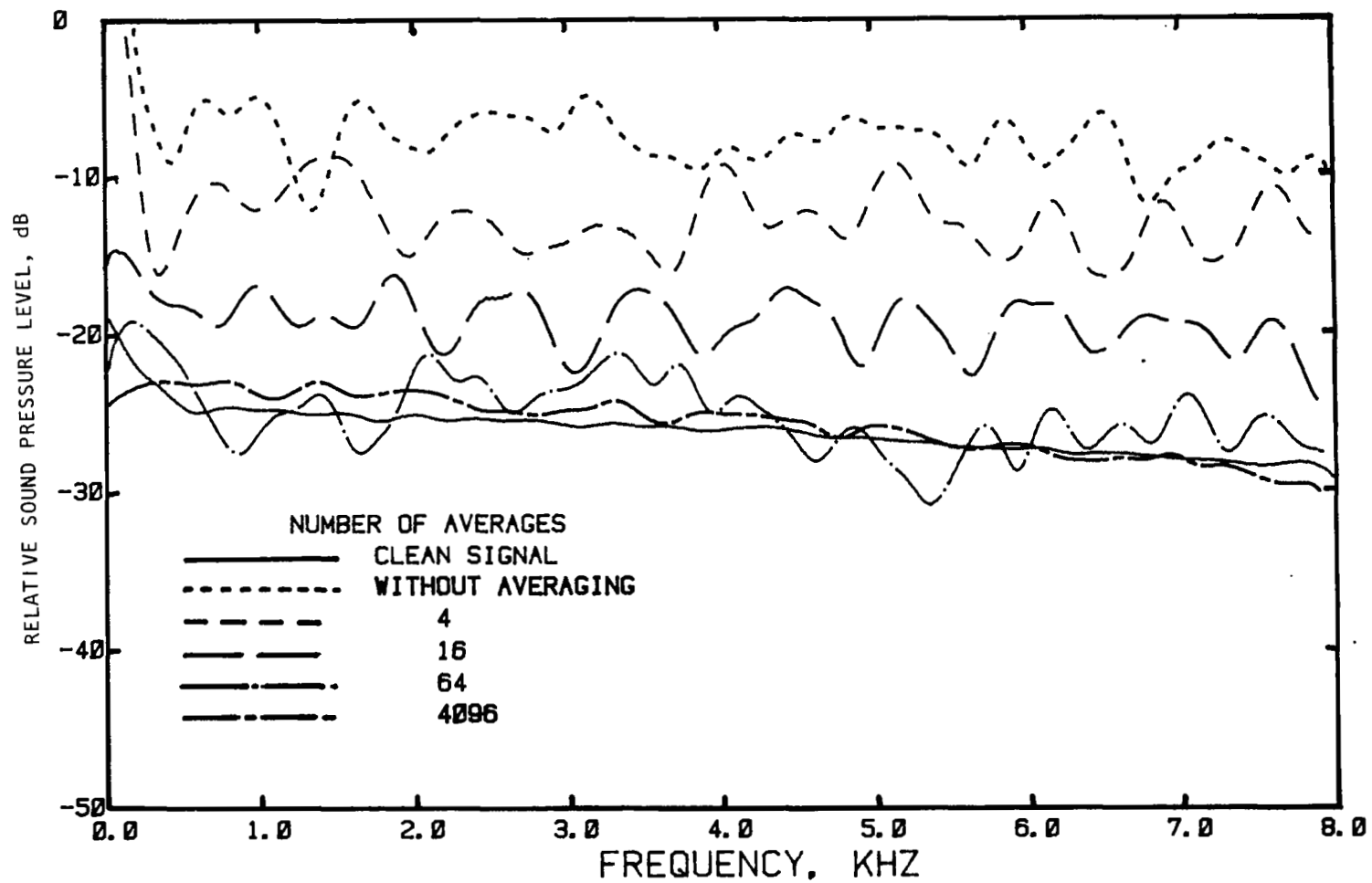


Figure 4.27 Effect of number of signal averages on the spectrum of a pulse completely buried in background noise (numerically smoothed)

far-field signals in real tests conducted at various jet flow Mach numbers for a straight duct and for a conical nozzle. To establish whether or not one needs different number of averages for far-field signals at different polar angles (for a fixed flow condition), the averaging procedure was carried out for several signals recorded at different polar angles. A flow Mach number of 0.6 for the 6.2 cm diameter nozzle was chosen for this exercise. The far-field signal at a polar angle of 60 degrees was averaged using different number of samples and the resultant time histories are presented in figure 4.28(a). It is clearly seen that the jet mixing noise superimposed on the signal reduces with increasing number of averages. After 1024 averages there is little improvement observed in the signal by increasing the averages to 4096. In other words, by applying 1024 averages the random jet noise level must have reduced to the background noise level, and hence, there was no further improvement by increasing the number of averages. The spectral distribution of these signals is presented in figure 4.28(b). The spectrum for the signal with 1024 averages coincides with the spectrum of the signal with 4096 averages which also indicates that there is no further improvement in the signal-to-noise ratio by increasing the number of averages beyond 1024.

To illustrate the effect of editing on the zero level extensions of the pulse, the jet mixing noise from these pulse extensions was zeroed out from each of the signals shown in figure 4.28(a). The edited signals are shown in figure 4.28(c), and the corresponding spectrum of each edited pulse is plotted in figure 4.28(d). It is interesting to note that the spectral distribution of the pulse with lesser number of averages (for example, 64 averages) with editing agrees well with that of the pulse with higher number of averages (for example, 4096 averages). This indicates that after a few averages the influence of jet mixing noise is largely eliminated from the main pulse (signal). However, the effect of the jet mixing noise remains only on the zero level extensions of the pulse and is, therefore, removed by the editing process (without introducing any error.) In summary, therefore, with an optimum number of averages and with the editing process described above, it is possible to recover the signal accurately from the background noise with a fewer number of averages compared to that derived from equation (4.17).

Similar results were also obtained for the signals at polar angles of 90 degrees and 120 degrees. These are shown in figures 4.29 and 4.30, respectively. It was found that for each of these polar angles the number of averages required to recover the signal is more or less the same - 1024).

Now to determine the effect of flow condition on the number of averages required to recover a pulse, a similar exercise was carried out with another jet flow Mach number, $M_j = 0.8$). This exercise was repeated only for one polar angle, $\theta = 90^\circ$. In this case it was found that more averages are needed to recover the signal compared to the case with flow Mach number of 0.6. The time histories with 1024 and 4096

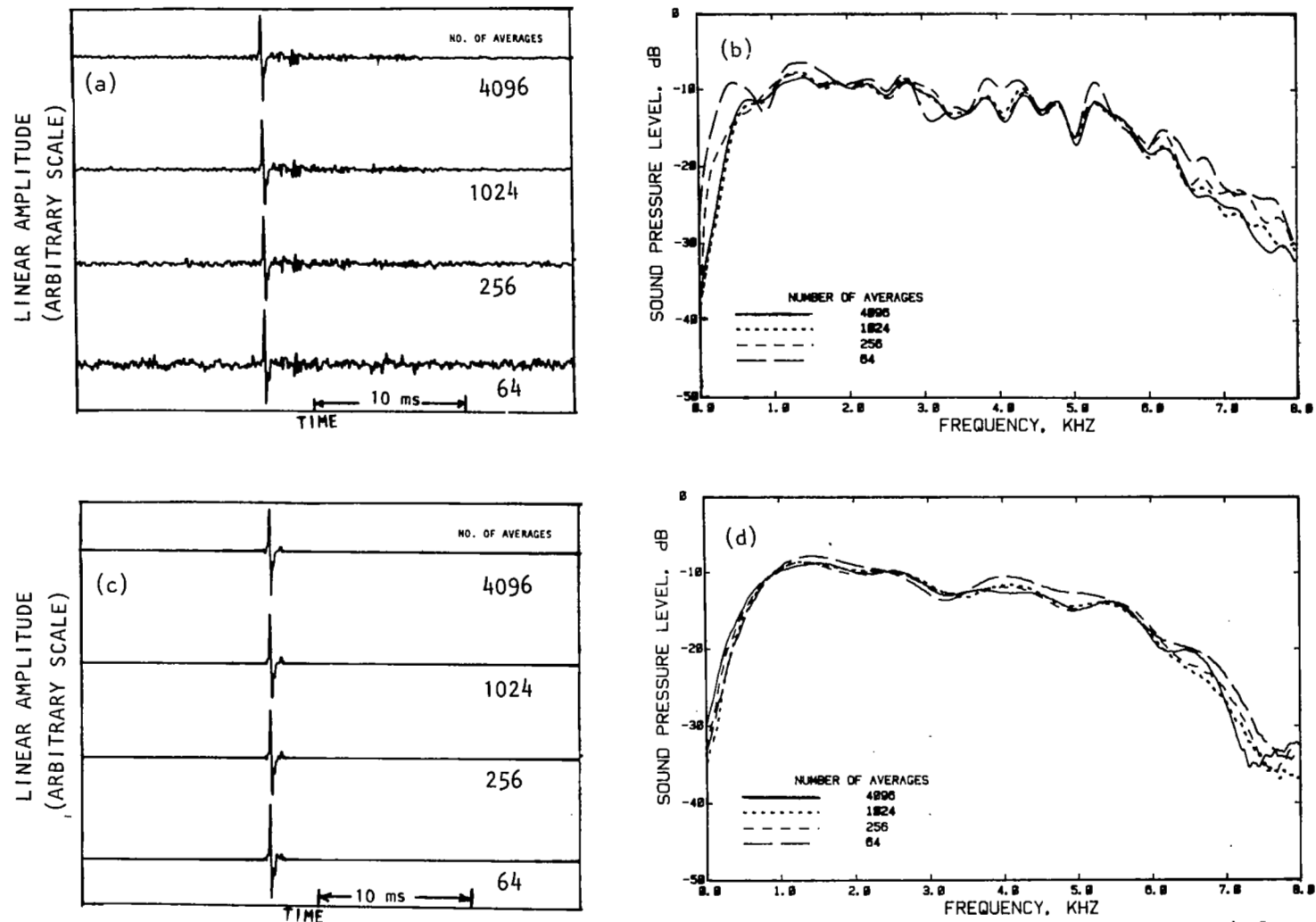


Figure 4.28 Effect of number of signal averages on far-field signal for a 6.2 cm diameter conical nozzle at $\theta = 60^\circ$ and $M_j = 0.6$; (a) time histories with different number of signal averages, (b) sound pressure level spectra of the pulses shown in (a) (numerically smoothed), (c) edited time histories after applying different number of signal averages, (d) sound pressure level spectra of the edited pulses shown in (c).

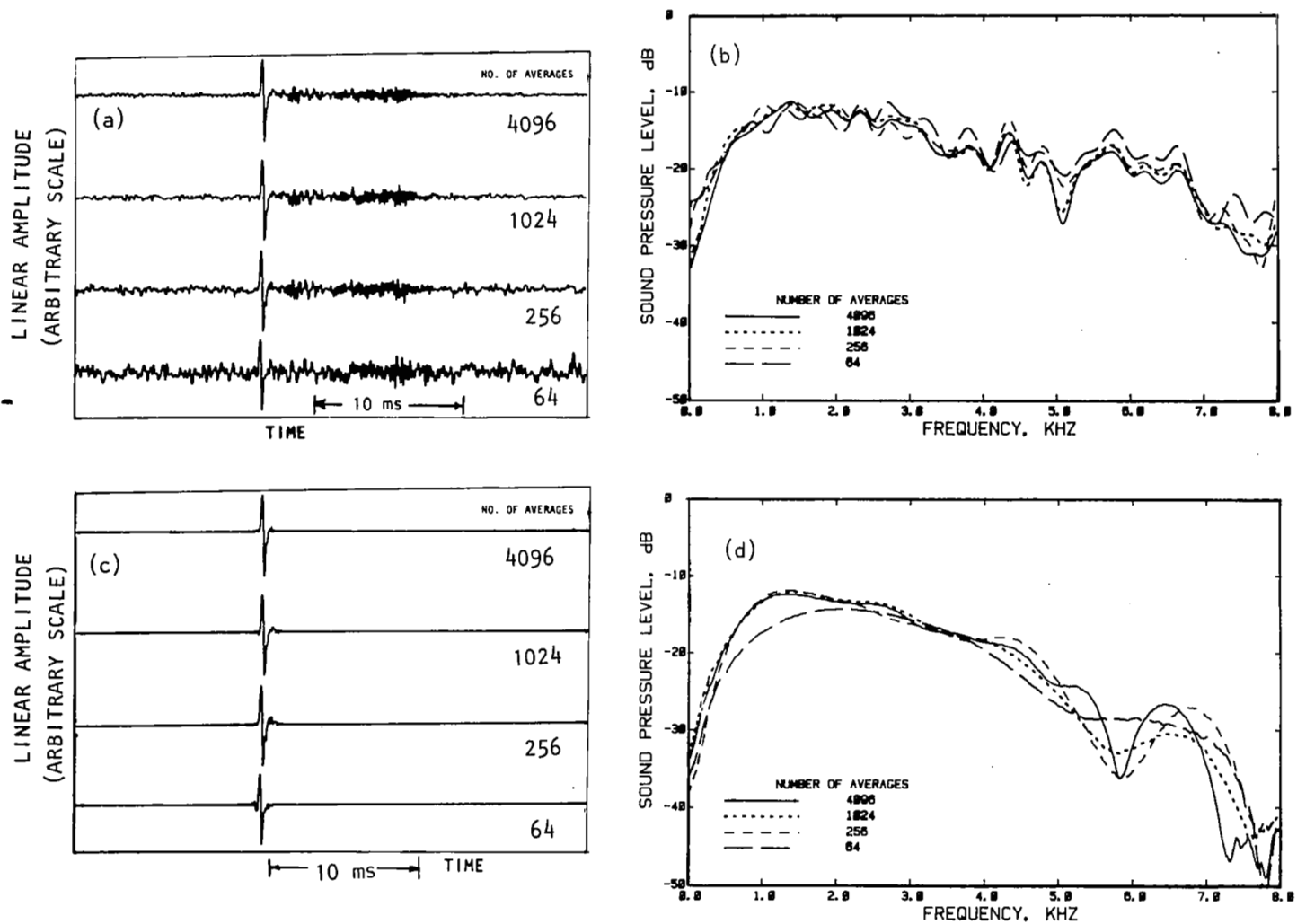


Figure 4.29 Effect of number of signal averages on far-field signal for a 6.2 cm diameter conical nozzle at $\theta = 90^\circ$ and $M_j = 0.6$; (a) time histories with different number of signal averages, (b) sound pressure level spectra of the pulses shown in (a) (numerically smoothed), (c) edited time histories after applying different number of signal averages, (d) sound pressure level spectra of the edited pulses shown in (c).

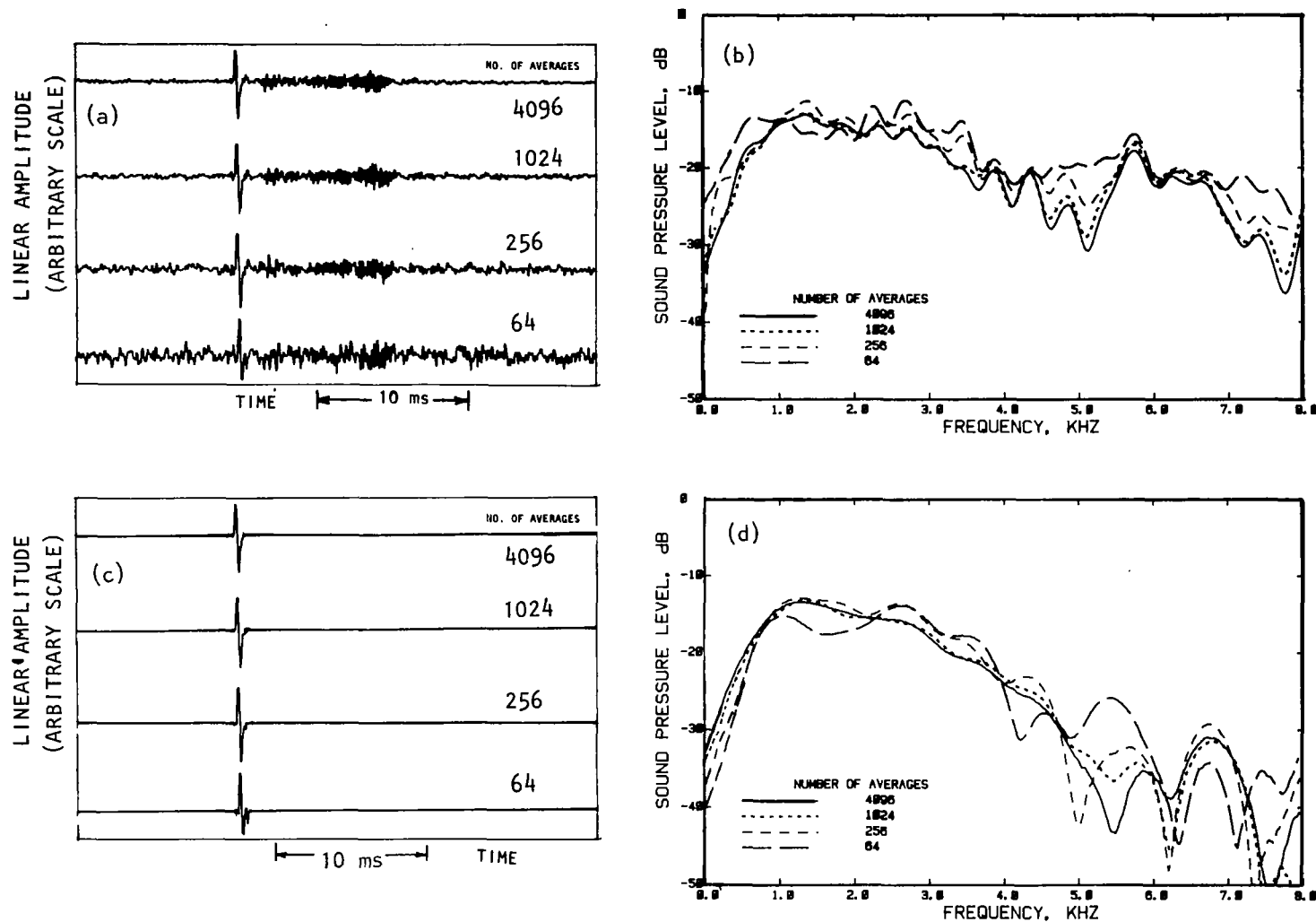


Figure 4.30 Effect of number of signal averages on far-field signal for a 6.2 cm diameter conical nozzle at $\theta = 120^\circ$ and $M_j = 0.6$; (a) time histories with different number of signal averages, (b) sound pressure level spectra of the pulses shown in (a) (numerically smoothed), (c) edited time histories after applying different number of signal averages, (d) sound pressure level spectra of the edited pulses shown in (c).

averages are shown in figure 4.31(a). It can be clearly seen that the time history with 4096 averages is cleaner than that with 1024 averages. Perhaps the signal-to-noise ratio would have increased even further by increasing the number of averages beyond 4096. However, the FFT analyzer (SD360) puts a limit on the maximum number of averages to 4096. Similar conclusions can also be drawn from the spectral plots of the corresponding signals without and with editing as shown in figures 4.31(b) and 4.31(d), respectively. Here, the spectral data with 1024 averages do not agree too well with those with 4096 averages even when the editing was applied to the signals.

To sum up, for a given test condition, the number of signal averages needed to recover the signals must be determined by applying different number of averages to the signal from one microphone channel, which has lowest signal to noise ratio and then the signals from other microphone channels should be averaged by this predetermined number of averages.

4.7 CONCLUSIONS

An improved impulse technique, using an electroacoustic driver instead of a spark discharge source for measuring the acoustic properties of a duct/nozzle system, with and without flow, has been presented in this section. The following conclusions can be drawn from the results presented in this section.

(1) Signal synthesis is successfully used to generate a desired sharp pulse (a) for a single-stream duct system with one-driver source at the centerline or a multiple driver source, and (b) for an annular duct system with a multiple driver source.

(2) Signal averaging process is a powerful means to minimize background noise.

(3) Signal editing as opposed to signal averaging is not a suitable means to recover the signal from the background noise when the signal-to-noise ratio is low.

(4) Spectral averaging does not improve the statistical accuracy of the spectral results when identical signals are generated and are signal averaged in time domain to remove the random noise.

(5) Numerically smoothed spectral data represent an overall spectral behavior. Since larger fluctuations in the spectral distribution are eliminated by numerical smoothing, such a representation is useful when data for different flow conditions or configurations are to be compared.

(6) Any extraneous noise superimposed on the signal reduces with increasing number of averages.

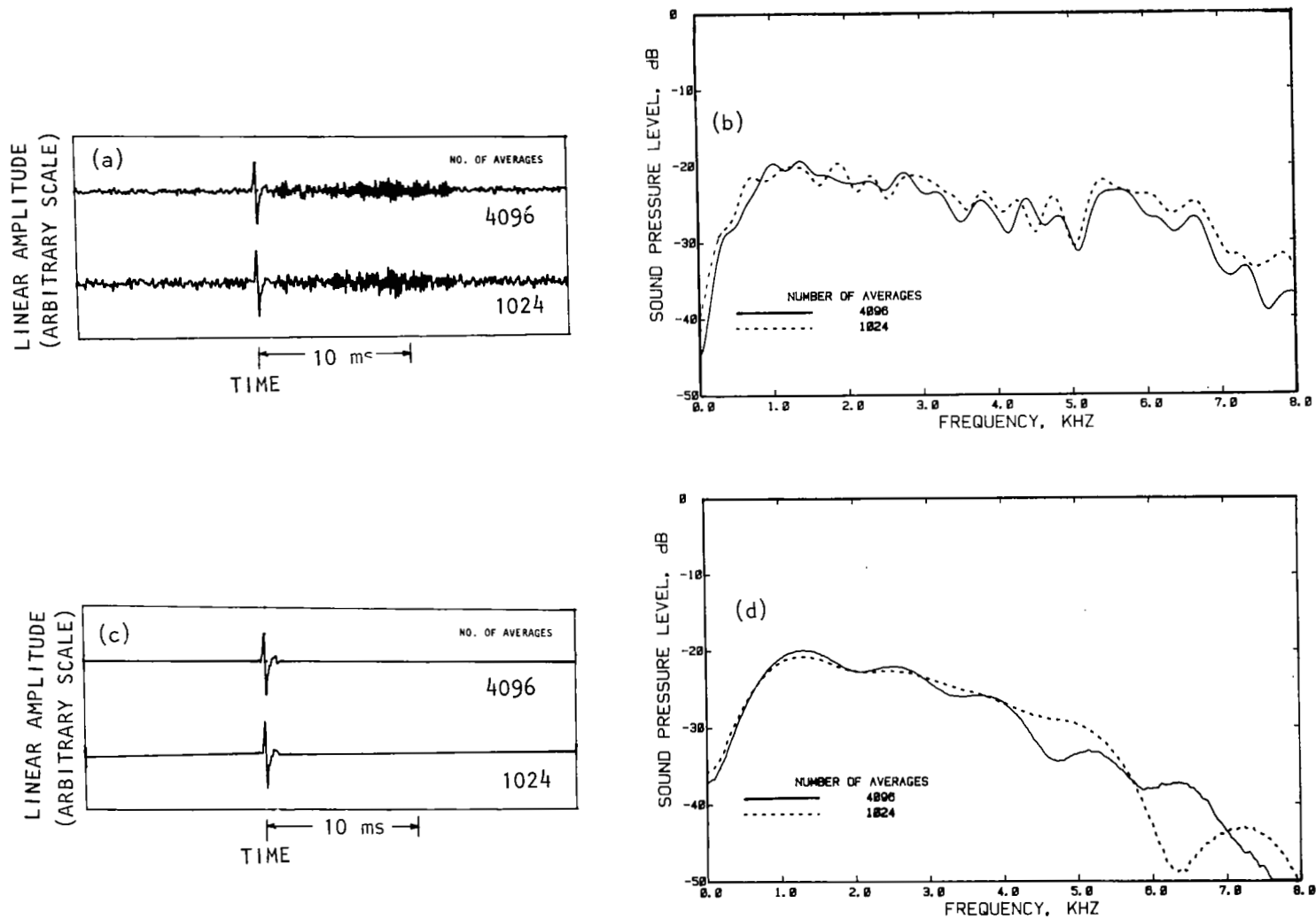


Figure 4.31 Effect of number of signal averages on far-field signal for a 6.2 cm diameter conical nozzle at $\theta = 90^\circ$ and $M_j = 0.8$; (a) time histories with different number of signal averages, (b) sound pressure level spectra of the pulses shown in (a) (numerically smoothed), (c) edited time histories after applying different number of signal averages, (d) sound pressure level spectra of the edited pulses shown in (c).

(7) The guideline to determine the number of signal averages needed for complete elimination of noise can be expressed as follows:

$$\text{Number of Averages} = \frac{\text{Mean Square Value of Flow Noise in the Absence of Signal}}{\text{Mean Square Value of Coherent Instrumentation Noise}}$$

This represents the point of diminishing returns for reducing the noise by signal averaging and is an upper limit. The actual number of averages needed to make the noise smaller relative to the signal (pulse) depends on the ratio of the signal to the noise and the extent of accuracy needed for the result. For example, from figure 4.27, the noise is about 20 dB above the clean signal. This is a ratio of noise to signal of 100. Thus 100 averages are needed to reduce the noise level to that of the signal. Some more averaging is needed to reduce the noise level further down compared to the signal depending upon the accuracy requirement.

(8) In practice, of a lesser number of signal averages (compared to the required number of averages) followed by signal editing allows an adequate recovery of the signal even under severe conditions.

5.0 IN-DUCT ACOUSTIC POWER MEASUREMENTS

The radiated sound power in the far field, W_f , can be calculated by integrating the measured far-field sound intensity over a sphere of polar radius R_m , as discussed in section 3. However, the determination of the induct sound power, namely, the incident or the reflected power, is not so simple due to the following reasons: (a) the duct sound field is critically sensitive to both duct mode structure and source position, (b) the mean-square pressure does not have any simple, universal relationship to the acoustic power, (c) the mean-square pressure in relatively short ducts may be dominated by contributions from cut-off modes, (d) both wall (and termination) acoustic absorption and effective internal source impedance may determine the response near a cut-on frequency, and (e) higher order modes can each carry as much as four times the plane wave mode acoustic power for point source and can be higher for other type of sources (ref. 16). A single-point induct measurement, therefore, may not be adequate to account for the modal power contributions due to the higher order modes. Therefore, following the refinement of the acoustic impulse technique as described in section 4, an experimental program was carried out to determine the proper procedure for measuring the acoustic power in a duct. The acoustic power for both incident and reflected sound fields, for circular ducts and annular ducts with and without nozzles, was examined at various flow conditions.

There has been a considerable interest recently in the measurement of acoustic intensities, rather than simply sound-pressure levels, since the mean-square pressure does not have any simple, universal relationship to the acoustic intensity. The intensity measurements indicate not only the noise level, but also the direction in which acoustic energy is flowing. Therefore, a knowledge of the intensity can be useful in locating noise sources. Furthermore, in noise emission standards and specifications, the total acoustic power output of a source is of interest. The acoustic power is simply a surface integral of the intensity.

The most promising technique for measuring the acoustic intensity involves the simultaneous measurement of the sound pressure at two points separated slightly in space (ref. 17). This is accomplished by means of two microphones. The acoustic intensity can be related mathematically to the imaginary part of the cross-spectral density between the two microphone signals, which in turn can be computed electronically (ref. 18).

Though the two-microphone technique seems to be capable of measuring the local intensity, it has several problems which make it very difficult to use it in practice. Statistical errors (ref. 19) and errors due to finite separation distance between the two microphones (ref. 20) seem to be quite severe, specially at low frequencies.

Moreover, to determine the acoustic power in a duct, it would be

necessary to measure the intensities at various locations, both in a radial and azimuthal. This would make the problem very difficult. Finally, in several applications, for example, in aircraft noise problems, it would be of interest to extend this type of measurement to a case in which there is a mean background flow. Unfortunately a complete knowledge of the time histories of the pressure and of the pressure gradient is not enough to determine the acoustic intensity at a point in the presence of mean flow (ref. 21).

In the present study, therefore, an alternate method has been developed to measure the acoustic power inside a single-stream or annular-stream duct when the direction of energy flux is known or when the power in a desired direction is required. In this method several radial and azimuthal pressure measurements are made and using these complex pressure data the modal content of the pressure field is determined. Therefore, the acoustic power due to each individual mode and also their total sum are derived. Moreover, the validity of single point pressure measurements to determine the acoustic power is also examined.

The experimental procedure and data analysis process are described in section 5.1. The radial and azimuthal variation of the induct pressure field, for both single and annular streams, is examined and the results are presented in section 5.2. The mathematical approach for the modal decomposition of induct acoustic power, and the results of modal decomposition are presented in section 5.3. Finally, the important observations are summarized in section 5.4.

5.1 EXPERIMENTAL PROCEDURE AND DATA ANALYSIS

The objective of this study was to determine the spatial distribution of the induct pressure field. To achieve this goal an induct pressure field survey was needed. For the single stream duct, where the azimuthal variation of the induct pressure field was assumed to be absent, only the radial variation of induct pressure field was obtained by traversing a probe from wall to the center of the duct and by measuring both the incident and the reflected pulses at several radial locations. However, for the annular duct, both radial and azimuthal pressure variations were obtained. To maintain the same flow condition during the pressure survey, a six-point measurement probe was used for the annular duct. This probe, as described in section 3, can measure pressure simultaneously at six radial locations. Several such measurements were taken at different azimuthal positions. The details of the measurement technique have been discussed in section 3.

The induct pressure time histories as measured by the probe were recorded on an analog tape recorder. Later on these signals were played back and analyzed on an FFT analyzer (SD-360) to derive complex pressure spectra for incident and reflected pressures at each induct measurement point. The amplitudes of these results were used to derive an area-

weighted pressure value in the duct. The complex pressures were used to carry out the modal decomposition exercise. In addition, the complex pressures could be used to derive the complex reflection coefficient and the radiation impedance spectra. Since the signal averaging process was applied (discussed in section 4), only one channel could be analyzed at a time using the FFT analyzer (SD-360). Therefore, an indirect procedure was used to derive the complex pressure spectra.

In this procedure, as illustrated in figure 5.1, once the signal averaging process is completed in the output memory of the machine (SD-360) the averaged signal (both incident and reflected pulses as shown in figure 5.1(a)) is transferred into the input memory of the machine (to each of the two channels, A & B, as shown in figure 5.1(b)). The incident pulse of the signal in channel B and the reflected pulse of the signal in channel A are taken out by the editing process (see figure 5.1(c)). Then the incident pulse is rotated in time domain by a fixed amount (say τ_0) to align it with the reflected pulse. The rotation is maintained same for all the radial and azimuthal measurements for a given test. Then, both the signals are rotated by the same amount to bring them to the center of the scope. Then a complex transfer function is obtained between the reflected and the incident pulses (see figure 5.1(d)). Let p_{ri} and ϕ_{ri} be the pressure and phase transfer functions of the reflected pulse with respect to the incident pulse for a given frequency, f . Then, the reflected pulse of channel B is removed and a delta function of a fixed amplitude is created in channel B, as shown in figure 5.1(e) at a fixed location with respect to the origin. Then a transfer function between the delta function and the incident pulse is derived. Let p_{di} and ϕ_{di} be the pressure and phase transfer functions of the delta function (signal created) with respect to the incident pulse for the same frequency, f . Using these values the complex pressure for the fixed delta function can be derived with respect to the reflected pulse and can be expressed as follows:

$$\left. \begin{aligned} p_{dr} &= p_{di} - p_{ri} \text{ (in dB scale)} \\ \phi_{dr} &= \phi_{di} - \phi_{ri} \end{aligned} \right\} \quad (5.1)$$

where p_{dr} and ϕ_{dr} are the pressure and phase transfer functions of the delta function with respect to the reflected pulse for the same frequency f .

The absolute pressure level for the incident and the reflected pulses can be derived using p_{di} and p_{dr} and the absolute pressure level of the delta function. The absolute phase values are not required. The phase difference between the measurement locations with respect to one representative location can easily be obtained from ϕ_{di} and ϕ_{dr} values

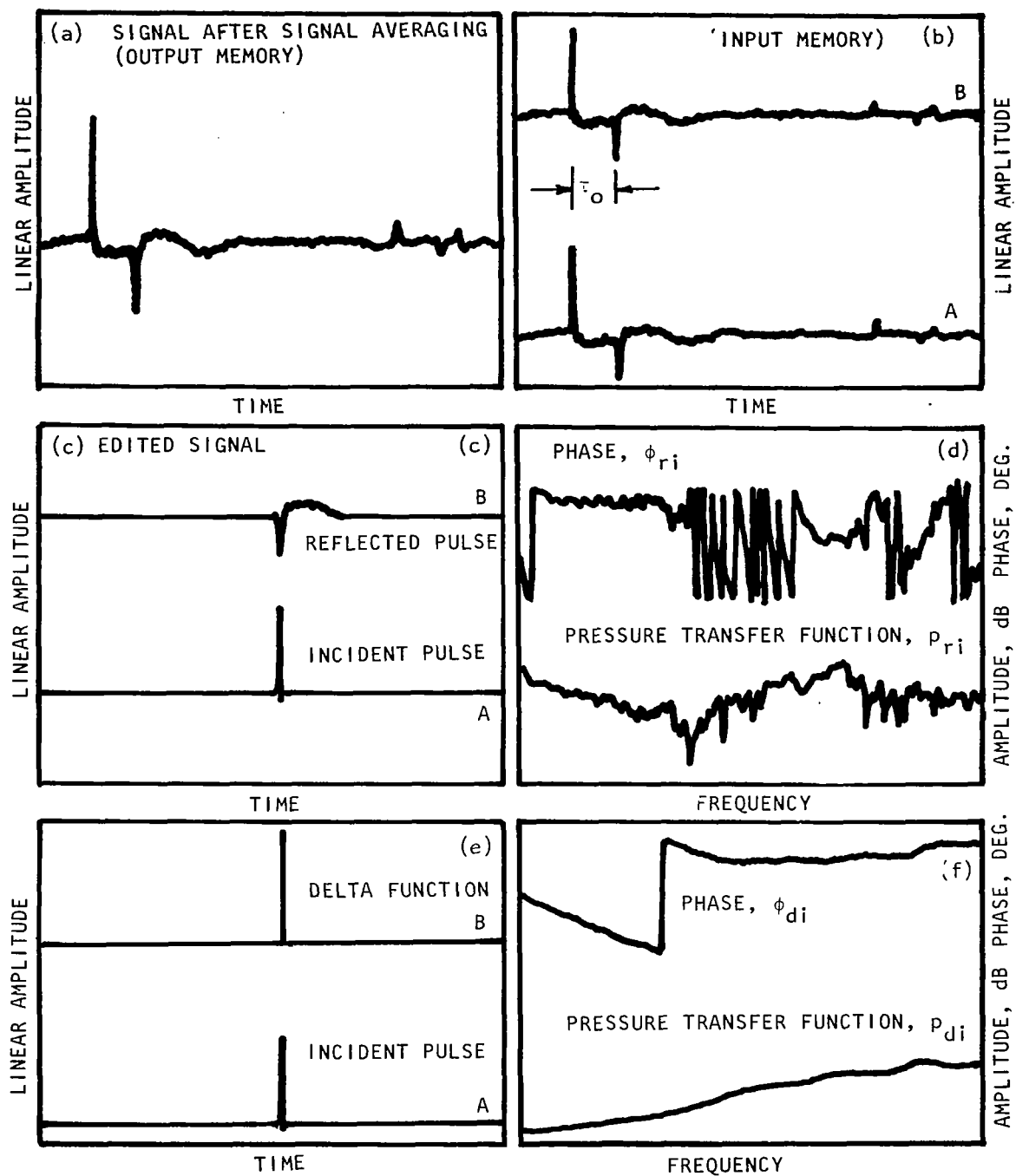


Figure 5.1 Illustration of a procedure to derive complex pressure spectra after applying the time domain signal averaging using the FFT analyzer (SD-360).

at different measurement locations. For the multi-point measurement probe, proper calibration is used to correct both amplitude and phase data.

The complex reflection coefficient for a given measurement location can be obtained using p_{ri} , ϕ_{ri} , τ_o , and the exact propagation time of the incident pulse from the probe location to the exit and back. Let τ_c be the exact propagation time which is derived using the physical length of the duct-nozzle system from the probe position to the exit, the sonic speed and the mean flow velocity. To obtain the complex reflection coefficient, the actual propagation time, τ_c , between the incident and the reflected pressure pulses needs to be removed. However, time τ_o has already been removed between these pulses by the relative rotation process applied during the analysis to evaluate the complex pressures. Therefore, a correction on the (already) derived complex transfer function, p_{ri} and ϕ_{ri} , due to the remaining time, $(\tau_c - \tau_o)$, needs to be applied. There is no effect of this relative rotation process on the pressure amplitude p_{ri} . Therefore, the correction is made only on the phase value in the following manner. The phase change due to relative time rotation is a function of frequency and is given by

$$\Delta\phi = 360f\Delta\tau, \text{ in Deg.}$$

f being the frequency in Hz. Therefore, the actual phase for the complex reflection coefficient is given by

$$(\phi_{ri})_c = \phi_{ri} + 360.f(\tau_c - \tau_o) \quad (5.2)$$

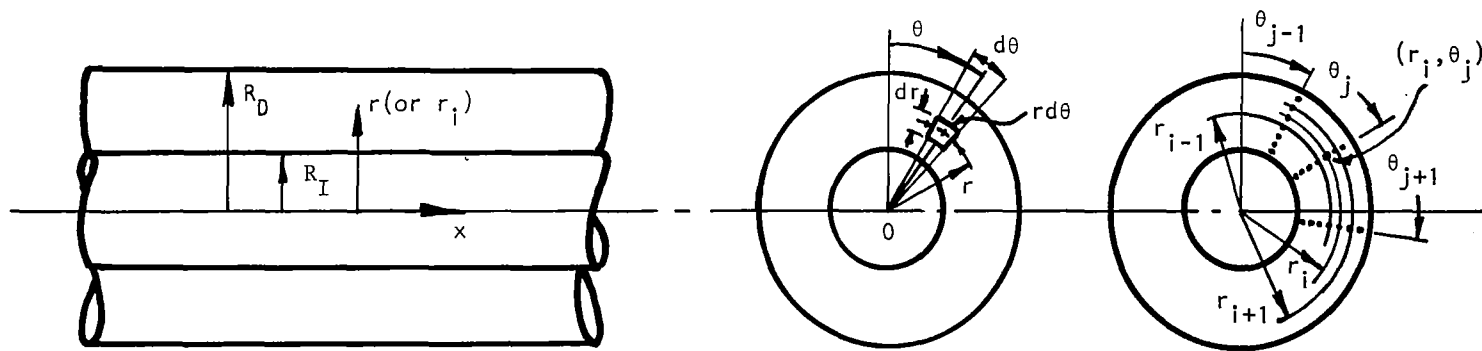
In this manner, the complex reflection coefficient (p_{ri} and $(\phi_{ri})_c$) is finally derived.

5.2 RADIAL AND AZIMUTHAL VARIATION OF IN-DUCT PRESSURE FIELD

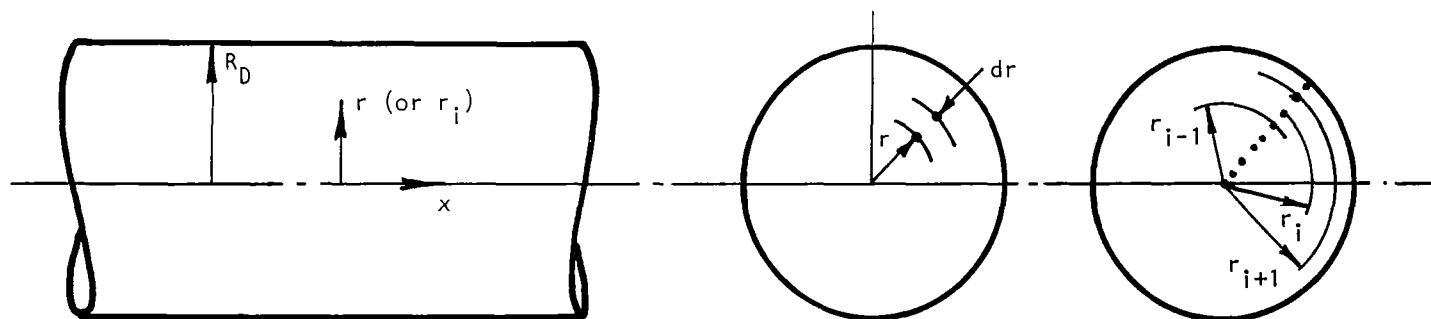
The induct sound pressure level spectra and the reflection coefficient amplitude spectra evaluated at various radial locations for a single stream duct, and various radial and azimuthal locations for an annular duct, are used to study the spatial variation of the induct sound pressure field. Also, these data are used to evaluate the corresponding area-weighted spectra. The area-weighted value, \bar{F} , of a function, F , for an annular duct with inner and outer radii of R_I and R_D , respectively, is defined as

$$\bar{F} = \frac{1}{\pi(R_D^2 - R_I^2)} \int_{R_I}^{R_D} \int_0^{2\pi} F(r, \theta) r dr d\theta, \quad (5.3)$$

where the radial co-ordinate, r , is measured from the center of the duct and θ is the azimuthal co-ordinate (see figure 5.2). For a finite number of measurements equation (5.3) can be rewritten as follows:



(a) ANNULAR FLOW SYSTEM



(b) SINGLE STREAM FLOW SYSTEM

Figure 5.2 Coordinate system and induct measurement locations.

$$\bar{F} = \frac{1}{\pi(R_D^2 - R_I^2)} \sum_{i=1}^N \sum_{j=1}^L F_{ij} r_i \cdot \Delta r \cdot \Delta \theta \quad (5.4)$$

Here, F_{ij} is the value of the function $F(r, \theta)$ at i th radial location and j th azimuthal location. N and L are the number of radial and azimuthal measurements, respectively.

$$\left. \begin{aligned} \Delta r &= (r_{i+1} - r_{i-1})/2 && \text{for } 1 < i < N \\ \Delta r &= (r_i + r_{i+1})/2 - R_I && \text{for } i=1 \\ \Delta r &= R_D - (r_i + r_{i-1})/2 && \text{for } i=N \end{aligned} \right\} \quad (5.5)$$

and

$$\Delta \theta = (\theta_{k^+} - \theta_{k^-})/2 \quad \text{for all values of } j \quad (5.6)$$

where $k^+ = j+1$ and $k^- = j-1$

If $k^+ > L$, then $k^+ = j+1-L$

If $k^- < 1$, then $k^- = j-1+L$

If $\Delta \theta < 0$, then $\Delta \theta = \Delta \theta + 2\pi$

When the azimuthal measurements are taken at fixed interval, then

$$\Delta \theta = \frac{2\pi}{L} \quad (5.7)$$

and equation (5.4) reduces to the following form

$$\bar{F} = \frac{2}{L(R_D^2 - R_I^2)} \sum_{i=1}^N \sum_{j=1}^L F_{ij} \cdot r_i \cdot \Delta r \quad (5.8)$$

For a single stream duct with radius R_D , with one azimuthal measurement (L becomes unity), the area-weighted value can be expressed as follows:

$$\bar{F} = \frac{2}{R_D^2} \sum_{i=1}^N F_i \cdot r_i \cdot \Delta r \quad (5.9)$$

The function F could be the incident pressure, reflected pressure or any other acoustic parameter.

5.2.1 Radial Variation of Induct Pressure Field for a Single Stream Duct and Validity of Single Point Measurement

5.2.1.1 Radial Traverse Mechanism

Two different traverse systems were fabricated to survey the radial variation of the induct sound field. A piezoelectric transducer (Sundstrand C206 model) was used in the first traverse mechanism (see figure 5.3). The hexagonal portion of the transducer, 1.6 cm in diameter, was not separable from the pressure sensing part. Moreover, the length of the transducer, 3.3 cm, was not long enough to traverse inside the 10 cm diameter duct to cover the entire radial range of 5 cm from the wall to the center. Therefore, the transducer was placed inside a metallic tube (see figure 5.3) whose outer diameter was 1.905 cm. This entire tube, holding the transducer, could traverse from the inner surface of the 10 cm duct to its center. The portion of the transducer projecting out of this 1.905 cm tube was 1.25 cm long with a diameter of 1.1 cm. Therefore, when the probe was projected less than 1.25 cm from the inner surface of the 10 cm duct, a cavity was formed between the 1.905 cm hole (through which the traverse mechanism was introduced) and the portion of the transducer outside the 1.905 cm diameter tube. Threaded sleeves with appropriate lengths were made to fill up these cavities when they were formed.

The size of this traverse mechanism in relation to the duct diameter was quite large. It was suspected that the induct sound field would be highly affected, especially in the presence of flow, when such a large probe was introduced into the duct. To determine the influence of the presence of this probe on the induct sound field and to have an alternate means to carry out this task, another traversing probe was fabricated using a Knowles microphone (see figure 5.4). The tube on which the microphone was attached was 0.3 cm in diameter. A small nose cone precisely made for the Knowles microphone was used. Therefore, it was expected that the presence of this probe would not affect the induct sound field appreciably.

5.2.1.2 Experiments

Tests were carried out using a straight duct termination and a 6.2 cm diameter conical nozzle termination at various flow conditions. The flow conditions for the respective terminations are outlined in Table 5.1.

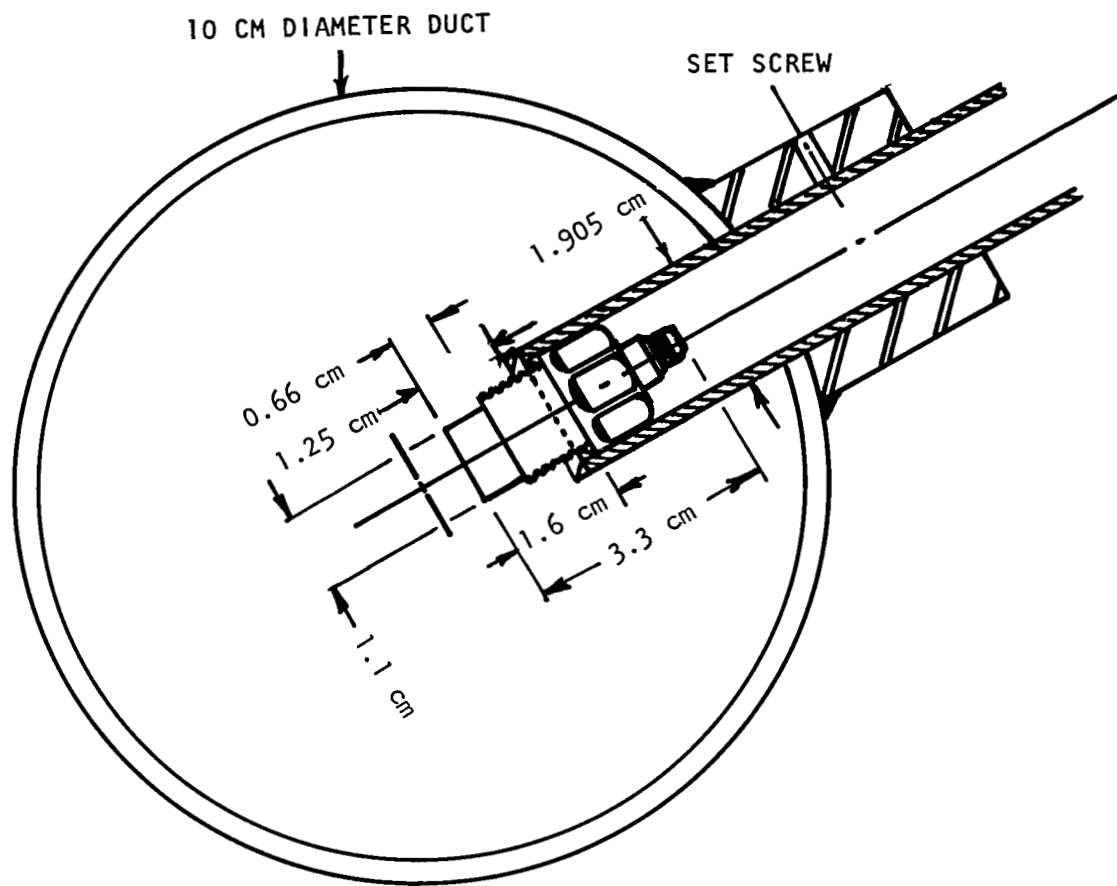


Figure 5.3 Radial traverse mechanism using a piezoelectric pressure transducer as the sensing device.

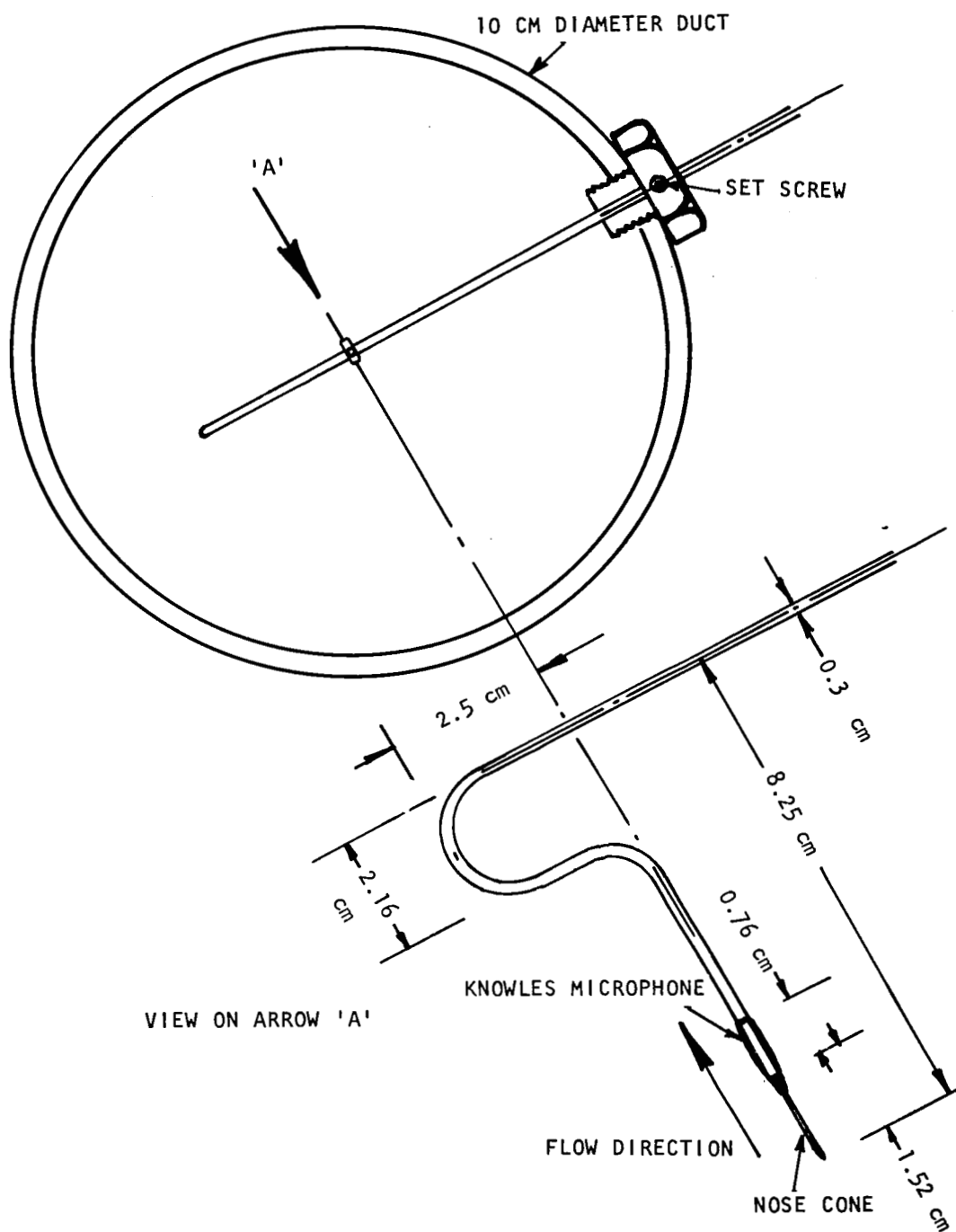


Figure 5.4 Radial traverse mechanism using a miniature Knowles microphone as the sensing device.

Table 5.1 Test conditions to survey the radial variation of induct sound field for single stream ducts

TERMINATION	JET FLOW MACH NUMBER
Straight Duct Termination (10 cm diameter)	0, 0.2
6.2 cm Diameter Conical Nozzle	0, 0.4, 0.6, 0.8

In each test, induct time histories were measured at nine radial locations, between the duct surface and the center, in steps of $r/D = 0.0625$, D being the duct diameter. These measurements were taken at a fixed axial location, about 76 cm upstream of the termination. Two sets of measurements were taken for the straight duct termination using the two different probes described earlier, whereas all the tests for the nozzle terminations were done using only the Knowles microphone probe. The measured data were used to evaluate the incident and the reflected sound pressure level spectra and the reflection coefficient spectra.

5.2.1.3 Experimental Results for the Duct Termination at No Flow Condition

The radial distribution and the area-weighted spectral data for the incident and the reflected sound pressure level for a straight duct termination measured by the Knowles microphone probe are presented in figure 5.5. Negligible difference is observed in the spectral data measured at various radial positions, at least up to about 3.5 KHz for the incident pressure field and up to about 3 KHz for the reflected pressure field. A small amount of radial variation does exist, for the incident pressure field, at higher frequencies. However, the spectral data measured at $r/D = 0.4375$ (i.e., 1/4 inch inside from the duct wall) coincide well with the area-weighted result (see figure 5.5(a)). Above 3 KHz the radial variation of the reflected sound pressure level is significant. However, the area-weighted results do not differ appreciably from the spectral data obtained at $r/D = 0.4375$ (see figure 5.5(b)).

These observations, for both the incident and the reflected pressure fields, are further demonstrated in figure 5.6 where the incident and the reflected sound pressure data at various frequencies are plotted with respect to the radial distance, r/D , measured from the center to the duct surface.

To establish further whether or not a single point measurement is adequate to determine the radiated power W_t , it is necessary to determine its relationship with the incident and reflected pressure

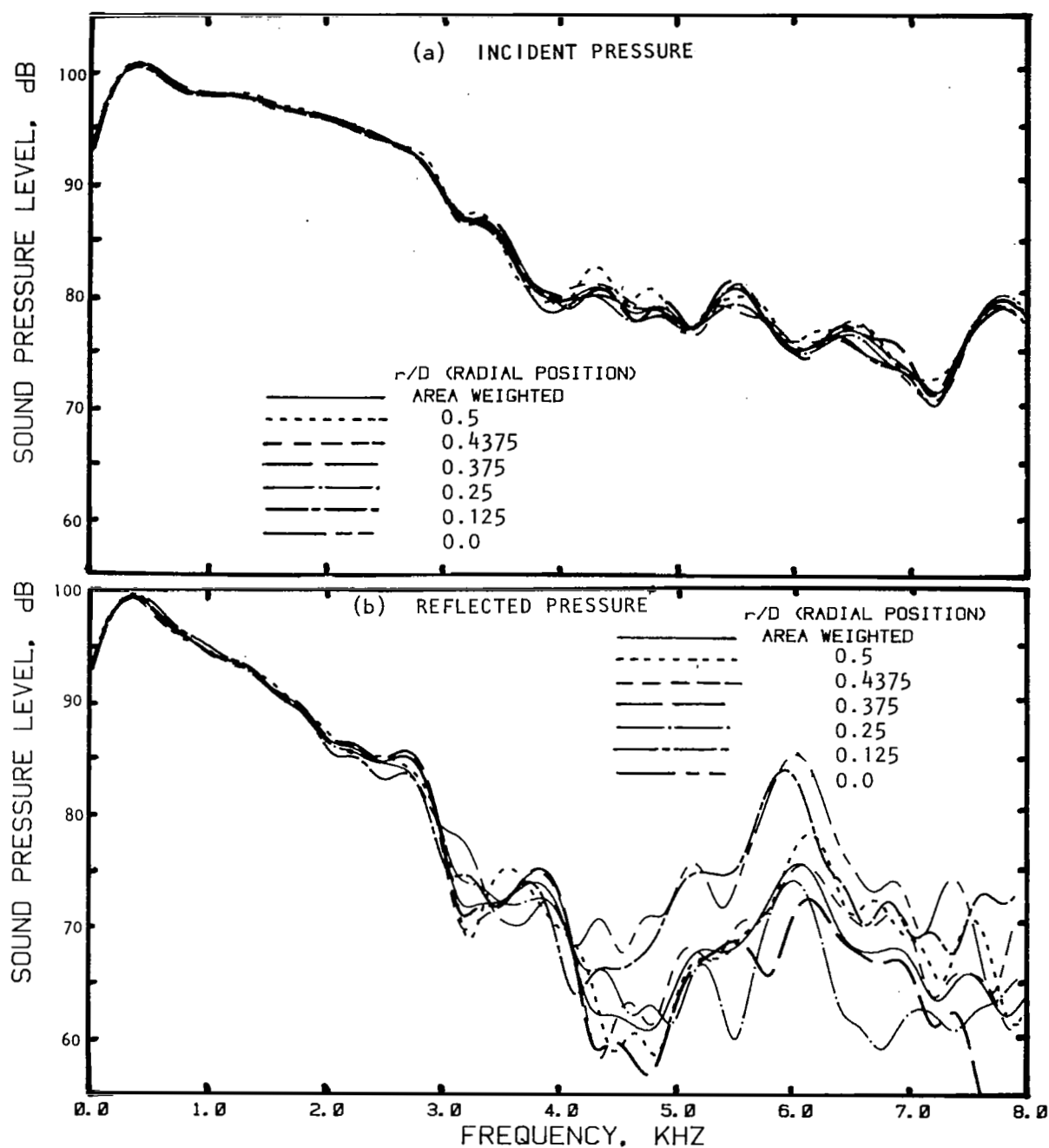
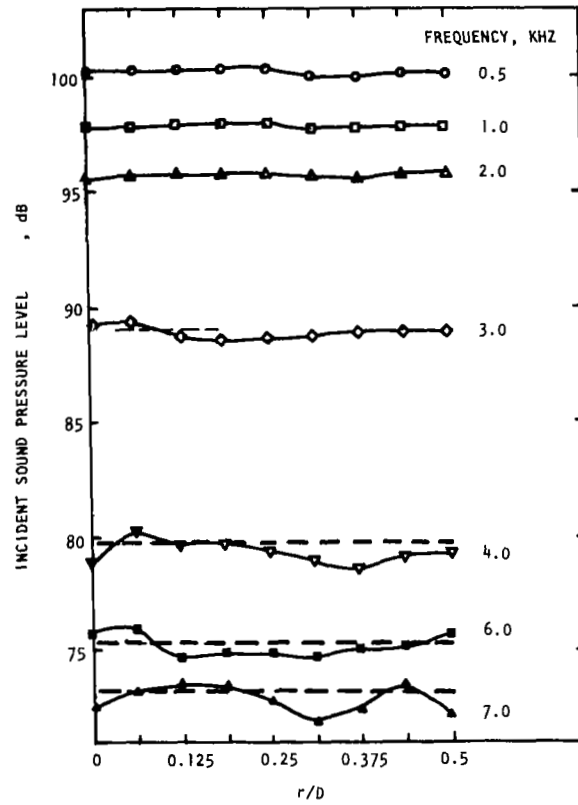
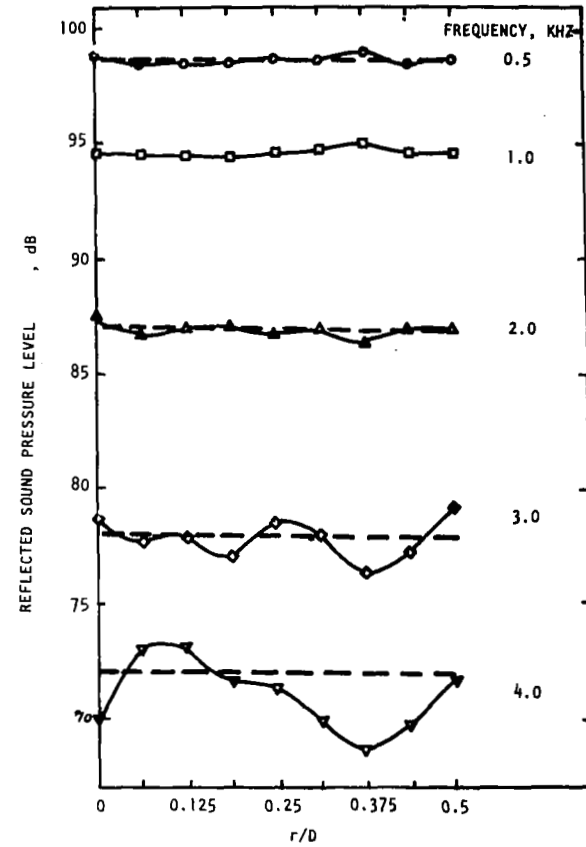


Figure 5.5 Radial variation of (a) incident and (b) reflected sound pressure level spectra and the corresponding area weighted spectrum measured by a Knowles microphone for a 10 cm diameter straight duct termination, $M_j = 0.0$.



(a)



(b)

Figure 5.6 Radial variation of (a) incident and (b) reflected sound pressure levels for a straight duct at various frequencies measured by a Knowles microphone probe, $M_j = 0.0$, (dashed lines represent area weighted levels).

fields in the duct.

The radiated power W_t for the plane wave mode can be expressed as a function of power reflection coefficient σ as follows:

$$W_t = \frac{A_D}{\rho_D c_D} (1 + M_D)^2 p_i^2 \left[1 - \sigma \left(\frac{1 - M_D}{1 + M_D} \right)^2 \right] \quad (5.10)$$

where

$$\sigma = \frac{p_r^2}{p_i^2} \quad (5.11)$$

In these expressions ρ_D , c_D and M_D are the mean density, sonic speed and flow Mach number inside the duct, respectively. A_D is the duct cross-sectional area and the incident and reflected pressures are represented by p_i and p_r , respectively. In the absence of flow equation (5.10) reduces to the following form

$$W_t = \frac{A_D}{\rho_D c_D} p_i^2 [1 - \sigma] \quad (5.12)$$

Equations (5.10) and (5.12) indicate that the radial distribution of the radiated power depends upon the radial distribution of the incident pressure p_i^2 , and the power reflection coefficient σ . Since the radial distribution of p_i^2 as shown in figure 5.5(a) indicates that a single-point measurement at a radial location $r/D = 0.4375$ is nearly the same as the area-weighted incident pressure field, it is necessary to examine the radial distribution of σ to determine the radial distribution of W_t .

The radial variation of the power reflection coefficient spectra and the area-weighted spectra are shown in figure 5.7. As expected from the incident and reflected pressure plots, an insignificant radial variation of σ occurs for frequencies upto about 2 KHz. Beyond 2 KHz the radial variation of σ is quite significant. However, the reflection coefficients derived at $r/D = 0.4375$ are somewhat close to the area weighted values. At some frequencies the difference in σ between the area-weighted values and those derived at $r/D = 0.4375$ are quite significant. However, at most of these frequencies the magnitudes of the area-weighted σ and the corresponding σ derived at $r/D = 0.4375$ are much smaller than unity (in dB, lower than zero value). Therefore, as can be seen from equation (5.12), the effect of σ on transmitted power, W_t , would be insignificant for such frequencies as long as p_i^2 measured at $r/D = 0.4375$ agrees well with its area-weighted value. Therefore, a single point measurement at $r/D = 0.4375$ at this test condition seems to be adequate in determining the transmitted power W_t .

The results derived from the measurements made by the pressure

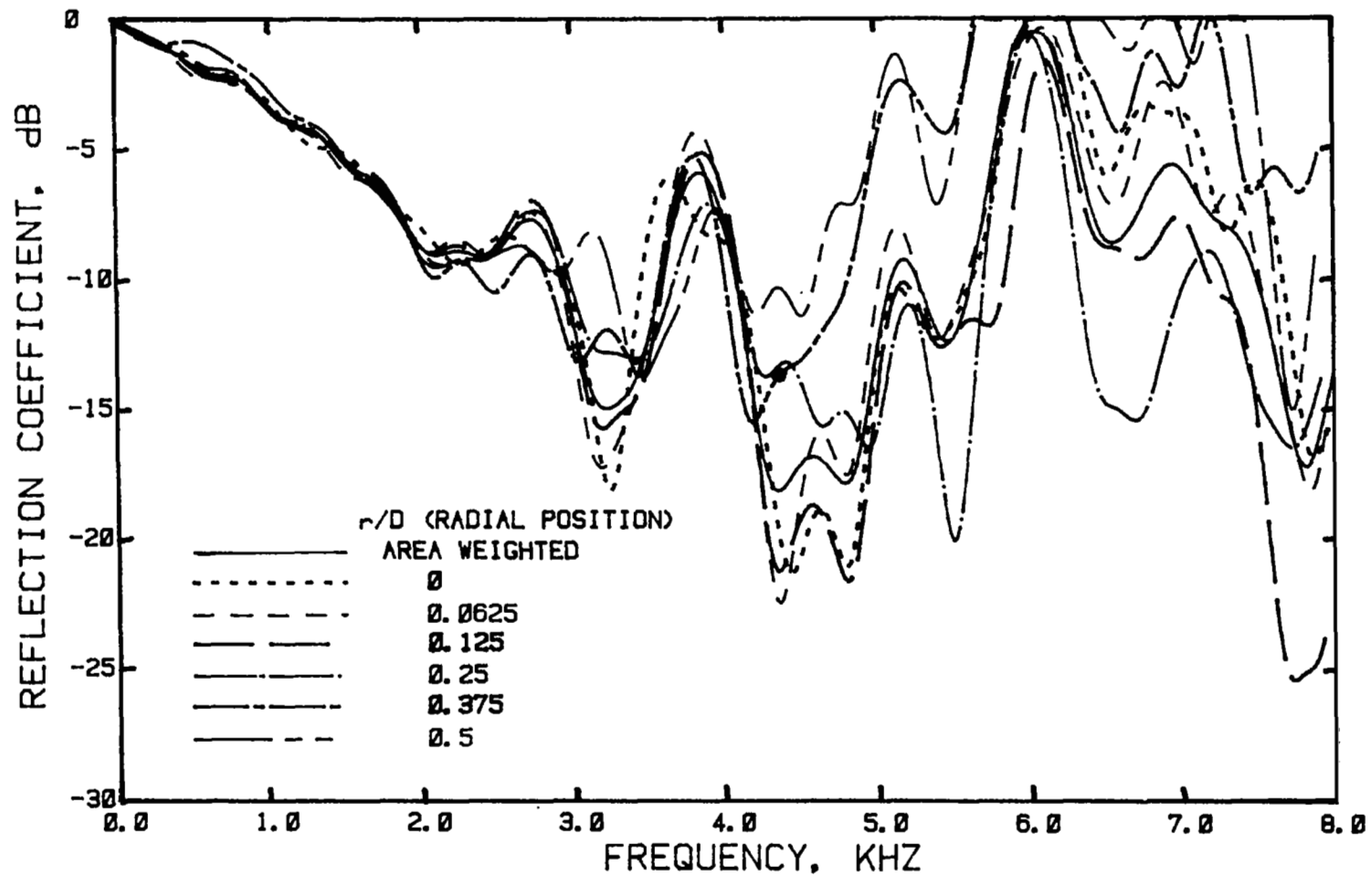


Figure 5.7 Radial variation of reflection coefficient spectrum and the corresponding area weighted spectrum measured by a Knowles microphone for a 10 cm diameter straight duct, $M_j = 0.0$.

transducer probe are also presented in this section in figures 5.8 through 5.10, similar to those presented in figures 5.5 through 5.7, respectively. This study was carried out to determine the effect of the pressure transducer probe on the induct sound field since the size of this probe was quite large compared to the duct-diameter. The following observations are made from the results presented in figures 5.8 through 5.10:

(1) The radial variation of the incident sound pressure level is insignificant upto about 4 KHz. Beyond 4 KHz, an appreciable difference is observed between the pressure levels measured at different radial locations. Moreover, the measurements at $r/D = 0.4375$ do not agree well with the area-weighted results (see figure 5.8(a)). This behavior is quite different from what is observed in figure 5.5(a) where the radial variation of the incident pressure levels obtained by using a Knowles microphone probe is small and the results derived at $r/D = 0.4375$ agree well with the area-weighted values. Since the Knowles microphone probe was smaller in dimension, the induct pressure field was not expected to be affected very much. Therefore, the incident pressure results obtained by using the pressure transducer probe, especially for higher r/D values, are affected due to the large dimension of the probe.

(2) The radial variation of the reflected sound pressure level is almost negligible upto about 2 KHz as shown in figure 5.8(b). Beyond this frequency, significant radial variation is observed for the reflected pressure, and the area-weighted levels do not agree well with the pressure levels derived at $r/D = 0.4375$.

(3) Similar conclusions can also be drawn by examining the radial variation of the incident and reflected pressure levels cross-plotted at various frequencies in figure 5.9.

(4) The spectral distributions for the reflection coefficient at various radial positions are shown in figure 5.10. Conclusions similar to those for the reflected pressure levels (see figure 5.8(b)) can be drawn for the reflection coefficients.

(5) At $r/D = 0.4375$, the pressure transducer probe remains close to the duct wall and, therefore, it was expected that the pressure field in the duct will not be influenced significantly at this position. Therefore, to verify this speculation, the reflection coefficients derived at $r/D = 0.4375$ by the pressure transducer probe are compared with those derived by the Knowles microphone probe in figure 5.11. It can be observed that at low frequencies (i.e., up to about 3 KHz) the reflection coefficients derived by both the probes are in good agreement. The difference at higher frequencies is mostly due to the presence of higher order modes which have different influence on these two probes since their orientations inside the duct during the tests were different.

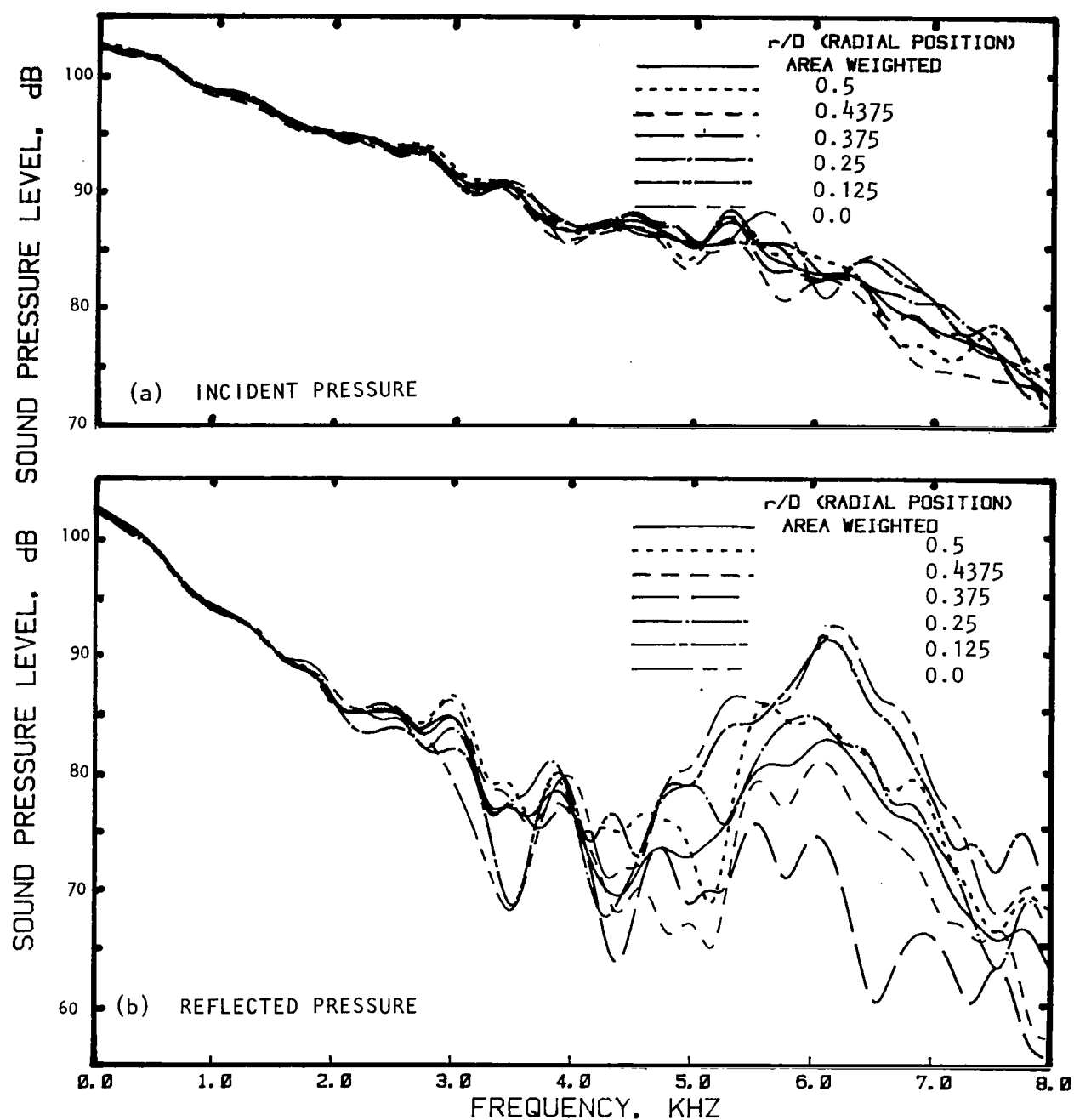


Figure 5.8 Radial variation of (a) incident and (b) reflected pressure level spectra and the corresponding area weighted spectrum measured by a pressure transducer for a 10 cm diameter duct termination, $M_j = 0.0$.

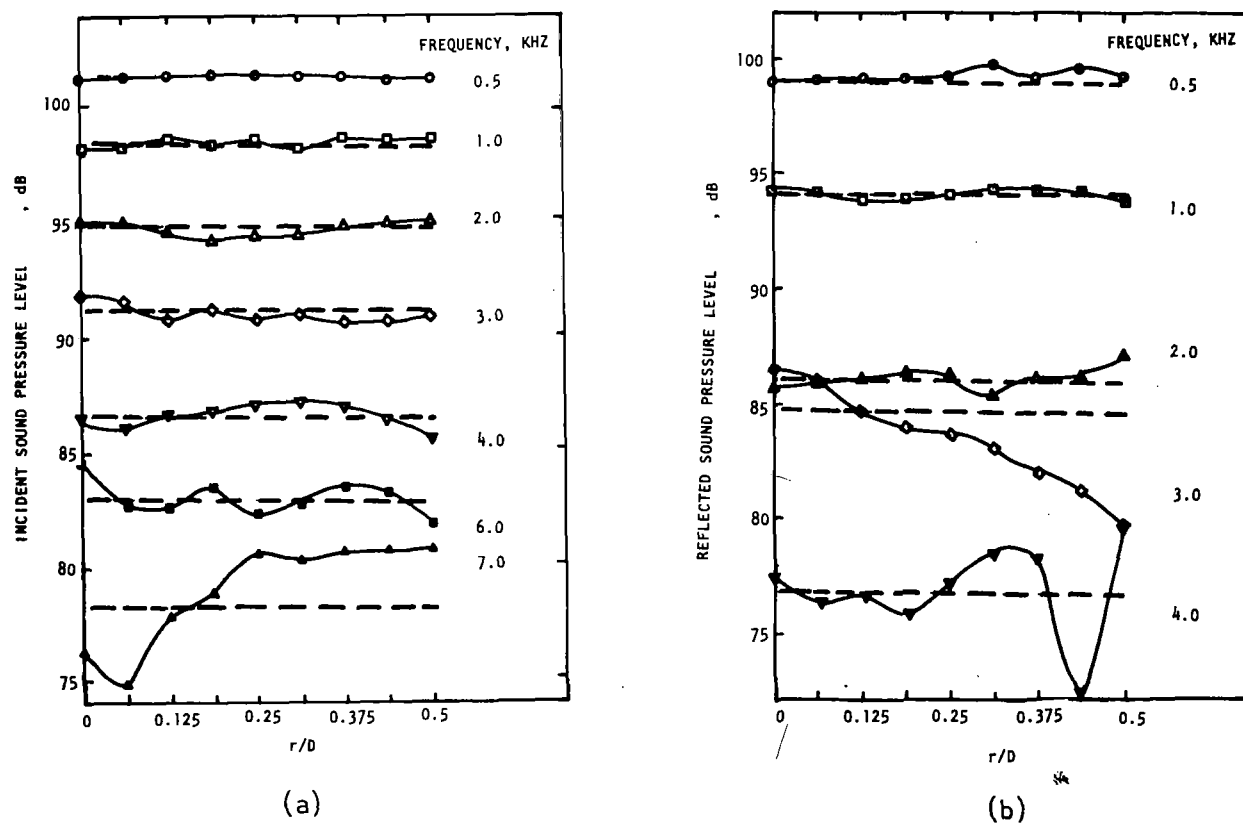


Figure 5.9 Radial variation of (a) incident and (b) reflected sound pressure levels for a straight duct at various frequencies measured by a pressure transducer probe, $M_j = 0.0$, (dashed lines represent the area weighted levels).

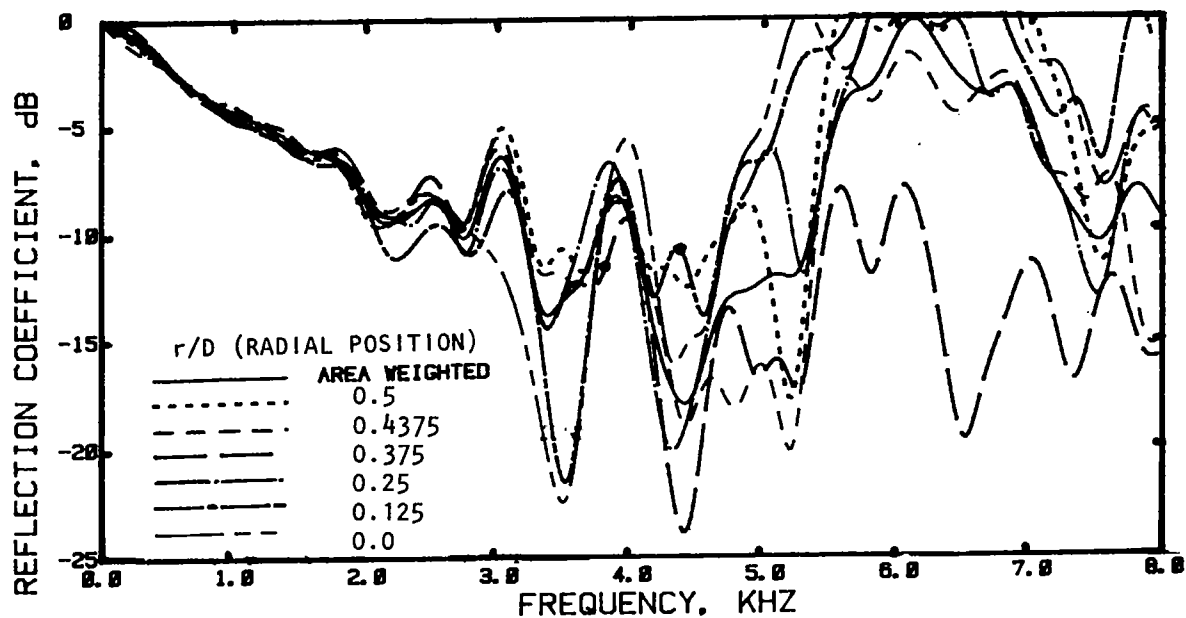


Figure 5.10 Radial variation of reflection coefficient spectrum and the area weighted spectrum measured by a pressure transducer for a 10 cm diameter duct termination, $H_j = 0.0$.

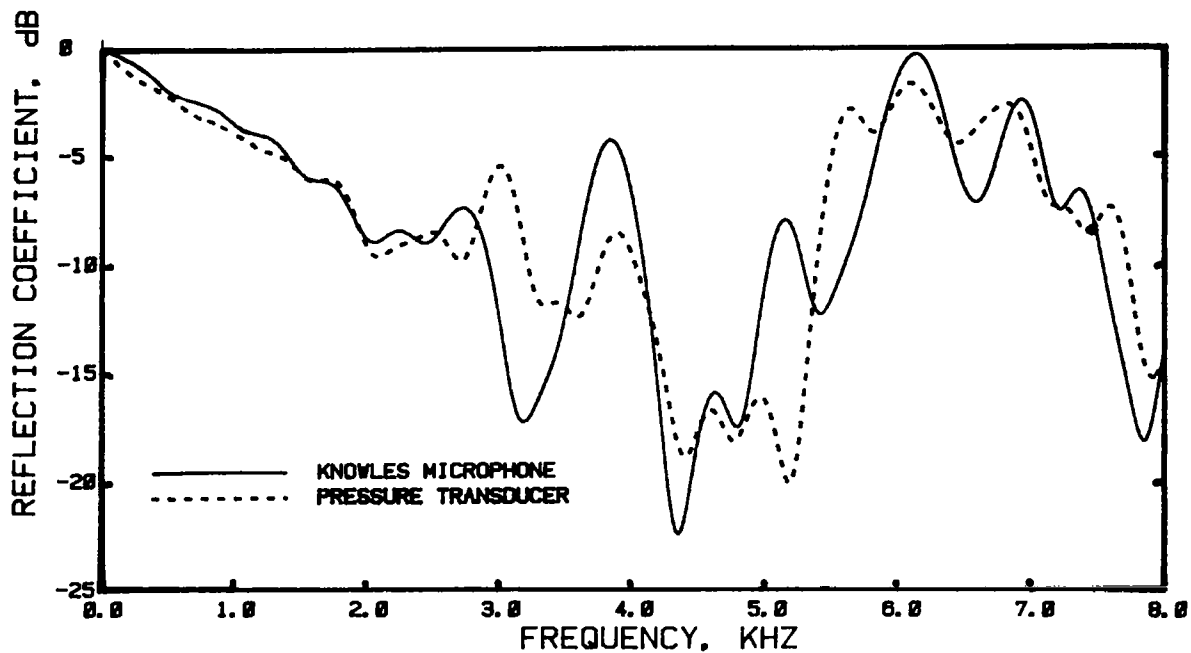


Figure 5.11 Comparison between the reflection coefficient spectra measured by Knowles microphone and by a pressure transducer for a 10 cm diameter duct termination, $M_j = 0.0$, $r/D = 0.4375$.

From the observations made so far it can be said that the effect of probe size on the induct acoustic pressure field is significant when the probe is projected sufficiently inside the duct. However, when the probe is at and near the duct surface, the effect of the probe size on the acoustic field is almost negligible.

It can be noted at this stage that the spectral distribution, for the incident or reflected pressure levels at a given r/D position, derived by the Knowles microphone probe, is slightly different compared to that derived by the pressure transducer. However, the spectral distribution of the reflection coefficients derived by both the probes are quite similar. This is due to the difference in the frequency responses of the individual probes. If the appropriate frequency response corrections are applied to the incident or reflected pressure levels the pressure level spectra derived by both the probes more or less come out to be identical. However, for this exercise, where the relative values, not the absolute values, are needed, such corrections are not needed.

5.2.1.4 Experimental Results for the Duct Termination at Flow Mach Number, $M_J = 0.2$

The radial variation results for incident pressure, reflected pressure, and reflection coefficient at $M_J = 0.2$ obtained by using both the probes are presented in figures 5.12 through 5.18 exactly in the same manner as the no flow results presented earlier. The following observations can be made by examining the results for $M_J = 0.2$:

(1) The results derived from the measurements made at $r/D = 0.4375$ using the Knowles microphone probe are compared with the area-weighted values computed by using all nine radial measurements in figures 5.12 through 5.14. Except for a few frequencies, the agreement between the results is very good for the complete frequency range.

(2) The power reflection coefficients, as shown in figure 5.14, become positive (i.e. greater than unity in linear scale) at some frequencies. However, as seen in equation (5.10), the Mach number term associated with the power reflection coefficient, in the calculation of W_t , would keep the product of σ and Mach number term well below 0 dB. Therefore, at frequencies where the agreement between the area-weighted power reflection coefficients and those measured at $r/D = 0.4375$ is not very good, the calculated radiated power will not be affected severely when σ values measured at $r/D = 0.4375$ are used instead of the area-weighted results.

(3) The influence of the pressure transducer probe on the induct pressure field is considerably increased at this flow condition compared to the no flow situation. The influence seems to be more when r/D is small (see figures 5.15 through 5.17).

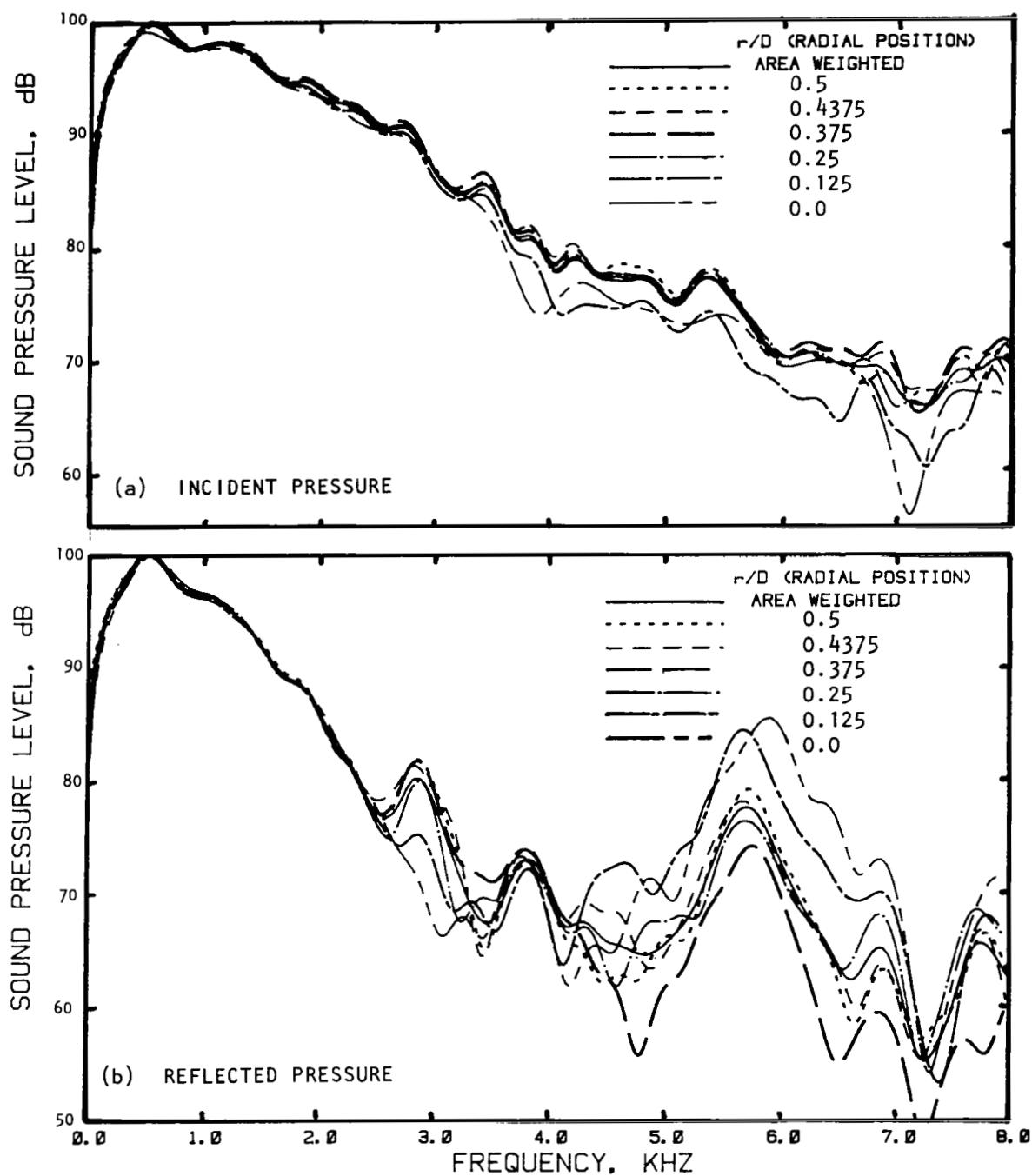
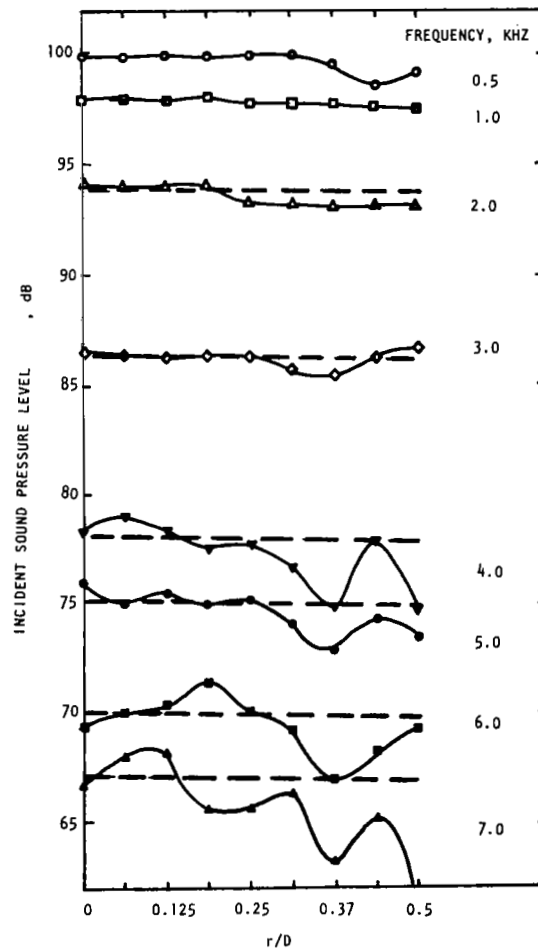
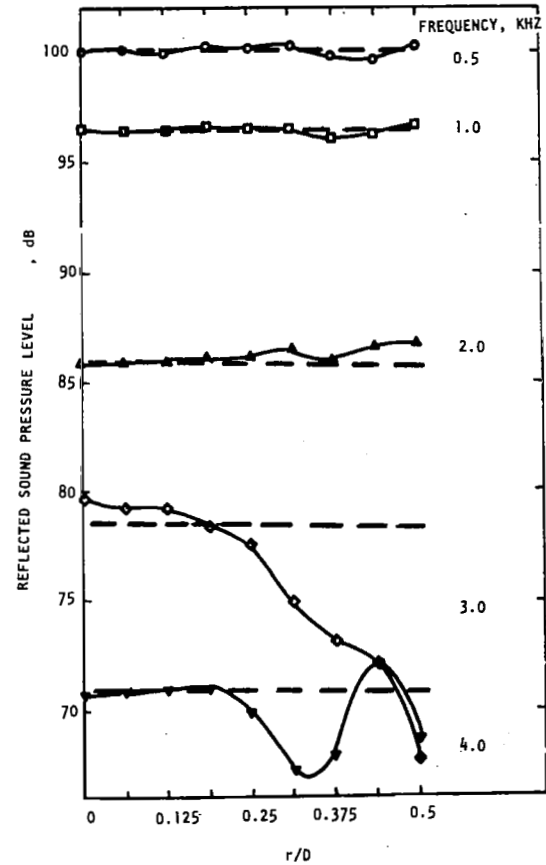


Figure 5.12 Radial variation of (a) incident and (b) reflected sound pressure level spectra; and the corresponding area weighted spectra measured by a Knowles microphone for a 10 cm diameter duct termination, $M_j = 0.2$.



(a)



(b)

Figure 5.13 Radial variation of (a) incident and (b) reflected sound pressure levels for a straight duct at various frequencies measured by a Knowles microphone probe, $M_j = 0.2$, (dashed lines represent area weighted levels).

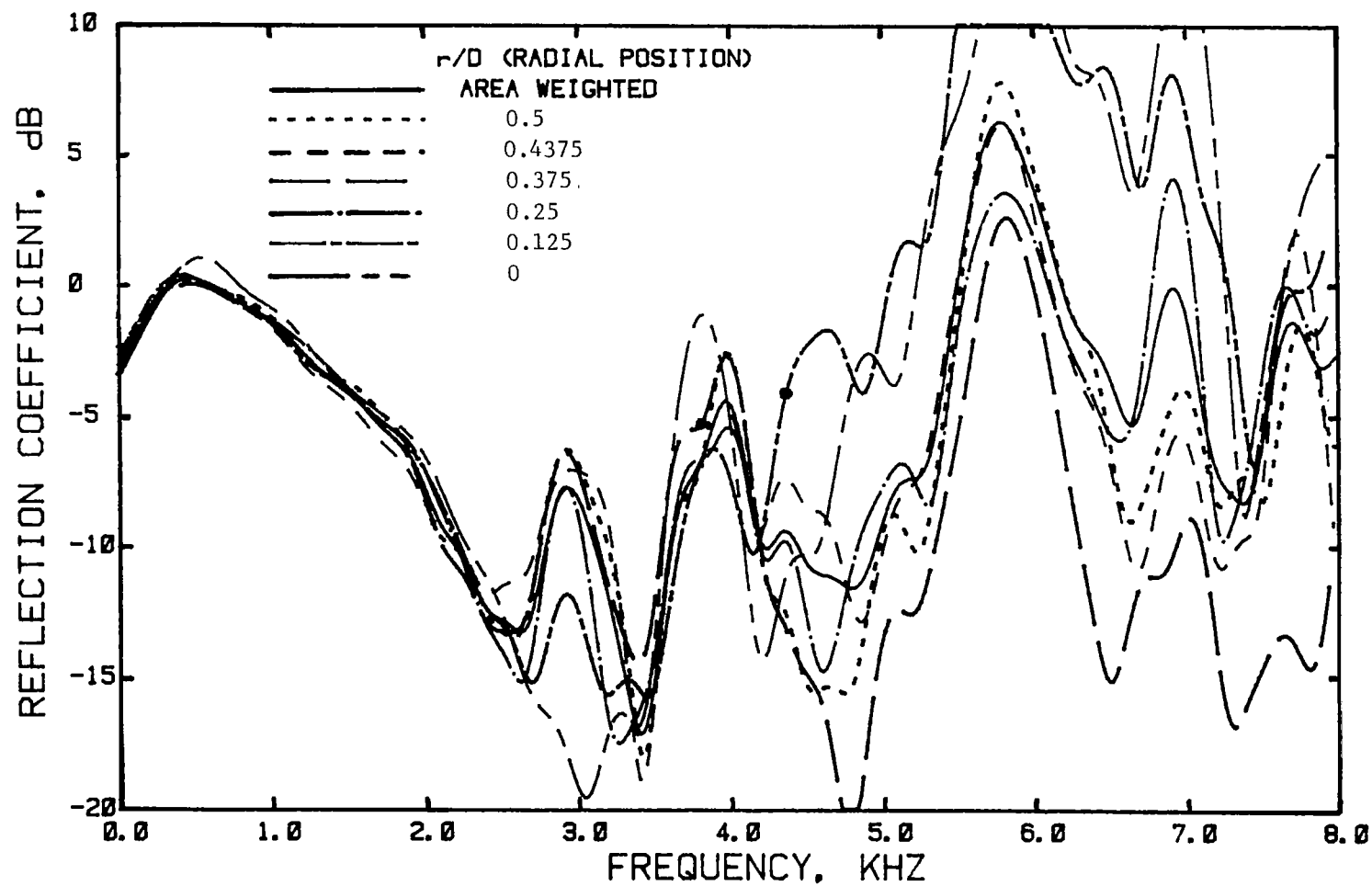


Figure 5.14 Radial variation of reflection coefficient spectrum and the corresponding area weighted spectrum measured by a Knowles microphone for a 10 cm diameter straight duct, $M_j = 0.2$.

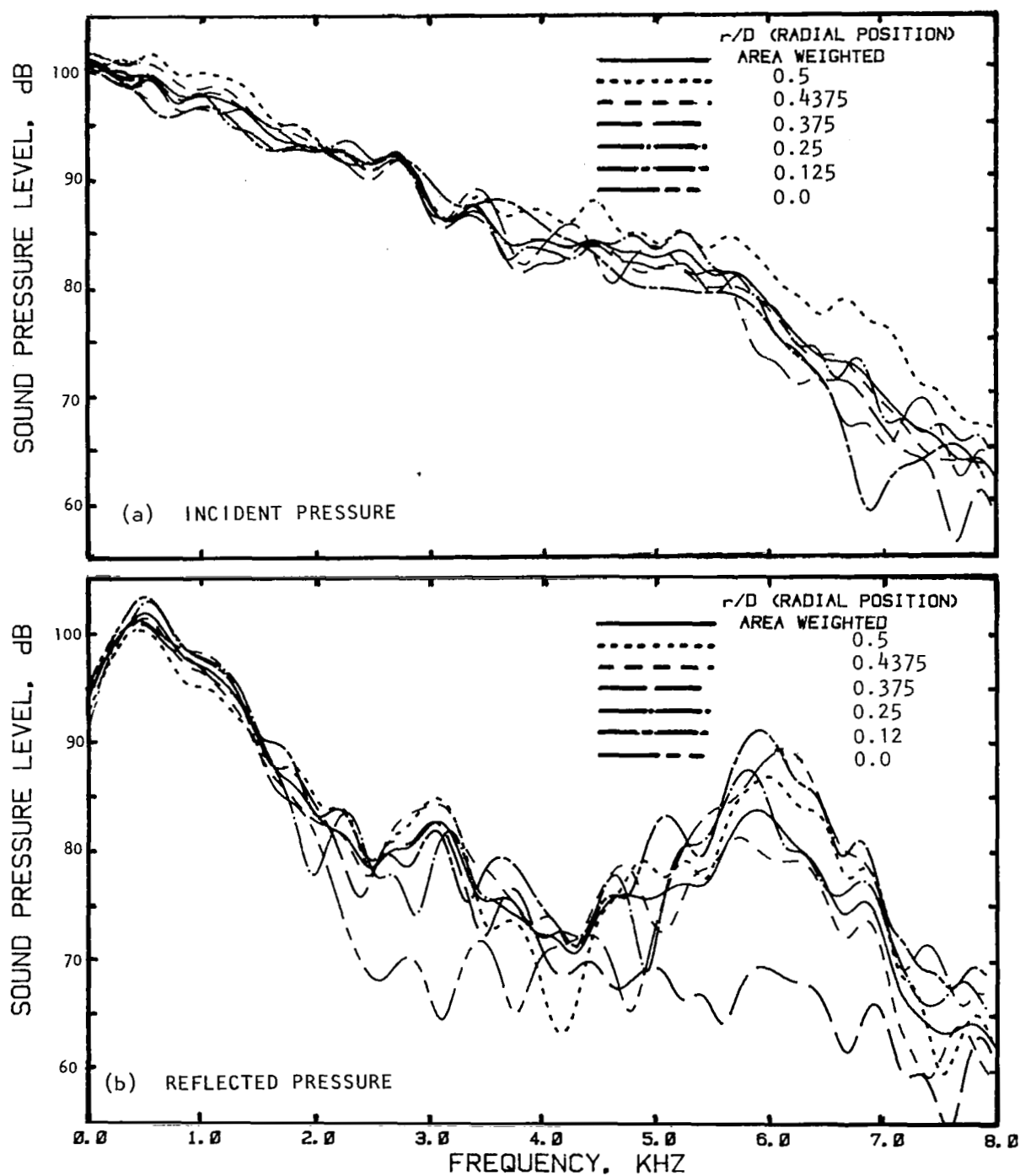
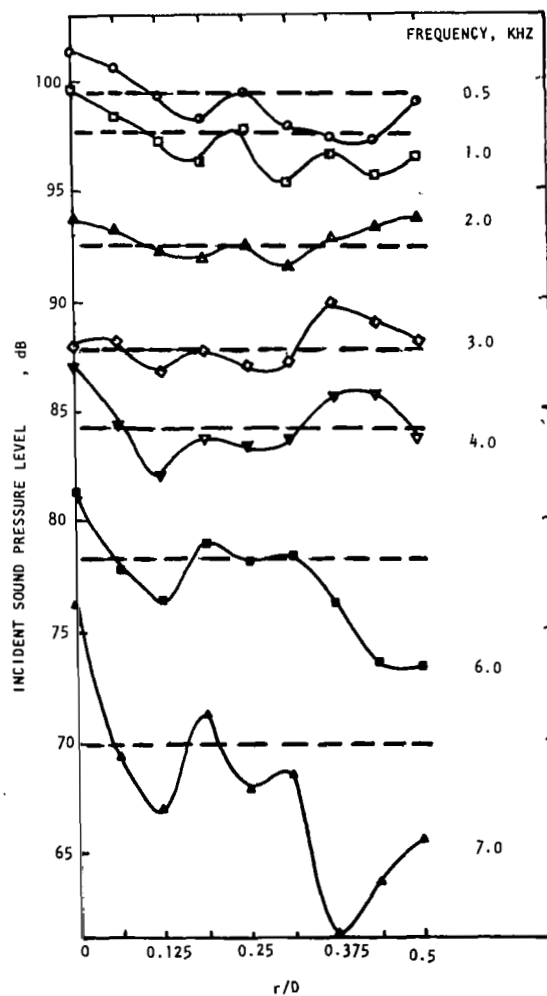
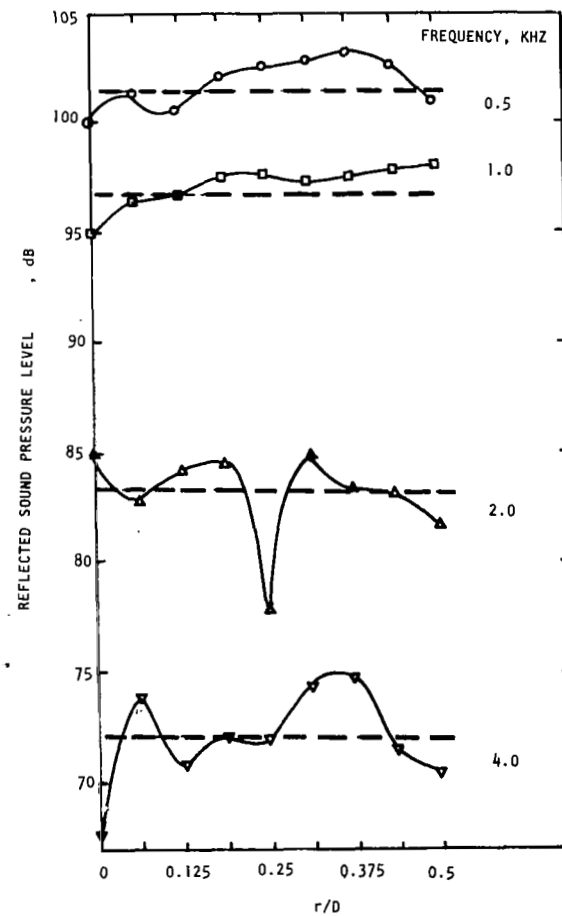


Figure 5.15 Radial variation of (a) incident and (b) reflected sound pressure level spectra and the corresponding area weighted spectra measured by a pressure transducer for a 10 cm diameter duct termination, $M_j = 0.2$.



(a)



(b)

Figure 5.16 Radial variation of (a) incident and (b) reflected sound pressure levels for a straight duct at various frequencies measured by a pressure transducer probe, $M_j = 0.2$, (dashed lines represent the area weighted levels).

(4) The reflection coefficients measured at $r/D = 0.4375$ using both the probes agree well for frequencies upto about 2.5 KHz (see figure 5.18).

5.2.1.5 Experimental Results for the Conical Nozzle Termination

(a) Incident Pressure Field

The radial variation of the incident sound pressure level spectrum and the corresponding area-weighted spectrum of the incident sound field for the conical nozzle termination are plotted in figure 5.19 for jet Mach numbers of 0.0, 0.4, 0.6 and 0.8. The radial variation of the incident sound pressure level at selected frequencies is cross plotted in figure 5.20 for jet Mach numbers of 0.0, 0.4, 0.6 and 0.8.

The following observations are made from the results presented in figures 5.19 and 5.20.

(1) The radial variation of the incident sound pressure level is insignificant up to about 4 KHz. Beyond 4 KHz, an appreciable difference is observed between the pressure levels measured at different radial locations.

(2) The incident pressure measurements at $r/D = 0.4375$ agree well with the area-weighted results up to about 6 KHz, beyond which the agreement deteriorates.

(b) Reflected Pressure Field

The radial variation of the reflected sound pressure level spectrum and the corresponding area-weighted spectrum of the reflected sound field for the conical nozzle termination are plotted in figure 5.21 for jet Mach numbers of 0.0, 0.4, 0.6 and 0.8. Cross plots of the reflected sound field with respect to radial distance, r/D , at various frequencies, corresponding to the spectral plots shown in figure 5.21 are also presented in figure 5.22.

The following observations are made from the results presented in figures 5.21 and 5.22.

(1) The radial variation of the reflected sound pressure level is insignificant up to about 2.5 KHz for jet Mach numbers of 0.0, 0.4 and 0.6. Beyond this frequency, significant radial variation is observed. However, for $M_J = 0.8$ (M_J being the jet Mach number) significant radial variation is noticed from about 1.5 KHz onward.

(2) The reflected pressure values measured at $r/D = 0.4375$ agree well with the area-weighted results up to about 4 KHz for jet flow Mach numbers of 0.0, 0.4 and 0.6. For $M_J = 0.8$, this agreement deteriorates

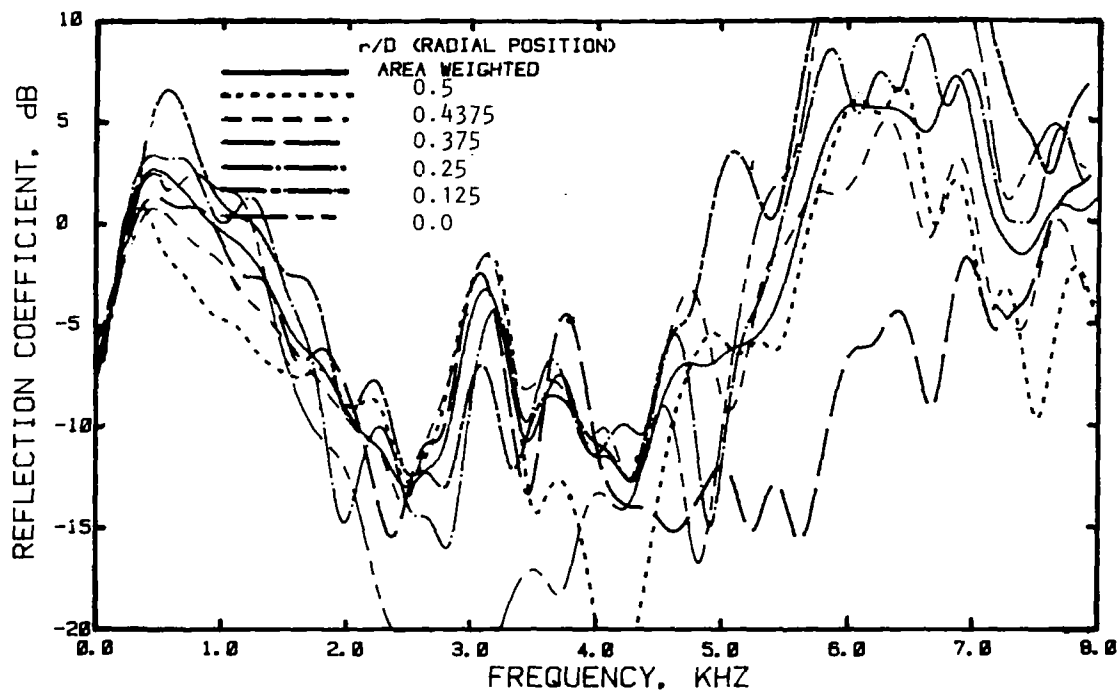


Figure 5.17 Radial variation of reflection coefficient spectrum and the corresponding area weighted spectrum measured by a pressure transducer for a straight duct, $M_j = 0.2$.

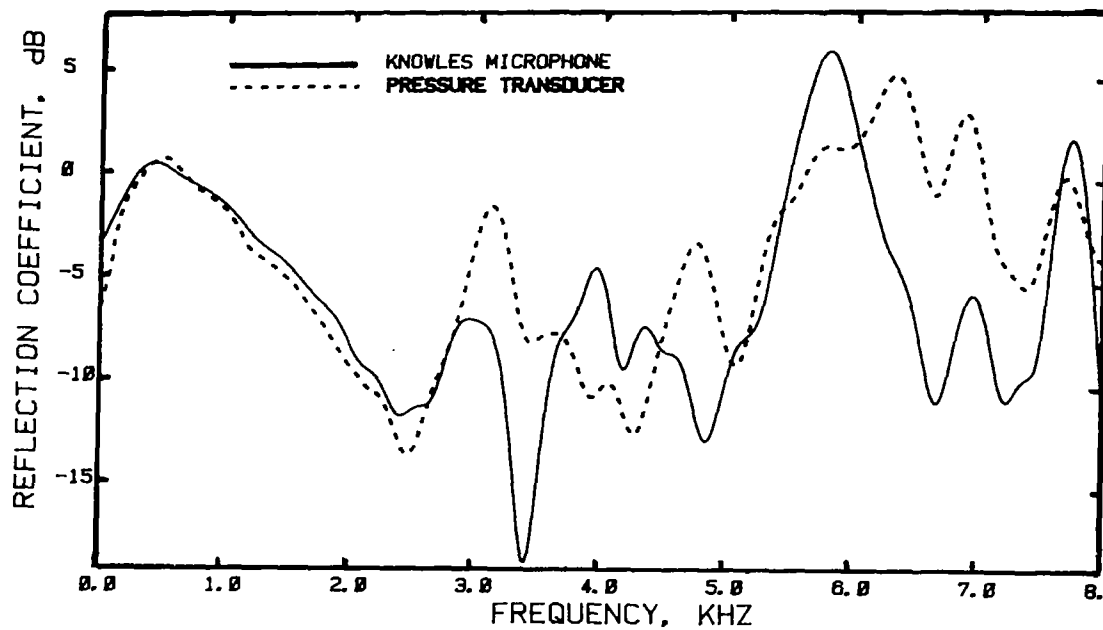


Figure 5.18 Comparison between the reflection coefficient spectra measured by a Knowles microphone and by a pressure transducer for a straight duct, $M_j = 0.2$, $r/D = 0.4375$.

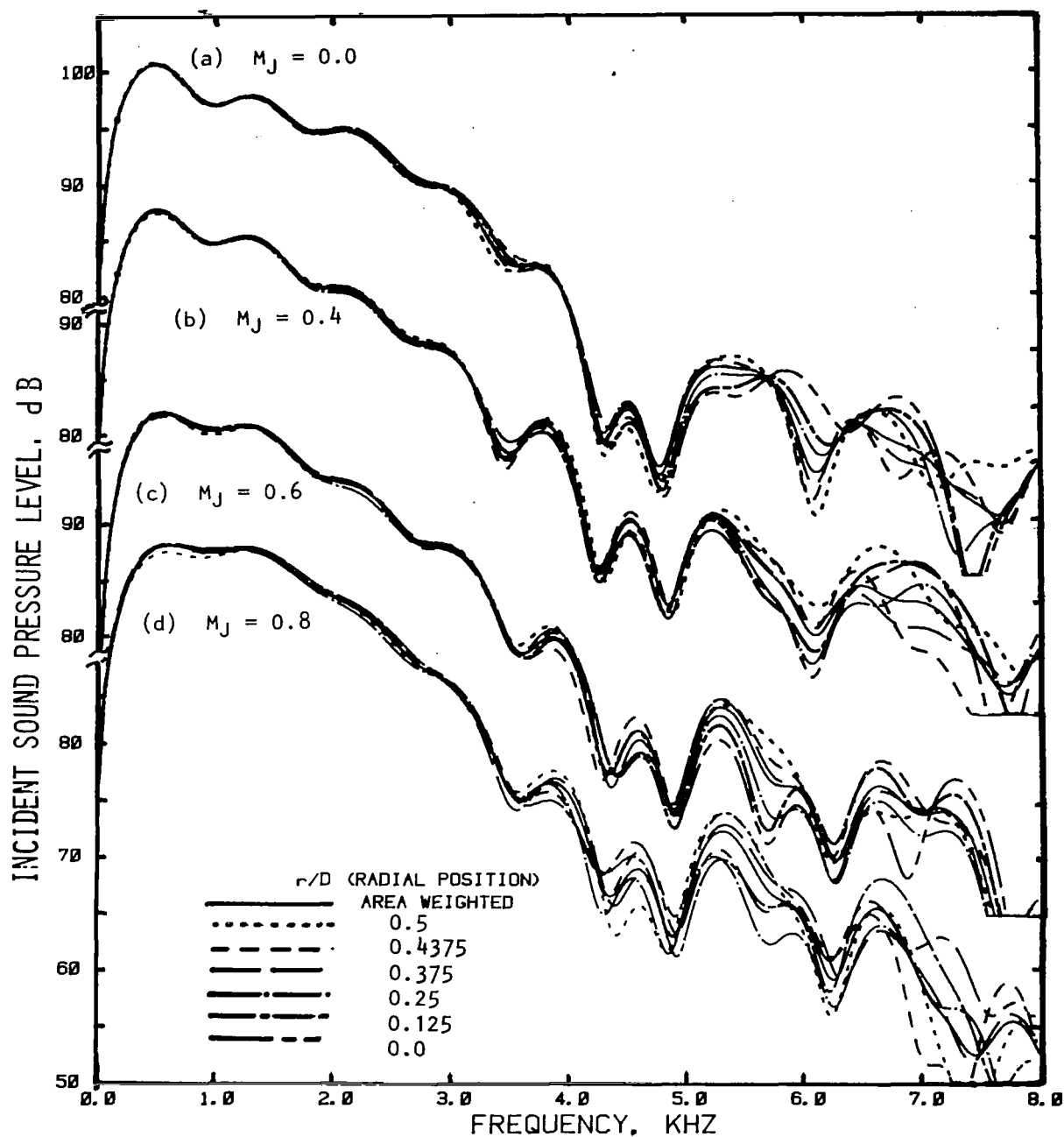


Figure 5.19 Radial variation of incident sound pressure level spectrum and the corresponding area weighted spectrum for a 6.2 cm diameter conical nozzle termination at various Mach numbers.

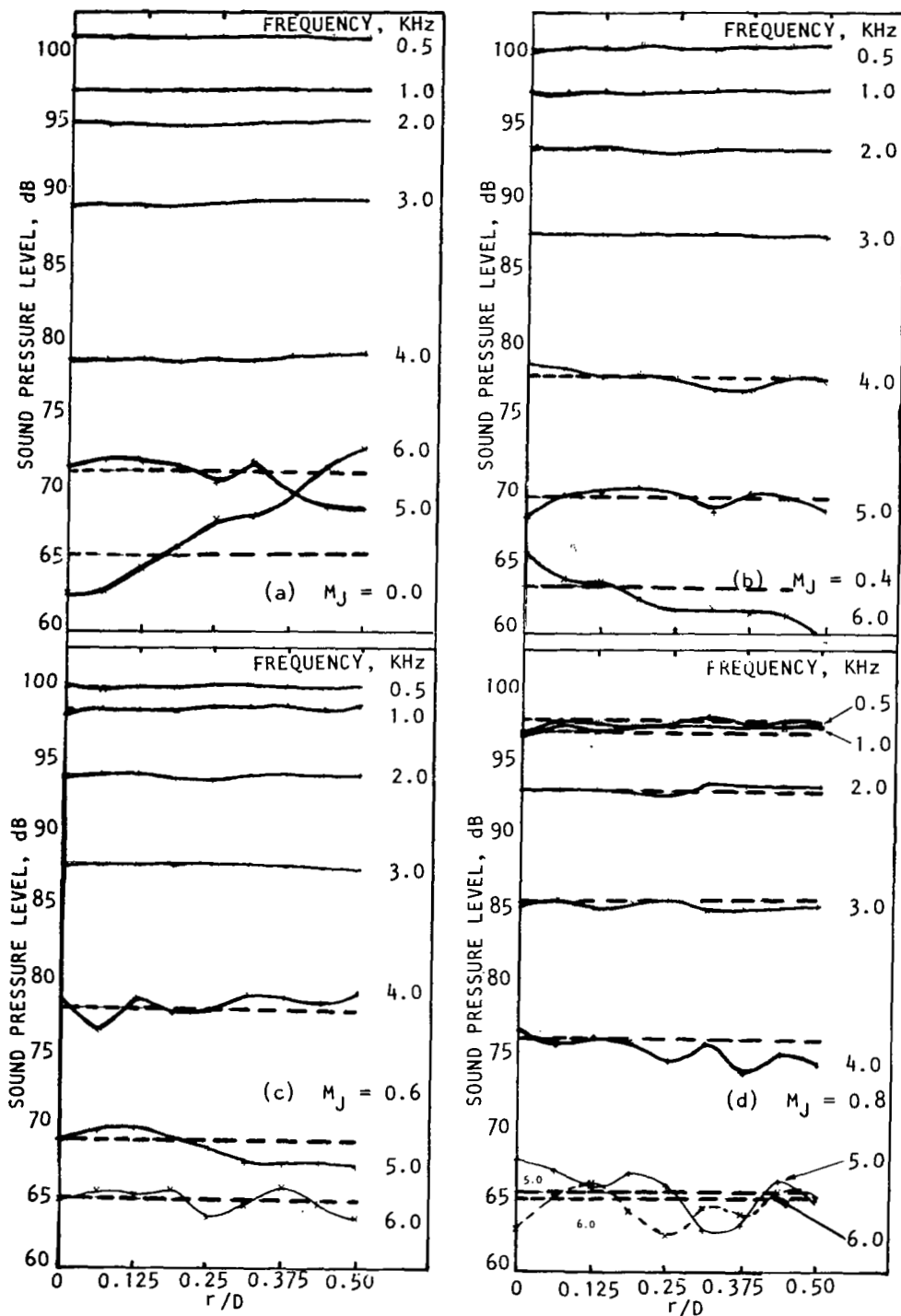


Figure 5.20 Radial variation of incident sound pressure levels at various frequencies for a 6.2 cm diameter conical nozzle termination at different Mach numbers, (dashed lines represent the area weighted levels)

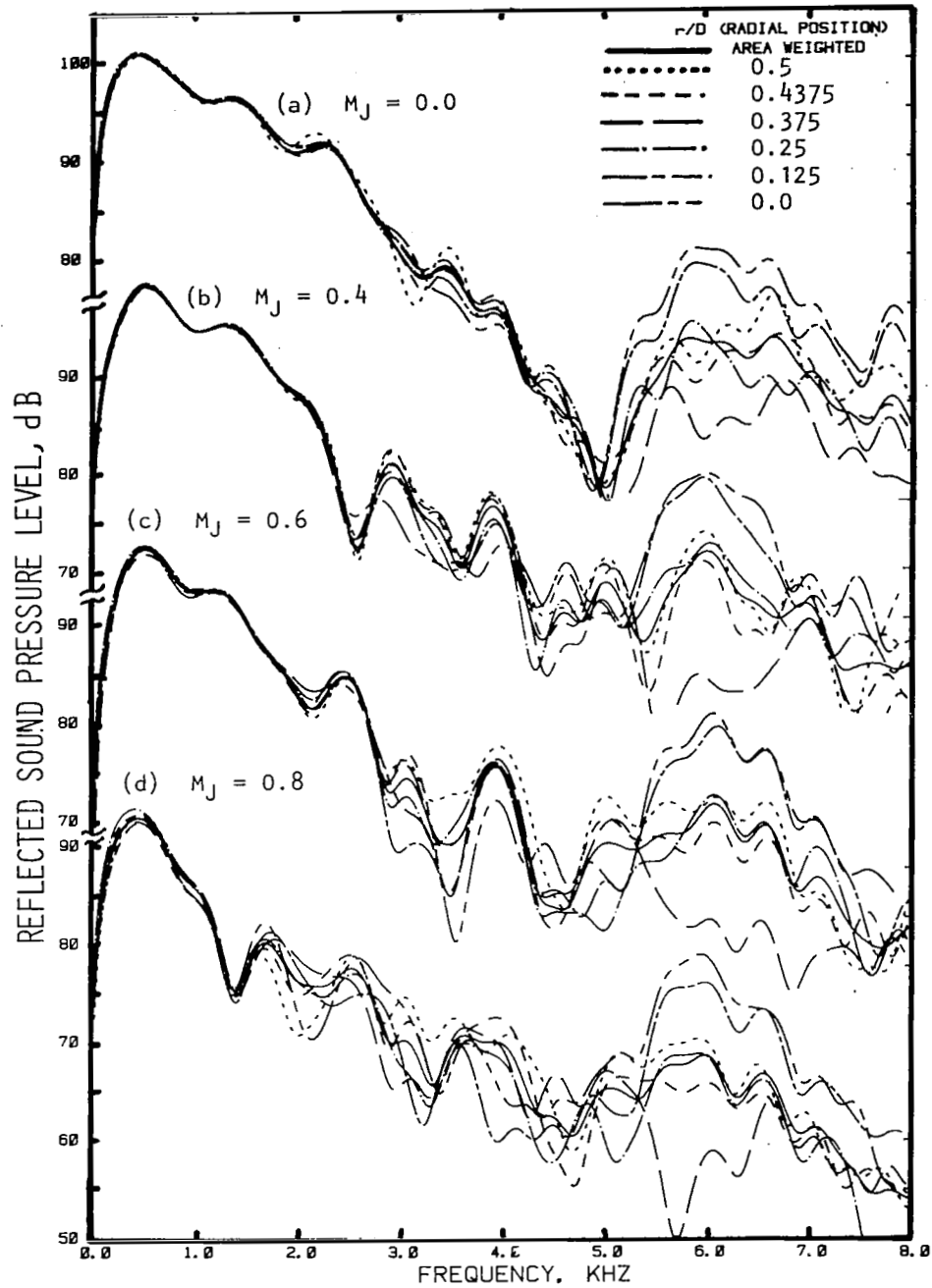


Figure 5.21 Radial variation of reflected sound pressure level spectrum and the corresponding area weighted spectrum for a 6.2 cm diameter conical nozzle at various Mach numbers.

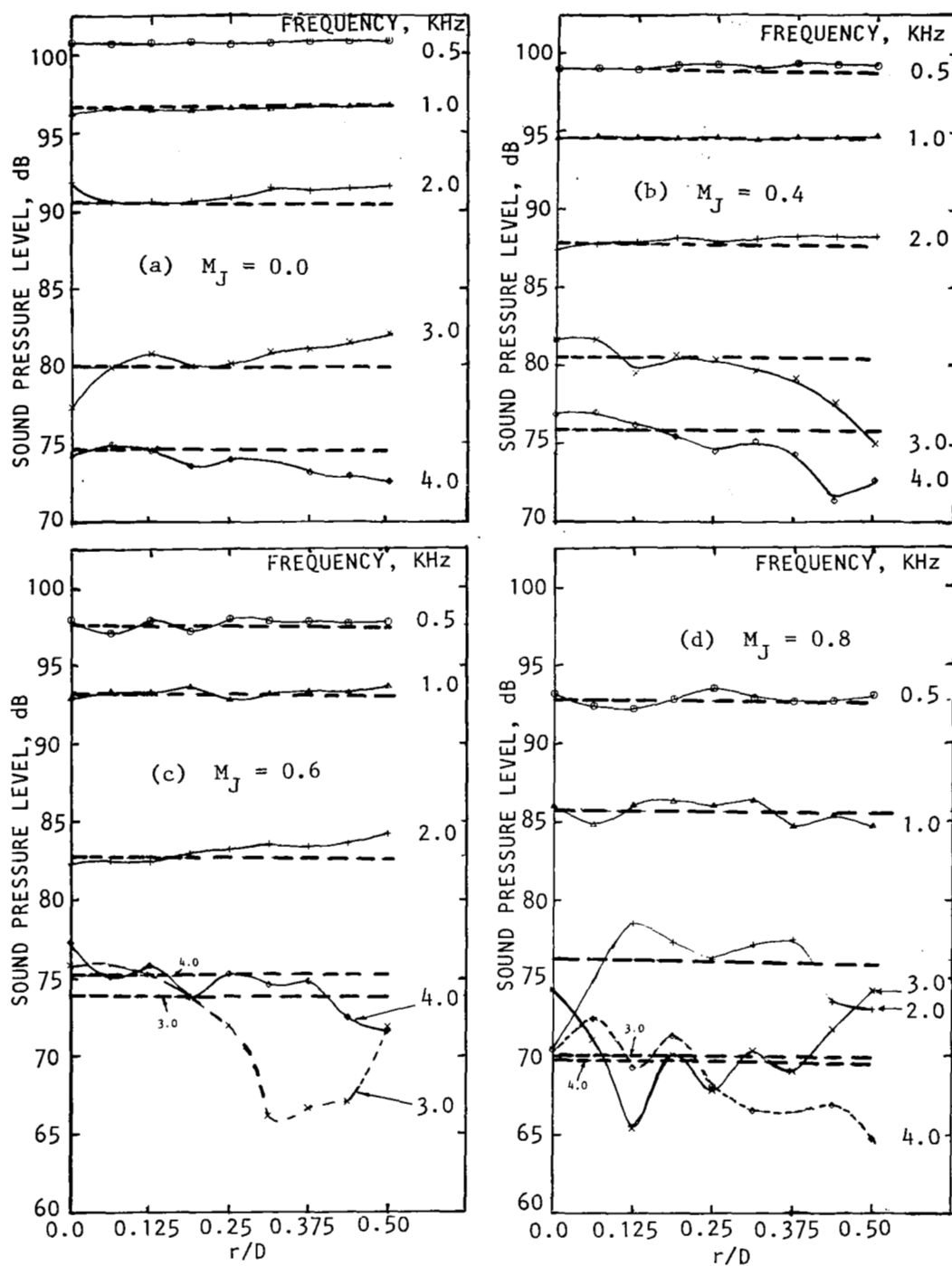


Figure 5.22 Radial variation of reflected pressure levels at various frequencies for a 6.2 cm diameter conical nozzle termination at various Mach numbers, (dashed lines represent the area weighted levels).

from about 1.5 KHz.

(c) Power Reflection Coefficient

The power reflection coefficient spectra at various radial locations and the corresponding area-weighted spectrum for the conical nozzle termination are plotted in figure 5.23 for jet Mach numbers of 0.0, 0.4, 0.6 and 0.8. The observations for these power reflection coefficients are similar to those for the reflected pressure fields.

(d) Transmitted Power for the Duct and the Nozzle Terminations

So far all the discussions were made concerning the incident mean-square pressure field, the reflected mean-square pressure field, and the power reflection coefficients. However, the main objective of the study was to determine whether or not the transmitted power computed by using a single-point measurement is comparable to the transmitted power computed by using the area-weighted values. Therefore the transmitted power was computed first by using the measured data at various radial locations and then by using the area-weighted values. The plane wave relationship of equation (5.10) was used to compute the transmitted power, W_t .

The transmitted power was computed for both the 10 cm diameter straight duct and for the 6.2 cm diameter conical nozzle. For conical nozzle, the transmitted power was computed only up to 4 KHz since the parameter

$$\frac{p_r^2}{p_i^2} \left[\frac{1 - M_D}{1 + M_D} \right]^2$$

in equation (5.10) becomes greater than unity at most of the frequencies beyond 4 KHz, which is physically not possible. The reason for this is the use of the plane wave relationship to compute W_t , which is not valid since the higher order modes are prominent at frequencies above approximately 4 KHz.

The transmitted powerspectra for the straight duct are plotted up to 8 KHz in figure 5.24 for jet flow Mach numbers of 0.0 and 0.2. The transmitted power spectra for the conical nozzle termination are plotted up to 4 KHz in figure 5.25 for jet flow Mach numbers of 0.0, 0.4, 0.6 and 0.8. In all these plots the transmitted power computed using the measured data at $r/D = 0.4375$ is compared with the transmitted power computed using the area-weighted values. The agreement is excellent. Therefore, it can be concluded that a single-point measurement at or near $r/D = 0.4375$ is adequate to compute the transmitted power for all frequencies considered in the present study (up to 8 KHz) for a straight duct, and for frequencies up to about 4 KHz, (first radial cut-on frequency) for the conical nozzle.

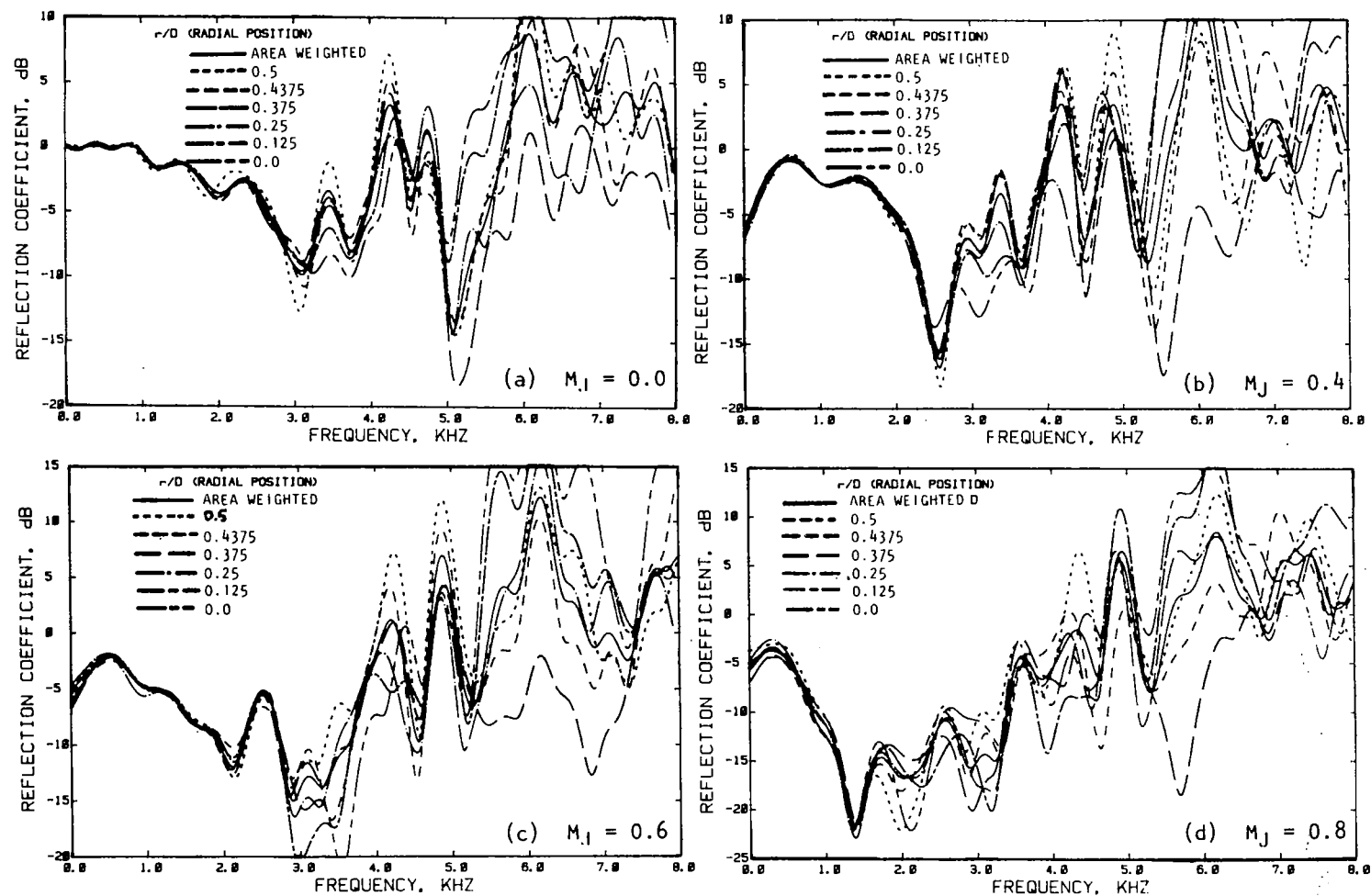


Figure 5.23 Radial variation of reflection coefficient spectrum and the corresponding area weighted spectrum for a 6.2 cm diameter conical nozzle at various Mach numbers.

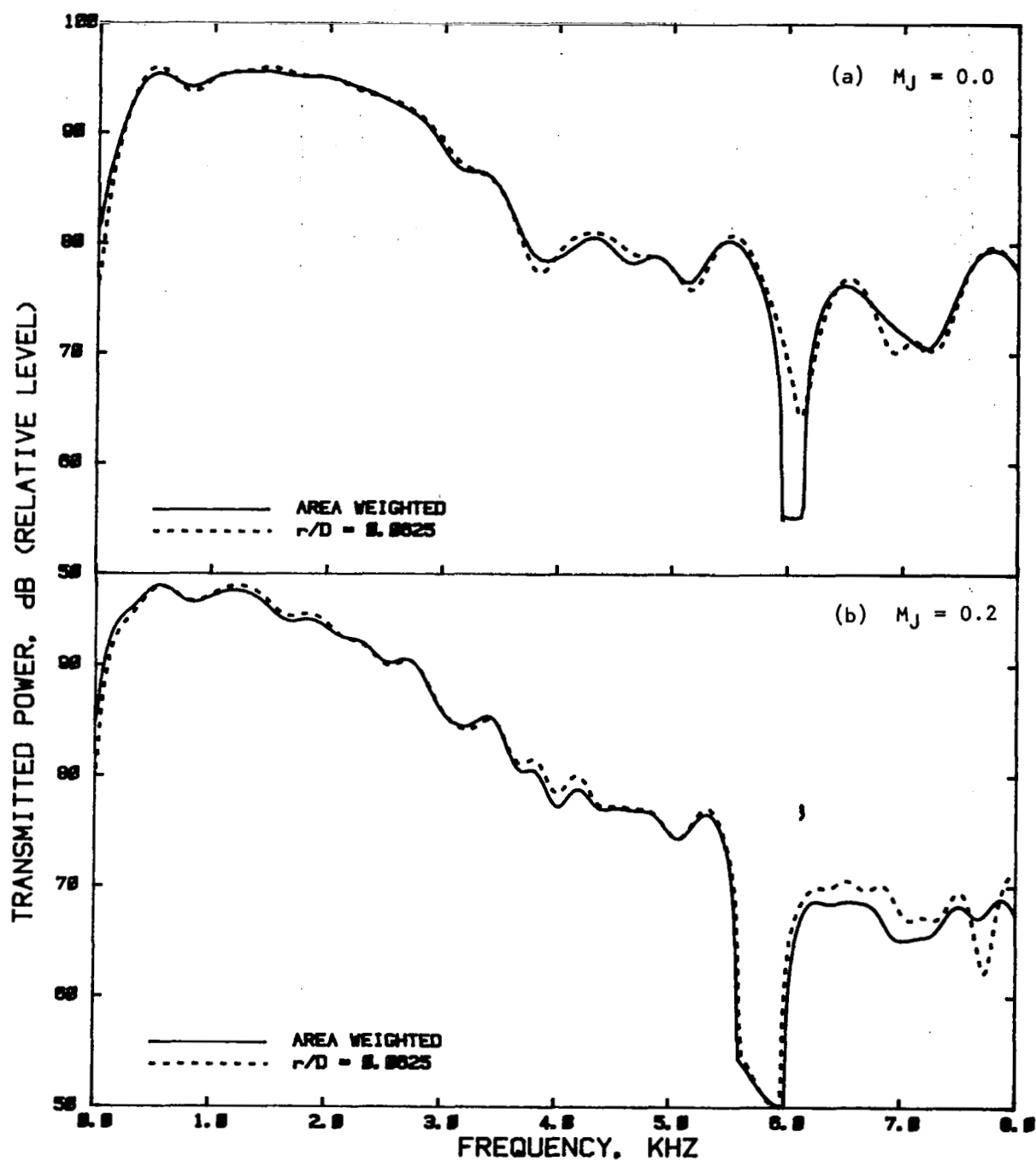


Figure 5.24 Comparison of transmitted power computed using area weighted pressure levels and corresponding pressure levels measured at $r/D = 0.4375$ for a 10 cm diameter duct at (a) $M_J = 0$ and (b) $M_J = 0.2$.

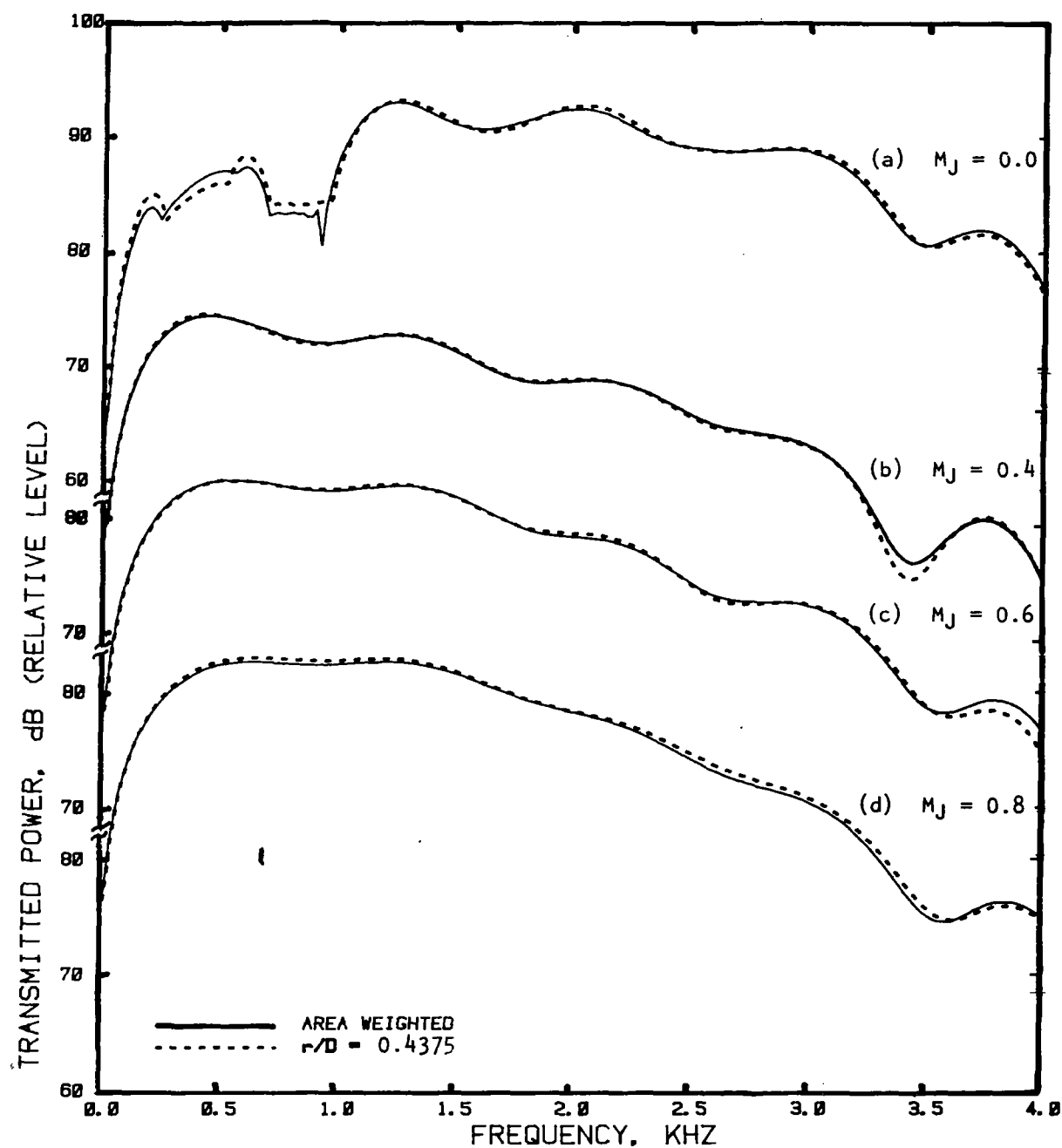


Figure 5.25 Comparison of transmitted power computed using area weighted pressure levels and the corresponding pressure levels measured at $r/D = 0.4375$ for a 6.2 cm diameter conical nozzle at (a) $M_J = 0.0$, (b) $M_J = 0.4$, (c) $M_J = 0.6$, and (d) $M_J = 0.8$.

5.2.2 Radial and Azimuthal Variation of Induct Pressure Field for Annular Duct, and Validity of Single Point Measurement

The annular facility and the six-point measuring probe described in section 3 were used in this study. Tests were carried out using a straight annular termination and a 6.2 cm outer conical nozzle termination at various flow conditions outlined in Table 5.2.

Table 5.2 Test conditions for annular duct experiments to survey radial and azimuthal variation of induct sound field

TERMINATION	JET FLOW MACH NUMBER
Straight Annular Termination	0, 0.2
Outer Conical Nozzle Annular Termination	0, 0.4, 0.6, 0.8

In addition to the tests described in Table 5.2, two more tests were conducted with the straight annular duct. In one of these, a rigid plate termination was used to block the termination opening, and in the second, 2.5 cm thick polyurethane foam, backed by a steel plate was used to block the termination opening.

In each test, induct time histories were measured at six radial locations in the annular cross section, between the outer and inner wall at six azimuthal positions, 60 degrees apart. The measured data were used to evaluate the incident and the reflected sound pressure level spectra and the reflection coefficient spectra.

5.2.2.1 Experimental Results for No Flow Condition

(1) Straight Annular Duct Termination:

The radial and azimuthal distribution and the area-weighted spectral data for the incident pressure field for the annular duct termination are presented in figures 5.26 and 5.27. The incident sound pressure level spectra measured at various radial locations for a number of fixed azimuthal angles are presented in figure 5.26. In this figure, six sets of plots are presented each one for a given azimuthal position, namely, 0°, 60°, 120°, 180°, 240° and 300°. Even though the measurements were made at six radial locations, only four radial measurements are presented in this figure for clarity. On each set of plots, the area-weighted spectrum, derived using all 36 spatial measurements, is superimposed. It can be seen from this figure that at frequencies up to 5 KHz a negligible amount of radial variation exists in the incident pressure field at each of the azimuthal positions. A small amount of radial variation is observed at higher frequencies.

The spectral distributions, as seen in figure 5.26, for various

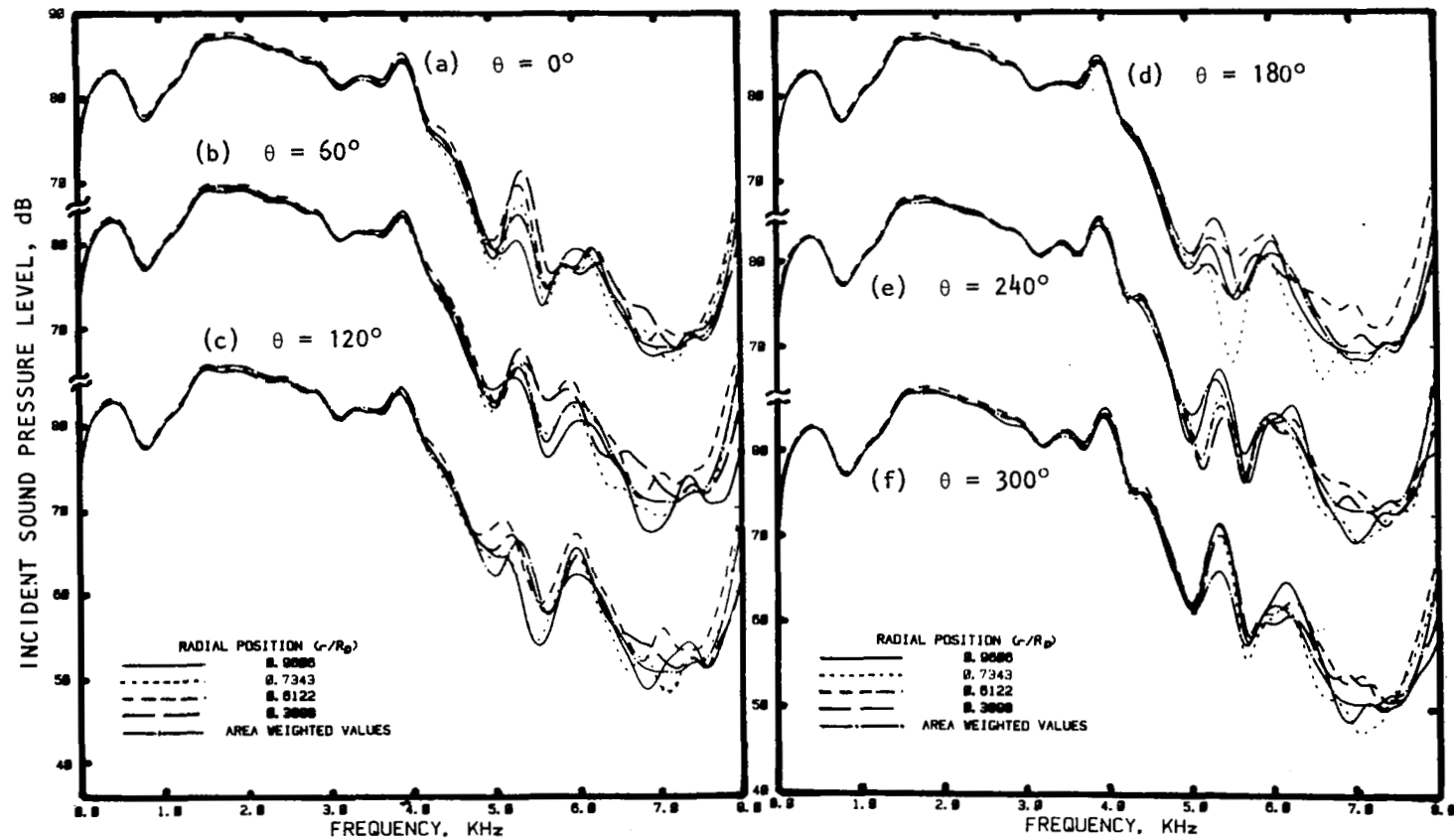


Figure 5.26 Radial variation of incident sound level spectrum and the corresponding area weighted spectrum for an annular duct at six azimuthal positions, $M_j = 0.0$.

radial locations agree very well with the area-weighted spectrum. This behavior indicates that the incident pressure field is quite uniform even in the azimuthal direction at least up to 5 KHz. To confirm this, spectral data for a number of fixed radial locations at six different azimuthal positions are plotted in figure 5.27. Four such sets are presented in this figure, each for a given radial position. Figure 5.27 indeed indicates that for frequencies up to about 5 KHz, the azimuthal variation of the incident pressure field is quite small.

The spectral variations, both radial and azimuthal, for the reflected pressure field are shown in figures 5.28 and 5.29, similar to figures 5.26 and 5.27 for the incident pressure field. Figure 5.28 shows that at frequencies up to about 5 KHz, very little radial variation exists at each of the azimuthal positions. However, figure 5.29 indicates a significant azimuthal variation of the reflected pressure field above 2 KHz. The sound pressure levels for the reflected field are considerably lower than the incident pressure field, specially at higher frequencies (above 2 KHz). Therefore, it can be expected that the transmitted power computed by using the area-weighted spectral data would coincide with the transmitted power computed by accounting for the contributions due to the spatial variation of the pressure field (i.e., accounting for the higher order modes), at least up to 5 KHz. In fact, this will be shown later to be true.

(2) Annular Duct System with Outer Conical Nozzle:

The induct measurements for all the annular configurations were taken in the straight portion of the annular duct system. Therefore, for the annular duct system with outer conical nozzle configuration, the incident pressure field is identical to that presented in figures 5.26 and 5.27 for a straight annular duct. In this section, therefore, the spatial variation of the reflected pressure field only is described. The reflected sound pressure level spectra measured at various radial locations for a number of fixed azimuthal angles are presented in figure 5.30. The area-weighted spectral results are also superimposed on each plot of figure 5.30. Similar to the straight annular duct termination, very little radial variation is observed at each of the azimuthal position, at least for frequencies up to 4.5 KHz. To examine the azimuthal variation, the spectral data for the six azimuthal positions at three fixed radial locations are compared in figure 5.31. Again, the behavior seems to be similar to that for the straight annular duct; that is, a significant azimuthal variation of the reflected pressure field exists above 2 KHz.

5.2.2.2 Experimental Results With Flow

A number of tests were conducted at various jet Mach numbers with the annular duct system. The acoustic results for different flow conditions exhibit similar behavior. Therefore, the results for a typical test case are discussed in this section. In this case, the

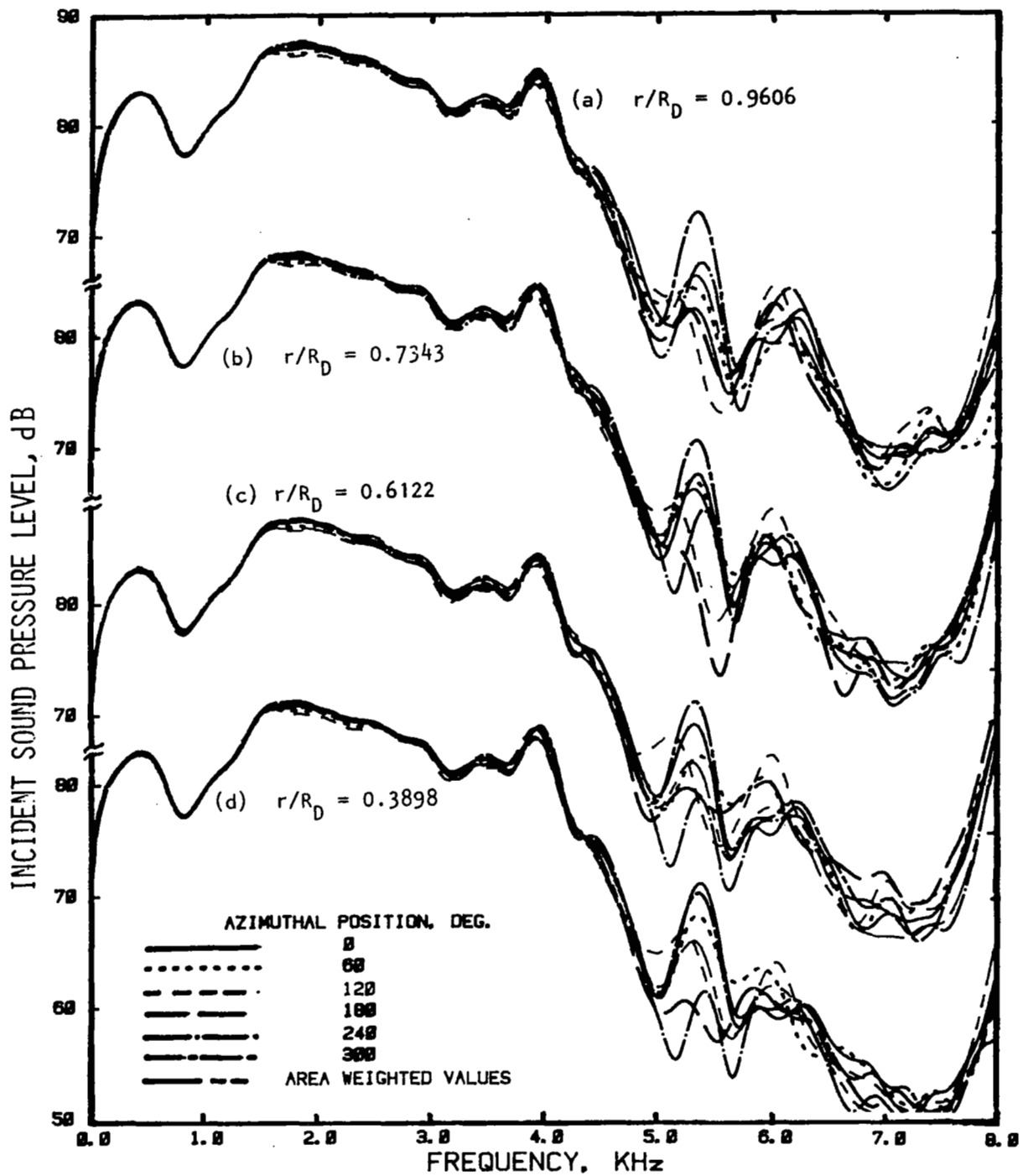


Figure 5.27 Azimuthal variation of incident sound pressure level spectrum and the corresponding area weighted spectrum for an annular duct at various radial locations, $M_j = 0.0$.

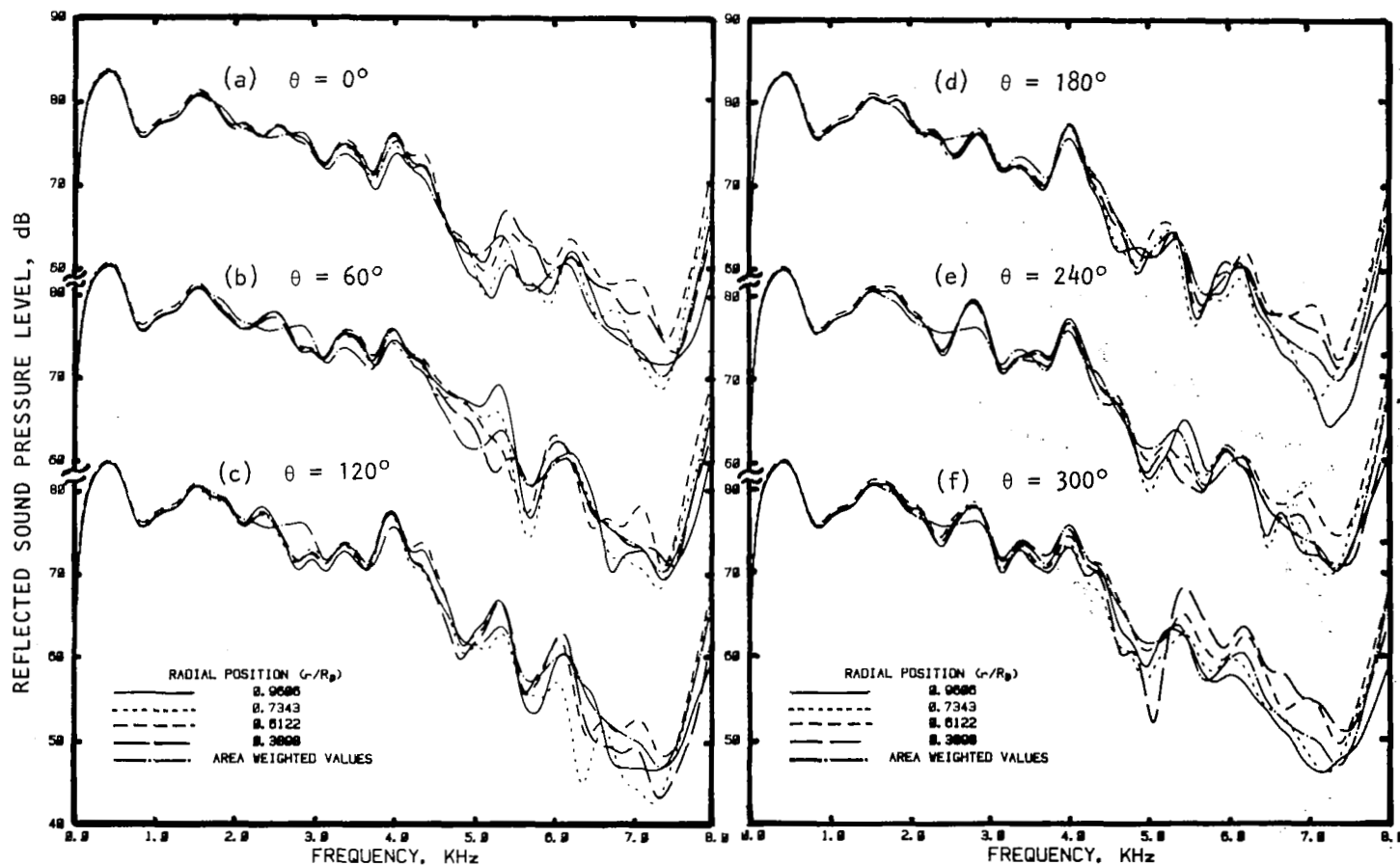


Figure 5.28 Radial variation of reflected sound pressure level spectrum and the corresponding area weighted spectrum for an annular duct at six azimuthal positions, $M_J = 0.0$.

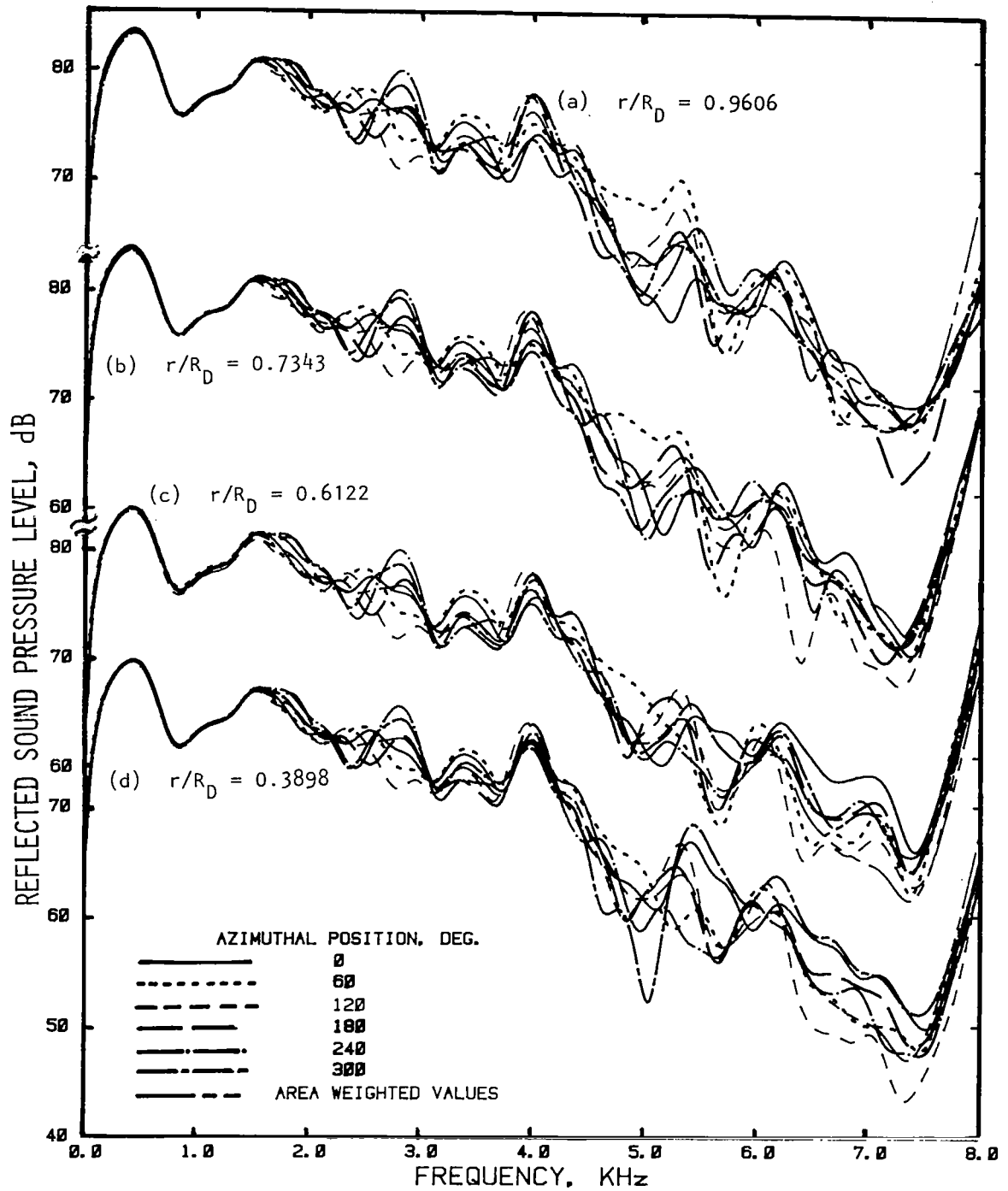


Figure 5.29 Azimuthal variation of reflected sound pressure level spectrum and the corresponding area weighted spectrum for an annular duct at various radial locations, $M_j = 0.0$.

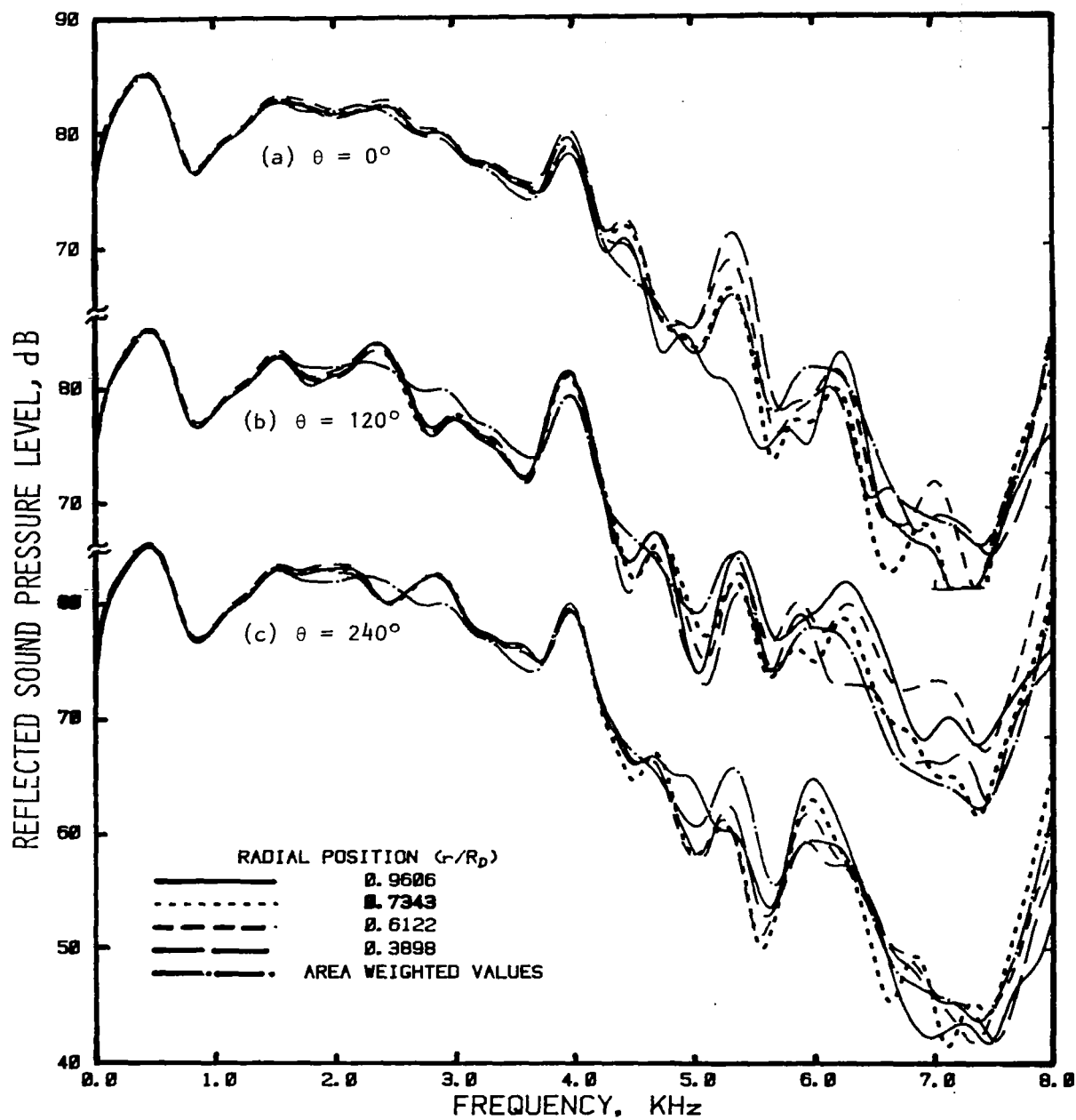


Figure 5.30 Radial variation of reflected sound pressure level spectrum and the corresponding area weighted spectrum for an annular conical nozzle at various azimuthal locations, $M_j = 0.0$.

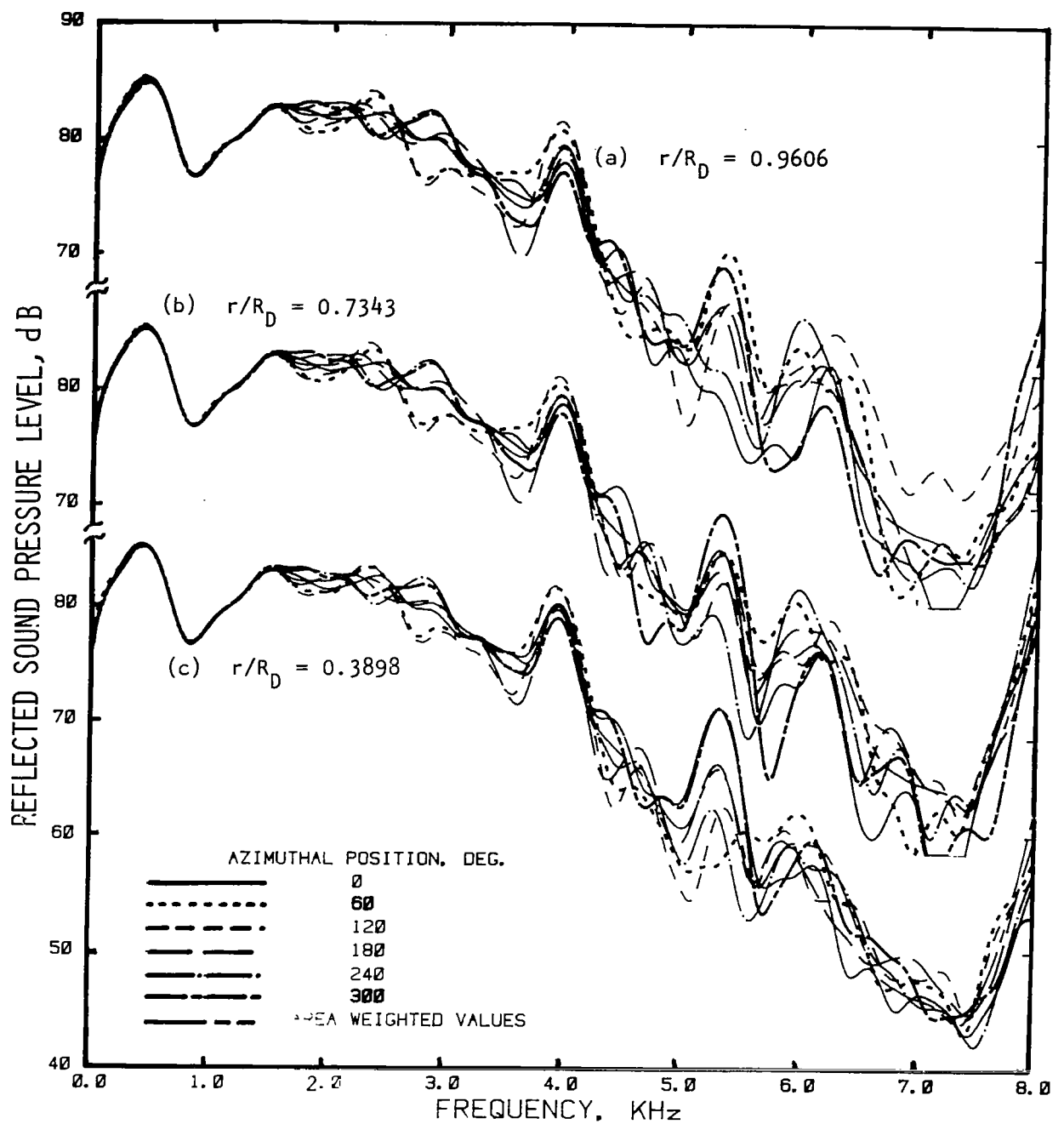


Figure 5.31 Azimuthal variation of reflected sound pressure level spectrum and the corresponding area weighted spectrum for an annular conical nozzle at various radial locations, $M_J = 0.0$.

annular duct system had an outer conical nozzle with 6.2 cm exit diameter and the annular jet flow Mach number was 0.6. However, there was no flow in the core region.

The variation of the induct pressure field for this case is illustrated in figures 5.32 through 5.35. Even in the presence of flow, the incident pressure field seems to be reasonably uniform in the annular cross section (see figures 5.32 and 5.33). However, the azimuthal distribution in figure 5.33 shows relatively more variation compared to the radial variation in figure 5.32. This reasonable uniformity of the incident pressure field exists up to about 4.5 KHz. At higher frequencies, significant variation, both in radial and azimuthal directions, is observed.

The radial variation of the reflected pressure field, as shown in figure 5.34, is quite significant. The azimuthal variation of the reflected pressure field (see figure 5.35) is even worse. However, the contribution of the reflected pressure field to the transmitted power may not be significant due to its lower sound pressure levels compared to the incident pressure levels. Moreover, the influence of the reflected pressure field decreases even further in the presence of flow since $(1 - M_D)^2$ is multiplied to the reflected power compared to $(1 + M_D)^2$ for the incident power. This effect will be seen later in this section where the acoustic powers for various test cases will be presented.

5.2.2.3 Experimental Results for the Straight Annular Duct with a Blocking Absorbing Material at the Termination

In this case a sample of 2.5 cm thick polyurethane foam was mounted to a steel plate at the exit plane of the annular pipe. The incident pressure field for this case is again identical to that of the open-ended annular duct in the absence of mean flow. Therefore, the spatial variation of the reflected pressure field only is shown in this section. The radial variation of the reflected pressure field at six azimuthal positions is shown in figure 5.36. A small amount of radial pressure variation is observed up to about 4.0 KHz. At higher frequencies the radial pressure variation seems to be quite significant. When these results are cross plotted to show the azimuthal variation of the reflected pressure field (see figure 5.37), a significant amount of variation is observed at frequencies above 2 KHz. This behavior indicates that the reflected pressure wave consists of higher order modes with significant pressure levels. This phenomena will be discussed later in this section.

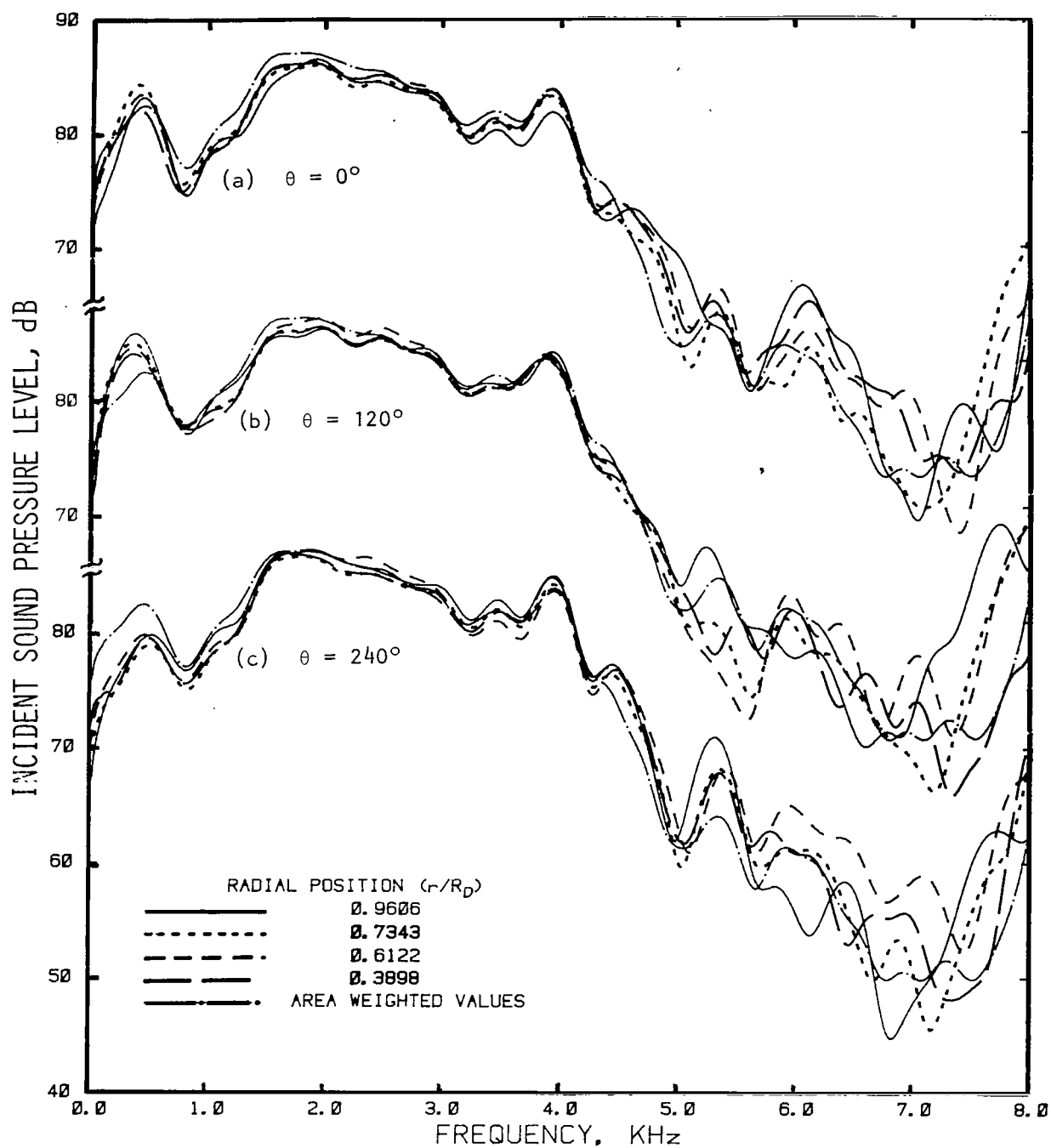


Figure 5.32 Radial variation of incident sound pressure level spectrum and the corresponding area weighted spectrum for an annular conical nozzle at various azimuthal locations, $M_J = 0.6$.

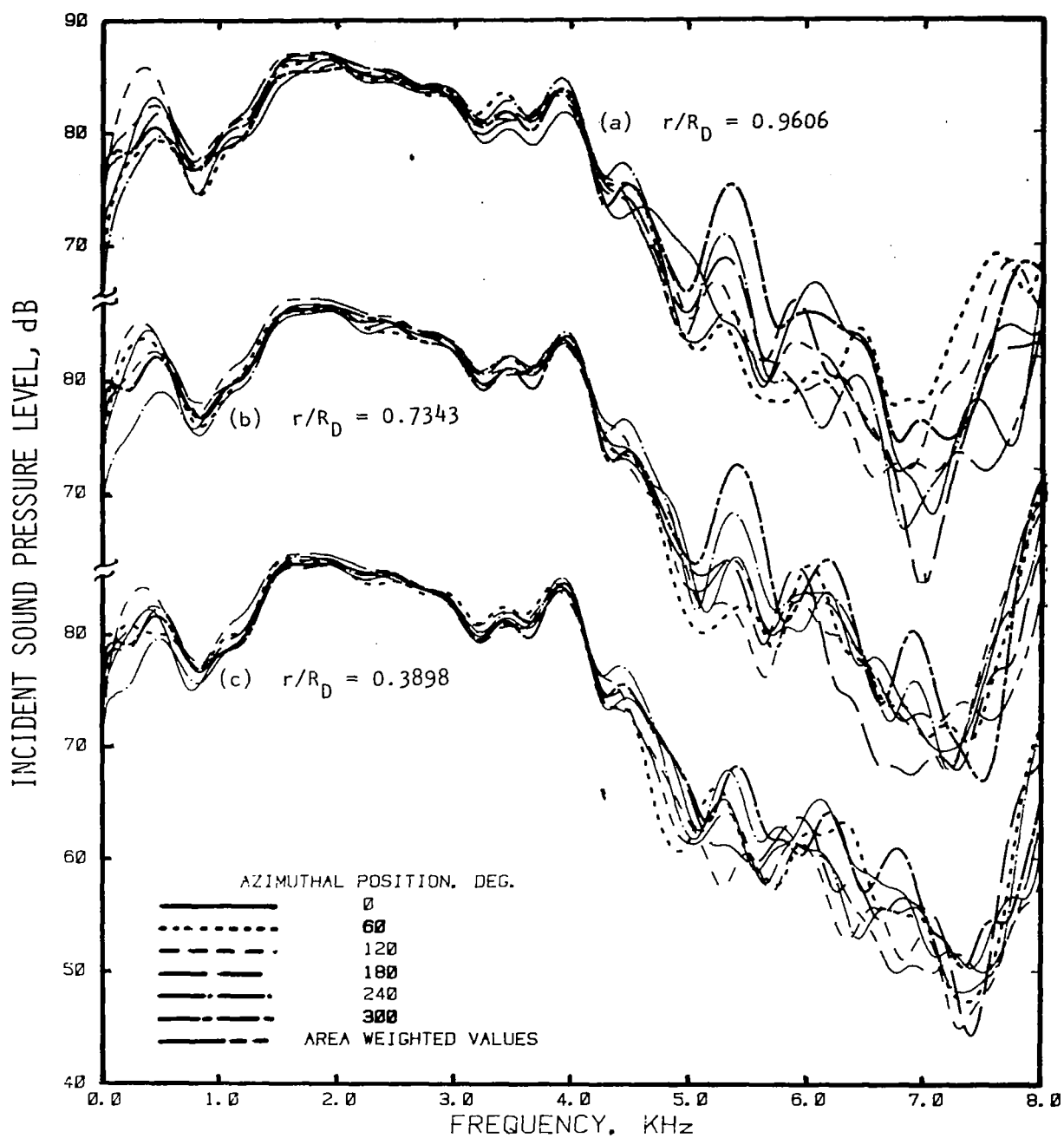


Figure 5.33 Azimuthal variation of incident sound pressure level spectrum and the corresponding area weighted spectrum for an annular conical nozzle at various radial locations, $M_J = 0.6$.

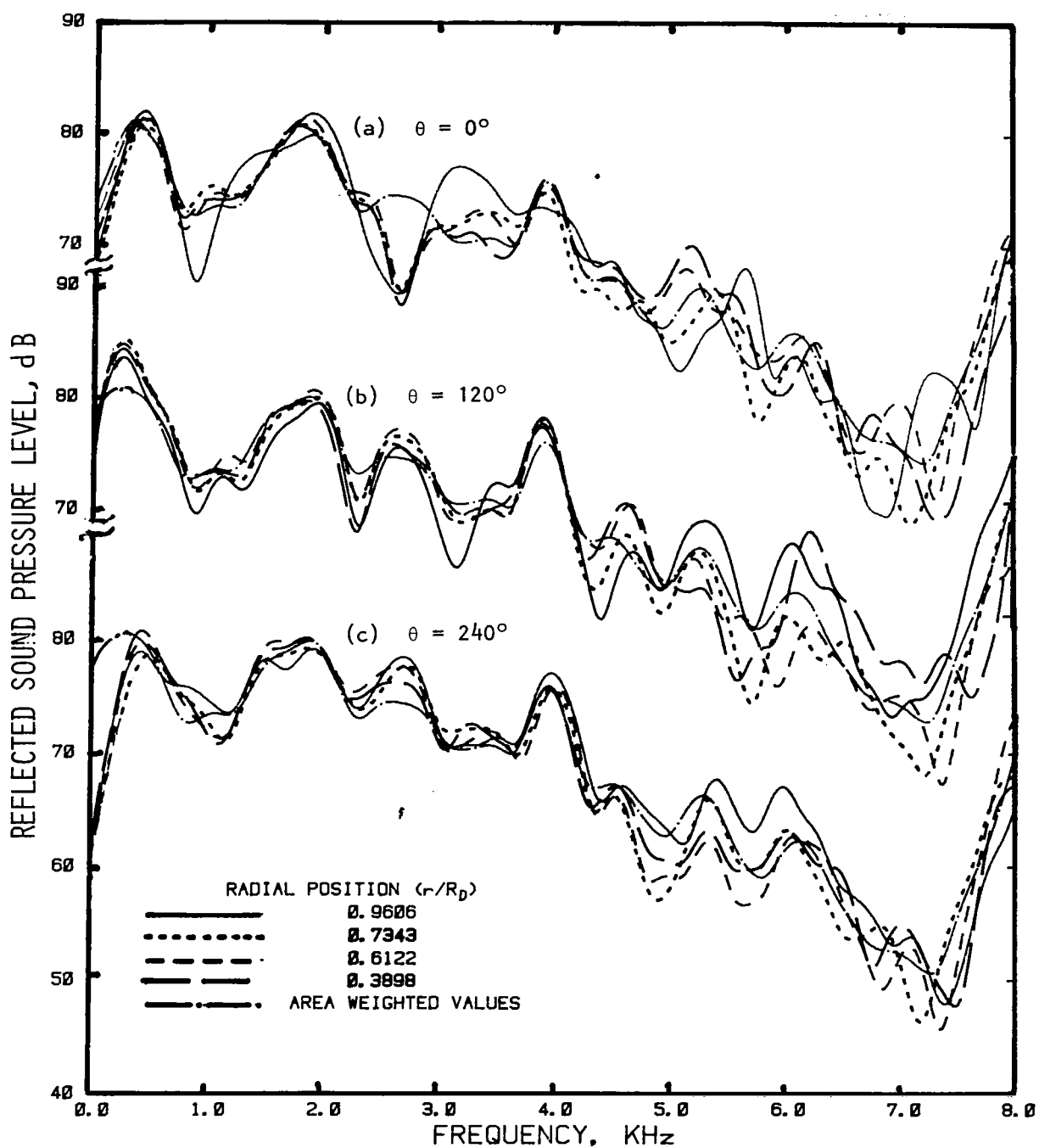


Figure 5.34 Radial variation of reflected sound pressure level spectrum and the corresponding area weighted spectrum for an annular conical nozzle at various azimuthal positions, $M_J = 0.6$.

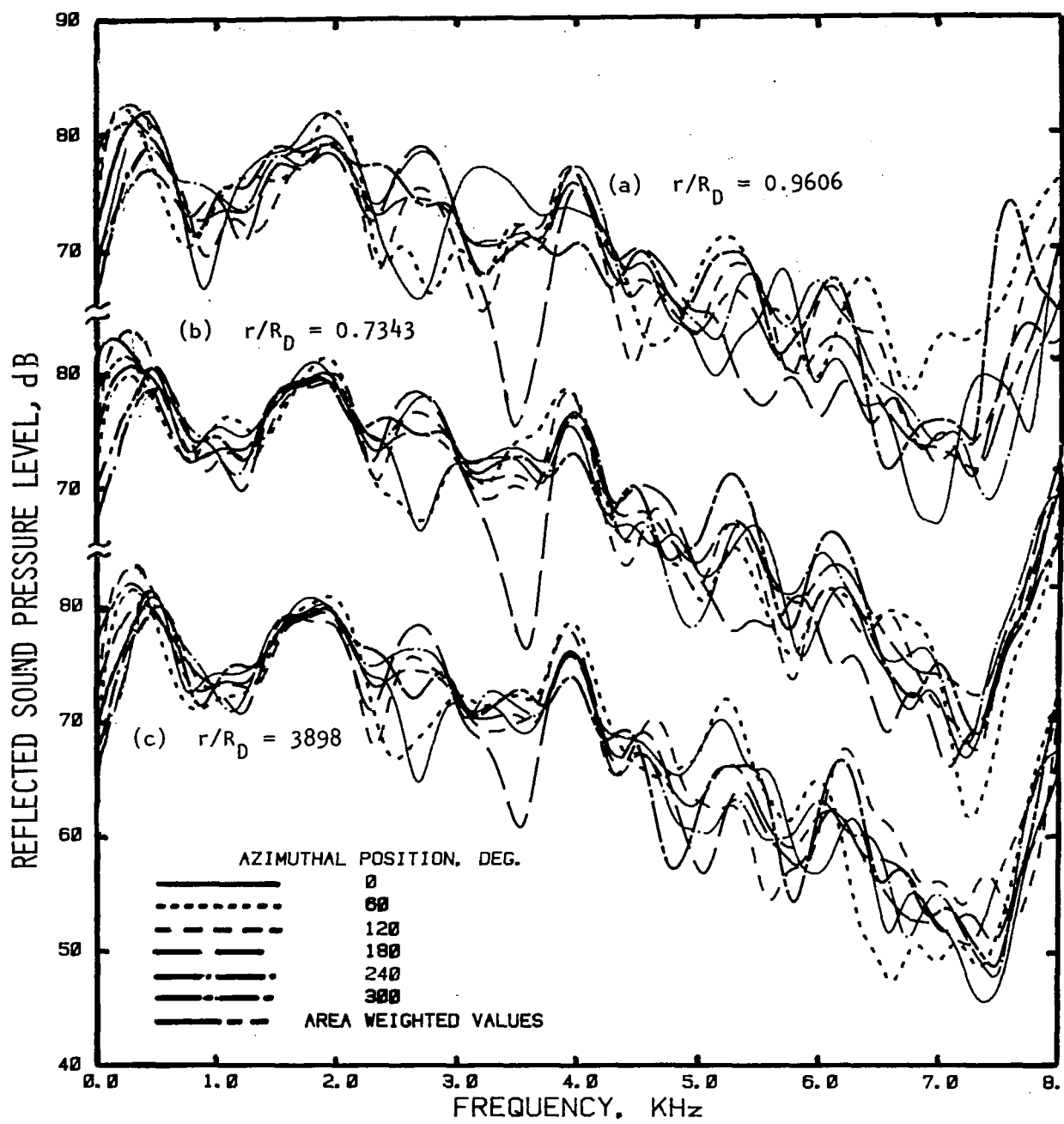


Figure 5.35 Azimuthal variation of reflected sound pressure level spectrum and the corresponding area weighted spectrum for an annular conical nozzle at various radial locations, $M_j = 0.6$.

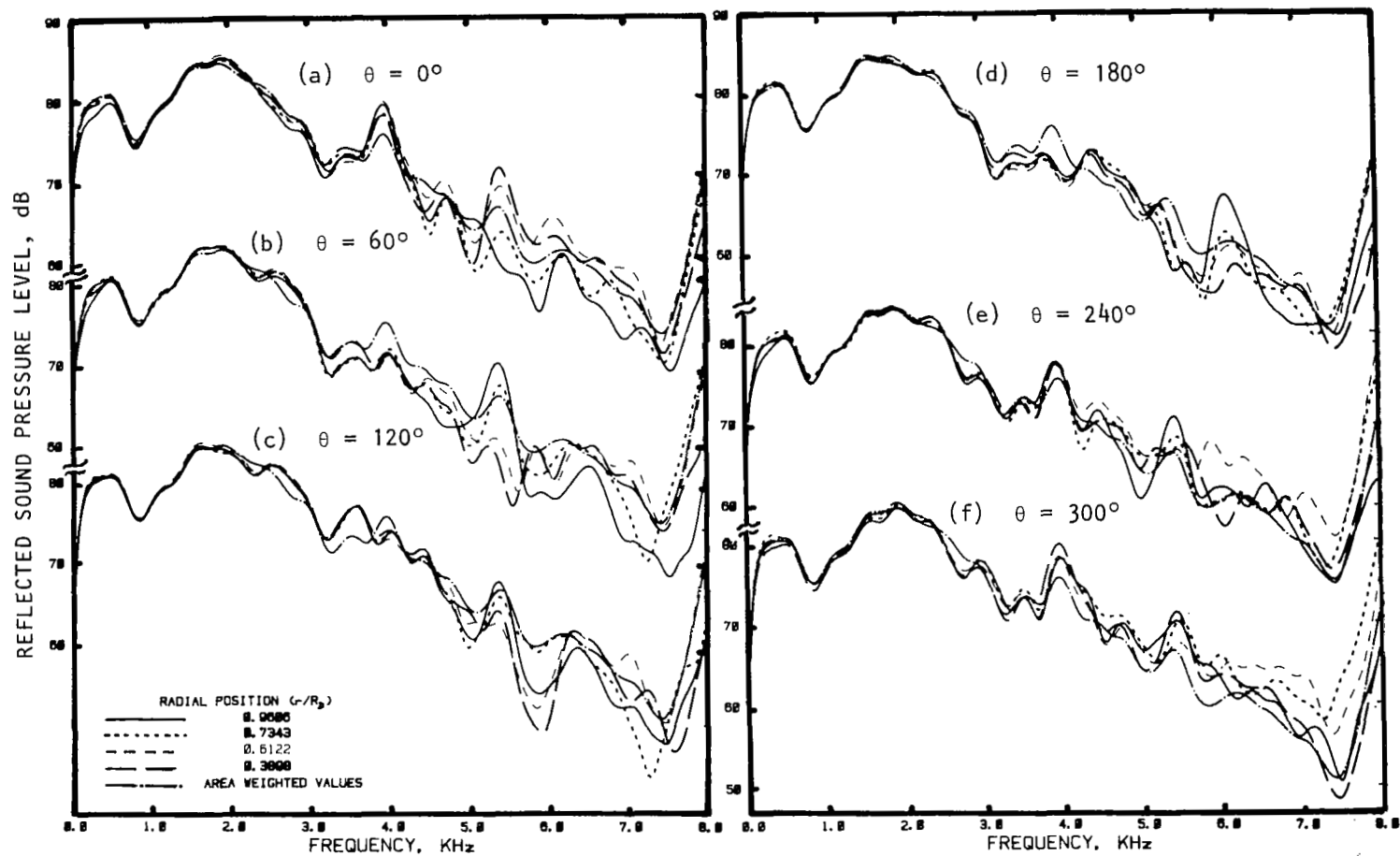


Figure 5.36 Radial variation of reflected pressure level spectrum and the corresponding area weighted spectrum due to a polyurethane foam sample mounted at the termination of an annular duct, at various azimuthal locations.

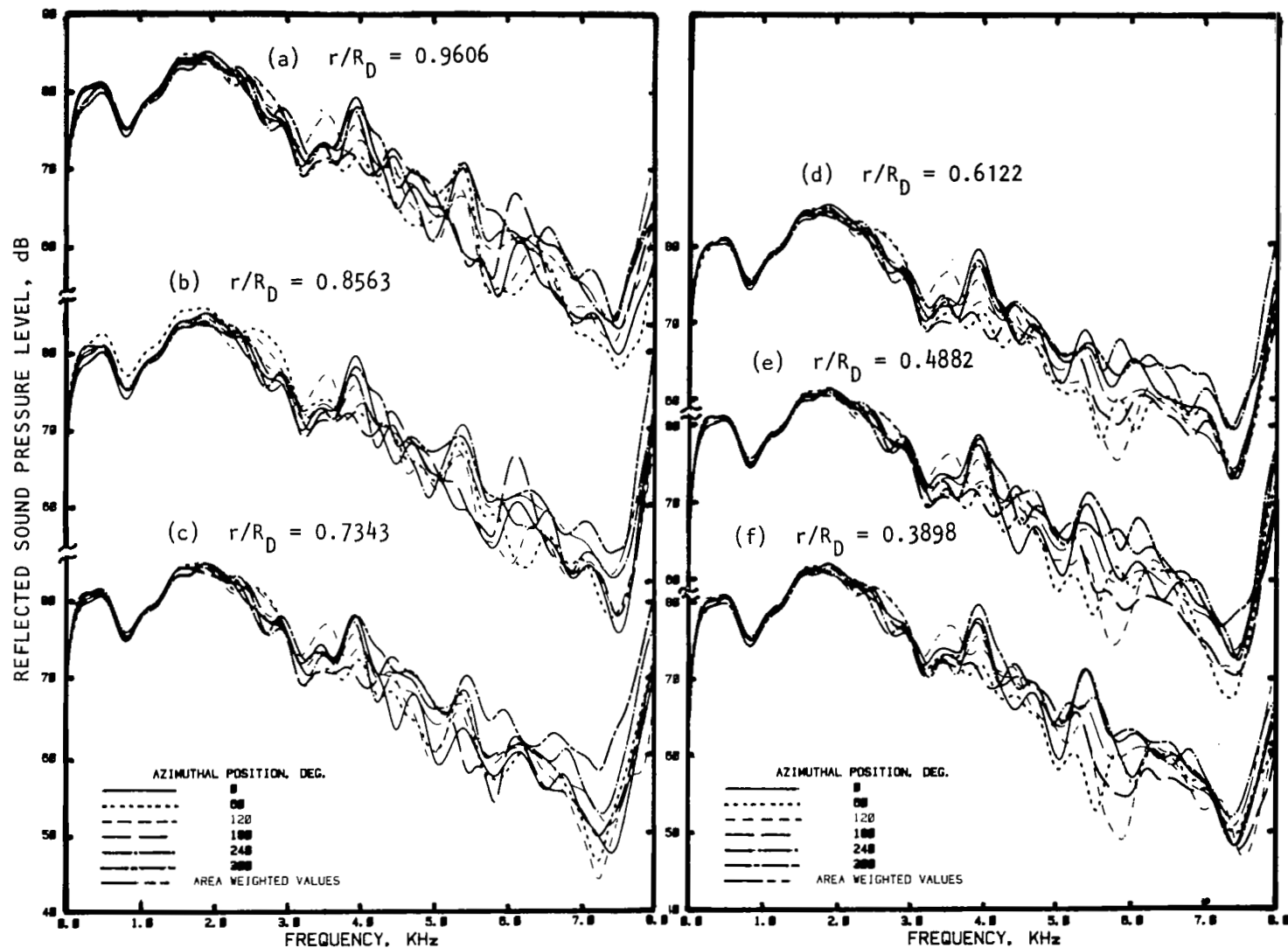


Figure 5.37 Azimuthal variation of reflected pressure level spectrum and the corresponding area weighted spectrum due to a polyurethane foam sample mounted at the termination of an annular duct at various radial locations.

5.3 MODAL DECOMPOSITION OF IN-DUCT ACOUSTIC POWER

A technique, which separates the modal components of internal noise in the form of impulsive sound source propagating inside circular or annular ducts using experimentally evaluated induct pressure distribution, is developed and presented in this section. This technique is also applicable to discrete frequency noise source with minor modification.

For hard-walled ducts, carrying no mean flow, three main factors determining the nature of the acoustic field are identified: (1) duct cross-section geometry, (2) the space-time pattern of the source distribution, and (3) acoustical termination conditions at the ends of the duct (refs. 16 and 22). However, in the presence of mean flow it is expected that the mean flow would be another determining factor of the induct acoustic field. In the theoretical analysis of reference 16 it has been shown that the excitation and transmission of sound by a source distribution in a hard-walled duct with non-reflecting terminations is controlled by two, relatively independent, sets of parameters.

The first set of parameters are the duct modes themselves. These are the denumerable number of particular sound fields that can exist in the duct for each given frequency of excitation, as permitted by the constraints imposed on the acoustic field by the hard walls. Each of these duct modes is a distinct interference pattern (each mode amplitude being proportional to a particular function of the duct cross-section position coordinates), which propagates along the duct with a particular speed, which is determined by the ratio of the driving frequency to the mode cut-on frequency and by the speed of sound in the acoustic medium contained in the duct. The mode cut-on frequencies themselves are determined by the duct cross-section geometry, the speed of sound in the acoustic medium, and the two mode index numbers. The index numbers of all the modes comprise a doubly infinite set of integers (m,n) . Modes with cut-on frequencies higher than the driving frequency do not propagate as waves in the usual sense, but decay in amplitude exponentially with distance from the plane of excitation. With non-reflecting terminations in a hard-walled duct such cut-off modes contribute to the acoustic pressure field in the duct but not at all to the mean acoustic energy flow.

The second set of parameters are those describing the nature of the space-time pattern of the source distribution, or externally applied force or stress system that is driving the acoustic field. The relative amplitudes of excitation of the duct modes, and their relative phases, are both especially sensitive to the space-time pattern of the source distribution. Hence the acoustic power transmitted down the duct is similarly sensitive to the space-time pattern.

When there is no reflection at the duct termination, the sound field in the region of the duct lying between the source distribution and the termination is made up only of modes that either propagate, or decay exponentially in amplitude, in the axial direction from the source distribution towards the termination. However, it is not generally true that there will be no reflection back into the duct from the termination.

Just as the duct geometry, wall impedance and ambient characteristics of the acoustic medium in the duct dictate that only certain acoustic modes of excitation are necessary and sufficient to describe any acoustic field inside the duct; so the geometry, boundary impedances and ambient characteristics of the region beyond the duct termination dictate that only certain acoustic modes of excitation are necessary and sufficient to describe any acoustic field outside the duct. Naturally, these "outside" modes are, in general, different in functional form from the "inside" modes. Therefore, in almost exactly the same way as the sound field in a duct of infinite length depends upon the matching between the source distribution space-time pattern and the duct modes, the acoustic field outside the duct depends upon the matching between the in-duct sound field space-time pattern over the termination cross-section to the acoustic modes of the outside region, which are determined by the conditions at the other boundaries of the region.

In the case of an infinite duct, it was found that the duct sound field exerted a back-reaction on the source distribution. For example, if, at a certain cross-section of the duct, the axial particle velocity is specified, then the space-time distribution of acoustic pressure over that cross-section cannot be independently specified, as it is already determined by the prescribed axial particle velocity distribution together with the constraints on the sound field imposed by the duct walls. In exactly the same way, the sound fields both inside and outside a duct of finite length depends, in general, just as much on the boundary conditions of the region outside the duct as they do on the space-time characteristics of the source distribution. Identical source distributions placed, for example, in an infinite-length duct and in a finite-length duct, respectively, will, in general, produce different sound fields in the ducts and will transmit different amounts of mean acoustic power down the ducts. This interdependence is an intrinsic feature of acoustic fields. A change in any of the boundary conditions, on any part of the boundary, can make itself felt through changes in all field quantities, throughout the field region (ref. 22).

In brief, the discussions made above clearly indicate that the sound field in the duct is very sensitive to the source distribution (orientation), duct cross-section geometry and the termination properties. Therefore, the modal characteristics of the incident wave (for impulsive sound source) need not be similar to those of the reflected wave. Moreover, these modal characteristics also would change when the flow conditions are altered. Therefore, the modal decomposition needs to be performed for both incident and reflected pulses for each flow condition and termination geometry to determine the total acoustic transmitted power.

5.3.1 Expression for Acoustic Pressure Field

The linearized equations of motion, governing the sound field in the presence of a mean flow \vec{V} , neglecting external and viscous forces, can be written as follows (ref. 23).

$$\text{Continuity:} \quad \left(\frac{\partial}{\partial t} + \vec{V} \cdot \vec{\nabla} \right) \hat{\rho} + \rho \sum_i \frac{\partial u_i}{\partial x_i} = 0 \quad (5.13)$$

$$\text{Momentum:} \quad \rho \left(\frac{\partial}{\partial t} + \vec{V} \cdot \vec{\nabla} \right) u_i = - \frac{\partial p}{\partial x_i} \quad (5.14)$$

$$\text{Energy:} \quad dp = c^2 d\hat{\rho} \quad (5.15)$$

where the subscript i refers to x, y , and z in cartesian coordinate or r, θ , and z in cylindrical coordinate, respectively. For brevity the subscript D is not used in this section for induct variables, such as, Mach number M , the speed of sound c , and the mean flow density ρ . From equations (5.13) through (5.15) the wave equation can be derived and can be expressed as follows

$$\frac{1}{c^2} \left(\frac{\partial}{\partial t} + \vec{V} \cdot \vec{\nabla} \right)^2 p = \nabla^2 p \quad (5.16)$$

$$\text{or } \frac{\partial^2 p}{\partial t^2} + 2 \sum_i V_i \frac{\partial}{\partial t} \frac{\partial p}{\partial x_i} + \sum_i V_i V_j \frac{\partial^2 p}{\partial x_i \partial x_j} = c^2 \nabla^2 p \quad (5.17)$$

When the mean flow \vec{V} is only along the axial direction x , equation (5.17) will reduce to the following form

$$\frac{\partial^2 p}{\partial t^2} + 2V \frac{\partial}{\partial t} \cdot \frac{\partial p}{\partial x} + V^2 \frac{\partial^2 p}{\partial x^2} = c^2 \nabla^2 p \quad (5.18)$$

For harmonic time dependence (i.e. $p \propto e^{i\omega t}$) equation (5.18) reduces to

$$\nabla^2 p + \left(\frac{\omega}{c} \right)^2 \left(p - 2 \frac{V}{\omega} i \frac{\partial p}{\partial x} - \frac{V^2}{\omega^2} \frac{\partial^2 p}{\partial x^2} \right) = 0 \quad (5.19)$$

In cylindrical coordinate as shown in figure 5.2 the Laplacian ∇^2 is given by

$$\nabla^2 = \frac{1}{r} \frac{\partial}{\partial r} \left(r \frac{\partial}{\partial r} \right) + \frac{1}{r^2} \frac{\partial^2}{\partial \theta^2} + \frac{\partial^2}{\partial x^2} \quad (5.20)$$

Therefore, equation (5.19) can be written as

$$\begin{aligned} \frac{1}{r} \frac{\partial}{\partial r} \left(r \frac{\partial p}{\partial r} \right) + \frac{1}{r^2} \frac{\partial^2 p}{\partial \theta^2} + \frac{\partial^2 p}{\partial x^2} + k^2 p - 2iMk \frac{\partial p}{\partial x} \\ - M^2 \frac{\partial^2 p}{\partial x^2} = 0 \end{aligned} \quad (5.21)$$

where $k = \omega/c$, the total wave number and $M = V/c$, the mean flow Mach number.

The above equation can also be written as

$$(1 - M^2) \frac{\partial^2 p}{\partial x^2} - 2iMk \frac{\partial p}{\partial x} + \frac{1}{r} \frac{\partial}{\partial r} \left(r \frac{\partial p}{\partial r} \right) + \frac{1}{r^2} \frac{\partial^2 p}{\partial \theta^2} + k^2 p = 0 \quad (5.22)$$

$$\text{Let } p = R(r) \cdot \Theta(\theta) \cdot X(x) \cdot e^{i\omega t} \quad (5.23)$$

Using the above functional form for p , equation (5.22) can be written as follows:

$$(1 - M^2) R\Theta X'' - 2iMk R\Theta X' + \frac{1}{r} \frac{d}{dr} (r\Theta X R') + \frac{1}{r^2} R X \Theta'' + k^2 R\Theta X = 0$$

$$\text{or } \left\{ (1 - M^2) \frac{X''}{X} - 2iMk \frac{X'}{X} + k^2 \right\} r^2 + \frac{r}{R} \frac{d}{dr} (r R') = -\frac{\Theta''}{\Theta} \quad (5.24)$$

The left hand side of equation (5.24) is a function of x and r , whereas the right hand side is a function of θ only. Therefore,

$$\frac{\Theta''}{\Theta} = \text{constant} \quad (5.25)$$

Let the constant be $-m^2$, m being a positive integer or zero. Therefore,

$$\Theta'' + m^2 \Theta = 0 \quad (5.26)$$

The solution of equation (5.26) is

$$\Theta = e^{\pm im\theta} \quad (5.27)$$

Now equation (5.24) can be rewritten in the following form

$$\left\{ (1 - M^2) \frac{X''}{X} - 2iMk \frac{X'}{X} + k^2 \right\} = \frac{-1}{rR} \frac{d}{dr} (r R') + \frac{m^2}{r^2} \quad (5.28)$$

Again the left hand side of equation (5.28) is a function of x only, whereas the right hand side is a function of r only. Therefore each side is a constant.

$$\text{Let } (1 - M^2) \frac{X''}{X} - 2iMk \frac{X'}{X} + k^2 = \lambda_{mn}^2 \quad (5.29)$$

where λ_{mn} is the transverse wave number. Equation (5.29) can be written as

$$(1 - M^2) X'' - 2Mk i X' + (k^2 - \lambda_{mn}^2) X = 0 \quad (5.30)$$

The solution of equation (5.30) can be derived by assuming

$$X = e^{-ik_{mn}x} \quad (5.31)$$

where k_{mn} is the longitudinal (axial) wave number. Therefore, equation (5.30) can be written as

$$-(1 - M^2)k_{mn}^2 - 2Mk k_{mn} + (k^2 - \lambda_{mn}^2) = 0 \quad (5.32)$$

Therefore,

$$k_{mn} = \frac{2Mk \pm \sqrt{4M^2k^2 + 4(1 - M^2)(k^2 - \lambda_{mn}^2)}}{-2(1 - M^2)} \quad (5.33)$$

$$\text{or } k_{mn} = \frac{-k}{(1 - M^2)} [\epsilon \eta + M] \quad (5.34)$$

where the factor

$$\eta = [1 - (\frac{\lambda_{mn}}{k})^2 (1 - M^2)]^{1/2} \quad (5.35)$$

and $\epsilon = \pm 1$, will be seen to characterize the direction of acoustic energy flow. If $k < \lambda_{mn} (1 - M^2)^{1/2}$, then η becomes imaginary. In this situation, the mode with λ_{mn} will be decaying as $e^{-|\eta|x}$. Therefore, the contribution due to this mn mode to the propagating wave is neglected.

Now equation (5.28) can be written as

$$\left. \begin{aligned} \lambda_{mn}^2 + \frac{1}{Rr} \frac{d}{dr} (r R') - \frac{m^2}{r^2} &= 0 \\ \text{or } \frac{1}{r} \frac{d}{dr} (r R') + (\lambda_{mn}^2 - \frac{m^2}{r^2}) R &= 0 \\ \text{or } R'' + \frac{1}{r} R' + (\lambda_{mn}^2 - \frac{m^2}{r^2}) R &= 0 \end{aligned} \right\} \quad (5.36)$$

The solution to equation (5.36) is the Bessel function.

The general solution of equation (5.36) is as follows:

$$R(r) = \frac{1}{2}[C_1 J_m(\lambda_{mn} r) + C_2 Y_m(\lambda_{mn} r)] \quad (5.37)$$

where

$J_m(\lambda_{mn} r)$ = Bessel function of the first kind, and

$Y_m(\lambda_{mn} r)$ = Bessel function of the second kind.

C_1 and C_2 are the constants evaluated on the basis of boundary condition.

Using the solution for R, θ , and X the acoustic pressure for a given mn mode can be written, from equation (5.23), as follows:

$$p_{mn}(x, r, \theta, t) = \frac{1}{2}[C_1 J_m(\lambda_{mn} r) + C_2 Y_m(\lambda_{mn} r)] \{e^{im\theta} + e^{-im\theta}\} e^{-ik_{mn}x} e^{i\omega t}$$

or

$$p_{mn}(x, r, \theta, t) = P_{mn} \Omega_m(\lambda_{mn} r) \cos m\theta e^{-ik_{mn}x} e^{i\omega t} \quad (5.38)$$

where

$$\Omega_m(\lambda_{mn} r) = J_m(\lambda_{mn} r) + \frac{C_2}{C_1} Y_m(\lambda_{mn} r) \quad (5.39)$$

and C_1 is the modal coefficient for the mn mode represented by P_{mn} .

To study the orthogonality characteristics of P_{mn} , with the weighting function r , the following integral needs to be evaluated.

$$\begin{aligned} I &= \int_a^{R_D} \int_0^{2\pi} r \Omega_m(\lambda_{mn} r) \cos m\theta \cdot \Omega_\mu(\lambda_{\mu\nu} r) \cos \mu\theta \, dr \, d\theta \\ &= \int_a^{R_D} r \Omega_m(\lambda_{mn} r) \Omega_\mu(\lambda_{\mu\nu} r) \, dr \cdot \int_0^{2\pi} \cos m\theta \cdot \cos \mu\theta \, d\theta \\ &= \epsilon_m \pi \delta_{m\mu} \int_a^{R_D} r \Omega_m(\lambda_{mn} r) \Omega_\mu(\lambda_{\mu\nu} r) \, dr \end{aligned} \quad (5.40)$$

where ϵ_m a factor assumes a value of 2 for $m=0$ and 1 for $m>0$, $\delta_{m\mu}$ is the Kronecker-delta function and a is the left-hand boundary point for r . Since $\delta_{m\mu}$ makes the value of the above integrand zero, when $m \neq \mu$, therefore, μ becomes identically equal to m within the integral sign in the above expression. Therefore,

$$I = \epsilon_m \pi \delta_{m\mu} \int_a^{R_D} r \Omega_m(\lambda_{mn}.r) \Omega_m(\lambda_{mv}.r) dr$$

To evaluate the above integral, equation (5.36) is expressed in the form of Liouville equation (ref. 24), as follows.

$$\frac{d}{dr} (rR') + [\lambda_{mn}^2 r - \frac{m^2}{r}] R = 0$$

The Sturm-Liouville problem is essentially the problem of determining the dependence of the general behavior of $R(r)$ on the parameter λ_{mn}^2 and the dependence of the eigenvalues of λ_{mn}^2 on the homogeneous boundary conditions imposed on $R(r)$. Assuming that R_1 and R_2 are solutions of the above equation, the procedure used to achieve this is to multiply the equation for R_1 by R_2 and the equation for R_2 by R_1 and subtract:

$$[R_2 \frac{d}{dr} (rR_1) + R_2 (\lambda_{mn}^2 r - \frac{m^2}{r})R_1] - [R_1 \frac{d}{dr} (rR_2) + R_1 (\lambda_{mv}^2 r - \frac{m^2}{r})R_2] = 0$$

$$\text{or } \frac{d}{dr} [R_2 r R_1' - R_1 r R_2'] = (\lambda_{mv}^2 - \lambda_{mn}^2) r R_1 R_2 \quad (5.41)$$

where λ_{mn}^2 and λ_{mv}^2 are the eigenvalues λ_{mn} for $R_1(r)$ and $R_2(r)$, respectively.

Now integrating equation (5.41) over r , beginning at the left-hand boundary point (let it be a in this case) and ending at some arbitrary point r , before reaching the right-hand boundary point, the following expression can be derived.

$$r(R_2 R_1' - R_1 R_2') - [r(R_2 R_1' - R_1 R_2')]_{r=a} = (\lambda_{mv}^2 - \lambda_{mn}^2) \int_a^r r R_1 R_2 dr$$

where the quantity in the parentheses would be the Wronskian for R_2 and R_1 if $\lambda_{mn}^2 = \lambda_{mv}^2$. But for the present purpose $\lambda_{mn}^2 \neq \lambda_{mv}^2$.

If a is a singular point of the differential equation (i.e., left-hand boundary point is at zero), the quantity in square bracket is zero as long as $R_1(r)$ and $R_2(r)$ are finite at the singular point. This is the situation for a hard-walled single-stream duct with uniform mean flow. If a is a regular point and the boundary condition is the homogeneous one (i.e., $\alpha R' - \beta R = 0$ at $r = a$, where α and β are independent of λ_{mn}^2), then $(R_1 R_2' - R_2 R_1') = (\beta/\alpha) (R_1 R_2 - R_2 R_1) = 0$ at $r = a$, and again the quantity in square bracket is zero. This is the case for an annular region of a co-

annular hard-walled duct with uniform mean flow. Therefore, for nearly any of the usual boundary conditions at $r = a$, the following expression is true.

$$r(R_2 R_1' - R_1 R_2') = (\lambda_{mv}^2 - \lambda_{mn}^2) \int_a^r r R_1 R_2 dr$$

The condition of orthogonality can be established on the basis of the boundary condition at the right-hand boundary point. For the present study for both the single stream and the annular stream, the boundary point is the inner radius of the outer-duct, R_D . The boundary condition at this point for single and annular stream ducts is $R'(R_D) = 0$. Therefore, at $r = R_D$ the left-hand side of the above equation goes to zero when $\lambda_{mn}^2 \neq \lambda_{mv}^2$. Therefore, the function $R(r)$ is orthogonal with the weighting function r for both the single and the annular stream ducts. Therefore,

$$\int_a^{R_D} r R_1 R_2 dr = \chi_{nn}^m \delta_{nv}$$

where,

$$\chi_{nn}^m = \int_a^{R_D} r R^2 dr$$

Since $R(r)$ and $\Omega_m(\lambda_{mn} r)$ are related with a constant factor of $\frac{1}{2} C_1$ (see equations (5.37) and 5.39)) equation (5.40) can be expressed as follows:

$$\int_a^{R_D} \int_0^{2\pi} r \Omega_m(\lambda_{mn} r) \cos m\theta \Omega_\mu(\lambda_{\mu v} r) \cos \mu\theta dr d\theta = C_0 \epsilon_m \pi \chi_{nn}^m \delta_{m\mu} \delta_{nv} \quad (5.42)$$

where C_0 is a constant.

Therefore, the expression for P_{mn} is orthogonal with the weighting function r for single and annular hard-walled ducts with uniform mean flow. This property will be used in this section to evaluate modal coefficients and acoustic power.

Equation (5.38) can be used either for right moving (i.e., incident) or for left moving (i.e., reflected) pressure waves, depending on the negative or positive sign of ϵ (see equation (5.34)), respectively. However, for a complete solution as per the discrete frequency pressure wave, the left moving pressure wave expression (i.e., the reflected wave) must be added to the right moving (i.e., incident wave) pressure wave expression. However, since the present analysis is for an impulsive wave the incident and the reflected pressure waves would appear separately, and, therefore, can be analyzed individually.

The total acoustic pressure, p , which is the contribution of all the modes, both radial, azimuthal (i.e., transverse), and cross modes can be obtained by summing the equation (5.38), over all the modes. Therefore,

$$p(x, r, \theta, t) = \sum_m \sum_n P_{mn} \Omega_m (\lambda_{mn} r) e^{i\omega t} \cos m\theta \cdot e^{-ik_{mn}x} \quad (5.43)$$

Using the time harmonic property of the pressure p as

$$p(x, r, \theta, t) = \hat{p}(x, r, \theta) e^{i\omega t},$$

equation (5.43) can be written as follows

$$\hat{p}(x, r, \theta) = \sum_m \sum_n P_{mn} \Omega_m (\lambda_{mn} r) \cos m\theta e^{-ik_{mn}x} \quad (5.44)$$

$\hat{p}(x, r, \theta)$ would be obtained from the measurements of $p(x, r, \theta, t)$ in the following manner,

$$\begin{aligned} p(x, r, \theta, t) &= \bar{p}(x, r, \theta) \cos [\omega t - \phi(r, \theta)] \cos m\theta \\ &= \text{Re} \{ \bar{p}(x, r, \theta) e^{i[(\omega t - \phi(r, \theta))]} \cdot e^{-im\theta} \} \\ &= \text{Re} \{ \bar{p}(x, r, \theta) e^{-i\phi(r, \theta)} e^{i\omega t} e^{-im\theta} \} \end{aligned}$$

Using the time harmonic property of the pressure the above expression can be written as

$$\begin{aligned} \hat{p}(x, r, \theta) &= \text{Re} \{ \bar{p}(x, r, \theta) e^{-i\phi(r, \theta)} e^{-im\theta} \} \\ &= \bar{p}(x, r, \theta) \cos \{m\theta + \phi(r, \theta)\} \end{aligned} \quad (5.45)$$

where $\bar{p}(r, \theta)$ and $\phi(r, \theta)$ are the pressure amplitude and phase at a given radial and azimuthal location r and θ , respectively. Therefore, using several radial and azimuthal measurements at x , the pressure field can be derived by equating equation (5.44) with equation (5.45), in the following manner

$$\bar{p}(x, r, \theta) \cos \{m\theta + \phi(r, \theta)\} = \sum_m \sum_n P_{mn} \Omega_m (\lambda_{mn} r) e^{-ik_{mn}x} \cos m\theta \quad (5.46)$$

or

$$\hat{p}(x, r, \theta) = \sum_m \sum_n P_{mn} \Omega_m (\lambda_{mn} r) \cos m\theta e^{-ik_{mn}x}$$

The following two cases are considered.

(1) Single Stream Duct: For this case the boundary conditions for equation (5.37) are

$$R'(R_D) = 0$$

and $R(r)$ is finite at all r including $r = 0$.

Since $Y_m(\lambda_{mn}r)$ at $r = 0$ becomes infinite, therefore to have a finite value of R at $r = 0$, C_2 becomes zero.

Therefore, from equations (5.37) and (5.39), respectively,

$$\left. \begin{aligned} R(r) &= \frac{1}{2} P_{mn} J_m(\lambda_{mn} r) \\ \text{and} \\ \Omega_m(\lambda_{mn} r) &= J_m(\lambda_{mn} r) \end{aligned} \right\} \quad (5.47)$$

The boundary condition therefore is $J'_m(\lambda_{mn} R_D) = 0$.

Therefore, using equation (5.46), the total acoustic pressure, $\hat{p}(x, r, \theta)$ for a single stream duct can be expressed as follows:

$$\hat{p}(x, r, \theta) = \sum_m \sum_n P_{mn} J_m(\lambda_{mn} r) \cdot \cos m\theta \cdot e^{-ik_{mn}x} \quad (5.48)$$

By letting $x = 0$ at the measurement point the above equation can be rewritten as

$$\hat{p}(r, \theta) = \sum_m \sum_n P_{mn} J_m(\lambda_{mn} r) \cos m\theta \quad (5.49)$$

Using the orthogonality principle of Bessel functions (ref. 24) by multiplying both sides of equation (5.49) by $r J_\mu(\lambda_{\mu\nu} r) \cos(\mu\theta)$ and by noting that

$$\begin{aligned} & \int \int r J_\mu(\lambda_{\mu\nu} r) \cos(\mu\theta) \cdot J_m(\lambda_{mn} r) \cos m\theta \, dr d\theta \\ &= \int_0^{R_D} r J_\mu(\lambda_{\mu\nu} r) \cdot J_m(\lambda_{mn} r) \, dr \cdot \int_0^{2\pi} \cos m\theta \cdot \cos \mu\theta \, d\theta \\ &= 2\pi N_{nn}^m \delta_{m\mu} \cdot \delta_{nv} \end{aligned} \quad (5.50)$$

where $\delta_{m\mu}$ and δ_{nv} are the Kronecker-delta functions, and

$$\begin{aligned}
N_{nn}^m &= \int_0^{R_D} r J_m^2(\lambda_{mn} r) dr \quad \text{for } m = 0 \\
&= \frac{1}{2} \int_0^{R_D} r \cdot J_m^2(\lambda_{mn} r) dr \quad \text{for } m > 0
\end{aligned} \tag{5.51}$$

the modal coefficient P_{mn} can be expressed as

$$P_{mn} = \frac{\int_0^{2\pi} \int_0^{R_D} r \cdot J_m(\lambda_{mn} r) \hat{p}(r, \theta) \cos m\theta dr d\theta}{2\pi N_{nn}^m} \tag{5.52}$$

The integral $\int_0^{R_D} r \cdot J_m^2(\lambda_{mn} r) dr$ can be evaluated as follows:

From reference 25,

$$\begin{aligned}
&\frac{d}{dt} [t^{-m} J_m(t)] = -t^{-m} J_{m+1}(t) \\
\text{and} \quad &\frac{d}{dt} [t^m J_m(t)] = t^m J_{m-1}(t) \\
\text{Therefore,} \quad &\frac{d}{dt} [t^2 \{J_m^2(t) - J_{m+1}(t)\}] = 2t J_m^2(t)
\end{aligned} \tag{5.53}$$

$$\begin{aligned}
\text{or} \quad &\int_0^z t J_m^2(t) dt = \frac{1}{2} z^2 [J_m^2(z) - J_{m+1}(z) \cdot J_{m-1}(z)] \\
\text{Therefore,} \quad &\int_0^{R_D} r \cdot J_m^2(\lambda_{mn} r) dr = \frac{R_D^2}{2} [J_m^2(\lambda_{mn} R_D) - J_{m+1}(\lambda_{mn} R_D) \cdot J_{m-1}(\lambda_{mn} R_D)]
\end{aligned} \tag{5.54}$$

As per boundary condition (see equation (5.47)) $J_m'(\lambda_{mn} R_D) = 0$

Considering the following properties of Bessel function,

$$\left. \begin{aligned} t \frac{d}{dt} J_m(t) &= -t J_{m+1}(t) + m J_m(t) \\ t \frac{d}{dt} J_m(t) &= t J_{m-1}(t) - m J_m(t) \end{aligned} \right\} \quad (5.55)$$

and letting t equal $\lambda_{mn} R_D$ the boundary condition would result in the following expression.

$$m^2 J_m^2(\lambda_{mn} \cdot R_D) = \lambda_{mn}^2 R_D^2 \cdot J_{m+1}(\lambda_{mn} \cdot R_D) \cdot J_{m-1}(\lambda_{mn} \cdot R_D) \quad (5.56)$$

From equations (5.54) and (5.56) the following expression is derived

$$\int_0^{R_D} r \cdot J_m^2(\lambda_{mn} \cdot r) dr = \frac{R_D^2}{2} \left(1 - \frac{m^2}{\lambda_{mn}^2 R_D^2}\right) \cdot J_m^2(\lambda_{mn} \cdot R_D) \quad (5.57)$$

$$\left. \begin{aligned} \text{Therefore } N_{nn}^0 &= \frac{R_D^2}{2} J_0^2(\lambda_{on} \cdot R_D), \quad m = 0 \\ \text{and } N_{nn}^m &= \frac{R_D^2}{4} \left[1 - \frac{m^2}{\lambda_{mn}^2 R_D^2}\right] J_m^2(\lambda_{mn} \cdot R_D), \quad m > 0 \end{aligned} \right\} \quad (5.58)$$

For the single duct experiments, since the sound is injected on the duct centerline or symmetrically around the periphery, the pressure field can be assumed to be azimuthally symmetric. In this situation, the higher order circumferential modes can be assumed to be absent (i.e., $m=0$). Therefore, the modal coefficients can be expressed as follows by letting $\hat{p}(r, \theta)$ equals $\bar{p}(r)$, independent of θ ;

$$p_{on} = \frac{1}{N_{nn}^0} \int_0^{R_D} r J_0(\lambda_{on} r) \bar{p}(r) dr \quad (5.59)$$

$$\text{and } N_{nn}^0 = \frac{R_D^2}{2} [J_0^2(\lambda_{on} R_D)] \quad (5.60)$$

The integral $\int_0^{R_D} r J_0(\lambda_{on} r) \bar{p}(r) dr$ is evaluated using a numerical integration scheme with six or more measured pressure data $\bar{p}(r)$.

Since there is no azimuthal variation of the induct pressure field, equation (5.36) can be written as

$$\frac{d}{dr^2} J_o(\lambda_{on} r) + \frac{1}{r} \frac{d}{dr} J_o(\lambda_{on} r) + \lambda_{on}^2 J_o(\lambda_{on} r) = 0 \quad (5.61)$$

and
$$\left. \frac{d}{dr} J_o(\lambda_{on} r) \right|_{at \ r = R_D} = 0 \quad (5.62)$$

Equation (5.62) can be simplified as follows:

$$-\lambda_{on} J_1(\lambda_{on} R_D) = 0 \quad (5.63)$$

Therefore,

$$\left. \begin{array}{l} J_1(\lambda_{on} R_D) = 0, \ n > 0 \\ \lambda_{oo} = 0, \ n = 0 \end{array} \right\} \quad (5.64)$$

and

The solution of equation (5.64) gives the values of λ_{on} , and they are:

$$\left. \begin{array}{l} \lambda_{oo} R_D = 0 \\ \lambda_{o1} R_D = 3.83 \\ \lambda_{o2} R_D = 7.02 \\ \lambda_{o3} R_D = 10.13 \end{array} \right\} \quad (5.65)$$

(2) Annular Stream Duct: For this case the boundary conditions for equation (5.37) are

$$\left. \begin{array}{l} R'(R_D) = 0 \\ R'(R_I) = 0 \end{array} \right\} \quad (5.66)$$

and

$$C_1 J'_m(\lambda_{mn} R_D) + C_2 Y'_m(\lambda_{mn} R_D) = 0$$

and
$$C_1 J'_m(\lambda_{mn} R_I) + C_2 Y'_m(\lambda_{mn} R_I) = 0$$

$$\frac{J'_m(\lambda_{mn} R_D)}{Y'_m(\lambda_{mn} R_D)} = \frac{J'_m(\lambda_{mn} R_I)}{Y'_m(\lambda_{mn} R_I)} \quad (5.67)$$

and

$$C_2 = -C_1 \frac{J'_m(\lambda_{mn} R_I)}{Y'_m(\lambda_{mn} R_I)}$$

Therefore, from equations (5.37) and (5.39), respectively,

$$\left. \begin{aligned} R(r) &= \frac{P_{mn}}{2} \left[J_m(\lambda_{mn} r) - \frac{J'_m(\lambda_{mn} R_I)}{Y'_m(\lambda_{mn} R_I)} Y_m(\lambda_{mn} r) \right] \\ \text{and} \\ Q_m(\lambda_{mn} r) &= J_m(\lambda_{mn} r) - \frac{J'_m(\lambda_{mn} R_I)}{Y'_m(\lambda_{mn} R_I)} \cdot Y_m(\lambda_{mn} r) \end{aligned} \right\} \quad (5.68)$$

Therefore, using equation (5.46) the total acoustic pressure $\hat{p}(x, r, \theta)$ for an annular stream duct can be expressed as follows:

$$\hat{p}(x, r, \theta) = \sum_m \sum_n P_{mn} Q_m(\lambda_{mn} r) \cos m\theta \cdot e^{-ik_{mn}x} \quad (5.69)$$

where

$$Q_m(\lambda_{mn} r) = J_m(\lambda_{mn} r) - \frac{J'_m(\lambda_{mn} R_I)}{Y'_m(\lambda_{mn} R_I)} Y_m(\lambda_{mn} r)$$

Letting $x = 0$ at the measurement point, equation (5.69) can be rewritten as

$$\hat{p}(r, \theta) = \sum_m \sum_n P_{mn} \cdot Q_m(\lambda_{mn} r) \cos m\theta \quad (5.70)$$

Using the orthogonality principle of Bessel functions (refs. 24 and 26), (proved earlier) by multiplying both sides of equation (5.70) by $r Q_\mu(\lambda_{\mu\nu} r) \cos(\mu\theta)$ and by noting that

$$\begin{aligned} & \int \int r Q_\mu(\lambda_{\mu\nu} r) \cos \mu\theta \cdot Q_m(\lambda_{mn} r) \cos m\theta \, dr d\theta \\ &= \int_{R_I}^{R_D} r \cdot Q_\mu(\lambda_{\mu\nu} r) \cdot Q_m(\lambda_{mn} r) \, dr \cdot \int_0^{2\pi} \cos \mu\theta \cdot \cos m\theta \, d\theta \\ &= \pi \epsilon_m \chi_{nn}^m \delta_{m\mu} \delta_{nv} \end{aligned} \quad (5.71)$$

where $\delta_{m\mu}$ and δ_{nv} are the Kronecker-delta functions, and

$$\chi_{nn}^m = \int_{R_I}^{R_D} r \cdot Q_m^2(\lambda_{mn} \cdot r) dr \quad (5.72)$$

The factor ϵ_m becomes 2 for $m = 0$ and 1 for $m > 0$, due to the fact that

$$\left. \begin{aligned} \int_0^{2\pi} \cos^2 m\theta \, d\theta &= 2\pi & \text{for } m=0 \\ &= \pi & \text{for } m>0 \end{aligned} \right\} \quad (5.73)$$

The integral

$$\int_{R_I}^{R_D} Q_m^2(\lambda_{mn} r) r dr = \left[\frac{1}{2} r^2 \left\{ \left(1 - \frac{m^2}{\lambda_{mn}^2 r^2} \right) Q_m^2(\lambda_{mn} \cdot r) + Q_m'^2(\lambda_{mn} r) \right\} \right]_{R_I}^{R_D} \quad (5.74)$$

The above integral is evaluated using reference 27 on the basis that

$$\left. \begin{aligned} Q_m(\lambda_{mn} \cdot r) &= J_m(\lambda_{mn} \cdot r) + A_o Y_m(\lambda_{mn} \cdot r) \\ \text{where } A_o = \text{constant} &= - \frac{J_m'^1(\lambda_{mn} R_I)}{Y_m'^2(\lambda_{mn} \cdot R_I)} \end{aligned} \right\} \quad (5.75)$$

Now

$$\begin{aligned} \left\{ r^2 \left(1 - \frac{m^2}{\lambda_{mn}^2 r^2} \right) Q_m^2(\lambda_{mn} \cdot r) \right\}_{R_I}^{R_D} &= R_D^2 \left(1 - \frac{m^2}{\lambda_{mn}^2 R_D^2} \right) Q_m^2(\lambda_{mn} R_D) \\ &- R_I^2 \left(1 - \frac{m^2}{\lambda_{mn}^2 R_I^2} \right) Q_m^2(\lambda_{mn} R_I) = R_D^2 [Q_m^2(\lambda_{mn} R_D) - \frac{m^2}{\lambda_{mn}^2 R_D^2} \cdot Q_m^2(\lambda_{mn} \cdot R_D) \\ &- \frac{R_I^2}{R_D^2} Q_m^2(\lambda_{mn} R_I) + \frac{m^2}{\lambda_{mn}^2 R_D^2} Q_m^2(\lambda_{mn} \cdot R_I)] = R_D^2 [Q_m^2(\lambda_{mn} R_D) \\ &- \frac{R_I^2}{R_D^2} Q_m^2(\lambda_{mn} R_I) - \frac{m^2}{\lambda_{mn}^2 R_D^2} \{ Q_m^2(\lambda_{mn} \cdot R_D) - Q_m^2(\lambda_{mn} R_I) \}] \end{aligned} \quad (5.76)$$

and

$$\begin{aligned}
r^2 Q_m'^2(\lambda_{mn} \cdot r) \Big|_{R_I}^{R_D} &= [\lambda_{mn}^2 \{J_m'(\lambda_{mn} \cdot r) - \frac{J_m'(\lambda_{mn} \cdot R_I)}{Y_m'(\lambda_{mn} \cdot R_I)} \cdot Y_m'(\lambda_{mn} \cdot r)\}^2 r^2]_{R_I}^{R_D} \\
&= \lambda_{mn}^2 [R_D J_m'(\lambda_{mn} \cdot R_D) - R_I J_m'(\lambda_{mn} \cdot R_I) - \frac{J_m'(\lambda_{mn} \cdot R_I)}{Y_m'(\lambda_{mn} \cdot R_I)} \\
&\quad \{R_D Y_m'(\lambda_{mn} \cdot R_D) - R_I Y_m'(\lambda_{mn} \cdot R_I)\}]^2 \\
&= \lambda_{mn}^2 R_D^2 [J_m'(\lambda_{mn} \cdot R_D) - J_m'(\lambda_{mn} \cdot R_I) \frac{R_I}{R_D} - \frac{J_m'(\lambda_{mn} \cdot R_I)}{Y_m'(\lambda_{mn} \cdot R_I)} \cdot Y_m'(\lambda_{mn} \cdot R_D) \\
&\quad + \frac{R_I}{R_D} J_m'(\lambda_{mn} \cdot R_I)]^2 \\
&= \frac{\lambda_{mn}^2 \cdot R_D^2}{Y_m'^2(\lambda_{mn} \cdot R_I)} [J_m'(\lambda_{mn} \cdot R_D) \cdot Y_m'(\lambda_{mn} \cdot R_I) \\
&\quad - J_m'(\lambda_{mn} \cdot R_I) \cdot Y_m'(\lambda_{mn} \cdot R_D)]^2 \quad (5.77)
\end{aligned}$$

The expression within the parenthesis goes to zero due to the boundary condition (see equation (5.67)).

Therefore,

$$[r^2 \{Q_m'^2(\lambda_{mn} \cdot r)\}]_{R_I}^{R_D} = 0 \quad (5.78)$$

Therefore,

$$\chi_{nn}^m = \frac{R_D^2}{2} [Q_m^2(\lambda_{mn} \cdot R_D) - \frac{R_I^2}{R_D^2} Q_m^2(\lambda_{mn} \cdot R_I) - \frac{m^2}{\lambda_{mn}^2 R_D^2} \{Q_m^2(\lambda_{mn} \cdot R_D) - Q_m^2(\lambda_{mn} \cdot R_I)\}] \quad (5.79)$$

Therefore, the modal coefficient P_{mn} can be express as

$$P_{mn} = \frac{\int_0^{2\pi} \int_{R_I}^{R_D} r \cdot Q_m(\lambda_{mn} \cdot r) \hat{p}(r, \theta) \cos m\theta \, dr \, d\theta}{\pi \epsilon_{mn} \chi_{nn}^m} \quad (5.80)$$

The above integral can be evaluated numerically using all the measured pressure data $\hat{p}(r, \theta)$. However, the above scheme is restricted to the orthogonal situation where the mean flow is uniform and boundary walls are rigid. Therefore, a generalized scheme to evaluate the modal coefficients, P_{mn} , is developed which can be used for both the orthogonal and nonorthogonal situations. P_{mn} , in this case, is evaluated from the several angular and radial pressure measurements in the following manner, by expressing equation (5.70) as

$$\begin{matrix} [A] & \{P_{mn}\} & = & \{\hat{p}(r, \theta)\} \\ \text{LXN} & \text{NX1} & & \text{LX1} \end{matrix} \quad (5.81)$$

where $[A] = Q_m (\lambda_{mn} \cdot r) \cdot \cos m\theta$, a coefficient matrix of the order, MXN

$\{P_{mn}\}$ = column matrix of the order $NX1$

$\{\hat{p}(r, \theta)\}$ = column matrix of the order $MX1$

L = total number of measurements both radial and azimuthal

N = total number of modes, radial, azimuthal and cross modes ($N \leq L$)

Equation (5.81) is an overdetermined system of linear equations, the matrix A having more rows than columns since the number of measurements, L , is greater than the number of unknowns, N . Overdetermined systems arise in experimental or computational work whenever more results are generated than would be required if accuracy were attainable. A least square solution is used to solve such an overdetermined system. In this method a residual vector, E , is defined as follows:

$$E = \sum_{\ell=1}^L \left(\sum_{j=1}^N a_{\ell j} x_j - b_{\ell} \right)$$

where $a_{\ell j}$, x_j and b_{ℓ} are the elements of matrices A , P_{mn} and $\hat{p}(r, \theta)$, respectively. Since E cannot ordinarily be reduced to the zero vector, an effort is made to choose x_j in such a way that E is minimized in some sense. This is achieved by the least-squares solution which makes the sum of the squares of the components of the residual vector a minimum. This process is carried out as follows:

Let

$$F = \sum_{\ell=1}^L \left(\sum_{j=1}^N a_{\ell j} x_j - b_{\ell} \right)^2$$

Therefore,

$$\frac{\partial F}{\partial x_i} = \sum_{\ell=1}^L 2 \left(\sum_{j=1}^N a_{\ell j} x_j - b_{\ell} \right) (a_{\ell i}), \quad i = 1, \dots, N$$

From equation (5.84) $\frac{\partial \hat{p}}{\partial x}$ can be derived as

$$\frac{\partial \hat{p}}{\partial x} = \sum_m \sum_n -ik_{mn} P_{mn} \Omega_m (\lambda_{mn} \cdot r) \cos m\theta \cdot e^{-ik_{mn}x} \quad (5.86)$$

Using equations (5.84) and (5.86) the intensity I can be expressed as

$$I = \sum_m \sum_n \bar{A} |P_{mn}|^2 \Omega_m^2 (\lambda_{mn} \cdot r) \cos^2 m\theta \quad (5.87)$$

where,

$$\bar{A} = 2 \left[-\frac{(1 - M^2)(1 + 3M^2)k_{mn}}{2\omega\rho} + \frac{M(1 + M^2)}{\rho c} + \frac{M(1 - M^2)^2}{2\rho c} \cdot \frac{c^2}{\omega^2} k_{mn}^2 \right] \quad (5.88)$$

The intensity expression contains only the contribution due to the individual modes (i.e., $|P_{mn}|^2$). The cross mode terms (i.e., $|P_{mn}| \cdot |P_{mn'}|$) do not appear in equation (5.87) due to the orthogonal behavior of the function Ω_m . Therefore, the acoustic power, W can be determined by integrating I over the duct cross section area.

$$W = \int_0^{2\pi} \int_{R_I}^{R_D} I \cdot r \cdot dr \cdot d\theta \quad (5.89)$$

Equation (5.89) gives the acoustic power for incident wave. However, the acoustic power for reflected wave can also be calculated using equation (5.89) by reversing the sign of the mean flow Mach number in the intensity expression, of equation (5.87).

1. For Single Stream Duct

For single stream duct equation (5.89) can be written as

$$\begin{aligned} W &= \int_0^{2\pi} \int_0^{R_D} \sum_m \sum_n \bar{A} |P_{mn}|^2 J_m^2(\lambda_{mn} r) \cdot \cos^2 m\theta \cdot r \cdot dr \cdot d\theta \\ &= \sum_m \sum_n \bar{A} |P_{mn}|^2 \int_0^{2\pi} \cos^2 m\theta d\theta \cdot \int_0^{R_D} J_m^2(\lambda_{mn} r) r dr \end{aligned} \quad (5.90)$$

or

$$\begin{aligned} W &= \sum_n \bar{A} \pi R_D^2 |P_{0n}|^2 J_0^2(\lambda_{0n} R_D) & \text{for } m = 0 \\ &= \sum_m \sum_n \bar{A} \pi R_D^2 |P_{mn}|^2 \cdot \left(1 - \frac{m^2}{\lambda_{mn}^2 R_D^2}\right) \cdot J_m^2(\lambda_{mn} R_D) & \text{for } m > 0 \end{aligned} \quad (5.91)$$

Equating the above expression to zero the following equations can be obtained.

$$\sum_{\ell=1}^L \sum_{j=1}^N a_{\ell j} a_{\ell i} x_j = \sum_{\ell=1}^L b_{\ell} a_{\ell i}, \quad i = 1, 2, \dots, N$$

$$\text{or} \quad \sum_{\ell=1}^L \sum_{j=1}^N a_{i\ell}^H a_{\ell j} x_j = \sum_{\ell=1}^L a_{i\ell}^H b_{\ell}, \quad i = 1, 2, \dots, N$$

where $a_{i\ell}^H$ is the transpose of conjugate of $a_{\ell i}$. The above equation, therefore, can be written in the following matrix form.

$$\begin{matrix} [A^H \cdot A] & \{P_{mn}\} & = & \{A^H \cdot \hat{p}(r, \theta)\} \\ \text{NXN} & \text{NX1} & & \text{NX1} \end{matrix} \quad (5.82)$$

where A^H is the transpose of conjugate of A .

$$\text{Therefore,} \quad \begin{matrix} \{P_{mn}\} \\ \text{NX1} \end{matrix} = \begin{matrix} [A^H \cdot A]^{-1} \\ \text{NXN} \end{matrix} \begin{matrix} \{A^H \cdot \hat{p}(r, \theta)\} \\ \text{NX1} \end{matrix} \quad (5.83)$$

The modal coefficients, therefore, can be derived from equation (5.83).

5.3.2 Derivation of Acoustic Power in Modal Form

The expressions for acoustic pressure for single stream duct as shown in equation (5.49) and that for annular stream duct as shown in equation (5.69) can be written in the following general form:

$$\hat{p}(x, r, \theta) = \sum_m \sum_n P_{mn} \Omega_m(\lambda_{mn} \cdot r) \cdot \cos m\theta e^{-ik_{mn}x} \quad (5.84)$$

$$\begin{aligned} \text{where} \quad \Omega_m(\lambda_{mn} r) &= J_m(\lambda_{mn} r) && \text{for single stream duct} \\ &= Q_m(\lambda_{mn} r) && \text{for annular stream duct.} \end{aligned}$$

The acoustic intensity in axial direction can be written as follows, from reference 21

$$\begin{aligned} \bar{I} = 2 \left[- \frac{(1-M^2)(1+3M^2)}{2\omega\rho} \text{IM}(\hat{p} \frac{\partial \hat{p}^*}{\partial x}) + \frac{M(1+M^2)}{\rho c} |\overline{\hat{p}}|^2 \right. \\ \left. + \frac{M(1-M^2)^2}{2\rho c} \cdot \frac{c^2}{\omega^2} \left| \frac{\partial \hat{p}}{\partial x} \right|^2 \right] \end{aligned} \quad (5.85)$$

Since \hat{p} is the rms value of the pressure, measured in the present study and used in the intensity expression of equation (5.85), a factor of 2 is multiplied to the original expression derived in reference 21.

The above integration is evaluated earlier and shown in equation (5.57).

An alternate expression for W is derived using the procedure outlined in reference 28.

$$W_{on}^{\pm} = \frac{2\pi}{\rho c} \frac{|P_{on}^{\pm}|^2 \eta (1 - M^2)^2}{(1 - \epsilon \eta M)^2} \int_0^{R_D} J_0^2(\lambda_{on} r) r dr$$

$$= \frac{\pi R_D^2}{\rho c} |P_{on}|^2 \frac{\eta (1 - M^2)^2}{(1 - \epsilon \eta M)^2} \cdot J_0^2(\lambda_{on} R_D) \quad (5.92)$$

where W_{on}^- is the acoustic power for the right moving pressure wave (i.e., incident) calculated when $\epsilon = +1$ and W_{on}^+ is the acoustic power for left moving pressure wave (i.e., reflected) when $\epsilon = -1$ for on mode. A summation over all the modes would result in the total power. Using equation (5.92) the following expression for the transmitted power $(W_{on})_t$ is derived.

$$(W_{on})_t = W_{on}^- - W_{on}^+$$

$$\text{or } (W_{on})_t = \frac{\pi R_D^2}{\rho c} \cdot J_0^2(\lambda_{on} R_D) \cdot \eta (1 + M)^2 |P_{on}^-|^2 \left\{ \frac{(1 - M)^2}{(1 - \eta M)^2} - \frac{|P_{on}^+|^2}{|P_{on}^-|^2} \cdot \frac{(1 - M)^2}{(1 + \eta M)^2} \right\} \quad (5.93)$$

The plane wave mode is a special case when n becomes zero. In this case, λ_{oo} becomes zero. Therefore,

$$\left. \begin{aligned} J_0(\lambda_{oo} R_D) &= 1 \\ \text{and } P_{oo} &= \frac{2}{R_D^2} \int_0^{R_D} \bar{P}(r) r dr \end{aligned} \right\} \quad (5.94)$$

Since no radial variation exists up to the first radial cut off frequency, in the present study, P_{oo} simply becomes $\bar{P}(r)$. Therefore, equations (5.92) and (5.93) for acoustic powers reduce to the plane wave equations (see equations (3.2) through (3.4)).

2. For Annular Stream Duct

For annular stream duct equation (5.89) can be written as

$$W = \int_0^{2\pi} \int_{R_I}^{R_D} \sum_m \sum_n \bar{A} |P_{mn}|^2 Q_m^2(\lambda_{mn} \cdot r) \cos^2 m\theta r dr d\theta$$

$$= \sum_m \sum_n \bar{A} |P_{mn}|^2 \int_0^{2\pi} \cos^2 m\theta d\theta \cdot \int_{R_I}^{R_D} Q_m^2(\lambda_{mn} \cdot r) dr \quad (5.95)$$

Using equation (5.79) the expression for W can be written as

$$W = \sum_m \sum_n \bar{A} |P_{mn}|^2 \epsilon_m \pi \chi_{nn}^m \quad (5.96)$$

where,

$$\chi_{nn}^m = \frac{R_D^2}{2} \left[Q_m^2(\lambda_{mn} \cdot R_D) - \left(\frac{R_I}{R_D} \right)^2 \cdot Q_m^2(\lambda_{mn} \cdot R_I) - \left(\frac{m}{\lambda_{mn} \cdot R_D} \right)^2 \{ Q_m^2(\lambda_{mn} \cdot R_D) - Q_m^2(\lambda_{mn} \cdot R_I) \} \right]$$

$$\begin{aligned} \epsilon_{mn} &= 2 & \text{for } m = 0 \\ &= 1 & m > 0 \end{aligned}$$

5.3.3 Derivation of Reflection Coefficient in Modal Form

The modal reflection coefficients are derived using the modal coefficients of the incident and the reflected pressures. Therefore, the complex modal power reflection coefficient, σ_{mn} , can be expressed as follows:

$$\sigma_{mn} = \frac{(P_{mn}^2)_r}{(P_{mn}^2)_i} \quad (5.97)$$

The modal power reflection coefficients can also be derived from modal incident and reflected power.

$$\bar{\sigma}_{mn} = \frac{(W_{mn})_r}{(W_{mn})_i} \quad (5.98)$$

σ_{mn} and $\bar{\sigma}_{mn}$ are related by a function of duct Mach number and can be expressed as follows

$$\bar{\sigma}_{mn} = \sigma_{mn} \cdot \frac{(\bar{A})_r}{(\bar{A})_i} \quad (5.99)$$

An overall power reflection coefficient $\bar{\sigma}$ can be derived from the ratio of reflected and incident power accounting for all the modal contributions. To compare the area weighted reflection coefficient, $(\sigma)_A$, with the modal and overall power reflection coefficient $\bar{\sigma}$, the amplitude of $\bar{\sigma}_{mn}$ or $\bar{\sigma}$ are approximately corrected for the duct Mach number as follows:

$$(|\bar{\sigma}|)_C = |\bar{\sigma}| \left\{ \frac{1+M}{1-M} \right\}^2 \quad (5.100)$$

5.3.4 Experimental Results for Single Stream Duct

Tests were carried out using a straight duct termination and a 6.2 cm diameter conical nozzle termination at various flow conditions, outlined in Table 5.1. The experimental procedure and the data analysis process to derive complex acoustic pressures at nine radial locations for each test are described in sections 5.1 and 5.2. The complex pressures thus derived were used in the analytical formulation described in sections 5.3.1 and 5.3.2 for modal decomposition exercise. A computer program was written to evaluate modal acoustic powers, incident, reflected and transmitted, using equations (5.91) and (5.92). Results derived by equation (5.91) are quite similar to those obtained with equation (5.92), except for very small differences at high frequencies when mean flow Mach numbers were significant. The results presented in this section, however, are evaluated using equation (5.92).

The incident power for the 10 cm diameter straight duct with $M_j = 0$ and 0.2 and for the 6.2 cm conical nozzle with $M_j = 0, 0.4, 0.6$ and 0.8 are presented in figures 5.38 and 5.39, respectively. In each figure the spectral distributions of the acoustic power due to plane wave mode, (0,0); sum of plane wave and first radial mode, (0,0 + 0,1); sum of plane wave and two radial modes, (0,0 + 0,1 + 0,2); and sum of plane wave and three radial modes, (0,0 + 0,1 + 0,2 + 0,3) are presented. Also the area weighted acoustic power, computed by plane wave power expressions using area weighted sound pressure values, is plotted in each of the figures.

The reflected acoustic power spectra and the transmitted acoustic power spectra similar to the incident acoustic power are plotted in figures 5.40 and 5.41, and figures 5.42 and 5.43, respectively. The observations made from these figures are summarized as follows:

- (1) Up to the first radial cut-off frequency, which is about 4.2 KHz in this case (i.e., $kR_D = 3.83$), the contributions to the incident, the reflected and the transmitted powers, due to the higher order modes, are negligible.
- (2) Up to the first radial cut-off frequency the area-weighted powers agree very well with the corresponding powers computed by summing the contributions of the plane wave mode and the higher order modes.
- (3) Beyond 4.2 KHz (i.e., $kR_D = 3.83$), the contribution due to the first radial mode is significant. However, the contributions due to other higher order modes seem to be insignificant. Since the second radial cut-off frequency is about 7.7 KHz ($kR_D = 7.02$), the contribution of the second radial mode, if important, would have been felt beyond this frequency. However, for the present exercise, since the frequency range is limited to 8 KHz, the power estimation can be done accurately by accounting for the contributions of only the plane wave and the first radial mode.

As shown in section 5.2, the radial variation of the incident and the transmitted powers is insignificant up to the first radial cut-off frequency, and in this frequency range, the single-point measurement results, at $r/D = 0.4375$, agree very well with the area-weighted values. Therefore, a single-point

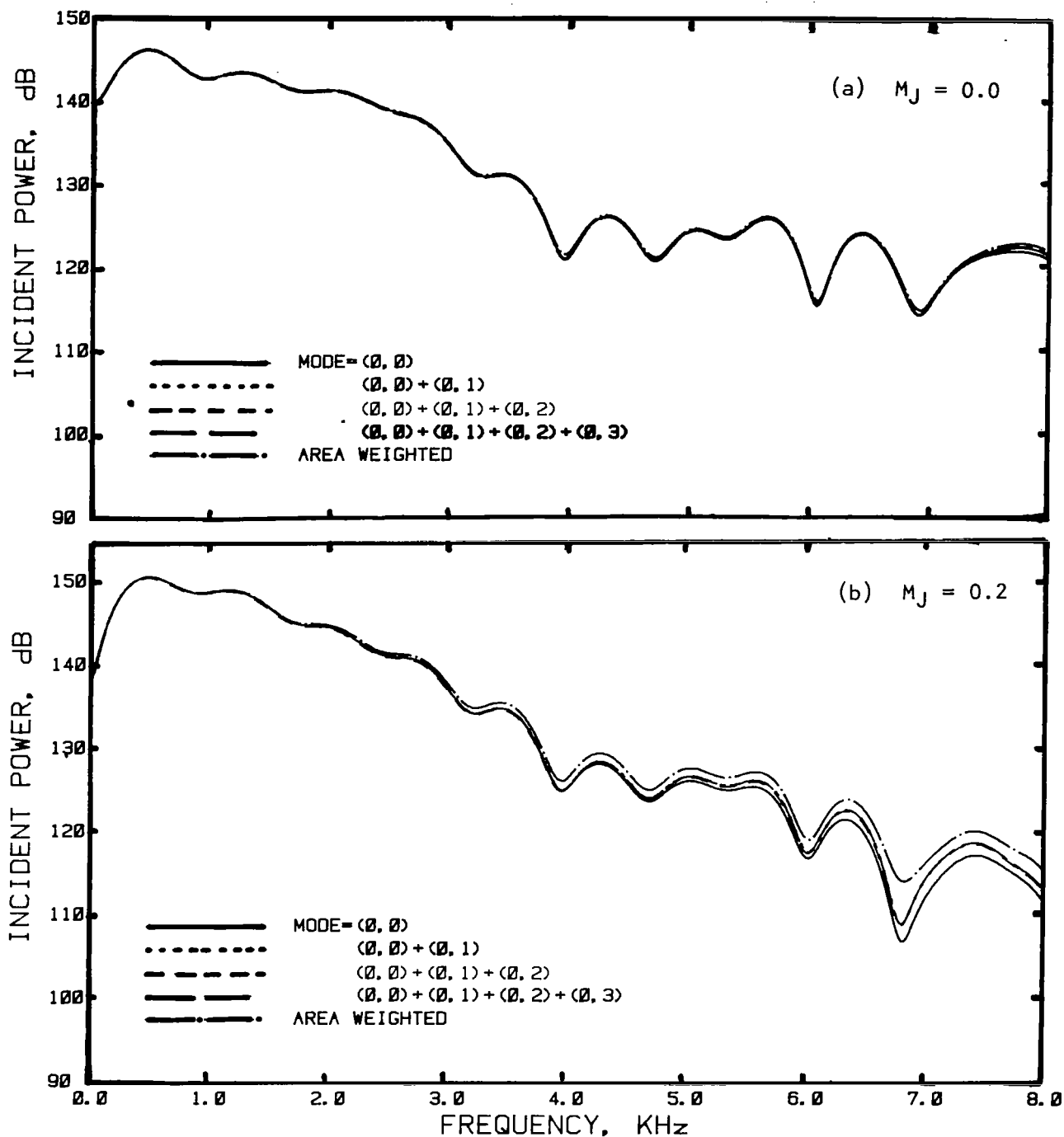


Figure 5.38 Contribution of higher order modes to the incident power for a 10 cm diameter duct at (a) $M_J = 0.0$, and (b) $M_J = 0.2$.

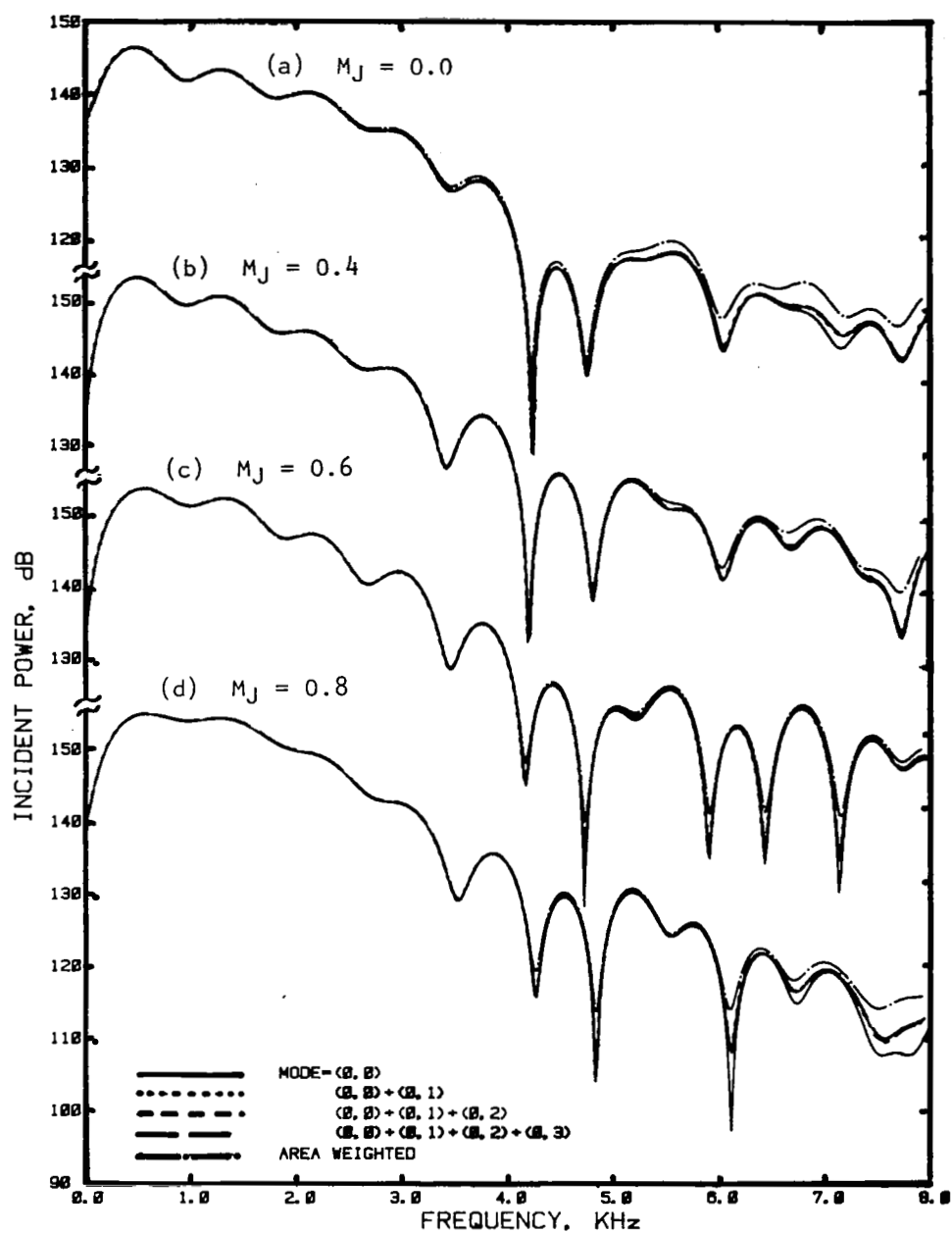


Figure 5.39 Contribution of higher order modes to the incident power for a 6.2 cm diameter conical nozzle at various Mach numbers.

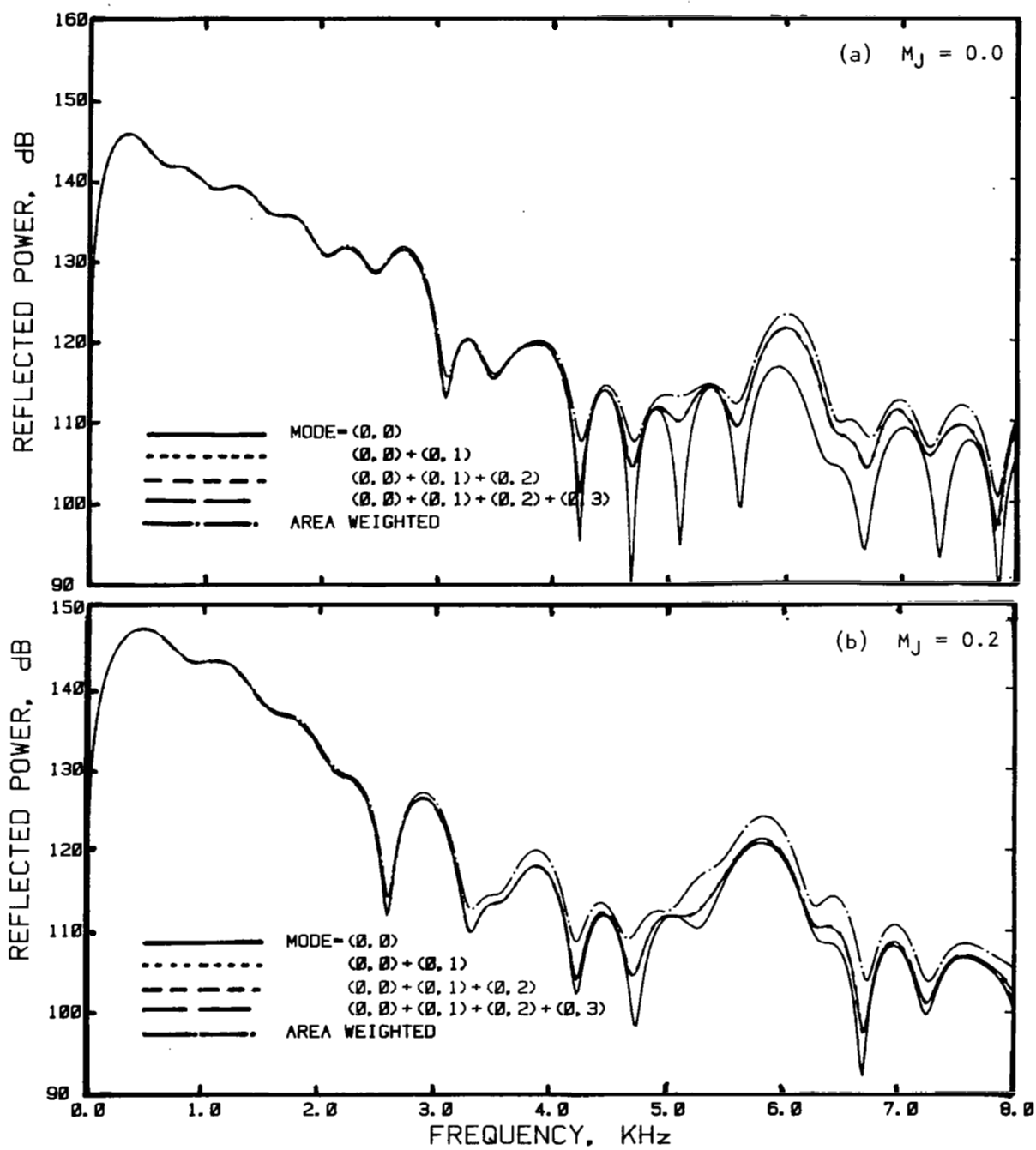


Figure 5.40 Contribution of higher order modes to the reflected power for a 10 cm diameter duct at (a) $M_J = 0.0$, and (b) $M_J = 0.2$.

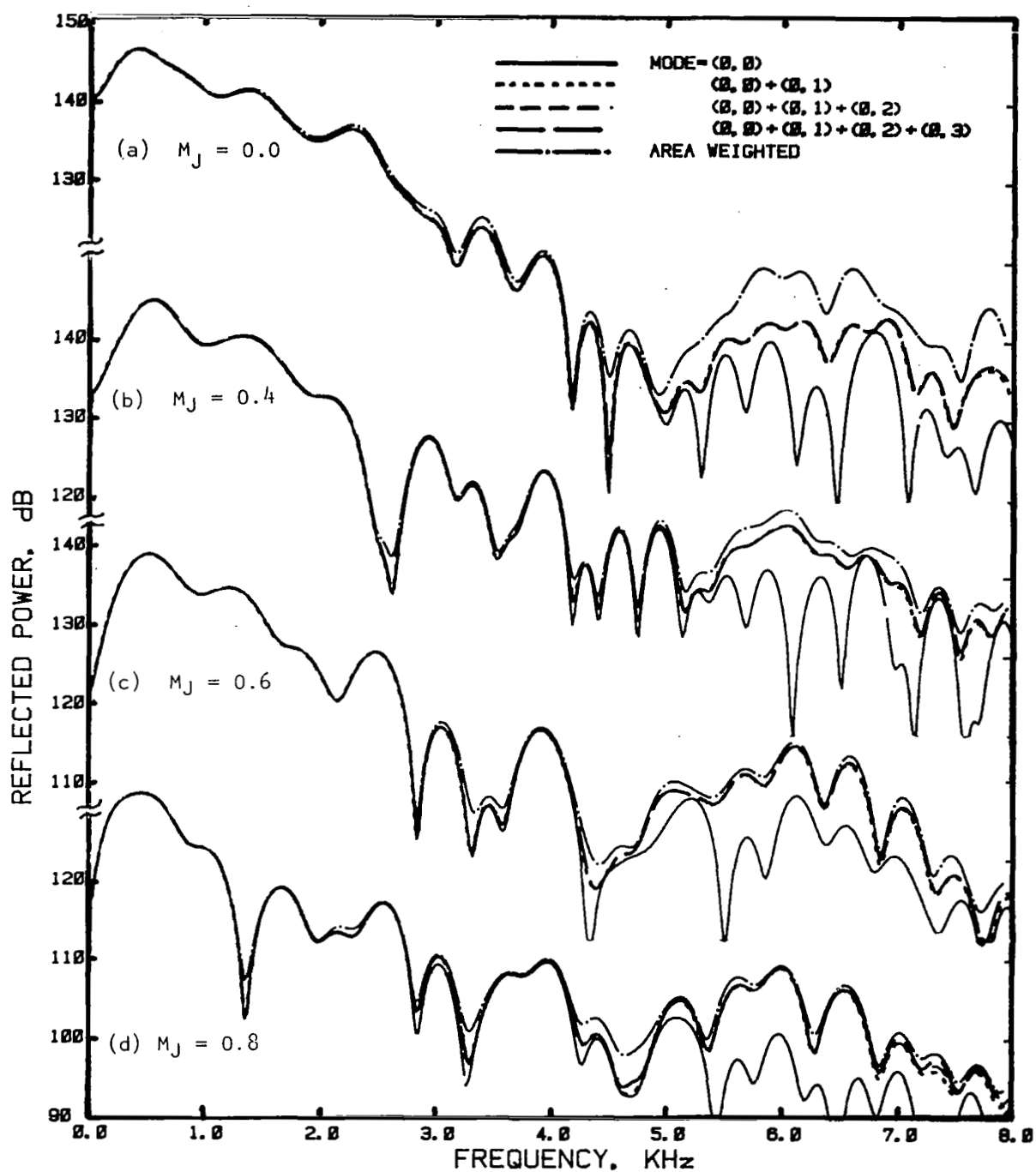


Figure 5.41 Contribution of higher order modes to the reflected power for a 6.2 cm diameter conical nozzle at various Mach numbers.

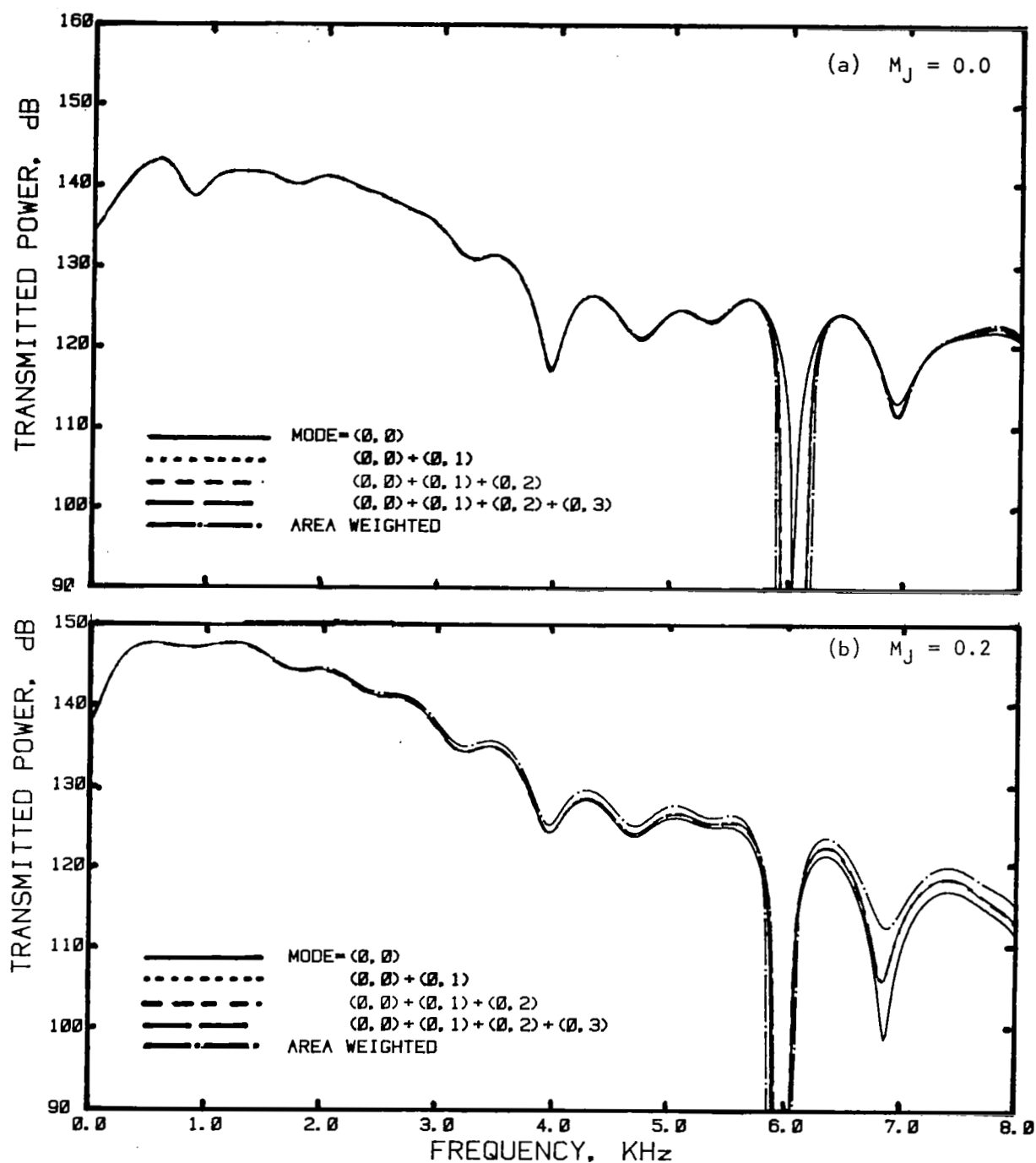


Figure 5.42 Contribution of higher order modes to the transmitted power for a 10 cm diameter duct at (a) $M_J = 0.0$, and (b) $M_J = 0.2$.

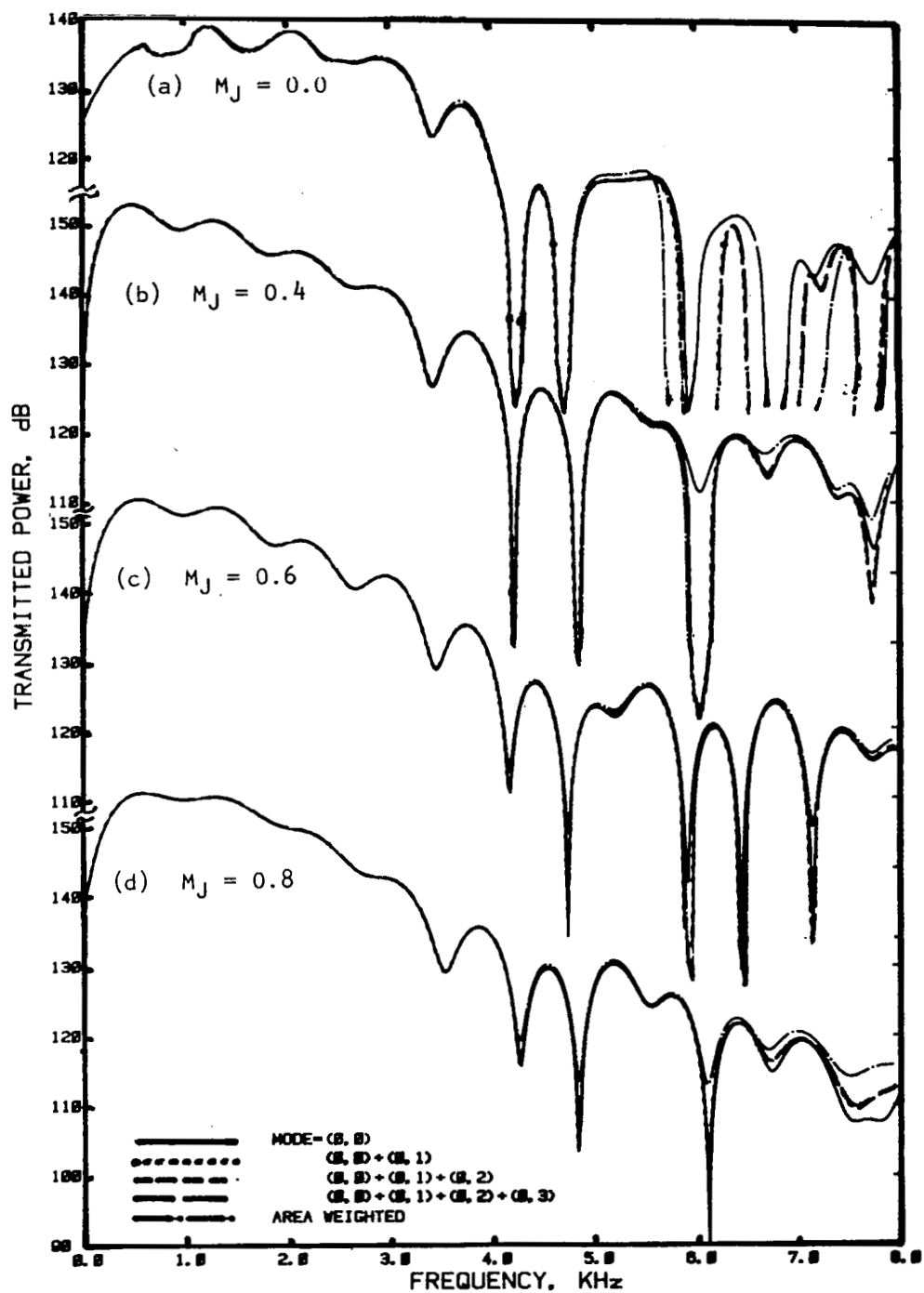


Figure 5.43 Contribution of higher order modes to the transmitted power for a 6.2 cm diameter conical nozzle at various Mach numbers.

measurement, at or near $r/D = 0.4375$, indeed accounts correctly for the incident and the transmitted acoustic field in the duct at least up to the first radial cut-off frequency.

5.3.5 Experimental Results for Annular Duct

Tests were conducted using a straight annular duct termination and with a 6.2 cm diameter conical nozzle annular termination at various flow conditions, outlined in Table 5.2. The experimental procedure and the data analysis process to derive complex acoustic pressure at 36 locations in the annular region are described in sections 5.1 and 5.2. The complex pressures thus derived were used in the analytical formulation for modal decomposition, described in section 5.3.1. A computer program was written to evaluate acoustic powers, incident, reflected and transmitted, using the appropriate expressions derived in section 5.3.2. For the present study, seven modal components (i.e., radial, circumferential and cross modes combined) are evaluated. The cut-on frequencies and the eigen values ($\lambda_{mn} R_I$) for various modes are derived from the boundary condition, equation (5.67). These values for the seven modes used in the present study are listed below in Table 5.3.

Table 5.3. Cut-on frequencies and eigen values for various modes.

CIRCUMFERENTIAL MODE m	RADIAL MODE n	$\lambda_{mn} \cdot R_I$	CUT-ON FREQUENCY, Hz
0	0	0.	0.
0	1	1.603	5196
1	0	0.508	1647
1	1	1.727	5595
2	0	0.967	3134
2	1	2.061	6677
3	0	1.370	4440

The incident power, the reflected power, the transmitted power and the reflection coefficient results for various test conditions are presented in this section. In each case the spectral distributions of the acoustic power (i.e., incident, reflected or transmitted) and the reflection coefficient due to plane wave mode, (0,0) and the six other higher modes, listed in Table 5.3, are calculated. These results are presented in two ways. In one set of results (i.e., incident and reflected modal power), the contributions of each mode to the acoustic power is plotted. In another set, the spectral distributions of the acoustic power (i.e., incident, reflected and transmitted) and the reflection coefficient due to the plane wave mode (0,0), sum of plane wave and first circumferential mode (i.e., $0,0 + 1,0$), sum of plane wave and three circumferential modes, ($0,0 + 1,0 + 2,0 + 3,0$), and sum of plane wave, three circumferential modes, one radial mode and two combination modes, ($0,0 + 1,0 + 2,0 + 3,0 + 0,1 + 1,1 + 2,1$) are presented. Also the corresponding area-weighted values are compared with the modal results.

1. Straight and Conical Annular Duct System:

Incident Power:

The incident pressure field for different configurations is measured upstream of the termination in the straight portion of the coannular duct system. Therefore, since the termination geometry does not influence the incident pressure field, the incident power spectra for a straight annular duct termination at $M_J = 0$ and for a conical nozzle annular termination at $M_J = 0.6$ are presented in figures 5.44 and 5.45, respectively, to study the effect of mean flow.

The incident powers due to individual modes are presented in parts (a) and the successive sums of the modal powers are presented in parts (b) of the respective figures. Figure 5.44(a) clearly indicates that, for the no flow condition, the incident power is dominated by the plane wave mode. The contributions of higher order modes are insignificant, even at higher frequencies (see figure 5.44(b)). For $M_J = 0.6$, the contribution of higher order modes seem to be significant at frequencies above 6.5 KHz, and are of the order of 2 to 3 dB as seen in figure 4.45(b).

The area-weighted incident power is higher compared to the sum of all the modal contributions, at higher frequencies above 4.5 KHz for the no flow condition and above 3.5 KHz for $M_J = 0.6$, as seen in figures 4.44(b) and 4.45(b), respectively.

Reflected Power:

Reflected acoustic power spectra are presented in figures 5.46 through 5.48 for an annular straight duct termination at $M_J = 0.0$, and for a 6.2 cm annular conical nozzle termination at $M_J = 0.0$ and $M_J = 0.6$, respectively. The individual modal reflected power spectra for each flow condition are presented in parts (a) and the successive sum of the modal powers are presented in parts (b) of the respective figures.

For the straight annular duct with no mean flow, contributions due to higher order modes at higher frequencies (above 5 KHz) seems to be significant (see figure 5.46(a)) compared to those for incident power in figure 5.44(a). This, in fact, is clear in figure 5.46(b) where the sum of all the modal contributions is slightly higher (about 1 or 2 dB) than the plane wave contribution, above 4.5 KHz.

By changing the termination, from a straight duct to an outer conical nozzle, the reflected powers due to higher order modes are relatively increased (see figure 5.47(a)). This effect is clearly seen in figure 5.47(b) where the total reflected power (i.e., sum of all the modal contributions) is higher compared to the plane wave reflected power (about 2 to 3 dB) at frequencies above 4.5 KHz.

With the initiation of flow, that is, with a conical nozzle at $M_J = 0.6$, the reflected powers due to higher order modes are significantly higher compared to those at $M_J = 0$ for the conical nozzle or the straight duct term-

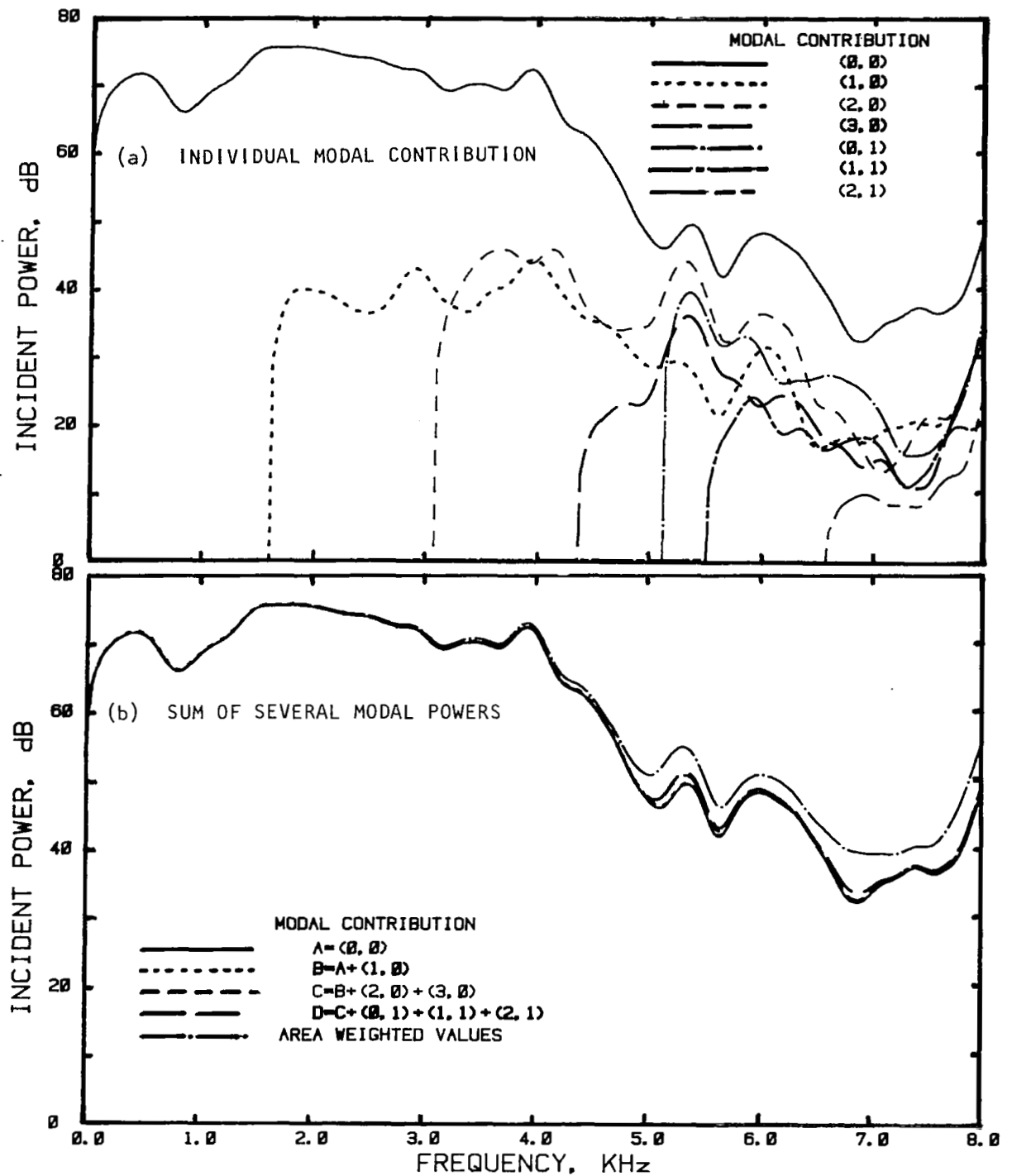


Figure 5.44 Contribution of various modals to the incident power for an annular duct at $M_j = 0.0$, (a) individual modal power, (b) sum of several modal powers.

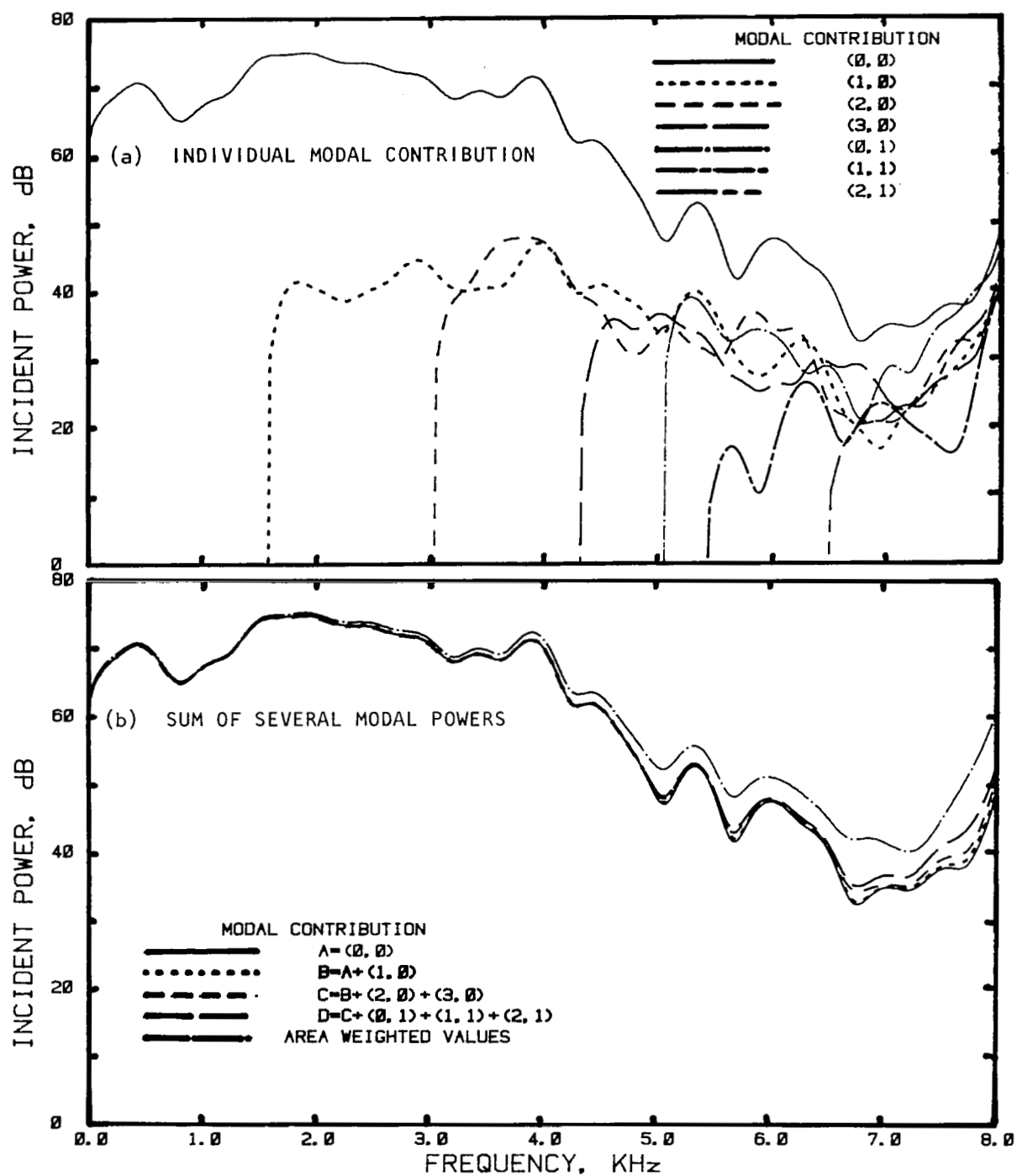


Figure 5.45 Contribution of various modes to the incident power for an annular conical nozzle at $M_j = 0.6$, (a) individual modal power, (b) sum of several modal powers.

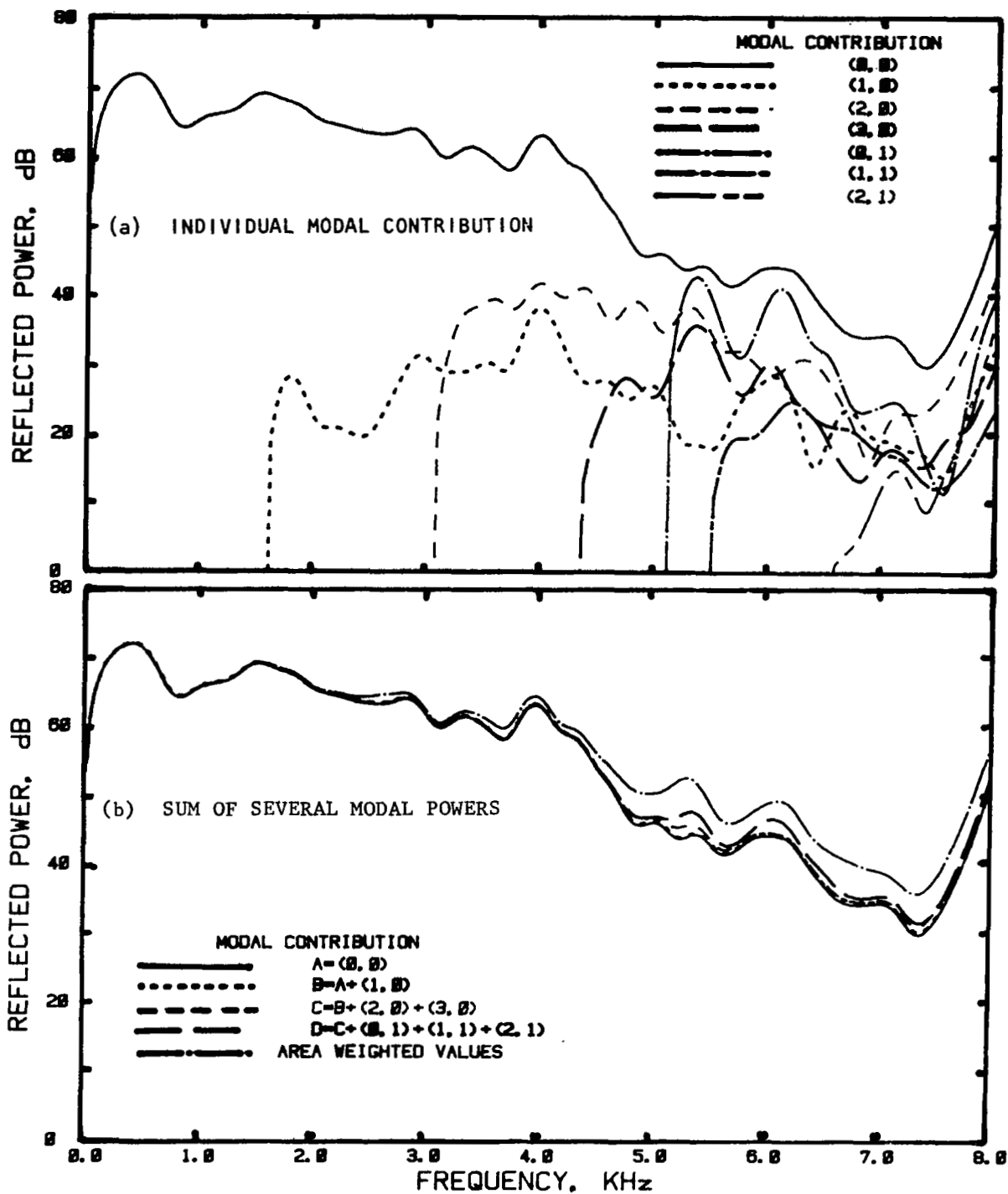


Figure 5.46 Contribution of various modes to the reflected power for an annular duct at $M_j = 0.0$, (a) individual modal power, (b) sum of several modal powers.

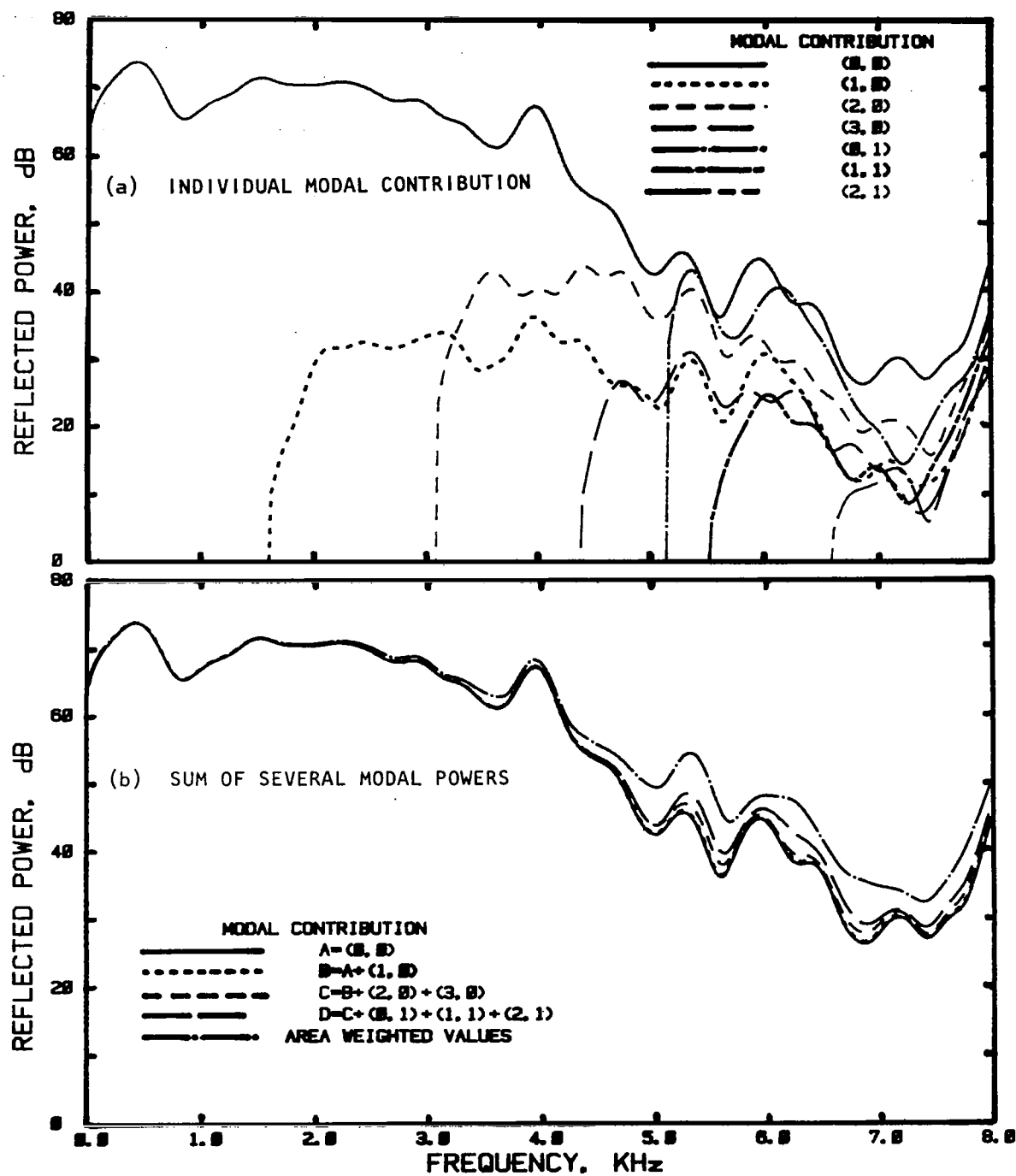


Figure 5.47 Contribution of various modes to the reflected power for an annular conical nozzle at $M_j = 0.0$, (a) individual modal power, (b) sum of several modal powers.

ination. This is clearly seen in figure 5.48(a) where the total reflected power above 4.5 KHz is about 3 to 8 dB higher compared to the plane wave reflected power.

As seen in figures 5.46 through 5.48, the area-weighted reflected powers are greater than the modal sums at frequencies above 2 to 3 KHz. The difference becomes large in the presence of mean flow.

Transmitted Power:

Transmitted power spectra for the straight annular duct with no mean flow, and the conical nozzle termination without and with mean flow are presented in figure 5.49. In this case the successive sum of various modal contributions are plotted. Even though a difference in the reflected power between the total and that due to plane wave mode is observed at higher frequencies, its effect on transmitted power is insignificant. This is due to the dominating effect of incident wave and due to the cancellation of the higher order mode contributions between incident and reflected powers in the process of transmitted power computation.

Another useful observation is that the area-weighted transmitted power spectra agree well with the total modal power. However, some difference does exist at higher frequencies, and the difference is relatively larger for the nozzle termination in the presence of flow.

The transmitted power for the nozzle termination with no mean flow seems to be negative at lower frequencies, below 500 Hz (see figure 5.49). This is due to higher reflected power compared to the incident power. Such a phenomena is not physically possible. The only explanation for this is an erroneous estimation of reflected power.

The most probable reason for this is the superimposition of a low-frequency pulse on the reflected signal. This unwanted low frequency pulse could have been generated by the reflection of the incident or reflected pulse from some object within the annular region, and this might have reached the induct measuring probe at the same time instant when the reflected pulse was recorded. However, at this stage one can simply ignore the data below 500 Hz.

Reflection Coefficients:

The modal reflection coefficients of the straight annular duct with no mean flow and the conical annular nozzle without and with mean flow are presented in figure 5.50. The successive sums of various modal reflection coefficient spectra are plotted in this figure. For the annular straight duct the reflection coefficient spectra due to the plane wave mode coincides well with the total reflection coefficient spectra up to about 5 KHz. (first radial cut on frequency). At frequencies above 5 KHz, appreciable difference is observed between the plane wave reflection coefficients and those due to the sum of all the modal contributions (see figure 5.50 (a)).

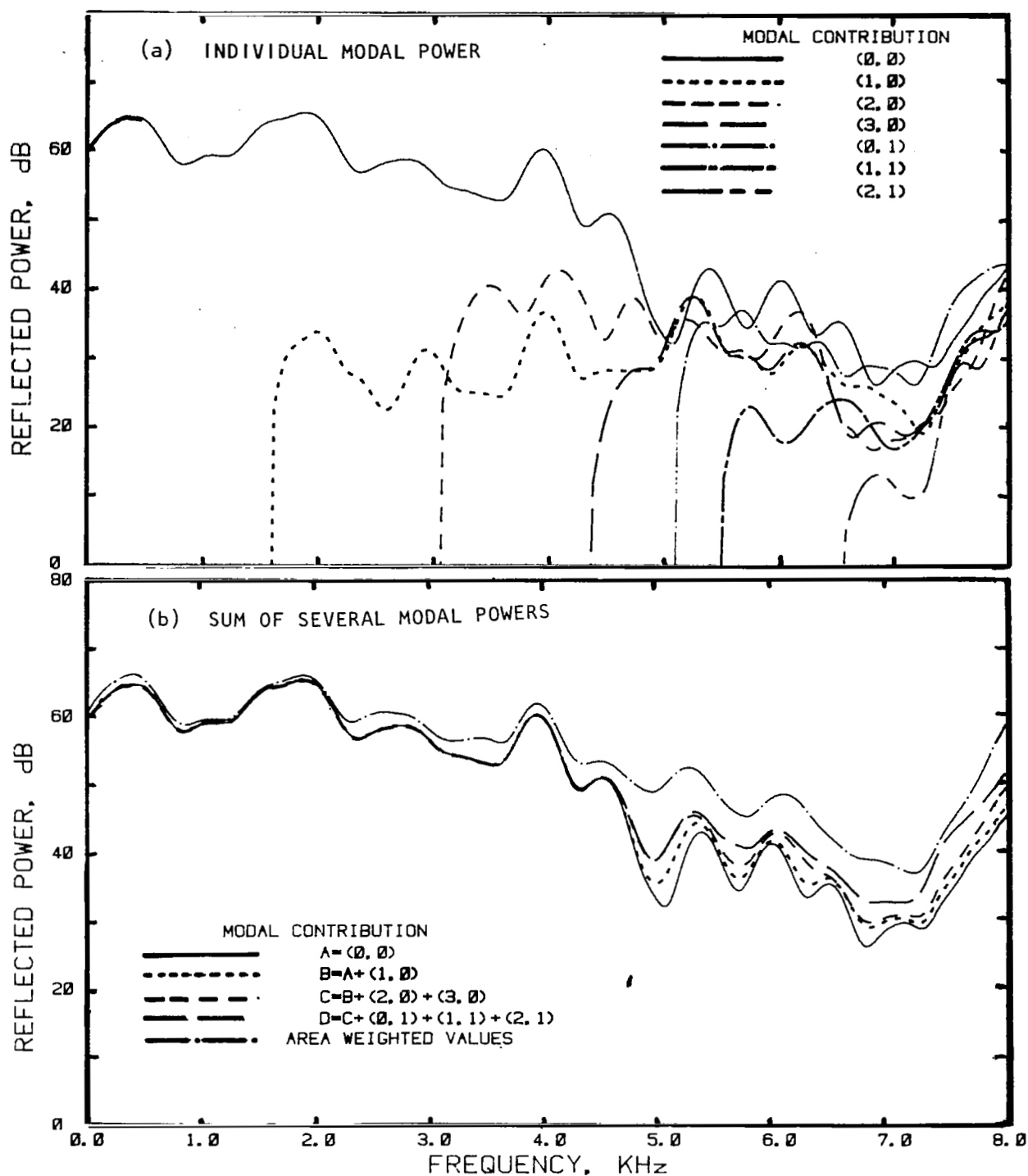


Figure 5.48 Contribution of various modes to the reflected power for an annular conical nozzle at $M_j = 0.6$, (a) individual modal power, (b) sum of several modal powers.

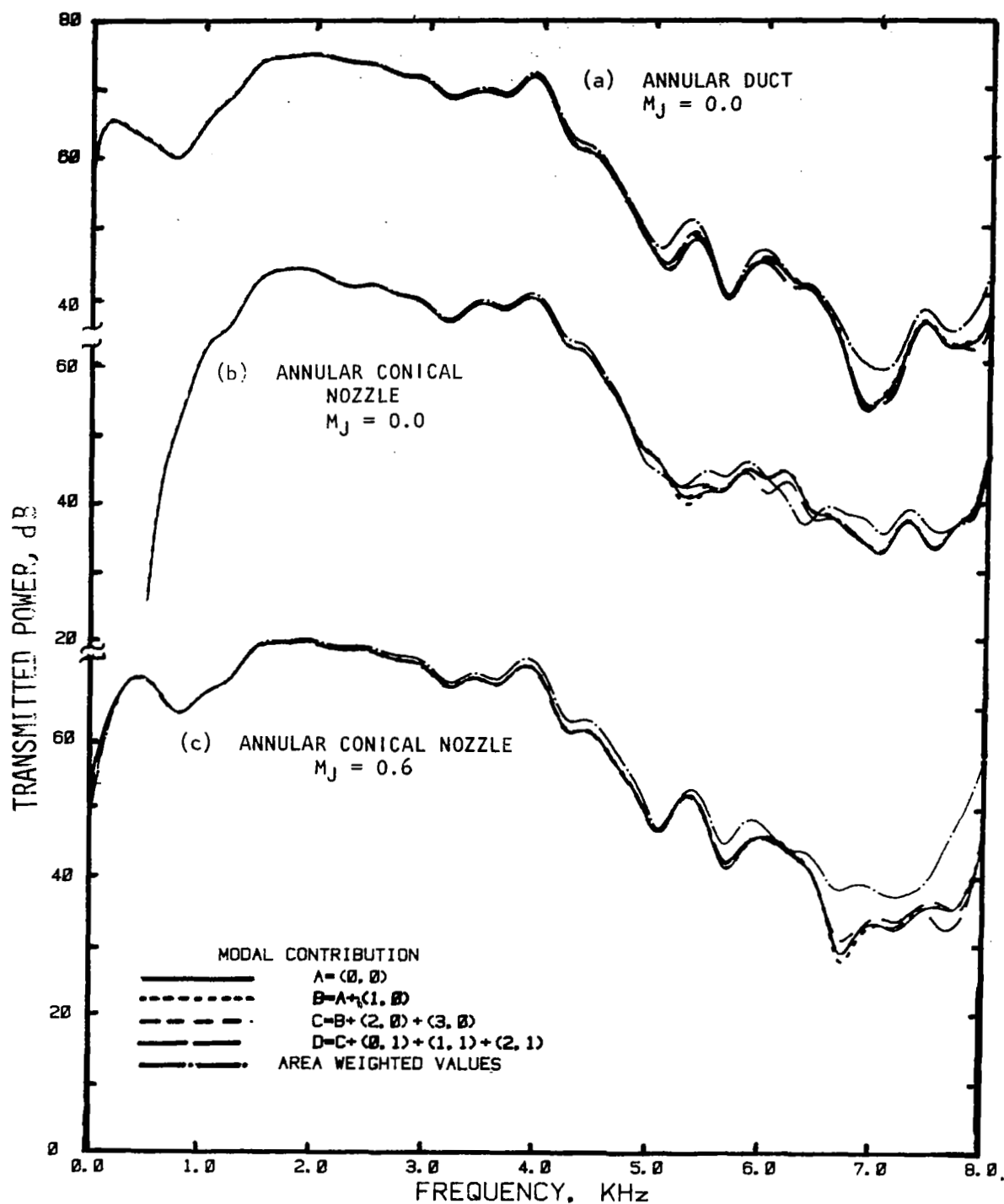


Figure 5.49 Contribution of various modes to the transmitted power for (a) annular duct, $M_J = 0.0$, (b) annular conical nozzle, $M_J = 0.0$, and (c) annular conical nozzle, $M_J = 0.6$.

The area-weighted reflection coefficient spectra for the no flow case compare well with the modal spectral distribution up to about 4.5 KHz for the straight duct and 3 KHz for the conical nozzle (see figure 5.50(a) and (b)). However, with mean flow ($M_j = 0.6$), the area-weighted reflection coefficient spectrum differs considerably from the modal results above 2 KHz.

2. Straight Annular Duct with Blocking Absorbing Material at the Termination

The reflected power spectra, the transmitted power spectra, and the reflection coefficient spectra for the annular duct with a 2.5 cm thick polyurethane foam mounted to a steel plate at the exit plane, are presented in figure 5.51. The contributions of higher order modes are quite insignificant even in higher frequency region (figure 5.51(a)). However, the area-weighted values of reflected power are much higher compared to the total modal data, above 3 KHz.

When the transmitted power spectra due to various modal contributions and the area-weighted spectrum are examined (see figure 5.51(b) very little difference is observed between them. The reflection coefficient spectra for the absorbing material are shown in figure 5.51(c).

3. Straight Annular Duct with a Rigid Steel Termination Blocking the Opening

The spectral distribution of the reflected power and the reflection coefficient for the rigid termination are presented in figure 5.52. The reflection coefficient values are expected to be unity (i.e., zero dB) for all the frequencies. However, a discrepancy of about 1 to 2 dB is found in the present results up to 3.5 KHz. For higher frequencies the spectral levels show much more deviations from zero dB, which indicates an inaccurate evaluation of reflected pressure field. The accuracy can be increased by accounting the contributions of other higher order modes and this is possible by increasing the number of radial and azimuthal measurements. The deviation of results from zero dB level could also be due to the slightly non-uniform annular height along the axial direction caused by fabrication inaccuracy.

5.4 CONCLUSIONS

Important conclusions derived from the results presented in this section are summarized below:

5.4.1 Single Stream Duct/Nozzle System

(1) Radial variation of incident pressure is insignificant up to about 4 KHz (first radial cut-on frequency, $kR_D = 3.83$), even in the presence of mean flow.

(2) The reflected pressure and the reflection coefficient are uniform across the cross section up to about 2 KHz.

(3) Transmitted power computed using area-weighted sound pressure levels agrees well with that computed using a single-point pressure measurement near the wall. Therefore, a single-point measurement near the duct wall is adequate for estimating the transmitted power.

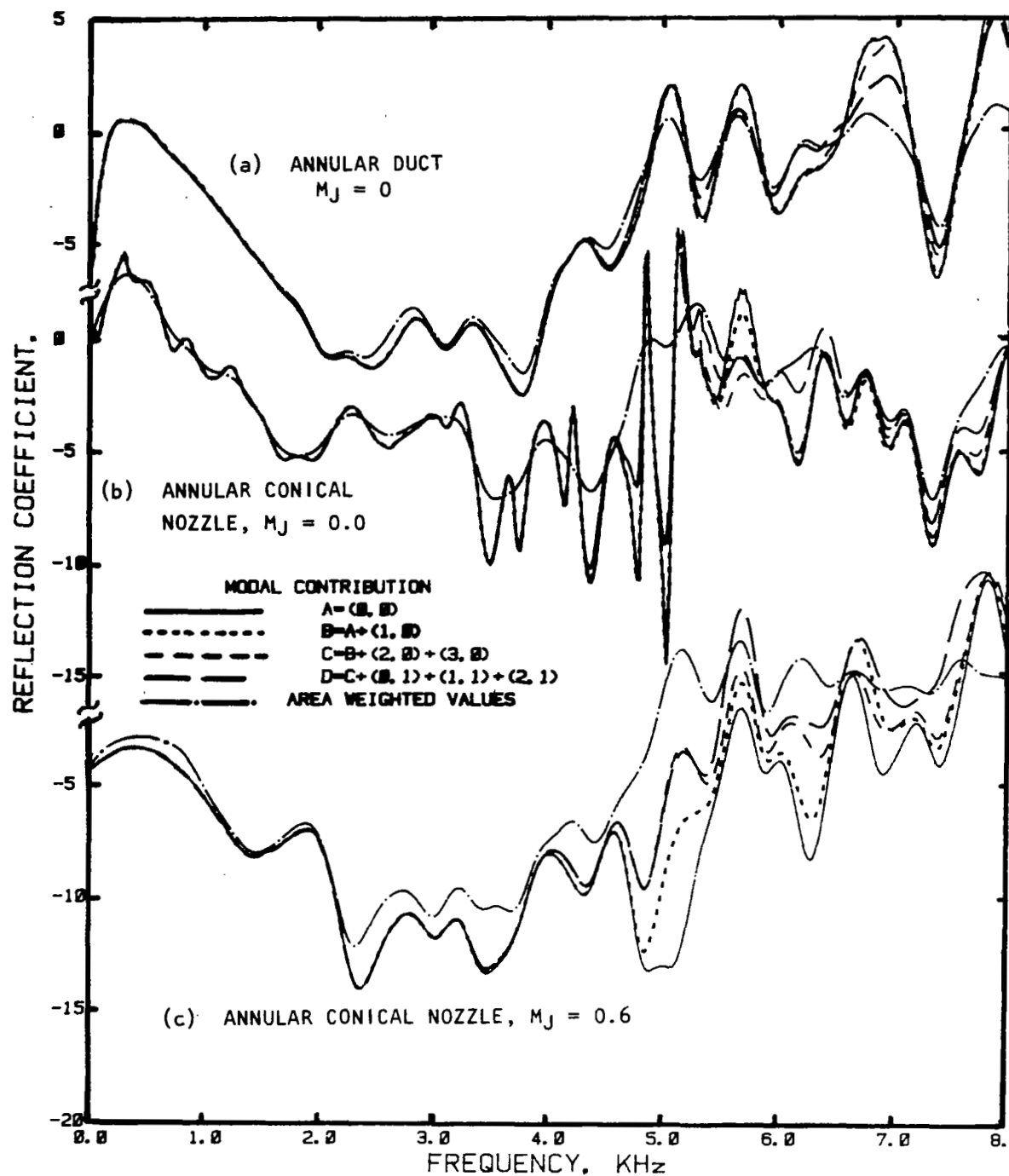


Figure 5.50 Contribution of various modes to the reflection coefficient for (a) annular duct, $M_J = 0.0$, (b) annular conical nozzle, $M_J = 0.0$, and (c) annular conical nozzle, $M_J = 0.6$.

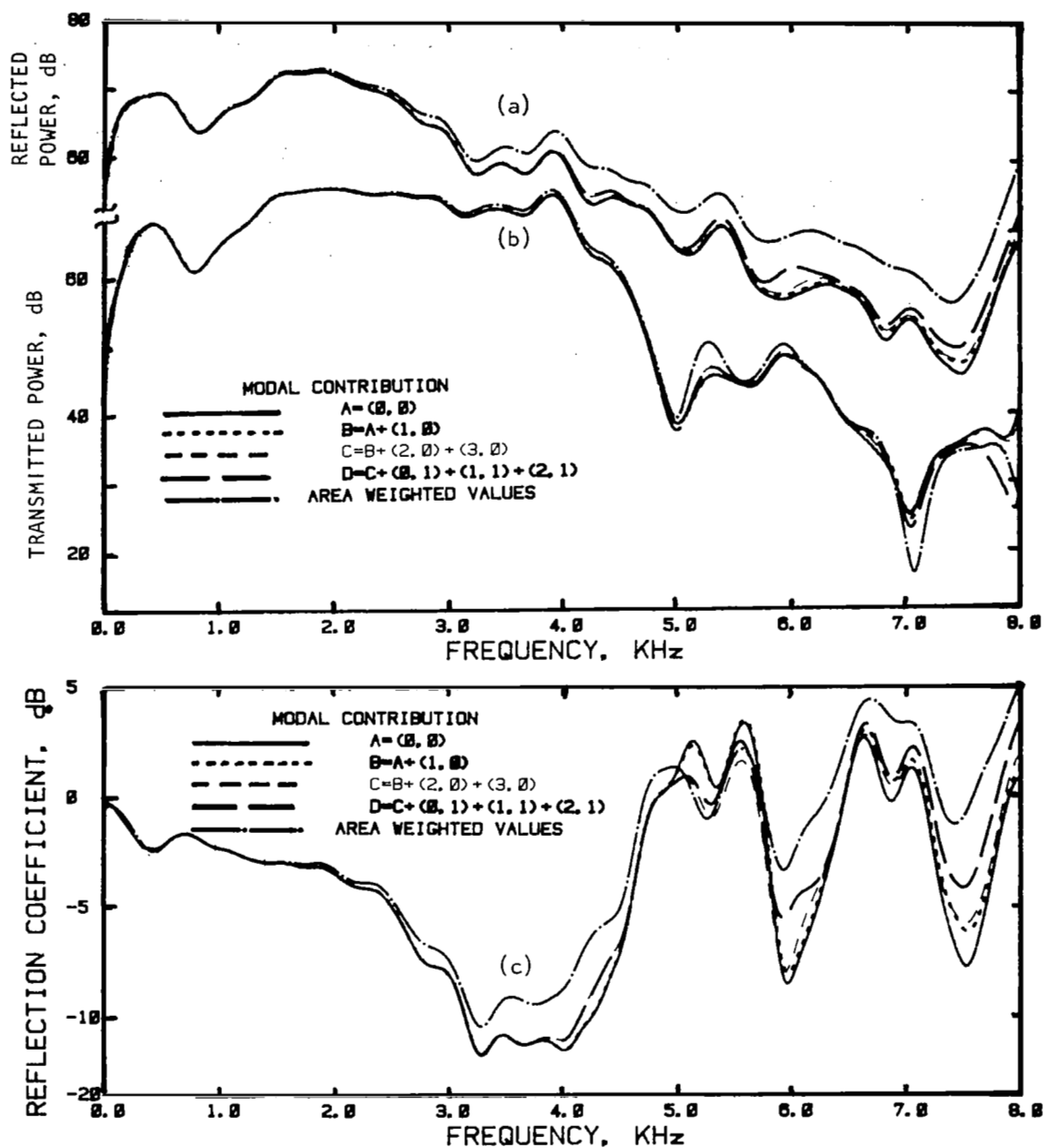


Figure 5.51 Contribution of various modes to (a) the reflected power, (b) the transmitted power, and (c) the reflection coefficient, due to a polyurethane foam sample mounted at the termination of annular duct.

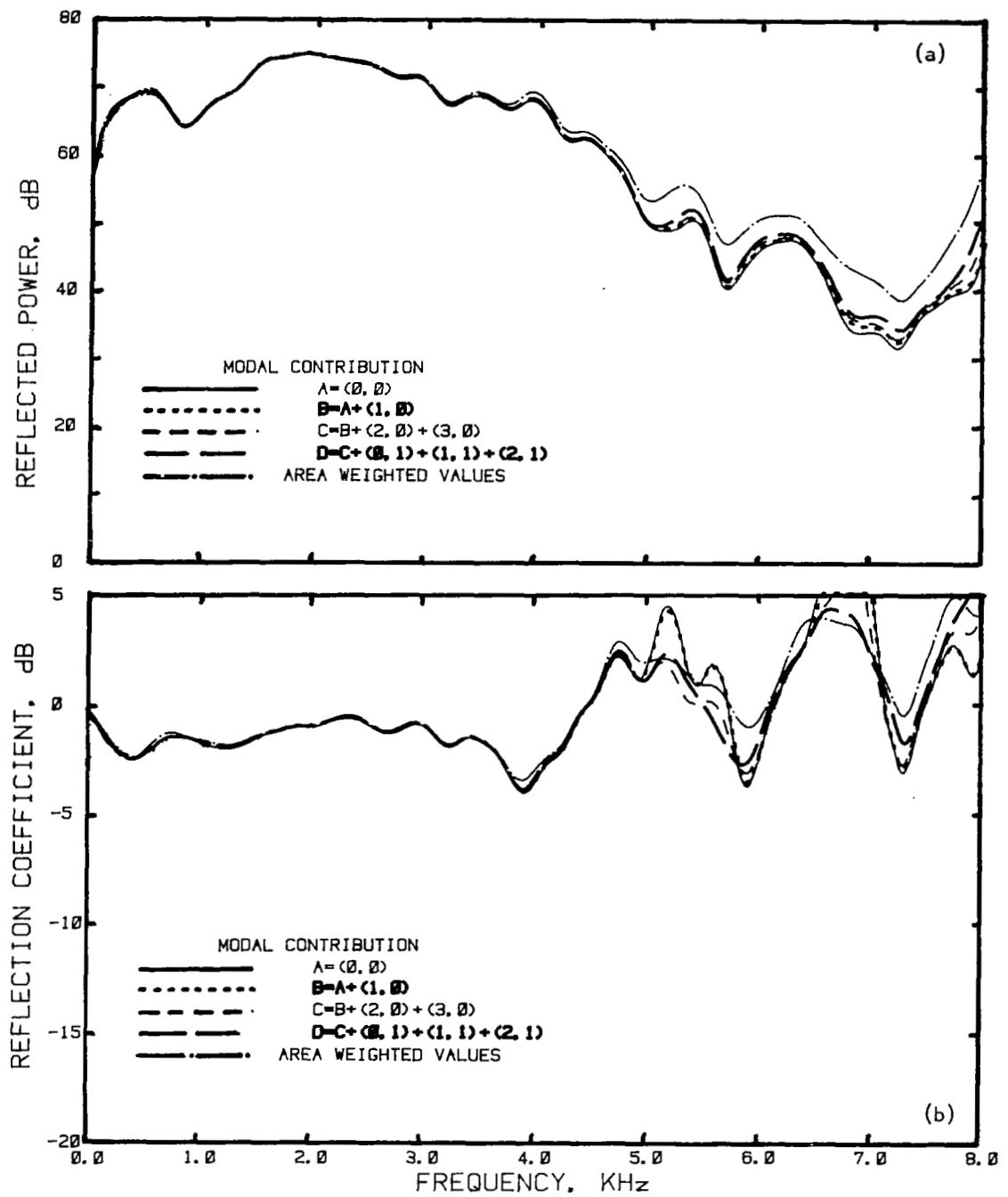


Figure 5.52 Contribution of various modes to (a) the reflected power and (b) the reflection coefficient due to a steel plate mounted at the termination of annular duct.

(4) The acoustic field is considerably influenced when a probe with large dimensions is traversed into the duct, and the effect is severe in the presence of flow. However, if the measurement is made near the wall, the acoustic field is not influenced much.

(5) The induct powers (i.e. incident, reflected and transmitted) computed using area-weighted pressure values agree well with the corresponding powers computed by summing the contributions of plane wave mode and the higher order modes.

(6) Contribution to the induct powers due to the first radial mode (beyond $kR_D = 3.83$) is significant.

5.4.2 Annular Stream Duct/Nozzle System

(1) Radial and azimuthal variation of incident pressure field, in the absence of mean flow, is insignificant up to about 5 KHz ($\lambda_{01}R_I = 1.603$). In the presence of flow, the radial variation remains insignificant but the azimuthal variation becomes noticeable even in the lower frequencies (below 5 KHz).

(2) Radial variation of reflected pressure field in the absence of flow is very small up to about 5 KHz, however, the azimuthal variation is significant at frequencies above 2 KHz. In the presence of mean flow, the radial variation of reflected pressure field becomes significant and the azimuthal variation is even larger.

(3) The incident power is mainly controlled by the plane wave mode pressure data. The contributions of higher order modes remain insignificant throughout the frequency range in the absence of mean flow. However, with mean flow, the contributions of higher order modes are felt at higher frequencies above 6 KHz.

(4) The contributions of higher order modes to the reflected power is felt at frequencies above 4.5 KHz. In the absence of flow, the contributions due to higher order modes are quite small compared to those with mean flow.

(5) Even though the higher order contributions are significant for the reflected power, the transmitted power seems to be little affected by higher order modes. This is a very useful observation: when only the transmitted power is needed, one can easily measure this parameter with a single-point measurement and can avoid all the laborious process of modal analysis, provided the acoustic source orientation is similar to that used in the present study where the annular pressure field is dominant by the plane wave mode.

6.0 VALIDATION OF ACOUSTIC IMPULSE TECHNIQUE

In this section, experimental results obtained by using the acoustic impulse technique are compared with results obtained mainly by the impedance tube method. These comparisons include (a) reflection coefficients, (2) far-field sound pressure level spectra, and (3) the power imbalance spectra (i.e., the difference between the far-field sound power W_f and the transmitted sound power W_t) for a 10 cm diameter duct and a 6.2 cm diameter conical nozzle terminations, with and without flow. In addition, the reflection coefficient spectra for an absorbing material and for a rigid termination derived using the annular facility are compared with the corresponding data measured in a classical impedance tube.

It has been established in section 5 that a single-point induct measurement at or near the duct wall is adequate to estimate the incident and the transmitted pressure field (and the associated acoustic power values) in the duct up to the first radial cut-off frequency. Therefore, the experimental results derived using the acoustic impulse technique with single-point induct measurements at $r/D = 0.4375$ are used in the validation exercise.

6.1 IMPLICATIONS OF FLOW IN IMPEDANCE TUBE MEASUREMENTS

The classical impedance tube setup consists of a tube with an acoustic driver at one end and the sample whose impedance is to be measured at the other end. During the actual experiment, the driver generates an incident wave of a desired frequency. This wave propagates along the tube until it impinges upon the sample under test. The interaction between the incident wave and the test sample results in a reflected wave with modified amplitude and phase. The reflected wave then combines with the incident wave to form a standing wave pattern in the tube whose structure depends, among other parameters, upon the impedance of the sample material. The structure of the standing wave is measured by traversing a microphone probe along the tube. The unknown impedance is then computed using an analytical solution for the standing wave which relates the wave structure to the sample impedance. The classical impedance tube experiment is restricted to situations involving no mean flow.

In the present investigation, the test sample was replaced by an open end (either a straight duct or a conical nozzle termination) and the driver end of the tube was connected to the air flow system. Therefore, a traverse mechanism similar to one used in the classical impedance tube could not be used. Instead, a modified traverse mechanism was needed to measure the structure of the standing wave in the tube with flow. Moreover, a simple microphone could not be used for the measurement, since the presence of flow would introduce strong hydrodynamic pressure fluctuations in the tube. Therefore, some modifications to the

microphone and to the measurement technique were necessary to eliminate the errors due to flow noise.

6.2 EXPERIMENTAL CONFIGURATION

For the impedance tube tests, the experimental configuration shown in figure 3.1 was modified by replacing the induct microphone with a microphone traverse mechanism. Figure 6.1 is the schematic of the microphone traverse mechanism specially designed for the present program. In this system a 183 cm long, 0.3 cm OD steel tube was used as the motion transmitter. This tube was introduced into the 10 cm diameter flow tube through a 0.635 cm OD tube which was fixed to the flow tube (see figure 6.1(b)) about 35 cm upstream of the termination. This 35 cm long tube was removable so that either a straight duct or a conical nozzle could be used as the termination. The microphone carriage system, shown in figure 6.1(a), was attached to the motion transmitter tube. The probe microphone was attached to the microphone support tube shown in figure 6.1(a). The shape of this support tube was such that it could also be used to traverse the microphone inside the conical nozzle. The probe microphone faced the driver end and stayed along the centerline of the 10 cm diameter flow tube. The connecting wire between the microphone and the microphone power supply ran inside the 0.3 cm OD motion transmitter tube. To keep the microphone carriage stable inside the flow tube, a triangular shaped structure, as shown in figure 6.1(a), was used to fit snugly against the inner surface of the flow tube. A conventional type of nose cone was used for the microphone to minimize the effect of flow noise in the measurements. A photographic view of the setup is shown in figure 6.2.

6.3 EXPERIMENTAL PROCEDURE

The experimental procedure, in principle, consists of measuring the minimum and maximum pressures, and the location of minimum pressure of the standing wave at each frequency, inside the duct, which could be used to determine the reflection coefficient and impedance values of the termination. The far-field sound pressure levels are also measured to determine the acoustic power transmission. However, in the presence of flow, the sound pressure levels inside the duct and in the far field cannot be measured directly. To get these pressure levels, the signal measured by each of the microphones needs to be averaged in time domain to eliminate the flow noise. The clean signal, after averaging, is Fourier transformed to get the sound pressure level. Therefore, inside the duct the probe microphone was placed at a number of axial locations and the corresponding signals were recorded on a tape recorder. These recorded signals were used to get the sound pressure levels at those locations. These acoustic pressure data and their corresponding axial locations were then used to determine the wave structure in the impedance tube. The information obtained included the incident and the reflected pressures, the complex reflection coefficient, and the radiation impedance using a modified impedance tube technique (refs. 29

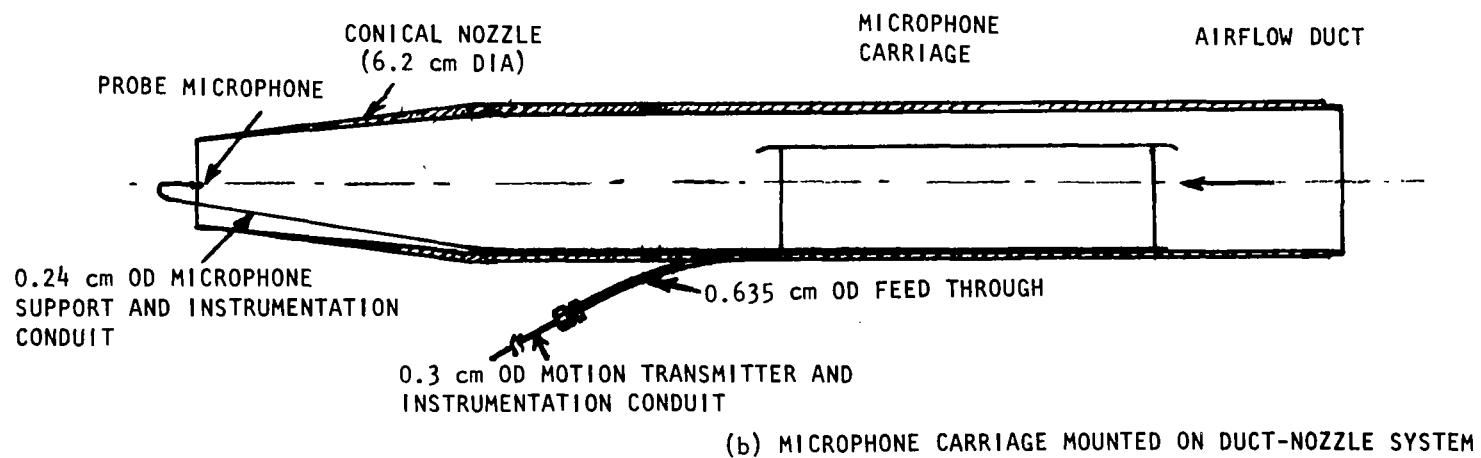
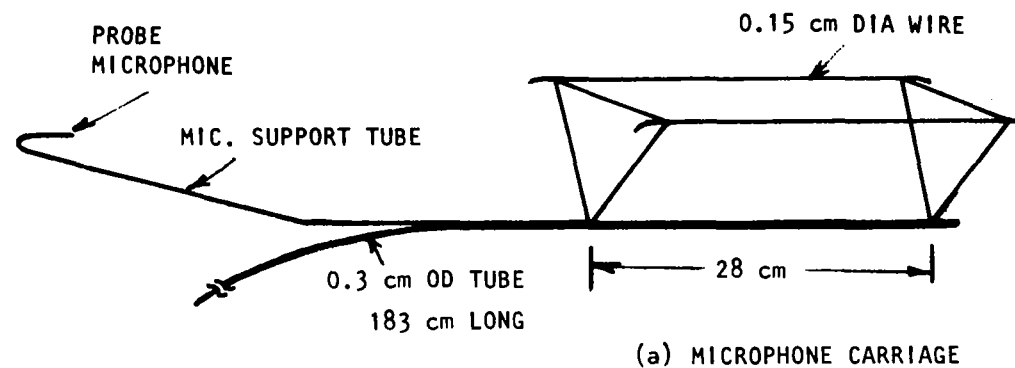


Figure 6.1 Schematic showing the microphone traverse mechanism for the impedance tube measurement.

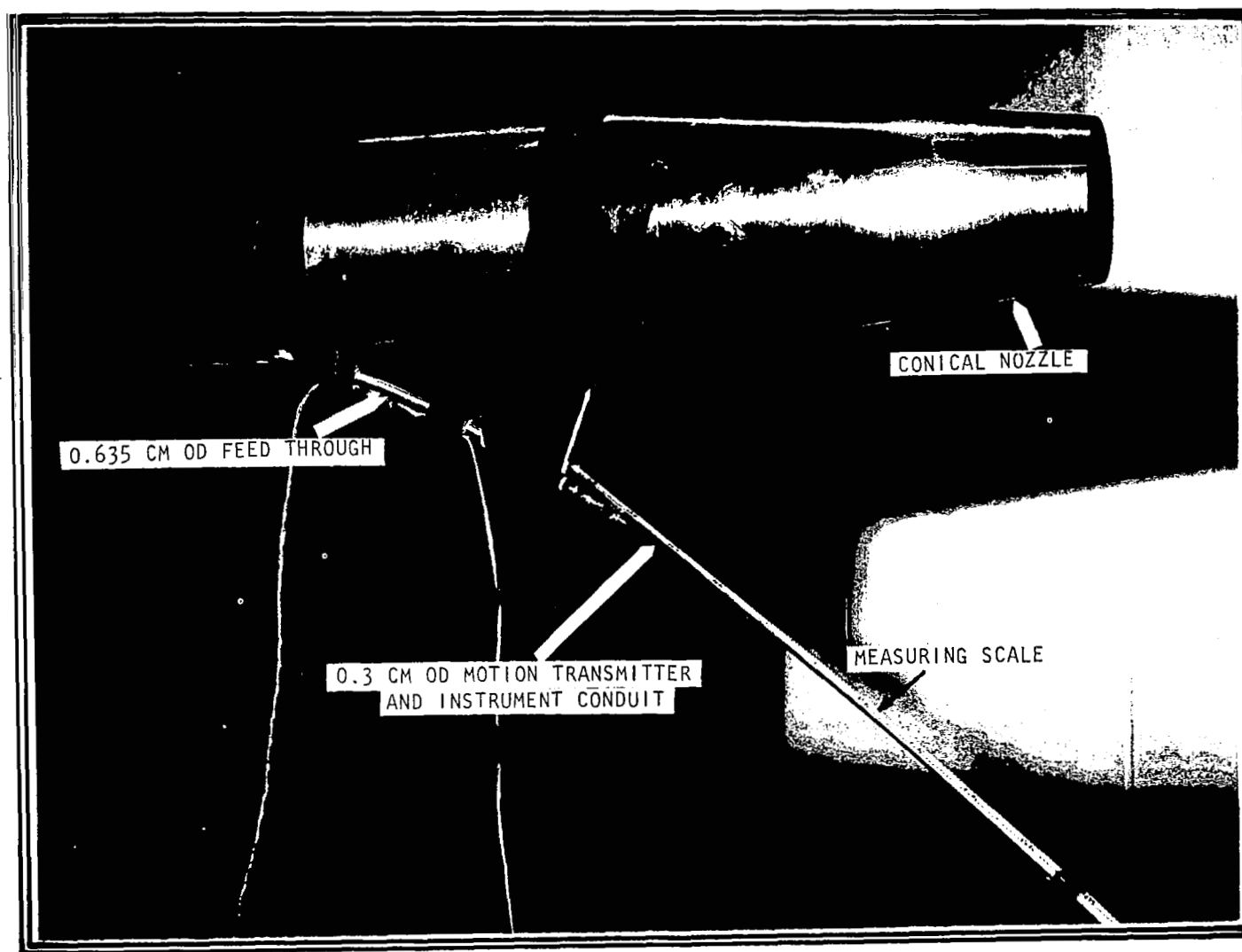


Figure 6.2 Photographic view of the impedance tube facility mounted on the flow duct.

and 30) with a nonlinear regression approach (ref. 31).

The signals measured by each of the microphones placed in the far field were also recorded in a tape recorder and were averaged in time domain to obtain the far-field sound pressure levels. The far-field, the incident, and the reflected sound pressure levels, thus obtained, were used to determine the incident (W_i), the reflected (W_r), the transmitted (W_t), and the far field (W_f) powers using plane wave relationship.

6.4 MATHEMATICAL APPROACH OF MODIFIED IMPEDANCE TUBE TECHNIQUE

The modified impedance tube technique to determine the termination impedance and reflection coefficient in the presence of non-uniform mean flow with axial mean temperature gradient and with axial acoustic loss due to particle interaction is described in reference 29. A corresponding situation with constant temperature and mean flow (i.e. isentropic flow condition) is presented in reference 30 where higher order modes were also considered. However, in the present study, for the validation of the impulse technique, the modified impedance tube technique is applied to the isentropic flow condition for plane wave propagation mode only. The analytical steps pertinent to this situation are as follows:

The one-dimensional conservation equations for isentropic flow, assuming periodic time dependent acoustic pressure and velocity can be written as:

$$\text{Continuity:} \quad i\omega\hat{p} + \rho \frac{du}{dx} + V \frac{d\rho}{dx} = 0 \quad (6.1)$$

$$\text{Momentum:} \quad i\omega u + V \frac{du}{dx} = - \frac{1}{\rho} \frac{dp}{dx} \quad (6.2)$$

$$\text{Energy:} \quad \hat{p} = \frac{p}{c^2} \quad (6.3)$$

The set of equations can be combined and expressed as follows:

$$(1 - M^2) \frac{d^2 p}{dx^2} - 2ikM \frac{dp}{dx} + k^2 p = 0 \quad (6.4)$$

$$\text{where: } \left. \begin{array}{l} M = V/c \\ k = \omega/c \end{array} \right\} \quad (6.5)$$

The solution of equation (6.4) can be represented as

$$p = A_+ e^{-\frac{ikx}{1+M}} + A_- e^{\frac{ikx}{1-M}} \quad (6.6)$$

and therefore,

$$\rho c u = A_+ e^{-\frac{ikx}{1+M}} - A_- e^{\frac{ikx}{1-M}} \quad (6.7)$$

Let

$$\left. \begin{aligned} A_+ &= \frac{1}{2} A e^{\pi\alpha - i\pi(\beta + \frac{1}{2})} \\ \text{and } A_- &= \frac{1}{2} A e^{-\pi\alpha + i\pi(\beta + \frac{1}{2})} \end{aligned} \right\} \quad (6.8)$$

where A_+ and A_- are the complex incident and reflected pressures at $x = 0$

$$\left. \begin{aligned} e^{-2\pi\alpha} &= \text{reflection coefficient amplitude} \\ \pi(2 + 1) &= \text{reflection coefficient phase at } x=0 \end{aligned} \right\} \quad (6.9)$$

Therefore,

$$p = -iAe^{iax} \sinh[\pi\alpha - i(\pi\beta + k_1 x)] \quad (6.10)$$

$$u = \frac{-iAe^{iax}}{\rho c} \{ \cosh[\pi\alpha - i(\pi\beta + k_1 x)] \} \quad (6.11)$$

$$\text{where } a = \frac{kM}{1-M^2}$$

$$k_1 = \frac{k}{1-M^2}$$

The termination impedance is defined as

$$Z = \frac{1}{\rho c} \cdot \left. \frac{p}{u} \right|_{x=0} = \tanh\{\pi(\alpha - i\beta)\} \quad (6.12)$$

Therefore, the resistance R and the reactance X can be expressed as

$$\left. \begin{aligned} R &= \frac{\sinh(2\pi\alpha)}{\cosh(2\pi\alpha) + \cos(2\pi\beta)} \\ \text{and } X &= \frac{-\sin(2\pi\beta)}{\cosh(2\pi\alpha) + \cos(2\pi\beta)} \end{aligned} \right\} \quad (6.13)$$

The termination reflection coefficient and impedance can be evaluated using equations (6.9) and (6.13), respectively, once the values of α and β are known.

Several methods are available for determining α and β experimentally which involve measurement of the standing wave pattern in the impedance tube. The dependence of the standing wave pattern for the pressure oscillations on the location in the tube is obtained from equation (6.10). These pressure oscillations are described by

$$p = |p| e^{i(\delta + \omega t)} \quad (6.14)$$

where the pressure amplitude $|p|$ is given by

$$|p| = A [\cosh^2 \pi\alpha - \cos^2 \pi(\beta + \frac{2x}{\lambda})]^{1/2} \quad (6.15)$$

where

$$\lambda = \frac{2\pi}{k_1} = \frac{2\pi}{k} (1-M^2) = \text{Axial wave length.}$$

$$\delta = \alpha x + \text{Arc tan}[\tanh \pi\alpha \cdot \cot \pi(\beta + \frac{2x}{\lambda})] \quad (6.16)$$

In this experiment, pressure amplitudes are measured in decibels. The sound pressure level in decibel, L , is defined as

$$L = 20 \log_{10} \frac{|p|}{p_{\text{ref}}} \quad (6.17)$$

where p_{ref} = reference pressure level

$$= 2 \times 10^{-4} \text{ dynes/cm}^2.$$

Therefore,

$$L = A_{\text{db}} + 10 \log_{10} [\cosh^2 \pi\alpha - \cos^2 \pi(\beta + \frac{2x}{\lambda})] \quad (6.18)$$

The most widely used method for finding α and β is the traversing microphone technique. It consists of a microphone probe which is used to traverse in the impedance tube in axial direction in order to measure

the standing wave pattern. By measuring the distance between two successive minima, the half-wave length $\lambda/2$ is determined. The value of β is then computed by measuring the distance x_{\min} from the sample to the first minimum. From equation (6.15) or equation (6.18), this minimum occurs when

$$\left. \begin{aligned} \cos^2 \pi \left(\beta + \frac{2x_{\min}}{\lambda} \right) &= 1 \\ \text{or when } \beta + \frac{2x_{\min}}{\lambda} &= 0 \\ \text{or } \beta &= - \frac{2x_{\min}}{\lambda} \end{aligned} \right\} \quad (6.19)$$

Then α is obtained by measuring a maximum pressure amplitude where

$$|p_{\max}| = A \cosh \pi \alpha$$

and a minimum pressure amplitude, where

$$|p_{\min}| = A \sinh \pi \alpha$$

Then

$$\begin{aligned} \tanh \pi \alpha &= \left| \frac{p_{\min}}{p_{\max}} \right| \\ \text{or } \alpha &= \frac{1}{2\pi} \ln \left\{ \frac{1 + \left| \frac{p_{\min}}{p_{\max}} \right|}{1 - \left| \frac{p_{\min}}{p_{\max}} \right|} \right\} \end{aligned} \quad (6.20)$$

However, in the present experimental technique, instead of determining the values of pressure maximum, pressure minimum, and the location of pressure minimum, the acoustic pressure is measured at several axial locations. Wave length λ is computed from the frequency and the induct static temperature and is given by

$$\lambda = \frac{2\pi}{k_1} = \frac{2\pi(1 - M^2)}{(2\pi f/c)} \quad (6.21)$$

where f = frequency in Hertz.

c is determined from temperature measurements. In principle, three pressure amplitude measurements $|p_1|$, $|p_2|$, $|p_3|$ at different axial locations x_1 , x_2 , x_3 are required to determine α , β and A .

$$\left. \begin{aligned} \alpha &= \frac{1}{2\pi} \ln (z + \sqrt{z^2-1}) \\ \beta &= \frac{1}{\pi} \ln (\text{Arc tan } y) \end{aligned} \right\} \quad (6.22)$$

where:

$$\left. \begin{aligned} z &= \frac{|A_{31}B_{21} - A_{21}B_{31}|}{\{[B_{21}(1-P_{31}) - B_{31}(1-P_{21})]^2 + [A_{21}(1-P_{31}) - A_{31}(1-P_{21})]^2\}^{\frac{1}{2}}} \\ y &= \frac{A_{21}(1-P_{31}) - A_{31}(1-P_{21})}{B_{21}(1-P_{31}) - B_{31}(1-P_{21})} \end{aligned} \right\} \quad (6.23)$$

$$\left. \begin{aligned} A_{n1} &= \cos \frac{4\pi}{\lambda} x_n - P_{n1} \cos \frac{4\pi}{\lambda} x_1 \\ B_{n1} &= \sin \frac{4\pi}{\lambda} x_n - P_{n1} \sin \frac{4\pi}{\lambda} x_1 \\ P_{n1} &= \left| \frac{P_n}{P_1} \right|^2 \text{ for amplitudes in psi} \\ \text{or } P_{n1} &= 10 \frac{(L_n - L_1)}{20} \text{ for amplitudes in dB} \end{aligned} \right\} \quad \begin{matrix} n = 2, 3 \\ (6.24) \end{matrix}$$

According to the above discussion any three accurate pressure measurements can be used to determine the unknown α, β and A . However, errors in experimental measurements result in errors in the computed α, β and A . These errors can be minimized by increasing the number of acoustic pressure measurements and utilizing a non-linear regression technique in the data reduction scheme (ref. 31).

Nonlinear regression consists of finding the values of α, β and A which give the best fit between the theoretical curve described by equation (6.15) and the experimental points. This is accomplished by computing the values of α, β and A which minimize the root-mean-square deviation between the theoretical curve and the experimental points. To find the minimum root-mean-square deviation, the following function F is minimized:

$$F = \sum_{i=1}^n [E_i - T_i(\alpha, \beta, A)]^2, \text{ 'A' in psi} \quad (6.25a)$$

$$\text{or } F = \sum_{i=1}^n [E_i - T_i(\alpha, \beta, A_{\text{db}})]^2, 'A_{\text{db}}' \text{ in decibels} \quad (6.25b)$$

The parameter E_i represents the pressure amplitude measured at a distance x_i from the termination where $i = 1, 2, \dots, n$. The corresponding theoretical prediction T_i is given as

$$\left. \begin{aligned} T_i(\alpha, \beta, A) &= A [\cosh^2 \pi \alpha - \cos^2 \pi (\beta + \frac{2x_i}{\lambda})]^{\frac{1}{2}} \\ \text{For Amplitudes in psi, and} \\ T_i(\alpha, \beta, A_{\text{db}}) &= A_{\text{db}} + 10 \log_{10} [\cosh^2 \pi \alpha - \cos^2 \pi (\beta + \frac{2x_i}{\lambda})] \\ \text{For Amplitudes measured in decibels} \end{aligned} \right\} \quad (6.26)$$

If a minimum for F exists, then

$$\frac{\partial F}{\partial \alpha} = \frac{\partial F}{\partial \beta} = \frac{\partial F}{\partial A} = \frac{\partial F}{\partial A_{\text{db}}} = 0 \quad (6.27)$$

$$\left. \begin{aligned} \sum_{i=1}^n (E_i - T_i) \frac{\partial T_i}{\partial \alpha} &= 0 \\ \sum_{i=1}^n (E_i - T_i) \frac{\partial T_i}{\partial \beta} &= 0 \\ \text{and } \sum_{i=1}^n (E_i - T_i) \frac{\partial T_i}{\partial A} &= 0 \\ \text{or } \sum_{i=1}^n (E_i - T_i) \frac{\partial T_i}{\partial A_{\text{db}}} &= 0 \end{aligned} \right\} \quad (6.28)$$

where, for pressure measured in psi,

$$\left. \begin{aligned} \frac{\partial T_i}{\partial \alpha} &= \frac{\pi A \cosh \pi \alpha \cdot \sinh \pi \alpha}{[\cosh^2 \pi \alpha - \cos^2 \pi (\beta + \frac{2x_i}{\lambda})]^{\frac{1}{2}}} \\ \frac{\partial T_i}{\partial \beta} &= \frac{\pi A \cos \pi (\beta + \frac{2x_i}{\lambda}) \sin \pi (\beta + \frac{2x_i}{\lambda})}{[\cosh^2 \pi \alpha - \cos^2 \pi (\beta + \frac{2x_i}{\lambda})]^{\frac{1}{2}}} \\ \text{and } \frac{\partial T_i}{\partial A} &= [\cosh^2 \pi \alpha - \cos^2 \pi (\beta + \frac{2x_i}{\lambda})]^{\frac{1}{2}} \end{aligned} \right\} \quad (6.29)$$

and, for pressure amplitudes in decibels,

$$\left. \begin{aligned}
\frac{\partial T_i}{\partial \alpha} &= (20\pi \log_e) \left[\frac{\sinh \pi \alpha \cdot \cosh \pi \alpha}{\cosh^2 \pi \alpha - \cos^2 \pi \left(\beta + \frac{2x_i}{\lambda} \right)} \right] \\
\frac{\partial T_i}{\partial \beta} &= (20 \log_e) \left[\frac{\sin \pi \left(\beta + \frac{2x_i}{\lambda} \right) \cos \pi \left(\beta + \frac{2x_i}{\lambda} \right)}{\cosh^2 \pi \alpha - \cos^2 \pi \left(\beta + \frac{2x_i}{\lambda} \right)} \right] \\
\text{and } \frac{\partial T_i}{\partial A_{db}} &= 1
\end{aligned} \right\} \quad (6.30)$$

Once equations (6.28) are solved, the values of α, β and A or A_{db} are obtained which provide the best fit between the theoretical curve described by equation (6.26) and the experimental data. Since equations (6.28) are nonlinear, an explicit solution for α, β and A or A_{db} cannot be derived and the equations must be solved numerically. Marquardt's algorithm (ref. 32) is used to solve equations (6.28). This algorithm is an extension of the Newton-Raphson method, and at the same time it improves the stability characteristics. To start the iteration, equation (6.15) or equation (6.18) is solved explicitly for α, β and A or A_{db} using various combinations of three amplitude measurements and equations (6.22). The value of α, β, A and A_{db} obtained from the combination which gives the minimum value of F from equation (6.25) are then used to start the iteration. The details of the iteration procedure are described in references 29 and 30.

6.5 CALIBRATION OF THE PROBE MICROPHONE

A Knowles microphone was used as the induct probe microphone for the impedance tube measurements. Before installing it in the impedance tube facility, it was calibrated with respect to a 6.2 mm B&K microphone at various flow conditions. The B&K microphone with nose cone and the probe microphone were mounted inside the flow duct side by side, both facing the flow direction (see figure 6.3). The acoustic driver, which was mounted upstream in the duct, was excited by sinusoidal signals at various frequencies. The corresponding outputs of each of the two microphones mounted inside the flow duct were recorded under the same flow conditions at which the actual impedance tube tests were to be conducted. These recorded signals were signal averaged and Fourier transformed subsequently and a relationship between the two microphones at each frequency and at each flow condition was derived which was used as the calibration for the Knowles microphone.

6.6 COMPARISON OF EXPERIMENTAL RESULTS FOR SINGLE STREAM DUCT

Some of the experimental results derived by using the refined acoustic impulse technique are compared with the corresponding results obtained by the impedance tube method. The impedance tube data were acquired at frequencies up to the first circumferential mode frequency of the duct. The first circumferential mode corresponds to $kR_D = 1.84$, k and R_D being the wave number and the duct radius, respectively.

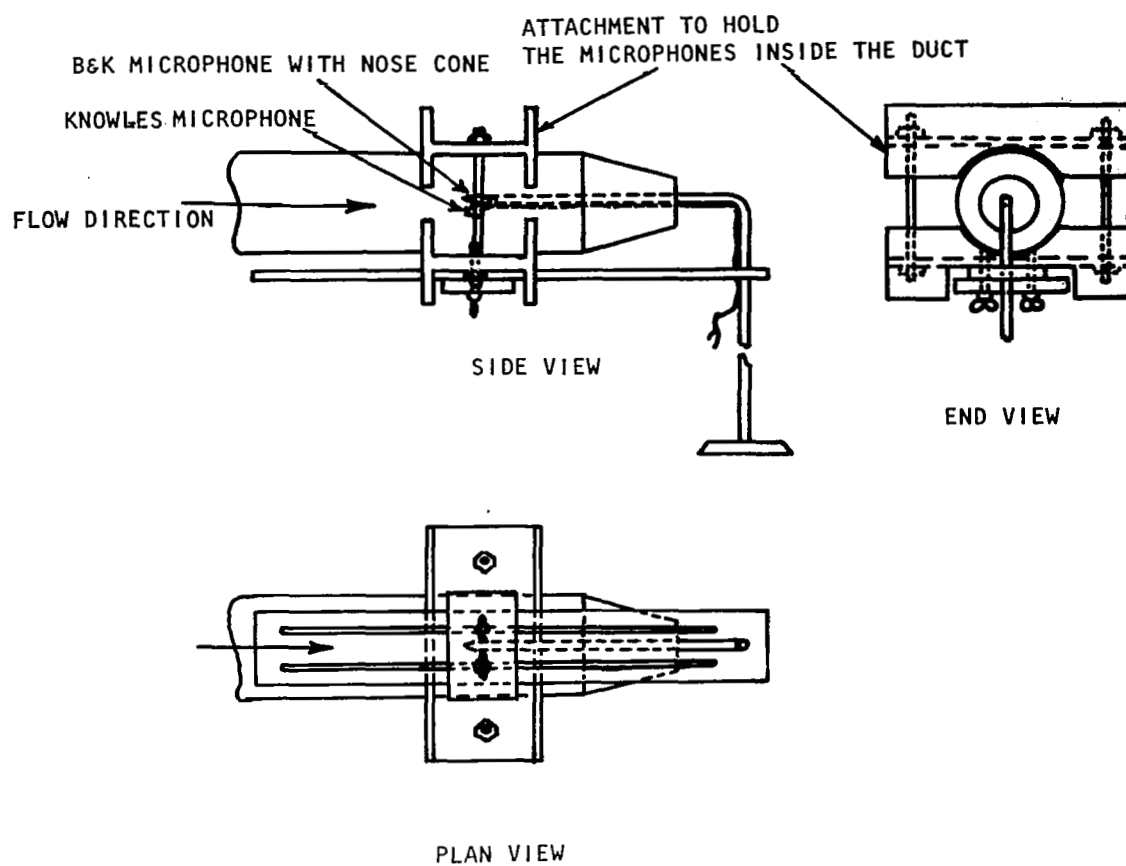


Figure 6.3 Knowles microphone calibration facility

(1) Reflection Coefficients

Figure 6.4 illustrates the comparison between the reflection coefficients for a 10 cm diameter duct termination, derived by the two methods, at $M_J = 0$ and at $M_J = 0.2$. For the no flow condition, the reflection coefficients are also compared with those derived by Levine and Schwinger's analysis (ref. 7) (see figure 6.4(a)). Figure 6.5 illustrates the comparison of reflection coefficients for a 6.2 cm diameter conical nozzle termination at $M_J = 0$ and at $M_J = 0.6$. The agreement between the reflection coefficient results derived by different methods for the duct as well as for the nozzle is excellent.

(2) Far-Field Sound Pressure Levels

Comparison of far-field sound pressure level spectra, normalized with respect to the incident sound pressure levels, at polar angles of 30 degrees, 60 degrees, and 120 degrees are presented in figures 6.6 and 6.7. Figure 6.6 illustrates the results for the 10 cm diameter straight duct at $M_J = 0$ (see figure 6.6(a)) and at $M_J = 0.2$ (see figure 6.6(b)), whereas, similar results for the 6.2 cm diameter conical nozzle attached to the 10 cm diameter flow duct at $M_J = 0$ and at $M_J = 0.6$ are shown in figure 6.7(a) and 6.7(b), respectively. The agreement between the results derived by the two methods is very good.

(3) Power Imbalance Results

Previous experimental studies at Lockheed-Georgia (refs. 2 through 6) have produced many interesting results. One of these is the transmission loss in acoustic power at low frequencies at all flow conditions including the no flow condition. Therefore, in the process of validating the acoustic impulse technique, it is worthwhile to compare the power imbalance (power loss) results obtained by the acoustic impulse tests with those derived by the impedance tube method to confirm the existence of the low-frequency power loss. Figure 6.8 illustrates the comparison of the power imbalance results derived for the 10 cm diameter duct at $M_J = 0.0$ and at $M_J = 0.2$. The comparison between the results shows very good agreement.

6.7 COMPARISON OF EXPERIMENTAL RESULTS FOR ANNULAR DUCT

The reflection coefficient spectra for a 2.5 cm thick polyurethane foam sample and for a rigid termination (a polished steel plate) were derived using the refined impulse technique in the annular duct. In these tests, as described in section 5, the induct measurements were taken at various radial and azimuthal positions and the modal decomposition scheme was used to derive the reflection coefficients. In addition, a standard B&K impedance tube (with single round tube) was

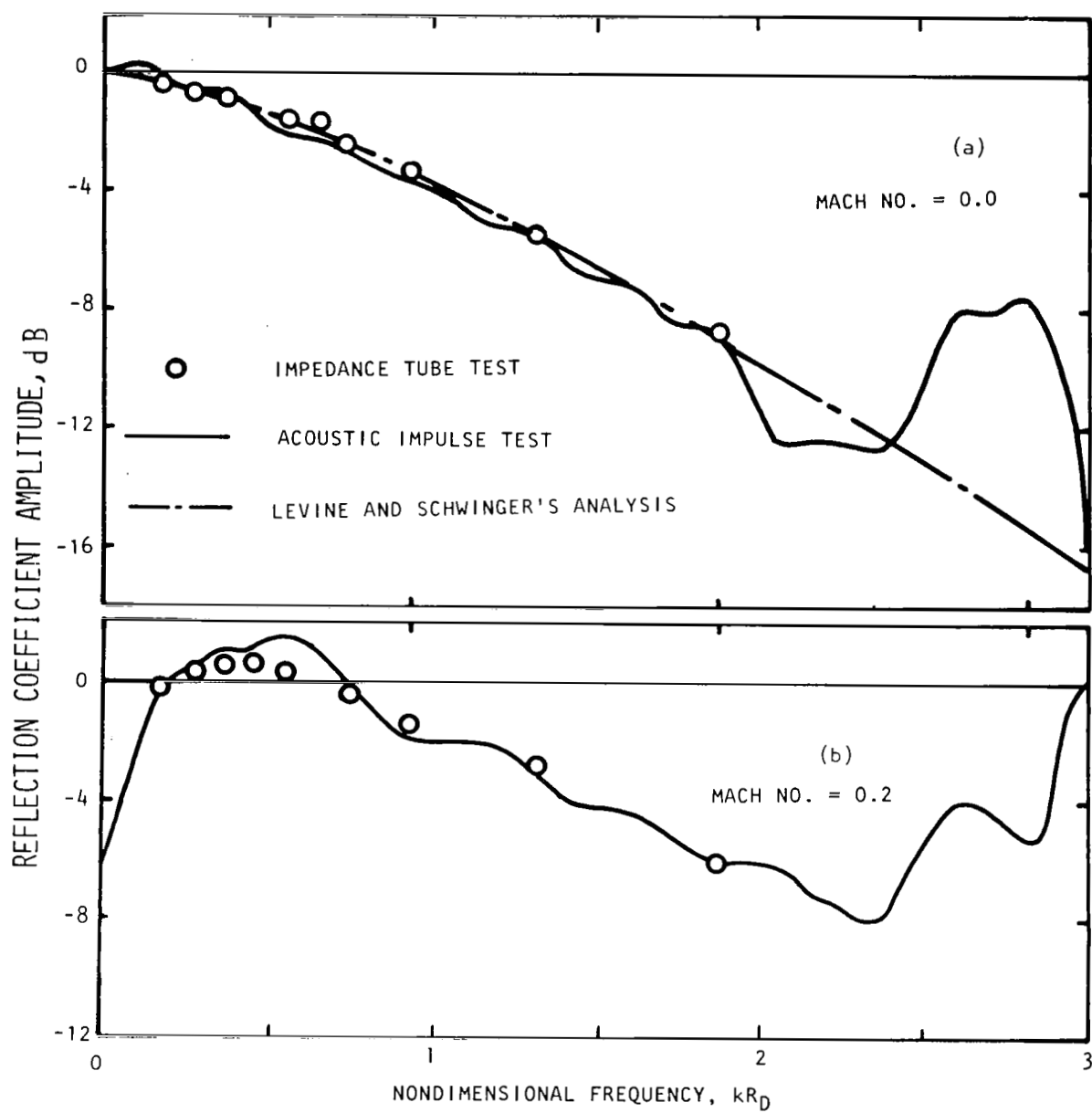


Figure 6.4 Reflection coefficient amplitude comparisons between the impulse method and other methods for a 10 cm diameter unflanged duct, (a) $M_J = 0$ and (b) $M_J = 0.2$.

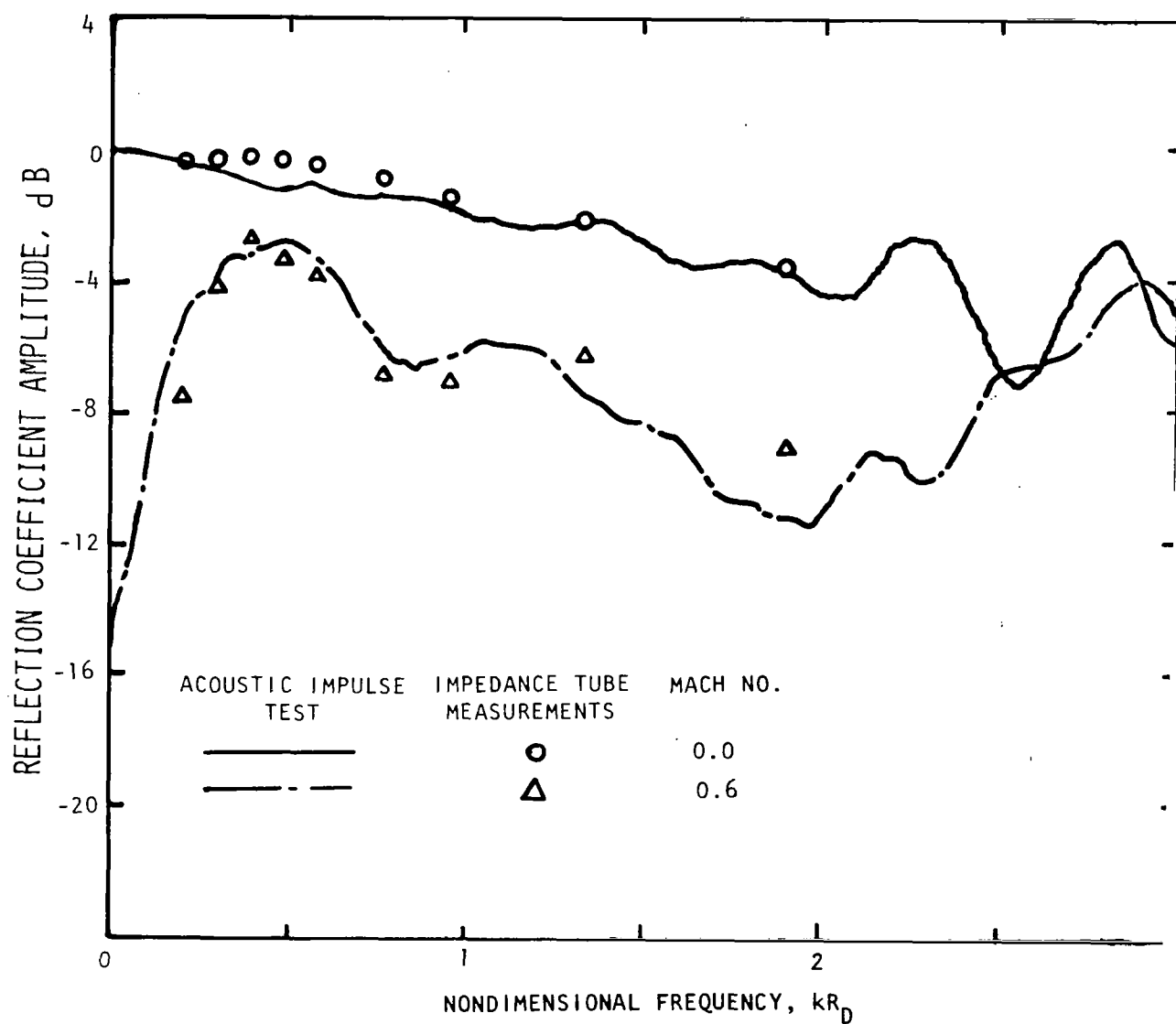


Figure 6.5 Reflection coefficient amplitude comparisons between the impulse method and the impedance tube technique for a 6.2 cm diameter conical nozzle at various flow Mach numbers.

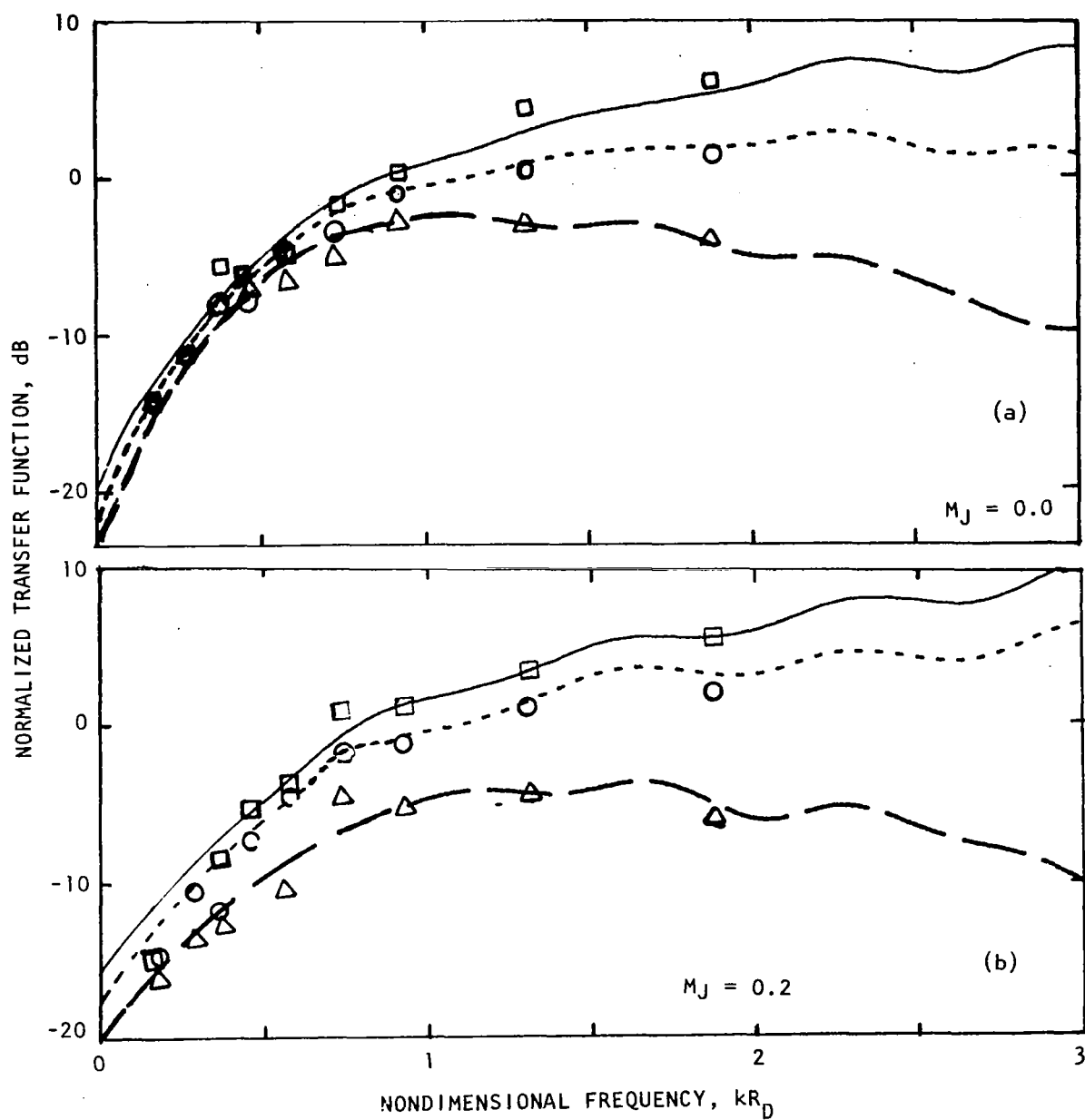


Figure 6.6 Normalized far field sound pressure level spectrum comparisons between the acoustic impulse technique and the impedance tube method for a 10 cm diameter duct at various polar angles, θ_T ; (a) $M_J = 0.0$; (b) $M_J = 0.2$.

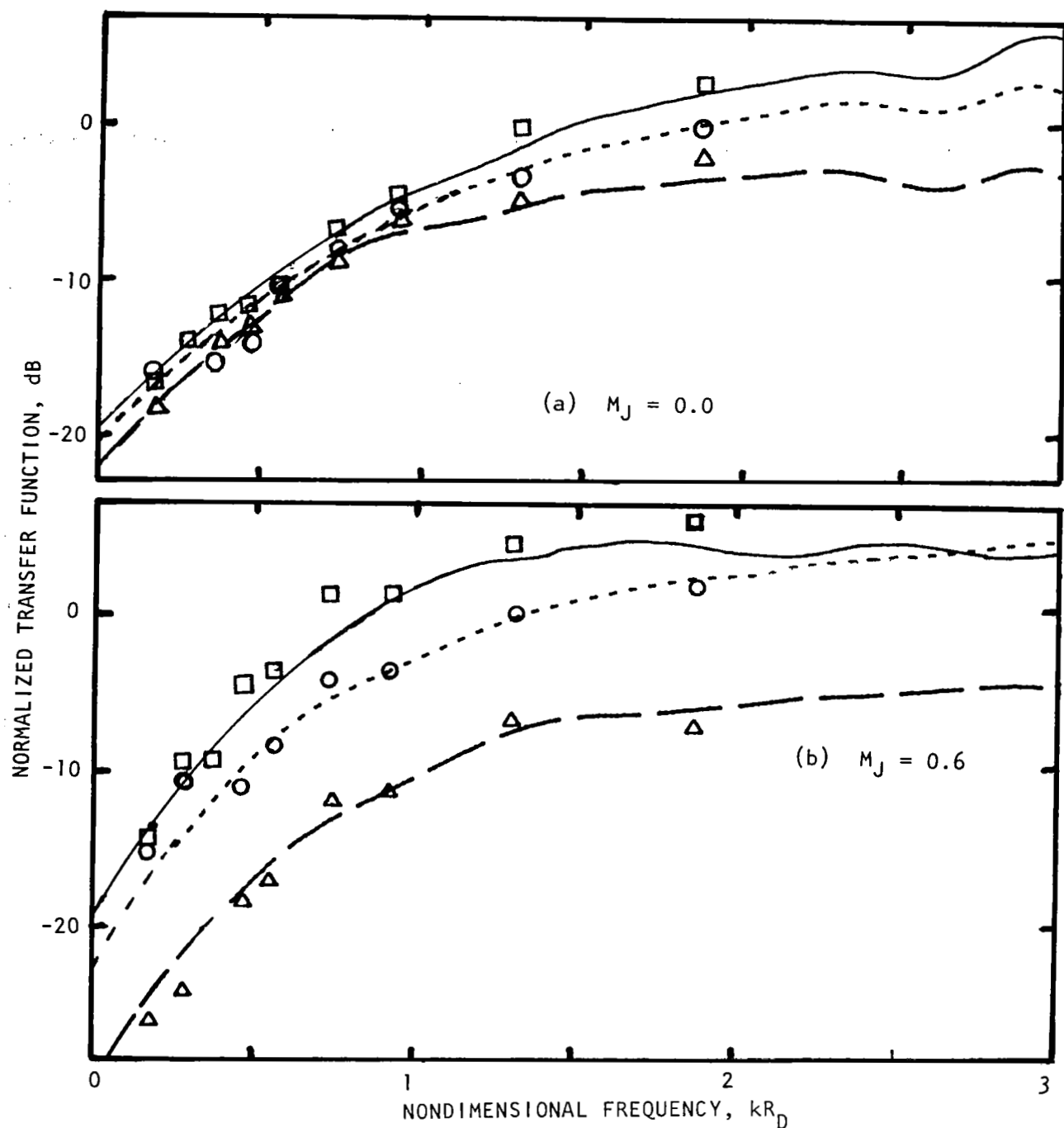


Figure 6.7 Normalized far field sound pressure level spectrum comparisons between the acoustic impulse technique and the impedance tube method for a 6.2 cm diameter conical nozzle at various polar angles, θ_T ; (a) $M_J = 0.0$; (b) $M_J = 0.6$.

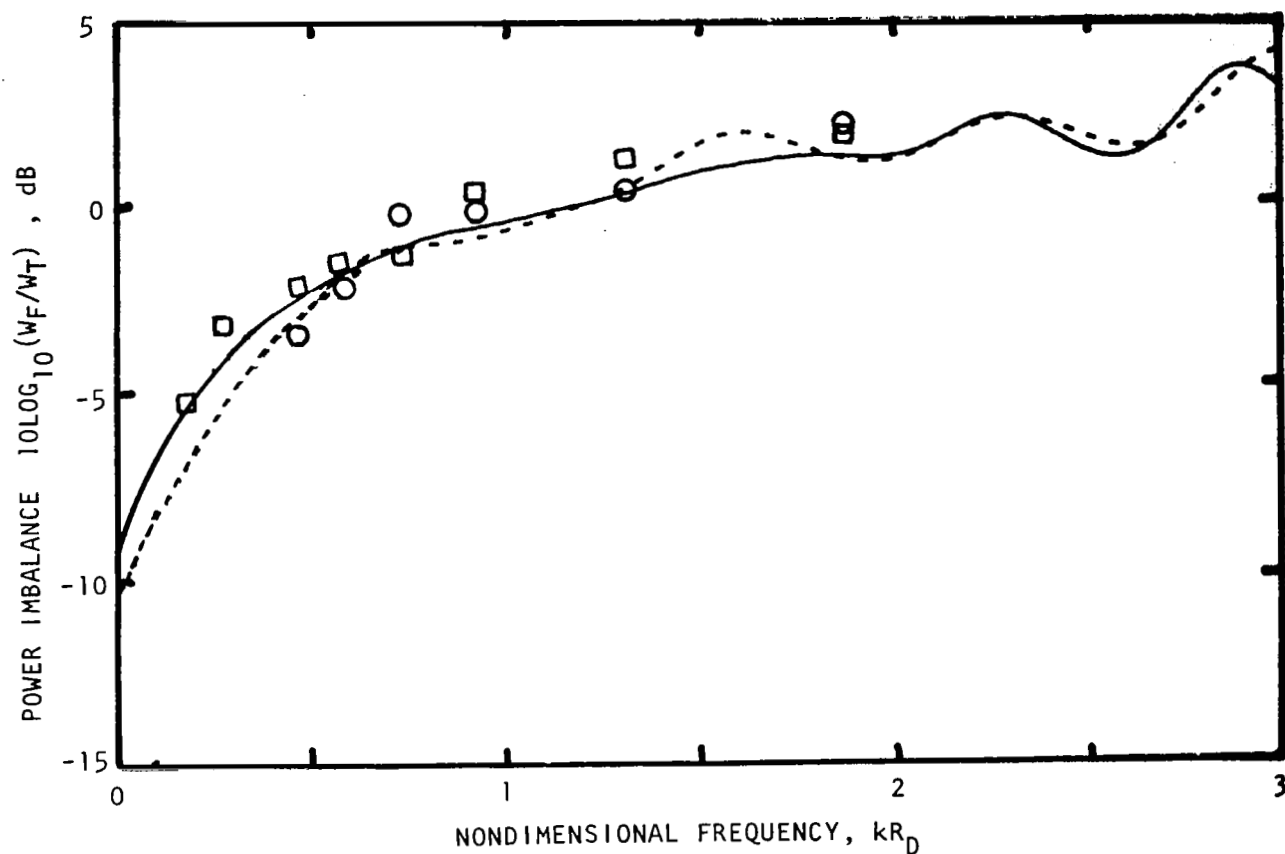


Figure 6.8 Far field power normalized with respect to transmitted power determined by acoustic impulse technique compared with similar results derived by the impedance tube method for a 10 cm diameter duct at different flow conditions.

used to measure the reflection coefficients for the above-mentioned samples. The results thus obtained are compared with those derived using the impulse technique in figure 6.9. The impulse technique results are derived by accounting for the contributions of higher order modes. In addition, the area-weighted reflection coefficients are also derived using all the induct measurements.

Comparison of the reflection coefficient spectra presented in figure 6.9(a) shows a good agreement except at lower frequencies (below 600 Hz) where a small amount of discrepancy (a maximum of 1.6 dB) is observed. A possible reason for this could be the nonuniform annulus height in the axial direction due to the fabrication inaccuracy in the annular setup. The nonuniformity was caused due to the sagging of the inner tube supported at a few axial locations. Therefore, a portion of the reflected wave might have reflected away from the distorted (bulging) surface of the inner tube. This phenomenon could easily lower the reflection coefficient level. The area-weighted levels are higher compared to the modal values at higher frequencies. This is to be expected since the area-weighted values were estimated on the basis of fundamental mode assumption whereas the actual pressure field contained other higher order modes.

Figure 6.9(b) shows the comparison of reflection coefficient spectra for a rigid termination. Again the small deviation of the impulse results from the impedance tube measurements (or from the zero dB level) is attributed to the same reason, namely the slight variations in annulus height with axial distance. In this case, however, the deviation is relatively more since the measurement becomes very sensitive when the reflection coefficients approach unity (i.e. zero dB).

6.8 CONCLUSION

The refined acoustic impulse method has been successfully validated by comparison with data obtained from other methods for single and dual stream duct nozzle systems, with and without mean flow.

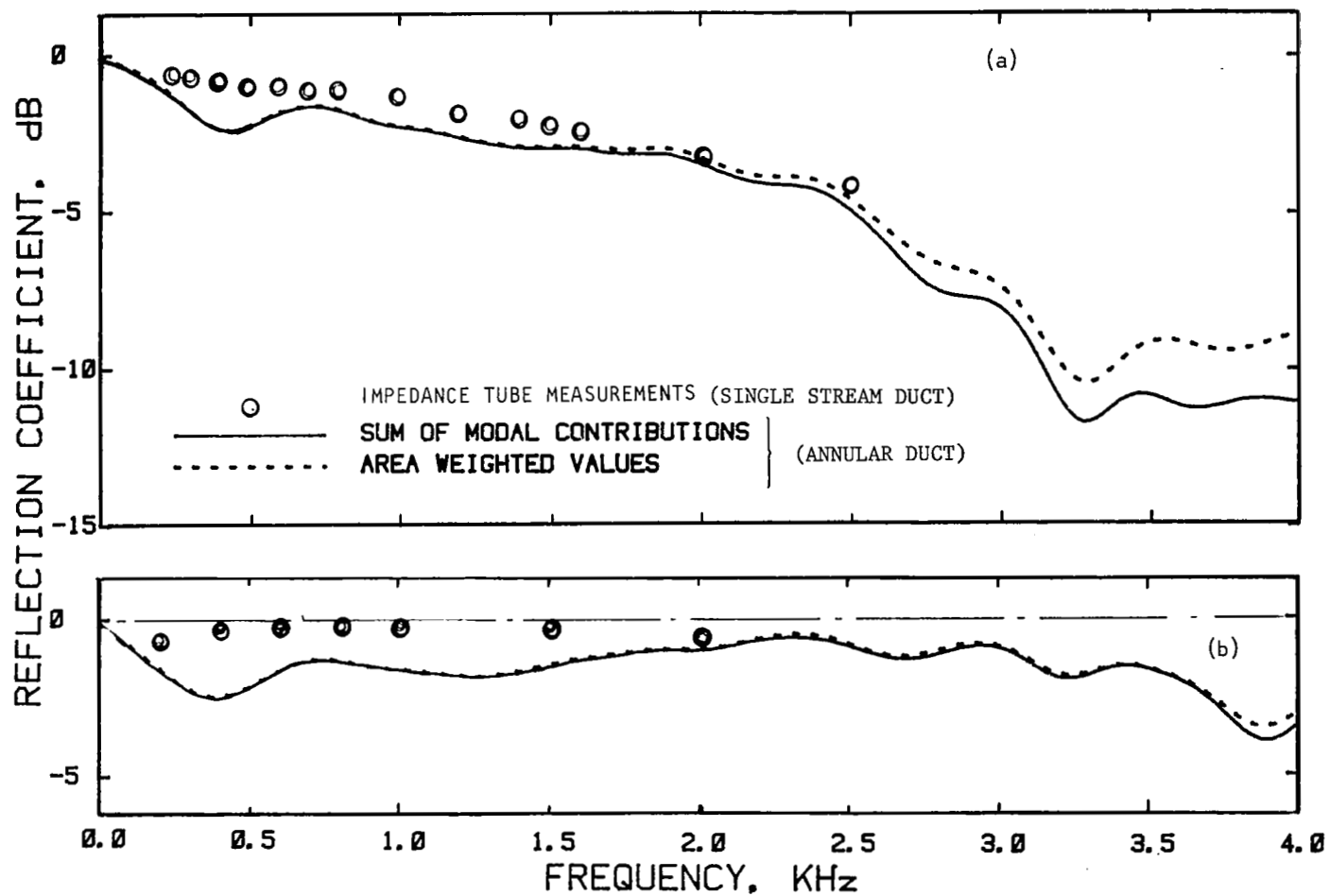


Figure 6.9 Reflection coefficient amplitude comparison between the impulse method and the impedance tube technique for (a) an absorbing material and (b) a rigid termination.

7.0 ACOUSTIC ENERGY LOSS MECHANISM

The comparison between the far-field power and the transmitted power, for a 10 cm diameter straight duct and a 6.2 cm diameter conical nozzle, as determined by using the improved acoustic impulse technique and presented in section 6, has indicated a loss in acoustic power, even for the no-flow condition. Therefore, the acoustic power loss mechanisms were investigated first by visual means, and the results are presented in section 7.1. Also, the amount of acoustic power loss has been quantitatively evaluated and these results are presented in section 7.2. In this case, using a theoretical model developed recently at Lockheed by Cummings and Eversman (refs. 33 and 34), the predicted power loss is compared with the corresponding measured power loss.

In the past few years, there has been a growth of interest in acoustic energy effects associated with the interaction between sound fields and free shear layers. In particular, the net acoustic energy absorption which is observed to occur when an acoustic wave is transmitted out through an air jet issuing from a pipe has been studied by several workers. Bechert's experimental and theoretical results (ref. 35) and Howe's theoretical analyses (refs. 36 and 37), for example, offer persuasive evidence that the absorption mechanism is the conversion of acoustic energy into vortical energy at a sharp edge, and the subsequent dissipation of this into heat, without further substantial interaction with the acoustic field.

It has also been noted that, in the absence of mean flow, energy can be dissipated by the same mechanism if the acoustic velocity is high enough to cause flow separation, and recent work at Lockheed-Georgia has shown this effect well in a comprehensive study of noise transmission through duct terminations (refs. 2,4,5,6,33,34, and 38).

In the present investigation the anticipated dissipative mechanism as the cause of energy loss is studied systematically by visual means as well as by quantitative estimation of energy loss.

7.1 FLOW VISUALIZATION

The mechanism of acoustic power loss, as anticipated, is due to the conversion of acoustic energy into vortical energy. Therefore, the first step to confirm this concept was to conduct some flow visualization experiments. In these experiments, the objective was to visualize the vortex formation as the acoustic pulse was transmitted out of the duct termination with and without mean flow. Smoke was used as the medium for the flow visualization technique in this study.

Flow visualization tests to study the implication of internal noise

on jets have been carried out by other researchers (refs. 39 and 40). In reference 39, Heavens studied the response of a subsonic round jet to internal excitation by an acoustic wave using flow visualization and noise measurements. The jet was subjected to pulse excitation and to harmonic excitation. In both cases large-scale vortex ring structures were observed in the jet mixing layer. With pulse excitation, interactions between the vortex rings were observed. However, he did not study any situation in the absence of flow. Some flow visualization studies in the absence of mean flow were carried out by Whiffen and Ahuja (ref. 40) using harmonic signal. They found a well defined vortex generated at the nozzle exit even in the absence of mean flow by harmonic sound generated upstream of the nozzle exit. However, in the present work, spark discharge pulses were used with varying intensities to study the above mentioned phenomenon in a systematic manner.

7.1.1 Test Set-up and Experimental Procedure

The flow visualization technique used for the present study consisted of a smoke generating mechanism synchronized with the acoustic pulse in such a way that a photograph of the smoke medium oriented according to the acoustic field due to the propagation of the transient pulse, just outside the duct nozzle termination, can be taken.

In this technique, a steel wire was placed diametrically at the duct/nozzle exit plane (see figures 7.1 and 7.2). Provision was made such that a stream of oil was flowing over this wire from one end to the other. The wire was electrically heated just before the escape of the acoustic pulse from the duct. Therefore, at the instant when the pulse was transmitted out, the wire would generate a smoke medium outside the termination due to the heating of the oil flowing over it. Using a synchronized light source for a short duration and a camera with the shutter open, a photograph of the smoke medium outside the termination, oriented according to the acoustic field, was taken. This photograph would indicate if a vortex was formed due to the transmission of the acoustic pulse.

The existing free-jet facility was used for the tests with mean flow. In this situation the sound source was located about 6 meters upstream of the termination. Since the flow duct in this facility was horizontal, the smoke generated in the absence of mean flow tended to rise upwards due to its lower intensity compared to air. This effect is shown in figure 7.3 where the vortex ring looks distorted due to the buoyancy force which arises due to the difference in densities between air and smoke. Therefore, another setup was built specially for the tests at zero flow. In this case the flow duct was kept vertical. The source was located about 2 meters upstream of the termination. The opposite end of the duct was terminated into a foam pad at about 1 meter from the source.

Two types of impulsive sources, one being a spark discharge source

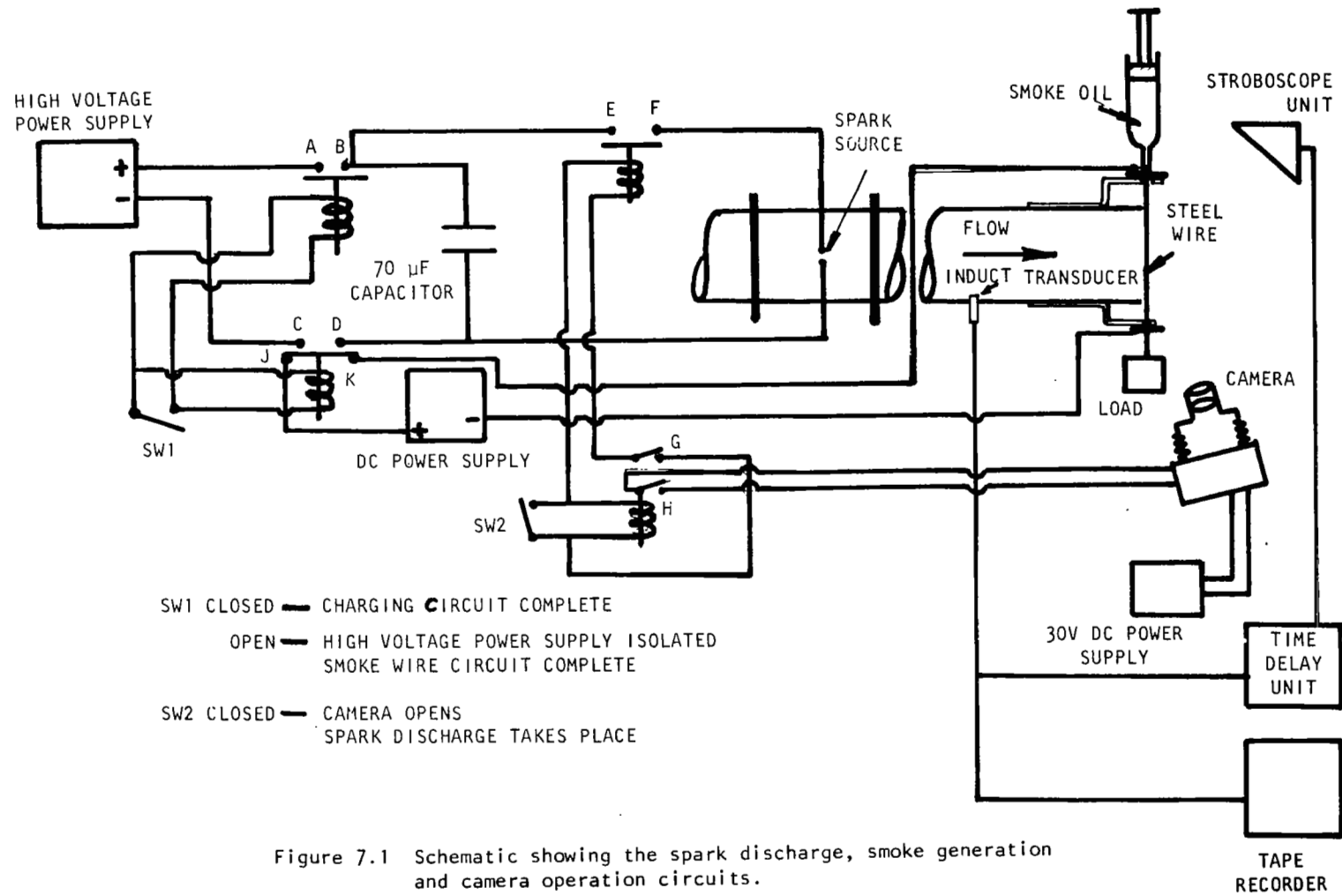


Figure 7.1 Schematic showing the spark discharge, smoke generation and camera operation circuits.

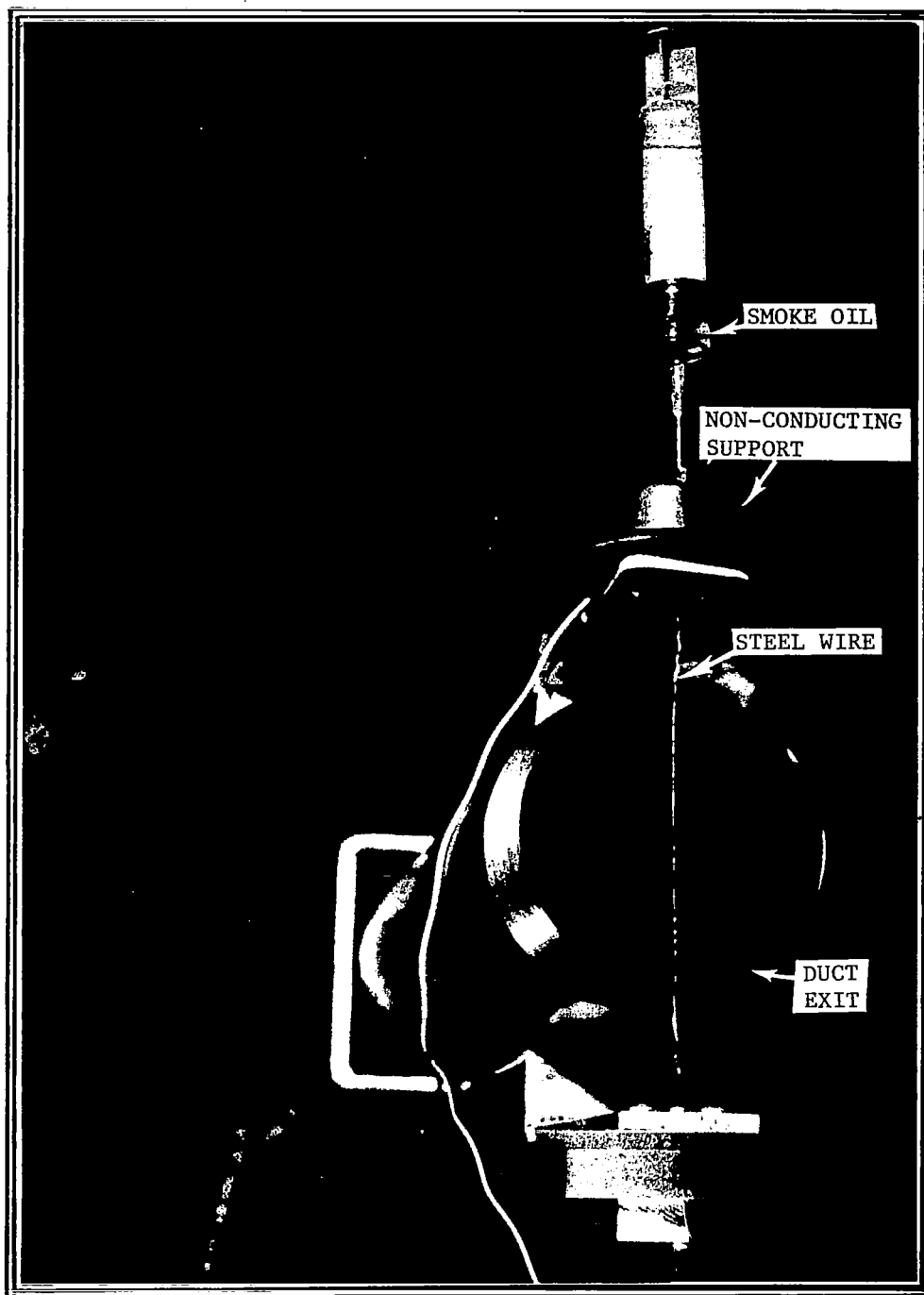


Figure 7.2 Photograph showing the smoke generating wire placed at the exit plane of a 10 cm diameter duct and the oil supply syringe attached to it.



Figure 7.3 Deformation of vortex ring, due to the lower buoyancy of the smoke, for a 10 cm diameter duct horizontal to the ground, $M_j = 0.0$.

and the other being an acoustic driver, were used for this study. The circuit diagram for the operation of spark discharge, smoke generation, and camera operation is shown in figure 7.1. When Switch 1 (SW1) was closed the charging circuit for the capacitor across the spark gap was complete. Once the charging was done, Switch 1 (SW1) was opened, which isolated the high voltage power supply from the circuit and completed the smoke generation circuit. When Switch 2 (SW2) was closed, the camera was opened and the spark discharge took place. The pulse, generated by the spark discharge, was recorded by an induct transducer, located about 1 meter upstream of the termination. This signal was used to trigger the stroboscopic light with appropriate time delay.

The same circuit was employed when an acoustic driver was used to generate the pulse. In this case the high-voltage power supply was not operated and the spark gap in the source section was replaced by an acoustic driver. The driver was fed with a repetitive input signal to generate a periodic chain of pulses. The Switch 1 (SW1) was opened, in this case, after the driver was switched on. The remaining operations were identical to the case when a spark discharge source was used.

Figure 7.2 is a photograph showing the smoke generating wire placed at the exit plane of a 10 cm diameter straight duct and an oil supply syringe attached to it. Figure 7.4 shows the orientation of the smoke generating wire for various terminations. Figure 7.5 is a photograph of the complete flow visualization instrumentation.

The transient pulse, generated by the spark discharge, was also measured by a pressure transducer inside the duct. The Fourier transform of the incident pulse was used to compute the pulse intensity.

7.1.2 Experimental Results

Tests were conducted using a straight duct with 10 cm diameter, two conical nozzles (one with 6.2 cm exit diameter and the other with 2.5 cm exit diameter), and a 12-lobe, 24-tube suppressor nozzle with an equivalent exit diameter of 6.2 cm. These tests were conducted to investigate the effects of pulse intensity, nozzle geometry, and flow velocity on the vortex ring formed at the termination due to the propagation of acoustic pulse.

(1) Flow Visualization Results in the Absence of Mean Flow

Flow visualization tests in the absence of mean flow were carried out using the vertical setup. To demonstrate the effect of pulse intensity on the vortex formation, two terminations, a 10 cm diameter straight duct and a 2.5 cm diameter conical nozzle attached to the 10 cm diameter flow duct, were chosen. Acoustic pulses of different intensities generated by spark discharge were used in this study. Figure 7.6 shows the effect of pulse intensity on the vortex formation at the exit plane of the straight duct and the conical nozzle. These

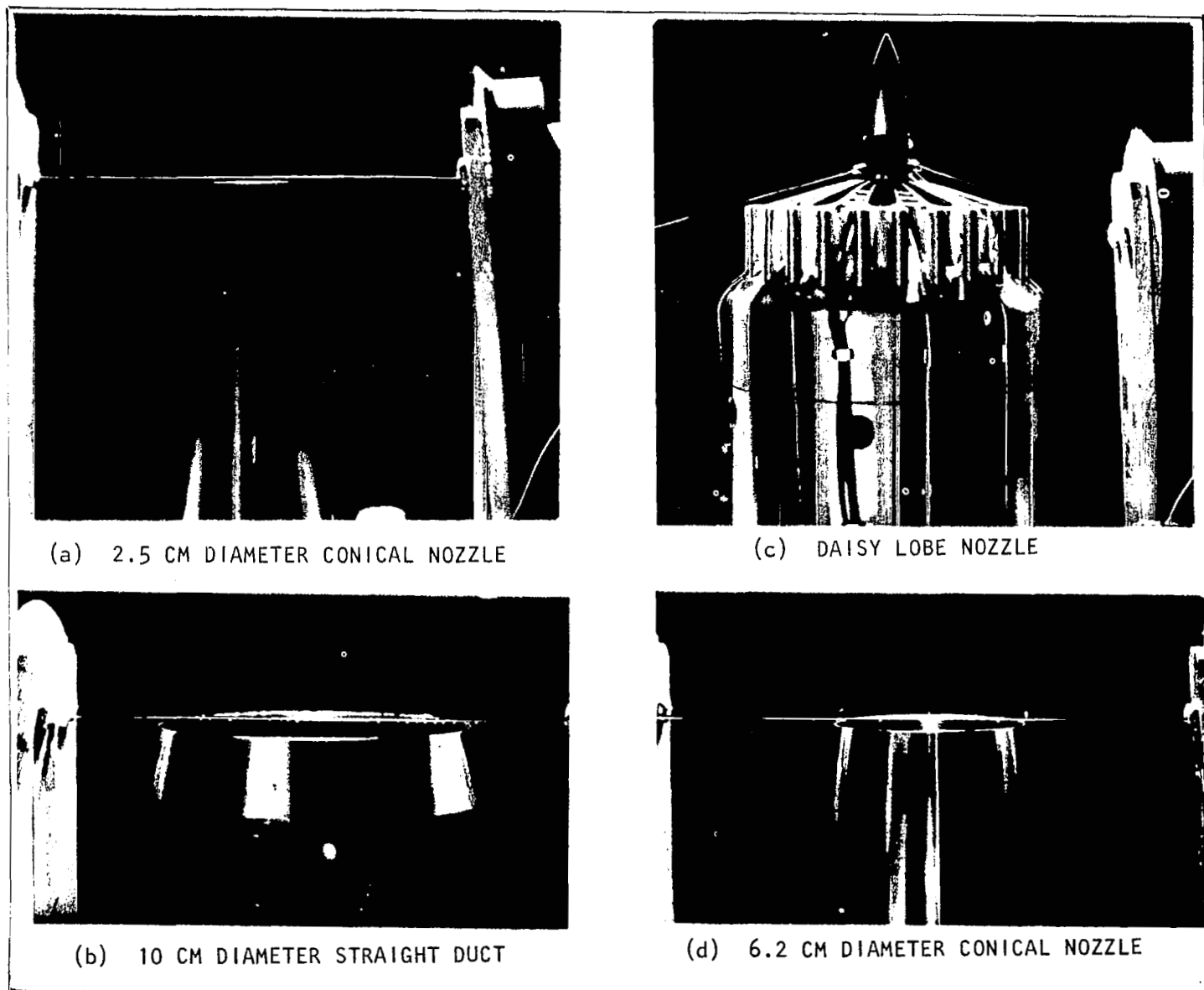


Figure 7.4 Orientation of smoke wire at the exit plane of various nozzle terminations.

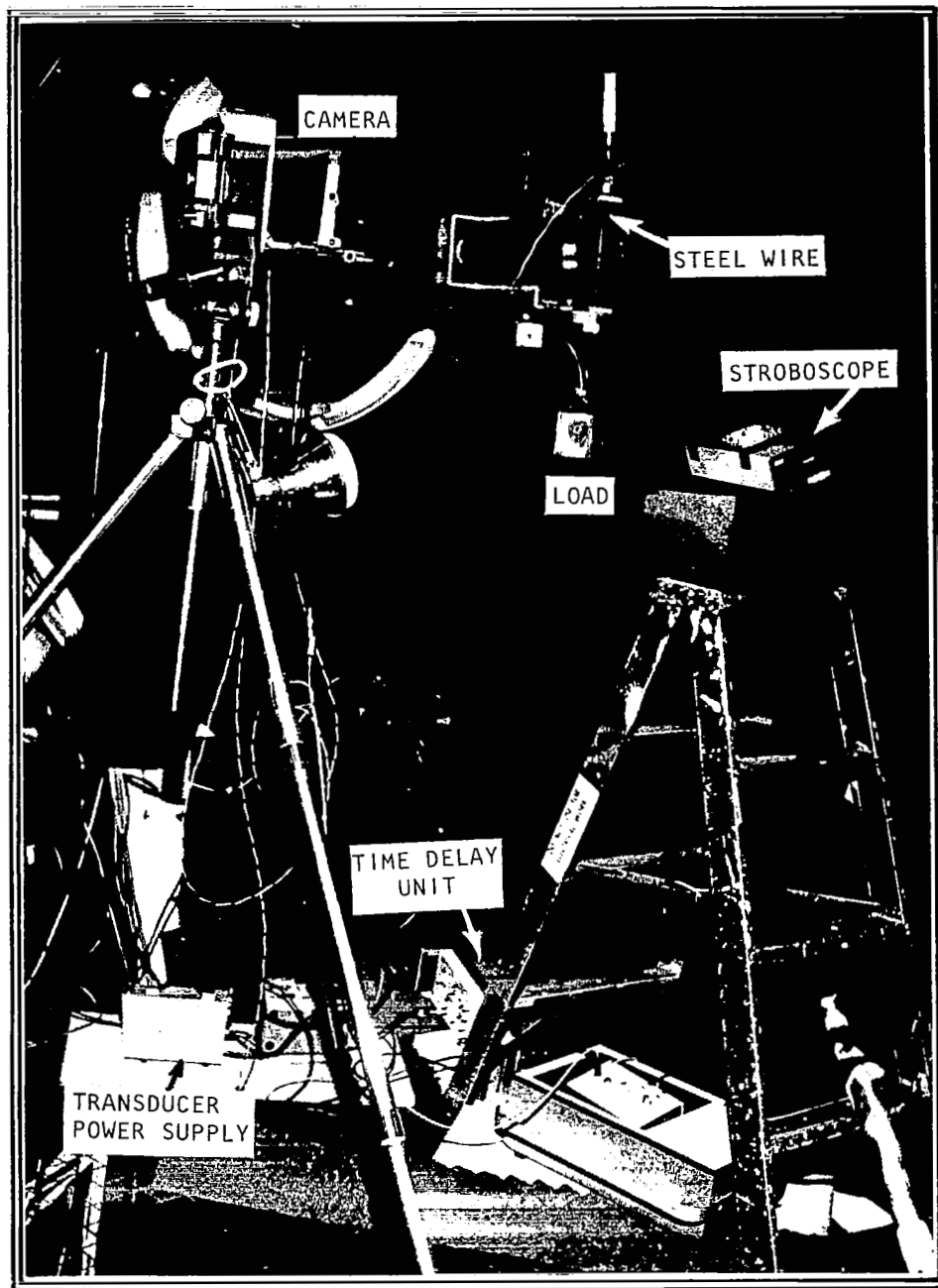


Figure 7.5 Photograph showing the flow visualization instrumentation.

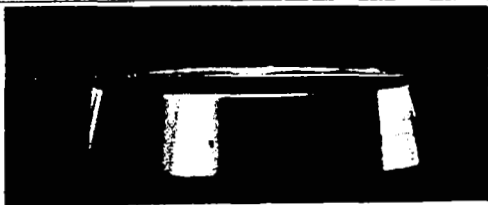

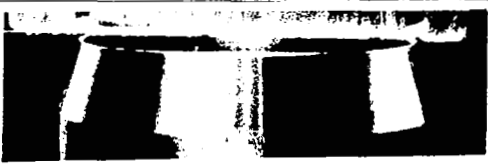






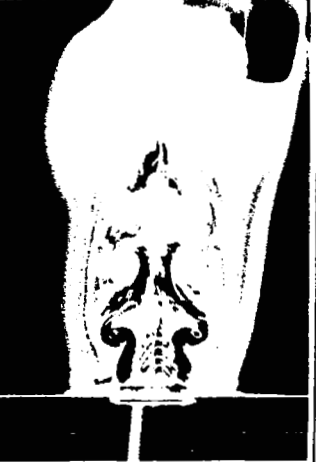
INTENSITY (dB)	(a) Duct	(b) Nozzle
NO PULSE		
137		
142		
149		
153		

Figure 7.6 Effect of pulse intensity on the vortex formation at the exit plane of (a) a 10 cm diameter duct and (b) a 2.5 cm diameter conical nozzle photographed 20 ms after the pulse propagated out of the exit plane, $M_j = 0.0$.

photographs were taken 20 ms after the pulse propagated out of the termination exit. Results in the absence of the acoustic pulse are also included in this figure for comparison. It can be clearly observed that the presence of an acoustic pulse is the cause of the formation of the vortex ring. With increasing intensity, one can see a more dominant vortex; also, the vortex moves away from the termination exit plane as the pulse intensity increases. Therefore, it can be concluded that a higher intensity pulse generates a stronger vortex ring and the propagation speed of that ring is relatively higher due to its higher particle velocity.

The induct pulse time histories (the incident pulse and the corresponding reflected pulse from the termination) corresponding to the various pulse intensities are plotted in figure 7.7. The incident pulse at a given intensity for both the configurations look identical. However, the reflected pulses are quite different due to the difference in termination geometry. At this stage one might expect that, since the incident pulses for both the terminations are identical (at a fixed intensity), the corresponding intensity (shape & size) of the vortices formed at the termination would be identical. However, this is not the case. The incident pulses shown in figure 7.7 were measured in the 10 cm diameter flow duct for both the terminations. For the straight duct, the incident pulse would propagate as it was, whereas for the conical nozzle, the intensity of the propagating incident pulse would increase due to the reduction in cross-sectional area, and would be sufficiently different at the exit compared to that for the straight duct termination. The formation of the vortex is basically controlled by this pulse at its final stage. Therefore, the vortex for the nozzle would be stronger compared to that of the straight duct. In fact, this can be seen in figure 7.6 where the vortex ring for the nozzle is stronger and moves faster compared to the corresponding vortex ring for the duct.

The optical results for the no flow condition indicate multiple vortex formation. The weaker vortices following the initial vortex ring, in this case, were due to the reflections of the main pulse from the opposite termination.

Figure 7.8 shows the formation of vortex rings due to acoustic pulses of various intensity for two nozzles of same exit open area, one being a conical nozzle and the other being a suppressor nozzle. The effect of intensity is quite similar to that observed in figure 7.6. However, the vortex ring for the suppressor nozzle is not similar to that for the conical nozzle, in spite of the fact that both the nozzles have the same exit open area. The vortex structures for the suppressor nozzle, as observed in figure 7.8, are dictated by the detailed nozzle geometry.

The effect of the nozzle geometry can also be seen from the corresponding time history plots in figure 7.9, where the reflected

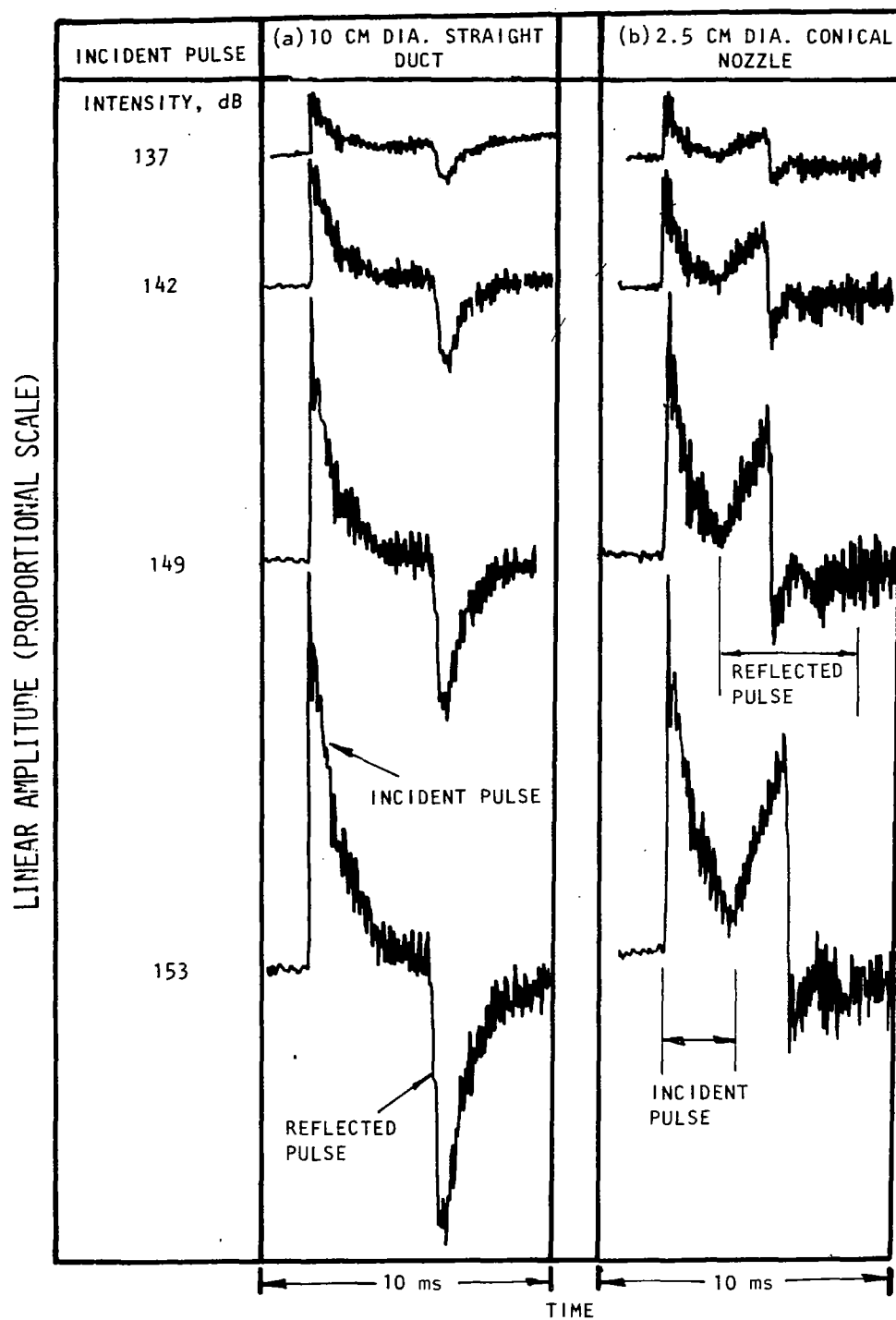


Figure 7.7 Induct time histories for (a) a 10 cm diameter straight duct and (b) a 2.5 cm diameter conical nozzle terminations at various incident pulse intensities, $M_j = 0.0$.

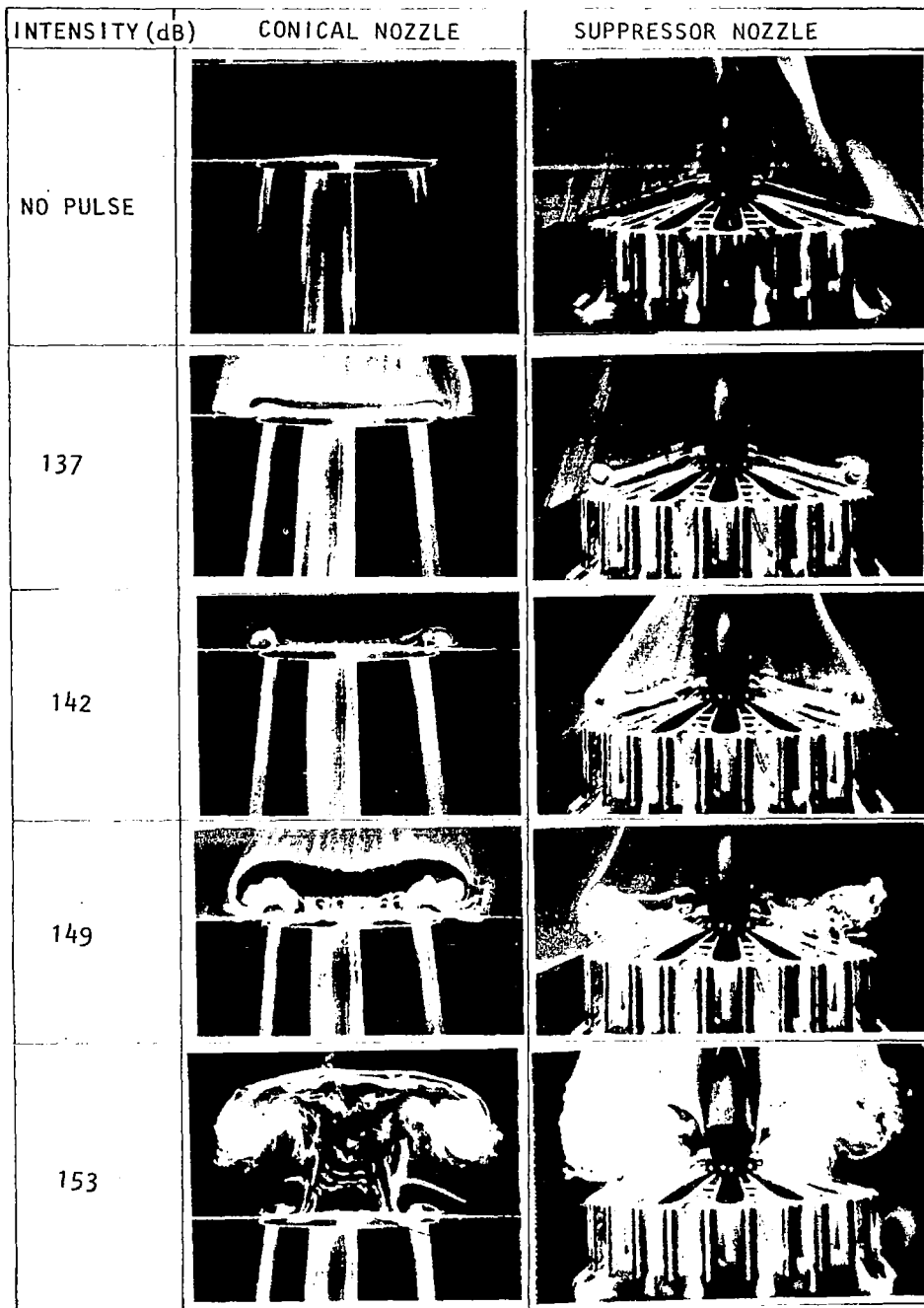


Figure 7.8 Effect of nozzle geometry (with same equivalent open area) on the vortex formation at the nozzle exits at various pulse intensities photographed 20 ms after the pulse propagated out of the exit plane, $M_J = 0.0$.

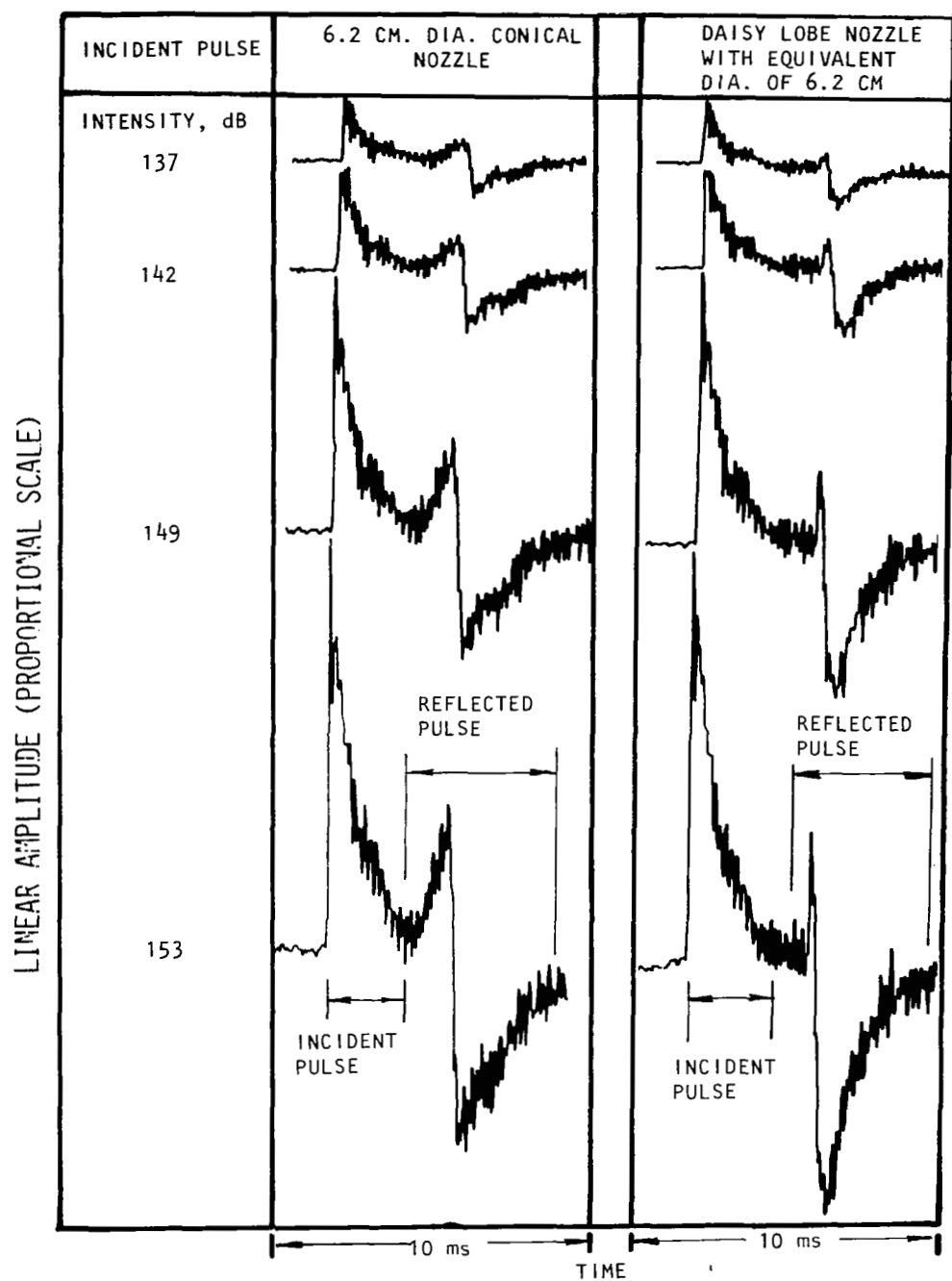


Figure 7.9 Induct time histories for (a) 6.2 cm diameter conical nozzle and (b) the daisy lobe nozzle with equivalent diameter of 6.2 cm terminations at various incident pulse intensities, $M_j = 0.0$.

pulses for the daisy lobe nozzle are quite different from those for the conical nozzle. The daisy lobe nozzle reflections indicate more blockage compared to the conical nozzle.

The fact that the vortex structures for the suppressor nozzle are dictated by its geometry is further demonstrated in figure 7.10, where the vortex structure photographed at the diametrical plane (the smoke wire passing over the center of two lobes) is compared with a similar photograph at off-diametrical plane (the smoke wire off-centered and passing over two tubes and portions of the lobes). In this figure, again the vortex structures are quite different in the two planes of the nozzle.

The flow fields, at the exit planes of various nozzle terminations, created by low-intensity acoustic pulses generated by an acoustic driver are shown in figure 7.11. The vortices formed in this case are very weak. The strength of these vortices, however, increases with decreasing area of the nozzle.

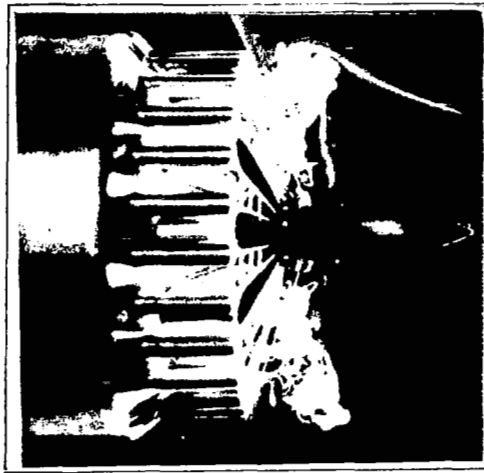
Figure 7.12 shows the propagation of the vortex rings for a fixed pulse intensity. In the absence of flow, the propagation speed of the vortex is the same as the particle velocity. The figure shows that, during a given time interval, the vortex ring shed from the conical nozzle propagated much faster compared to that shed from the straight duct termination. Figure 7.13 shows the propagation of vortex rings for the 6.2 cm diameter conical nozzle compared to that for the suppressor nozzle. Even though the vortex structures are different for the two nozzles, the propagation speed seems to be the same at a given intensity. Therefore, the size of the exit open area is the controlling factor for the vortex intensity and travel speed.

(2) Flow Visualization Results with Mean Flow

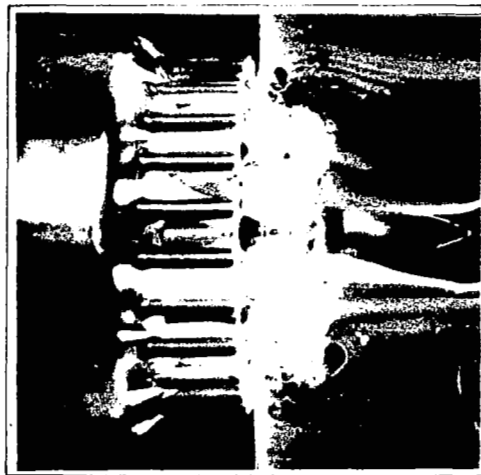
Optical results with mean flow were obtained only for very low Mach numbers, since it was difficult to generate uniform smoke at high flow velocities. Tests in the presence of mean flow were conducted using the horizontal setup.

Figure 7.14 demonstrates the effect of an acoustic pulse propagating out through a straight duct at various flow Mach numbers. The corresponding optical results in the absence of the pulse are also presented here. The propagation speed for the vortex ring, in this case, is the sum of the particle velocity of the pulse and the mean flow velocity. Therefore, the vortex ring formed in the presence of flow has propagated further downstream compared to that at no flow condition. Figure 7.15 is identical to figure 7.14, except that the results in this case are obtained for a 6.2 cm diameter conical nozzle.

The effects of pulse intensity on the formation of vortex rings in the presence of mean flow for a straight duct and a conical nozzle are



(a) Vortex structure in the plane of the exit diameter, covering two lobes.



(b) Vortex structure at an off diameter plane, covering the lobes and the tubes.

Figure 7.10 Vortex formation at various planes at the exit of a suppressor nozzle; the pulse intensity was 149 dB and the photographs were taken 20 ms after the pulse propagated out of the exit plane, $M_j = 0.0$.

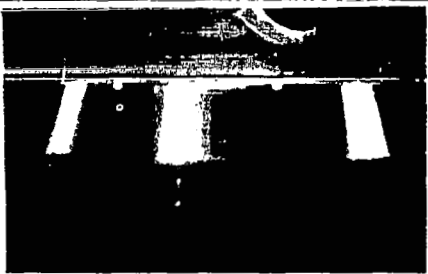

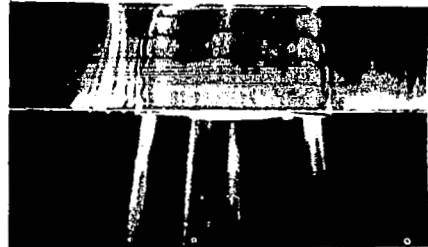
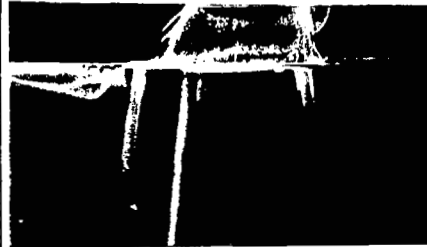
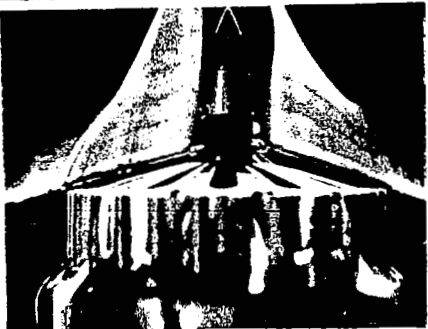

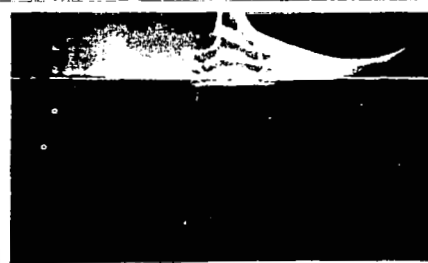

INTENSITY, dB→	120	114
10 CM DIAMETER DUCT		
6.2 CM DIAMETER CONICAL NOZZLE		
SUPPRESSOR NOZZLE WITH AN EQUIVALENT DIAMETER OF 6.2 CM		
2.5 CM DIAMETER CONICAL NOZZLE		

Figure 7.11 Acoustic field at the exits of various nozzle terminations, created by low-intensity acoustic pulses generated from an acoustic driver, $M_j = 0.0$.

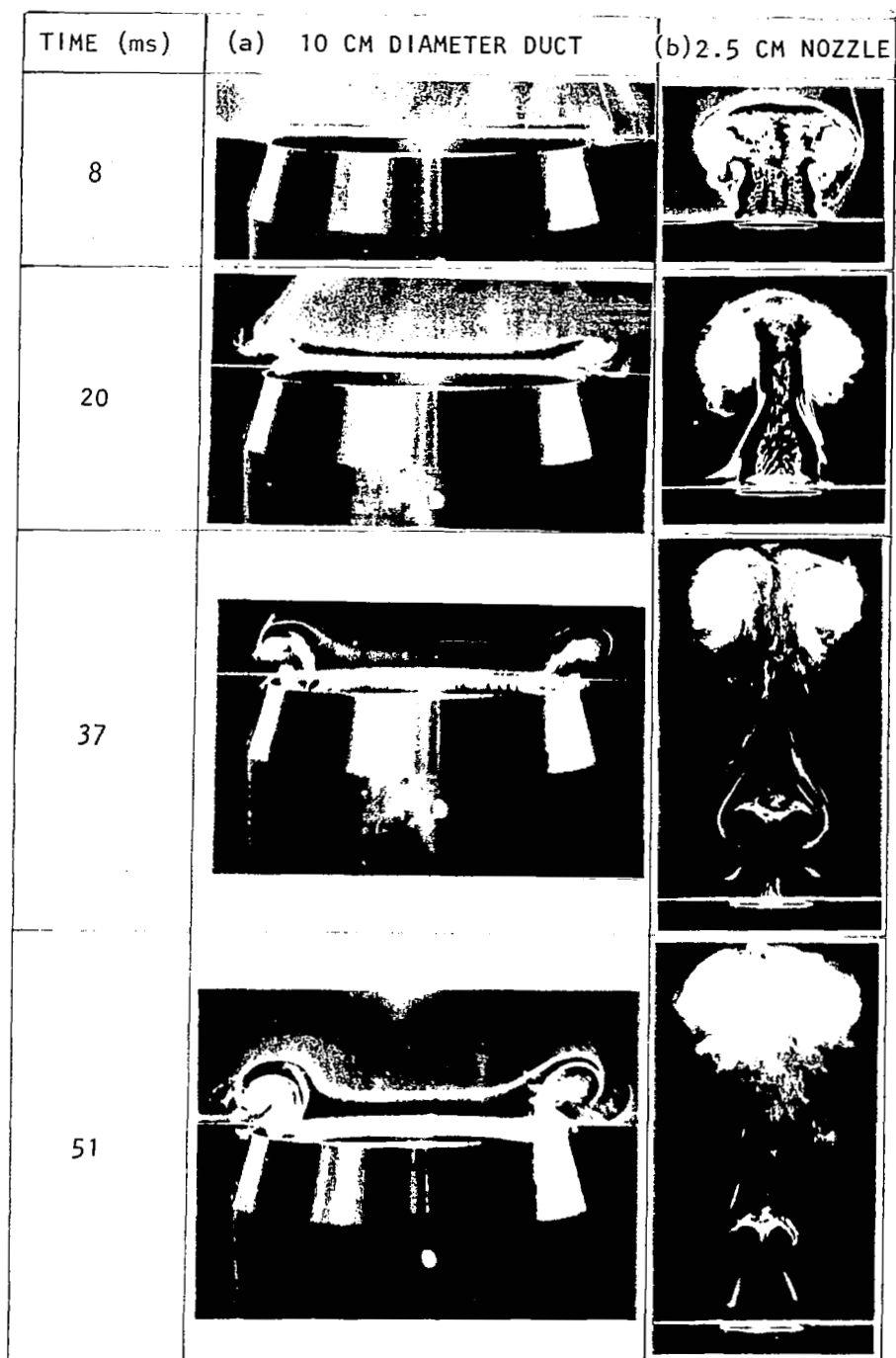


Figure 7.12 Propagation of vortex rings created by a pulse with an intensity of 149 dB for (a) a straight duct and (b) a conical nozzle, $M_J = 0.0$.

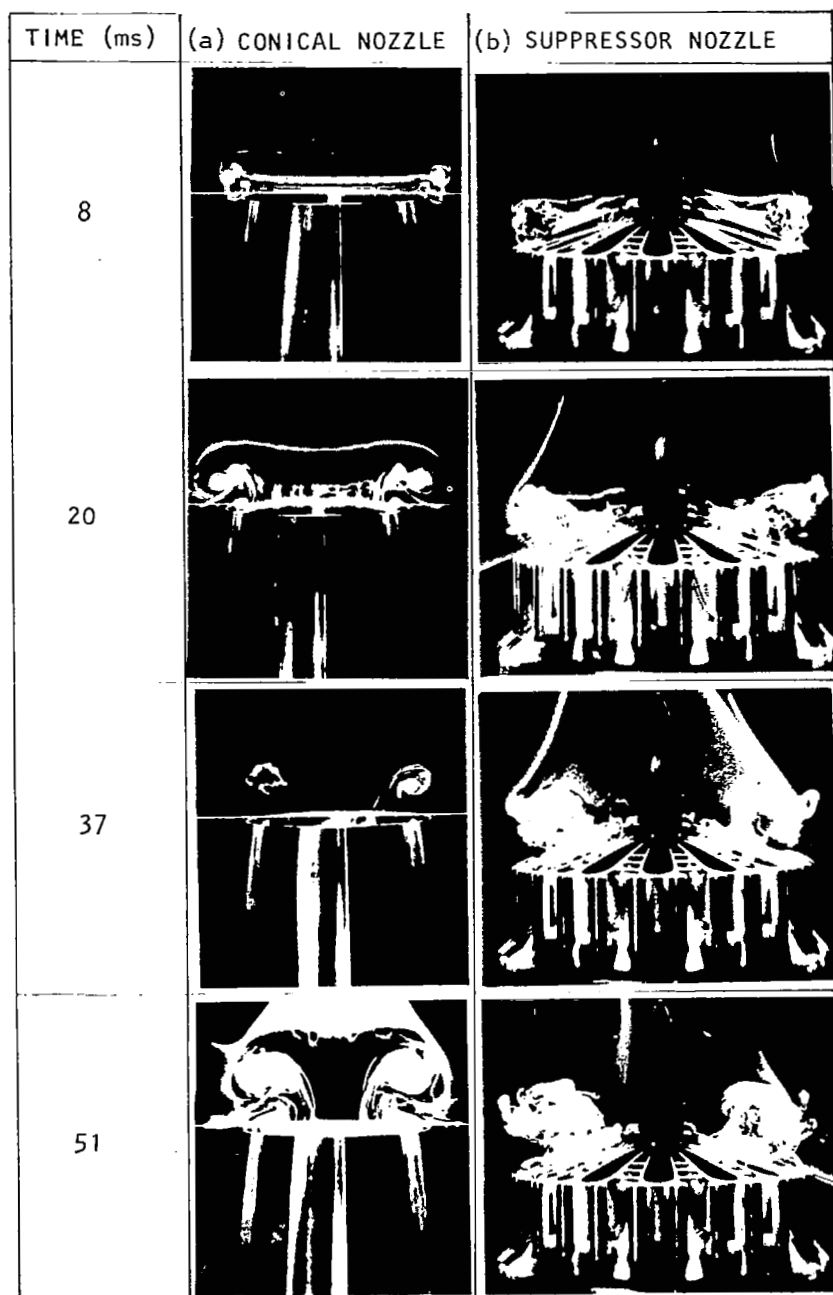


Figure 7.13 Propagation of vortex rings created by a 149 dB pulse for (a) a conical nozzle and (b) a suppressor nozzle with the same equivalent exit open area.

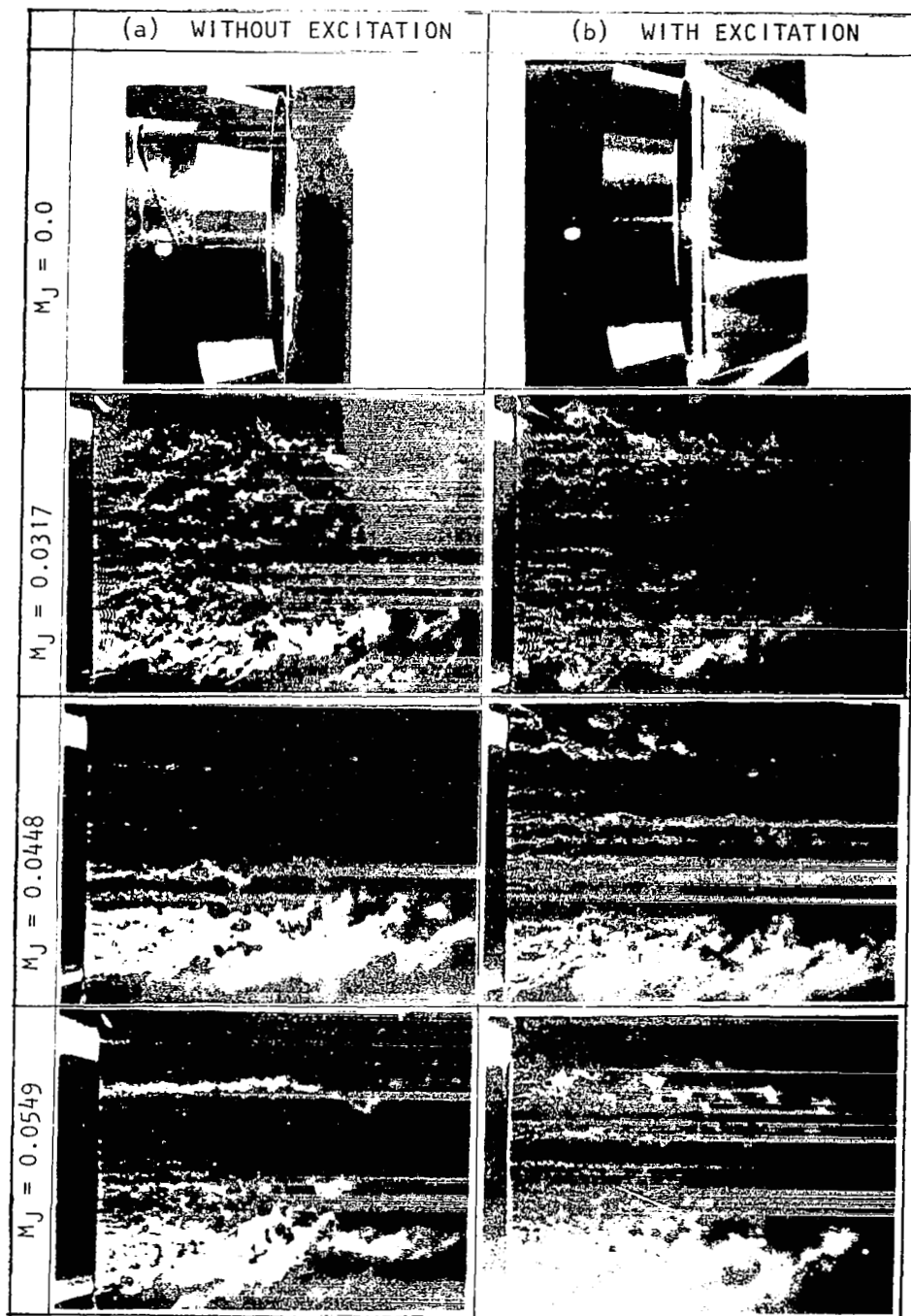


Figure 7.14 Excitation of the jet by a 149 dB pulse for a 10 cm diameter straight duct at various Mach numbers, M_J ; photographed 6 ms after the pulse propagated out of the duct exit.

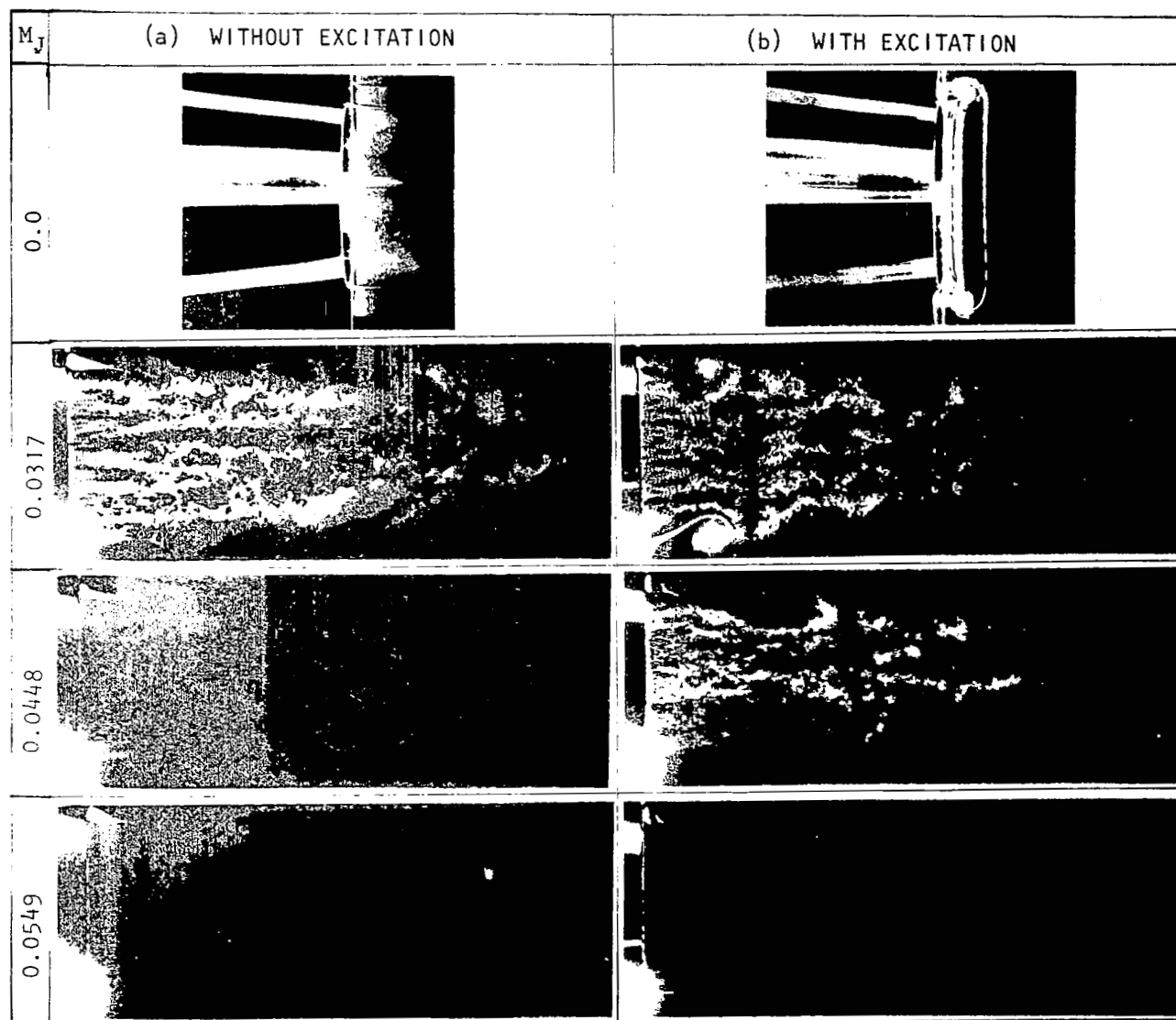


Figure 7.15 Excitation of the jet by a 149 dB pulse for a 6.2 cm diameter conical nozzle at various Mach numbers, M_J ; photographed 6 ms after the pulse propagated out of the nozzle exit; (a) without excitation, (b) with excitation.

shown in figure 7.16. As observed previously for the no flow condition, the strength of the vortex ring is higher for a pulse with higher intensity, and the vortex ring has propagated more downstream compared to a low intensity ring. However, in the presence of flow, the effect of pulse intensity is not as dominant as that seen in the absence of flow. Therefore, the nonlinear effects of the high-intensity pulses are considerably less in the presence of flow. This is because the particle velocity of the pulse is much smaller compared to the mean flow velocity. Therefore, it is expected that at higher flow conditions, the nonlinear effects of high intensity signals would be almost negligible. This effect is not shown in this section since it was not possible to generate uniform smoke at higher flow velocities using the present smoke technique. However, this is shown quantitatively in the next section.

Figure 7.17 demonstrates the effect of nozzle exit area on the formation of vortex rings in the presence of flow. In this figure, at a fixed flow condition (Mach number $M_J = 0.0317$) and with a fixed pulse intensity (i.e., 143 dB), the formation of the vortex ring for the 10 cm diameter straight duct is compared with that for the 6.2 cm diameter conical nozzle. As observed previously for the no flow condition, the strength of the vortex ring for the nozzle seems to be higher than that for the straight duct. However, the effect is not as dominant as that for the no-flow condition. The reason discussed above applies here as well.

Figure 7.18 illustrates the flow field due to a low-intensity repetitive pulse generated by an acoustic driver in the presence of mean flow. The effect seems to be insignificant for the straight duct whose open exit area is larger compared to that for the 6.2 cm diameter conical nozzle.

Figure 7.19 shows the position of the vortex ring formed due to a 143 dB pulse at various time instances, for a straight duct at $M_J = 0.0317$. As expected, the vortex ring moves downstream with time.

From all the results presented in this section, it can be concluded that the acoustic energy transmitted out of a termination in the form of a pulse is partly converted into vortical energy. This phenomenon is observed with and without mean flow. In the next section, it is shown quantitatively that a power loss occurs in the transmission of the pulse from induct to far field, and that the amount of power loss (or power imbalance) is higher for a pulse with higher intensity.

7.2 QUANTITATIVE EVALUATION OF POWER LOSS

The optical results presented in section 7.1 show the formation of vortex rings when a finite amplitude pulse (or signal) propagates out through the termination. The intensity of the vortex ring increases as the propagating pulse intensity increases. These observations indicate that some portion of the acoustic energy contained in the pulse is

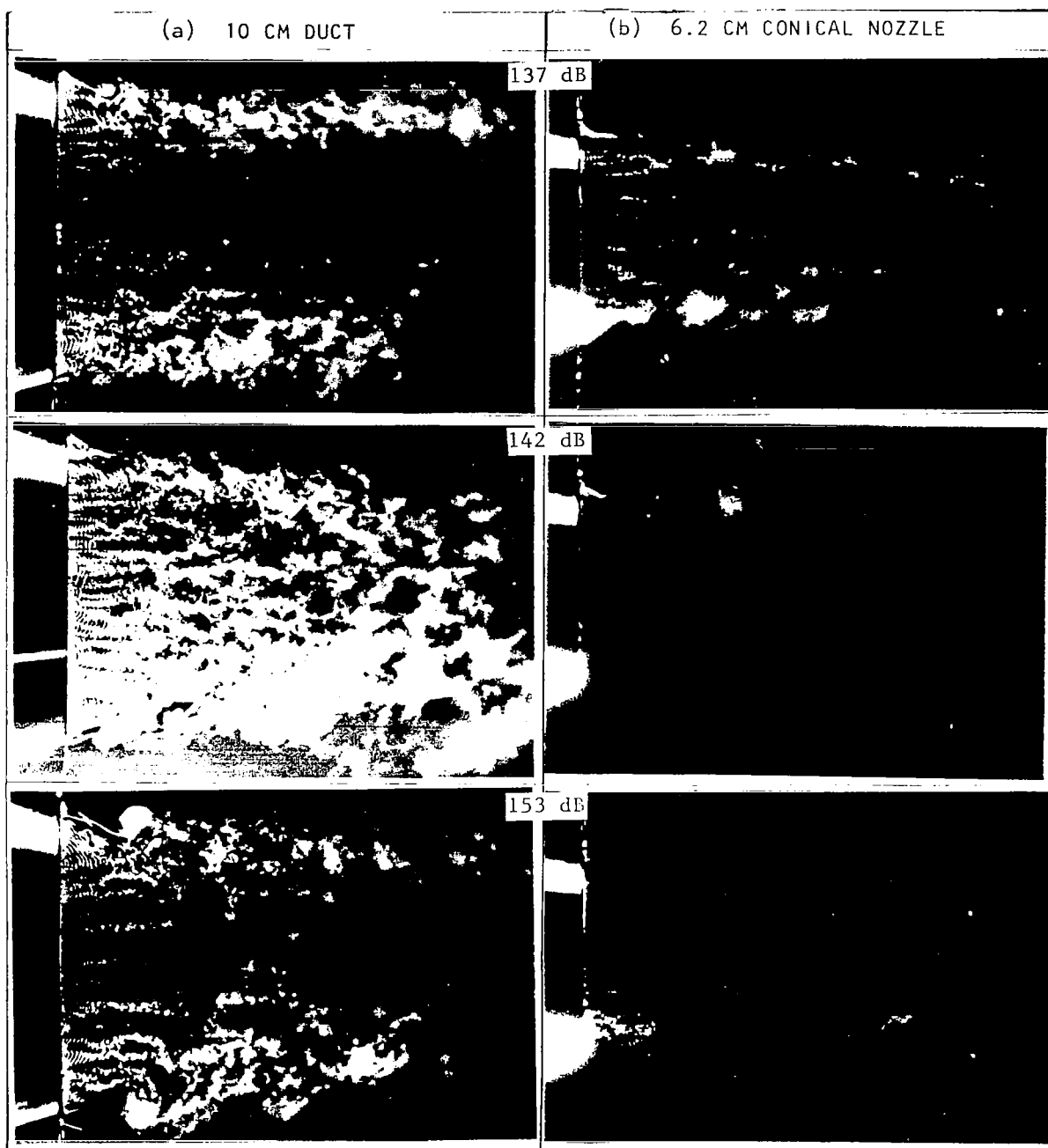
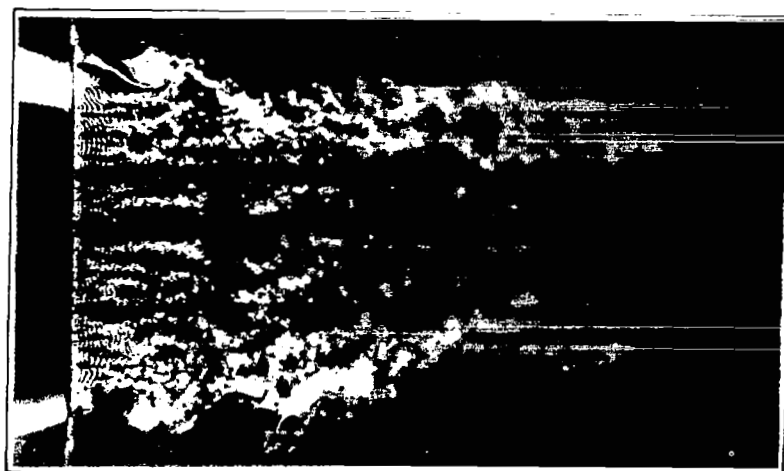


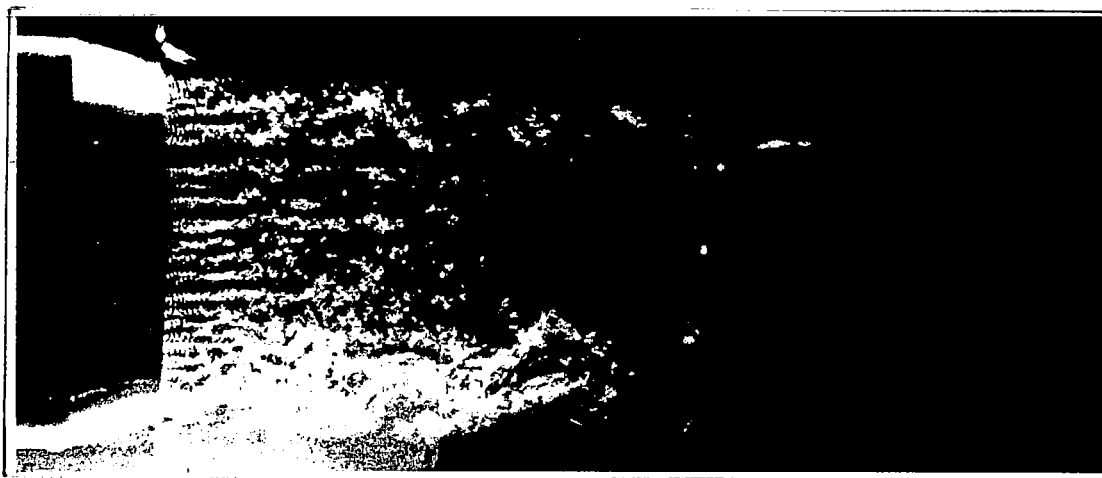
Figure 7.16 Effect of pulse intensity on the vortex formation at the exit of (a) a 10 cm diameter duct at $M_j = .0448$; photographed 6 ms after the pulse propagated out of the exit plane.



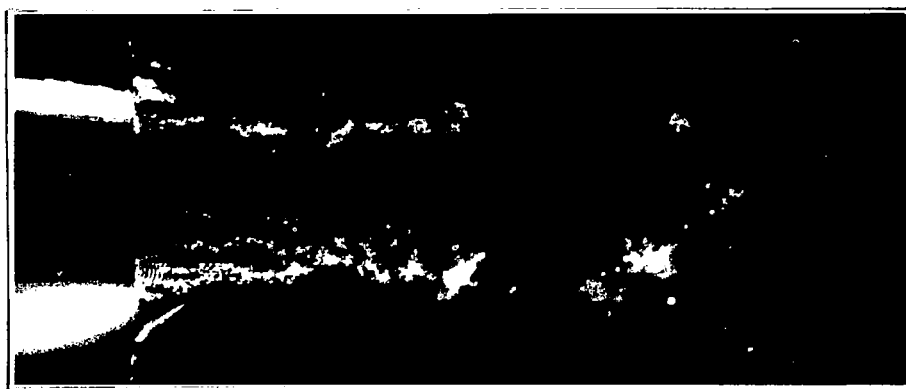
(a) 10 CM STRAIGHT DUCT



Figure 7.17 Propagation of vortex ring in the jet formed by a 149 dB pulse, photographed 6 ms after it propagated out of the exit plane of (a) a 10 cm diameter duct and (b) a 6.2 cm conical nozzle; $M_j = 0.0317$.



(a) 10 CM STRAIGHT DUCT



(b) 6.2 CM CONICAL NOZZLE

Figure 7.18 Excitation of the jet, by low intensity, 114 dB, repetitive acoustic pulse generated by an acoustic driver; (a) a 10 cm diameter duct and (b) a 6.2 cm conical nozzle; $M_J = 0.0317$.

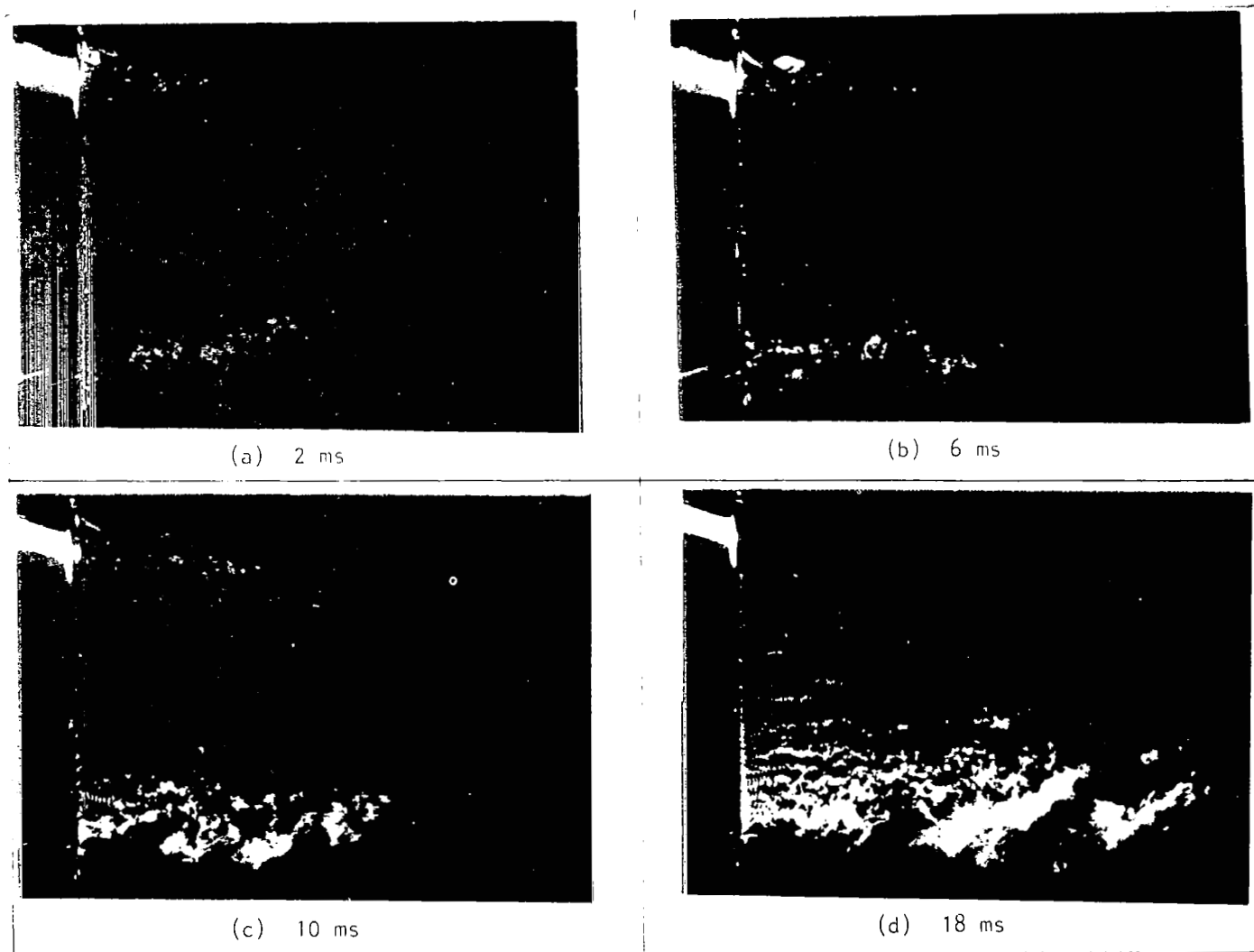


Figure 7.19 Propagation of vortex rings created by a 149 dB pulse for a 10 cm diameter straight duct, $M_J = 0.0317$.

converted into vortical energy when the pulse propagates out to the far field. In other words, the acoustic power reaching the far field has to be smaller than the radiated power estimated on the basis of induct measurement which does not account for any kind of power loss at the termination. This behavior was distinctly observed in previous investigations at Lockheed-Georgia (refs. 2,4,5,6 and 38), and also by others (refs. 35 through 37).

In the present study, a systematic investigation was carried out to evaluate the acoustic power loss quantitatively with varying intensity of the impulsive sound source, using various terminations with and without mean flow. The quantitative assessment of the power loss was done both experimentally and by using a prediction scheme.

The experimental procedure and data analysis scheme used for the present investigation are identical to those used in Phase II (ref. 2) of this contract. A brief description of the experimental procedure and data analysis scheme is presented in section 2 of this report. The experimental configuration is shown in figure 2.2. In brief, the experimental procedure consisted of discharging a capacitor across a spark gap located inside the flow duct at the source section, and measuring the resulting incident and reflected pressure pulses by an induct pressure transducer, and the transmitted pulse by several far-field microphones. The induct measurement is used to estimate the transmitted power (W_t) and the far-field measurements are used to evaluate the far-field power (W_f). The difference between far field and transmitted powers gives the amount of power loss or power imbalance. The intensity of the incident pulse inside the duct is controlled by the charging voltage and the spark gap.

The acoustic power loss was quantitatively estimated using the theoretical model developed by Cummings and Eversman (refs. 31 and 32). In this model, a simple radiation condition is imposed at the duct end to calculate the reflections and thus the transmitted power. A Kirchhoff type of model with analogous monopole and dipole representations of the duct end is used to calculate the radiated field. Nonlinear impedance conditions are incorporated in this model. This model is based upon plane wave mode. The incident pulse intensities derived from the experiments are used in the analytical model to estimate the power loss. This model is used for various terminations with and without mean flow. The controlling parameters used here are the intensity of the pulse, the ratio of the termination open area to the duct cross-sectional area, and a discharge coefficient (C_D). The discharge coefficient used for all the terminations except for the straight duct is 0.61, which is a very reasonable value as justified by Cummings and Eversman (ref. 33). The discharge coefficient for the straight-duct in reference 33 was 0.05 for the no-flow condition only on the basis of a good agreement between experiment and prediction. However, for the duct with mean flow, this parameter was not determined in reference 33. Therefore, in the present study for the straight duct termination in the presence of mean flow,

the power loss estimations are done using two values of C_D , namely, 0.61 and 0.05.

7.2.1 Effect of Acoustic Intensity on Power Loss

The experimentally evaluated power loss results in this section are compared with the corresponding predicted values. Figure 7.20 shows the power imbalance (power loss) spectra for a 10 cm diameter straight duct termination at various pulse intensities at $M_J = 0.0$. The experimental power loss results are compared with the corresponding predicted values for two different discharge coefficients, 0.05 and 0.61, in figures 7.20(a) and 7.20(b), respectively. The low-frequency spectral distribution, experimentally evaluated, clearly indicates that the amount of power loss increases as the pulse intensity increases. The predicted results also show the same trend throughout the frequency range. The predicted power loss values agree well with the measured values for $C_D = 0.05$. However, the predicted power loss values for $C_D = 0.61$ are small compared to the corresponding measured values and this disagreement seems to be more at lower frequencies. Therefore $C_D = 0.05$ is an appropriate value to predict the power loss for a straight duct in the absence of flow.

Figure 7.21 shows the effect of pulse intensity on the power imbalance spectra for the daisy lobe nozzle at $M_J = 0.0$. The predicted values evaluated using $C_D = 0.61$ agree well with the measured values. Both experimental and predicted results show more low frequency power loss with increasing intensity.

Figures 7.22 and 7.23 show the effect of pulse intensity on the power imbalance spectra for a 10 cm diameter straight duct at $M_J = 0.1$ and $M_J = 0.2$, respectively. In each case, the predicted power loss using discharge coefficient values of 0.05 and 0.61 are presented. In the presence of mean flow as seen in figure 7.22, the power loss at each intensity remains more or less the same. However, at $M_J = 0.2$ (see figure 7.23) the amount of power loss seems to be less for the lower intensity pulses. This reduction is not entirely due to the effect of intensity. Most likely, at $M_J = 0.2$ for the straight duct, the signal (far field) was contaminated due to the jet mixing noise, which in turn introduced some error in the results mainly for the low-intensity cases where the signal to noise ratio was poor.

The predicted power loss values for $C_D = 0.61$ agree well with the experimental results for both the Mach numbers. They both show that, in the presence of flow, the pulse intensity (i.e. nonlinear behavior) has a negligible effect on the power loss mechanism. The predicted power loss levels for both the flow conditions are higher when $C_D = 0.05$. Therefore, $C_D = 0.61$ seems to be an appropriate discharge coefficient to predict the power loss for a straight duct in the presence of flow.

Similar comparisons are made to show the effect of pulse intensity

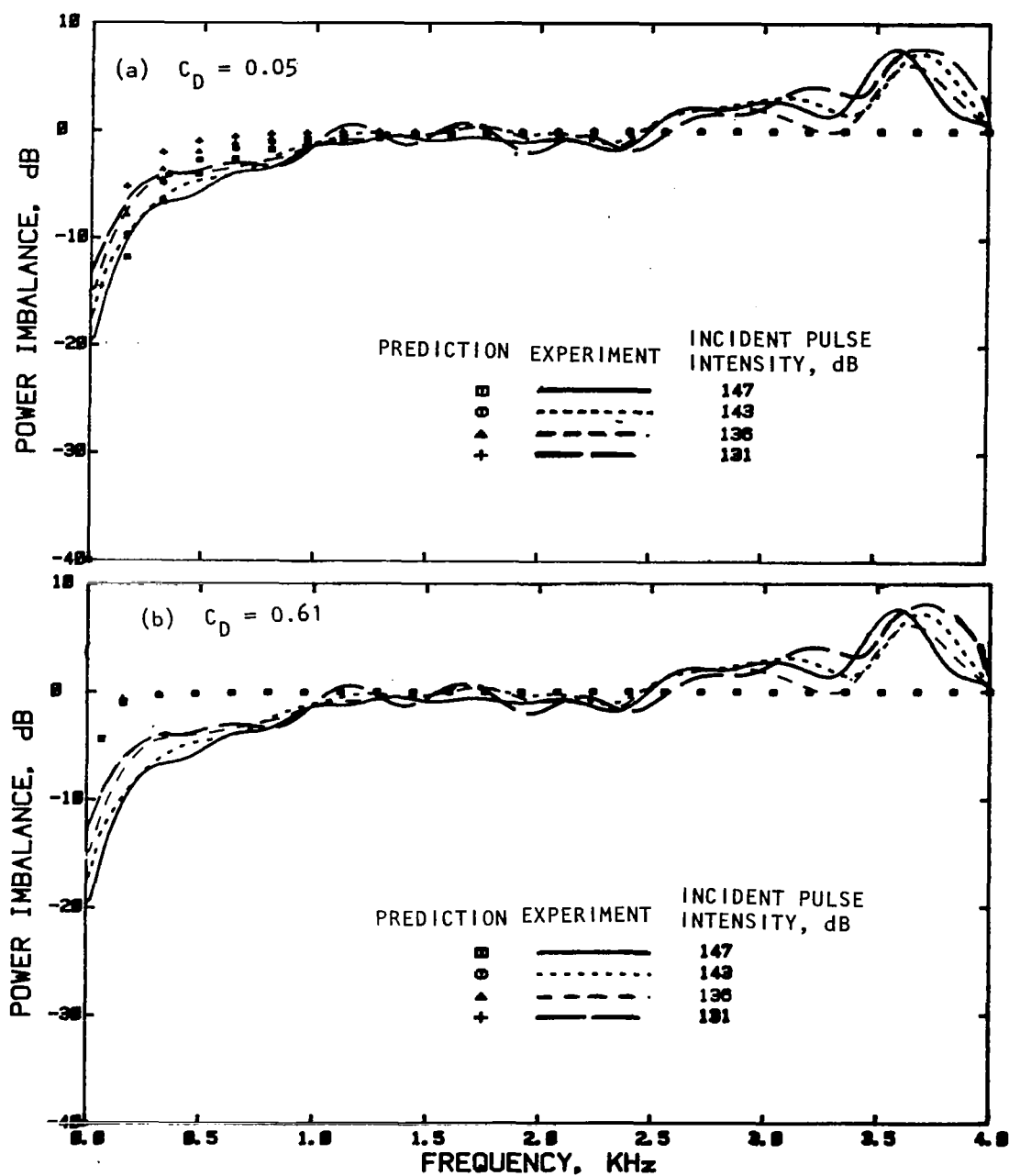


Figure 7.20 Effect of incident pulse intensity on the power imbalance spectra for a 10 cm diameter straight duct at $M_j = 0.0$ derived experimentally and by a prediction scheme.

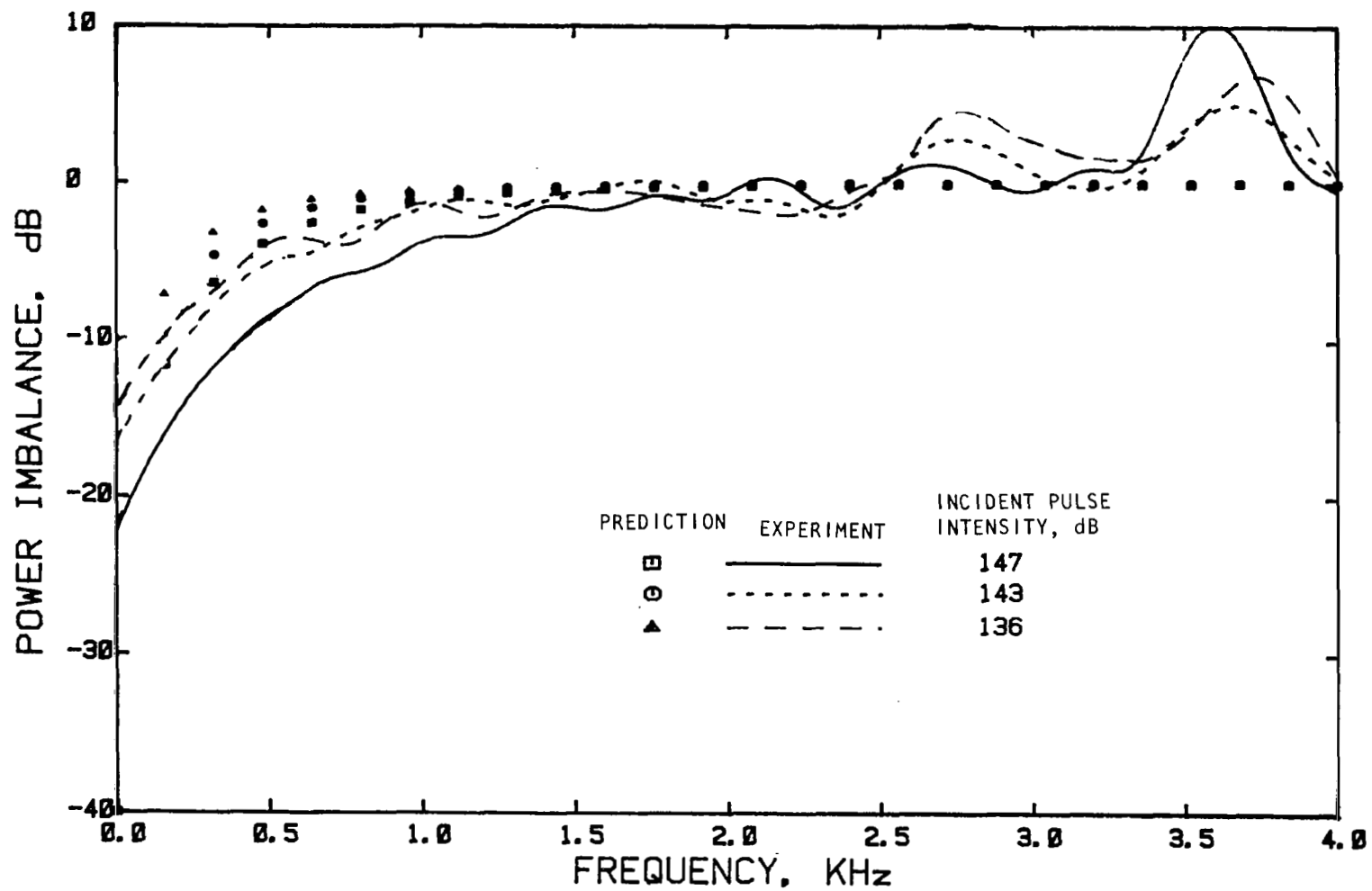


Figure 7.21 Effect of incident pulse intensity on the power imbalance spectra for the daisy lobe nozzle at $M_J = 0.0$, derived experimentally and by a prediction scheme, $C_D = 0.61$.

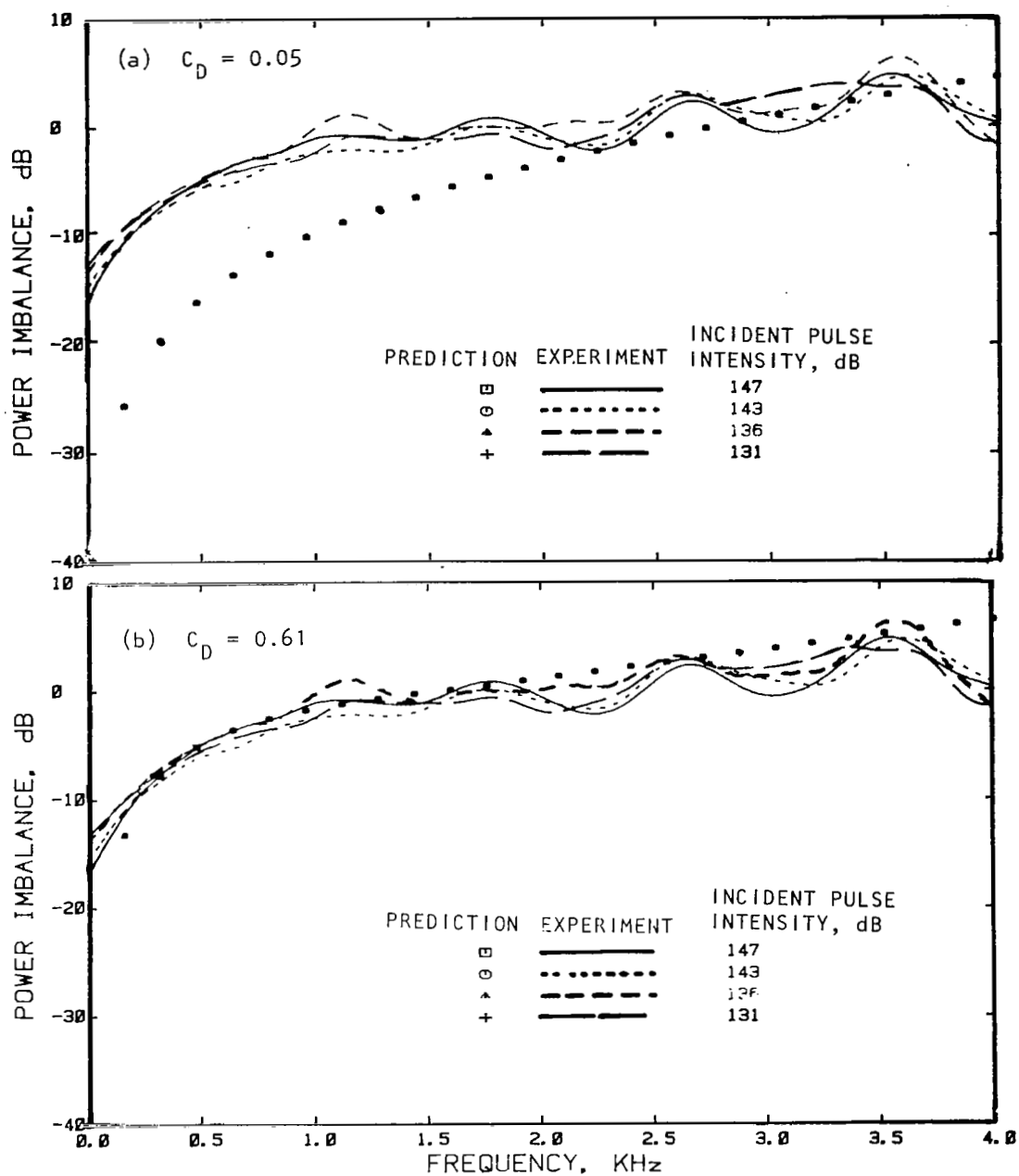


Figure 7.22 Effect of incident pulse intensity on the power imbalance spectra for a 10 cm diameter straight duct at $M_j = 0.1$ derived experimentally as well as by a prediction scheme.

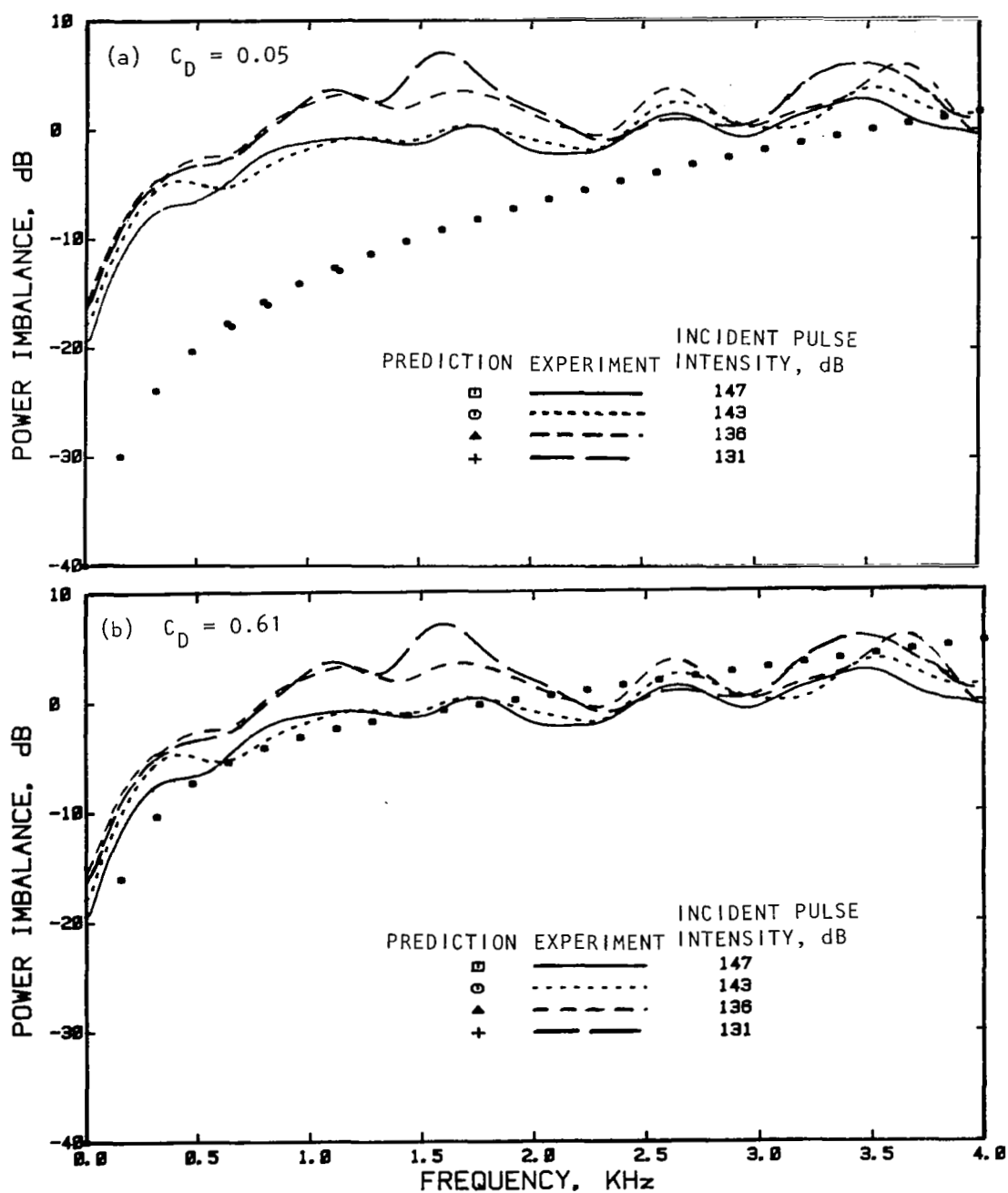


Figure 7.23 Effect of incident pulse intensity on the power imbalance spectra for a 10 cm diameter straight duct at $M_j = 0.2$ derived experimentally as well as by a prediction scheme.

on the power loss for a 6.2 cm conical nozzle at $M_J = 0.1$ (see figure 7.24(a)) and $M_J = 0.4$ (see figure 7.24(b)). The conclusions here are similar to those for the straight duct. That is, in the presence of mean flow, the nonlinear effects become negligible. The predicted results here agree very well with the experimental results for $M_J = 0.1$. For $M_J = 0.4$, the prediction shows higher power loss compared to the experiment.

7.2.2 Effect of Nozzle Exit Area on Power Loss

The power loss spectra evaluated at a fixed pulse intensity of 147 dB for conical nozzles with 2.5 cm and 6.2 cm diameters are compared with those for a 10 cm diameter straight duct at $M_J = 0.0$ in figure 7.25. The nozzle with lower exit diameter (area) exhibits more power loss compared to the nozzle with higher diameter. The predicted results also behave in the same manner. This observation also agrees with the optical results.

Similar results evaluated for a 6.2 cm diameter conical nozzle are compared with those for a 10 cm diameter straight duct for a fixed pulse intensity of 143 dB at $M_J = 0.032$ (see figure 7.26(a)) and $M_J = 0.1$ (see figure 7.26(b)). The power loss spectra for both the terminations are quite alike except at the lower frequencies where the nozzle exhibits more power loss compared to the straight duct. The predicted results agree well with the measurements.

7.2.3 Effect of Nozzle Geometry on Power Loss

The measured and predicted power loss spectra for a conical nozzle are compared with those for a daisy lobe nozzle for two different pulse intensities, at $M_J = 0.0$ in figure 7.27. The open exit area for both the nozzles was 30.2 sq cm (i.e. a diameter of 6.2 cm). However, the geometry of the daisy lobe nozzle was quite different from the conical nozzle. The predicted results for both the nozzles are identical since the analytical model did not include the effect of termination shape. The experimental results show small differences between the two nozzles at low frequencies. For the pulse intensity of 147 dB (see figure 7.27(a)) the daisy lobe nozzle shows more power loss compared to the conical nozzle. However, for the pulse intensity of 143 dB (see figure 7.27(b)) there is very little difference observed between the two nozzles. Therefore, the nozzle geometry seems to have very little effect on the power loss values.

7.2.4 Effect of Mean Flow on Power Loss

The induct time histories for a 10 cm diameter duct and a 6.2 cm diameter conical nozzle with a fixed pulse intensity of 143 dB are plotted in figure 7.28 at various low flow Mach numbers. In this range of Mach numbers, the induct time histories do not show much change.

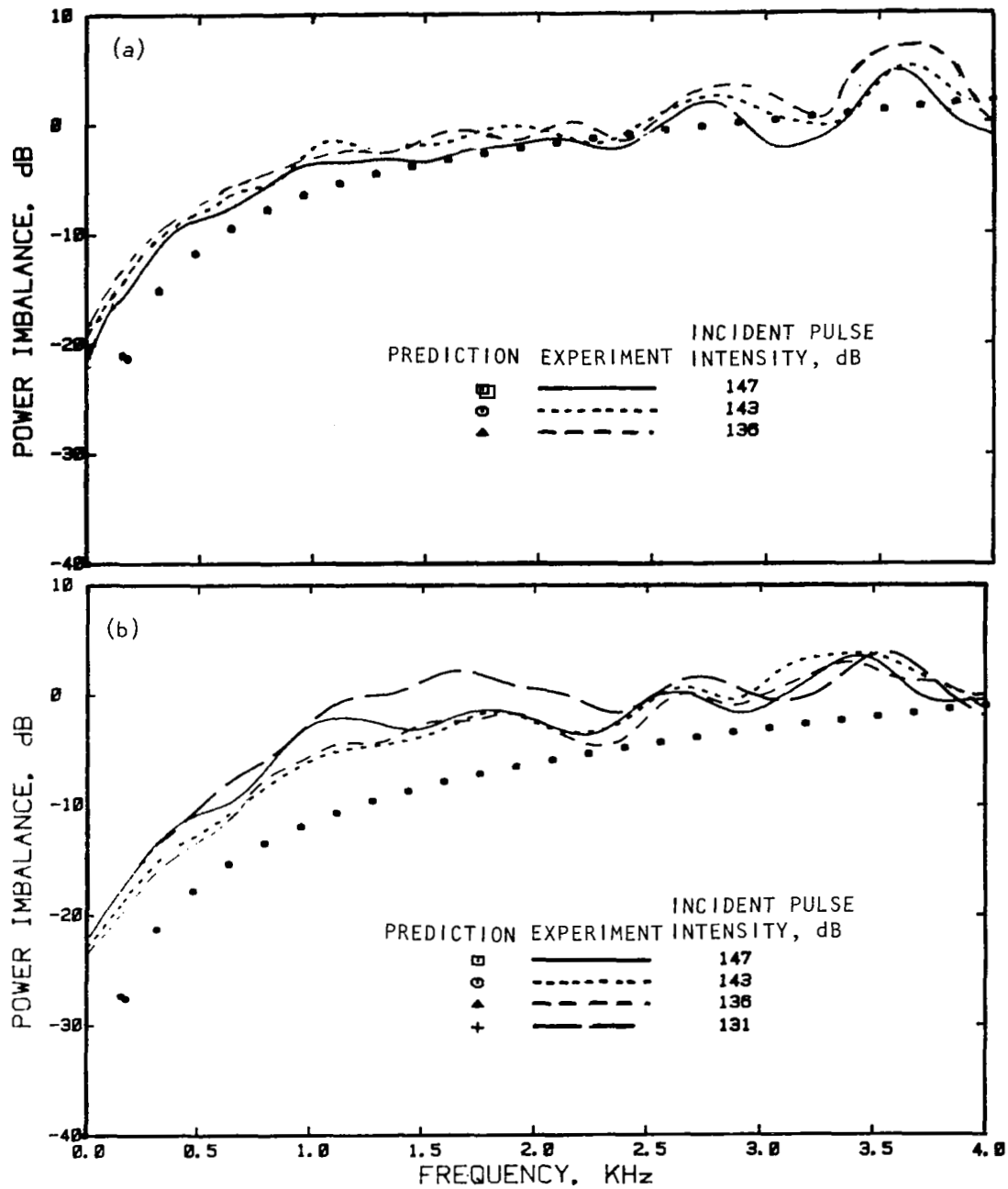


Figure 7.24 Effect of incident pulse intensity on the power imbalance spectra for a 6.2 cm diameter conical nozzle derived experimentally as well as by a prediction scheme, $C_D = 0.61$, (a) $M_J = 0.1$, (b) $M_J = 0.4$.

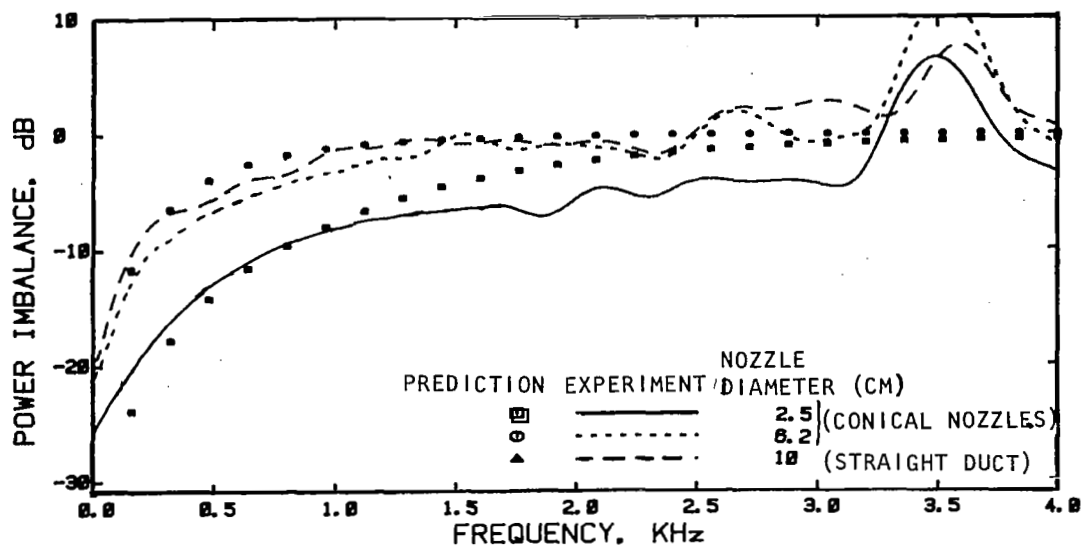


Figure 7.25 Comparison of power imbalance spectra between two conical nozzles of 2.5 cm and 5.2 cm exit diameters, and a 10 cm diameter straight duct, the incident pulse intensity was 147 dB, $M_J = 0.0$, C_D for the nozzle was 0.61 and for the duct was 0.05.

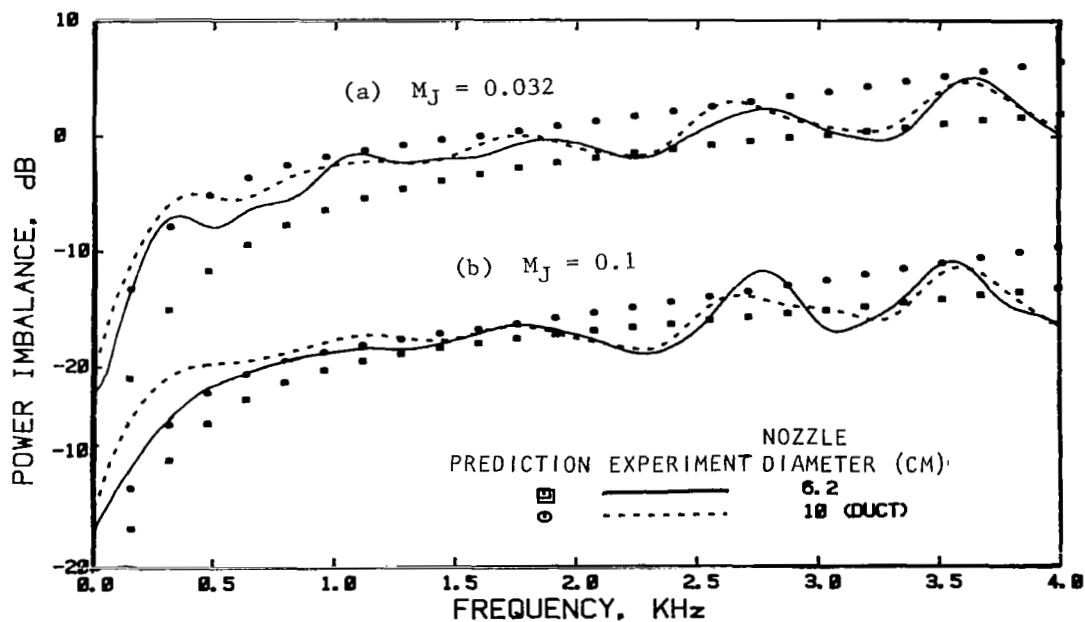


Figure 7.26 Comparison of power imbalance spectra between a 6.2 cm diameter conical nozzle and a 10 cm diameter duct, the incident pulse intensity being 143 dB and $C_D = 0.61$; (a) $M_J=0.032$ and (b) $M_J=0.1$.

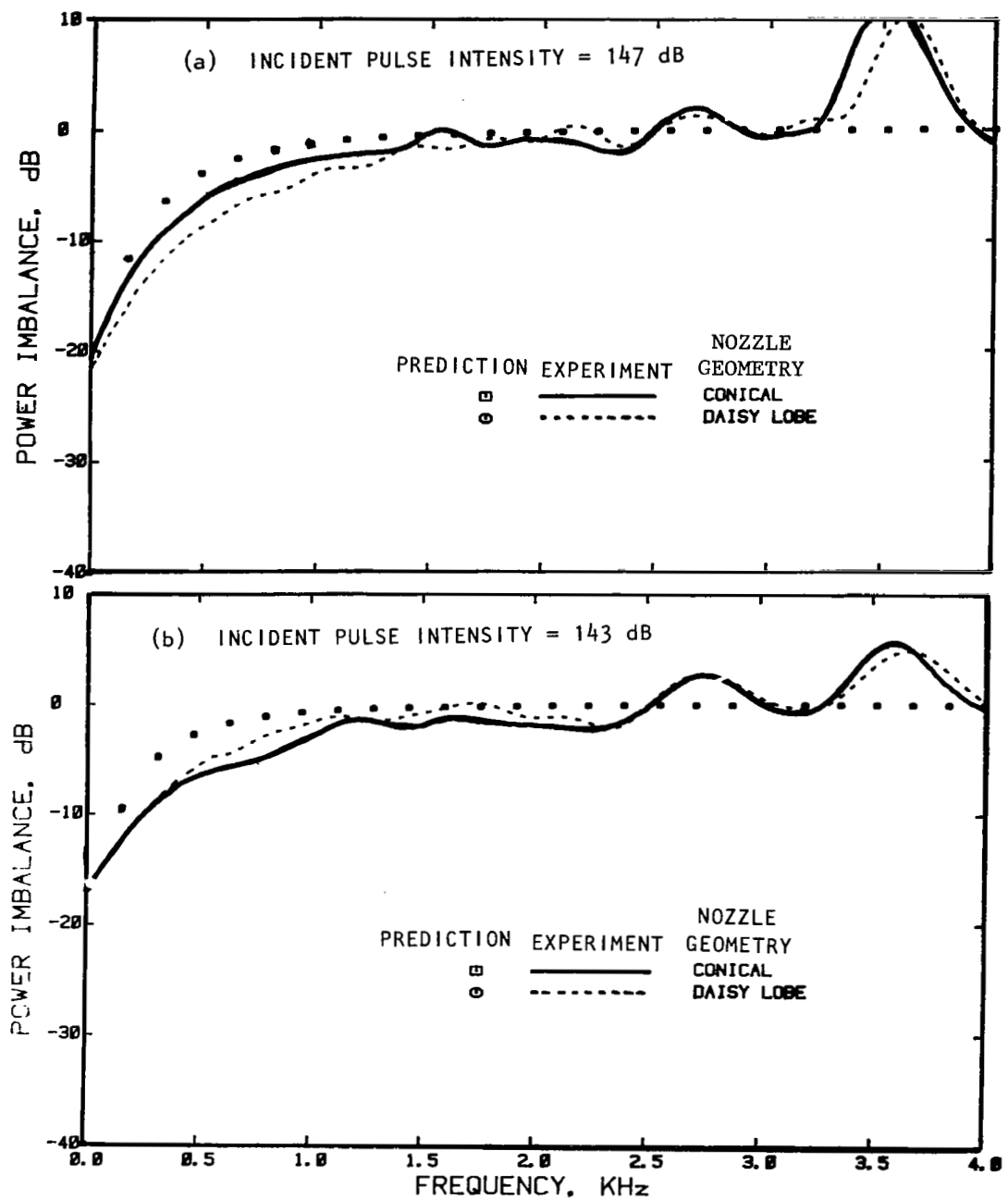


Figure 7.27 Effect of nozzle geometry with same exit open area on the power imbalance spectra for different incident pulse intensity at $M_J=0.0$ and $C_D=0.61$; incident pulse intensity: (a) 147 dB and (b) 143 dB.

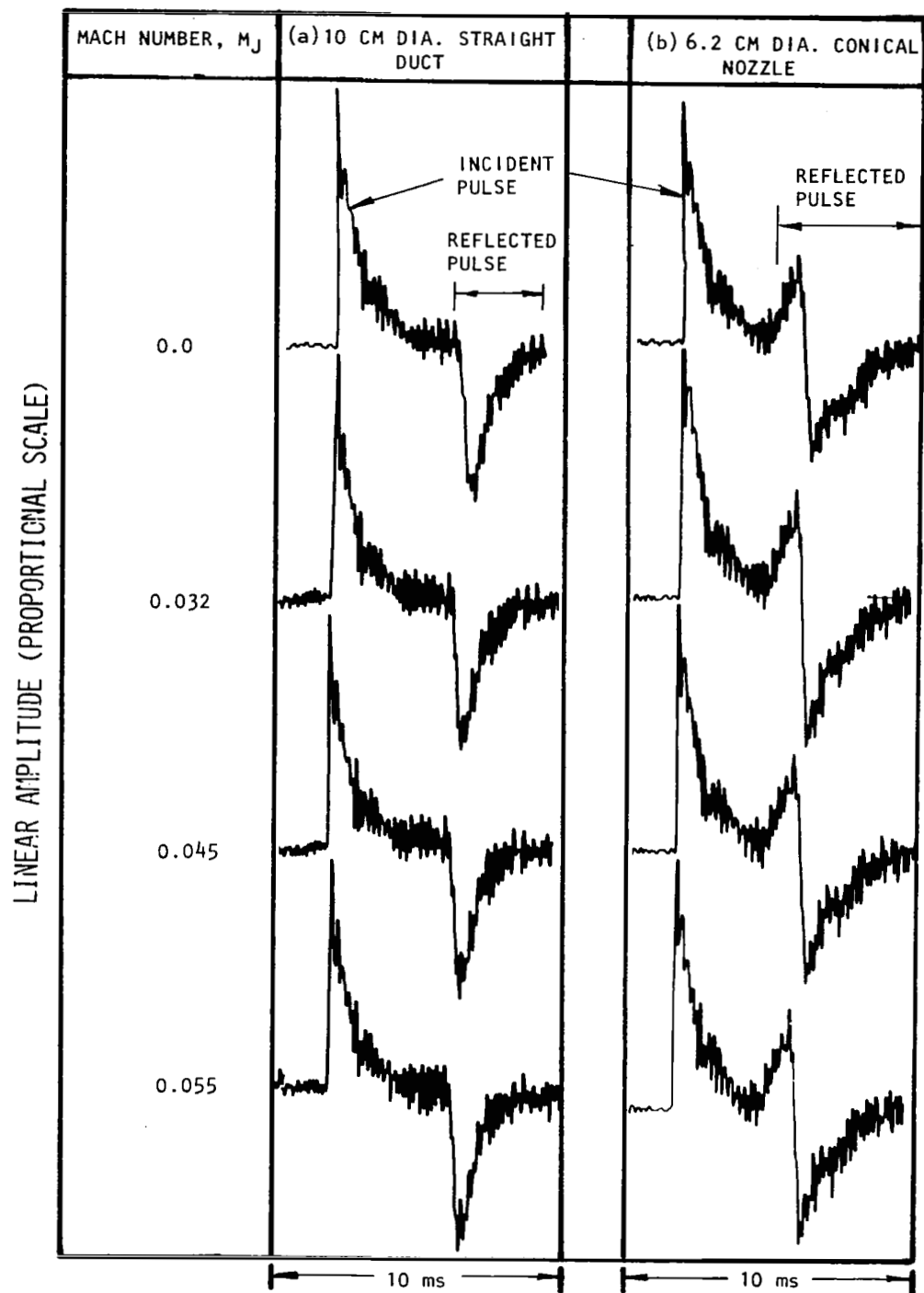


Figure 7.28 Effect of flow on the induct time histories for (a) 10 cm diameter straight duct and (b) a 6.2 cm diameter conical nozzle with incident pulse intensity of 143 dB.

The corresponding measured power loss spectra for the duct at various Mach numbers are plotted in figure 7.29. The effect of Mach number on the power loss seems to be very small. At lower frequencies, the power loss increases slightly with Mach number. However, at higher frequencies there is no apparent difference in the power loss levels.

The predicted results shown in figure 7.29 were evaluated using $C_D = 0.05$ for no flow condition and $C_D = 0.61$ for flow cases. The predicted values show the increasing power loss with Mach number and this effect is more prominent at lower frequencies.

The power loss spectra for the 6.2 cm diameter nozzle at various Mach numbers are plotted in figure 7.30. The effect of Mach number is more clearcut in this case. The low-frequency power loss increases with increasing Mach number. The predicted results also follow the same trend. The agreement between experiment and prediction is very good except for higher Mach numbers where the prediction shows more power loss.

7.3 CONCLUSIONS

The important observations are summarized in this section:

- (1) The presence of an acoustic pulse (signal) is the cause of the formation of the vortex ring at the termination exit.
- (2) A higher intensity pulse (or signal) generates a stronger vortex ring and increases the propagation speed of the ring.
- (3) The vortex structure is dependent on the termination geometry.
- (4) The low-frequency power loss increases due to the increase in the propagating pulse intensity.
- (5) For a fixed pulse intensity, the amount of power absorption (or power loss) appears to be controlled primarily by the open area at the exit and not as much by the shape of the termination.
- (6) With mean flow the power absorption increases with increasing Mach number.
- (7) Nonlinear effects of high intensity pulses are considerably reduced in the presence of mean flow.
- (8) A discharge coefficient of 0.05 seems to be appropriate for power loss prediction for a straight duct termination in the absence of flow. However, in the presence of flow a discharge coefficient of 0.61 is suitable for all the terminations including a straight duct for power loss prediction.

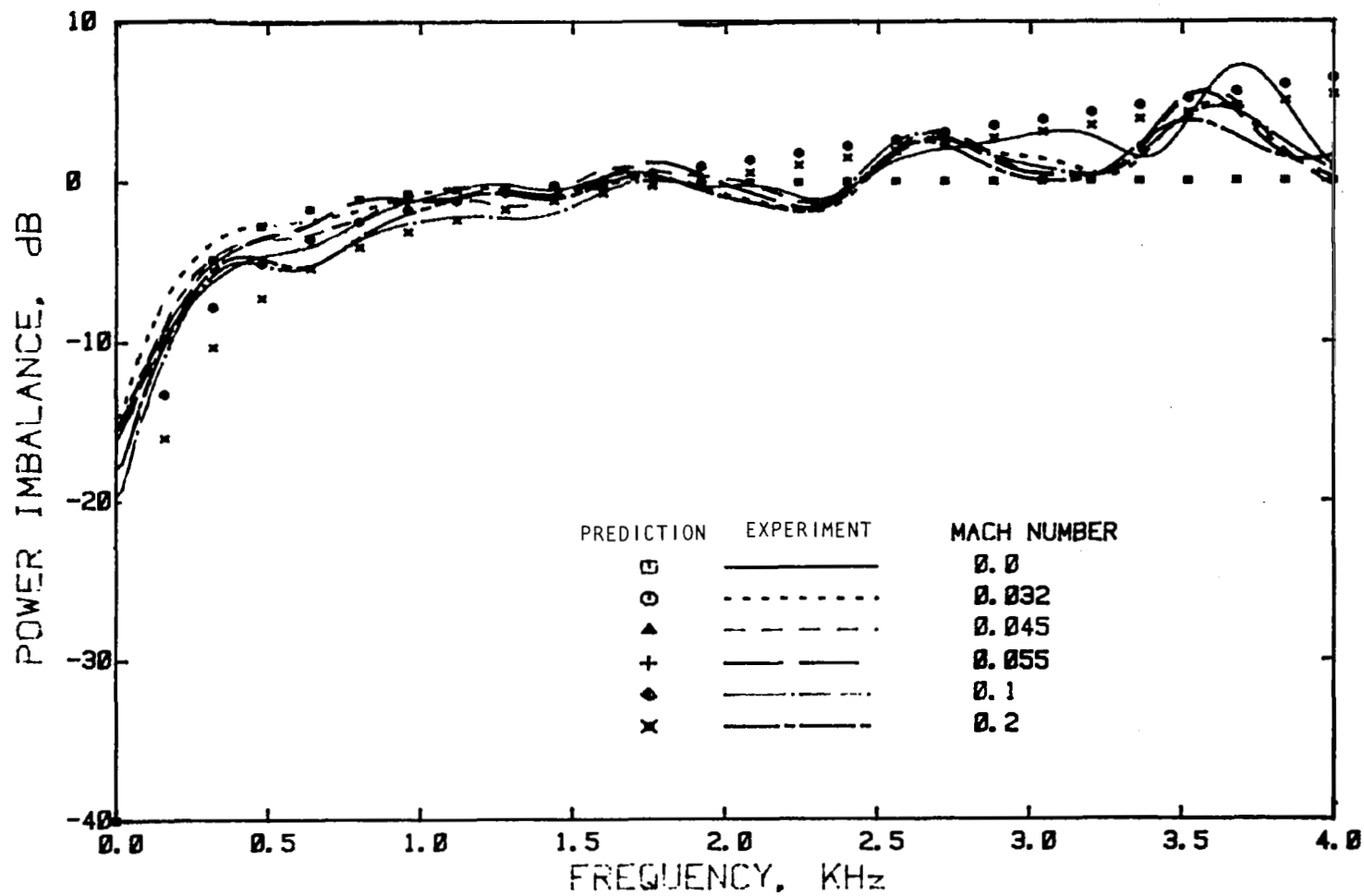


Figure 7.29 Effect of Mach number on the power imbalance spectra evaluated experimentally and by a prediction scheme for a 10 cm diameter duct, the incident pulse intensity being 143 dB.

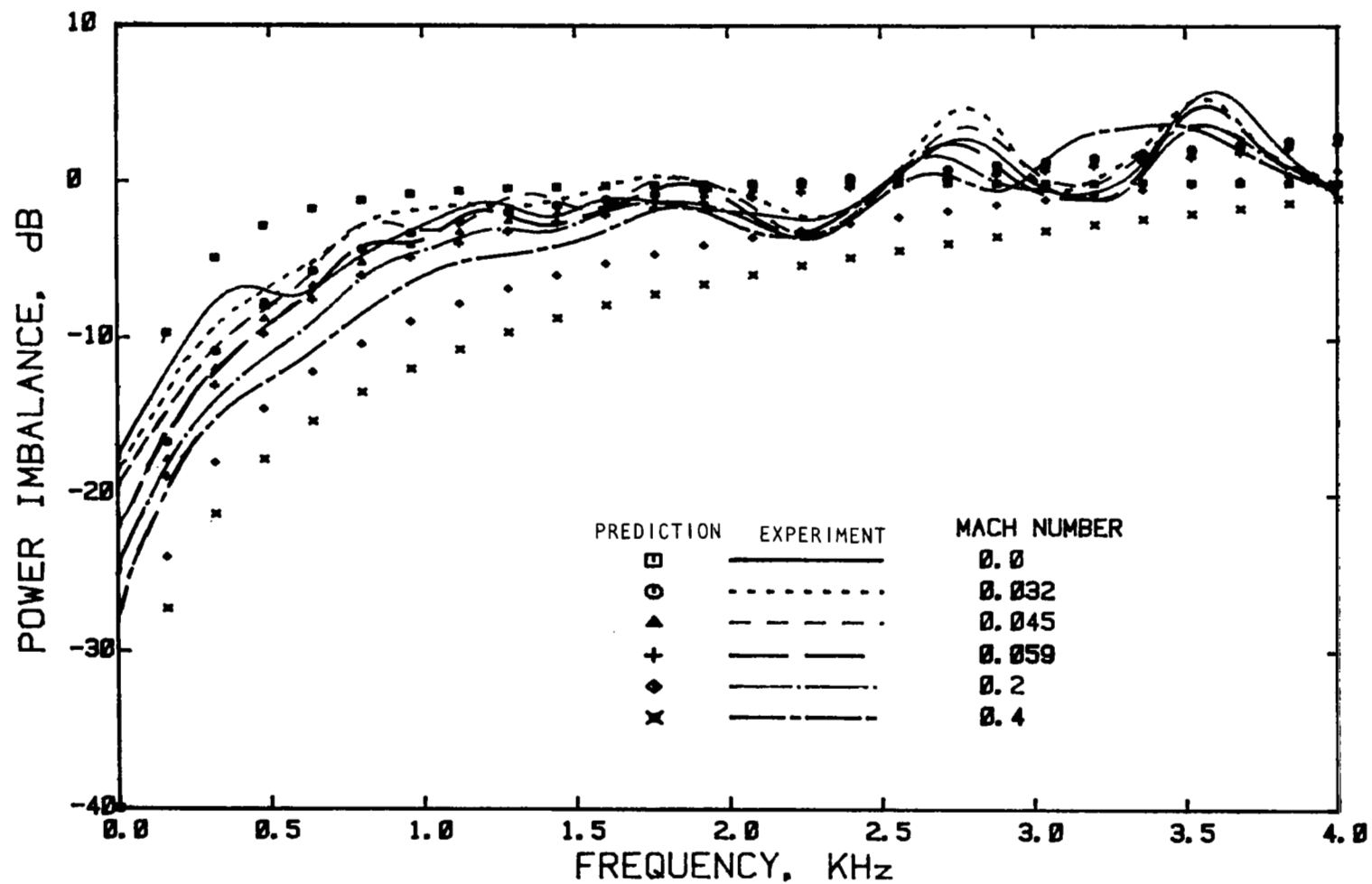


Figure 7.30 Effect of Mach number on the power imbalance spectra evaluated experimentally and by a prediction scheme for a 6.2 cm diameter conical nozzle, the incident pulse intensity being 143 dB, and $C_D = 0.61$.

8.0 APPLICATION OF IMPROVED ACOUSTIC IMPULSE TECHNIQUE

The acoustic impulse test technique has been improved in many areas under the present contract as described in sections 4 and 5. In particular, the "signal synthesis" and "signal averaging" processes have been successfully incorporated in the acoustic impulse technique to generate a desired impulsive signal from an acoustic driver and to eliminate the background noise (flow noise) from the induct and the far-field signals. The contribution of higher order modes in the computation of incident and reflected powers can also be accounted for using the modal decomposition process described in section 5.

At this stage, the refined acoustic impulse technique can be applied to study more accurately the acoustic characteristics of various nozzles. Therefore, experiments using this technique were conducted for a 6.2 cm diameter conical nozzle and a daisy lobe suppressor nozzle (with an equivalent exit diameter of 6.2 cm), at various flow conditions. Both of these nozzles were tested earlier in the Phase II of the present contract. A few typical results obtained then have been presented in this report in section 2.

The acoustic measurements for determining the transmission coefficients were carried out in the anechoic free-jet facility. The experimental setup, the induct and far-field instrumentation, the experimental procedure and the data analysis schemes have been described fully in section 3. For completeness, however, a brief description of the nozzles, the test plan, the instrumentation, the experimental procedure and the data analysis scheme is given in section 8.1 here. Following this, the experimental results, showing the effect of nozzle geometry, jet Mach number and free jet Mach number, are presented in section 8.2. Finally, a summary and general conclusions are presented in section 8.3.

8.1 TEST CONFIGURATIONS AND EXPERIMENTAL PROCEDURE

The single-stream flow facility has been described in section 3.1 (see figure 3.1). The source sections with single and multiple acoustic drivers are shown in figures 3.2 and 3.3, respectively. Tests were carried out using a conical nozzle with 6.2 cm exit diameter and a multilobe multitube suppressor nozzle, which is referred to as the "daisy lobe nozzle" for convenience.

8.1.1 Nozzle Description

(1) Daisy Lobe Nozzle

Two photographic views of this nozzle are shown in figures 8.1(a) and 8.1(b). A cross-sectional view of the nozzle with important

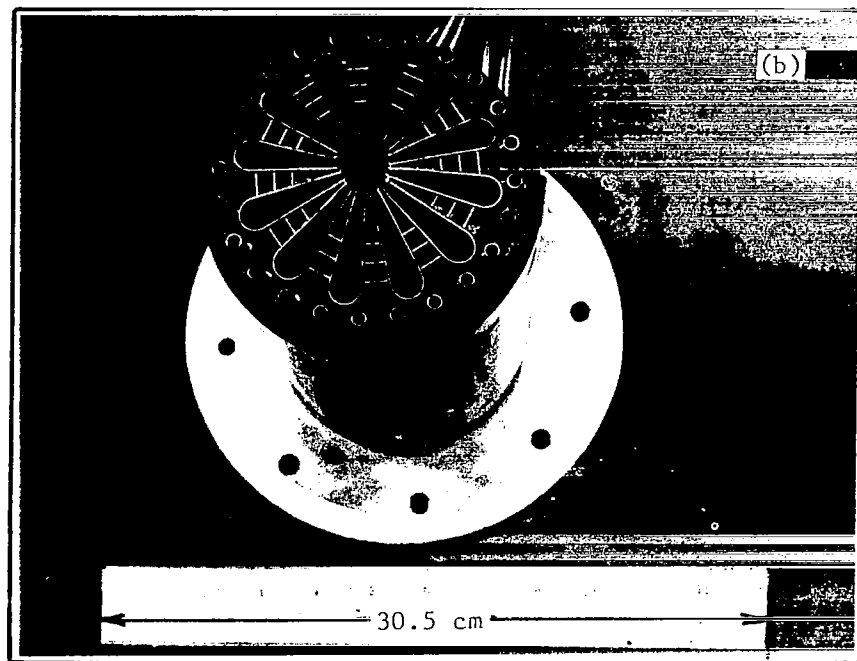
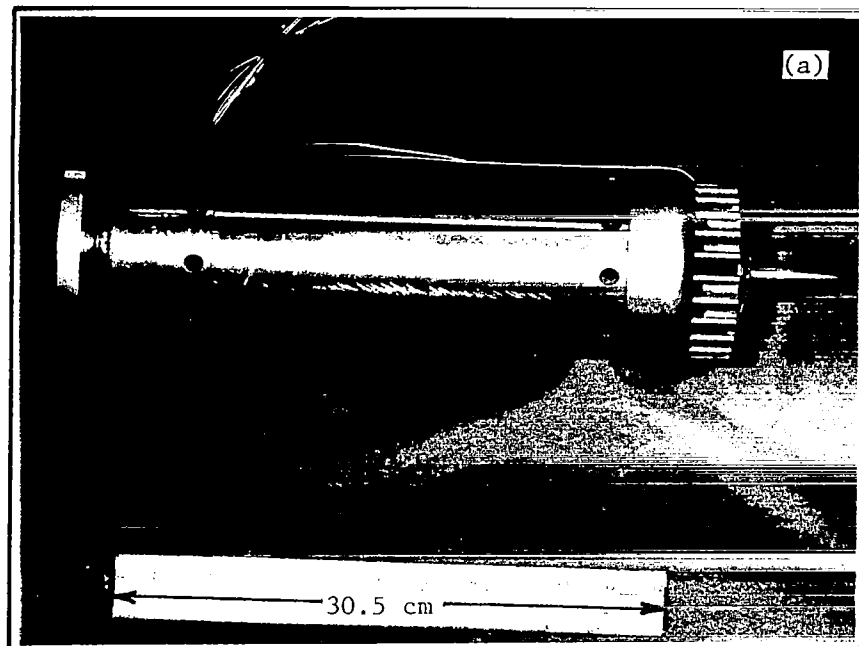


Figure 8.1 The 12-lobe, 24-tube suppressor nozzle.

dimensions is shown in figure 8.2. The total flow area through the 12-lobes and 24 tubes is 30.21 cm and is equivalent to that of a round nozzle with a diameter equal to 6.21 cm (2.44 in). Both the tubes and the lobes are attached to a conic section which makes an angle of 50 degrees with the nozzle axis. The 24 tubes are equispaced on a circle of diameter 9.59 cm. The tube diameter is 0.409 cm and the tube wall thickness is 0.762 mm. The inlets of these tubes are well rounded for smooth flow entry and the exits are chamfered to minimize flow separation at the lip.

The 12 daisy lobes are also equispaced and each lobe consists of two straight and two rounded walls (see fig. 8.2). The lobe angle is 15 degrees and the flow area of each lobe is 2.26 sq. cm. This provides a ratio of total area of the lobes and that of the tubes equal to 9.6. Three stiffener pins of diameter 0.80 mm are inserted between the adjacent walls of each pair of lobes.

A plug is mounted in the center of the nozzle. It is ogival in shape, has a maximum diameter of 1.58 cm, and protrudes beyond the lobe exit by 4.95 cm. It extends upstream into the 10.16 cm diameter test duct by 7.08 cm and has an elliptical leading edge (major axis = 6.34 cm, minor axis = 1.58 cm). The plug is actually detachable from the main body of the nozzle such that tests can be carried out with a different plug or no plug at all, if required.

To obtain a measure of the drag on this nozzle, seven static pressure sensing ports have been provided, four in the entrainment area between the lobes, and three on the plug itself. Exact locations of these ports are shown in figure 8.2.

(2) Reference Conical Nozzle

The reference nozzle is a round conical convergent nozzle of flow area equal to that of the daisy lobe nozzle with an exit diameter = 6.21 cm (2.44 in). Pertinent dimensions of this nozzle are given in figure 8.3. The nozzle is designed such that when mounted on the 10.16 cm diameter supply duct, the distances of the induct sound source and the induct probe from the exit plane remains the same as those from the exit of the daisy lobe nozzle.

8.1.2 Test Plan

The flow conditions for which the above-mentioned nozzles were tested are given in Table 8.1. Basically the above-mentioned two single-stream nozzles were tested for the no-flow case, three subsonic and one supersonic Mach numbers, and three tunnel Mach numbers. All the tests were conducted at ambient temperature condition.

Table 8.1 Test Conditions For The Daisy Lobe And The Reference Conical Nozzle

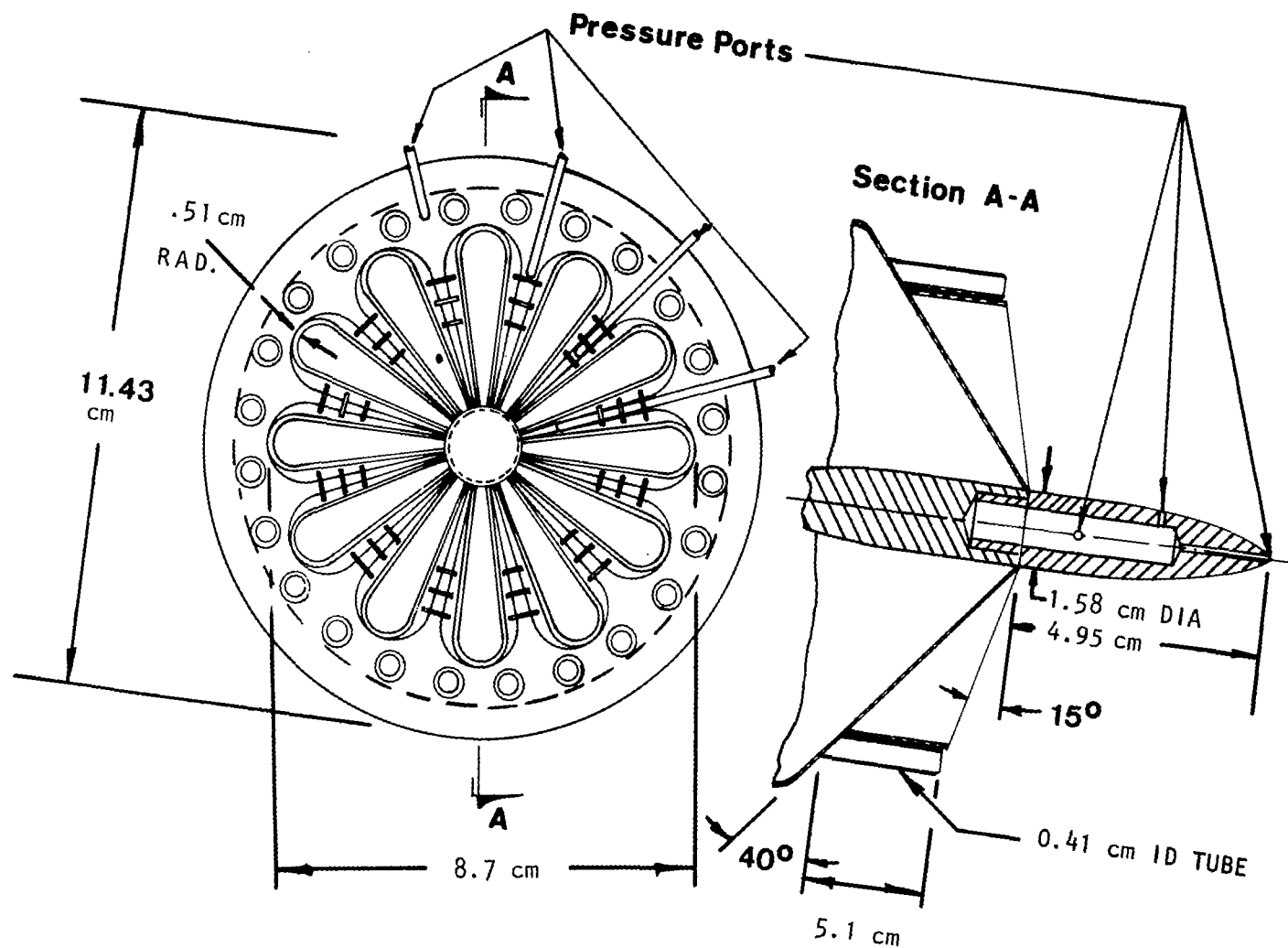


Figure 8.2 A cross-sectional view of the daisy lobe nozzle

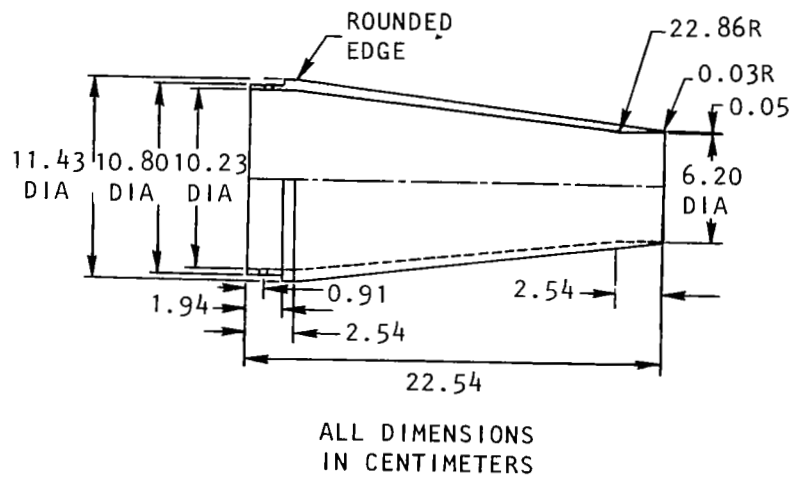
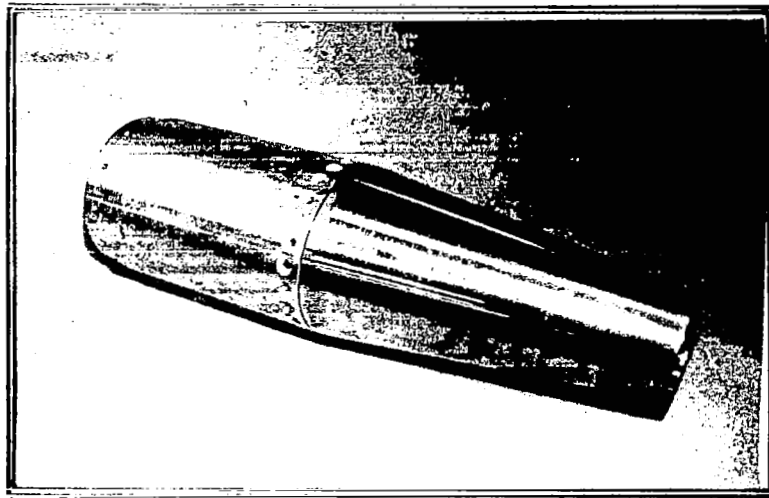


Figure 8.3 The reference conical nozzle (dia = 6.21 cm)

FULLY-EXPANDED JET MACH NO., M_J	TUNNEL MACH NO., M_T
0.0	0.0, 0.24
0.4	0.0, 0.24
0.6	0.0, 0.08, 0.16, 0.24
0.8	0.0, 0.24
1.2	0.0, 0.24

8.1.3 Instrumentation

The general outline for the instrumentation has been described in section 3. The specific instruments used in this study are described here.

A special six-microphone probe was fabricated for the induct measurements. In this probe (see figure 8.4), six miniature Knowles microphones were used. The length of the probe which remains inside the duct cross section was exactly the same as the duct radius, 5 cm. This covered the entire radius of the duct with six radial measurement locations 1.0 cm apart. The rest of the details about this probe are identical to those for the annular duct probe, which has been described in section 3.2.

All the subsonic flow tests were conducted using the single acoustic driver system as the sound source, whereas for the supersonic flow case (i.e. $M_J = 1.2$), the four driver-system was used to increase the signal to noise ratio, specially in the far field.

8.1.4 Experimental Procedure and Data Analysis Scheme

The experimental procedure consisted of measuring the induct pressure field using the six-microphone probe, and the far-field pressures at various polar angles.

The data analysis scheme is outlined in figure 8.5. The induct pressure field as measured at six radial locations was used to derive the incident, the reflected, and the transmitted powers, and the reflection coefficients accounting for the higher radial mode contributions. The details of this procedure have been described in section 5. Using the computed induct powers and the far-field pressure measurements, the normalized transmission coefficients (conveniently called the nozzle transfer function, NTF), the power transfer functions and the related parameters were evaluated (the details are described in

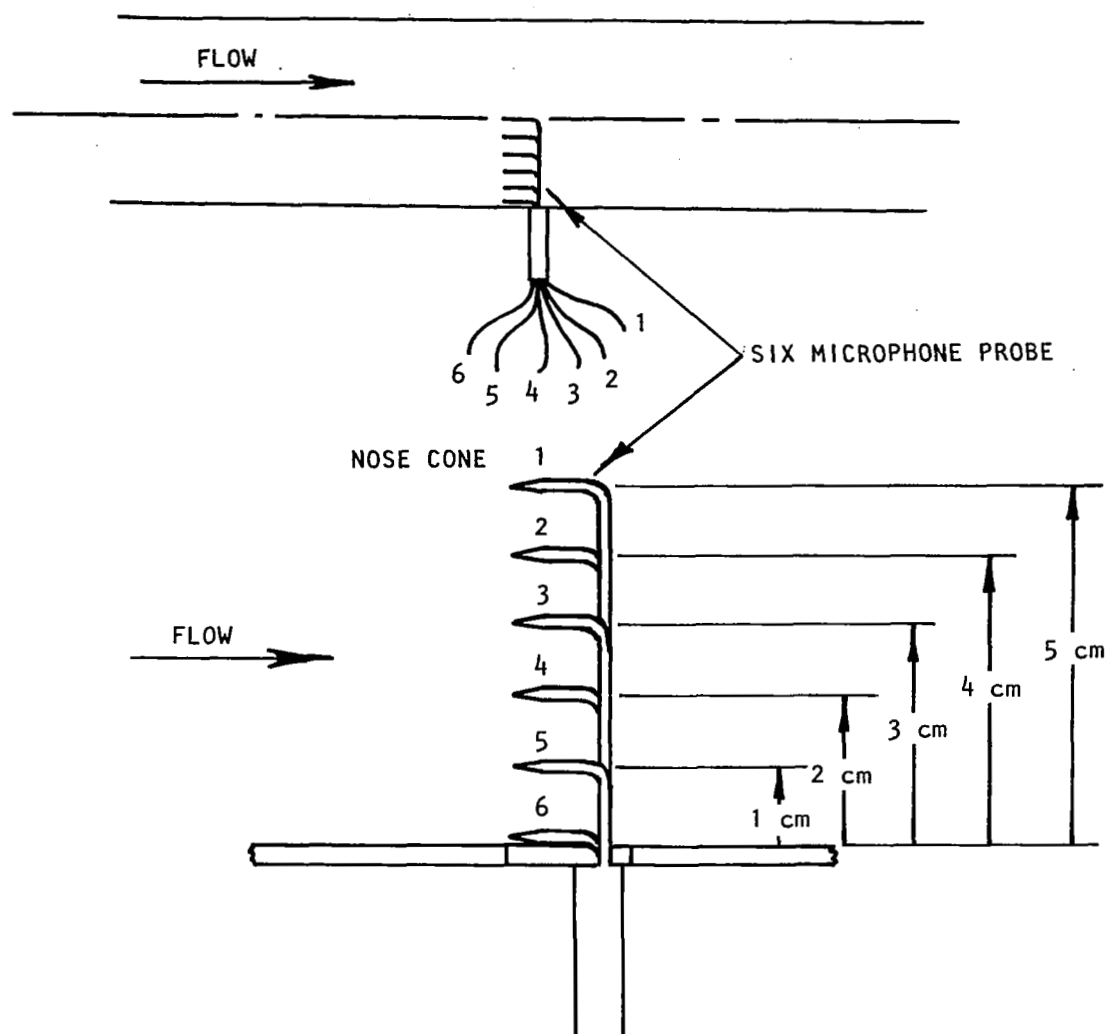


Figure 8.4 Six microphone probe for radial survey of induct pressure field for a single stream duct of 10 cm diameter.

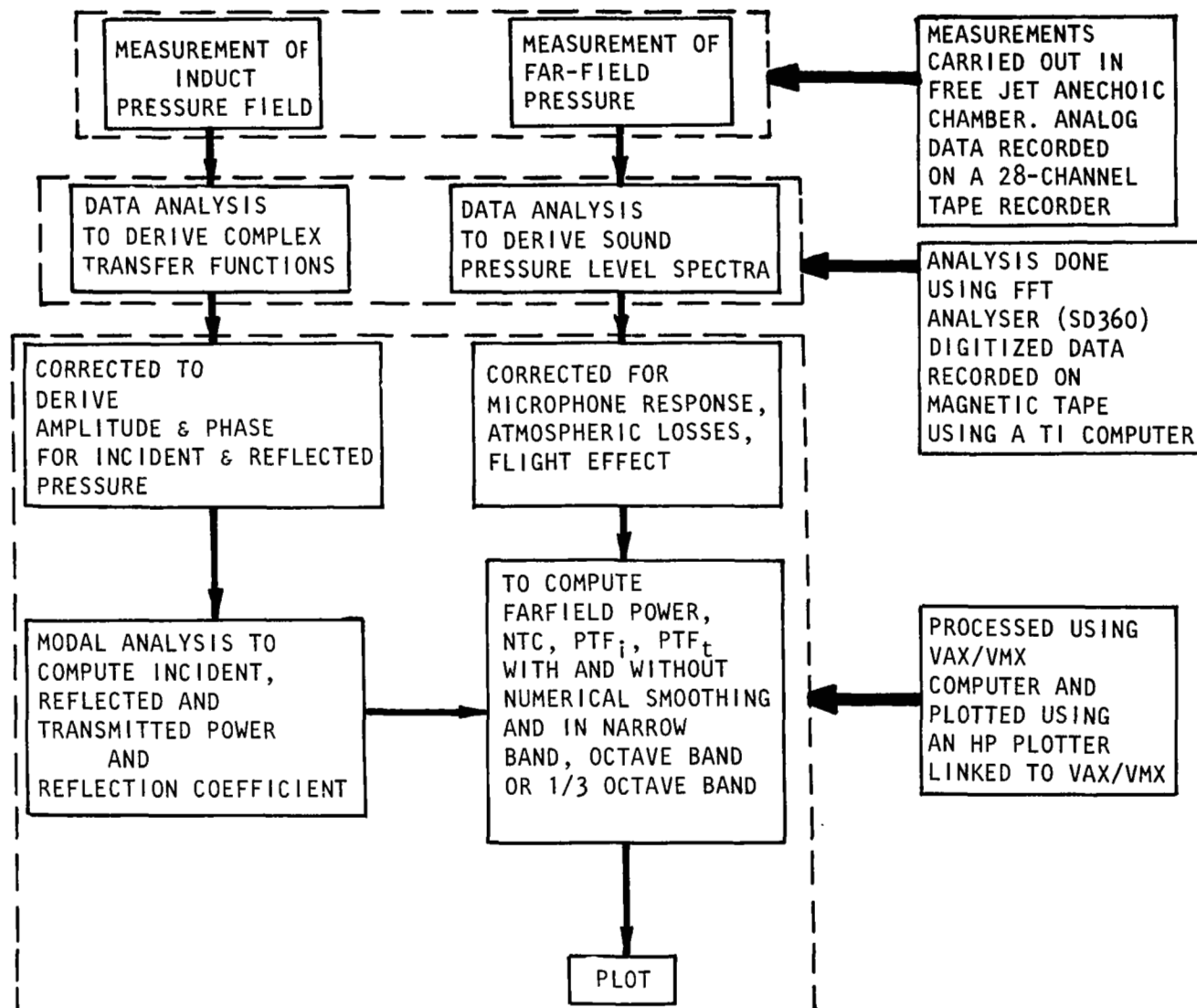


Figure 8.5 Schematic showing the data analysis procedure to derive various nozzle transmission parameters.

section 3). Finally, various parameters were plotted to show the effects of nozzle geometry, jet Mach number, and free-jet Mach number.

8.2 EXPERIMENTAL RESULTS

The characteristics of internal noise radiation from the 12-lobe 24-tube suppressor nozzle (i.e., the daisy lobe nozzle) and the reference conical nozzle, both with the same exit open area (equivalent diameter of 6.2 cm), tested statically and under flight simulation, are presented here. The effects of jet Mach number on the in-duct and far-field time histories, reflection coefficients, nozzle transfer functions and power transfer functions are first described in section 8.2.1. Following this, the results showing the effects of flight simulation on the same transmission parameters are then described in section 8.2.2.

8.2.1 Effects of Jet Mach Number

(1) In-Duct Time Histories

The induct time histories measured at six radial locations for the daisy lobe nozzle and the conical nozzle, without any jet flow, are shown in figure 8.6. It has already been observed from the results presented in section 5 that very little radial variation exists for the incident pressure pulse, especially for the no-flow condition. However, a hasty look at figure 8.6 indicates that the incident pulse measured at the center of the duct is quite different from the rest of the radial measurements. But, in reality, that is not the case. The apparent difference in pulse shapes is due to the difference in the frequency response of the microphones of the six-point probe. Although every effort was made to retain the same frequency response for each of the six microphones used in the probe, the one at the center did not come out that way due to the variation in tube length connecting the microphone to the flow field. However, this difference in frequency response is immaterial in deriving the final results, as long as it is properly accounted for in the data reduction.

Figure 8.6 clearly indicates the difference in the reflected wave between the two nozzles, even though the exit open area for the two are the same. The reflected pulse for the daisy lobe nozzle has two distinct portions, one due to the solid part reflection, in phase with the incident pulse, and the other due to the exit opening, out-of-phase with the incident pulse. In contrast, the reflected pulse for the reference conical nozzle is dominated by the open end reflection, out-of-phase to the incident pulse.

Figures 8.7 through 8.10 are the induct time histories for the daisy lobe nozzle and the reference conical nozzle at jet Mach numbers of 0.4, 0.6, 0.8 and 1.2, respectively. In each of these figures, six radial measurements are shown. For the daisy lobe nozzle, the open end

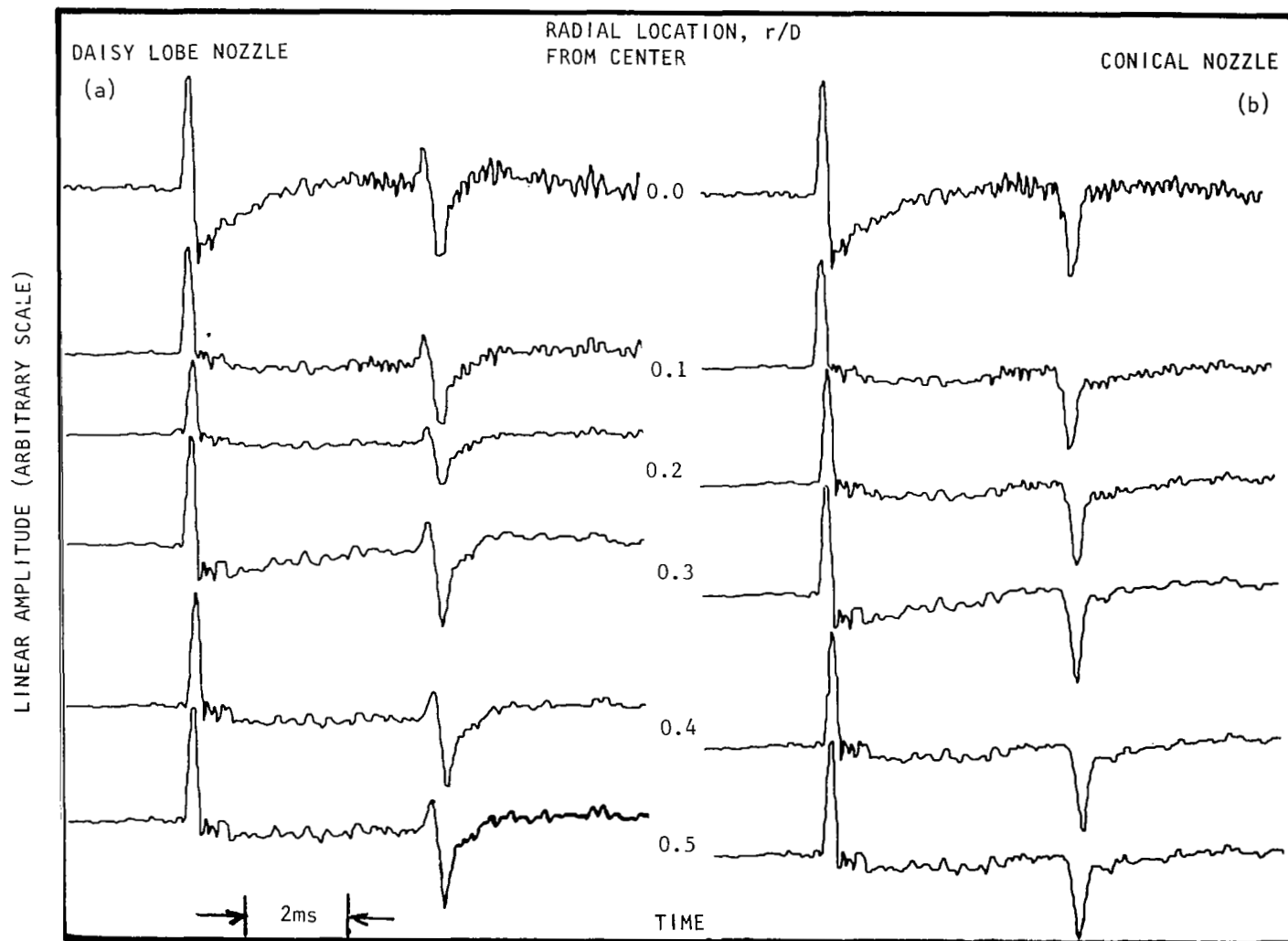


Figure 8.6 Induct time histories for (a) the daisy lobe nozzle and (b) the reference conical nozzle, showing the radial variation at $M_J = 0$ and $M_T = 0.00$.

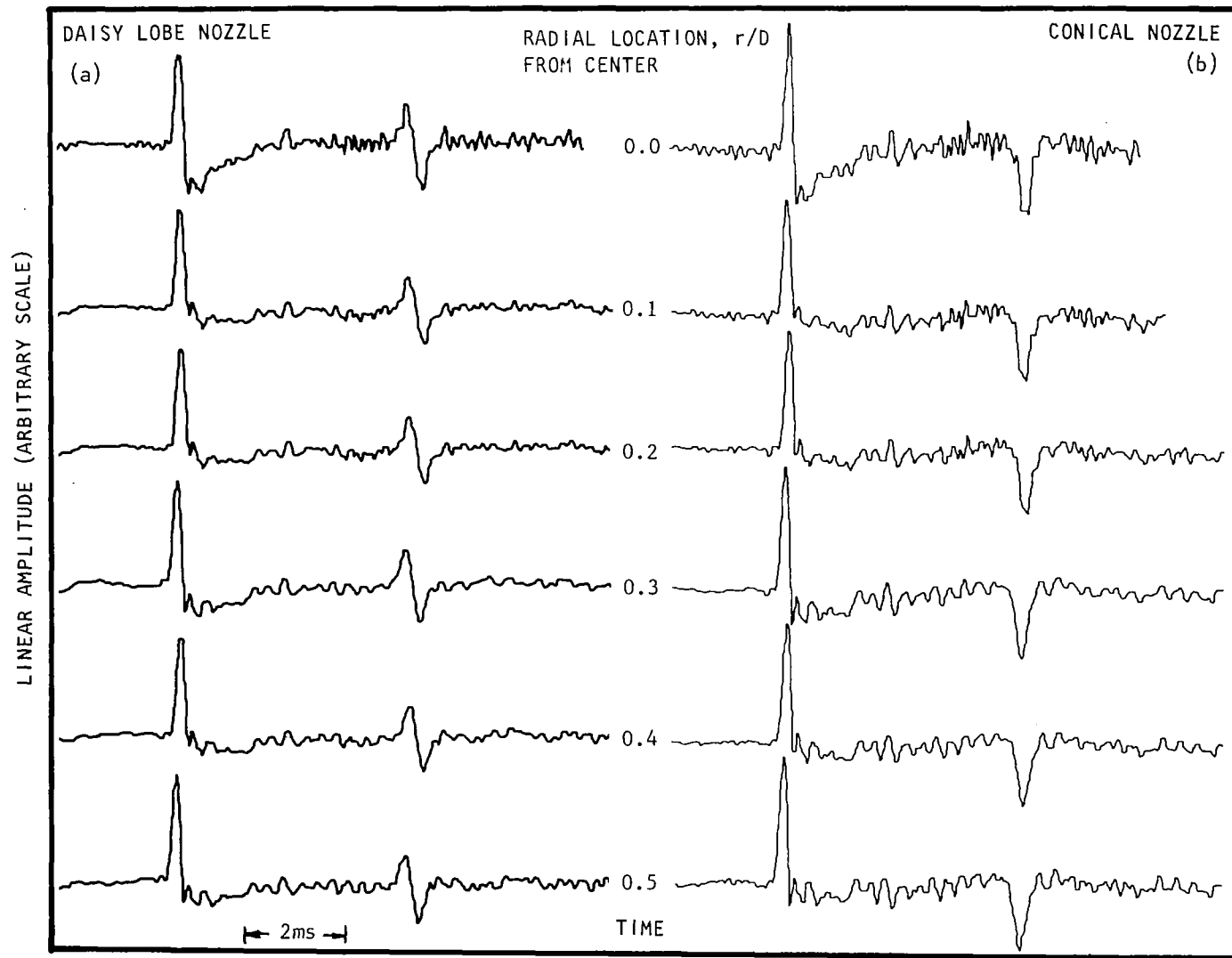


Figure 8.7 Induct time histories for (a) the daisy lobe nozzle and (b) the reference conical nozzle, showing the radial variation at $M_J = 0.4$ and $M_T = 0.00$.

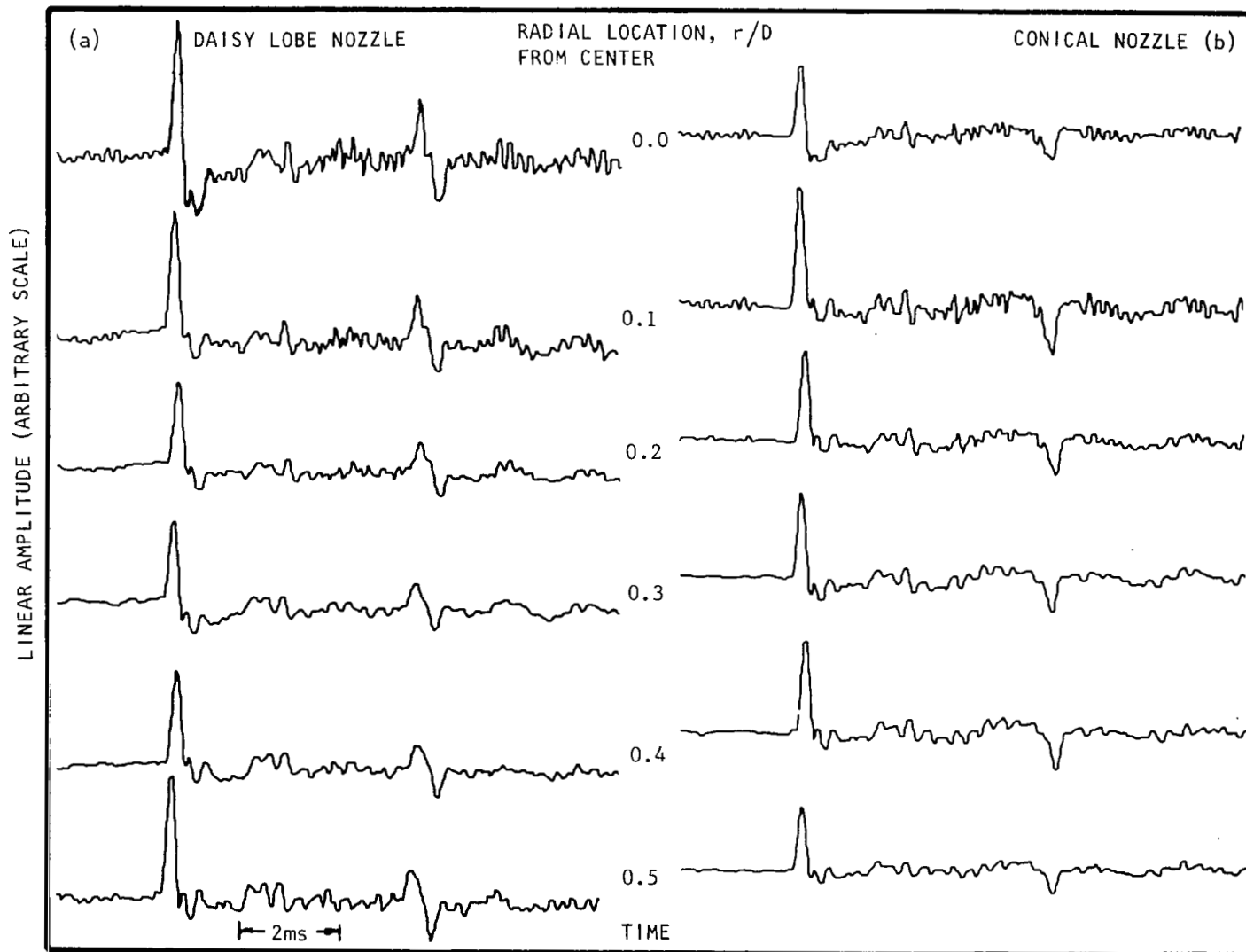


Figure 8.8 Induct time histories for (a) the daisy lobe nozzle and (b) the reference conical nozzle, showing the radial variation at $M_J = 0.6$ and $M_T = 0.00$.

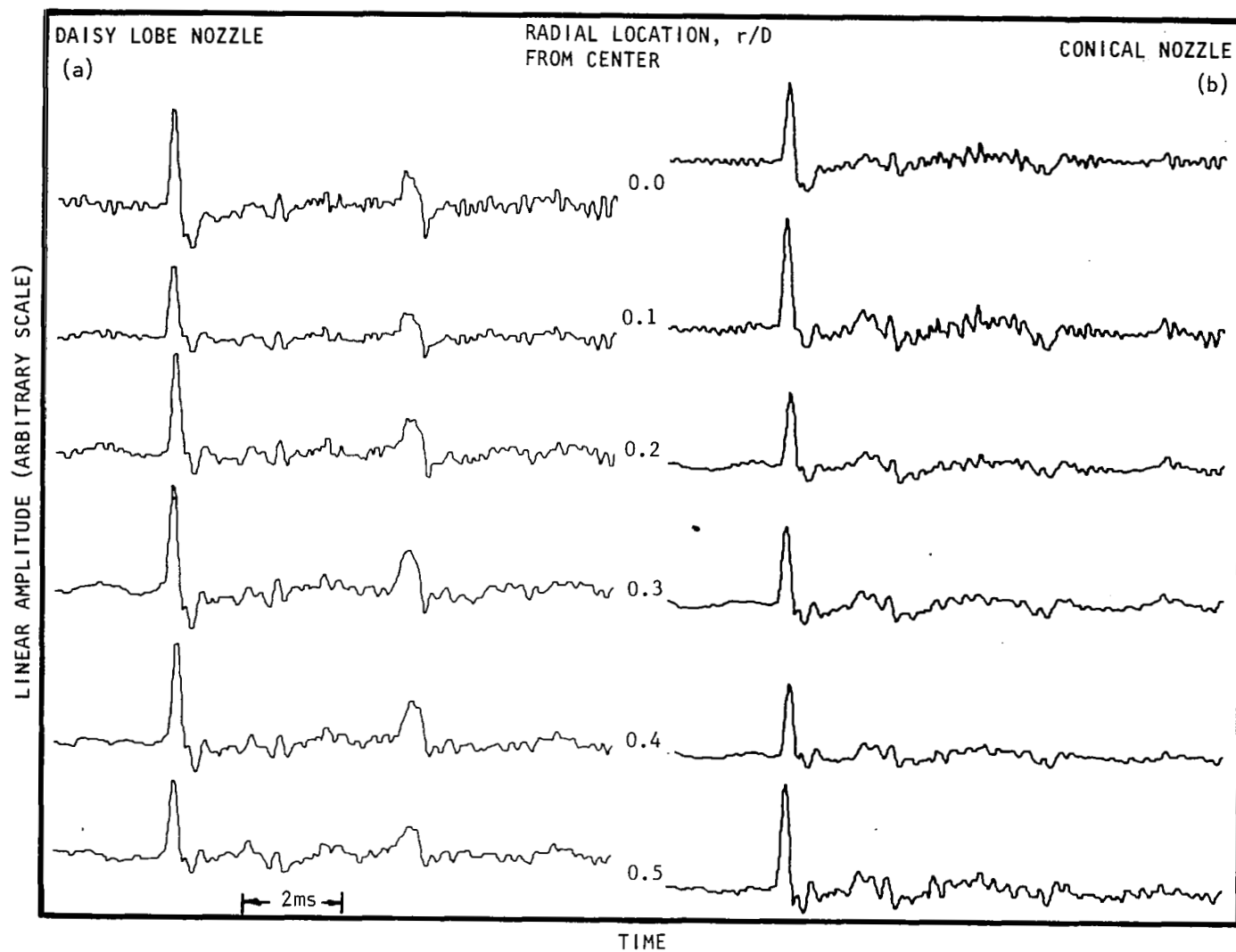


Figure 8.9 Induct time histories for (a) the daisy lobe nozzle and (b) the reference conical nozzle, showing the radial variation at $M_J = 0.8$ and $M_T = 0.00$.

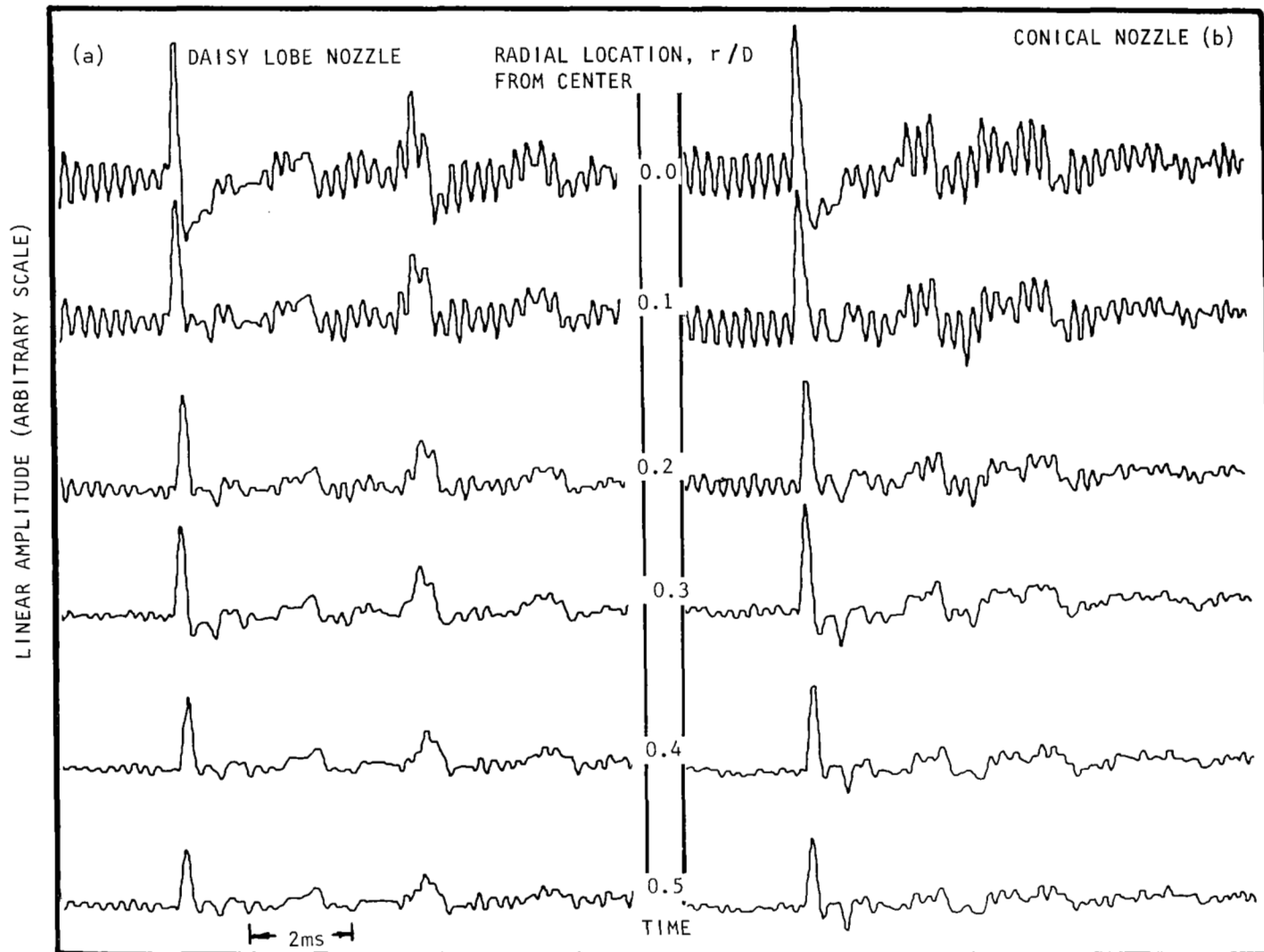


Figure 8.10 Induct time histories for (a) the daisy lobe nozzle and (b) the reference conical nozzle, showing the radial variation at $M_J = 1.2$ and $M_T = 0.00$.

reflection gradually diminishes with increasing jet flow. For $M_J = 0.8$ and $M_J = 1.2$, very small portion of this out-of-phase reflection is left. The in-phase reflection gradually gets wider with increasing flow, indicating less high-frequency content in it. For the conical nozzle, however, the reflected pulse (out-of-phase) gradually gets smaller with increasing flow and becomes almost insignificant at $M_J = 0.8$ and $M_J = 1.2$, indicating complete transmission of the incident pulse. Therefore, from these observations, it can be expected that with increasing flow the daisy lobe nozzle will have higher reflection coefficient compared to the reference conical nozzle. Later in this section, it will be shown that this is indeed the case.

(2) Reflection Coefficients

The reflection coefficients for the daisy lobe nozzle (σ_{DL}) and the reference conical nozzle (σ_C), showing the effects of jet Mach number, are presented in figure 8.11. As expected from the reflected time histories, the reflection coefficients decrease with increasing jet Mach number in the frequency range of 1 KHz to 3 KHz. At higher frequencies the trend seems to be reversed, although the high-frequency behavior is not consistent. Moreover, the reflection coefficient spectrum for $M_J = 1.2$ does not behave in the manner as that observed for other Mach numbers, specially for the reference conical nozzle.

To show the effect of nozzle geometry, the reflection coefficient spectra for the daisy lobe nozzle are compared with those for the reference conical nozzle at various jet Mach numbers in figure 8.12. At lower jet Mach numbers (i.e. for $M_J = 0, .4$ and $.6$), the difference between these spectra is relatively small. However, at higher Mach numbers (i.e. at $M_J = 0.8$ and 1.2), the conical nozzle reflection coefficients are considerably lower than those for the daisy lobe nozzle, specially in the lower frequency range (below 5 KHz).

The spectral behavior for the daisy lobe nozzle reflection coefficient, as observed in the present study, is similar to that for the reference conical nozzle, which is in contrast with the observations made from the results derived in Phase II of this contract. This is further addressed in the last section of this report, where all the relevant conclusions are presented.

(3) Far-Field Time Histories

Typical far-field time histories for the daisy lobe nozzle and the reference conical nozzle are shown in figures 8.13 and 8.14, respectively. Data for $M_J = 0.0, 0.6$ and 1.2 are shown at $\theta = 30^\circ, 60^\circ, 90^\circ$ and 120° . The time histories shown here have fixed time scale but arbitrary amplitude scale. The main purpose of these figures, however, is to examine the narrowing or widening of the pulses as a function of angle and jet Mach number.

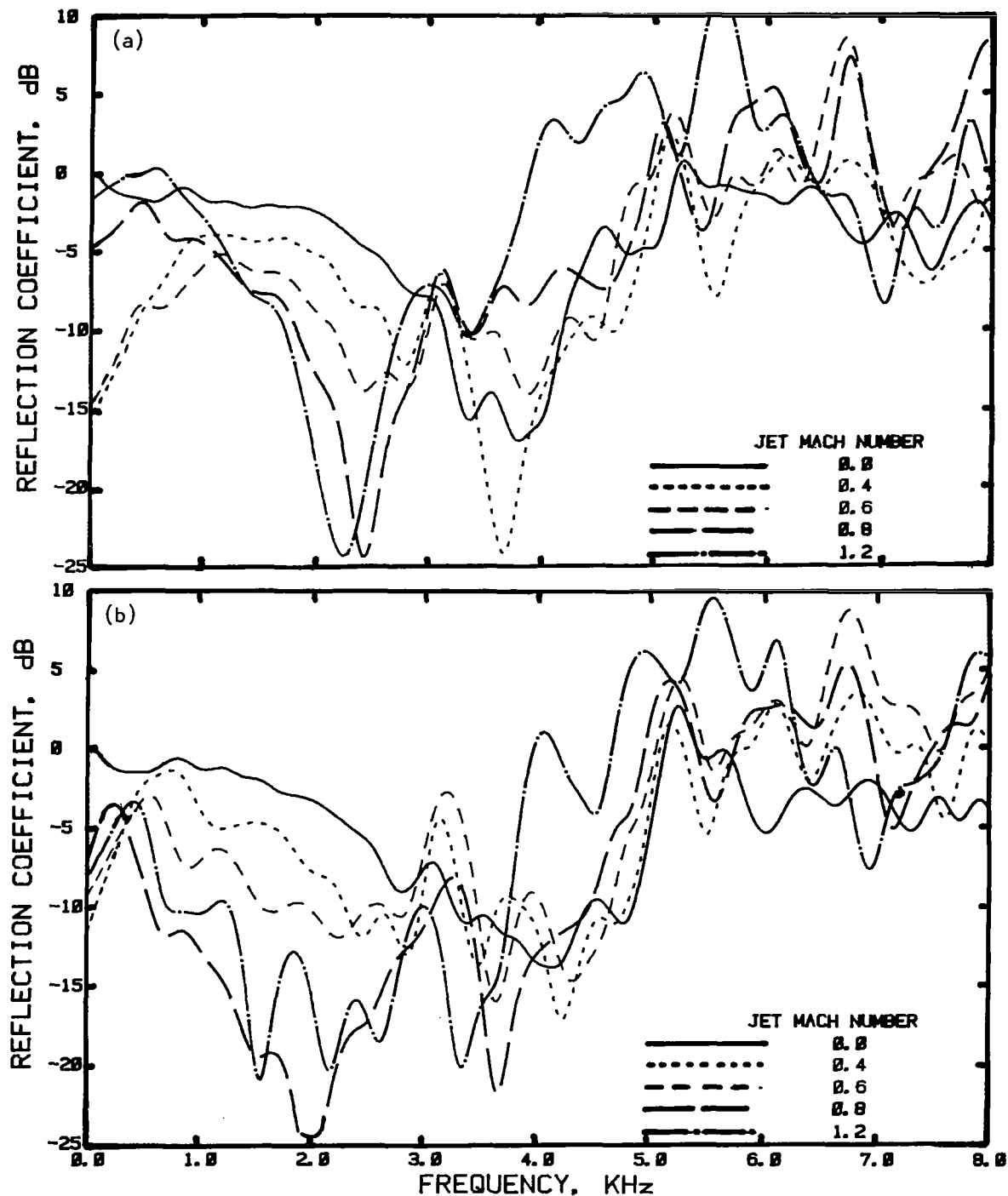


Figure 8.11 Effect of jet Mach number on the reflection coefficient spectra for (a) the daisy lobe nozzle and (b) the reference conical nozzle, $M_T = 0.00$

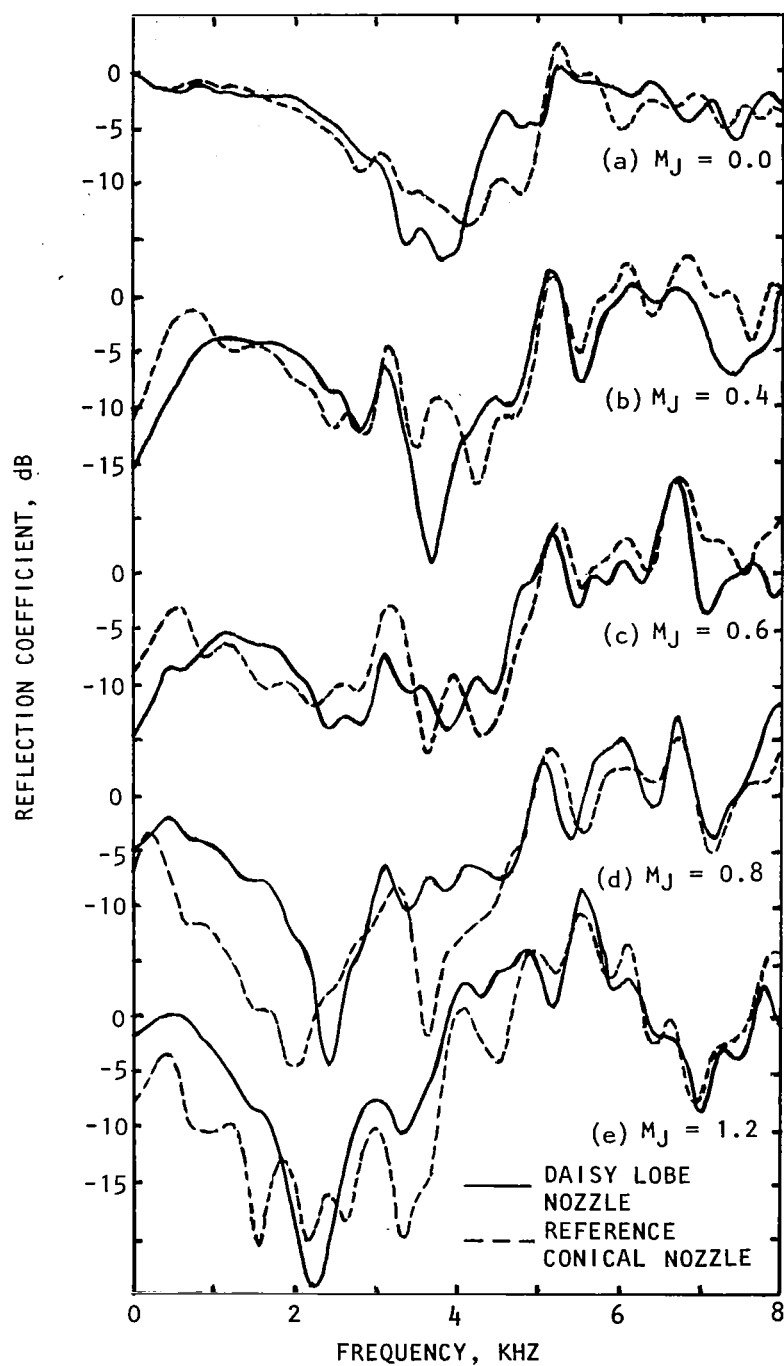


Figure 8.12 Effect of nozzle geometry on reflection coefficient spectra for various jet Mach numbers, $M_T = 0.00$.

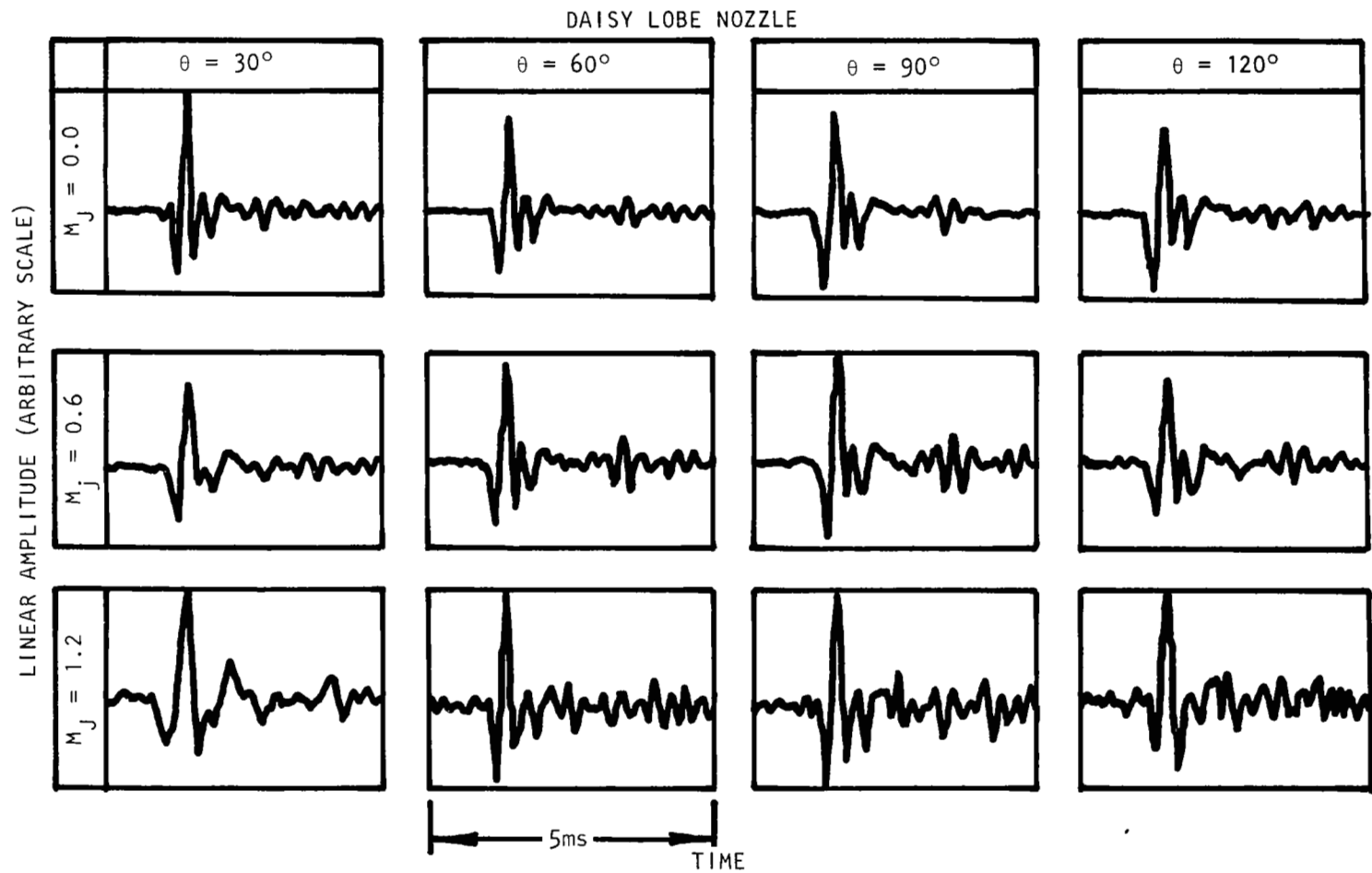


Figure 8.13 Far field time histories for the daisy lobe nozzle at various polar angles, θ and jet Mach numbers, M_j ; $M_T = 0.00$.

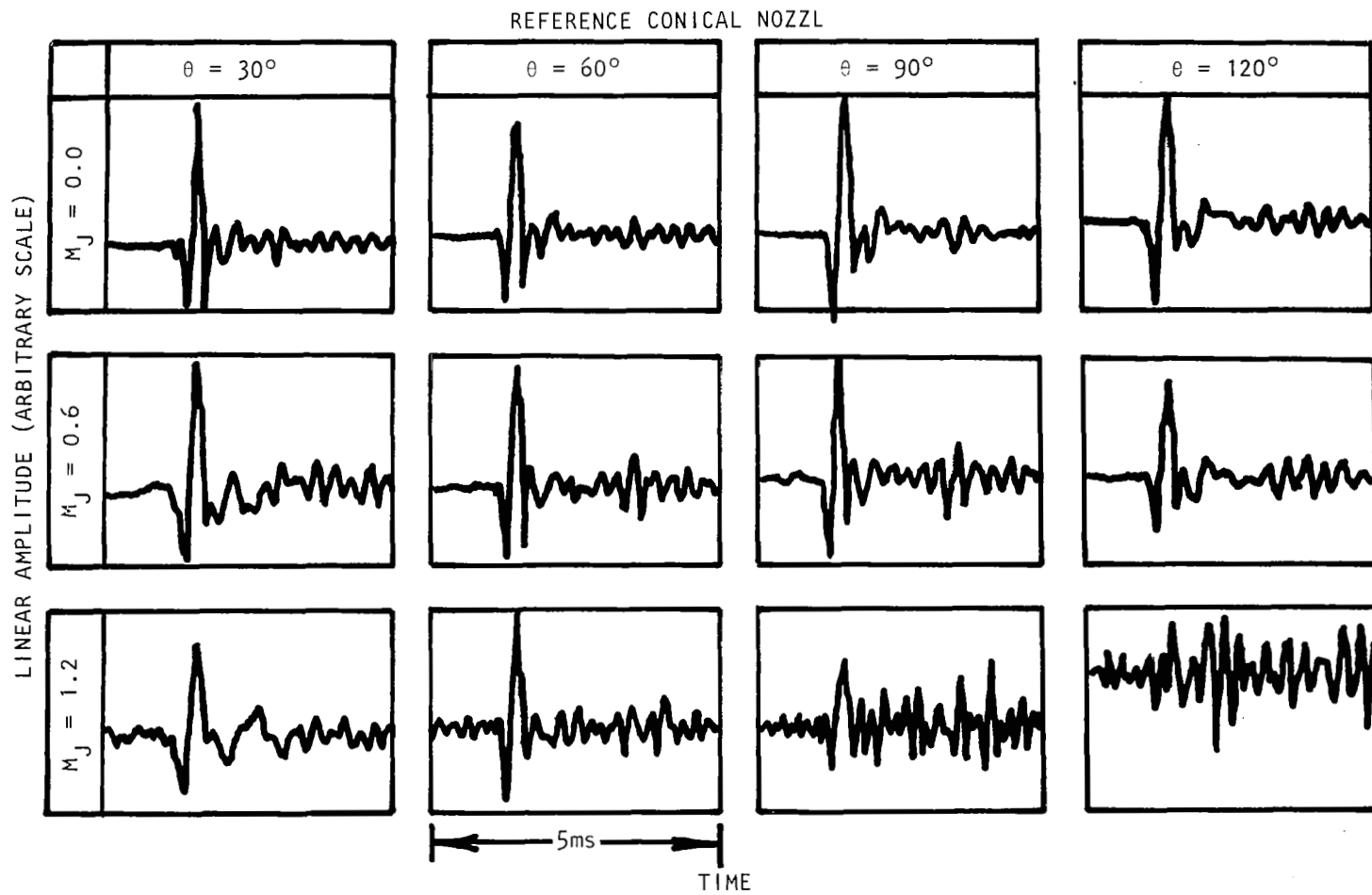


Figure 8.14 Far field time histories for the reference conical nozzle at various polar angles, θ and jet Mach numbers, M_J ; $M_T = 0.00$.

There are only minor differences in the far-field signals for the two nozzles. For zero flow, both nozzles display narrower pulses at small angles compared to the large angles, thus indicating more high-frequency radiation at small angles. As the jet Mach number is increased, the effect of refraction becomes important in that the pulse at small angles (i.e., $\theta = 30^\circ$) becomes wider, indicating depletion of high-frequency sound which apparently has been refracted to larger angles (i.e., $\theta = 60^\circ$). This effect becomes stronger as the jet Mach number is increased from $M_j = 0.6$ to 1.2.

(4) Nozzle Transfer Function (NTF) (Normalized Transmission Coefficient)

Typical nozzle transfer function (NTF) spectra for the daisy lobe nozzle and the reference conical nozzle at $\theta = 30^\circ, 60^\circ, 90^\circ$ and 120° for $M_j = 0.0, 0.4, 0.6$ and 0.8 are presented in figures 8.15 and 8.16, respectively. These figures show that at zero flow condition the radiation is predominantly towards the jet axis since the spectral content of NTF values at smaller polar angles are higher compared to those at higher polar angles. The NTF spectral distributions in the presence of flow indicate increasing convection effect with the increasing jet velocity.

To examine the effect of refraction due to the increase of jet Mach number, the nozzle transfer functions for the daisy lobe nozzle and the reference conical nozzles are plotted for different jet Mach numbers with fixed polar angles θ , in figures 8.17 and 8.18, respectively. The increase of refraction effect at high frequencies is noticeable in these figures as the jet Mach number is increased. This is seen as a high frequency decrease in NTF level at $\theta = 30^\circ$ and a corresponding increase at $\theta = 60^\circ$.

These refraction effects can be seen more clearly by examining the radiation directivities at various frequencies and jet Mach numbers as shown in figures 8.19 and 8.20 for the daisy lobe nozzle and the reference conical nozzle, respectively. Here, the directivities for $M_j = 0.0, 0.4, 0.6$ and 0.8 are plotted for three frequencies, namely, 1 KHz, 2 KHz and 4 KHz. These results show that as the jet Mach number is increased, the refraction effect becomes more important. This is indicated by the fact that the NTF values at small angles to the jet axis decrease with increasing Mach number, and the effect is greater at high frequencies. A shift in the peak in directivity with increasing Mach number is also quite evident.

A comparison of the nozzle transfer function for the two nozzles at $\theta = 30^\circ, 60^\circ, 90^\circ$ and 120° is made for $M_j = 0.0, 0.6$ and 1.2 in figures 8.21 through 8.23, respectively. For all the jet Mach numbers, the nozzle transfer functions in the lower frequency range up to about 4 KHz have the same values for the two nozzles. At higher frequencies, small differences are observed in the NTF values between the two nozzles.

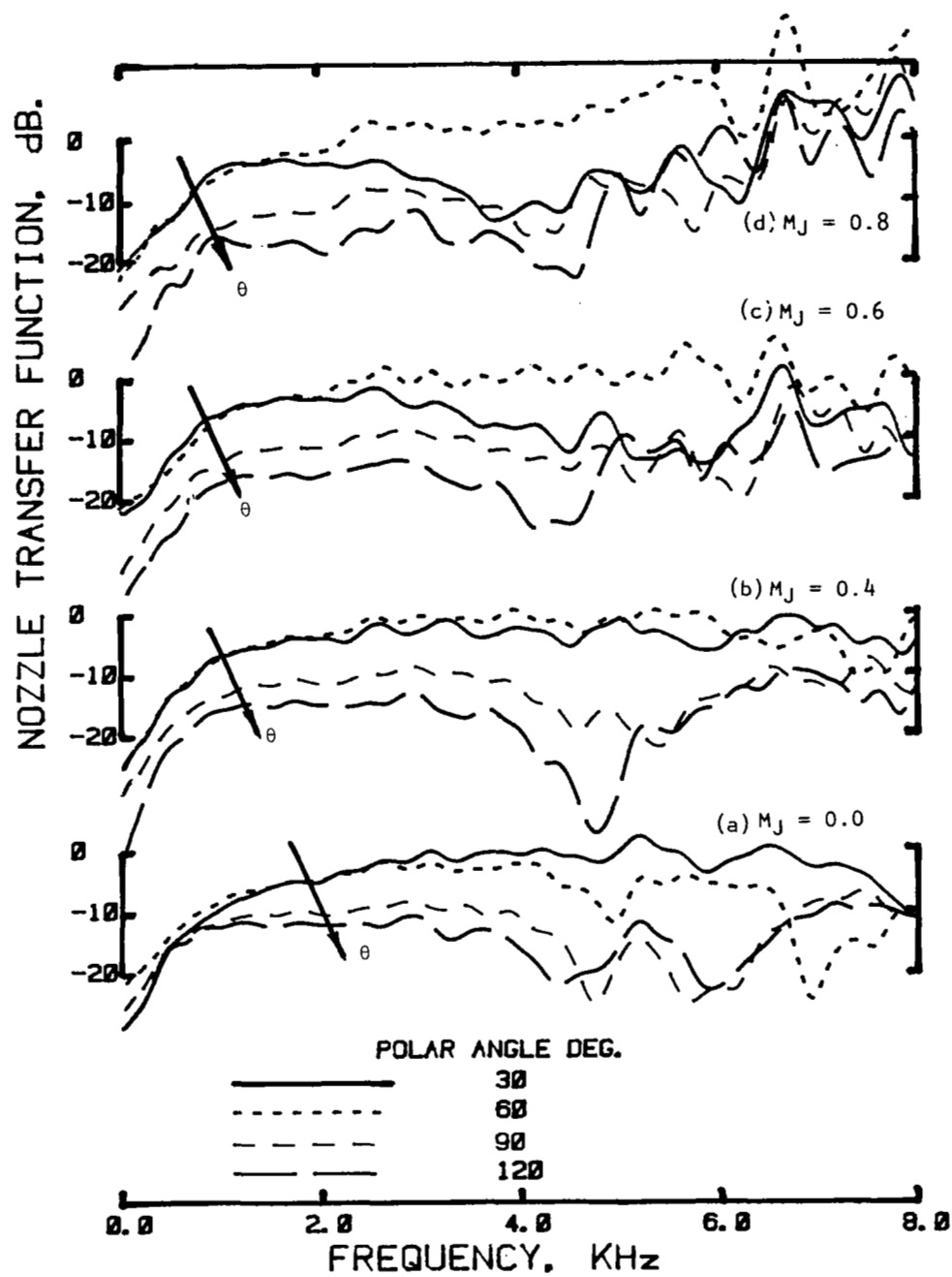


Figure 8.15 Variation of nozzle transfer function spectra with polar angle θ at various jet Mach numbers, M_J for daisy lobe nozzle; $M_T = 0.00$.

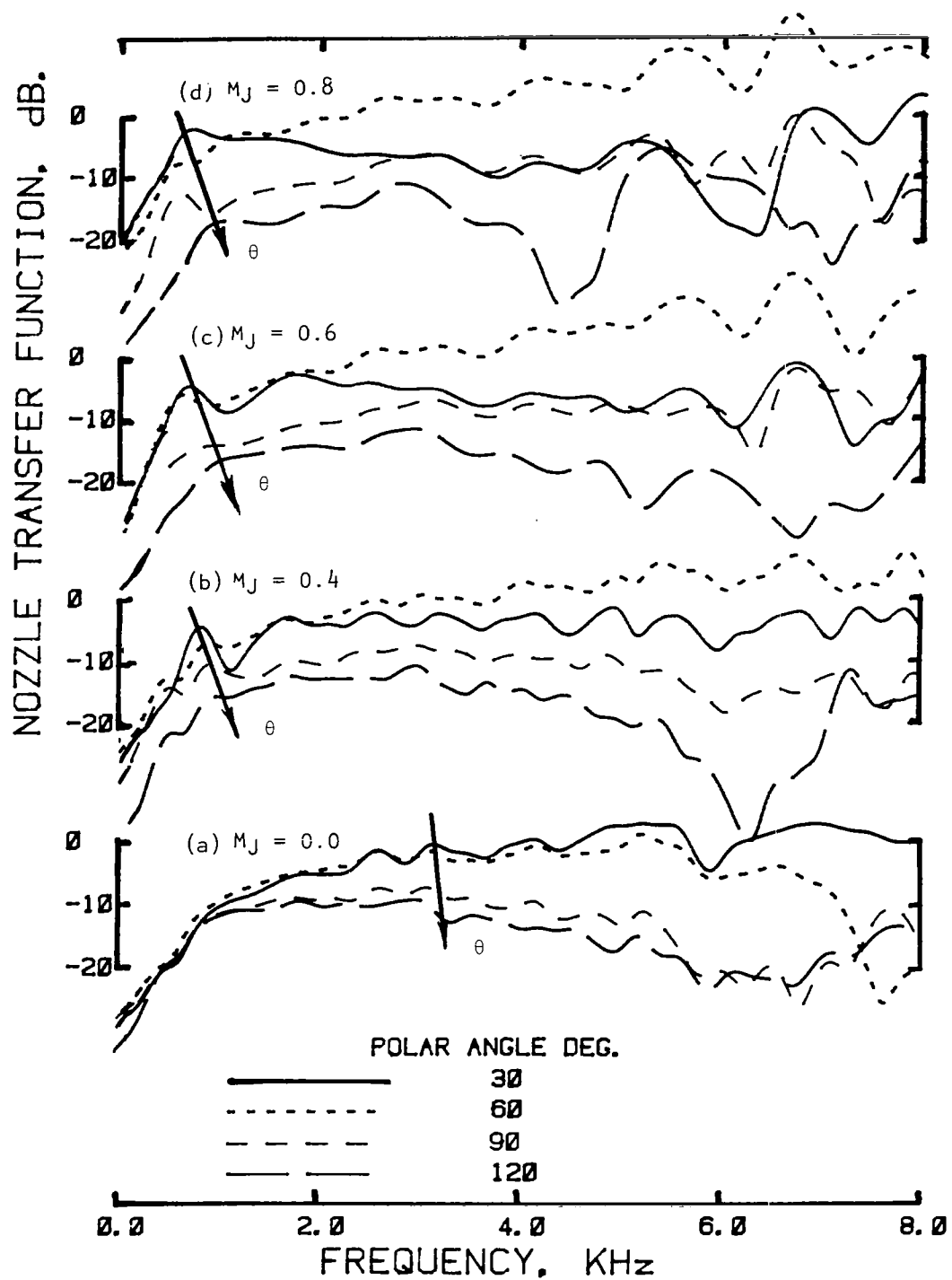


Figure 8.16 Variation of nozzle transfer function spectra with polar angle θ at various jet Mach numbers, M_J for reference conical nozzle; $M_T = 0.00$.

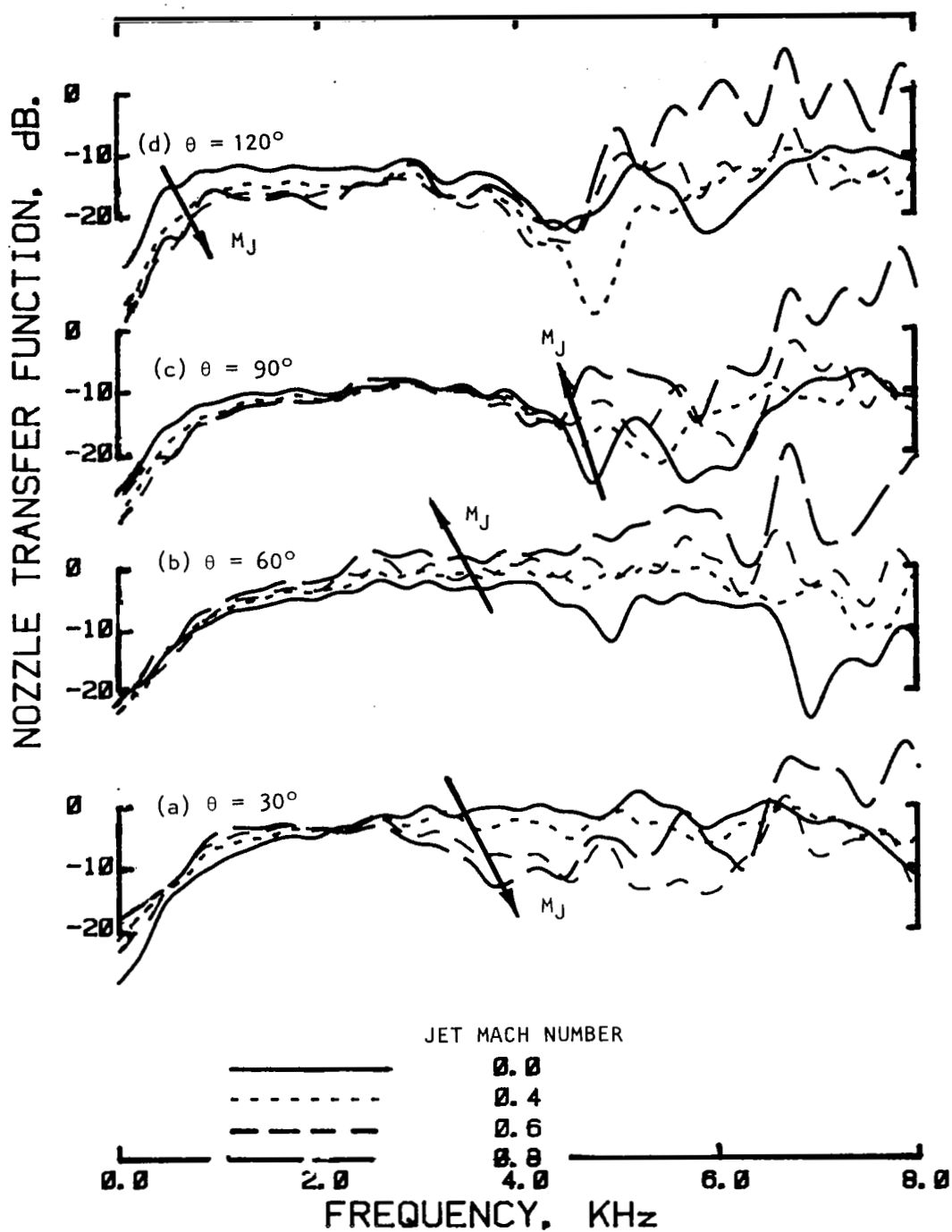


Figure 8.17 Variation of nozzle transfer function spectra with jet Mach number M_J at various polar angles, θ for daisy lobe nozzle; $M_T = 0.00$.

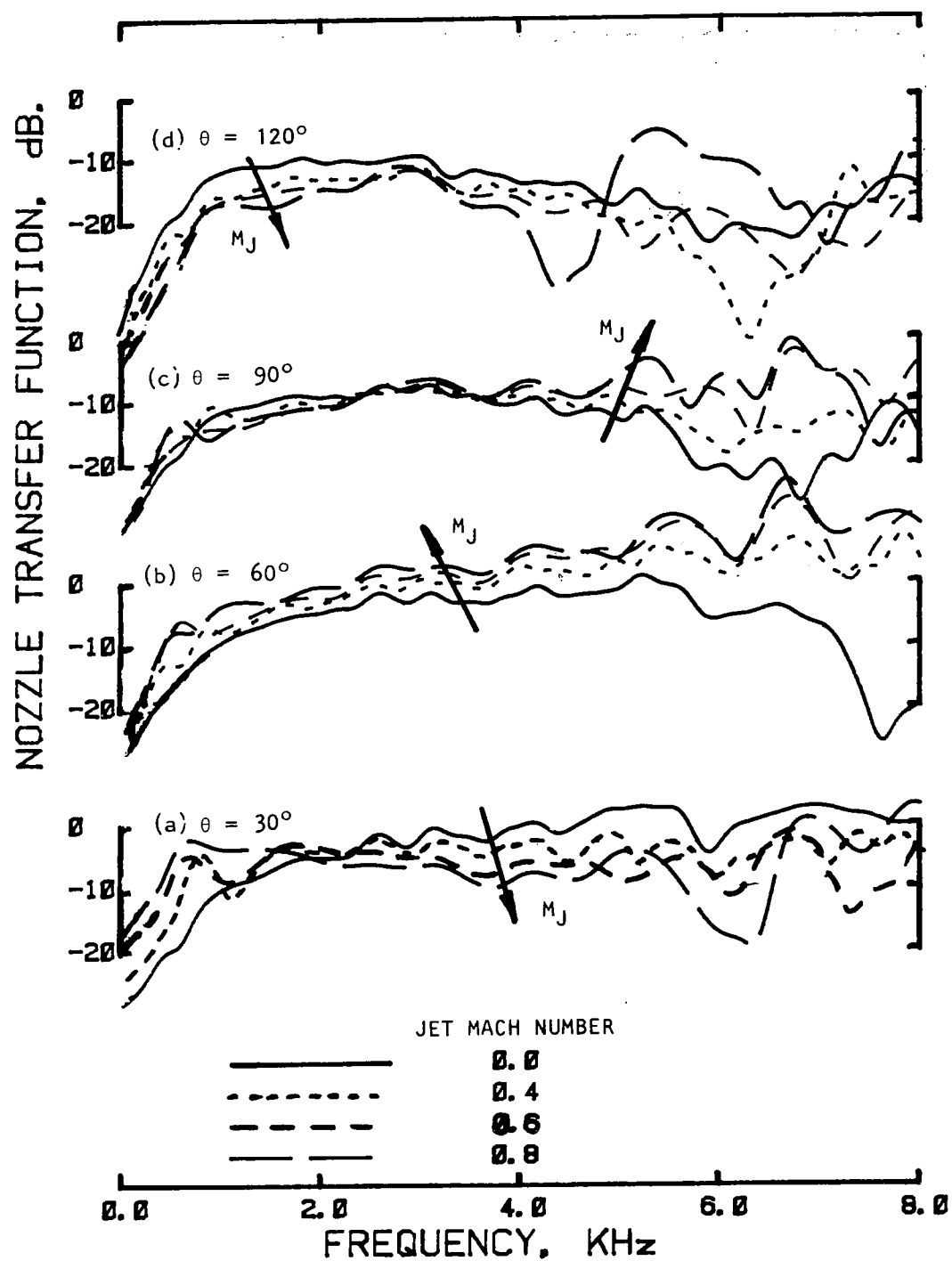


Figure 8.18 Variation of nozzle transfer function spectra with jet Mach number M_J at various polar angles, θ for reference conical nozzle; $M_T = 0.00$.

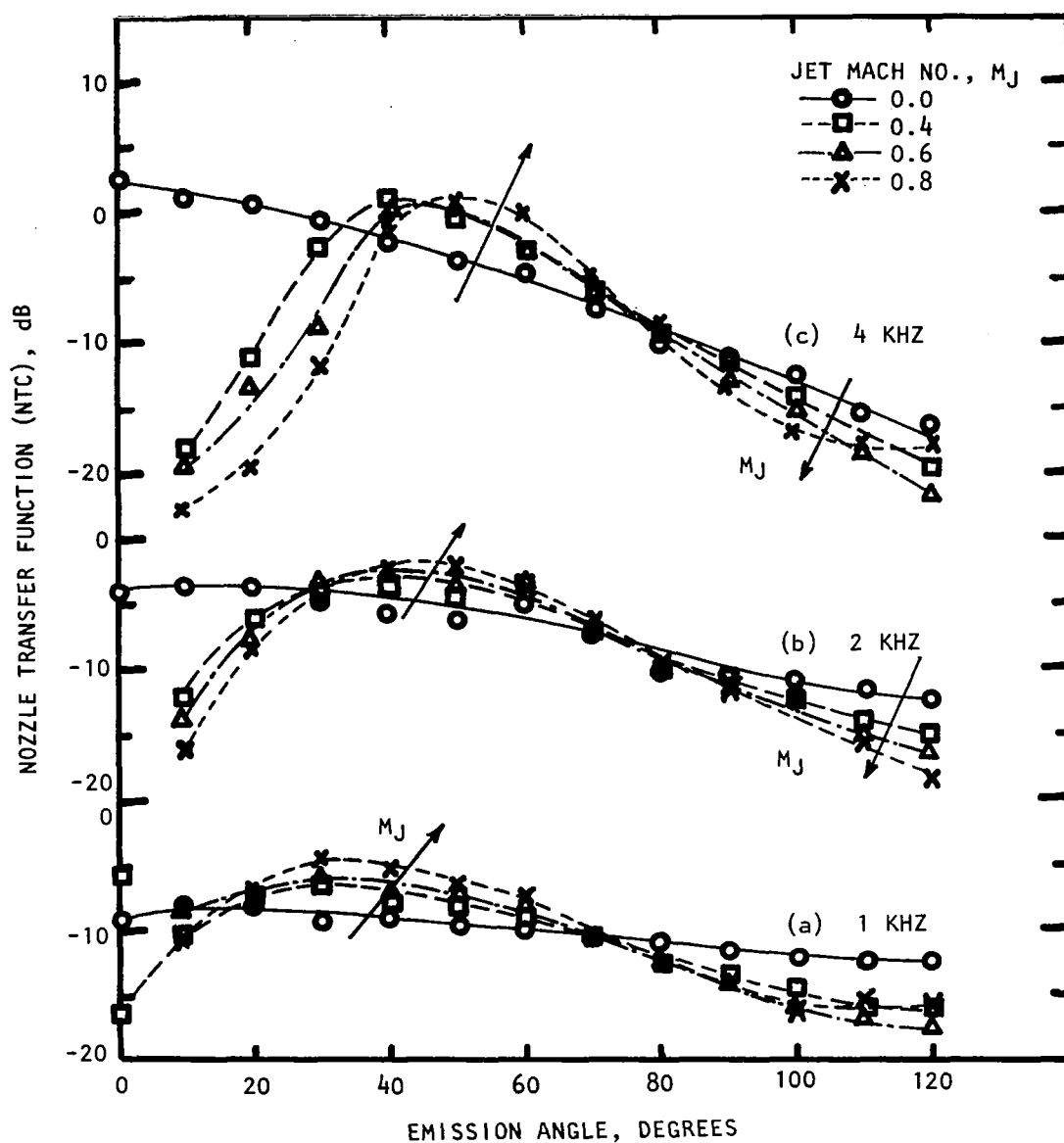


Figure 8.19 Effect of jet Mach number on the nozzle transfer function directivities for the daisy lobe nozzle at various frequencies; $M_T = 0.00$, (a) 1 KHZ, (b) 2 KHZ, (c) 4 KHZ.

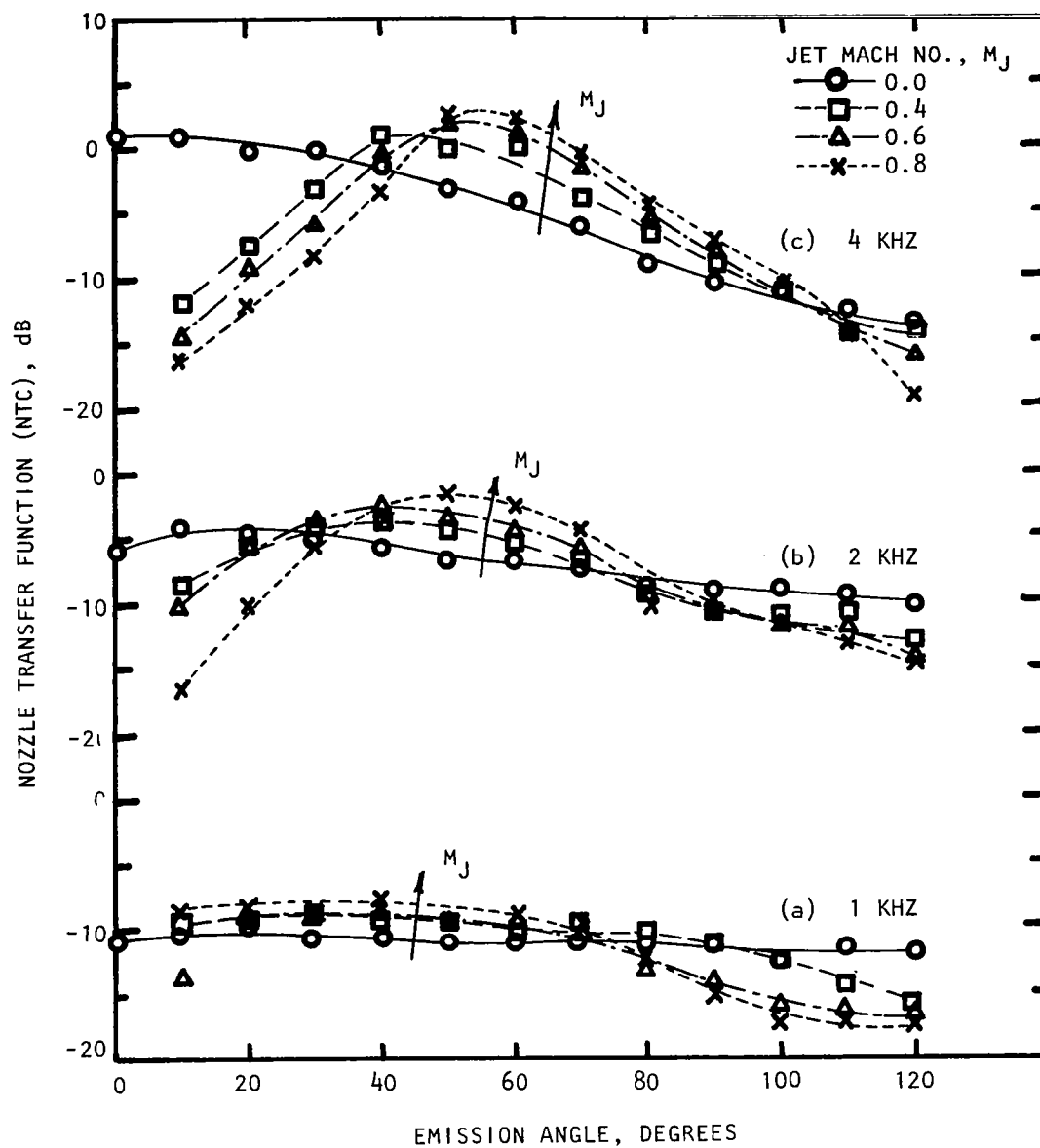


Figure 8.20 Effect of jet Mach number on the nozzle transfer function directivities for the reference conical nozzle at various frequencies; $M_T = 0.00$; (a) 1 KHZ, (b) 2 KHZ, (c) 4 KHZ.

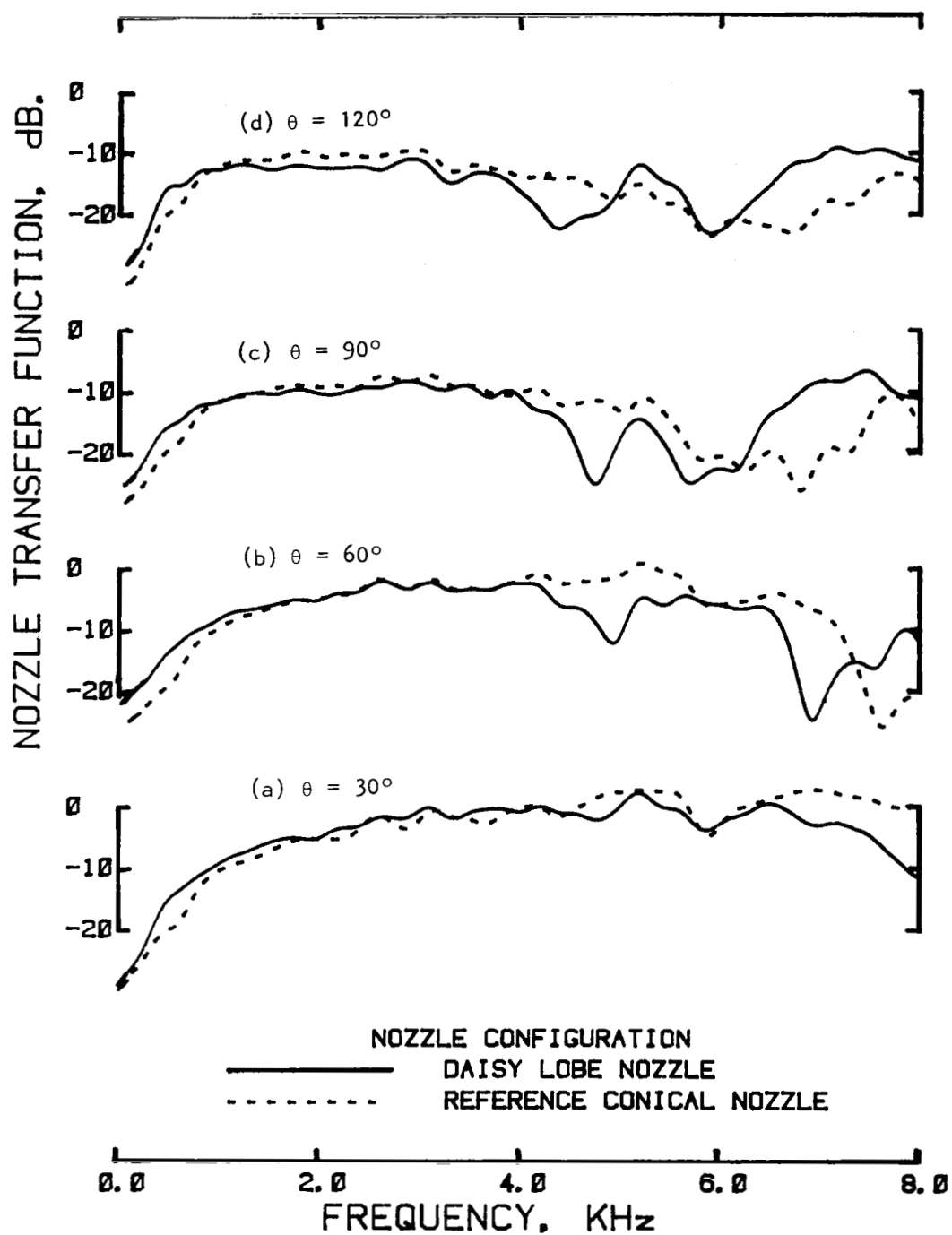


Figure 8.21 Effect of nozzle geometry on nozzle transfer function spectra at various polar angles, θ ; $M_J = 0.0$; $M_T = 0.00$.

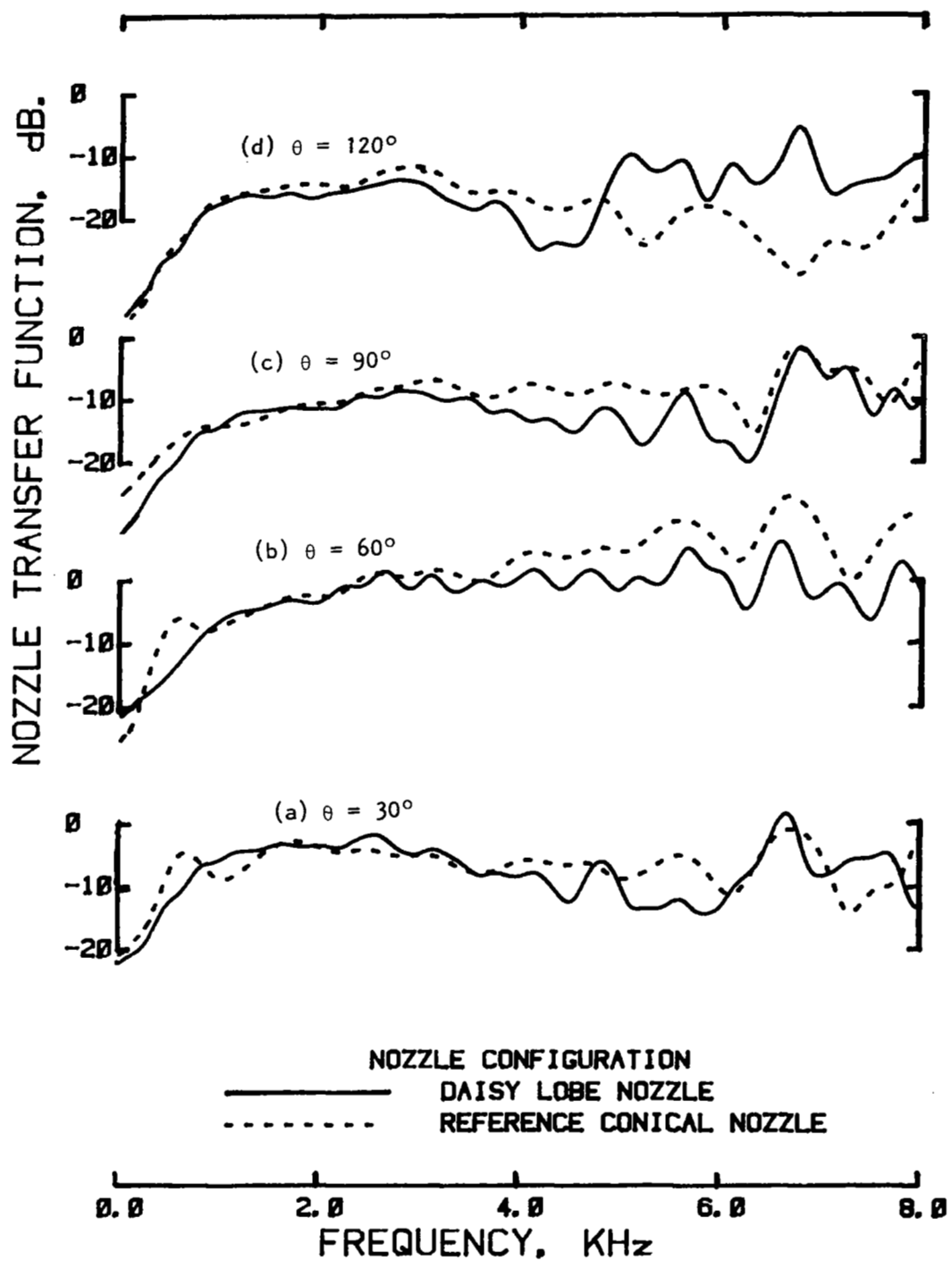


Figure 8.22 Effect of nozzle geometry on nozzle transfer function spectra at various polar angles, θ ; $M_j = 0.6$; $M_T = 0.00$.

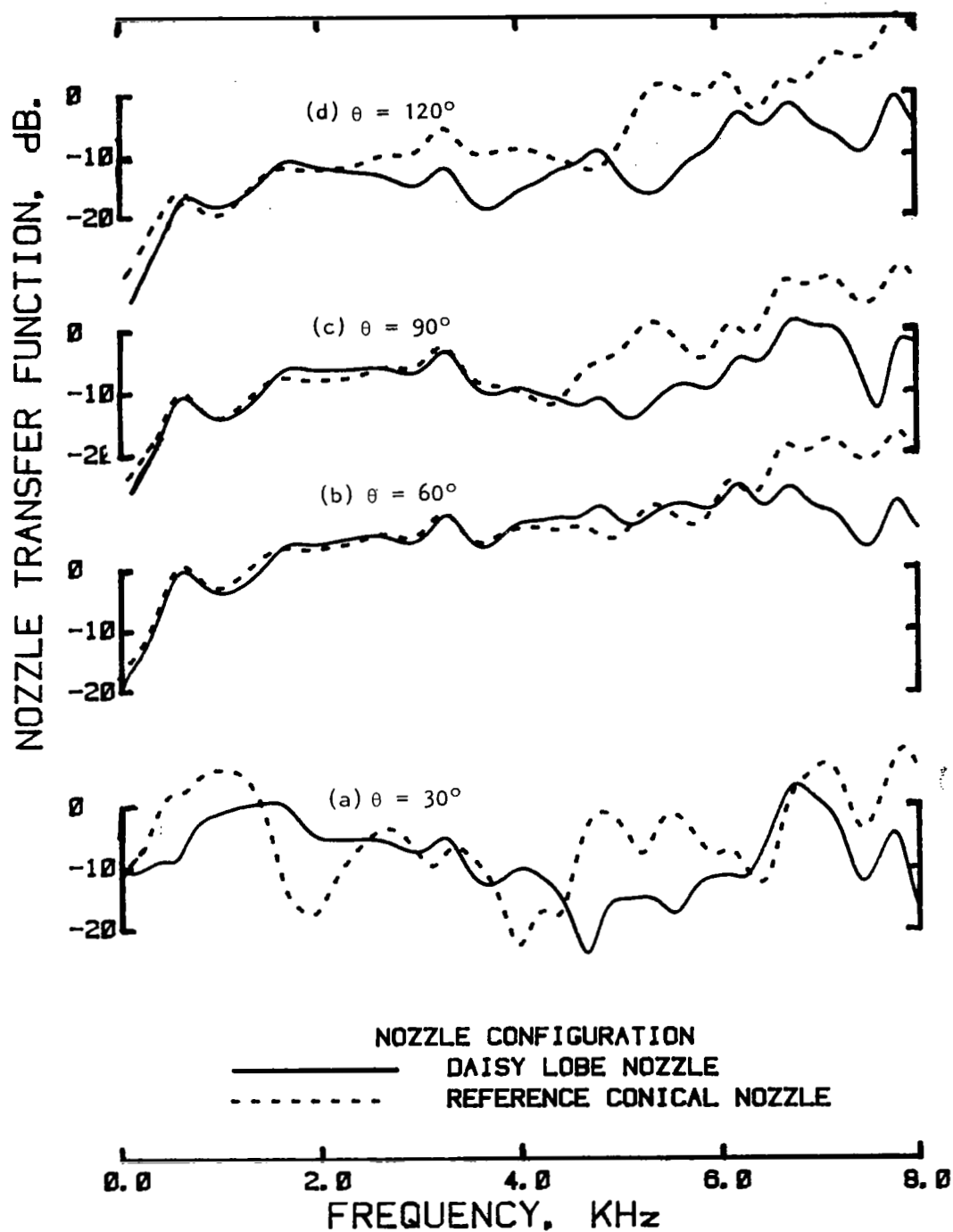


Figure 8.23 Effect of nozzle geometry on nozzle transfer function spectra at various polar angles, θ ; $M_J = 1.2$; $M_T = 0.0$.

However, the overall shape of the NTF spectra remains the same for the two nozzles for all flow conditions and at each polar angle.

Similar conclusions can also be drawn from the directivity plots shown in figures 8.24 through 8.26, where the NTF directivities for the two nozzles are compared at frequencies of 1 KHz, 2 KHz and 4 KHz at flow Mach numbers of 0.0, 0.6 and 1.2. This behavior indicates that it is the exit open area, and not the termination geometry, that predominantly controls the acoustic radiation.

A more accurate way to determine which of the two nozzles radiates internal noise more efficiently is to compare the far-field acoustic power radiated by each nozzle for the same incident power. Such a comparison is discussed in the next paragraph.

(5) Far-Field Power Normalized with Respect to Incident Power (PTF_i)

Figure 8.27 shows the effect of jet Mach number on the far-field power normalized with respect to incident power (PTF_i) for the daisy lobe nozzle and the reference conical nozzle. For both the nozzles, a small increase in far-field power is observed due to the increasing jet Mach number in the subsonic range. However, for $M_j = 1.2$, the increase in PTF_i is considerably higher over the whole frequency range, compared to the no-flow condition.

Figure 8.28 shows a comparison of the far-field acoustic power spectra normalized with respect to the incident power spectra for the daisy lobe nozzle and the reference conical nozzle for $M_j = 0.0, 0.4, 0.6, 0.8$ and 1.2 . For almost all flow conditions, the results show little difference in the radiated acoustic power levels for the two nozzles. Just like the NTF spectra and the directivities, the shapes of these PTF_i spectra are also almost identical for the two nozzles, thus further confirming that equivalent diameter is a good parameter to incorporate in frequency scaling to compare acoustic results from nozzles of different shapes.

(6) Far-Field Power Normalized With Respect to Transmitted Power (PTF_t)
- Power Imbalance

Figure 8.29 shows the effect of jet Mach number on the far-field power normalized with respect to transmitted power (PTF_t), which is nothing but the power imbalance, for the daisy lobe nozzle and the reference conical nozzle. These results are quite interesting in the low frequency range. Instead of obtaining power balance, a decrease in acoustic power is noticed at low frequencies for all jet Mach numbers including $M_j = 0$. Of course the levels at low frequencies can be expected to be higher (by about 2.5 dB), since the far-field power has been calculated for the angular range of 0° to 125° with the downstream jet axis. This does not, however, account for the 8 to 10 dB loss for $M_j = 0.0$. With the initiation of jet flow, the low-frequency power loss is

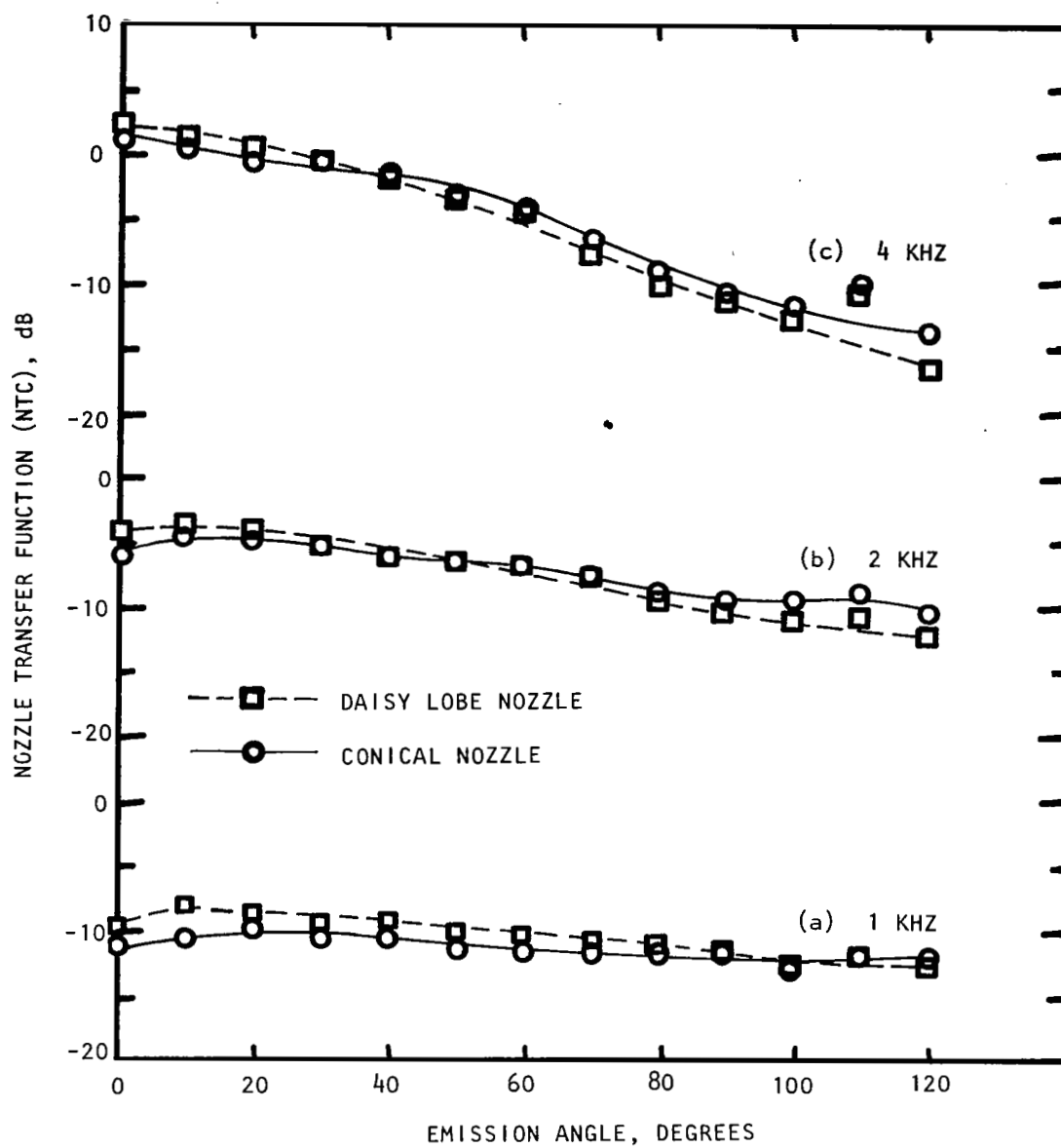


Figure 8.24 Effect of nozzle geometry on the nozzle transfer function directivities at various frequencies; $M_J = 0.0$, $M_T = 0.00$; (a) 1 KHZ, (b) 2 KHZ, (c) 4 KHZ.

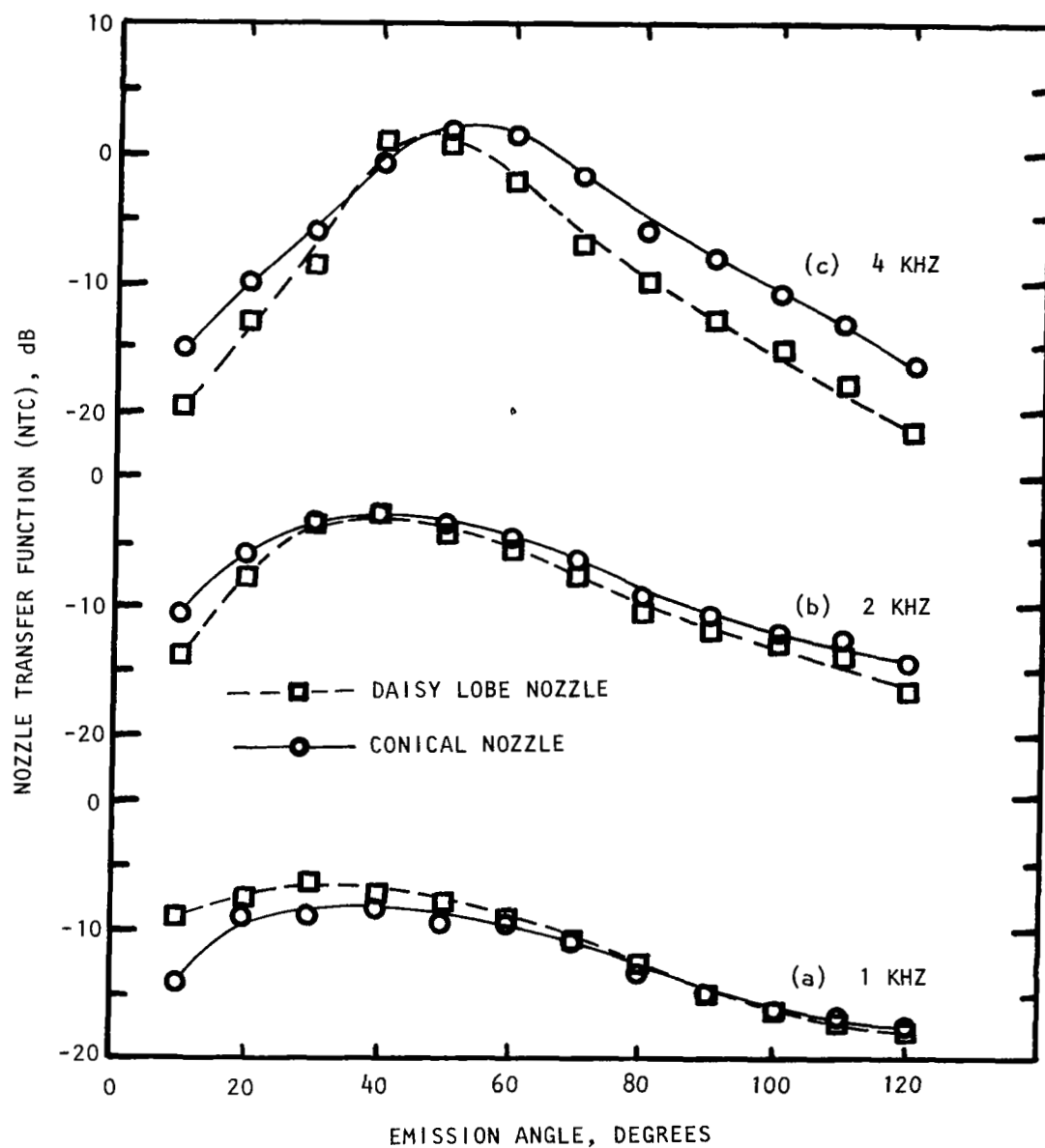


Figure 8.25 Effect of nozzle geometry on the nozzle transfer function directivities at various frequencies; $M_J = 0.6$, $M_T = 0.00$; (a) 1 KHz, (b) 2 KHz, (c) 4 KHz.

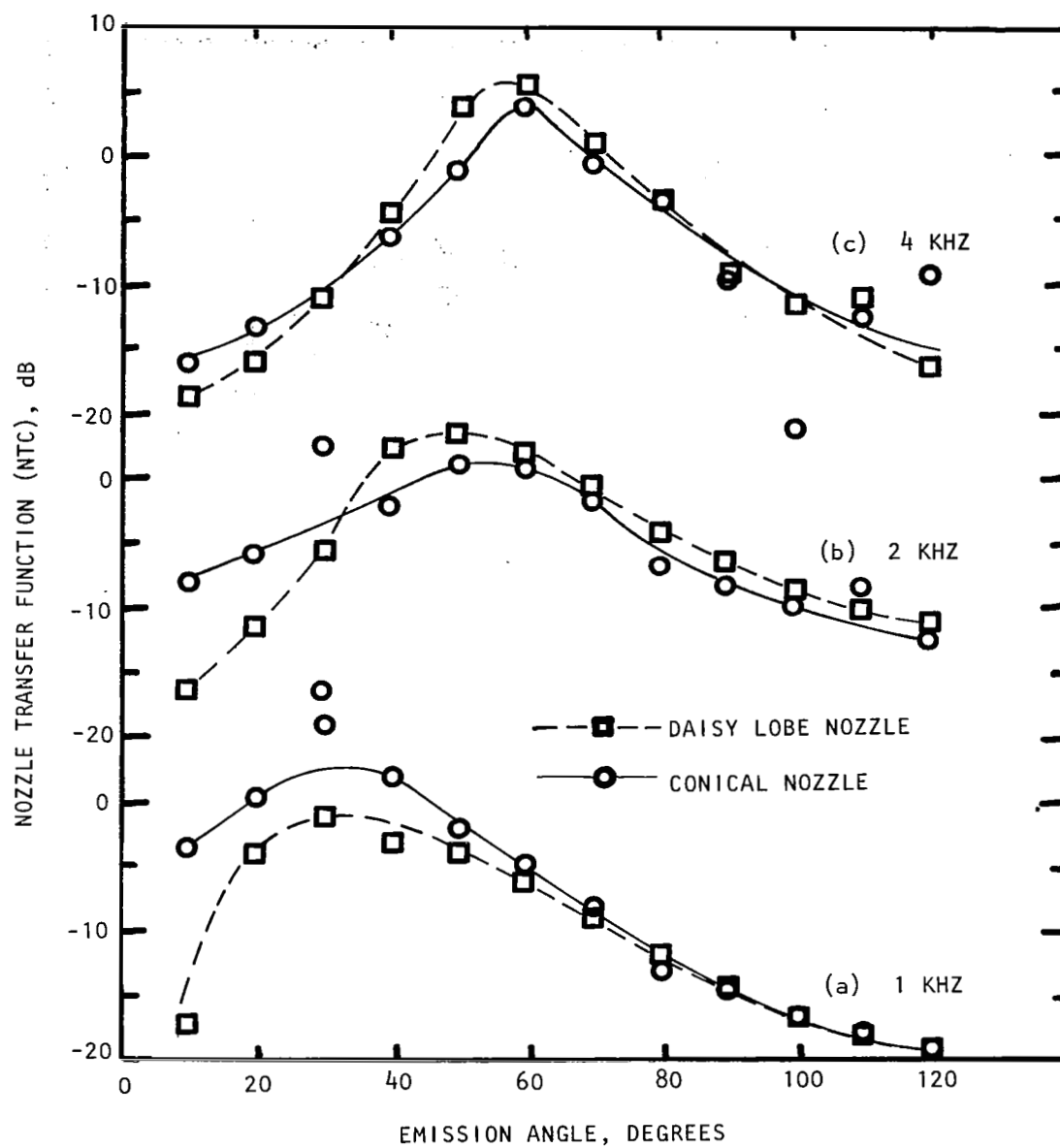


Figure 8.26 Effect of nozzle geometry on the nozzle transfer function directivities at various frequencies; $M_J = 1.2$, $M_T = 0.00$; (a) 1 KHz, (b) 2 KHz, (c) 4 KHz.

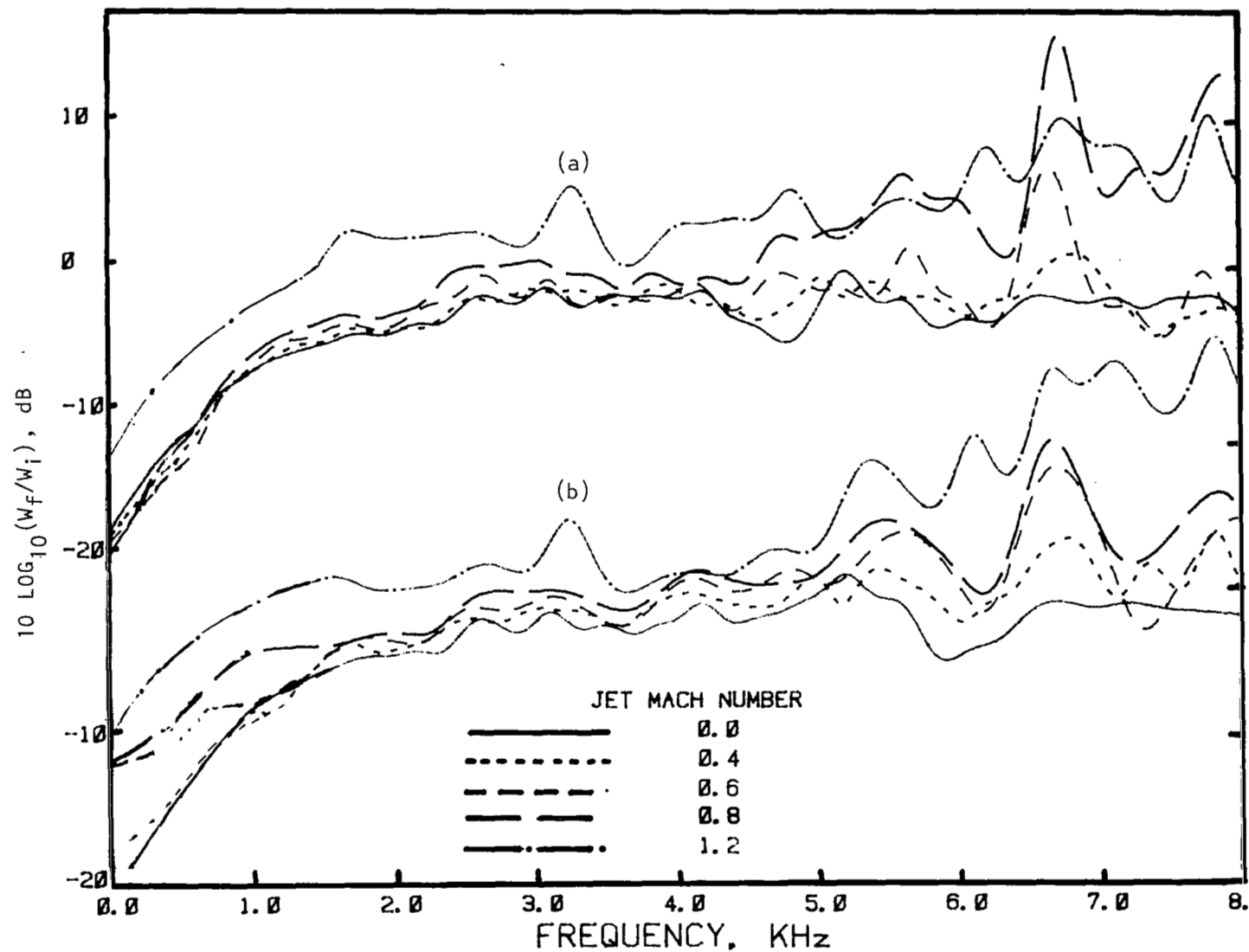


Figure 8.27 Effect of jet Mach number on far-field acoustic power normalized with respect to incident power (PTF_i) for (a) the daisy lobe nozzle, and (b) the reference conical nozzle; $M_T = 0.00$.

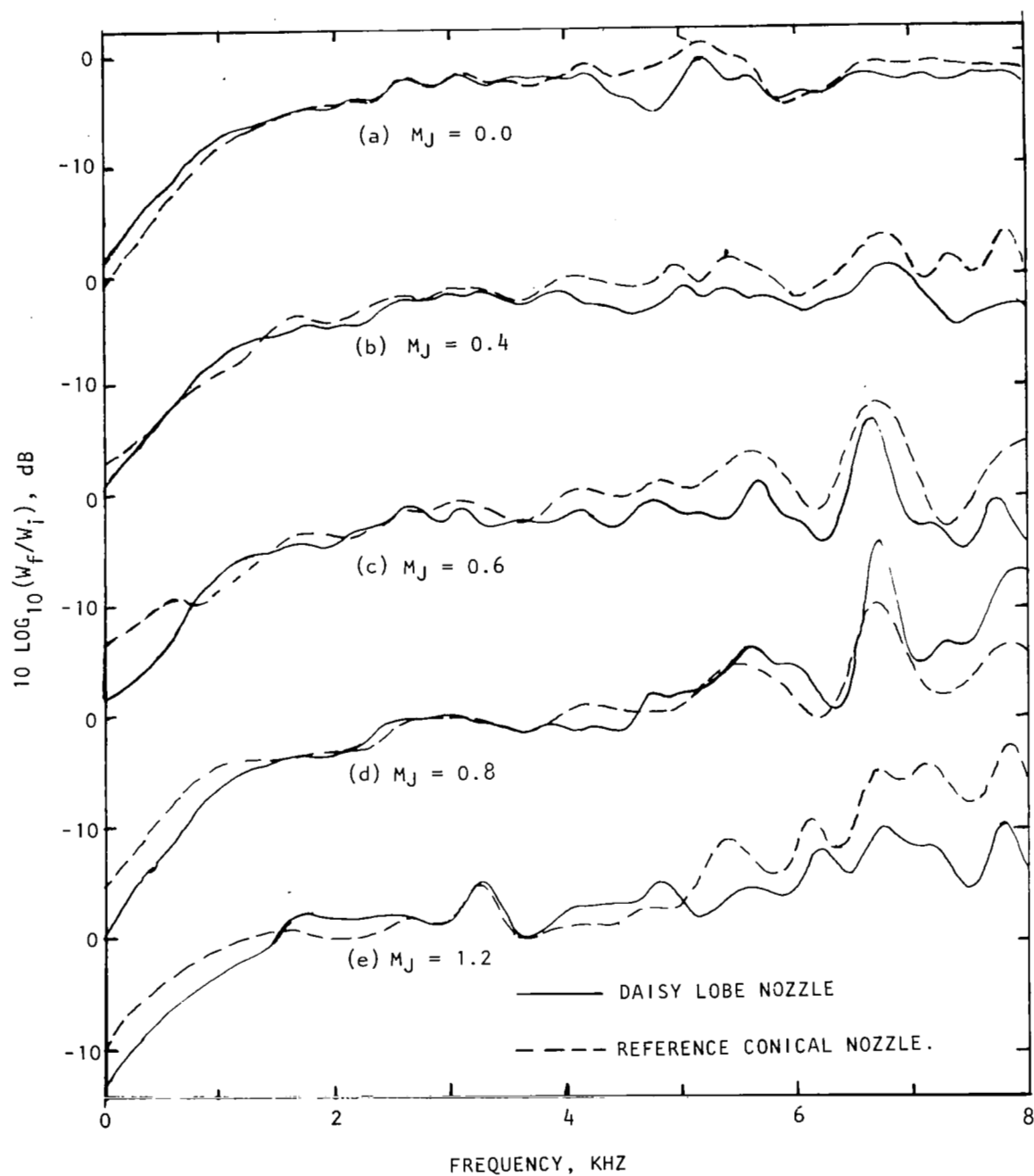


Figure 8.28 Effect of nozzle geometry on far-field acoustic power normalized with respect to incident power (PTF_i) for various jet Mach numbers; $M_T = 0.00$.

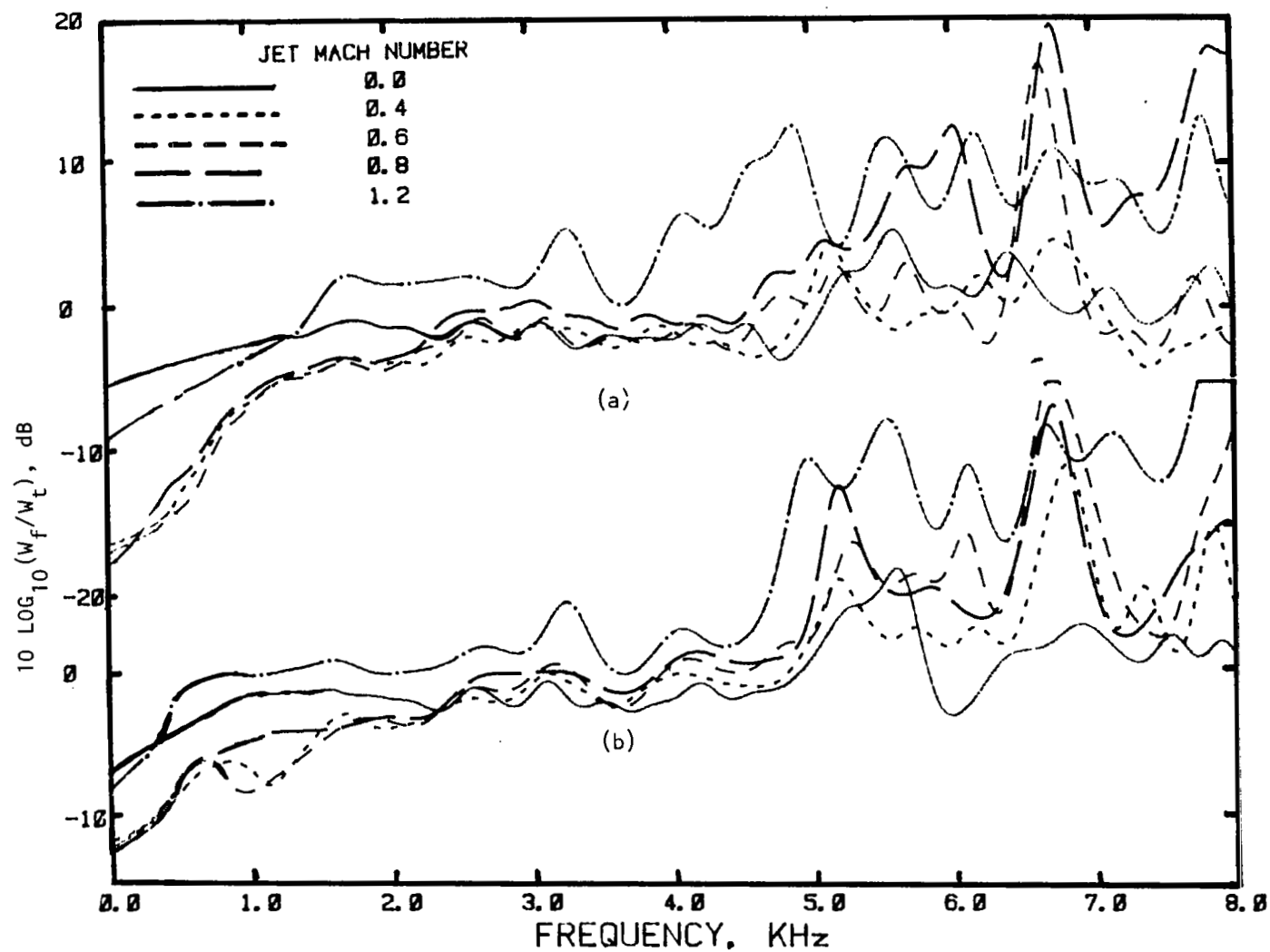


Figure 8.29 Effect of jet Mach number on far-field acoustic power normalized with respect to transmitted power (PTF_t) for (a) the daisy lobe nozzle, and (b) the reference conical nozzle; $M_T = 0.00$.

increased considerably, and it is relatively higher for the daisy lobe nozzle. However, the amount of power loss seems to be the same for all the subsonic jet Mach numbers for both the nozzles. For the supersonic case (i.e. $M_J = 1.2$), the amount of power loss decreases considerably.

Except for $M_J = 1.2$, the PTF_t levels remain below 0 dB up to about 5 KHz. Beyond this frequency, however, the PTF_t levels become positive at many frequencies. The transmitted power calculation is done on the basis of modal decomposition, which accounts for the power contributions due to higher order modes. Therefore, it is expected to have either a power balance or a power loss, but not an excess far-field power as seen here for higher frequencies. This discrepancy could have happened due to the following two reasons:

(a) In the modal decomposition for the single-stream duct, it is assumed that the induct pressure field is axisymmetric, and thereby, the circumferential modes are assumed to be absent. In practice this assumption may not be valid, since the modal structure is highly dependent on the orientation of the source in the flow field. For the present study, even though the output of the acoustic driver was injected at the centerline of the duct, the physical positioning could have been slightly off-center. Therefore, the computed transmitted power might have been affected due to this assumption.

(b) In the present investigation, the frequency response of the induct microphones is slightly different from that of the far-field microphones. When the signal synthesis was applied, the output of the driver measured by the induct microphones consisted of single pulses. However, the transmitted pulses, as measured by the far-field microphones, were made up of multiple peaks. Therefore, some degree of inaccuracy might have been introduced in the editing process applied to the far-field pulses.

For supersonic flow (i.e. $M_J = 1.2$), the spectral level does not follow the trend for other subsonic flow conditions. At present, the reason for this behavior is not known. However, for the supersonic flow case, the inaccuracy associated with the derivation of the PTF_t results may be more compared to that for the subsonic conditions. For the supersonic flow case, instead of a single driver in the center, four drivers were used in the periphery as the internal sound source. Hence, the assumption of axisymmetric induct pressure field might have introduced more error in this case compared to the single driver case. In addition, the signal-to-noise ratio in this case was quite low. Therefore, in the estimation of far-field power, significant amount of inaccuracy could have been introduced.

The low-frequency power loss in the presence of jet flow has been well established by many researchers (refs. 35,36,37, and 41) and the general conclusion is that the acoustic energy which escapes from the nozzle is partially converted into vortical energy, thereby causing a

power imbalance, since the converted vortical energy is not accounted for in the far-field power estimation.

The low-frequency power loss in the absence of mean flow observed in the present study is considerably lower compared to what is reported in reference 2, derived using high-intensity spark discharge pulses during Phase II study of this contract. The higher losses measured at that time were due to the severe nonlinear propagation effects of high intensity pulses (ref. 6). However, in the present study, very low intensity pulses were used, yet these pulses were of finite amplitude. Therefore, a small amount of nonlinear effect must be present even in the propagation of these low intensity pulses. This may be the reason for the low-frequency power loss (about 6 dB) observed with the daisy lobe nozzle and the reference conical nozzle at $M_J = 0.0$.

The power imbalance results for the daisy lobe nozzle are compared with the corresponding results for the reference conical nozzle at various jet Mach numbers in figure 8.30. The power imbalance spectra show the same shape between the two nozzles, and almost the same level in the mid-frequency range (i.e., between 1.5 KHz and 5 KHz). However, the daisy lobe nozzle shows more low-frequency power loss and this difference is higher in the presence of flow. Again, this could be due to the nonlinear effects which may be relatively more severe for the daisy lobe nozzle due to its complicated shape, especially the narrow tubes and lobes through which the induct pressure pulses propagate out.

8.2.2 Flight Effects

Results similar to those presented in section 8.2.1 for the static conditions are presented in this section for both the nozzles operated under flight simulation. All data presented here are corrected to ideal wind tunnel conditions using a free-jet shear layer propagation program developed at Lockheed (ref. 42). It should be noted that whenever reference is made to an angle, it is the emission angle and not the measured polar angle. All the data presented in this section are for a fixed jet Mach number, $M_J = 0.6$.

(1) Time Histories

Time histories, both in-duct and far field, measured under flight simulation had shapes very similar to those measured statically. Figure 8.31 shows the induct time histories for the daisy lobe nozzle and the reference conical nozzle at $M_J = 0.6$ with different free jet Mach numbers, M_T . There is hardly any qualitative difference, due to change in M_T values, observed in figure 8.31.

(2) Reflection Coefficients

The reflection coefficient spectra for the daisy lobe nozzle and

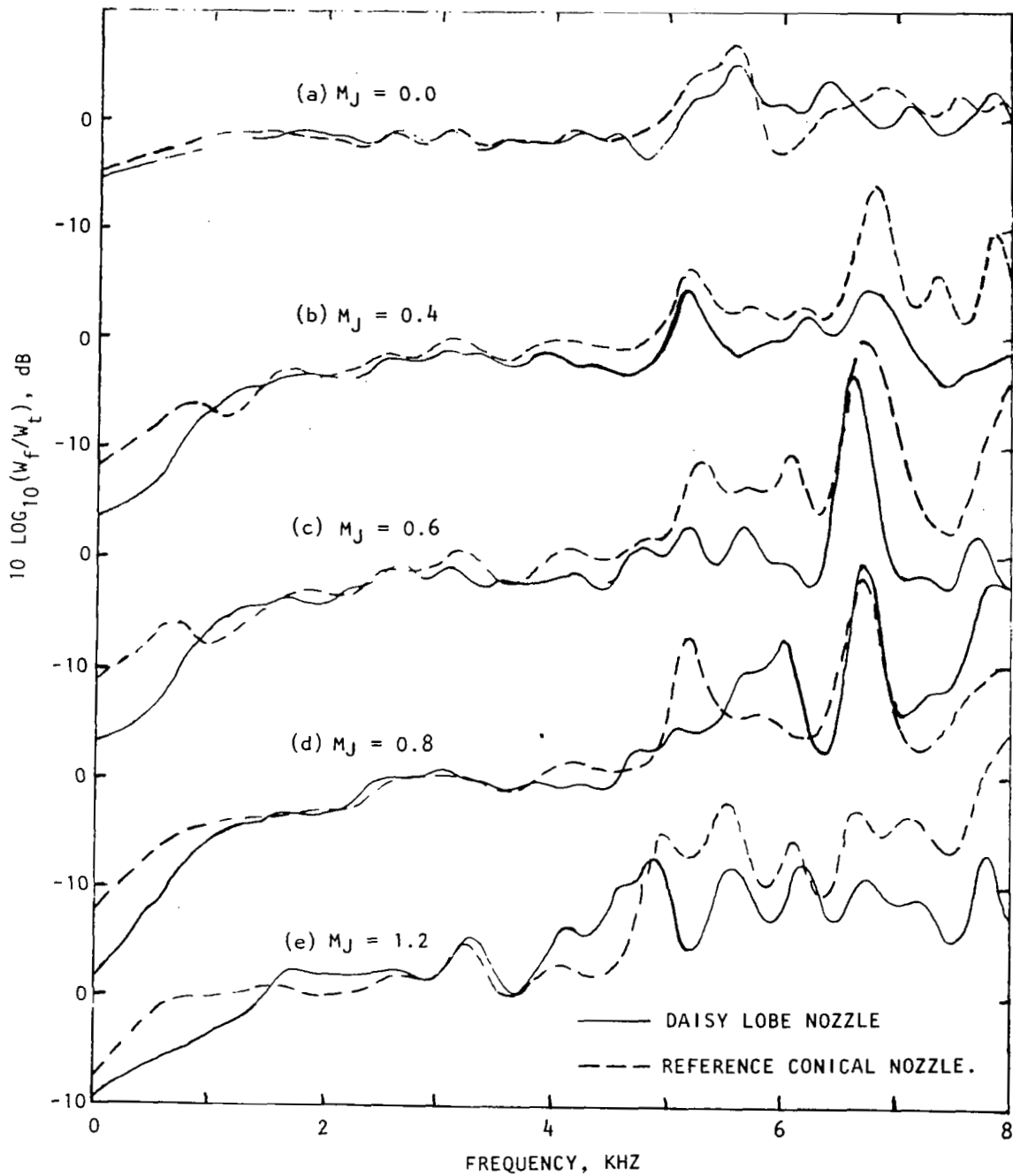


Figure 8.30 Effect of nozzle geometry on far-field acoustic power normalized with respect to transmitted power (PTF_t) for various jet Mach numbers; $M_T = 0.00$.

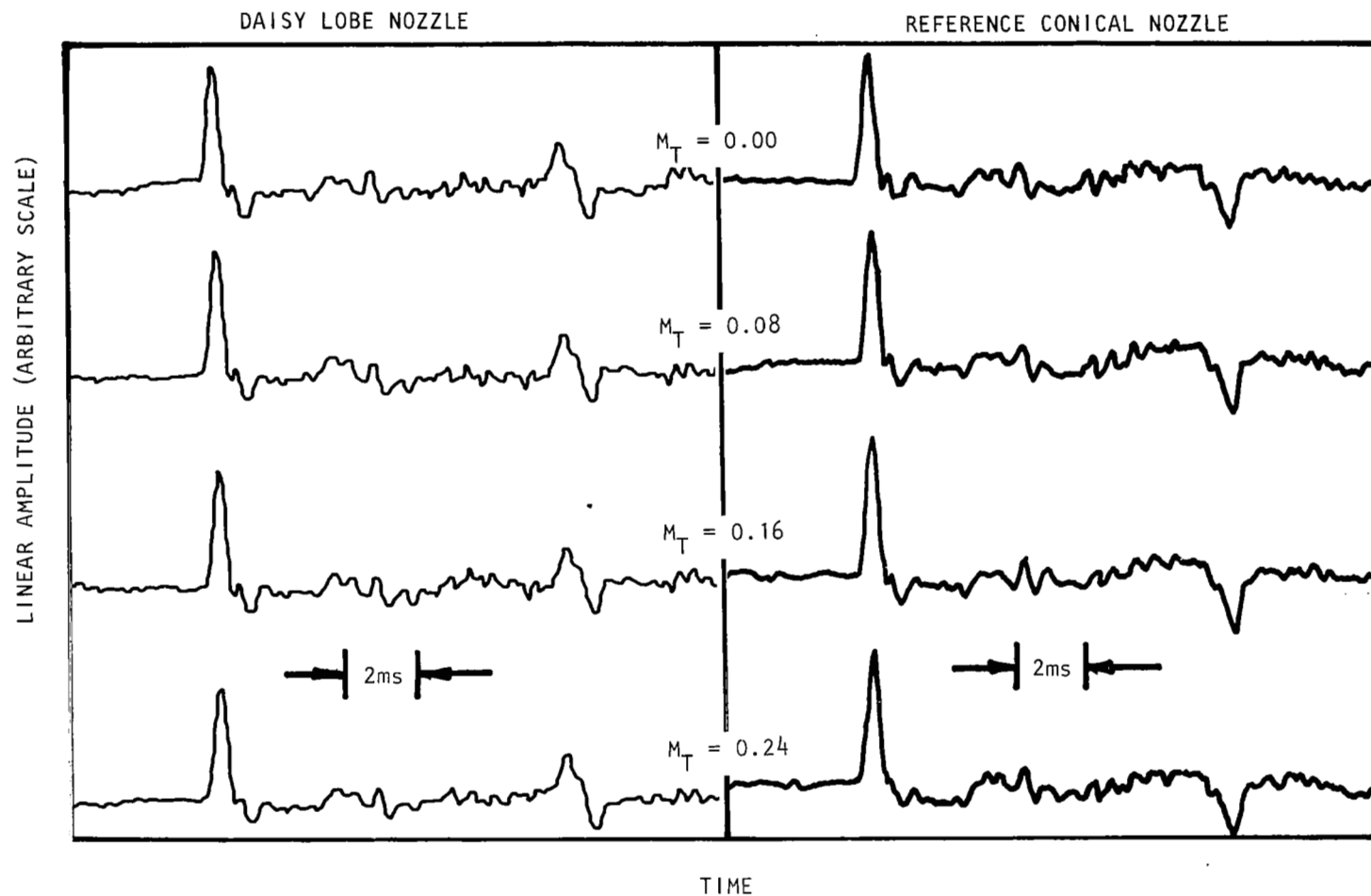


Figure 8.31 Induct time histories for (a) the daisy lobe nozzle and (b) the reference conical nozzle at various free jet Mach numbers; measured at $r/R_D = 0.4$; $M_J = 0.6$

the reference conical nozzle at $M_J = 0.6$ with various free jet Mach numbers (i.e. $M_T = 0.00, 0.08, 0.16$ and 0.24) are plotted in figure 8.32. There is very little effect of free-jet Mach number on the reflection coefficients for the nozzles. To determine the effect of nozzle geometry on the reflection coefficient spectra in the presence of free-jet flow, the results for both the nozzles at $M_J = 0.6$ are plotted for different values of M_T in figure 8.33. In the plane wave range of frequency, the daisy lobe nozzle seems to have a lower reflection coefficient at very low frequencies (below 1 KHz), and then the trend is reversed between 1 KHz and 2.5 KHz, after which the trend is again reversed. This behavior is observed for all free-jet flow conditions including $M_T = 0$.

(3) Nozzle Transfer Function (NTF)

The nozzle transfer function spectra at free jet Mach numbers of 0.00, 0.08, 0.16 and 0.24 are compared at four emission angles, namely, 30 degrees, 60 degrees (rear arc), 90 degrees and 110 degrees (forward arc) in figures 8.34 and 8.35 for the daisy lobe nozzle and the reference conical nozzle, respectively. For both the nozzles, at each free jet flow condition, the NTF spectral level goes up for 60 degrees and then gradually goes down with increasing emission angle compared to the spectral levels at 30 degrees. With increasing free jet Mach number, the difference between the NTF spectral levels for different emission angles starts decreasing. The effect is less pronounced for the reference conical nozzle.

The effect of free jet Mach number is further studied by plotting the NTF spectra at emission angles of 30 degrees, 60 degrees, 90 degrees and 110 degrees for various free jet Mach numbers, namely, 0.00, 0.08, 0.16 and 0.24, in figures 8.36 and 8.37 for the daisy lobe nozzle and the reference conical nozzle, respectively. A closer examination of the data presented here discloses that flight simulation reduces noise in the rear arc, has little change at 90 degrees, and increases noise in the forward arc, similar to what was found in earlier studies (ref. 2). This behavior is further established by plotting the NTF directivities at three frequencies, namely, 1 KHz, 2 KHz and 4 KHz, for various tunnel Mach numbers in figures 8.38 and 8.39, respectively for the daisy lobe nozzle and the reference conical nozzle.

To show the effect of nozzle geometry on the NTF spectra under flight simulation, the NTF spectra for both the nozzles are compared at emission angles 30 degrees, 60 degrees, 90 degrees and 110 degrees for three free jet Mach numbers, namely, 0.08, 0.16 and 0.24, in figures 8.40 through 8.42, respectively. There is no significant difference observed in the NTF spectra between the two nozzles. This is further confirmed from the directivity plot in figures 8.43, where the NTF directivities for the two nozzles are compared at frequencies of 1 KHz, 2 KHz and 4 KHz, at $M_T = 0.24$ and $M_J = 0.6$.

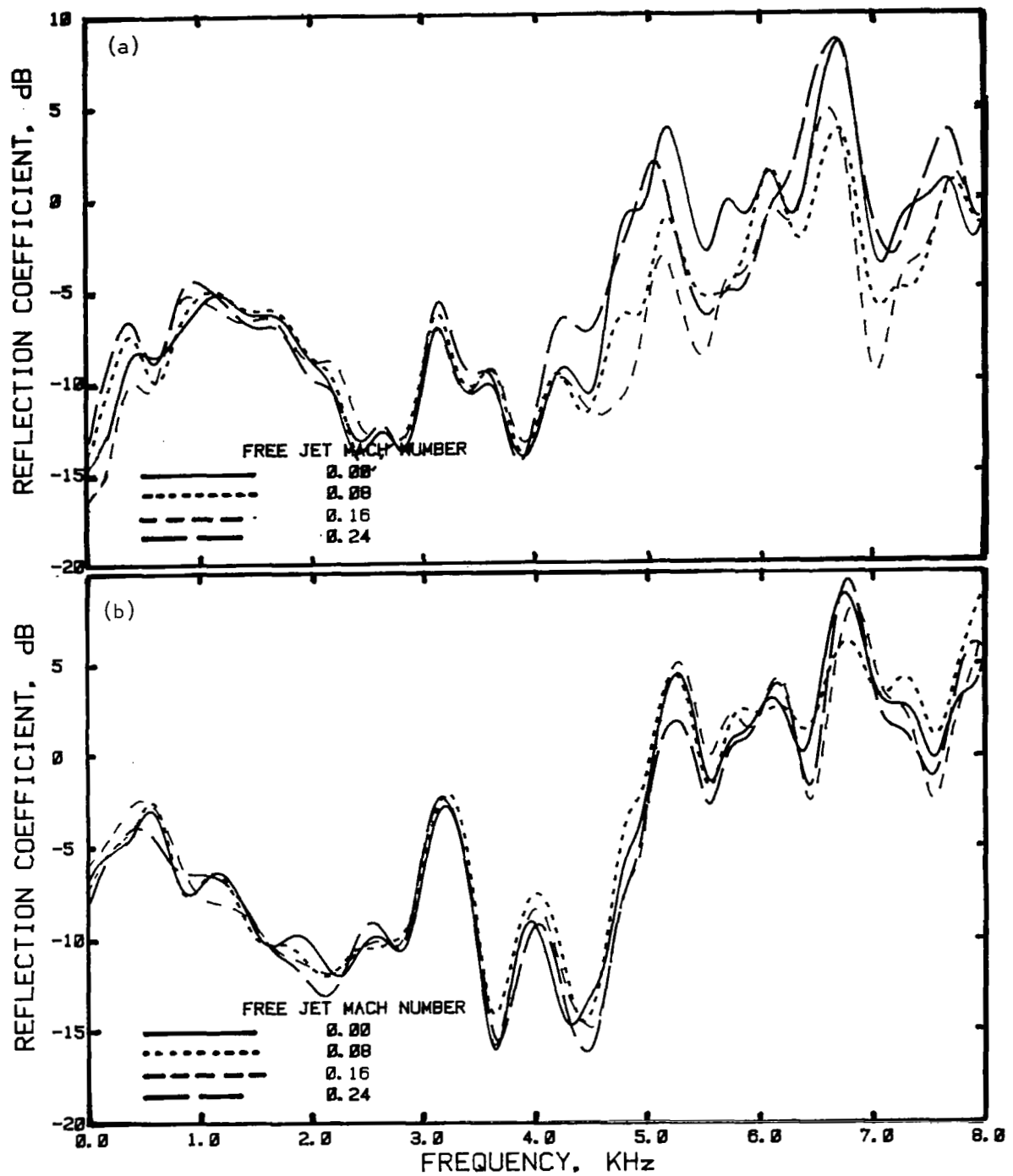


Figure 8.32 Effect of free jet Mach number on the reflection coefficient spectra for (a) the daisy lobe nozzle, and (b) the reference conical nozzle; $M_j = 0.6$.

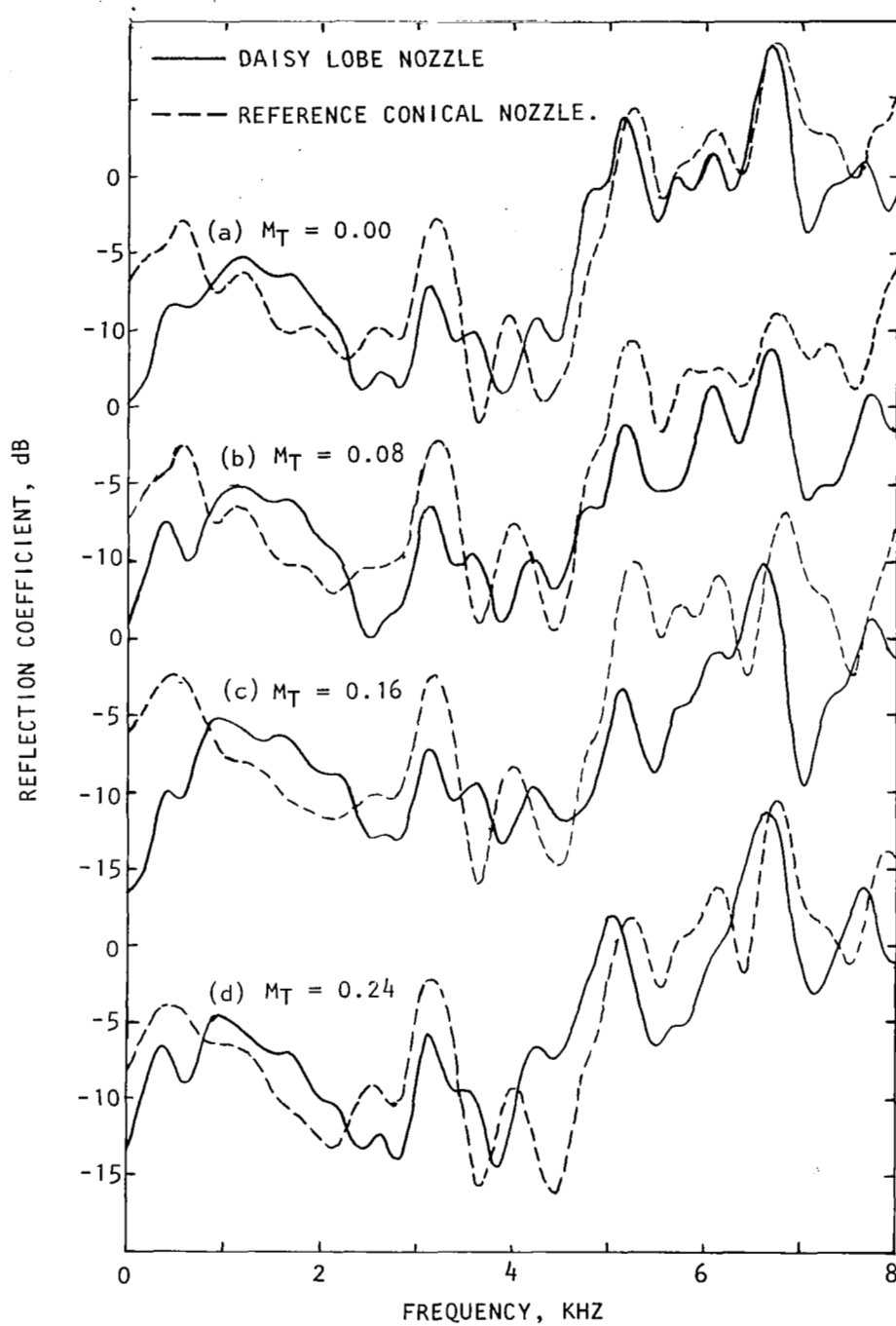


Figure 8.33 Effect of nozzle geometry on reflection coefficient spectra for various free jet Mach numbers; $M_J = 0.6$.

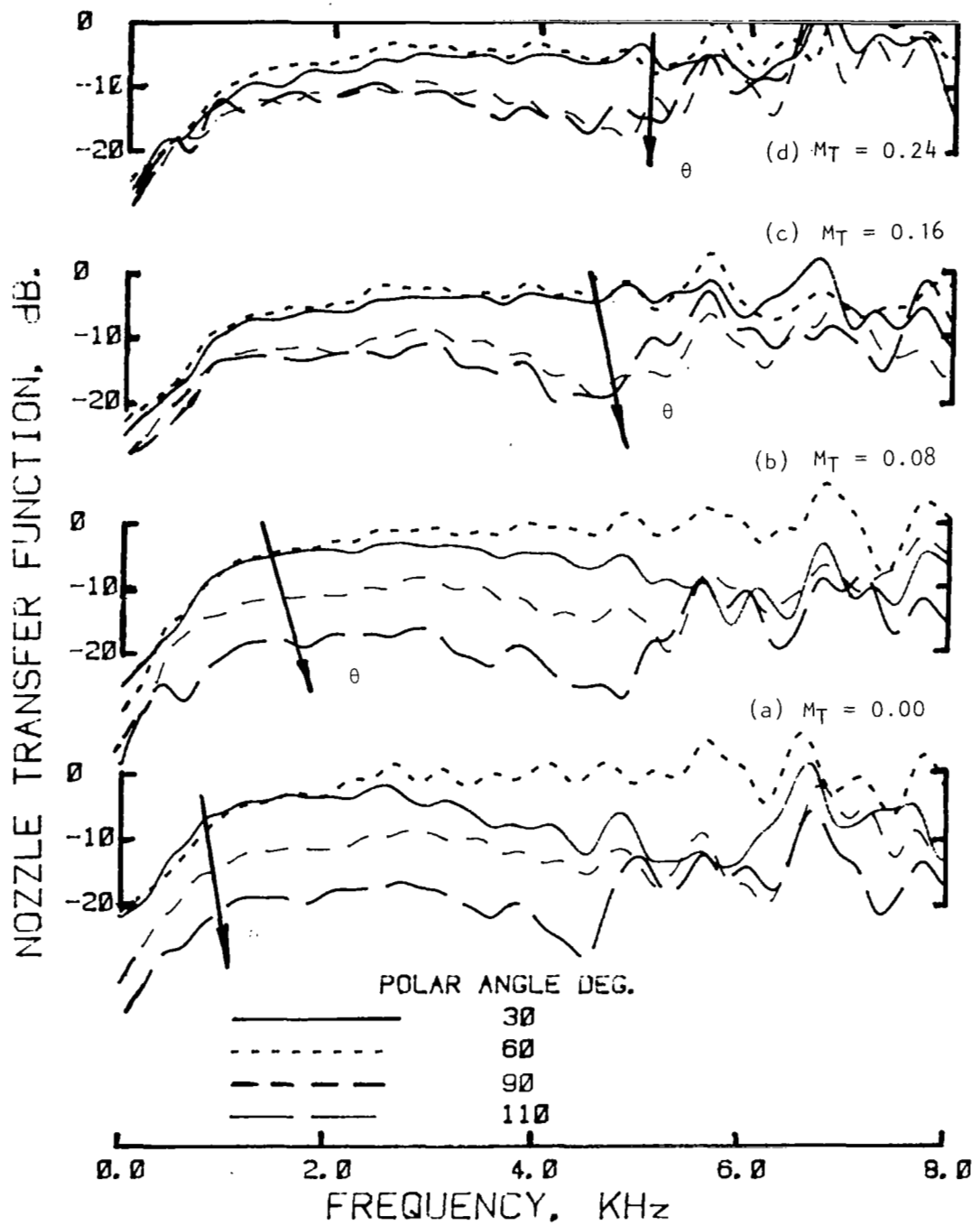


Figure 8.34 Variation of nozzle transfer function spectra with polar angle θ at various free jet Mach numbers, M_T for daisy lobe nozzle; $M_J = 0.6$.

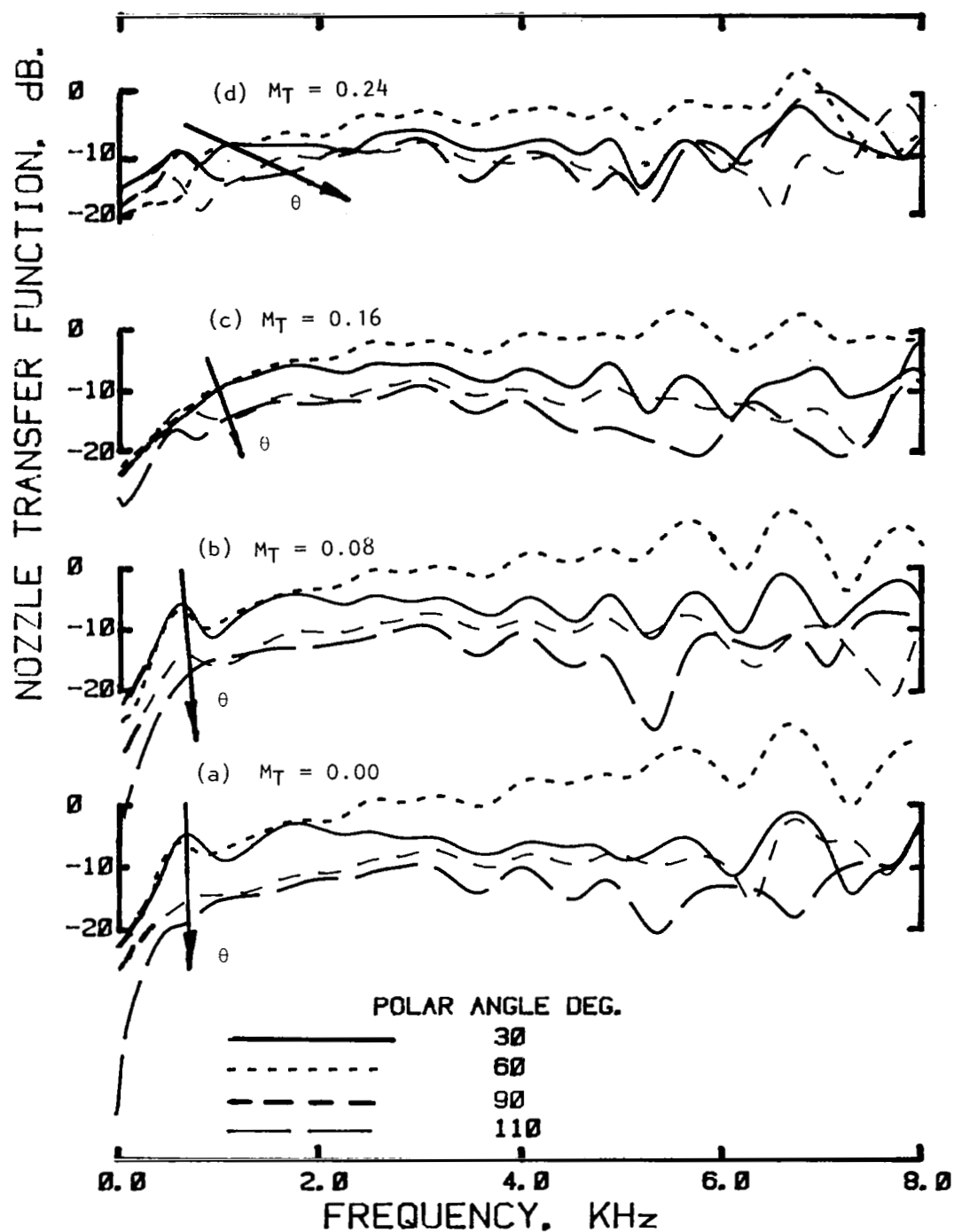


Figure 8.35 Variation of nozzle transfer function spectra with polar angle θ at various free jet Mach numbers, M_T for reference conical nozzle; $M_J = 0.6$.

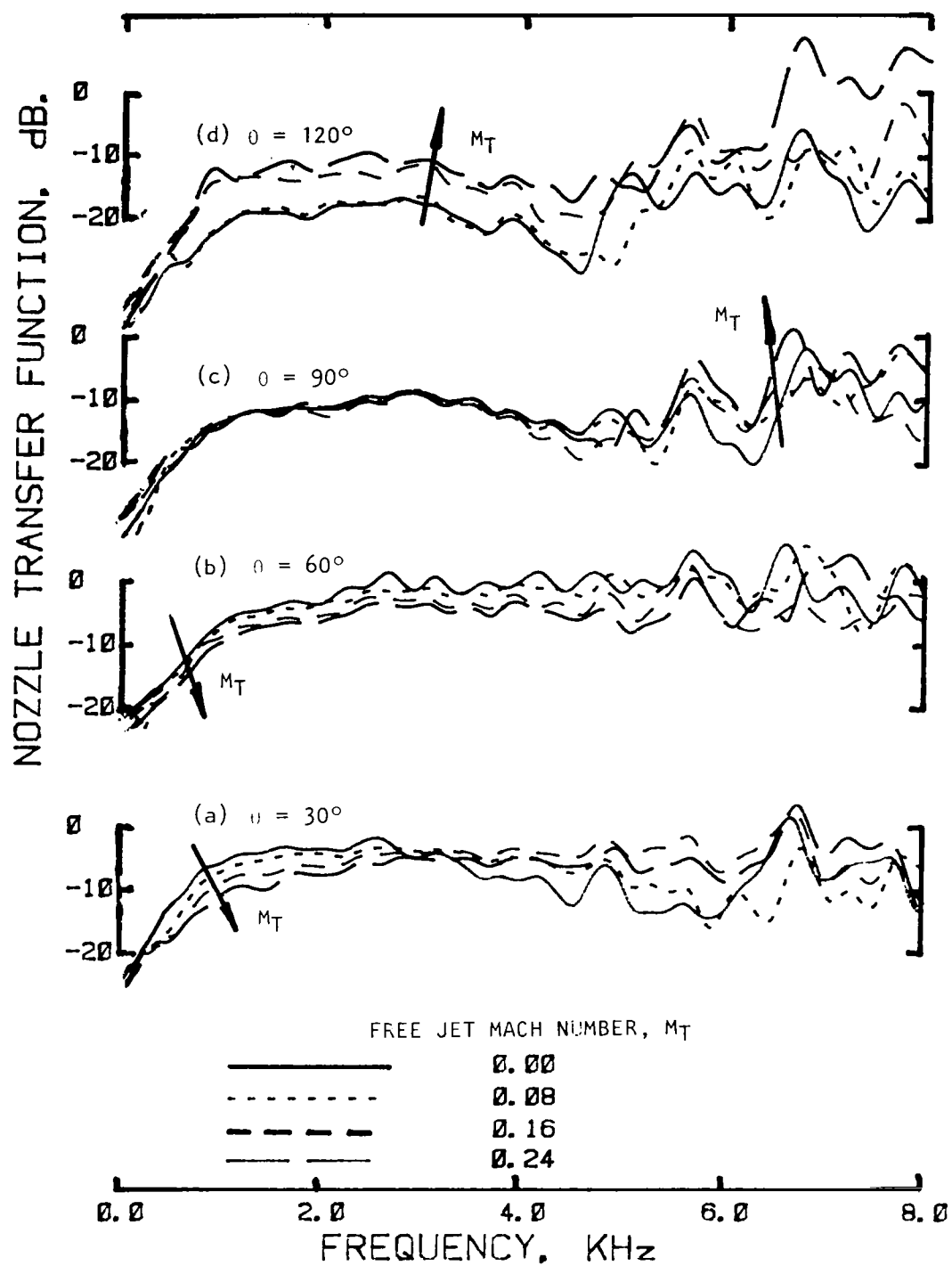


Figure 8.36 Variation of nozzle transfer function spectra with free jet Mach number M_T at various polar angles, θ for daisy lobe nozzle; $M_J = 0.6$.

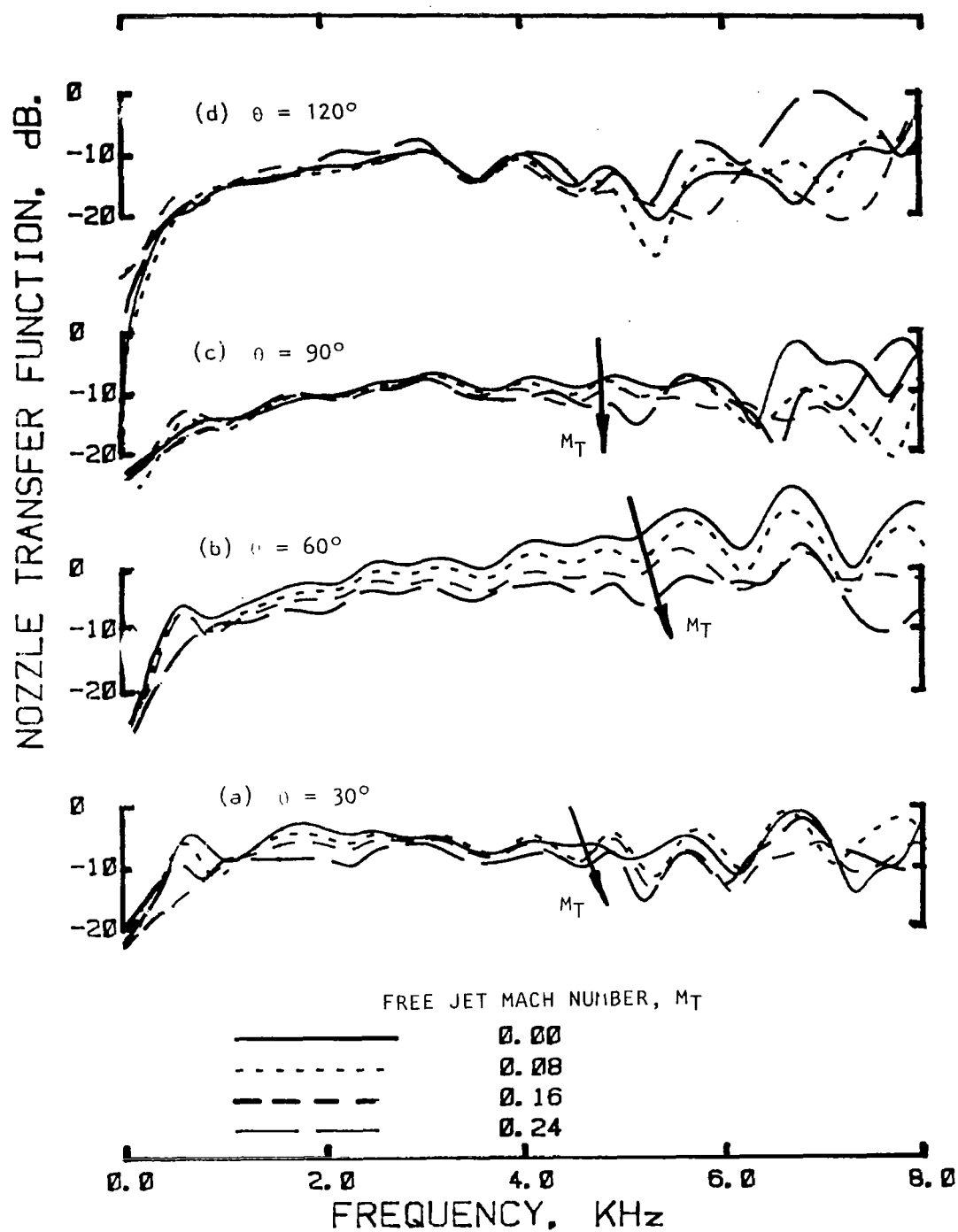


Figure 8.37 Variation of nozzle transfer function spectra with free jet Mach number M_T at various polar angles, θ for reference conical nozzle; $M_J = 0.6$.

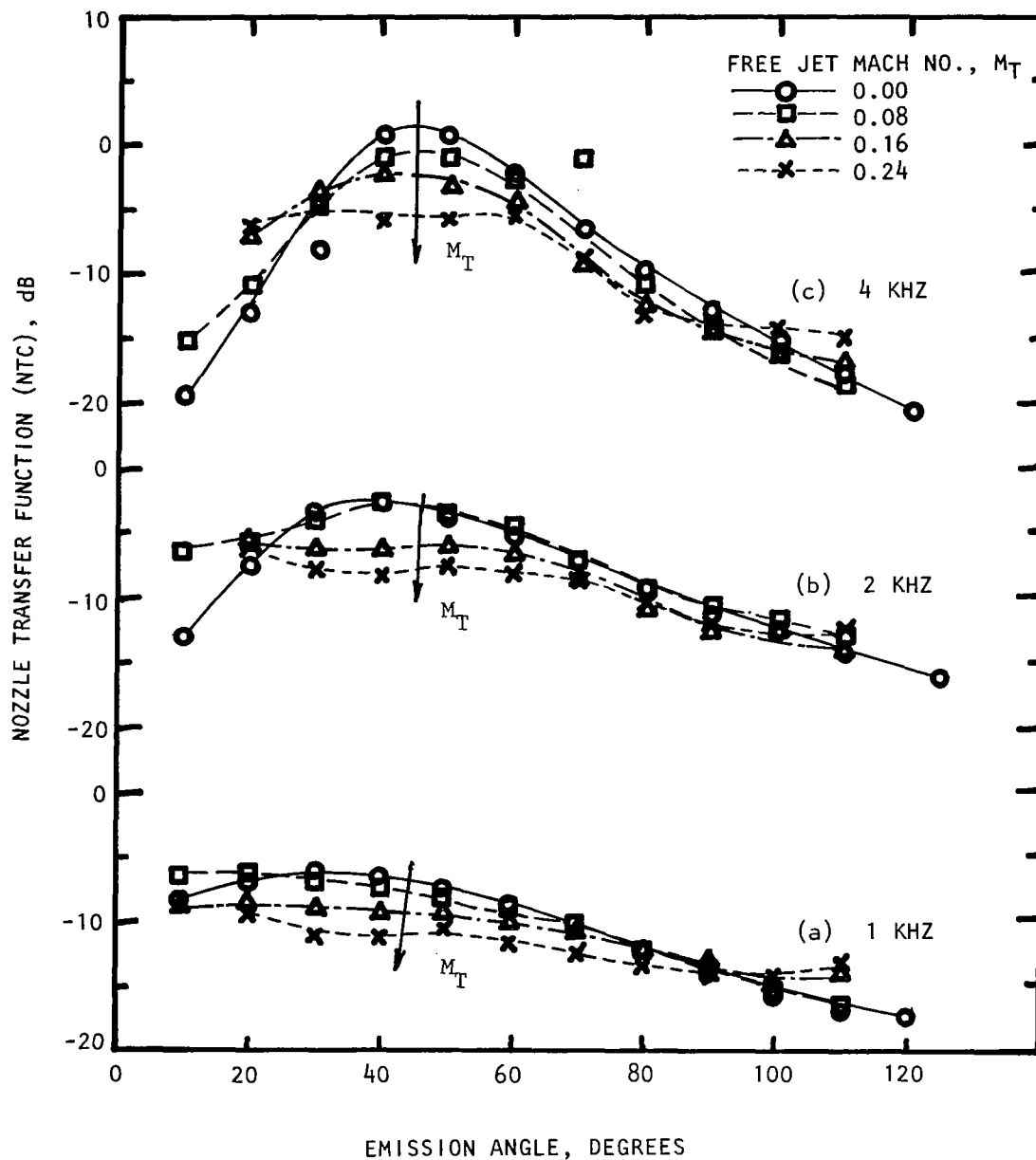


Figure 8.38 Effect of free jet Mach number on the nozzle transfer function directivities for the daisy lobe nozzle at various frequencies; $M_J = 0.6$; (a) 1 KHz, (b) 2 KHz, (c) 4 KHz.

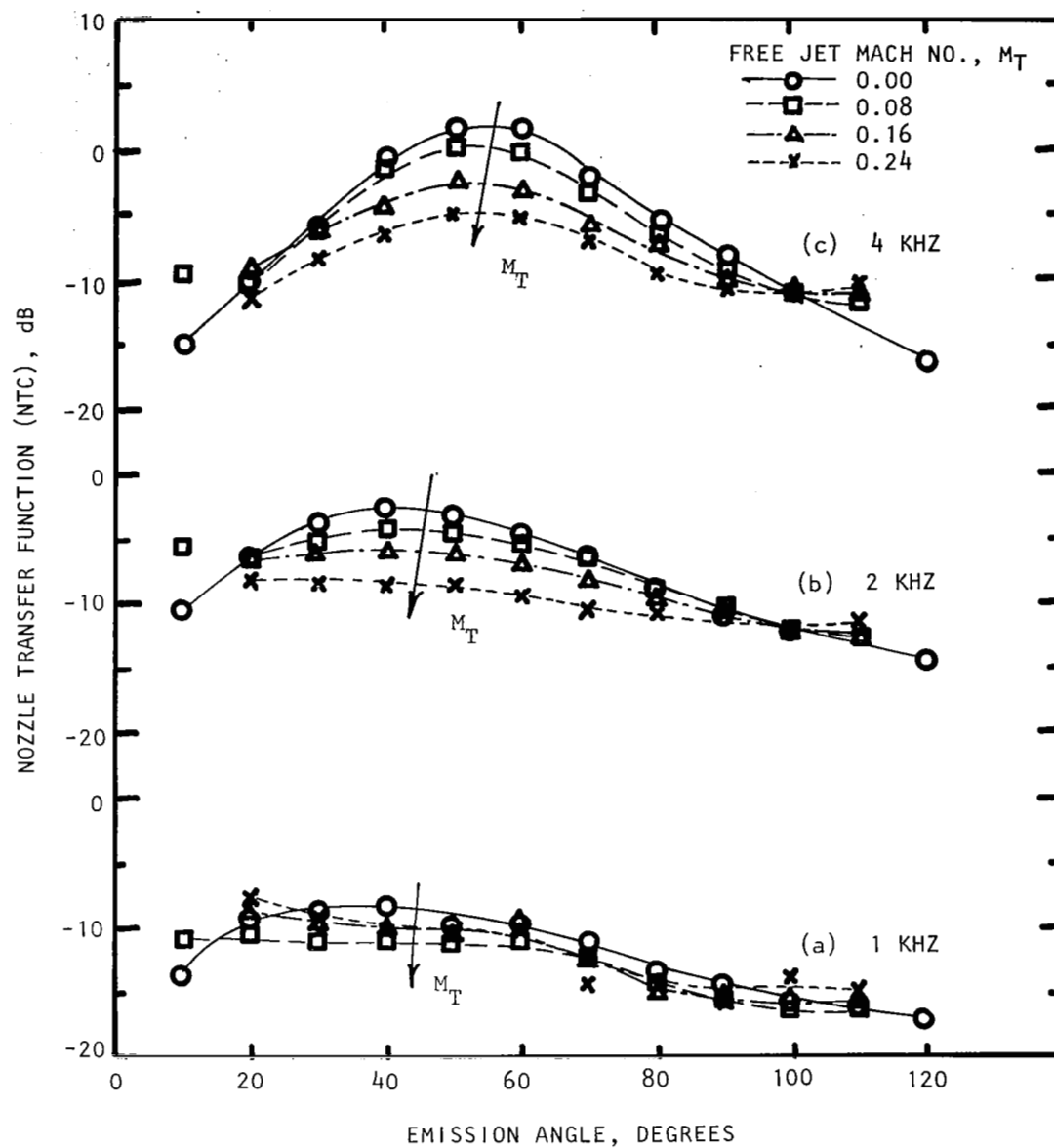


Figure 8.39 Effect of free jet Mach number on the nozzle transfer function directivities for the reference conical nozzle at various frequencies; $M_J = 0.6$; (a) 1 KHz, (b) 2 KHz, (c) 4 KHz.

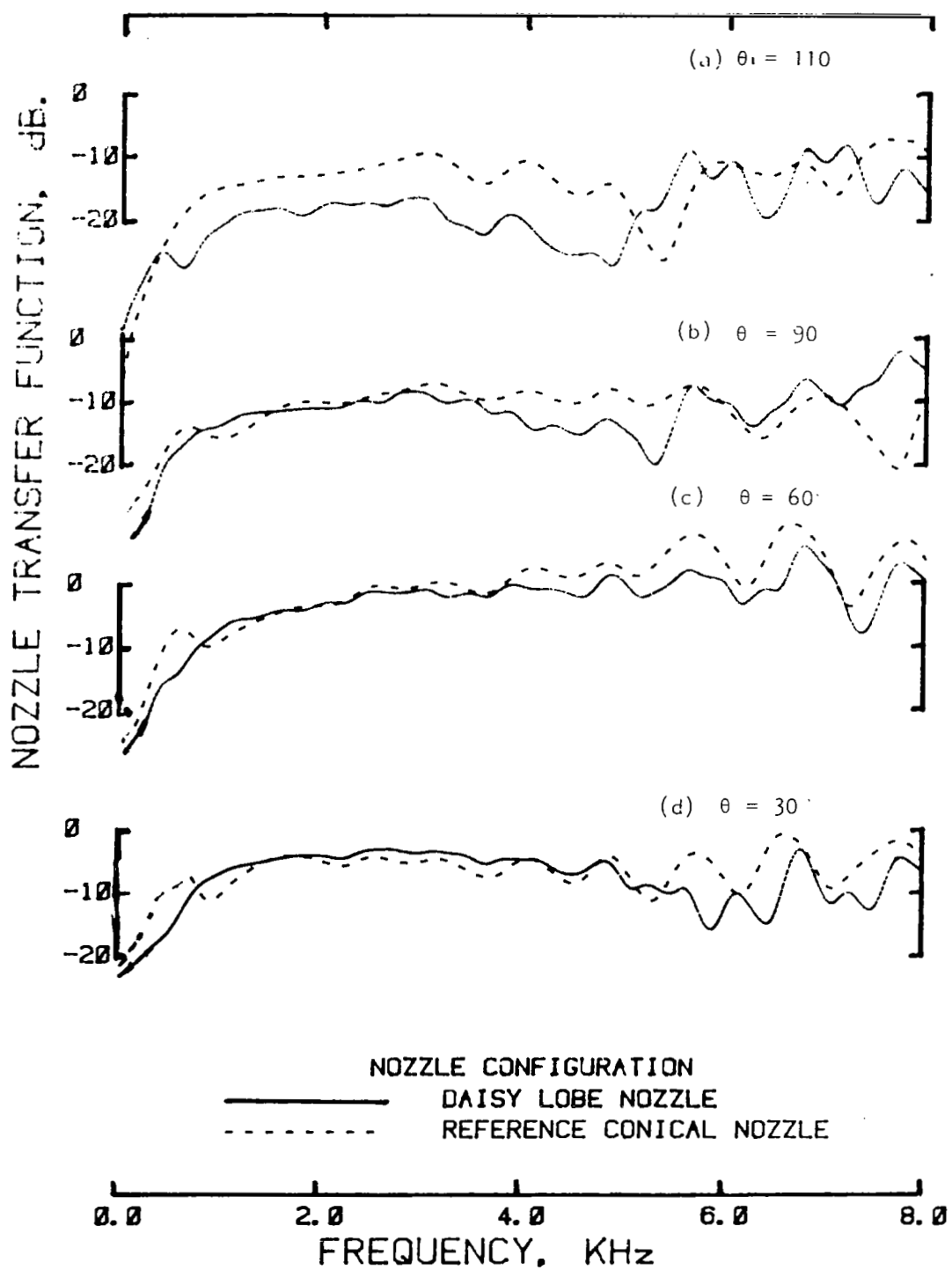


Figure 8.40 Effect of nozzle geometry on nozzle transfer function spectra at various polar angles, θ ; $M_J = 0.6$; $M_T = 0.08$.

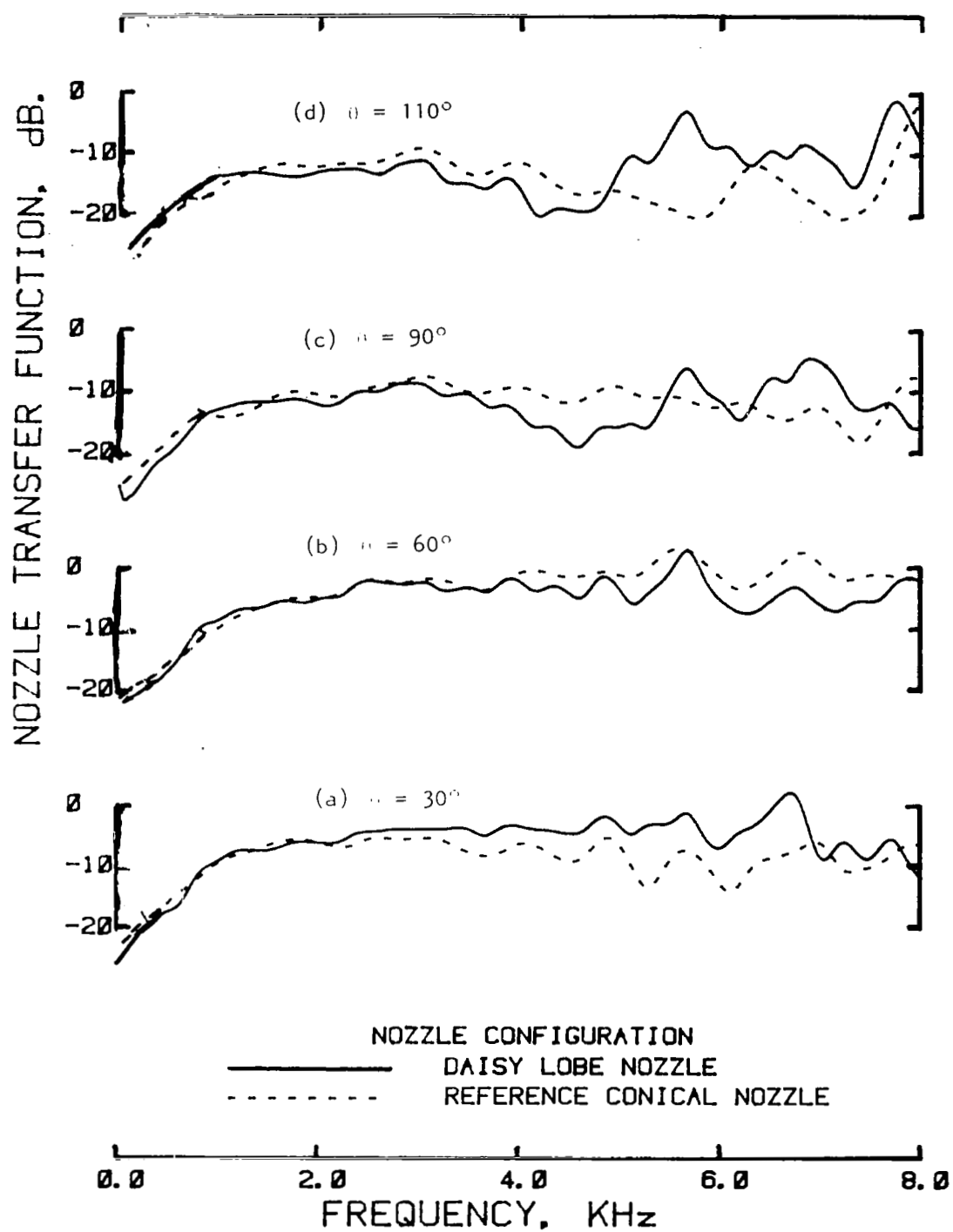


Figure 8.41 Effect of nozzle geometry on nozzle transfer function spectra at various polar angles, θ ; $M_j = 0.6$; $M_T = 0.16$.

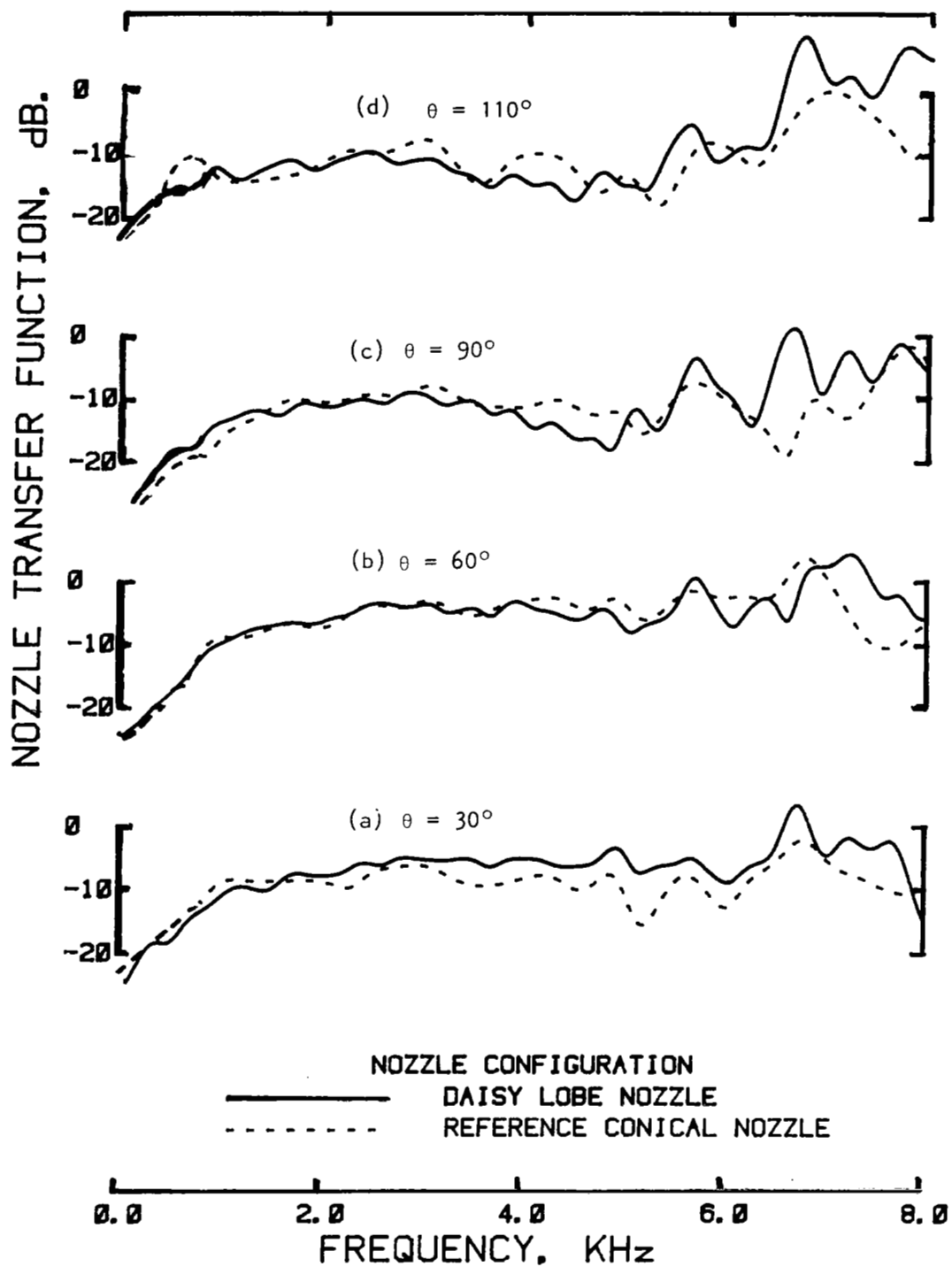


Figure 8.42 Effect of nozzle geometry on nozzle transfer function spectra at various polar angles, θ ; $M_J = 0.6$; $M_T = 0.24$.

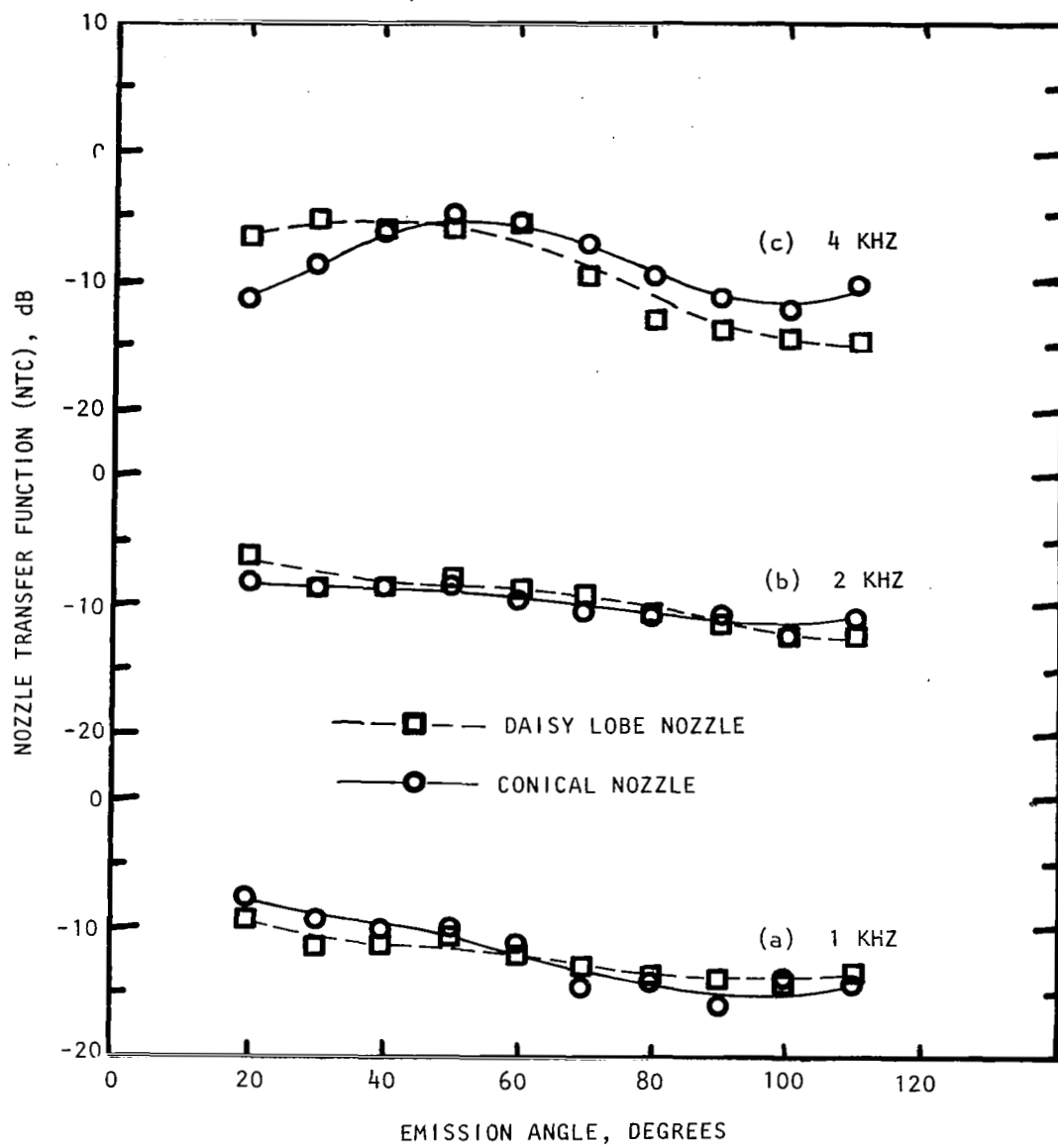


Figure 8.43 Effect of nozzle geometry on the nozzle transfer function directivities at various frequencies; $M_J = 0.6$, $M_T = 0.24$; (a) 1 KHz, (b) 2 KHz, (c) 4 KHz.

(4) Far-Field Power Normalized With Respect to Incident Power (PTF_i)

Far-field power spectra normalized with respect to incident power spectra (PTF_i) for various free jet Mach numbers at $M_J = 0.6$ are plotted in figure 8.44 for the daisy lobe nozzle and the reference conical nozzle. For both the nozzles, it is clearly observed that the far-field acoustic powers decrease with forward velocity. It is seen that there is up to about 10 dB reduction in the far-field power due to a free jet Mach number of 0.24 compared to the static condition. This effect is relatively more dominant for the conical nozzle compared to the daisy lobe nozzle. To determine further the effect of nozzle geometry, the PTF_i spectra for the two nozzles are compared in figure 8.45 at $M_J = 0.6$ for different free jet Mach numbers. At low frequencies (below 1 KHz) the far-field acoustic power is considerably lower for the daisy lobe nozzle compared to the reference conical nozzle. This difference seems to be independent of M_T and, therefore, is due to the reasons discussed in the previous section (8.2.1). However, due to the increase in M_T value, the PTF_i spectral level for the conical nozzle start coinciding with that for the daisy lobe nozzle in higher frequency range.

(5) Far-Field Power Normalized With Respect to Transmitted Power (PTF_t)
- Power Imbalance

To determine the effect of flight on the low-frequency power imbalance noticed in section 8.2.1 for the static case, the far-field power spectra normalized with respect to the transmitted power spectra (PTF_t), for $M_J = 0.6$ at different M_T values, for the daisy lobe nozzle and the reference conical nozzle are plotted in figure 8.46. The effect of free jet Mach number is similar to that observed in figure 8.44 for the PTF_i spectra. Throughout the frequency range, the power loss increases as the tunnel Mach number increases.

The PTF_t spectra are further replotted in figure 8.47, comparing the results between the two nozzles at different M_T for fixed $M_J = 0.6$. Similar to the PTF_i results, there is almost no effect of M_T on low-frequency power loss. However, at higher frequencies, the PTF_t level for the daisy lobe nozzle is lower compared to the conical nozzle at lower values of M_T . This difference diminishes at higher tunnel flows and becomes negligible at $M_T = 0.24$.

8.3 CONCLUSIONS

Important conclusions from the results presented in this section are as follows:

- (1) The trend in the variation of reflection coefficient spectra for the daisy lobe nozzle is similar to that for the reference conical nozzle.

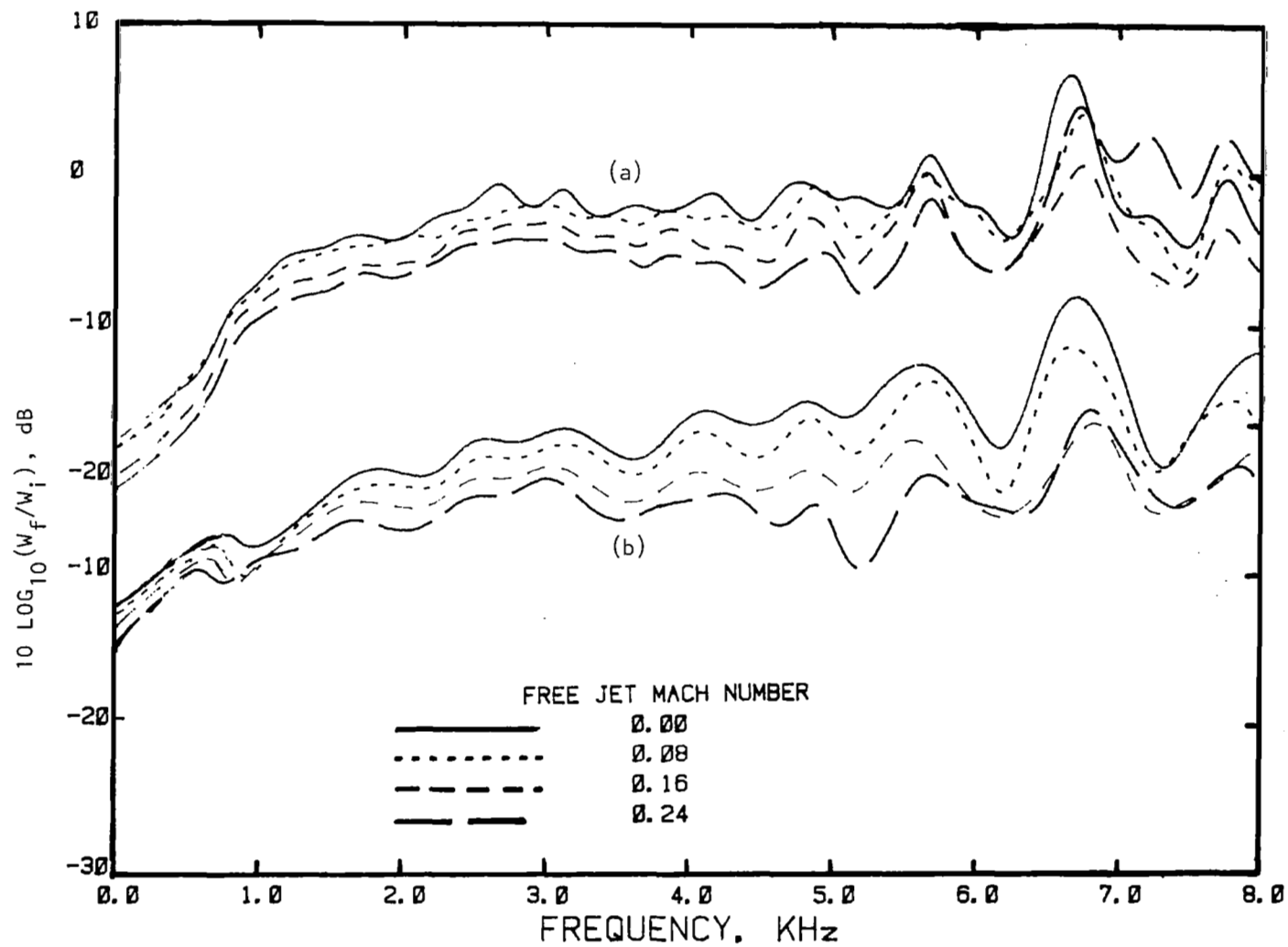


Figure 8.44 Effect of free jet Mach number on far-field power normalized with respect to incident power (PTF_i) for (a) the daisy lobe nozzle, and (b) the reference conical nozzle; $M_j = 0.6$.

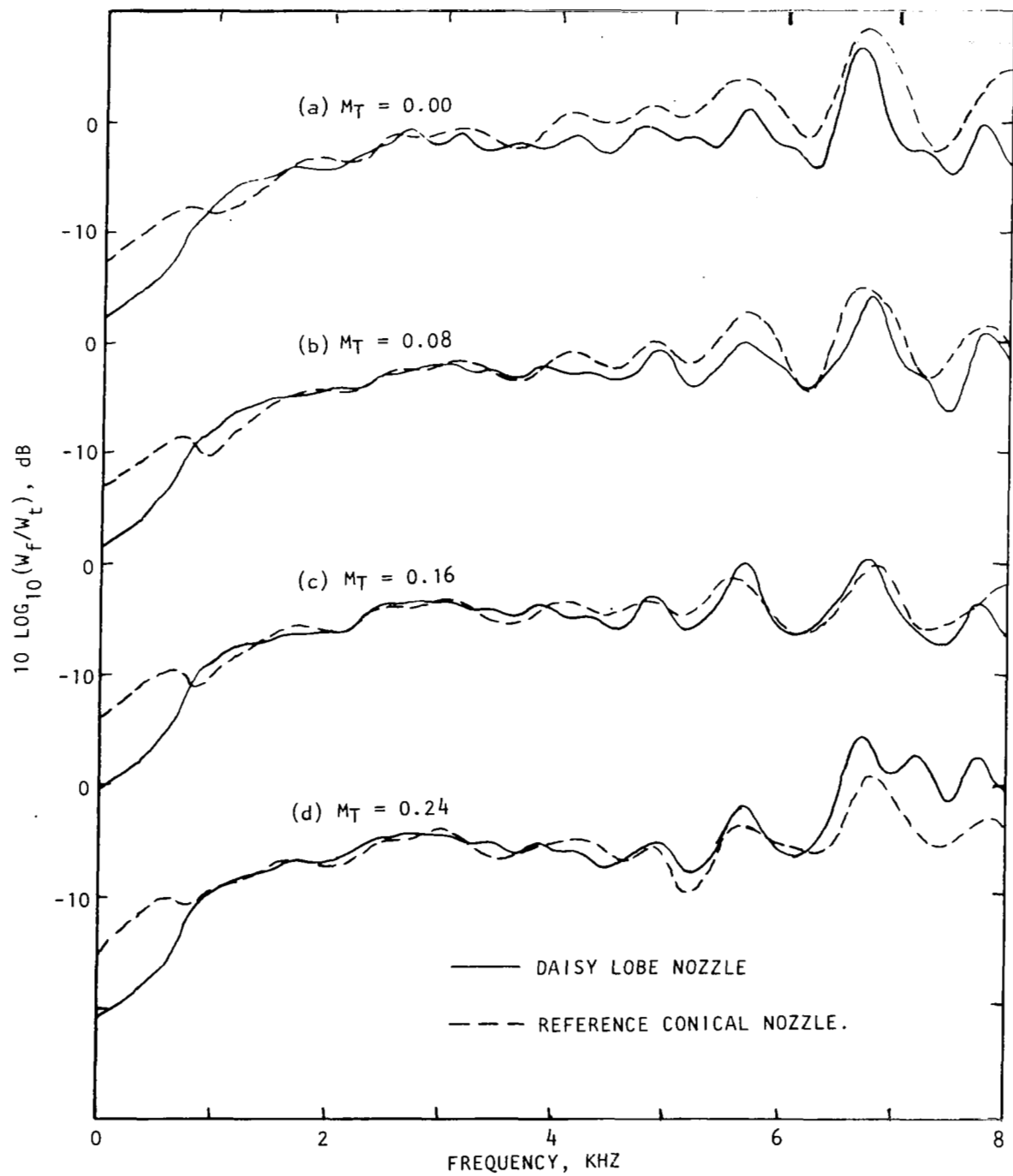


Figure 8.45 Effect of nozzle geometry on far-field acoustic power normalized with respect to incident power (PTF_i) for various free jet Mach numbers; $M_j = 0.6$.

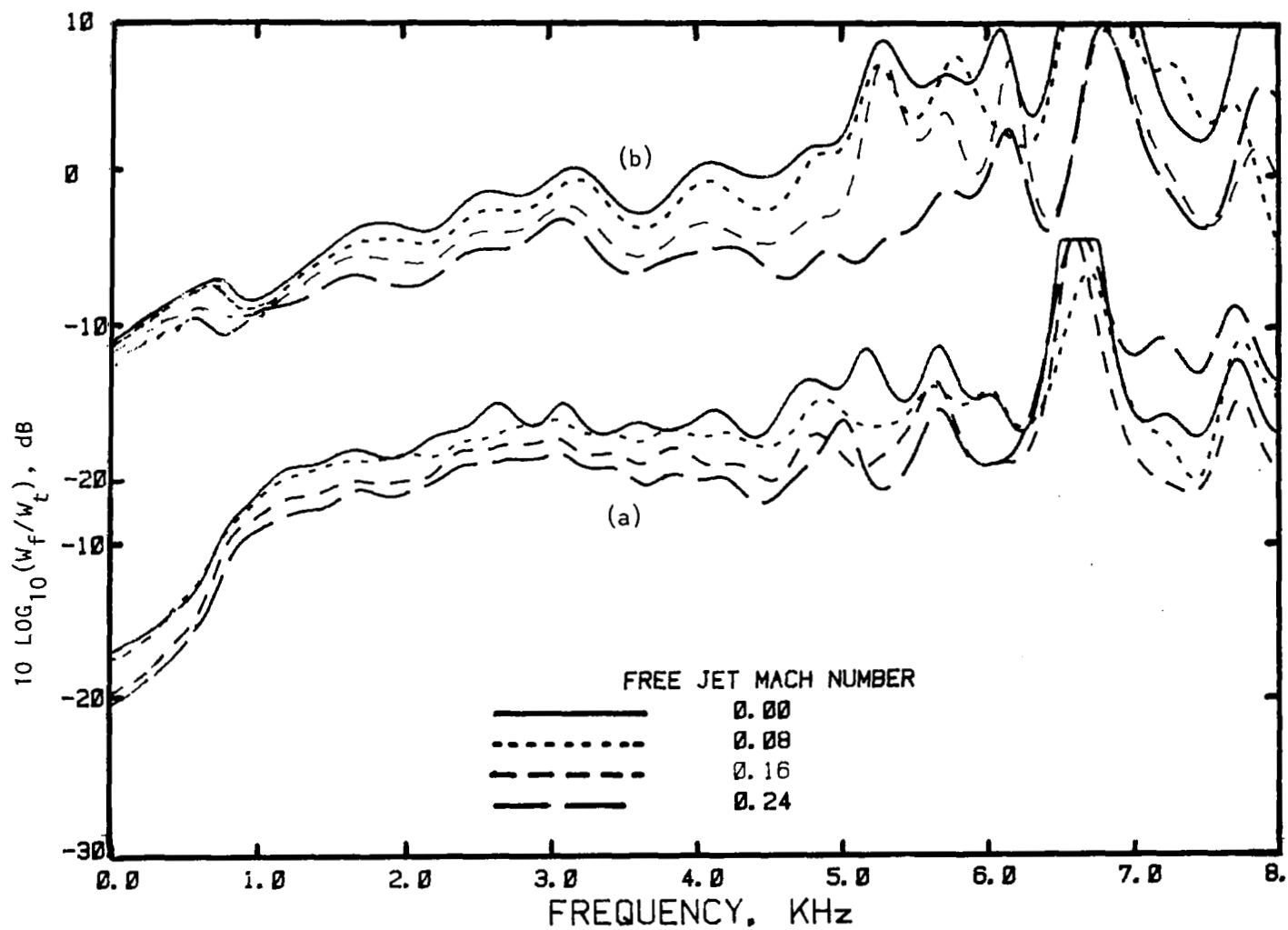


Figure 8.46 Effect of free-jet Mach number on far-field acoustic power normalized with respect to transmitted power (PTF_t) for (a) the daisy lobe nozzle, and (b) the reference conical nozzle; $M_J = 0.6$.

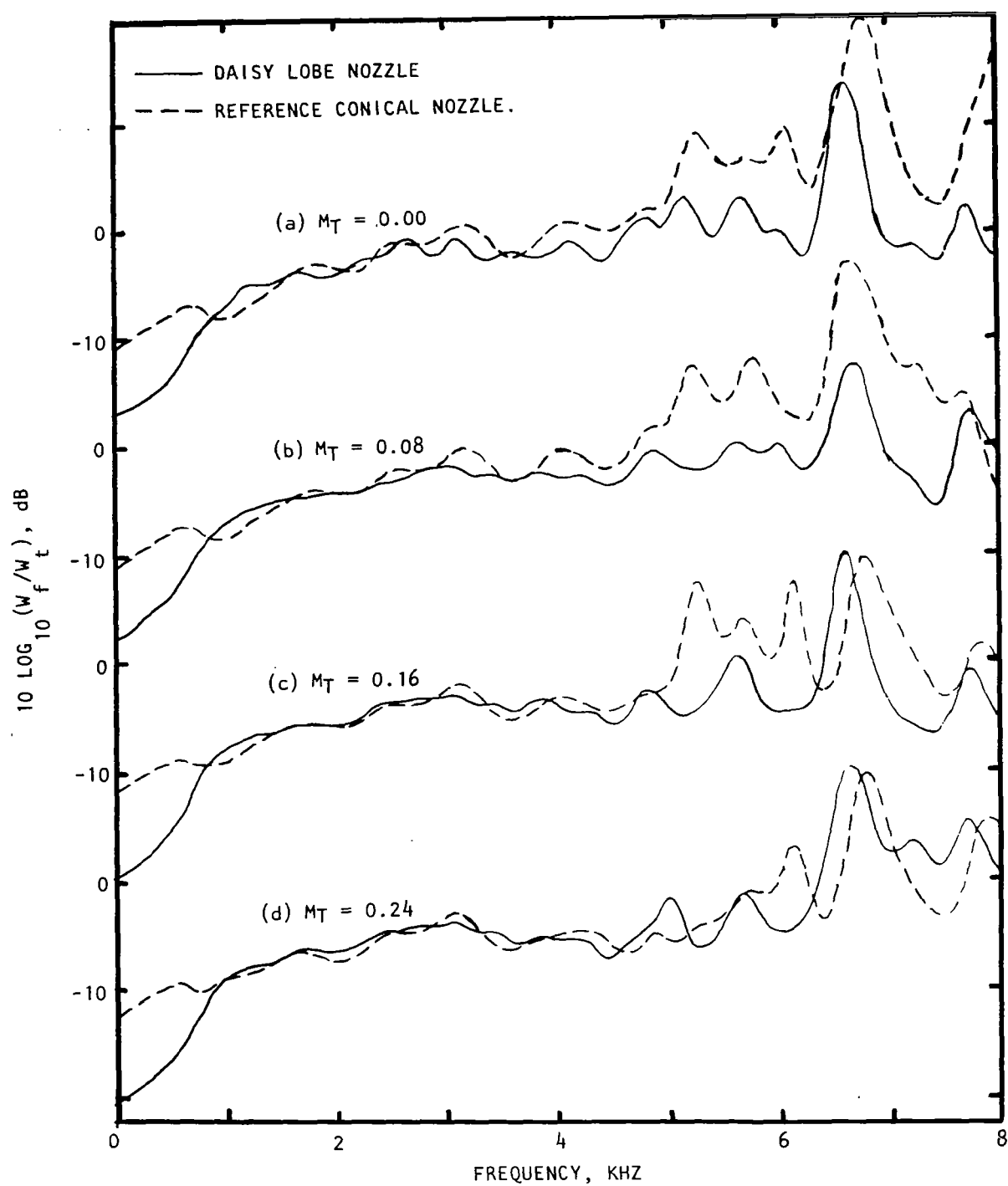


Figure 8.47 Effect of nozzle geometry on far-field acoustic power normalized with respect to transmitted power (PTF_t) for various free jet Mach numbers, $M_j = 0.6$.

(2) At $M_J = 0$, the reflection coefficients for the daisy lobe nozzle are more or less the same compared to the reference conical nozzle data. However, with increasing jet Mach number, the reflection coefficients for the conical nozzle start decreasing compared to those for the daisy lobe nozzle.

(3) At zero flow conditions, the radiation is predominantly towards the downstream of the jet axis. With flow, refraction becomes important and the peaks in the directivities shift towards higher angles.

(4) Exit open area of the nozzle, and not the nozzle geometry, is the controlling parameter that determines the shape and levels of the far-field spectra.

(5) A low-frequency power loss is observed for all Mach numbers. However, this is quite small for the no-flow condition. Initiation of flow increases the power loss levels. But, further increase in jet velocity does not alter the power loss levels appreciably.

(6) Forward velocity has very little effect on reflection coefficients.

(7) Forward velocity decreases the NTF in the rear arc, has little effect at and around 90 degrees, and increases radiation in the forward arc.

(8) Far-field power (PTF_1) is reduced under flight simulation.

(9) Power imbalance increases with increasing flight simulation velocity.

9.0 CONCLUDING REMARKS

The work described in this report presents an improved acoustic impulse technique to study the acoustic transmission characteristics of both single and dual stream duct/nozzle systems.

The objective of this program was to investigate the various problems associated with the spark-discharge impulse technique used in the first two phases of the present contract and to determine the means to overcome those problems. In addition, the refined impulse technique was to be used to obtain a better understanding of the acoustic transmission properties of selected nozzle geometries.

To accomplish these objectives, various problems associated with the spark-discharge impulse technique were first studied. Electroacoustic driver(s) instead of a spark discharge source was used as the impulsive source in the present impulse technique. Then the various processes to improve the impulse technique were implemented. These included (1) synthesizing an acoustic impulse with acoustic driver(s), (2) time-domain signal averaging, (3) signal editing, (4) spectral averaging, and (5) numerical smoothing.

The induct acoustic power measurement technique was improved by taking multiple induct measurements and by utilizing a modal decomposition process to account the contribution of higher order modes in the power computation. The improved acoustic impulse technique was then validated by comparing the results derived using this technique with similar results derived by other established methods.

The mechanism of acoustic power loss, that occurs when sound is transmitted through nozzle terminations, was investigated first by visual means. In addition, the amount of power loss was evaluated experimentally and by a theoretical prediction method.

Finally, the refined impulse technique was applied to obtain more accurate results for the acoustic characteristics of a conical nozzle and a multi-lobe multi-tube suppressor nozzle, both of which were tested earlier in the Phase II of this contract.

The important conclusions obtained from this work were listed in the respective sections; therefore, they are not repeated in this section. Instead, the specific improvements achieved due to the refined impulse technique are summarized in section 9.1. Also, some general comments on the future application of this technique are made in section 9.2.

9.1 IMPROVEMENT OF THE QUALITY OF RESULTS USING THE REFINED IMPULSE TECHNIQUE

Typical earlier results obtained by using the spark-discharge

impulse source and the possible errors associated with the impulse technique have been described in section 2. In this section, the improvements on those results are summarized.

(1) Reflection Coefficients: The reflection coefficient results, shown in figures 2.8 and 2.9, obtained by using high-intensity spark-discharge pulses, were influenced significantly by nonlinear effects. However, with the use of the refined acoustic impulse technique, the nonlinear effects are almost eliminated. This is shown in figure 6.4, where the reflection coefficient spectra for a straight duct termination, obtained by the refined technique, are in good agreement with Levine and Schwinger's analytical results (ref. 7).

(2) Induct Reflection Time Histories and Reflection Coefficient Spectrum for Daisy Lobe Nozzle: The effect of jet Mach number on the reflection time histories for the daisy lobe nozzle, obtained by using spark-discharge pulses, is shown in figure 2.10. Here, as the jet Mach number increases, the reflection from the open end decreases, and the reflection from the solid part of the nozzle termination increases. In fact, at $M_J = 1.2$, the incident and the reflected pulses appear to be of the same amplitude. This implies that, at higher jet Mach numbers, the incident sound field is almost completely reflected by the nozzle termination, and the corresponding reflection coefficient results shown in figures 2.12 and 2.13 confirm this.

In contrast, the induct time histories for the daisy lobe nozzle, obtained with the refined impulse technique and presented here in figure 9.1, show a different outcome. From this figure, it can be seen that although the open end reflection gradually diminishes with increasing jet Mach number, the in-phase reflection from the solid part becomes wider as the Mach number increases, and its peak amplitude does not approach the incident pulse amplitude at high M_J . This indicates that the reflected pulse contains less high-frequency energy (which must have been transmitted out of the nozzle). The reflection coefficient spectra plotted in figure 8.11 in fact support this; the reflection coefficient levels now decrease not only with increasing M_J , but also with increasing frequency. Hence, these results for the daisy lobe nozzle are similar to the results for the equivalent conical nozzle.

(3) Far-Field Time Histories: The far-field time histories for the daisy lobe nozzle (at various jet Mach numbers) obtained from the spark-discharge experiments are compared in figure 9.2 with similar results obtained by the refined impulse technique. The pulses with the spark-discharge sound source are contaminated with jet mixing noise, especially in the forward arc and at higher Mach numbers. In fact, at $M_J = 1.2$, the far-field pulses are not identifiable. In contrast, the far-field signals from the refined impulse technique are clearly visible at all polar angles even at $M_J = 1.2$. This is achieved by eliminating or minimizing the jet mixing noise contamination by using the signal averaging process.

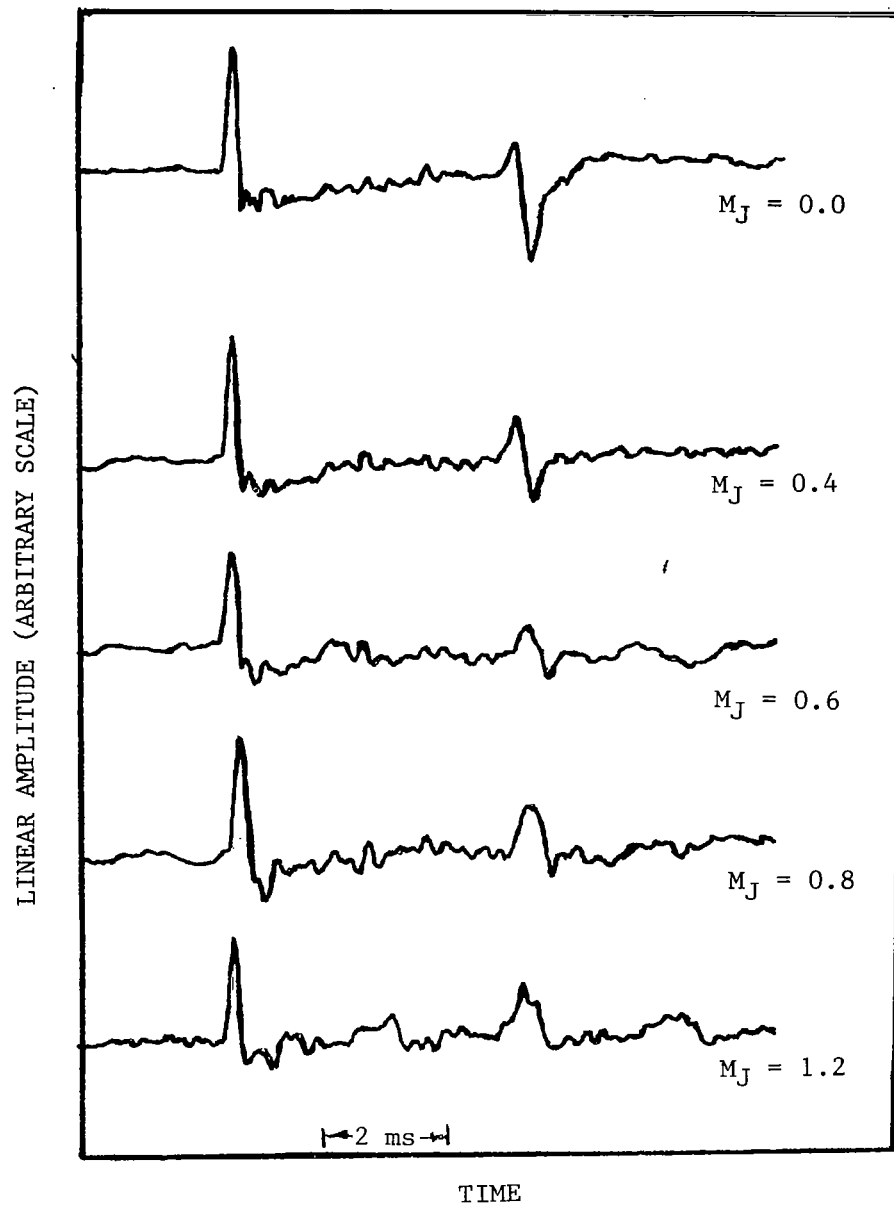


Figure 9.1 Induct time histories for the daisy lobe nozzle measured at various jet Mach numbers.

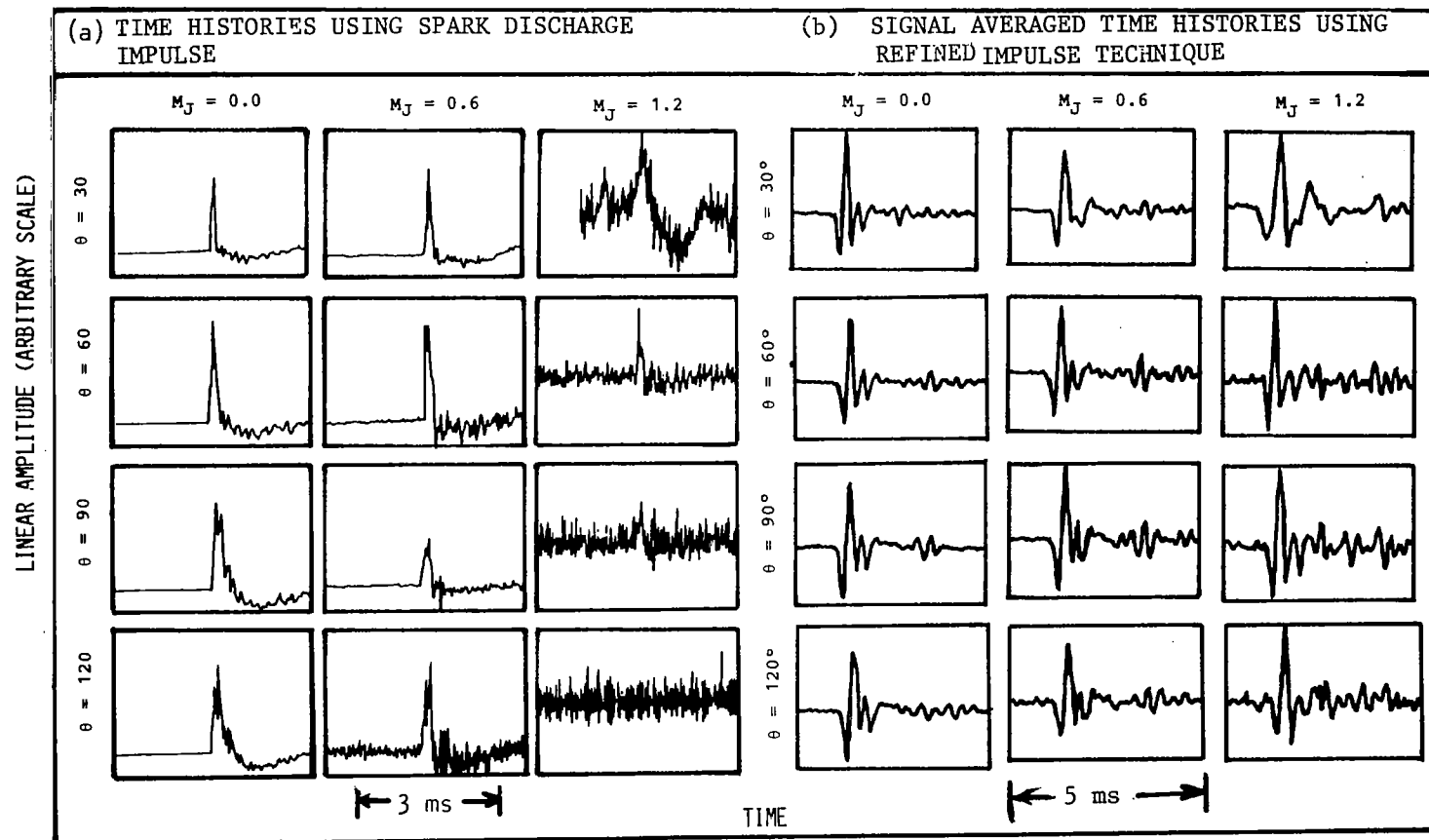


Figure 9.2 Far-field time-histories for the daisy lobe nozzle at various jet Mach numbers measured at different polar angles.

(4) Far-Field Power: In the earlier measurements using the spark-discharge impulse method to study the acoustic transmission characteristics of the daisy lobe nozzle as a function of jet Mach number, an opposite trend was found between the far-field power results and the reflection coefficient results. However, in the present work using the refined acoustic impulse technique, this inconsistency has been successfully resolved.

(5) Power Balance: In the previous work using high-intensity spark-discharge pulses, a large amount of low-frequency power loss was observed for the conical and the daisy lobe nozzles at all flow conditions including $M_J = 0$ (see figure 2.18). On the other hand, the present results using the refined impulse technique (with low-intensity pulses) do not show such a high power loss for the no-flow condition. However, the small power loss still observed at $M_J = 0$ is a real effect, and it has been confirmed by independent power imbalance measurements using the impedance tube technique (see Figure 6.8).

(6) Time Histories Due to Multipoint Source in Annular Region: In the earlier work to study the acoustic transmission characteristics of the multi-chute coaxial nozzle, severe problems were encountered when a multipoint spark-discharge source was used in the annular plenum. As indicated by figures 2.19 and 2.20, both the induct and the far-field signals are very complex in this case. As a result, an accurate separation and editing of the incident, reflected, and far-field pulses was not possible, and in particular, the reflection coefficients of the nozzle could not be determined. In contrast, as demonstrated in figure 9.3, the use of signal synthesis in the present refined technique (using acoustic drivers) allows a much better generation and separation of single incident and reflected pulses, even in the presence of flow. Furthermore, the far-field pulses are also much cleaner.

9.2 GENERAL COMMENTS ON THE APPLICATION OF THE ACOUSTIC IMPULSE TECHNIQUE

(1) A major limitation of this technique is associated with the frequency response of the acoustic driver. The acoustic driver is incapable of generating signals at frequencies outside its frequency band limits. Therefore, in practice, more than one driver with different frequency band widths may be necessary to cover a complete frequency range of interest.

(2) Signal synthesis is used to generate a desired, sharp, single incident pulse. However, if the frequency responses of the induct and the far-field microphones are not identical (more strictly, if the responses are not flat), then a sharp single pulse as measured by the induct microphones, may not be measured so by the far-field microphones.

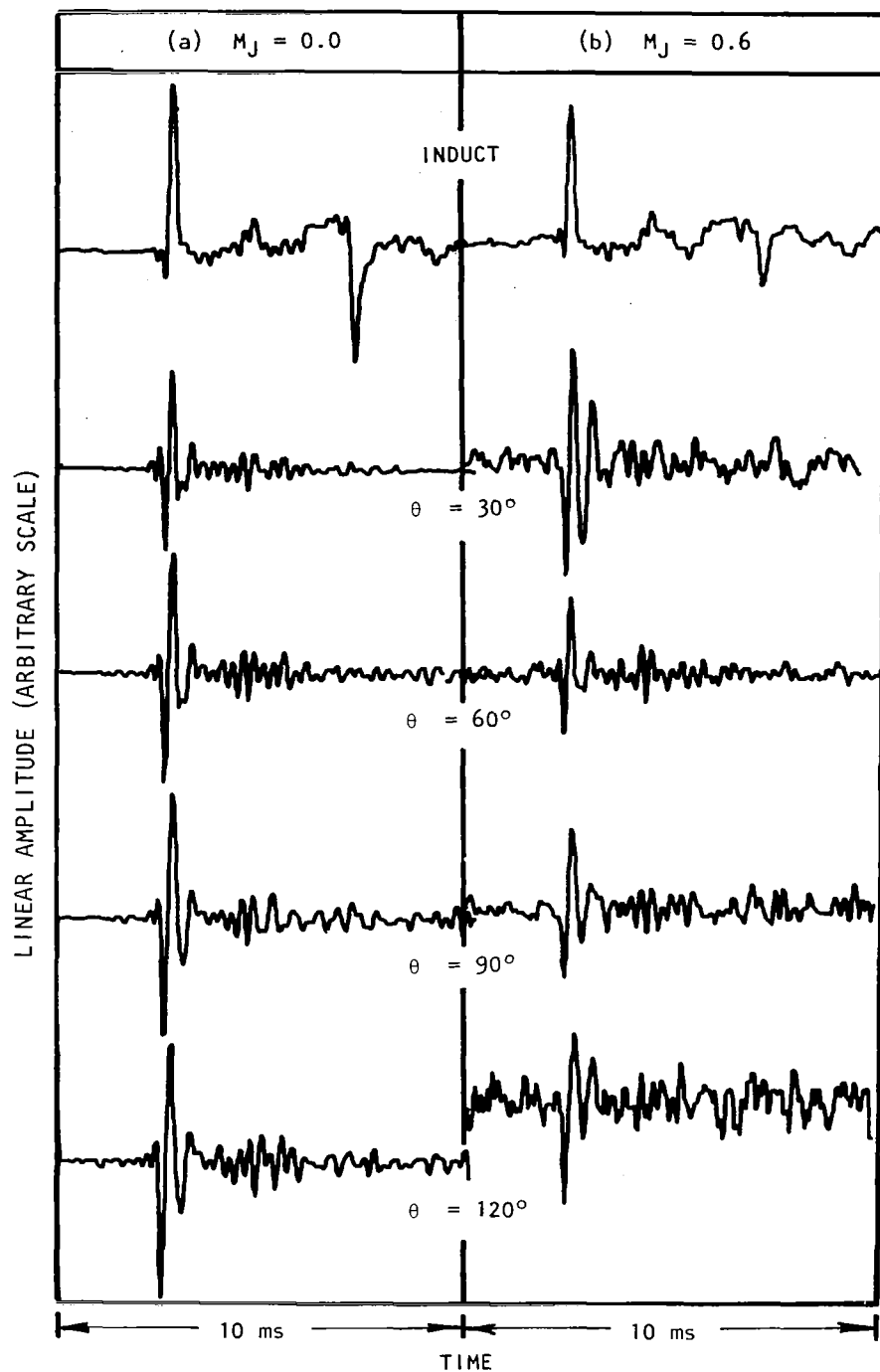


Figure 9.3 Induct and far field time histories for a conical annular nozzle, (a) $M_J = 0.0$, (b) $M_J = 0.6$.

An example of this effect is illustrated in figure 9.4 where the induct and far-field time histories for a straight duct are presented. The results presented in figure 9.4(a) are obtained by using a multipoint induct probe and 12.7 mm B&K microphones in the far field. The frequency responses of the induct probe microphones were not flat and thereby not similar to that for the B&K microphones. When signal synthesis was applied for the induct probe, the incident pulse came out to be a single pulse as desired. However, the pulses measured in the far field had multiple peaks. When a similar exercise was conducted by replacing the induct probe with a pressure transducer whose frequency response was similar to that for the B&K microphones, the results obtained with signal synthesis are quite different, as shown in figure 9.4(b). In this case, not only the incident and the reflected signals are single pulses, but also the far-field pulses are well defined with one negative and one positive peak.

(3) Since the intensity of the incident pulses due to acoustic driver(s) is about 30 dB lower compared to a spark discharge pulse, the signal-to-noise ratio for the far-field signals is quite poor at higher Mach numbers, even after signal averaging. This introduces considerable amount of error in the process of editing.

This problem can be avoided in principle by increasing the number of signal averages, which is a difficult and time-consuming process. Alternatively, a high-intensity spark-discharge pulse can be used for higher flow conditions, where the nonlinear effects of the pulse would be almost negligible due to the presence of flow. The spark discharge must be repeated several times to carry out a few signal averages to reduce the jet mixing noise to acceptable level. Therefore, a combination of the spark-discharge impulse technique and the presently-developed impulse technique appears to be more suitable to cover all flow conditions of practical interest.

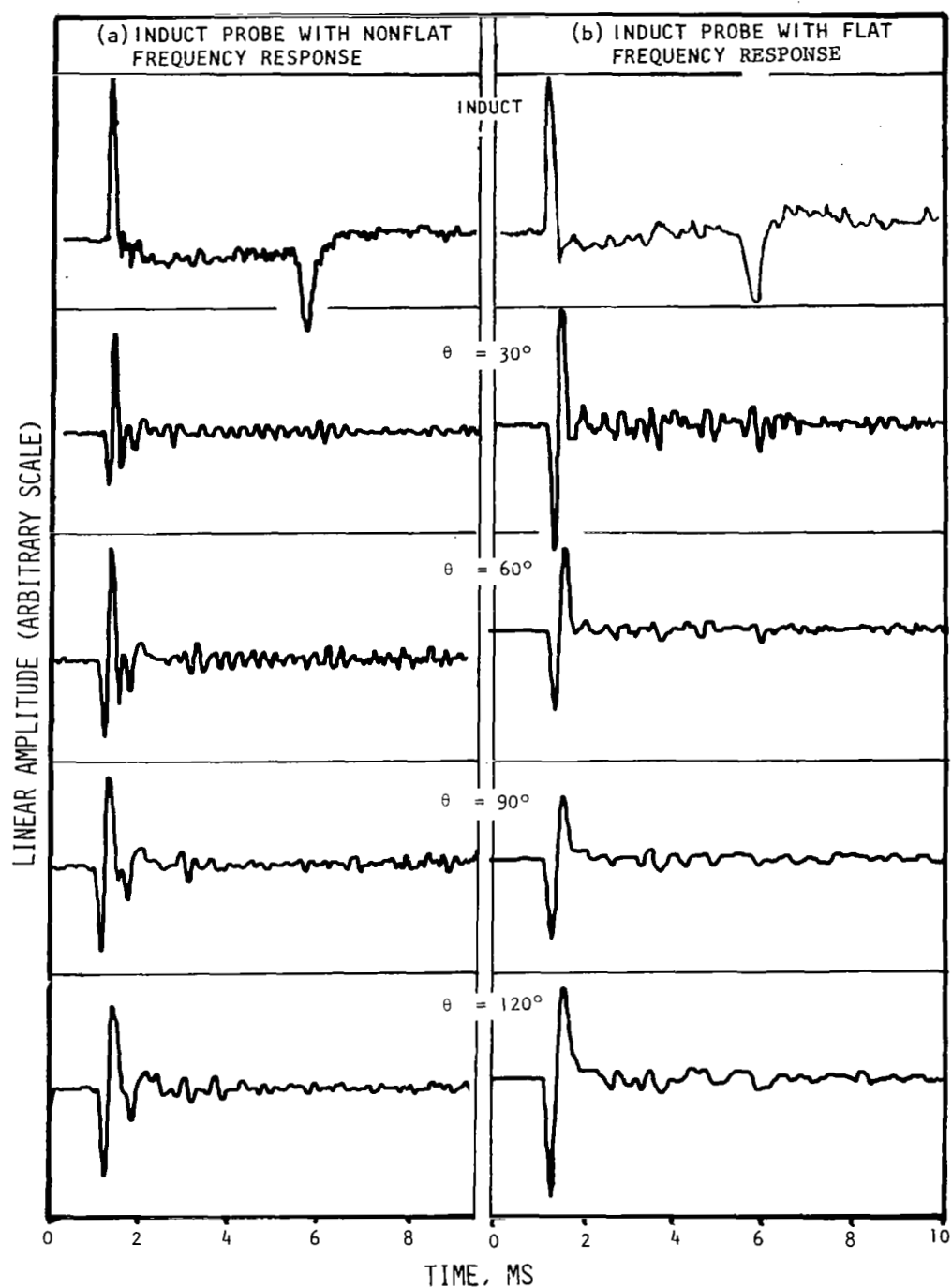


Figure 9.4 Induct and far-field time histories for a straight duct at $M_j = 0.0$, using two different induct probes, with (a) non-flat and (b) flat frequency response, the farfield microphones being same for both cases with flat frequency response.

APPENDIX A

NOMENCLATURE

A	cross-sectional area of the duct
c	speed of sound
D	diameter
f	frequency
h	annulus width
I	acoustic intensity
k	wave number, $2\pi f/c$
L	protrusion of primary exit beyond the fan exit
NTC(\equiv NTF)	normalized transmission coefficient (\equiv nozzle transfer function)
M	Mach number
m	circumferential mode number
n	radial mode number
p	acoustic pressure amplitude
\bar{p}	mean pressure
P_{mn}	modal coefficient for mn mode
PTF	power transfer function
R	radius, also resistance
R_I	inner duct radius of coannular system
R_m	polar arc radius
r	radial coordinate
t	time
T	temperature
u	oscillatory flow velocity
V	mean velocity

W	acoustic power
X	reactance
x	axial coordinate
Z	radiation impedance
λ	wave length
ρ	density
$\hat{\rho}$	oscillatory density
σ	reflection coefficient amplitude
θ	azimuthal coordinate (in chapter 5), also. far-field measurement angle (degrees) with the jet axis (polar angle, also emission angle)
ϕ	convergence angle of the nozzle
τ	time

Subscripts and Superscripts

0	relating to the ambient
c	relating to the conical nozzle
D	relating to the duct
DL	relating to the daisy lobe nozzle
f	relating to the far-field
i	relating to the incident wave
J	relating to the fully-expanded jet condition (for single stream and for annular stream)
r	relating to the reflected signal
t	relating to the transmitted signal
T	relating to the free-jet
'	relating to the first derivative
''	relating to the second derivative

APPENDIX B

DATA REDUCTION COMPUTER PROGRAMS

The major computer programs used for the present investigation are listed in this Appendix. These programs are written in FORTRAN V interpretive language compatible with the VAX/VMS machine language compiler. The computer programs are divided into four groups. The first group consisting of a single program with two subroutines used to synthesize acoustic signals to generate a desired signal from acoustic driver system. The second group consisting of five main programs was used for modal decomposition exercise for single and annular stream ducts. The third group consisting of a single program with two subroutines was used to evaluate complex reflection coefficient and specific nozzle impedance using impedance tube measurements. The fourth group consisting of a single program with five subroutines was used to compute induct and far-field parameters for single or annular stream duct-nozzle systems.

B.1 SIGNAL SYNTHESIS

The signal synthesis is defined as the procedure to obtain a distorted waveform from the response of the driver system. The calculated distorted wave form, when fed back to the driver system, completes a feed-back loop and the output of the driver system is then the desired signal.

MSYNTH: This is the main program to compute the distorted waveform to generate a desired signal. The input to the program includes the time history of an arbitrary input signal to the driver system and the corresponding output of the driver system. The desired output signal time history is also fed to the program when it is different from the arbitrary input signal to the driver system.

FFT: This subroutine to MSYNTH is used to calculate the Fourier transform of the input time histories to the main program and to calculate the inverse transform of the synthesized output.

BITREV: This subroutine to MSYNTH is used to reverse the data from inverse binary to normal.

```

C
C PROGRAM NAME: MSYNTH.FOR
C
C *****
C
C TO CALCULATE A SYNTHESIZED SIGNAL BY CONVOLUTION
C
C *****
C
C DIMENSION IA(3,1024),NR1(3)
C
C COMPLEX CC(1024),DD(1024),RA(1024),D(1024),CD(1024)
C
C CHARACTER FNAME*13
C
C PI=3.1415926
C
C ***** INPUT DATA *****
C
C READ(5,*)N,IYES,IDES,IDX,NR1(1),NR1(2),NNO
C -----
C IF(IDES.EQ.1)READ(5,*)NR1(3)
C -----
C
C N = EXPONENT OF 2 TO DETERMINE TOTAL NUMBER OF
C POINTS IN THE RECORD.
C IYES = CONTROL PARAMETER TO EDIT FREQUENCY SPECTRUM
C TO AVOID POOR LOW AND HIGH END DRIVER'S RESPONSE
C = 0, NO EDITING
C = 1, EDITING REQUIRED
C IDES = CONTROL PARAMETER TO DECIDE ON DESIRED SIGNAL
C = 0, DESIRED SIGNAL IS SAME AS ORIGINAL INPUT SIGNAL
C = 1, DESIRED SIGNAL IS DIFFERENT FROM ORIGINAL INPUT
C SIGNAL AND DATA FOR THIS SIGNAL IS SUPPLIED
C IDX = CONTROL PARAMETER FOR GETTING PRINTOUT
C = 0, NO PRINTOUT
C = 1, INPUT AND VARIOUS OUTPUT DATA ARE PRINTED
C NR1(1) = RUN NUMBER FOR ORIGINAL INPUT SIGNAL
C NR1(2) = RUN NUMBER FOR OUTPUT SIGNAL
C NR1(3) = RUN NUMBER FOR DESIRED SIGNAL IF IT IS NOT
C SAME AS ORIGINAL INPUT SIGNAL
C NNO = NUMBER OF LOW FREQUENCY POINTS FOR WHICH THE
C DRIVER'S RESPONSE WOULD BE KEPT ZERO
C = ATLEAST 1
C *****
C
C N1=2**N
C N2=N1/2

```

```

      JK0=2
      IF(IDES.EQ.1)JK0=3
C
C      ***** INPUT DATA FROM FILES STORED IN DISC *****
C
      DO 100 JK=1,JK0
      NR=NR1(JK)
      NP=100*JK
      IF(JK.EQ.3)NP=100
C      JK = 1, INPUT TO DRIVER
C      JK = 2, OUTPUT MEASURED BY PROBE
C      JK = 3, DESIRED OUTPUT
C      (IF IDES=0, DESIRED OUTPUT IS SAME AS INPUT TO DRIVER)
      ENCODE(13,110,FNAME)NR,NP
110  FORMAT(2I3,'SYN.RDT')
      OPEN(UNIT=9,NAME=FNAME,STATUS='OLD')
      READ(9,270)(IA(JK,I),I=1,N1)
      IF(IDX.EQ.1)WRITE(6,120)NR,NP
120  FORMAT(1H1,10X,2I8//)
      IF(IDX.EQ.1)WRITE(6,270)(IA(JK,I),I=1,N1)
      CLOSE(9)
100  CONTINUE
C
C      *****
C
      DO 150 I=1,N1
      A1=IA(1,I)
      A2=IA(2,I)
      DD(I)=CMPLX(A1,0.)
      CC(I)=CMPLX(A2,0.)
150  CONTINUE
      IF(IDX.EQ.1)WRITE(6,130)(DD(I),I=1,N1)
      IF(IDX.EQ.1)WRITE(6,130)(CC(I),I=1,N1)
      CALL FFT(N,DD,D)
      CALL BITREV(N,DD)
      CALL FFT(N,CC,D)
      CALL BITREV(N,CC)
      IF(IDX.EQ.1)WRITE(6,140)(DD(I),I=1,N1)
      IF(IDX.EQ.1)WRITE(6,140)(CC(I),I=1,N1)
130  FORMAT(10F8.0)
140  FORMAT(10F10.2)
      IF(IDES.NE.1)GO TO 170
      DO 160 I=1,N1
      A1=IA(3,I)
      CD(I)=CMPLX(A1,0.)
160  CONTINUE
      CALL FFT(N,CD,D)
      CALL BITREV(N,CD)

```



```

      GO TO 190
170  CONTINUE
      DO 180 I=1,N1
180  CD(I)=DD(I)
190  CONTINUE
      DO 200 I=1,N1
      RA(I)=CD(I)*DD(I)/CC(I)
      IF(I.LF.NN0)RA(I)=(0.,0.)
      RA(I)=CONJG(RA(I))
200  CONTINUE
      IF(IYES.EQ.0)GO TO 210
      READ(5,*) ALF,AUF,FRE
      ANL=(N2-1)*ALF/FRE
      AUP=(N2-1)*AUF/FRE
      NL=ANL+1
      NU=AUP+1
      WRITE(6,*) ALF,AUF,FRE,NL,NU
      IF(NL.LE.2) GO TO 230
      DO 220 I=2,NL
      RA(I)=DD(I)
      RA(N1+2-I)=DD(I)
220  CONTINUE
230  CONTINUE
      IF(NU.GE.N2) GO TO 210
      DO 240 I=NU,N2
      RA(I)=DD(I)
      RA(N1+2-I)=DD(I)
240  CONTINUE
210  CONTINUE
      CALL FFT(N,RA,D)
      CALL BITREV(N,RA)
      DO 250 I=1,N1
      RA(I)=CONJG(RA(I))/N1
250  CONTINUE
      DO 260 I=1,N1
      IA(2,I)=REAL(RA(I))+.5
260  CONTINUE
C
C      ** DATA STORED IN FOR020 IS COPIED TO A MAG ***
C      TAPE FOR SUBSEQUENT USE
C
      WRITE(20,270) (IA(2,I),I=1,N1)
270  FORMAT(10I8)
      STOP
      END

```

```

C
C      SUBROUTINE FFT(IGAM,XVAL,W)
C
C      *****
C
C      TO CALCULATE THE 'Z' TRANSFORM OF 2**N SETS OF POINTS
C
C      *****
C
C      IGAM = EXPONENT OF 2 TO DETERMINE TOTAL NO OF POINTS
C      INUM = NUMBER OF POINTS
C      XVAL(1) = VALUE AT T=0
C      XVAL(INUM/2+1) = VALUE AT T=PERIOD/2
C      XVAL(INUM/2+2) = VALUE AT T=-PERIOD/2+DELT
C      XVAL(INUM)      = VALUE AT T=-DELT
C
C      XVAL IS RETURNED AS THE FOURIER TRANSFORM S(F) IN STEPS
C      OF DELF=1/PERIOD. S(F) IS FOLDED ABOUT F=IUNM/2*PERIOD
C
C      FOR A FREQUENCY TRANSFORM THE CALLING ROUTINE MUST
C      MULTIPLY BY DELT TO OBTAIN THE POWER SPECTRUM.
C
C      *****
C
C      IMPLICIT INTEGER*2 (I-N)
C
C      DIMENSION XVAL(1),W(1)
C
C      COMPLEX XVAL,W,VAL,XDUM,WC
C
C      DATA IONCE/0/
C
C      PI=3.1415926
C      IG=1
C      IF(IGAM.LT.0)IG=-1
C      IGAM=IABS(IGAM)
C      NUM=2**(IGAM-1)
C      INUM=2*NUM
C      ANUM=IG*NUM
C      IF(IONCE.EQ.IGAM)GO TO 110
C      XDUM=CMPLX(0.0,-PI/ANUM)
C      W(1)=(1.0,0.0)
C      WC=CEXP(XDUM)
C      DO 120 KKK=2,NUM
C      K1=2*(KKK-1)
C      IC=K1
C      I4=K1
C      IBITV=INUM
C      DO 170 I=1,IGAM
C      IBITV=IBITV/2
C      IB=IC/2

```

```

      K1=(IC-2*IB)*IBITV+K1
      IC=IB
      I1=I4/IBITV
      I1=IBITV*I1
      K1=K1-I1
      I4=I4-I1
170  CONTINUE
      W(KKK)=WC**K1
120  CONTINUE
      IONCE=IGAM*IG
110  CONTINUE
      N2=1
      IGM2=NUM
      DO 140 IOUT=1,IGAM
      DO 200 KK=1,IGM2
      KVAL=KK+IGM2
      XDUM=XVAL(KK)
      VAL=XVAL(KVAL)
      XVAL(KK)=XDUM+VAL
200  XVAL(KVAL)=XDUM-VAL
      IF(N2.EQ.1)GO TO 210
      DO 150 KKK=2,N2
      LLL=2*(KKK-1)*IGM2
      DO 160 KK=1,IGM2
      IVAL=KK+LLL
      KVAL=IVAL+IGM2
      XDUM=XVAL(IVAL)
      VAL=W(KKK)*XVAL(KVAL)
      XVAL(IVAL)=XDUM+VAL
      XVAL(KVAL)=XDUM-VAL
160  CONTINUE
150  CONTINUE
210  N2=2*N2
      IGM2=IGM2/2
140  CONTINUE
      RETURN
      END

```

```

C      SUBROUTINE BITREV(IGAM,XVAL)
C
C      *****
C
C      TO REVERSE THE DATA FROM INVERSE BINARY TO NORMAL
C
C      *****
C
C      IGAM = EXPONENT OF 2 TO DETERMINE THE NUMBER OF
C              POINTS IN THE DATA STRING
C      XVAL = A COMPLEX ARRAY OF 2**IGAM TO BE BITREVERSED
C
C      IMPLICIT INTEGER*2 (I-N)
C
C      DIMENSION XVAL(1)
C
C      COMPLEX XVAL,XDUM
C
C      INUM=2**IGAM
C      NUM1=INUM-1
C      ITOP=INUM/2
C      IG=1
C      N1=1
C      DO 100 I=1,NUM1
C      IC=1
C      NUP=ITOP
C      ITMP=0
C      IF(I.LE.N1)GO TO 110
C      N1=2*N1
C      IG=IG+1
110   DO 120 J=1,IG
C      IB=IC/2
C      ITMP=(IC-2*IB)*NUP+ITMP
C      IC=IB
C      NUP=NUP/2
120   CONTINUE
C      IVAL=I+1
C      ITMP=ITMP+1
C      IF(IVAL.GT.ITMP)GO TO 100
C      XDUM=XVAL(IVAL)
C      XVAL(IVAL)=XVAL(ITMP)
C      XVAL(ITMP)=XDUM
100   CONTINUE
C      RETURN
C      END

```

B.2 MODAL DECOMPOSITION

In modal decomposition procedure several radial and azimuthal pressure measurements are made and using these complex pressure data the modal contents of the pressure field is determined. Therefore, the acoustic power due to each individual mode and also their total sum are derived.

B.2.1 Radial Modal Decomposition for Single Stream Duct-Nozzle System

(1) SIDCOR: This program is used to evaluate absolute sound pressure level and the relative phase of the incident and the reflected pressure fields measured at various radial locations. The input to the program consists of the complex reflection coefficient and the complex transfer function of a reference delta function with respect to the incident pressure for various radial measurements.

(2) MMMODAL: This is the radial modal decomposition program for single stream duct-nozzle systems. The program computes the area-weighted pressures, area-weighted induct powers, individual modal induct powers and successive summation of modal induct powers. The induct powers include the incident, the reflected and the transmitted powers. Input to the program includes the output of SIDCOR and other parameters defined in the program listing.

BES12: This subroutine to program MMMODAL is used to calculate Bessel functions (first kind) of zero and first order for real arguments.

QSF: This subroutine to program MMMODAL is used to compute the integral of a given table of six or more equispaced values.

```

C
C PROGRAM; SIDCOR.FOR
C
C *****
C
C TO EVALUATE THE ABSOLUTE SOUND PRESSURE LEVEL
C OF THE INCIDENT AND REFLECTED PRESSURE FIELDS
C USING THE REFLECTION COEFFICIENT DATA AND THE
C TRANSFER FUNCTION OF THE REFERENCE DELTA
C FUNCTION WITH RESPECT TO THE INCIDENT PRESSURE
C FOR A SINGLE STREAM DUCT-NOZZLE SYSTEM, IN-DUCT
C PRESSURE FIELD MEASURED USING A MULTI-POINT PROBE
C
C *****
C
C DIMENSION C(501),AMP(6),CR(501),AC(501),PC(501),
C *AD(501),PD(501),PH1(501),AM(6,501),PH(6,501),
C *F(501),RAD(501),RPD(501)
C
C CHARACTER FNAME*13
C
C ***** INPUT DATA *****
C
C READ(5,*)INDX,NR,NP80,NR0,NR10,A1
C -----
C INDX=0, WITHOUT MEAN FLOW
C      =1, WITH MEAN FLOW
C NR=RUN NUMBER
C NP80=200+NUMBER OF POINTS TAKEN AWAY BETWEEN
C      INCIDENT PULSE & REFLECTED PULSE TO EVALUATE
C      REFLECTION COEFFICIENT
C NR0=RUN NUMBER FOR AMPLITUDE CALIBRATION
C NR10=RUN NUMBER FOR PHASE CALIBRATION
C A1=ATTENUATION ON CHANNEL A DURING AVERAGING
C
C READ(5,*)(AMP(K),K=1,6)
C -----
C AMP(K)=AMPLIFICATION FOR THE MICROPHONES USED IN
C      SIX POINT PROBE
C K=1 CORRESPONDS TO THE MIC AT THE CENTERLINE OF
C      THE DUCT; K BEING THE NO OF INDUCT MEASUREMENTS.
C
C IB=501
C NPO=103
C
C IB=NUMBER OF DATA POINTS IN A FILE
C NPO=THREE DIGITS ASSOCIATED WITH NR0 TO NAME
C      THE AMPLITUDE CALIBRATION DATA FILE

```

```

C
C   SPLR0=114.-37.9+20.-50.+(A1+5.)
C
C   SPLR=SPLR0-AMP(K)
C       =114.-37.9+(20.-AMP(K))-50.+(A1+5.)
C
C   114. dB (WITH 25.+25.=50. dB ATTN) WITH RESPECT TO
C   1800 LINEAR COUNT (WITH 5 dB ATTN) READS -37.9;
C   THEREFORE A FACTOR 114.-37.9-50. COMES INTO PICTURE.
C
C   ATTN OF ACTUAL SIGNAL (IN CH A) WAS A1+A2 dB
C   ATTN OF REF. SIGNAL (1800 COUNT IN CH B) WAS 5. dB
C   DURING DECODING ATTN A2 dB OF CH A WAS SUBSTRUCTED
C   FROM AND ATTN OF 5. dB OF CH B WAS ADDED TO THE DATA ,
C   (i.e.,-A2+5. dB ADDED). IN OTHER WORDS A2-5. dB IS
C   INCORPORATED IN SPLR INDIRECTLY. SO THE REMAINING
C   A1+5. dB OUT OF A1+A2 dB (i.e., [A1+A2]-[A2-5.]=A1+5.)
C   IS ADDED TO SPLR.
C
C   AMPLIFICATION DURING CAL WAS 20. dB AND DURING ACTUAL
C   TEST WAS AMP(K) dB. SO A FACTOR OF 20.-AMP(K) IS TO
C   BE ADDED TO SPLR.
C
C   CR(I)=FREQUENCY RESPONSE OF B&K MIC USED IN CALIBRATION
C
C   C(I)=TF AMPLITUDE OF THE PROBE MIC AT CENTERLINE
C       WRT A B&K MICROPHONE.
C
C   AC(I)=AMPLITUDE CALIBRATION OF PROBE MICS
C       WRT THE MIC AT CENTERLINE
C
C   PC(I)=PHASE CALIBRATION OF PROBE MICS WRT
C       THE MIC AT CENTERLINE ( INCLUDES TAPE
C       RECORDER PHASE CALIBRATION )
C
C   *****
C
C   DO 200 I=1,IB
C   F(I)=(I-1)*20.
C   X=F(I)
C   IF(I.LE.31)CR(I)=-5.33+.0318*X-.639E-04*X*X
C   *+.426E-07*X*X*X
C   IF(I.GT.31.AND.I.LE.51)CR(I)=0.
C   IF(I.GT.51)CR(I)=-.0876+.229E-03*X-.172E-06*X*X
C   *+.181E-10*(X**3)-.725E-15*(X**4)
200  CONTINUE
C
C   ***** INPUT DATA FROM DISC *****

```

```

C      ENCODE(13,140,FNAME)NR0,NP0
      OPEN(UNIT=9,NAME=FNAME,STATUS='OLD')
      READ(9,130)(C(I),I=1,IB)
      CLOSE(9)
      DO 360 NZ=1,2
      DO 100 K=1,6
      SPLR=SPLR0-AMP(K)
110    FORMAT(2I3,'SID.RDT')
130    FORMAT(10F8.3)
      NP2=102+K
      NP4=302+K
      IF(K.EQ.1)GO TO 240
      ENCODE(13,140,FNAME)NR0,NP2
140    FORMAT(2I3,'SMT.CAL')
      OPEN(UNIT=9,NAME=FNAME,STATUS='OLD')
      READ(9,130)(AC(I),I=1,IB)
      CLOSE(9)
      ENCODE(13,140,FNAME)NR10,NP4
      OPEN(UNIT=9,NAME=FNAME,STATUS='OLD')
      READ(9,130)(PC(I),I=1,IB)
      CLOSE(9)
240    CONTINUE
      ENCODE(13,110,FNAME)NR,NP2
      OPEN(UNIT=9,NAME=FNAME,STATUS='OLD')
      READ(9,130)(AD(I),I=1,IB)
      READ(9,130)(PD(I),I=1,IB)
      CLOSE(9)
      IF(NZ.EQ.1)GO TO 390
      NP8=NP80+K*100
      ENCODE(13,110,FNAME)NR,NP8
      OPEN(UNIT=9,NAME=FNAME,STATUS='OLD')
      READ(9,130)(RAD(I),I=1,IB)
      READ(9,130)(RPD(I),I=1,IB)
      CLOSE(9)
C
C      *****
C
      RPD(1)=0.
      DA=(RAD(16)-RAD(11))/5.
      DO 410 I=1,15
      IF(INDX.EQ.0)RAD(I)=RAD(16)*(I-1)/15.
      IF(INDX.EQ.1.AND.I.LT.9)RAD(I)=RAD(9)-(9-I)*DA
410    CONTINUE
      DO 400 I=1,IB
      AD(I)=AD(I)-RAD(I)
      PD(I)=PD(I)-RPD(I)
400    CONTINUE

```



```

390  CONTINUE
      DO 180 I=1,IB
      IF(K.NE.1)GO TO 150
      AM(K,I)=SPLR-AD(I)-C(I)-CR(I)
      PH(K,I)=-PD(I)
      PH1(I)=PH(1,I)
      GO TO 170
150  CONTINUE
      AM(K,I)=SPLR-AD(I)-C(I)-AC(I)-CR(I)
      PH(K,I)=-PD(I)-PC(I)
170  CONTINUE
      PH(K,I)=PH(K,I)-PH1(I)
530  CONTINUE
      IF(PH(K,I).LT.180.)GO TO 520
      PH(K,I)=PH(K,I)-360.
      GO TO 530
520  CONTINUE
      IF(PH(K,I).GE.-180.)GO TO 540
      PH(K,I)=PH(K,I)+360.
      GO TO 520
540  CONTINUE
180  CONTINUE
C
C    *** OUTPUT DATA STORED IN DISC *****
C
      IF(NZ.EQ.2)NP2=302+K
      ENCODE(13,190,FNAME)NR,NP2
190  FORMAT(2I3,'COR.RDT')
      OPEN(UNIT=9,NAME=FNAME,STATUS='NEW')
      WRITE(9,130)(AM(K,I),I=1,IB)
C    AM = ABSOLUTE PRESSURE AMPLITUDE, dB
      WRITE(9,130)(PH(K,I),I=1,IB)
C    PH = PHASE DIFFERENCE BETWEEN PRESSURES MEASURED
C          AT A RADIAL LOCATION WITH RESPECT TO THAT
C          AT A REFERENCE POINT (AT WALL)
      CLOSE(9)
100  CONTINUE
C
C    ***** PRINTOUT OF OUTPUT DATA *****
C
      WRITE(6,320)
      IF(NZ.EQ.1)WRITE(6,280)NR
      IF(NZ.EQ.2)WRITE(6,160)NR
280  FORMAT(10X,'INCIDENT WAVE AMPLITUDE FOR
* RUN NO = ',I3//)
160  FORMAT(10X,'REFLECTED WAVE AMPLITUDE FOR
* RUN NO = ',I3//)
      WRITE(6,290)(F(I),(AM(K,I),K=1,6),I=1,IB,5)

```

```

290  FORMAT(F10.0,6F13.3)
      WRITE(6,320)
      IF(NZ.EQ.1)WRITE(6,210)NR
      IF(NZ.EQ.2)WRITE(6,370)NR
210  FORMAT(1H,10X,'INCIDENT WAVE PHASE FOR RUN NO = ',I3//)
370  FORMAT(1H,10X,'REFLECTED WAVE PHASE FOR RUN NO = ',I3//)
      WRITE(6,290)(F(I),(PH(K,I),K=1,6),I=1,18,5)
360  CONTINUE
320  FORMAT(1H1)
      STOP
      END

```

```

C
C PROGRAM NAME: MMMODAL.FOR
C
C *****
C
C MODAL DECOMPOSITION PROGRAM FOR SINGLE STREAM
C DUCT-NOZZLE SYSTEM FOR RADIAL MODES.
C
C *****
C
C DIMENSION W(3,4,510),WI(3,4,510),RCP(4,510),RCPI(4,510)
C *,POS(10),BESO(10,10),PRESA(501),PRES(501),AMPL(6,501),
C *PRE1(10),PRE2(10),FRQ(510),ARWA(2,501),ARWP(3,501)
C *,RCAW(501),POWT(501),RCIND(4,501)
C
C COMPLEX JAY,CC(1024),C1(1024),EPS,PCOMX(10,510),D(2,10)
C *,PCOFF(2,4,501)
C
C REAL MACH
C
C CHARACTER FNAME*13
C
C COMMON/BK11/RMN(151)
C
C DATA PI/3.14159265/,GAM/1.402/,FACT/3.7396751/,JAY/(0.,1.)/
C
C ***** INPUT DATA *****
C
C ( ASSIGNED TO MODAL.DAT)
C
C NR=RUN NUMBER
C NF=NUMBER OF FREQUENCIES
C NRM=NUMBER OF RADIAL MODES
C RAD=DUCT RADIUS, INCHES
C DELF=FREQUENCY BAND PER DATA POINT
C NPOS=NUMBER OF RADIAL MEASUREMENTS
C INDX=1,DATA TO BE STORED IN FILE
C INDX1=1,MODAL POWER CALCULATED USING INGARD'S
C EXPRESSION
C
C READ(5,*) NR,NF,NRM,RAD,DELF,NPOS,INDX,INDX1
C -----
C
C POS(I)=r/RAD FOR I th MEASUREMENT POINT FROM CENTERLINE
C
C READ(5,*) (POS(I),I=1,NPOS)
C -----
C

```

```

C      PAMB=AMBIENT PRESSURE, PSIA
C      PT=TOTAL PRESSURE, PSIG
C      PS=STATIC PRESSURE, PSIG
C      TR=TOTAL TEMPERATURE, F
C
C      READ(5,*)PAMB,PT,PS,TR
C      -----
C
C      RMN(1)=0.
C      RMN(2)=3.83
C      RMN(3)=7.02
C      RMN(4)=10.13
C      HH=POS(2)-POS(1)
C      RAD=RAD/12.
C      DO 280 I=1,NPOS
C      DO 280 J=1,NRM
C      X1=RMN(J)*POS(I)
C      CALL BES12(X1,AJ0,AJ1,0)
C      BES0(I,J)=AJ0
280    CONTINUE
C      DO 400 I=1,NF
C      FRQ(I)=(I-1)*DELF
400    CONTINUE
C
C      DO 190 NZ=1,2
C
C      NZ=1, INCIDENT PRESSURE FIELD
C      =2, REFLECTED PRESSURE FIELD
C
C      ****TO READ PRESSURE AMPLITUDE & PHASE FROM DATA FILES****
C
C      DO 170 J=1,NPOS
C      NP=102+J+(NZ-1)*200
C      ENCODE(13,200,FNAME)NR,NP
200    FORMAT(2I3,'COR.RDT')
C      OPEN(UNIT=9,NAME=FNAME,STATUS='OLD')
C      READ(9,240)(PRESA(I),I=1,NF)
C      READ(9,240)(PRESP(I),I=1,NF)
C      CLOSE(9)
240    FORMAT(10F8.3)
C      PRESA(1)=PRESA(2)
C      PRESP(1)=PRESP(2)
C
C      *****CONVERSION OF PRESSURE DATA INTO COMPLEX FORM*****
C
C      DO 100 I=1,NF
C      ACA=PRESA(I)
C      ACP=PRESP(I)*PI/180.

```

```

    ACA=10.** (ACA/20.)
    AMPL(J,I)=ACA
    CACP=COS(ACP)
    SACP=SIN(ACP)
    ACP=ACA*SACP
    ACA=ACA*CACP
    PCOMX(J,I)=CMPLX(ACA,ACP)
100  CONTINUE
170  CONTINUE
C
C      ***** EVALUATION OF VARIOUS PARAMETERS *****
C
C      MACH=DUCT MACH NUMBER
C      TS=STATIC TEMPERATURE IN THE DUCT, R
C      CNOT=SONIC SPEED, FT/SEC.
C      RC=PRODUCT OF DENSITY & SONIC SPEED, SLUG/(FT*FT*SEC)
C
    G=(GAM-1.)/2.
    GI=1./G
    GACI=(GAM-1.)/GAM
    PR=PT-PS
    PSA=PS+PAMB
    MACH=SQRT(((1.+PR/PSA)**GACI-1.)*GI)
    IF(NZ.EQ.2)MACH=-MACH
    BETA=1.-MACH*MACH
    AMACH2=MACH*MACH
    TS=(TR+460.)/(1.+G*AMACH2)
    CNOT=49.0166*SQRT(TS)
    RC=GAM*PSA*144./CNOT
    PII=BETA*BETA*PI/RC
C
C      ***** EVALUATION OF AREA WEIGHTED PRESSURE & POWER
C
    ARW=10.*ALOG10((1.+MACH)*(1.+MACH)*RAD*RAD*PI/RC)
    DO 500 I=1,NF
    ARWA(NZ,I)=0.
    ARWP(NZ,I)=0.
500  CONTINUE
    DO 360 J=1,NPOS
    DAJ=((POS(J+1)-POS(J-1))*(POS(J-1)+POS(J+1)+2.*POS(J)))/4.
    IF(J.EQ.NPOS)DAJ=1.-(POS(J)+POS(J-1))*(POS(J)+POS(J-1))/4.
    IF(J.EQ.1)DAJ=(POS(J)+POS(J+1))*(POS(J)+POS(J+1))/4.
    DO 320 I=1,NF
    ARWA(NZ,I)=ARWA(NZ,I)+AMPL(J,I)*DAJ
320  CONTINUE
360  CONTINUE
    DO 330 I=1,NF
    ARWA(NZ,I)=20.*ALOG10(ARWA(NZ,I))

```

```

      ARWP(NZ,I)=ARWA(NZ,I)+ARW+FACT
330  CONTINUE
C
C      *****EVALUATION OF POWER BY VARIOUS MODES*****
C
      DO 410 I=1,NF
      FREQ=FRQ(I)
      X1=2.*PI*FREQ/CNOT
      IF(X1.EQ.0.)X1=.001
      DO 420 IRM=1,NRM
      DO 430 IPOS=1,NPOS
      EPS=PCOMX(IPOS,I)*BESO(IPOS,IRM)*POS(IPOS)
      PRE1(IPOS)=REAL(EPS)
      PRE2(IPOS)=AIMAG(EPS)
430  CONTINUE
      CALL QSF(HH,PRE1,ZA,NPOS)
      CALL QSF(HH,PRE2,ZB,NPOS)
      D(NZ,IRM)=2.*CMPLX(ZA,ZB)/((BESO(NPOS,IRM))**2.)
      PCOFF(NZ,IRM,I)=D(NZ,IRM)
420  CONTINUE
      IF(INDX1.EQ.1)GO TO 960
      W(NZ,1,I)=PI1*(((CABS(D(NZ,1)))*RAD/(1.-MACH))**2.)
      WI(NZ,1,I)=W(NZ,1,I)
      DO 450 IRM=2,NRM
      X3=RMN(IRM)/RAD
      X4=BETA*X3/X1*X3/X1
      EP=SQRT(ABS(1.-X4))
      IF(X4.GT.1.) EP=0.
      X2=(CABS(D(NZ,IRM))*RAD*BESO(NPOS,IRM)/(1.-MACH*EP))**2.
      WI(NZ,IRM,I)=X2*EP*PI1
      W(NZ,IRM,I)=W(NZ,IRM-1,I)+X2*EP*PI1
450  CONTINUE
      GO TO 970
960  CONTINUE
C
C      ***** INGARD'S EXPRESSION *****
C
      DO 980 IRM=1,NRM
      X3=RMN(IRM)/RAD
      X4=BETA*X3/X1*X3/X1
      EP=SQRT(ABS(1.-X4))
      IF(X4.GT.1.)EP=0.
      AKMN=-X1*(EP-MACH)/BETA
      TERM1=BETA*(1.+AMACH2*3.)*AKMN/(2.*X1*RC)
      TERM2=MACH*(1.+AMACH2)/RC
      TERM3=MACH*BETA*BETA*AKMN/X1*AKMN/(2.*X1*RC)
      PW1=2.*PI*(-TERM1+TERM2+TERM3)*((CABS(D(NZ,IRM)))*
      *BESO(NPOS,IRM)*RAD)**2)

```

```

      IF(EP.EQ.0.)PW1=0.
      WI(NZ,IRM,I)=PW1
      IF(IRM.EQ.1)W(NZ,IRM,I)=PW1
      IF(IRM.GT.1)W(NZ,IRM,I)=W(NZ,IRM-1,I)+PW1
980  CONTINUE
970  CONTINUE
410  CONTINUE
190  CONTINUE
      DO 470 I=1,NF
      DO 470 J=1,NRM
      W(3,J,I)=W(1,J,I)-W(2,J,I)
      WI(3,J,I)=WI(1,J,I)-WI(2,J,I)
470  CONTINUE
      ICH=1
      DO 480 I=1,NF
      DO 480 K=1,3
      DO 480 J=1,NRM
      NEX=2
      IM=I
910  CONTINUE
      IF(W(K,J,I).GT.0.)GO TO 900
      IM=IM+(-1)**NEX
      IF(IM.GE.NF)NEX=1
      W(K,J,I)=W(K,J,IM)
      IF(IM.LE.1)W(K,J,I)=.0001
      GO TO 910
900  CONTINUE
      W(K,J,I)=10.*ALOG10(W(K,J,I))+FACT
      IN=I
      NEY=2
      IF(I.GT.ICH)GO TO 670
      IF(WI(K,J,I).EQ.0.)ICH=I+1
      IF(WI(K,J,I).EQ.0.)GO TO 480
670  CONTINUE
      IF(WI(K,J,I).GT.0.)GO TO 920
      IN=IN+(-1)**NEY
      IF(IN.GE.NF)NEY=1
      WI(K,J,I)=WI(K,J,IN)
      IF(IN.LE.1)WI(K,J,I)=.0001
      GO TO 670
920  CONTINUE
      WI(K,J,I)=10.*ALOG10(WI(K,J,I))+FACT
480  CONTINUE
      DO 490 I=1,NF
      DO 490 J=1,NRM
      RCP(J,I)=W(2,J,I)-W(1,J,I)
      RCPI(J,I)=WI(2,J,I)-WI(1,J,I)
      RCL=CABS(PCOFF(2,J,I)/PCOFF(1,J,I))

```

```

      IF(RCL.LE.0.)RCL=.001
      RCIND(J,I)=20.*ALOG10(RCL)
490  CONTINUE
      DO 510 I=1,NF
      RCAW(I)=ARWA(2,I)-ARWA(1,I)
      POWT(I)=10.**(ARWP(1,I)/10.)-10.**(ARWP(2,I)/10.)
510  CONTINUE
      DO 950 I=1,NF
      NEZ=2
      IL=I
940  CONTINUE
      IF(POWT(I).GT.0.)GO TO 930
      IL=IL+(-1)**NEZ
      IF(IL.GE.NF)NEZ=1
      POWT(I)=POWT(IL)
      IF(IL.LE.1)POWT(I)=.0001
      GO TO 940
930  CONTINUE
      ARWP(3,I)=10.*ALOG10(POWT(I))
950  CONTINUE
C
C      *****PRINT OUTPUT *****
C
      WRITE(6,140)NR
      WRITE(6,540)
      WRITE(6,340)
      WRITE(6,590)(FRQ(I),(W(1,J,I),J=1,NRM),ARWP(1,I),I=1,NF,5)
      WRITE(6,150)NR
      WRITE(6,540)
      WRITE(6,340)
      WRITE(6,590)(FRQ(I),(W(2,J,I),J=1,NRM),ARWP(2,I),I=1,NF,5)
      WRITE(6,160)NR
      WRITE(6,540)
      WRITE(6,340)
      WRITE(6,590)(FRQ(I),(W(3,J,I),J=1,NRM),ARWP(3,I),I=1,NF,5)
      WRITE(6,140)NR
      WRITE(6,530)
      WRITE(6,350)
      WRITE(6,580)(FRQ(I),(WI(1,J,I),J=1,NRM),I=1,NF,5)
      WRITE(6,150)NR
      WRITE(6,530)
      WRITE(6,350)
      WRITE(6,580)(FRQ(I),(WI(2,J,I),J=1,NRM),I=1,NF,5)
      WRITE(6,160)NR
      WRITE(6,530)
      WRITE(6,350)
      WRITE(6,580)(FRQ(I),(WI(3,J,I),J=1,NRM),I=1,NF,5)
      WRITE(6,770)NR

```



```

WRITE(6,540)
WRITE(6,340)
WRITE(6,590)(FRQ(I),(RCP(J,I),J=1,NRM),RCAW(I),I=1,NF,5)
WRITE(6,770)NR
WRITE(6,530)
WRITE(6,350)
WRITE(6,580)(FRQ(I),(RCIND(J,I),J=1,NRM),I=1,NF,5)
770  FORMAT(1H1,/,10X,'REFLECTION COEFFICIENT, RUN NO = ',I3/)
140  FORMAT(1H1,/,10X,'INCIDENT POWER, RUN NO = ',I3/)
150  FORMAT(1H1,/,10X,'REFLECTED POWER, RUN NO = ',I3/)
160  FORMAT(1H1,/,10X,'TRANSMITTED POWER, RUN NO = ',I3/)
590  FORMAT(F11.0,5F11.3)
580  FORMAT(F11.0,4F11.3)
530  FORMAT(10X,'INDIVIDUAL MODAL POWER',/)
540  FORMAT(10X,'SUCCESSIVE SUMMATION OF MODAL POWER',/)
340  FORMAT(1X,'FREQUENCY,HZ',2X,'A=(0,0)',4X,'B=A+(0,1)'
*,2X,'C=B+(0,2)',2X,'D=C+(0,3)',2X,'AREA WEIGHTED',/)
350  FORMAT(1X,'FREQUENCY,HZ',3X,'(0,0)',7X,'(0,1)',6X,
*'(0,2)',6X,'(0,3)',/)
IF(INDX.NE.1)GO TO 800

C
C ***** OUTPUT STORE IN DISK FILES *****
C      K=1; INCIDENT
C      =2; REFLECTED
C      =3; TRANSMITTED
C
NP=109
ENCODE(13,700,FNAME)NR,NP
700  FORMAT(2I3,'PRS.RDT')
OPEN(UNIT=9,NAME=FNAME,STATUS='NEW')
DO 710 K=1,2
WRITE(9,240)(ARWA(K,I),I=1,NF)
C  ARWA = AREA-WEIGHTED PRESSURE
710  CONTINUE
CLOSE(9)
ENCODE(13,730,FNAME)NR,NP
730  FORMAT(2I3,'POW.RDT')
OPEN(UNIT=9,NAME=FNAME,STATUS='NEW')
DO 720 K=1,3
WRITE(9,240)(ARWP(K,I),I=1,NF)
C  ARWP = AREA-WEIGHTED POWER
720  CONTINUE
DO 810 K=1,3
DO 810 J=1,NRM
WRITE(9,240)(W(K,J,I),I=1,NF)
C  W = SUCCESSIVE SUMMATION OF MODAL POWER
810  CONTINUE
DO 820 K=1,3

```

```

      DO 820 J=1,NRM
      WRITE(9,240)(WI(K,J,I),I=1,NF)
C      WI = INDIVIDUAL MODAL POWER
      820 CONTINUE
      CLOSE(9)
      ENCODE(13,830,FNAME)NR,NP
      830 FORMAT(2I3,'RCS.RDT')
      OPEN(UNIT=9,NAME=FNAME,STATUS='NEW')
      WRITE(9,240)(RCAW(I),I=1,NF)
C      RCAW = AREA-WEIGHTED REFLECTION COEFFICIENT
      DO 840 J=1,NRM
      WRITE(9,240)(RCIND(J,I),I=1,NF)
C      RCIND = INDIVIDUAL MODAL REFLECTION COEFFICIENT
C      EVALUATED USING COMPLEX PRESSURE COEFFICIENTS
      840 CONTINUE
      DO 850 J=1,NRM
      WRITE(9,240)(RCP(J,I),I=1,NF)
C      RCP = SUCCESSIVE SUMMATION OF MODAL REFLECTION
C      COEFFICIENT EVALUATED USING MODAL POWER
      850 CONTINUE
      DO 860 J=1,NRM
      WRITE(9,240)(RCPI(J,I),I=1,NF)
C      RCPI = INDIVIDUAL MODAL REFLECTION COEFFICIENT
C      EVALUATED USING MODAL POWER
      860 CONTINUE
      CLOSE(9)
      800 CONTINUE
      STOP
      END

```

```

C
SUBROUTINE BES12(XX,AJO,AJ1,N)
C
C *****
C
C CALCULATES BESSEL FUNCTIONS OF ZERO AND FIRST
C ORDER FOR REAL ARGUMENTS
C
C *****
C
C XX = REAL POSITIVE OR NEGATIVE ARGUMENTS
C AJO = ZERO ORDER BESSEL FUNCTION
C AJ1 = FIRST ORDER BESSEL FUNCTION
C N = 0, CALCULATES ONLY AJO
C     = 1, CALCULATES BOTH AJO AND AJ1
C
C *****
C
X=ABS(XX)
IF(X.GT.3)GO TO 200
X1=X/3.
X2=X1*X1
X4=X2*X2
X6=X4*X2
X8=X4*X4
X10=X8*X2
X12=X6*X6
AJO=1.-2.2499997*X2+1.2656208*X4-.3163866*X6
*+.0444479*X8-.0039444*X10+.00021*X12
IF(N.EQ.0)RETURN
AJ1=.5-.56249985*X2+.21093573*X4-.03954289*X6
*+.00443319*X8-.00031761*X10+.00001109*X12
AJ1=X*AJ1
IF(XX.LT.0.)AJ1=-AJ1
RETURN
200 CONTINUE
X0=SQRT(X)
X1=3./X
X2=X1*X1
X3=X2*X1
X4=X3*X1
X5=X4*X1
X6=X5*X1
F0=.79788456-.00000077*X1-.0055274*X2-.00009512*X3
*+.00137237*X4-.00072805*X5+.000144476*X6
T0=X-.78539816-.04166397*X1-.00003954*X2+.00262573*X3
*-.00054125*X4-.00029333*X5+.00013558*X6
AJO=F0/X0*COS(T0)
IF(N.EQ.0)RETURN
F1=.79788456+.00000156*X1+.01659667*X2+.00017105*X3
*-.00249511*X4+.00113653*X5-.00020033*X6

```

```
T1=X-2.35619449+.12499612*X1+.0000565*X2-.00637879*X3
*+.00074348*X4+.00079824*X5-.00029166*X6
AJ1=F1/X0*COS(T1)
IF (XX.LT.0.)AJ1=-AJ1
RETURN
END
```

```

C      SUBROUTINE QSF(H,Y,Z,NDIM)
C
C      *****
C
C      TO COMPUTE THE INTEGRAL OF A GIVEN TABLE OF
C      SIX OR MORE EQUIDISTANT VALUES
C
C      *****
C
C      H = INCREMENT OF ARGUMENT VALUES
C      Y = INPUT TABLE OF FUNCTIONAL VALUES
C      Z = RESULTING INTEGRAL
C      NDIM = DIMENSION OF Y
C
C      *****
C
C      DIMENSION Y(1)
C
C      HT=H/3.
C      IF(NDIM.LE.5)GO TO 800
C      SUM1=Y(2)+Y(2)
C      SUM1=SUM1+SUM1
C      SUM1=HT*(Y(1)+SUM1+Y(3))
C      AUX1=Y(4)+Y(4)
C      AUX1=AUX1+AUX1
C      AUX1=SUM1+HT*(Y(3)+AUX1+Y(5))
C      AUX2=HT*(Y(1)+3.875*(Y(2)+Y(5))+2.625*(Y(3)+Y(4))+Y(6))
C      SUM2=Y(5)+Y(5)
C      SUM2=SUM2+SUM2
C      SUM2=AUX2-HT*(Y(4)+SUM2+Y(6))
C      AUX=Y(3)+Y(3)
C      AUX=AUX+AUX
C      IF(NDIM.LE.6)GO TO 500
C
C      *** INTEGRATION LOOP ***
C
C      DO 400 I=7,NDIM,2
C      SUM1=AUX1
C      SUM2=AUX2
C      AUX1=Y(I-1)+Y(I-1)
C      AUX1=AUX1+AUX1
C      AUX1=SUM1+HT*(Y(I-2)+AUX1+Y(I))
C      IF(I.GE.NDIM)GO TO 600
C      AUX2=Y(I)+Y(I)
C      AUX2=AUX2+AUX2
C      AUX2=SUM2+HT*(Y(I-1)+AUX2+Y(I-1))
400  CONTINUE
500  Z=AUX2
      RETURN
600  Z=AUX1

```

```
      RETURN
800  WRITE(6,100)
100  FORMAT(1H,'ERROR IN QSF. NUMBER OF POINTS < 6',//)
      RETURN
      END
```

B.2.2 Radial and Azimuthal Modal Decomposition for Annular Stream Duct-Nozzle System

(1) AIDCOR: This program is used to evaluate absolute sound pressure level and relative phase of the incident and the reflected pressure fields measured at various radial and azimuthal locations. The input to the program consists of the complex reflection coefficient and the complex transfer function of a reference delta function with respect to the incident pressure for various radial and azimuthal measurements.

(2) MODANU: This is the radial and azimuthal modal decomposition program for annular stream duct-nozzle system. The program computes either the incident or the reflected acoustic parameters. These parameters include the area-weighted pressure, area-weighted acoustic power, individual modal acoustic powers and successive summation of the modal powers. Input to the program includes the output of AIDCOR and other parameters defined in the program listing.

INVERT: This subroutine to program MODANU is used to invert a complex matrix.

BESLJY: This subroutine to MODANU is used to calculate Bessel functions of first and second kinds for real arguments.

(3) REFTRA: This program is used to evaluate reflection coefficient and transmitted power. Input to this program consists of the output of MODANU for both incident and reflected pressure fields.

```

C
C PROGRAM; AIDCOR.FOR
C
C *****
C
C TO EVALUATE THE ABSOLUTE SOUND PRESSURE LEVEL
C OF INCIDENT AND REFLECTED PRESSURE FIELDS
C USING THE REFLECTION COEFFICIENT DATA AND THE
C TRANSFER FUNCTION OF THE REFERENCE DELTA
C FUNCTION WITH RESPECT TO THE INCIDENT PRESSURE
C FOR AN ANNULAR STREAM DUCT-NOZZLE SYSTEM, INDUCT
C PRESSURE FIELD MEASURED USING A MULTI-POINT PROBE
C
C *****
C
C DIMENSION NR(6),C(501),PT(501),AC(501),PC(501),
C *AD(501),PD(501),PH1(2,501),AM(6,501),PH(6,501),
C *F(501),RAD(501),RPD(501),CR(501)
C
C CHARACTER FNAME*13
C
C ***** INPUT DATA *****
C
C READ(5,*)INDX,NP80,A1,AMPI
C -----
C INDX=0, NO MEAN FLOW
C      =1, WITH MEAN FLOW
C NP80=NO OF POINTS ROTATED BETWEEN INCIDENT & REFLECTED
C      WAVES TO EVALUATE REFLECTION COEFFICIENT +200
C A1= ATTENUATION ON CHANNEL A DURING AVERAGING
C AMPI= AMPLIFICATION OF INDUCT PROBE MICROPHONES
C
C IB=501
C NR0=855
C NR1=998
C NP0=210
C
C IB=NUMBER OF DATA POINTS STORED PER FILE
C NR0=RUN NUMBER FOR AMPLITUDE CALIBRATION OF THE
C      REFERENCE PROBE MICROPHONE WITH RESPECT TO A
C      STANDARD B&K MICROPHONE
C NR1=RUN NUMBER FOR TAPE RECORDER PHASE CALIBRATION
C NP0=THREE DIGIT NUMBER ASSIGN AFTER NR0 TO NAME THE
C      AMPLITUDE CALIBRATION DATA FILE
C
C SPLR=114.-37.9+(16.-AMPI)-50.+(A1+5.)
C
C 114. dB (WITH 25.+25.=50. dB ATTN) WITH RESPECT TO

```



```

C      1800 LINEAR COUNT (WITH 5 dB ATTN) READS -37.9;
C      THEREFORE A FACTOR  $114.-37.9-50$ . COMES INTO PICTURE.
C
C      ATTN OF ACTUAL SIGNAL (IN CH A) IS  $A1+A2$  dB
C      ATTN OF REF. SIGNAL (1800 COUNT IN CH B) IS 5. dB
C      DURING DECODING ATTN  $A2$ . dB OF CH A WAS SUBTRACTED
C      FROM AND ATTN OF 5. dB OF CH B WAS ADDED TO THE DATA,
C      (i.e.,  $-A2+5$ . dB ADDED). IN OTHER WORDS  $A2-5$ . dB IS
C      INCORPORATED IN SPLR INDIRECTLY. SO THE REMAINING
C       $A1+5$ . dB OUT OF  $A1+A2$  dB (i.e.,  $[A1+A2]-[A2-5.] = A1+5.$ )
C      IS ADDED TO SPLR.
C
C      AMPLIFICATION DURING CAL WAS 16. dB AND DURING ACTUAL
C      TEST WAS AMPI dB. SO A FACTOR OF  $16.-AMPI$  IS ADDED TO SPLR
C
C       $C(I) = TF$  AMPLITUDE OF THE PROBE MIC AT OUTER WALL
C      WRT A B&K MICROPHONE.
C
C       $PT(JL, I) =$  PHASE CALIBRATION OF THE TAPE RECORDER
C      CHANNELS USED FOR PROBE MICS WRT THE
C      PROBE MIC CHANNEL FOR DUCT OUTER WALL
C
C       $AC(I) =$  AMPLITUDE CALIBRATION OF PROBE MICS
C      WRT THE MIC AT OUTER WALL
C
C       $PC(I) =$  PHASE CALIBRATION OF PROBE MICS WRT
C      THE MIC AT OUTER WALL
C
C       $CR(I) =$  FREQUENCY RESPONSE OF A 1/2 INCH B&K MIC.
C
C      DO 200 I=1, IB
C      F(I) = (I-1)*20.
C      X1 = F(I)
C      X2 = X1*X1
C      X3 = X2*X1
C      X4 = X2*X2
C      IF (I.LE.31) CR(I) = -5.33+.0318*X1-.639E-04*X2
C      *+.426E-07*X3
C      IF (I.GT.31.AND.I.LE.51) CR(I) = 0.
C      IF (I.GT.51) CR(I) = -.0876+.229E-03*X1-.172E-06*X2
C      *+.181E-10*X3-.725E-15*X4
200 CONTINUE
C
C      *** INPUT DATA FROM DISC *****
C      *** AND OUTPUT STORED IN DIDC ****
C
C      ENCODE(13,140,FNAME)NRO,NPO
C      OPEN(UNIT=9,NAME=FNAME,STATUS='OLD')

```

```

      READ(9,130)(C(I),I=1,IB)
      CLOSE(9)
      READ(5,*)(NR(K),K=1,6)
C      -----
C      NR(K)RUN NUMBER ASSOCIATED WITH ONE AZIMUTHAL
C      MEASUREMENT
C
      DO 100 J=1,6
      NP1=102+J
      ENCODE(13,510,FNAME)NR1,NP1
510  FORMAT(2I3,'TAP.CAL')
110  FORMAT(2I3,'AID.RDT')
      OPEN(UNIT=9,NAME=FNAME,STATUS='OLD')
      DO 120 K=1,2
      READ(9,130)(PT(I),I=1,IB)
120  CONTINUE
      CLOSE(9)
130  FORMAT(10F8.3)
      NR2=848+J
      NP2=223+10*J
      NP4=423+10*J
      IF(J.EQ.1)GO TO 240
      ENCODE(13,140,FNAME)NR2,NP2
140  FORMAT(2I3,'SMT.CAL')
      OPEN(UNIT=9,NAME=FNAME,STATUS='OLD')
      READ(9,130)(AC(I),I=1,IB)
      CLOSE(9)
      ENCODE(13,140,FNAME)NR2,NP4
      OPEN(UNIT=9,NAME=FNAME,STATUS='OLD')
      READ(9,130)(PC(I),I=1,IB)
      CLOSE(9)
240  CONTINUE
      DO 360 NZ=1,2
      DO 160 K=1,6
      NR3=NR(K)
      NP3=102+J
      IF(NZ.EQ.2)NP8=NP80+J*100
      ENCODE(13,110,FNAME)NR3,NP3
      OPEN(UNIT=9,NAME=FNAME,STATUS='OLD')
      READ(9,130)(AD(I),I=1,IB)
      READ(9,130)(PD(I),I=1,IB)
      CLOSE(9)
      IF(NZ.EQ.1)GO TO 390
      ENCODE(13,110,FNAME)NR3,NP8
      OPEN(UNIT=9,NAME=FNAME,STATUS='OLD')
      READ(9,130)(RAD(I),I=1,IB)
      READ(9,130)(RPD(I),I=1,IB)
      CLOSE(9)

```

```

      RPD(1)=0.
      DA=(RAD(16)-RAD(11))/5.
      DO 410 I=1,15
      IF(INDX.EQ.0)RAD(I)=RAD(16)*(I-1)/15.
      IF(INDX.EQ.1.AND.I.LT.9)RAD(I)=RAD(9)-(9-I)*DA
410  CONTINUE
      DO 400 I=1,IB
      AD(I)=AD(I)-RAD(I)
      PD(I)=PD(I)-RPD(I)
400  CONTINUE
390  CONTINUE
      DO 180 I=1,IB
      PT1=PT(I)
      IF(J.NE.1)GO TO 150
      AM(K,I)=SPLR-AD(I)-C(I)-CR(I)
      PH(K,I)=PT1-PD(I)
      IF(K.EQ.1)PH1(NZ,I)=PH(1,I)
      GO TO 170
150  CONTINUE
      AM(K,I)=SPLR-AD(I)-C(I)-AC(I)-CR(I)
      PH(K,I)=PT1-PD(I)-PC(I)
170  CONTINUE
      PH(K,I)=PH(K,I)-PH1(NZ,I)
530  CONTINUE
      IF(PH(K,I).LT.180.)GO TO 520
      PH(K,I)=PH(K,I)-360.
      GO TO 530
520  CONTINUE
      IF(PH(K,I).GE.-180.)GO TO 540
      PH(K,I)=PH(K,I)+360.
      GO TO 520
540  CONTINUE
180  CONTINUE
      IF(NZ.EQ.2)NP3=302+J
      ENCODE(13,190,FNAME)NR3,NP3
190  FORMAT(2I3,'COR.RDT')
      OPEN(UNIT=9,NAME=FNAME,STATUS='NEW')
      WRITE(9,130)(AM(K,I),I=1,IB)
C     ABSOLUTE PRESSURE LEVEL, dB
      WRITE(9,130)(PH(K,I),I=1,IB)
C     PH = PHASE DIFFERENCE BETWEEN PRESSURES MEASURED
C           AT A SPATIAL LOCATION WITH RESPECT TO THAT
C           AT A REFERENCE POINT (AT THE INNER WALL WITH
C           ZERO AZIMUTHAL POSITION)
      CLOSE(9)
160  CONTINUE
      WRITE(6,320)
      WRITE(6,280)NP3

```

```

280  FORMAT(10X,'AMPLITUDE FOR MIC NO = ',I3//)
      WRITE(6,290)(F(I),(AM(K,I),K=1,6),I=1,IB,5)
290  FORMAT(F10.0,6F13.3)
      WRITE(6,320)
      WRITE(6,210)NP3
210  FORMAT(1H,10X,'PHASE FOR PROBE MIC NO = ',I3//)
      WRITE(6,290)(F(I),(PH(K,I),K=1,6),I=1,IB,5)
360  CONTINUE
100  CONTINUE
320  FORMAT(1H1)
      STOP
      END

```

```

C
C PROGRAM NAME: MODANU.FOR
C
C *****
C MODAL DECOMPOSITION PROGRAM FOR ANNULAR DUCT.
C *****
C
C IMPLICIT REAL*8 (A-H,O-Z)
C LOGICAL YKIND
C REAL*8 MACH,MACH2
C CHARACTER FNAME*13
C
C COMPLEX*16 JAY,PRES(50),COEF(50,50),A(11,11),B(50),SUM,RV
C 1,NMODES(20),NMODES1(20),AB(50,50),ABC(50,50),PCOMX(501,50)
C
C DIMENSION AJ(101),AY(101),PRESA(501,50),PRES(501,50),
C 1FREQ(20),TPOS1(20),JC(20),POWER(501,10),FRD(501),NR3(6),
C 2AFREQ(20),AZEROS(20),PWIND(501,10),ARWA(501),ARWP(501)
C 3,RPOS(15),TPOS(15),ZEROS(20),FAC(20),FACN(20)
C
C DATA JAY/(0.D00,1.0D00)/,PI/3.14159265/,YKIND/.TRUE./
C DATA GAM/1.402/,FACT/3.7396751/
C
C *****
C INPUT DATA ASSIGN TO FOR007 WITH FILE NAME 'NRNO'ANU.DAT
C
C IDX1=1,INCIDENT FIELD
C =2,REFLECTED FIELD
C IDX2=1,PRINTOUT FOR EIGEN VALUES AND MATRICES
C =2,NO PRINTOUT
C IDX3=1,PRINTOUT FOR POWER COEFF. & POWER VALUES AT
C CERTAIN FREQUENCIES
C =2,NO PRINTOUT
C .....
C NRNO=RUN NUMBER
C NR=NO OF RADIAL MEASUREMENTS
C NT=NO OF AZIMUTHAL MEASUREMENTS
C NM=NO OF MODES (RADIAL+CIRCUMFERENCIAL)
C BA=RATIO OF INNER TO OUTER DIAMETERS OF COANNULAR DUCT
C NFREQ=NO OF FREQUENCIES POINT
C HH=FREQUENCY BAND PER POINT
C RAD=RADIUS OF THE OUTER DUCT, INCH
C .....
C PAMB=AMBIENT PRESSURE, PSIA
C PT=TOTAL PRESSURE, PSIG
C PS=STATIC PRESSURE, PSIG
C TR=TOTAL TEMPERATURE, F
C .....
C RPOS=RADIAL MEASUREMENT POINTS WITH RESPECT TO

```

```

C      OUTER DUCT RADIUS MEASURED FROM CENTERLINE
C      .....
C      TPOS=AZIMUTHAL MEASUREMENT POINTS, DEG.
C      .....
C      NR3=RUN NUMBER CORRESPOND TO AN AZIMUTHAL POSITION
C      .....
C      NMODES=MODES WITH INCREASING ORDER OF THEIR VALUE,
C      FOR EXAMPLE, (0,1),(0,2),(1,1),(1,2) ETC.
C      ZEROS=EIGEN VALUES (ALPHA NM) FOR 'NMODES'
C      FREQ=CUT-ON FREQUENCY FOR 'NMODES', HZ.
C      .....
C      NMODES1=MODES WITH INCREASING VALUE OF CUT-ON
C      FREQUENCY
C      AZEROS=EIGEN VALUES (ALPHA NM) FOR 'NMODES1'
C      AFREQ=CUT-ON FREQUENCY FOR 'NMODES1', HZ.
C      .....
C
C      READ(7,*) IDX1,IDX2,IDX3
C      -----
C      READ(7,*) NRNO,NR,NT,NM,BA,NFREQ,HH,RAD
C      -----
C      READ(7,*) PAMB,PT,PS,TR
C      -----
C      READ(7,*) (RPOS(I),I=1,NR)
C      -----
C      READ(7,*) (TPOS(I),I=1,NT)
C      -----
C      READ(7,*)(NR3(I),I=1,NT)
C      -----
C      READ(7,*) (NMODES(I),ZEROS(I),FREQ(I),I=1,NM)
C      -----
C      READ(7,*) (NMODES1(I),AZEROS(I),AFREQ(I),I=1,NM)
C      -----
C      *****
C
C      INPUT DATA STORED IN FILES
C
C      PRESA=PRESSURE AMPLITUDE, dB.
C      PRESF=PHASE, DEG.
C
C      IF (IDX1.EQ.1) NPNP=100
C      IF (IDX1.EQ.2) NPNP=300
C      NPPI=NPNP+9
C      NPNP AS 4th 5th AND 6th DIGIT FOR POWER FILE NAME
C      NPPI AS 4th 5th AND 6th DIGIT FOR AWT POWER FILE NAME
C      DO 280 J=1,NT
C      DO 290 K=1,NR

```

```

NP3=102+K
IF (IDX1.EQ.2) NP3=302+K
L=(J-1)*NR+K
ENCODE(13,270,FNAME) NR3(J),NP3
270  FORMAT(2I3,'COR.RDT')
      OPEN(UNIT=9,NAME=FNAME,STATUS='OLD')
C
      READ(9,580)(PRESA(I,L),I=1,NFREQ)
C
C   PRESA = ABSOLUTE PRESSURE AMPLITUDE, dB
C
      READ(9,580)(PRESA(I,L),I=1,NFREQ)
C
C   PRESA = RELATIVE PRESSURE PHASE, DEG
C
      CLOSE(9)
      PRESA(1,L)=PRESA(2,L)
      PRESA(1,L)=PRESA(2,L)
290  CONTINUE
280  CONTINUE
C
C   ***** EVALUATION OF VARIOUS PARAMETERS *****
C
C   MACH=ANNULAR DUCT MACH NUMBER
C   TS=STATIC TEMPERATURE IN THE DUCT, R
C   CNOT=SONIC SPEED, FT/SEC.
C   RHOC=PRODUCT OF DENSITY & SONIC SPEED, SLUG/(FT*FT*SEC)
C
      RAD=RAD/12.
      G=(GAM-1.)/2.
      GI=1./G
      GACI=(GAM-1.)/GAM
      PR=PT-PS
      PSA=PS+PAMB
      MACH=SQRT(((1.+PR/PSA)**GACI-1.)*GI)
      IF (IDX1.EQ.2) MACH=-MACH
      NEQ=NR*NT
      RV=(1.,0.)
      AMACH=1.-MACH*MACH
      AMACH2=SQRT(AMACH)
      MACH2=MACH*MACH
      TS=(TR+460.)/(1.+G*MACH2)
      CNOT=49.0166*SQRT(TS)
      RHOC=GAM*PSA*144./CNOT
C
C   ***** EVALUATION OF AREA WEIGHTED PRESSURE & POWER
C
      ARW=10.*LOG10((1.+MACH)*(1.+MACH)*RAD*RAD*(1.-BA*BA)*PI/RHOC)

```

```

DO 190 K=1,NFREQ
ARWA(K)=0.
ARWP(K)=0.
190 CONTINUE
DO 200 I=1,NT
DO 210 J=1,NR
DAJ=((RPOS(J-1)-RPOS(J+1))*(RPOS(J-1)+RPOS(J+1)+2.*RPOS(J)))/4.
IF(J.EQ.1)DAJ=1.-(RPOS(J)+RPOS(J+1))*(RPOS(J)+RPOS(J+1))/4.
IF(J.EQ.NR)DAJ=(RPOS(J)+RPOS(J-1))*(RPOS(J)+RPOS(J-1))/4.-BA*BA
L=(I-1)*NR+J
DO 220 K=1,NFREQ
AMP=10.**(PRESA(K,L)/20.)
ARWA(K)=ARWA(K)+AMP*DAJ
220 CONTINUE
210 CONTINUE
200 CONTINUE
DO 230 K=1,NFREQ
ARWA(K)=20.*LOG10(ARWA(K)/(NT*(1.-BA*BA)))
ARWP(K)=ARWA(K)+ARW+FACT
230 CONTINUE
C
C ***** EVALUATION OF EIGEN VALUES *****
C
DO 110 J=1,NM
ZEROS(J)=ZEROS(J)/BA
AZEROS(J)=AZEROS(J)/BA
110 CONTINUE
DO 120 J=2,NM
M=DREAL(NMODES(J))
NMAX=M+3
X=ZEROS(J)*BA
CALL BESLJY(X,NMAX,YKIND,AJ,AY)
AXJ=-AJ(M+2)+M*AJ(M+1)/X
AXY=-AY(M+2)+M*AY(M+1)/X
FAC(J)=AXJ/AXY
120 CONTINUE
DO 130 J=2,NM
M=DREAL(NMODES1(J))
NMAX=M+3
X=AZEROS(J)*BA
CALL BESLJY(X,NMAX,YKIND,AJ,AY)
AXJ=-AJ(M+2)+M*AJ(M+1)/X
AXY=-AY(M+2)+M*AY(M+1)/X
PHIB=AJ(M+1)-AXJ/AXY*AY(M+1)
X=AZEROS(J)
CALL BESLJY(X,NMAX,YKIND,AJ,AY)
PHIA=AJ(M+1)-AXJ/AXY*AY(M+1)
PA2=PHIA*PHIA

```



```

PB2=PHIB*PHIB
FACN(J)=PA2-BA*BA*PB2-((M/X)**2.)*(PA2-PB2)
130 CONTINUE
FACN(1)=1.-BA*BA
DO 140 J=1,NM
140 FACN(J)=FACN(J)*RAD/2.*RAD
FAC(1)=0.
DO 150 I=1,NR
DO 150 J=1,NM
IF(J.EQ.1) GO TO 160
M=DREAL(NMODES(J))
AX=ZEROS(J)
X=AX*RPOS(I)
NMAX=M+3
CALL BESLJY(X,NMAX,YKIND,AJ,AY)
COEF(I,J)=(AJ(M+1)-FAC(J)*AY(M+1))
GO TO 150
160 COEF(I,J)=(1.,0.)
150 CONTINUE
DO 170 I=1,NR
DO 170 J=1,NM
M=DREAL(NMODES(J))
DO 170 LT=2,NT
LLT=(LT-1)*NR
TPOS1(LT)=TPOS(LT)*PI/180.
SUM=TPOS1(LT)*JAY*M
170 COEF(I+LLT,J)=COEF(I,J)*COS(TPOS1(LT)*M)
IF(IDX2.EQ.1)WRITE(6,500)
500 FORMAT(1H1)
IF(IDX2.EQ.1.AND.NM.EQ.6)WRITE(6,410)((COEF(I,J),J=1,NM),I=1,NEQ)
IF(IDX2.EQ.1.AND.NM.EQ.7)WRITE(6,930)((COEF(I,J),J=1,NM),I=1,NEQ)
410 FORMAT(1H ,6F12.5)
930 FORMAT(1H,7F12.5)
DO 420 K=1,NM
DO 420 L=1,NM
SUM=(0.,0.)
DO 430 M=1,NEQ
430 SUM=SUM+CONJG(COEF(M,K))*COEF(M,L)
C SUM=COEF(K,L)
AB(K,L)=SUM
420 A(K,L)=SUM
IF(IDX2.EQ.1)WRITE(6,500)
IF(IDX2.EQ.1.AND.NM.EQ.6)WRITE(6,410)((A(I,J),J=1,NM),I=1,NM)
IF(IDX2.EQ.1.AND.NM.EQ.7)WRITE(6,930)((A(I,J),J=1,NM),I=1,NM)
CALL INVERT(A,NM,11)
C CALL CGJR(A,50,50,NM,MC,JC,RV)
IF(IDX2.EQ.1)WRITE(6,500)
IF(IDX2.EQ.1.AND.NM.EQ.6)WRITE(6,410)((A(I,J),J=1,NM),I=1,NM)

```

```

      IF (IDX2.EQ.1.AND.NM.EQ.7) WRITE(6,930)((A(I,J),J=1,NM),I=1,NM)
      DO 730 K=1,NM
      DO 730 L=1,NM
      SUM=(0.,0.)
      DO 740 M=1,NM
      SUM=SUM+A(K,M)*AB(M,L)
740  CONTINUE
730  ABC(K,L)=SUM
      IF (IDX2.EQ.1) WRITE(6,500)
      IF (IDX2.EQ.1.AND.NM.EQ.6) WRITE(6,410)((ABC(I,J),J=1,NM),I=1,NM)
      IF (IDX2.EQ.1.AND.NM.EQ.7) WRITE(6,930)((ABC(I,J),J=1,NM),I=1,NM)
C
C  ***** EVALUATION OF POWER BY VARIOUS MODES ***
C
      IFQ=1
      OMEGA=-HH
      DO 440 IFREQ=1,NFREQ
      OMEGA=OMEGA+HH
      AKA=2.*PI/CNOT*OMEGA
      IF (AKA.EQ.0.) AKA=.001
      FRD(IFREQ)=OMEGA
      DO 450 IJ=1,NEQ
      AMP=PRESA(IFREQ,IJ)
      AMP=10.** (AMP/20.)
      PHA=PRESP(IFREQ,IJ)*PI/180.
      AMPR=AMP*COS(PHA)
      AMPI=AMP*SIN(PHA)
450  PRES(IJ)=DCMLX(AMPR,AMPI)
      DO 460 K=1,NM
      SUM=(0.D00,0.D00)
      DO 470 M=1,NEQ
470  SUM=SUM+CONJG(COEF(M,K))*PRES(M)
460  B(K)=SUM
      DO 480 K=1,NM
      SUM=(0.,0.)
      DO 490 M=1,NM
490  SUM=SUM+A(K,M)*B(M)
      PRES(K)=SUM
      PCOMX(IFREQ,K)=PRES(K)
480  CONTINUE
      NPOWER=0
      DO 520 J=1,NM
      AROOTS=AZEROS(J)/RAD*AMACH2
      IF (AKA.GE.AROOTS) NPOWER=J
520  CONTINUE
      SUM1=0.
      DO 530 J=1,NPOWER
      EPS=1.

```

```

      IF(J.EQ.1) EPS=2.
      AKMN=SQRT(AKA*AKA-(AMACH*((AZEROS(J)/RAD)**2.)))
      AKMN=(AKA*MACH-AKMN)/AMACH
      TERM1=AMACH*(1.0+MACH2*3.)*AKMN/(2.*AKA*RHOC)
      TERM2=MACH*(1.0+MACH2)/RHOC
      TERM3=MACH*AMACH*AMACH*AKMN/AKA*AKMN/(AKA*2.*RHOC)
      PW1=(ABS(PRES(J))**2.)*FACN(J)*EPS*PI
      1*(-TERM1+TERM2+TERM3)*2
      IF(PW1.LE.0.)GO TO 390
      PWIND(IFREQ,J)=10.*LOG10(PW1)+FACT
390  CONTINUE
      SUM1=SUM1+PW1
      IF(SUM1.LE.0.)GO TO 400
      POWER(IFREQ,J)=10.*LOG10(SUM1)+FACT
400  CONTINUE
530  CONTINUE
      IF(NPOWER.EQ.NM)GO TO 810
      NP1=NPOWER+1
      DO 820 J=NP1,NM
      POWER(IFREQ,J)=POWER(IFREQ,NPOWER)
820  CONTINUE
810  CONTINUE
      IF(IDX3.NE.1)GO TO 440
      IF(IFREQ.NE.IFQ)GO TO 440
      IFQ=IFQ+10
      WRITE(6,100) OMEGA
100  FORMAT(//////1H ,5X,'FREQUENCY= ',F10.0/)
      WRITE(6,540)
540  FORMAT(3X,'AZIMUTHAL      RADIAL      CUT-ON',10X,
1'MODAL COEFFICIENTS',/5X,'MODE',8X,'MODE      FREQUENCY',
29X,'REAL      IMAGINARY'////)
      DO 550 I=1,NM
      M=DREAL(NMODES(I))
      N=DIMAG(NMODES(I))
      WRITE(6,560) M,N,FREQ(I),PRES(I)
560  FORMAT(2X,I5,7X,I5,5X,F7.0,10X,2F12.3)
550  CONTINUE
      IF(IDX1.EQ.1)WRITE(6,570) POWER(IFREQ,NPOWER),ARWP(IFREQ)
      IF(IDX1.EQ.2)WRITE(6,590)POWER(IFREQ,NPOWER),ARWP(IFREQ)
440  CONTINUE
      ENCODE(13,240,FNAME)NRNO,NPNP
240  FORMAT(2I3,'PRS.RDT')
      OPEN(UNIT=9,NAME=FNAME,STATUS='NEW')
      DO 330 K=1,NM
      WRITE(9,780)(PCOMX(I,K),I=1,NFREQ)
C    PCOMX = COMPLEX PRESSURE COEFFICIENT
780  FORMAT(6E13.5)
330  CONTINUE

```

```

        CLOSE(9)
        ENCODE(13,620,FNAME)NRNO,NPPI
620    FORMAT(2I3,'COR.RDT')
        OPEN(UNIT=9,NAME=FNAME,STATUS='NEW')
        WRITE(9,580)(ARWA(I),I=1,NFREQ)
C      ARWA = AREA-WEIGHTED PRESSURE AMPLITUDE
        CLOSE(9)
        ENCODE(13,250,FNAME)NRNO,NPNP
250    FORMAT(2I3,'POW.RDT')
        OPEN(UNIT=9,NAME=FNAME,STATUS='NEW')
        DO 300 J=1,NM
        WRITE(9,580) (POWER(I,J),I=1,NFREQ)
C      POWER = SUCCESSIVE SUMMATION OF MODAL POWER
300    CONTINUE
        DO 310 J=1,NM
        WRITE(9,580) (PWIND(I,J),I=1,NFREQ)
C      PWIND = INDIVIDUAL MODAL POWER
310    CONTINUE
        CLOSE(9)
        ENCODE(13,600,FNAME)NRNO,NPPI
600    FORMAT(2I3,'POW.RDT')
        OPEN(UNIT=9,NAME=FNAME,STATUS='NEW')
        WRITE(9,580) (ARWP(I),I=1,NFREQ)
C      ARWP = AREA-WEIGHTED POWER
        CLOSE(9)
570    FORMAT(/1H,'THE INCIDENT POWER =',2F10.2,' dB')
590    FORMAT(/1H,'THE REFLECTED POWER =',2F10.2,' dB')
580    FORMAT(10F8.3)
        WRITE(6,500)
        IF(NM.EQ.6)WRITE(6,320)
        IF(NM.EQ.7)WRITE(6,920)
320    FORMAT(/1H,10X,'SUCCESSIVE SUMMATION OF MODAL POWER',//,
15X,'FREQUENCY',2X,'A=(0,1)',2X,'B=A+(1,1)',2X,'C=B+(2,1)
2',2X,'D=C+(0,2)',2X,'E=D+(1,2)',2X,'F=E+(2,2)',2X,
3'AREA WTD POWER',//)
920    FORMAT(/1H,10X,'SUCCESSIVE SUMMATION OF MODAL POWER',//,
15X,'FREQUENCY',2X,'A=(0,1)',2X,'B=A+(1,1)',2X,'C=B+(2,1)
2',2X,'D=C+(3,1)',2X,'E=D+(0,2)',2X,'F=E+(1,2)',2X,'G=F+(2,2)
3',2X,'AREA WTD POWER',//)
        IF(NM.EQ.6)WRITE(6,380)(FRD(I),(POWER(I,J),J=1,NM),ARWP(I)
1,I=1,NFREQ,5)
        IF(NM.EQ.7)WRITE(6,980)(FRD(I),(POWER(I,J),J=1,NM),ARWP(I)
1,I=1,NFREQ,5)
380    FORMAT(F11.0,7F11.2)
980    FORMAT(F11.0,8F11.2)
        WRITE(6,500)
        IF(NM.EQ.6)WRITE(6,340)NRNO,MACH
        RMCH=-MACH

```

```

      IF(NM.EQ.7)WRITE(6,990)NRNO, RMCH
340  FORMAT(/1H,10X,'INDIVIDUAL MODAL POWER',5X,'RUN NO = ',I3,
      15X,'DUCT MACH NO = ',F5.3,/,5X,'FREQUENCY',3X,'(0,1)',6X,
      2'(1,1)',6X,'(2,1)',5X,'(0,2)',6X,'(1,2)',6X,'(2,2)',/)
990  FORMAT(/1H,10X,'INDIVIDUAL MODAL POWER',5X,'RUN NO = ',I3,
      15X,'DUCT MACH NO = ',F5.3,/,5X,'FREQUENCY',3X,'(0,1)',6X,
      2'(1,1)',6X,'(2,1)',5X,'(3,1)',5X,'(0,2)',6X,'(1,2)',6X,'(2,2)',/)
      IF(NM.EQ.6)WRITE(6,350)(FRD(I),(PWIND(I,J),J=1,NM),I=1,NFREQ,5)
      IF(NM.EQ.7)WRITE(6,890)(FRD(I),(PWIND(I,J),J=1,NM),I=1,NFREQ,5)
350  FORMAT(F11.0,6F11.2)
890  FORMAT(F11.0,7F11.2)
      STOP
      END

```

```

SUBROUTINE INVERT(A,N,MAXRA)
.....
C
C
C      PURPOSE
C      INVERT A COMPLEX MATRIX.
C
C      USAGE
C      CALL INVERT(A,N,MAXRA)
C      A = MATRIX TO BE INVERTED AND THE RESULTANT INVERSE.
C      N = ORDER OF MATRIX A.
C      MAXRA = ROW DIMENSION OF A IN THE CALLING PROGRAM.
C
C      METHOD
C      GAUSSIAN ELIMINATION IN PLACE.
C
C      REMARKS
C      THIS ALGORITHM WAS ORIGINALLY PUBLISHED IN THE 1620 USER'S
C      GROUP NEWSLETTER, AUTHOR UNKNOWN.
C
C      SUBROUTINE AND FUNCTION SUBPROGRAMS REQUIRED
C      NONE
C
C      .....
C
C      SPECIFICATION STATEMENTS
C      COMPLEX*16 DCONJG,DCMPLX,CDSQRT,CDCOS,CDSIN
C      COMPLEX*16 A(MAXRA,1),STORE,ONE/(1.D00,0.D00)/,ZERO/(0.D00,0.D00)/
C
C      DO 100 I=1,N
C      STORE=A(I,I)
C      A(I,I)=ONE
C      DO 110 J=1,N
110  A(I,J)=A(I,J)/STORE
C      DO 100 K=1,N
C      IF(K.EQ.I) GO TO 100
C      STORE=A(K,I)
C      A(K,I)=ZERO
C      DO 120 J=1,N
120  A(K,J)=A(K,J)-STORE*A(I,J)
100  CONTINUE
C      RETURN
C      END

```

```

C      SUBROUTINE BESLJY(X,NMAX,YKIND,J,YY)
C
C      *****
C      TO COMPUTE BESSEL FUNCTIONS OF FIRST AND SECOND
C      KINDS (ZERO AND FIRST ORDER) FOR REAL ARGUMENTS
C      *****
C
C      IMPLICIT REAL*8 (A-H,O-Z)
C      DIMENSION J(101),YY(101),ENPLUS(26)
C      REAL*8 J
C      LOGICAL YKIND
C
C      PI=3.1415926
C      IFACT=20
C      IFACT1=IFACT+1
C      IF(X.GT.3) GO TO395
C      X32=(X/3.)**2
C      A2=-2.2499997
C      A4=1.2656208
C      A6=-.3163866
C      A8=.0444479
C      A10=-.0039444
C      A12=.00021
C      BJO=((((A12*X32+A10)*X32+A8)*X32+A6)*X32+A4)*X32+A2)*X32+1.
C      IF(.NOT.YKIND) GO TO 100
C      Y=(2./PI)*LOG(X/2.)*BJO
C      Y0=.36746691
C      Y2=.60559366
C      Y4=-.74350384
C      Y6=.25300117
C      Y8=-.04261214
C      Y10=.00427916
C      Y12=-.00024846
C      BY0=(((Y12*X32+Y10)*X32+Y8)*X32+Y6)*X32+Y4)*X32+Y2)*X32+Y0+Y
100  H0=.5
C      H2=-.56249985
C      H4=.21093573
C      H6=-.03954289
C      H8=.00443319
C      H10=-.00031761
C      H12=.1109E-04
C      H1X=(((H12*X32+H10)*X32+H8)*X32+H6)*X32+H4)*X32+H2)*X32+H0
C      BJ1=H1X*X
C      IF(.NOT.YKIND) GO TO 760
C      D=(2./PI)*X*LOG(X/2.)*BJ1
C      D0=-.6366198
C      D2=.2212091

```

```

D4=2.1682709
D6=-1.3164827
D8=.3123951
D10=-.0400976
D12=.0027873
Y1X=(((((D12*X32+D10)*X32+D8)*X32+D6)*X32+D4)*X32+D2)*X32+D0+D
BY1=Y1X/X
GO TO 760
395 X3=3./X
C0=.79788456
C1=-.77E-06
C2=-.0055274
C3=-.00009512
C4=.00137237
C5=-.00072805
C6=.00014476
F0((((C6*X3+C5)*X3+C4)*X3+C3)*X3+C2)*X3+C1)*X3+C0
T0=-.78539816
T1=-.04166397
T2=-.3954E-04
T3=.00262573
T4=-.00054125
T5=-.00029333
T6=.00013558
THETA0((((T6*X3+T5)*X3+T4)*X3+T3)*X3+T2)*X3+T1)*X3+T0+X
BJ0=(1./SQRT(X))*F0*COS(THETA0)
IF(.NOT.YKIND) GO TO 500
BY0=(1./SQRT(X))*F0*SIN(THETA0)
500 B0=.79788456
B1=.156E-05
B2=.01659667
B3=.00017105
B4=-.00249511
B5=.00113653
B6=-.0002033
F1((((B6*X3+B5)*X3+B4)*X3+B3)*X3+B2)*X3+B1)*X3+B0
G0=-2.35619449
G1=.12499612
G2=.00005650
G3=-.00637879
G4=.00074348
G5=.00079824
G6=-.00029166
THETA1((((G6*X3+G5)*X3+G4)*X3+G3)*X3+G2)*X3+G1)*X3+G0+X
BJ1=(1./SQRT(X))*F1*COS(THETA1)
IF(.NOT.YKIND) GO TO 760
BY1=(1./SQRT(X))*F1*SIN(THETA1)
760 J(1)=BJ0

```



```

      J(2)=BJ1
      IF(.NOT.YKIND) GO TO 800
      YY(1)=BY0
      YY(2)=BY1
800  IF(NMAX.LT.2) GO TO 900
      DO 895 N=2,NMAX
      ENM1=N-1
      TNM10X=2.*ENM1/X
      INDN=N+1
      INDNM1=N
      INDNM2=N-1
      IF(.NOT.YKIND) GO TO 820
      YY(INDN)=TNM10X*YY(INDNM1)-YY(INDNM2)
820  IF(X.LT.ENM1) GO TO 878
      J(INDN)=TNM10X*J(INDNM1)-J(INDNM2)
      GO TO 895
878  FACT=1.
      ENPLUS(IFACT1)=N+IFACT
      DO 890 I=1,IFACT
      II=IFACT1-I
      ENPLUS(II)=N+II-1
      FACT=1.-X*X/(4.*ENPLUS(II)*ENPLUS(II+1)*FACT)
890  CONTINUE
      J(INDN)=J(INDNM1)*X/(2.*DFLOAT(N)*FACT)
895  CONTINUE
900  RETURN
      END

```

```

C
C PROGRAM NAME: REFTRA.FOR
C
C *****
C
C TO EVALUATE REFLECTION COEFFICIENT AND TRANSMITTED
C POWER USING MODAL INCIDENT AND REFLECTED PRESSURES
C AND POWERS.
C
C *****
C
C IMPLICIT REAL*8(A-H,O-Z)
C CHARACTER FNAME*13
C
C COMPLEX*16 PCOMX(2,501,50)
C
C DIMENSION POWER(2,501,10),PWIND(2,501,10),ARWA(2,501),
C 1ARWP(2,501),FRD(501),RCAW(501),ARWT(501),POWET(501,7),
C 2PWINT(501,7),RCIND(501,7),AIR(501),RCPW(501,7)
C
C READ(5,*)NR,PT,PS,PA
C -----
C NR=RUN NUMBER
C PT=TOTAL PRESSURE, PSIG
C PS=STATIC PRESSURE, PSIG
C PA=ATMOSPHERIC PRESSURE, PSIA
C
C GAM=1.402
C GI=2./(GAM-1.)
C GACI=(GAM-1.)/GAM
C PR=PT-PS
C PSA=PS+PA
C DMAC=SQRT(((1.+PR/PSA)**GACI-1.)*GI)
C FCTDM=20.*LOG10((1.+DMAC)/(1.-DMAC))
C
C FCTDM=FACTOR CORRECTING THE POWER REFLECTION
C COEFFICIENT DERIVED FROM INCIDENT AND
C REFLECTED POWER DUE TO DUCT MACH NUMBER.
C
C NM=7
C NM=NO OF MODES(RADIAL+CIRCUMFERENTIAL)
C NFR=501
C DF=20.
C ***** INPUT DATA FROM DISC *****
C DO 100 J=1,2
C J=1, INCIDENT FIELD
C =2, REFLECTED FIELD
C NP=(J-1)*200+100

```

```

      NPP=NP+9
      ENCODE(13,110,FNAME)NR,NP
110  FORMAT(2I3,'PRS.RDT')
      OPEN(UNIT=9,NAME=FNAME,STATUS='OLD')
      DO 130 K=1,NM
      READ(9,140)(PCOMX(J,I,K),I=1,NFR)
C    PCOMX=MODAL PRESSURE COEFFICIENTS
130  CONTINUE
      CLOSE(9)
140  FORMAT(6F13.5)
      ENCODE(13,150,FNAME)NR,NP
150  FORMAT(2I3,'POW.RDT')
      OPEN(UNIT=9,NAME=FNAME,STATUS='OLD')
      DO 160 K=1,NM
      READ(9,170)(POWER(J,I,K),I=1,NFR)
C    POWER=SUCCESSIVE SUMMATION OF MODAL POWER
160  CONTINUE
      DO 180 K=1,NM
      READ(9,170)(PWIND(J,I,K),I=1,NFR)
C    PWIND=INDIVIDUAL MODAL POWER
180  CONTINUE
      CLOSE(9)
170  FORMAT(10F8.3)
      ENCODE(13,190,FNAME)NR,NPP
190  FORMAT(2I3,'COR.RDT')
      OPEN(UNIT=9,NAME=FNAME,STATUS='OLD')
      READ(9,170)(ARWA(J,I),I=1,NFR)
C    ARWA=AREA-WEIGHTED PRESSURE VALUES
      CLOSE(9)
      ENCODE(13,200,FNAME)NR,NPP
200  FORMAT(2I3,'POW.RDT')
      OPEN(UNIT=9,NAME=FNAME,STATUS='OLD')
      READ(9,170)(ARWP(J,I),I=1,NFR)
C    ARWP=AREA-WEIGHTED POWER
      CLOSE(9)
100  CONTINUE
C    *****
C    ***** COMPUTATION *****
      DO 210 I=1,NFR
      FRD(I)=(I-1)*DF
      RCAW(I)=ARWA(2,I)-ARWA(1,I)
      AI=10.**(ARWP(1,I)/10.)
      AR=10.**(ARWP(2,I)/10.)
      AIR(I)=AI-AR
      IF(AIR(I).LE.0.)AIR(I)=AIR(I-1)
      IF(AIR(I).LE.0.)AIR(I)=.001
      ARWT(I)=10.*LOG10(AIR(I))
      DO 220 K=1,NM

```

```

RCPW(I,K)=POWER(2,I,K)-POWER(1,I,K)+FCTDM
AI=10.**(POWER(1,I,K)/10.)
AR=10.**(POWER(2,I,K)/10.)
AIR(I)=AI-AR
IF(AIR(I).LE.0.)AIR(I)=AIR(I-1)
IF(AIR(I).LE.0.)AIR(I)=.001
POWET(I,K)=10.*LOG10(AIR(I))
IF(PWIND(1,I,K).EQ.0.)GO TO 400
AI=10.**(PWIND(1,I,K)/10.)
AR=10.**(PWIND(2,I,K)/10.)
AIR(I)=AI-AR
IF(AIR(I).LE.0.)AIR(I)=AIR(I-1)
IF(AIR(I).LE.0.)AIR(I)=.001
PWINT(I,K)=10.*LOG10(AIR(I))
400  CONTINUE
RCL=ABS(PCOMX(2,I,K)/PCOMX(1,I,K))
RCIND(I,K)=20.*LOG10(RCL)
220  CONTINUE
210  CONTINUE
C *****
C ***** STORING IN THE DISC*****
C
ENCODE(13,230,FNAME)NR,NP
230  FORMAT(2I3,'RCS.RDT')
OPEN(UNIT=9,NAME=FNAME,STATUS='NEW')
WRITE(9,170)(RCAW(I),I=1,NFR)
C RCAW=AREA-WEIGHTED REFLECTION COEFFICIENT
DO 350 K=1,NM
WRITE(9,170)(RCPW(I,K),I=1,NFR)
C RCPW=SUCCESSIVE MODAL SUMMATION OF REFLECTION COEFFICIENT
350  CONTINUE
DO 240 K=1,NM
WRITE(9,170)(RCIND(I,K),I=1,NFR)
C RCIND=INDIVIDUAL MODAL REFLECTION COEFFICIENT
240  CONTINUE
CLOSE(9)
ENCODE(13,250,FNAME)NR,NP
250  FORMAT(2I3,'POT.RDT')
OPEN(UNIT=9,NAME=FNAME,STATUS='NEW')
WRITE(9,170)(ARWT(I),I=1,NFR)
C ARWT=AREA WEIGHTED TRANSMITTED POWER
DO 260 K=1,NM
WRITE(9,170)(POWET(I,K),I=1,NFR)
C POWET=SUCCESSIVE SUMMATION OF MODAL TRANSMITTED POWER
260  CONTINUE
DO 270 K=1,NM
WRITE(9,170)(PWINT(I,K),I=1,NFR)
C PWINT=INDIVIDUAL MODAL TRANSMITTED POWER

```

270 CONTINUE
CLOSE(9)

C

C

C

***** PRINT OUT *****

WRITE(6,290)

WRITE(6,360)NR

360 FORMAT(/1H,10X,'SUCCESSIVE SUMMATION OF MODAL REFLECTION
1 COEFFICIENT',5X,'RUN NO = ',I3,/,5X,'FREQUENCY',2X,'A=(0,1)
2 ',2X,'B=A+(1,1)',2X,'C=B+(2,1)',2X,'D=C+(3,1)',2X,'E=D+(0,2)
3 ',2X,'F=E+(1,2)',2X,'G=F+(2,2)',2X,'AREA WTD VALUES',//)
WRITE(6,300)(FRD(I),(RCPW(I,J),J=1,NM),RCAW(I),I=1,NFR,5)
WRITE(6,290)

290 FORMAT(1H1)

WRITE(6,280)NR

280 FORMAT(/1H,10X,'INDIVIDUAL MODAL REFLECTION COEFFICIENT'
1,5X,'RUN NO = ',I3,/,5X,'FREQUENCY',3X,'(0,1)',6X,'(1,1)',
2,6X,'(2,1)',5X,'(3,1)',5X,'(0,2)',6X,'(1,2)',6X,'(2,2)',//)
WRITE(6,330)(FRD(I),(RCIND(I,K),K=1,NM),I=1,NFR,5)

300 FORMAT(F11.0,8F11.2)

WRITE(6,290)

WRITE(6,310)NR

310 FORMAT(/1H,10X,'SUCCESSIVE SUMMATION OF MODAL TRANSMITTED
1 POWER',5X,'RUN NO = ',I3,/,5X,'FREQUENCY',2X,'A=(0,1)',
2,2X,'B=A+(1,1)',2X,'C=B+(2,1)',2X,'D=C+(3,1)',2X,'E=D+(0,2)',
3,2X,'F=E+(1,2)',2X,'G=F+(2,2)',2X,'AREA WTD POWER',//)
WRITE(6,300)(FRD(I),(POWET(I,J),J=1,NM),ARWT(I),I=1,NFR,5)
WRITE(6,290)

WRITE(6,320)NR

320 FORMAT(/1H,10X,'INDIVIDUAL MODAL TRANSMITTED POWER',5X,
1 'RUN NO = 'I3,/,5X,'FREQUENCY'3X,'(0,1)',6X,'(1,1)',6X,
2 '(2,1)',5X,'(3,1)',5X,'(0,2)',6X,'(1,2)',6X,'(2,2)',//)
WRITE(6,330)(FRD(I),(PWINT(I,K),K=1,NM),I=1,NFR,5)

330 FORMAT(F11.0,7F11.2)

STOP

END

B.3 NONLINEAR REGRESSION TECHNIQUE FOR MODIFIED IMPEDANCE TUBE DATA ANALYSIS

NLR: The modified impedance tube technique to determine the termination impedance and reflection coefficient in the presence of mean flow with fixed temperature is programmed in NLR. The input to this program consists of the measured induct pressure amplitudes (dB) and the corresponding relative locations. The other parameters (i.e., flow parameters and conversion factors, etc.) needed for this program are defined in the listing.

SR8: This subroutine to program NLR is used to solve a set of simultaneous equations.

INITIAL: This subroutine to program NLR uses combinations of three pressure amplitude measurements to compute initial values of Γ , β , and A. The set of values which gives the minimum rms error between the theoretical and the experimental values of the pressure amplitudes is used as the initial set in NLR.

```

C
C PROGRAM NAME: NLR.FOR
C
C *****
C
C NONLINEAR REGRESSION TECHNIQUE USED TO
C
C EVALUATE COMPLEX REFLECTION COEFFICIENT
C
C AND SPECIFIC NOZZLE IMPEDANCE USING
C
C IMPEDANCE TUBE MEASUREMENTS WITH FLOW.
C
C *****
C
C DIMENSION W11(10),TC1(10),IR1(50),AP(50),X3(50),
*PRA(500),XYZ(500),Z(3),TDB(50),DT(3,50),A(3,4),
*E(3),AZ(3),V(4),X4(50),F1(50),B(6,50),F2(50),ER6(50)
*,X5(50),CALP(50),DEL(500),Z1(50,3)
C
C CHARACTER FNAME*13
C
C PIE=3.1415926
C GAM=1.4
C ALR=8.68589
C ALR=20/LOGe(10) :TO RELATE NATURAL LOG WITH LOG BASE 10
C FACX=64.4375
C FACX=FACTOR TO DERIVE EXACT X-COORDINATE
C
C ***** INPUT DATA *****
C
C READ(5,*)PB1,NO1,NZ1,PR,PS,FACP
C *****
C
C PB1=ATMOSPHERIC PRESSURE,PSI
C NO1=RUN NO
C NZ1=NUMBER OF FREQUENCIES
C PR=TOTAL PRESSURE PSIG
C PS=STATIC PRESSURE,PSIG
C FACP=FACTOR TO GET ABSOLUTE PRESSURE
C
C READ(5,*)(W11(I),TC1(I),IR1(I),CALP(I),I=1,NZ1)
C *****
C
C W11=FREQUENCY
C TC1=TEMPERATURE,F
C IR1=NUMBER OF MEASUREMENT POINTS
C CALP=CALIBRATION FOR PRESSURE
C
C GF=(GAM-1.)/GAM
C AM=SQRT((((PB1+PR)/(PB1+PS))**GF-1.)*2./(GAM-1.))

```

```

DO 235 IM1=1,NZ1
W1=W11(IM1)
IR=IR1(IM1)
TC=TC1(IM1)
C=49.0116*SQRT(460.+TC)
READ(5,*)(AP(I),I=1,IR)
C *****
READ(5,*)(X3(I),I=1,IR)
C *****
READ(5,*)(X4(I),I=1,IR)
C *****
C AP=MEASURED PRESSURE AMPLITUDES, dB
C X3=MEASURED X-DISTANCE IN INCHES
C X4=MEASURED X-DISTANCE IN 1/16 th OF AN INCH
C *****
C
DO 323 I=1,IR
X5(I)=FACX-(X3(I)+X4(I)/16.)
X3(I)=-X5(I)
AP(I)=AP(I)-CALP(IM1)+FACP
323 CONTINUE
C
C AP=PRESSURE, DB
C X3=COORDINATES OF DATA POINTS, INCH
C
W=2.*PIE*W1
ALM=2.*PIE*(1.-AM*AM)*C/W
C
C ALM=WAVE LENGTH IN FEET
C
CAILL INITIAL(ALM,AP,X3,Z,NUM,IR,PRMS)
C $$$$$$$$$$$$$$$$$$$$$$$$$$$$$$$$$$$$$$$$$$$$$$$$$$$$$$$$$
C
C Z(1)=ALPHA
C Z(2)=BFTA
C Z(3)=A
C
DO 285 IQ=1,10
CSH=COSH(PIE*Z(1))
CSHS=CSH**2
SNH=SINH(PIE*Z(1))
SNHS=SNH**2
DO 300 IX=1,IR
BTX=PIE*(Z(2)+X3(IX))/(6.*ALM)
SN=SIN(BTX)
CS=COS(BTX)
CSS=CS**2

```



```

      TDN=CSHS-CSS
      TDB(IX)=Z(3)+10.*ALOG10(TDN)
      DT(1,IX)=PIE*ALR*(SNH*CSH/TDN)
      DT(2,IX)=PIE*ALR*(SN*CS/TDN)
      DT(3,IX)=1.
C
C      DT(1,IX)=DERIVATIVE OF PRESSURE W.R.T ALPHA
C      DT(2,IX)=DERIVATIVE OF PRESSURE W.R.T BETA
C      DT(3,IX)=DERIVATIVE OF PRESSURE W.R.T A
C
300  CONTINUE
      DO 320 K=1,3
      A(K,4)=0.
      DO 320 I=1,IR
320  A(K,4)=A(K,4)+(AP(I)-TDB(I))*DT(K,I)
      DO 330 K=1,3
      DO 330 J=1,3
      A(K,J)=0.
      DO 330 I=1,IR
330  A(K,J)=A(K,J)+DT(K,I)*DT(J,I)
      V(1)=4.
      CALL SR8(A,3,4,3,4,JC,V)
C      $$$$$$$$$$$$$$$$$$$$$$$$$$$$
C
      DO 275 K=1,3
      AZ(K)=Z(K)
      E(K)=ABS(A(K,4))
275  CONTINUE
      DO 280 K=1,3
      E1=ABS(AZ(K)*.0025)
      IF(K.EQ.3)E1=.025
      IF(E(K)-E1)280,280,286
280  CONTINUE
      GO TO 290
286  CONTINUE
      DO 287 K=1,3
      Z(K)=Z(K)+A(K,4)
287  CONTINUE
285  CONTINUE
290  CONTINUE
      DO 291 K=1,3
      Z1(IM1,K)=Z(K)
291  CONTINUE
      E6=0.
      DO 310 I=1,IR
      E6=E6+ABS(AP(I)-TDB(I))
310  CONTINUE
      E6=E6/IR

```

```

ER6(IM1)=E6
EXM=EXP(-Z(1)*2.*PIE)
EXH=EXP(Z(1)*PIE)
EXMH=EXP(-Z(1)*PIE)
SNH=SINH(2.*PIE*Z(1))
CSH=COSH(2.*PIE*Z(1))
CSHH=COSH(Z(1)*PIE)
SNHH=SINH(Z(1)*PIE)
D=CSH+COS (2.*PIE*Z(2))
B(1,IM1)=SNH/D
B(2,IM1)=-SIN(2.*PIE*Z(2))/D
B(3,IM1)=ALR*ALOG(EXM)
B(4,IM1)=180.*(2.*Z(2)+1.)
DO 200 JK=1,10
IF(B(4,IM1).GT.360.)B(4,IM1)=B(4,IM1)-360.
IF(B(4,IM1).LT.-360.)B(4,IM1)=B(4,IM1)+360.
IF(B(4,IM1).LT.360..AND.B(4,IM1).GT.-360.)GO TO 210
200 CONTINUE
210 CONTINUE
B(5,IM1)=Z(3)+ALR*ALOG(.5*EXH)
B(6,IM1)=Z(3)+ALR*ALOG(.5*EXMH)
F1(IM1)=PIE*2.013/(6.*ALM)
F2(IM1)=F1(IM1)*(1.-AM*AM)
IB=356
H=1./120.
XZ=0.
AA=2.*PIE*AM/ALM
DO 500 IT=1,IB
XYZ(IT)=-XZ
CAX=COS(AA*XZ)
SAX=SIN(AA*XZ)
BTX=PIE*(Z(2)+XZ*2./ALM)
SN=SIN(BTX)
CS=COS(BTX)
CSS=CS**2
TDN=CSHS-CSS
PRA(IT)=Z(3)+10.*ALOG10(TDN)
AAT=SAX*SNHH*CS-CAX*CSHH*SN
BBT=-SAX*CSHH*SN-CAX*SNHH*CS
DEL1=ATAN(BBT/AAT)
IF(AAT.LT.0.)DEL1=DEL1+PIE
IF(DEL1.GT.2.*PIE)DEL1=DEL1-2.*PIE
IF(DEL1.LT.-2.*PIE)DEL1=DEL1+2.*PIE
DEL(IT)=DEL1*180./PIE
XZ=XZ-H
500 CONTINUE
WRITE(6,510)NO1,AM,W11(IM1)
C @@@@@@@@@@@@@@@@@@@@@@@@@@@@@@@@@@@@@@@@@@@@@@@@@@@@@@@@@

```

```

510  FORMAT(1H1,///,10X,'RUN NO = ',I3,5X,'MACH NO = ',F5.3
*,5X,'FREQUENCY,HZ = ',F6.0,///,6X,'AXIAL LOCATION, INCH'
*,2X,'MEASURED AMP.DB',2X,'COMPUTED AMP.DB',/)
WRITE(6,520)(X5(I),AP(I),TDB(I),I=1,IR)
C  @@@@@@@@@@@@@@@@@@@@@@@@@@@@@@@@@@@@@@@@@@@@@@@@@@@@@@@@@
520  FORMAT(3F18.3)
WRITE(6,540)NO1,AM,W11(IM1)
C  @@@@@@@@@@@@@@@@@@@@@@@@@@@@@@@@@@@@@@@@@@@@@@@@@@@@@@@@@
540  FORMAT(1H1,///,10X,'RUN NO = ',I3,5X,'MACH NO = ',F5.3
*,5X,'FREQUENCY,HZ = ',F6.0,///,8X,'AXIAL LOCATION, FT'
*,6X,'COMPUTED AMP.DB',6X,'COMPUTED PHASE, DEG',/)
WRITE(6,530)(XYZ(I),PRA(I),DEL(I),I=1,IB)
C  @@@@@@@@@@@@@@@@@@@@@@@@@@@@@@@@@@@@@@@@@@@@@@@@@@@@@@@@@
530  FORMAT(3F20.3)
DO 700 I=1,IR
X5(I)=X5(I)/12.
700  CONTINUE
IW11=W11(IM1)
NO2=NO1*10+IW11/1000
IW12=IW11-(IW11/1000)*1000
IF(IW12.EQ.0)NO2=NO2*1000
IF(IW12.NE.0)ENCODE(13,600,FNAME)NO2,IW12
C  .....
IF(IW12.EQ.0)ENCODE(13,610,FNAME)NO2
C  .....
600  FORMAT(I4,I3,'IM.DAT')
610  FORMAT(I7,'IM.DAT')
OPEN(UNIT=9,NAME=FNAME,STATUS='NEW')
C  .....
WRITE(9,620)(X5(I),I=1,IR)
C  ~~~~~
C  X5=AXIAL LOCATION CORRESPOND TO MEASUREMENT POINTS
WRITE(9,620)(AP(I),I=1,IR)
C  ~~~~~
C  AP=MEASURED PRESSURE AMPLITUDES
WRITE(9,620)(XYZ(I),I=1,IB)
C  ~~~~~
C  XYZ=AXIAL LOCATION CORRESPOND TO COMPUTED PRESSURE
WRITE(9,620)(PRA(I),I=1,IB)
C  ~~~~~
C  PRA=COMPUTED PRESSURE AMPLITUDES
WRITE(9,620)(DEL(I),I=1,IB)
C  ~~~~~
C  DEL=COMPUTED PRESSURE PHASE
620  FORMAT(10F8.3)
CLOSE(9)
C  .....
235  CONTINUE

```

```

      WRITE(6,150)NO1,AM
C      @@@@@@@@@@@@@@@@@@
150  FORMAT(1H1,///,5X,'ACOUSTIC PROPERTIES OF OPEN DUCT TERMINATION'
      *,//,6X,'USING IMPEDANCE TUBE METHOD, RUN NO = ',I3,2X,
      *'MACH NO = ',F5.3,/)
      WRITE(6,130)
C      @@@@@@@@@@@@@@@@@@
130  FORMAT(2X,'FREQ,HZ',2X,'KR',4X,'KR/(1-M*M)',2X,'RESISTANCE',
      *1X,'REACTANCE'1X,'REF. AMP.',2X,'REF.PHAE',2X,'INC. AMP',3X,
      *'REF. AMP',4X,'ALPHA',5X,'BETA',4X,'AMP. CONST',2X,'ERROR',/)
      WRITE(6,190)(W11(I),F2(I),F1(I),(B(K,I),K=1,6),(Z1(I,J),J=1,3)
C      @@@@@@@@@@@@@@@@@@@@@@@@@@@@@@@@@@@@@@@@@@@@@@@@@@@@@@@@@@@@@@
      *,FR6(I),I=1,NZ1)
C      @@@@@@@@@@@@@@@@@@
190  FORMAT(1X,F6.0,2X,F7.3,2X,F7.3,F11.3,F10.3,2X,F8.3,2X,F11.3
      *,6F10.3/)
      STOP
      END

```

```

SUB ROUTINE SR8(A,NR,NC,N,MC,JC,V)
C
C *****
C
C TO SOLVE A SET OF SIMULTANEOUS EQUATIONS.
C
C *****
C
C NC=MAXIMUM NO OF COLS IN MATRIX A
C NR=MAXIMUM NO OF ROWS IN MATRIX A
C N=SIZE OF PART MATRIX TO BE INVERTED
C MC=NO OF COLS OF PART MATRIX
C DIMENSION A(NR,NC),JC(N),V(N)
C IW=V(1)
C M=1
C S=1.
C L=N+(MC-N)*(IW/4)
C KD=2-MOD(IW/2,2)
C IF(KD.EQ.1)V(2)=0.
C KI=2-MOD(IW,2)
C IF(KI.EQ.2)GO TO 105
C DO 100 I=1,N
100 JC(I)=I
105 DO 165 I=1,N
C IF(KI.EQ.1) GO TO 110
C M=I
110 IF(I.EQ.N) GO TO 130
C X=-1.
C DO 115 J=I,N
C IF(X.GT.ABS(A(J,I))) GO TO 115
C X=ABS(A(J,I))
C K=J
115 CONTINUE
C IF(K.EQ.I) GO TO 130
C S=-S
C IF(KI.EQ.2) GO TO 120
C MU=JC(I)
C JC(I)=JC(K)
C JC(K)=MU
120 DO 125 J=M,L
C X=A(I,J)
C A(I,J)=A(K,J)
125 A(K,J)=X
130 IF(ABS(A(I,I)).GT.0.) GO TO 145
C IF(KD.EQ.1)V(1)=0.
C JC(1)=I-1
C WRITE(6,135)
135 FORMAT('O INVERSION TROUBLE'/)
C WRITE(6,140)JC(1)
140 FORMAT('OJC(1)+',I4/)

```

```

      STOP
145  IF(KD.EQ.2) GO TO 150
      IF(A(I,I).LT.0.)S=-S
      V(2)=V(2)+ALOG(ABS(A(I,I)))
150  X=A(I,I)
      A(I,I)=1.
      DO 155 J=M,L
      A(I,J)=A(I,J)/X
155  CONTINUE
      DO 165 K=1,N
      IF(K.EQ.I) GO TO 165
      X=A(K,I)
      A(K,I)=0.
      DO 160 J=M,L
      A(K,J)=A(K,J)-X*A(I,J)
160  CONTINUE
165  CONTINUE
      IF(KI.EQ.2) GO TO 190
      DO 185 J=1,N
      IF(JC(J).EQ.J) GO TO 185
      JJ=J+1
      DO 170 I=JJ,N
      IF(JC(I).EQ.J) GO TO 175
170  CONTINUE
175  JC(I)=JC(J)
      DO 180 K=1,N
      X=A(K,I)
      A(K,I)=A(K,J)
180  A(K,J)=X
185  CONTINUE
190  JC(1)=N
      IF(KD.EQ.1) V(1)=S
      RETURN
      END

```

```

C      SUB ROUTINE INITIAL(ALM,AP,X3,Z,NUM,IR,PRMS)
C
C      *****
C
C      TO COMPUTE VALUES OF ALPHA BETA AND A USING
C      COMBINATION OF THREE PRESSURE MEASUREMENTS AND
C      TO DETERMINE A SET OF ALPHA BETA AND A WITH
C      MINIMUM rms ERROR BETWEEN THEORETICAL AND
C      EXPERIMENTAL VALUES OF PRESSURE AMPLITUDES
C      TO BE USED AS INITIAL VALUES
C
C      *****
C
C      DIMENSION AP(50),X3(50),Z(3)
C
C      PIE=3.1415926
C      R1=4.*PIE/ALM
C      NUM=0
C      PRMS=1000
C      AVALP=0
C      AVBET=0
C      AVAMP=0
C      JP=IR-2
C      DO 110 J=1,JP
C      JJ=J+1
C      JJP=JP+1
C      DO 120 K=JJ,JJP
C      KK=K+1
C      DO 130 L=KK,IR
C      P1=AP(J)
C      P2=AP(K)
C      P3=AP(L)
C      D1=X3(J)/12.
C      D2=X3(K)/12.
C      D3=X3(L)/12.
C      CO=COS(R1*D1)
C      SI=SIN(R1*D1)
C      P12=10.**((P2-P1)*.1)
C      P13=10.**((P3-P1)*.1)
C      A12=COS(R1*D2)-P12*CO
C      A13=COS(R1*D3)-P13*CO
C      B12=SIN(R1*D2)-P12*SI
C      B13=SIN(R1*D3)-P13*SI
C      F1=A13*B12-A12*B13
C      FA=A12*(1.-P13)-A13*(1.-P12)
C      FB=B12*(1.-P13)-B13*(1.-P12)
C      DNM=SQRT(FA*FA+FB*FB)
C      IF(DNM.EQ.0.)GO TO 130
C      X=ABS(F1/DNM)
C      IF(X*X-1.)132,135,135
132  Z(1)=.001

```

```

GO TO 137
135 Z(1)=(1./(2.*PIE))*ALOG(X+SQRT(X*X-1))
137 FABP=-FB/FA+SQRT((FB/FA)*(FB/FA)+1)
FABM=-FB/FA-SQRT((FB/FA)*(FB/FA)+1)
Z(2)=ATAN(FABP)/PIE
CH2=COSH(PIE*Z(1))**2
C12=COS(PIE*Z(2)+R1*D1/2)**2
C22=COS(PIE*Z(2)+R1*D2/2)**2
C32=COS(PIE*Z(2)+R1*D3/2)**2
CC2=(CH2-C22)/(CH2-C12)
CC3=(CH2-C32)/(CH2-C12)
DB12P=ABS(P12-CC2)
DB13P=ABS(P13-CC3)
Z(2)=ATAN(FABM)/PIE
CH2=COSH(PIE*Z(1))**2
C12=COS(PIE*Z(2)+R1*D1/2)**2
C22=COS(PIE*Z(2)+R1*D2/2)**2
C32=COS(PIE*Z(2)+R1*D3/2)**2
CC2=(CH2-C22)/(CH2-C12)
CC3=(CH2-C32)/(CH2-C12)
DB12M=ABS(P12-CC2)
DB13M=ABS(P13-CC3)
IF(DB12P*DB13P-DB12M*DB13M)140,140,150
140 Z(2)=ATAN(FABP)/PIE
C12=COS(PIE*Z(2)+R1*D1/2)**2
C22=COS(PIE*Z(2)+R1*D2/2)**2
C32=COS(PIE*Z(2)+R1*D3/2)**2
150 NUM=NUM+1
Z(3)=(P1-10.*ALOG10(CH2-C12)+P2-10.*ALOG10(CH2-C22)
*+P3-10.*ALOG10(CH2-C32))/3
AVALP=AVALP+Z(1)
AVBET=AVBET+Z(2)
AVAMP=AVAMP+Z(3)
F=0.
DO 170 I=1,IR
PBD=PIE*(Z(2)+2.*X3(I)/(12.*ALM))
C=COS(PBD)
C2=C*C
PT=Z(3)+10.*ALOG10(CH2-C2)
170 F=F+(AP(I)-PT)**2
PRMS1=SQRT(F/IR)
IF(PRMS-PRMS1)165,165,160
160 PRMS=PRMS1
ALP1=Z(1)
BET1=Z(2)
AL=Z(3)
165 CONTINUE
130 CONTINUE
120 CONTINUE
110 CONTINUE
IF(NUM.EQ.0.)GO TO 100

```



```

AVALP=AVALP/NUM
AVBET=AVBET/NUM
AVAMP=AVAMP/NUM
F=0.
DO 180 I=1,IR
PBD=PIE*(AVBET+2.*X3(I)/(12.*ALM))
C2=COS(PBD)**2
CH2=COSH(PIE*AVALP)**2
PT=Z(3)+10.*ALOG10(CH2-C2)
180 F=F+(AP(I)-PT)**2
PRMS1=SQRT(F/IR)
IF (PRMS-PRMS1)190,190,185
185 PRMS=PRMS1
Z(1)=AVALP
Z(2)=AVBET
Z(3)=AVAMP
GO TO 100
190 Z(1)=ALP1
Z(2)=BET1
Z(3)=A1
100 CONTINUE
RETURN
END

```

B.4 COMPUTATION OF INDUCT AND FAR-FIELD ACOUSTIC PARAMETERS

MSEP39: This program computes the induct parameters (namely, reflection coefficient amplitude, incident power, reflected power and transmitted power), far-field parameters (namely, far-field sound pressure levels at 100 nozzle diameters away from the exit and far-field power), and the power imbalance. In addition, normalized power and far-field sound pressures are also computed. The normalizing parameters could be either the incident power or the transmitted power. The results can be obtained either at narrow band frequencies, at octave or one-third octave frequencies. The output data can also be numerically smoothed, if desired. The program can be used to both single and annular stream duct nozzle systems.

The input to the program includes inducts and far-field data. The far-field data are supplied in the form of measured sound pressure levels at several polar angles. The induct data are supplied in two ways. When a single induct measurement is made, the incident and the reflected sound pressure levels are supplied as they are measured. For multiple point measurements as needed for modal decomposition, the modal summation of the incident, the reflected and the transmitted powers are fed to the program. For single stream duct-nozzle system these data are obtained from the output of the program MPMODAL. For annular duct-nozzle system the output of MODANU and REFTRA are fed to MSEP39.

HUMCAL: This subroutine to MSEP39 corrects the input data for humidity, for microphone position to a standard polar radius, the effect of wind screen (if used for a microphone) and converts the corrected data to absolute sound pressure level using microphone calibrations.

FLIGHT: This subroutine to MSEP39 transforms noise data measured in a free jet simulation facility to the ideal wind-tunnel simulation.

OCTAVE: This subroutine to MSEP39 is used to convert the narrow band data into octave or one-third octave bands.

POWER: This subroutine to MSEP39 computes various acoustic power and power imbalance spectra.

SMOOTHING: This subroutine to MSEP39 is used to smooth numerically the sound pressure level spectrum or the power spectrum or any normalized transfer function spectrum.

```

C
C PROGRAM NAME: MSEP39.FOR
C
C *****
C
C GENERALIZED PROGRAM TO COMPUTE INDUCT AND FARFIELD
C SPL SPECTRA; FARFIELD TRANSFER FUNCTION SPECTRA AT
C EACH POLAR ANGLE; AND INCIDENT, TRANSMITTED AND
C FARFIELD ACOUSTIC POWER SPECTRA
C
C *****
C
C DIMENSION AM(16,501),F(501),IANG(16),ADUM(501),AM1(16,501)
C *,TITL1(40),TITL2(40),TITL3(40)
C
C CHARACTER FNAME*13
C
C ***** INPUT DATA *****
C ( ASSIGNED TO MSEP39.DAT )
C
C READ(5,580)TITL1
C -----
C TITL1 SPECIFIFS NOZZLE TERMINATION IN THE PRINTOUT
C
C READ(5,580)TITL2
C -----
C TITL2 SPECIFIES BAND WIDTH AND TYPE OF ANALYSIS
C
C READ(5,580)TITL3
C -----
C TITL3 IS THE HEADING FOR EMISSION ANGLES
C
C READ(5,*)IDX,IDX1,IDX2,IDX3,IDX4,IDX5,IDX6
C -----
C
C READ(5,*)NR,IC,IB,NF,NSTF,LO,L1,DF,RE,RMP
C -----
C
C READ(5,*)PA,PR,PS,PT,PM,TR,TA
C -----
C
C LMX=L1-LO+1
C
C IF (IDX.EQ.2) READ(5,*)(IANG(I),I=1,LMX)
C -----
C
C IF (IDX1.GT.1) READ(5,*)NFO
C -----

```

```

C
C      IF (IDX1.GT.1) READ(5,*) (F(I), I=1, NFO)
C      -----
C
C      IDX=1; WHEN POLAR ANGLES ARE WITH FIXED INCREAMENTS
C      =2; WHFN POLAR ANGLES ARE NOT WITH FIXED
C      INCREMENT AND ARE READ SEPARATELY
C
C      IDX1=1; NARROW BAND FREQUENCY ANALYSIS
C      =2; ONE-THIRD OCTAVE FREQUENCY ANALYSIS
C      =3; OCTAVE FREQUENCY ANALYSIS
C
C      IDX2=1; WITHOUT SMOOTHING
C      =2, WITH SMOOTHING
C
C      IDX3=1; POWER CALCULATIONS ARE DONE USING INDUCT & FARFIELD
C      SPL SPECTRA
C      =2; NO POWER CALCULATION
C      =3; INDUCT POWER DATA SUPPLIED FROM SEPARATE COMPUTATION
C
C      IDX4=1; WIND SCREENS USED UPTO 5TH MIC
C      =2; NO WIND SCREE USED
C
C      IDX5=1; WITH FLIGHT SIMULATION CORRECTION
C      =2; NO FLIGHT SIMULATION
C
C      IDX6=1; SINGLE STREAM DUCT-NOZZLE SYSTEM
C      =2; COANNULAR DUCT-NOZZLE SYSTEM
C
C      $$$$$$$$$$$$$$$$$$$$$$$$$$$$$$$$$$$$$$$$$$$$$$$$$$$$$$$$$$$$$
C
C      NR= RUN NUMBER
C
C      IC=NUMBER OF FREQUENCY POINTS STORED IN THE DATA FILE
C
C      IB=NUMBER OF FREQUENCY POINTS USED IN COMPUTATION
C
C      NF=NUMBER OF FREOUENCIES PRINTED OUT
C
C      NSTF=INTERVAL OF FREQUENCY POINTS FOR DATA PRINTOUT
C
C      LO=FIRST POLAR ANGLE NUMBER
C
C      LI=LAST POLAR ANGLE NUMBER
C
C      DF=BAND WIDTH FOR NARROW BAND ANALYSIS, HZ
C
C      RE=NOZZLE EXIT RADIUS, INCH

```

```

C      (FOR ANNULAR CASE, OUTER NOZZLE RADIUS)
C
C      RMP=STANDARD POLAR DISTANCE, FT
C
C      $$$$$$$$$$$$$$$$$$$$$$$$$$$$$$$$$$$$$$$$$$$$$$$$$$$$$$$$$$$$
C
C      PA=ATMOSPHERIC PRESSURE, PSIA
C
C      PR=TOTAL PRESSURE, PSIG
C
C      PS=STATIC PRESSURE IN THE DUCT, PSIG
C
C      PT=TOTAL PRESSURE IN TUNNEL, PSIG
C
C      PM=DIFFERENCE OF ATMOSPHERIC PRESSURE
C          BETWEEN THE CHAMBER AND LAB., INCH OF WATER
C
C      TR=TEMPERATURE IN THE DUCT, F
C
C      TA=CHAMBER TEMPERATURE, C
C
C      $$$$$$$$$$$$$$$$$$$$$$$$$$$$$$$$$$$$$$$$$$$$$$$$$$$$$$$$$$$$
C
C      IANG(I)=MEASUREMENTS MADE AT THESE POLAR ANGLES
C
C      $$$$$$$$$$$$$$$$$$$$$$$$$$$$$$$$$$$$$$$$$$$$$$$$$$$$$$$$$$$$
C
C      NFO=NUMBER OF OCTAVE OR 1/3 OCTAVE FREQUENCIES
C
C      F(I)=RESULTS EVALUATED AT THESE FREQUENCIES
C
C      $$$$$$$$$$$$$$$$$$$$$$$$$$$$$$$$$$$$$$$$$$$$$$$$$$$$$$$$$$$$
C
C      ***** COMPUTATION OF VARIOUS MACH NUMBERS *****
C          AND FACTORS
C
C
580  FORMAT(20A4)
      PI=3.1415926
      POWF=3.7396751
      GAM=1.402
      G=(GAM-1.)/2.
      GI=1./G
      GAC=GAM/(GAM-1.)
      GACI=1./GAC
      CF=14.7/408.8
C
C      CF=CONVERSION OF INCH OF WATER TO PSI

```

C

```

TA=TA*1.8+32.
CO=49.016*SQRT(TA+460.)
PJ=PR+PM*CF
IF (PR.EQ.0.)PJ=0.
PD=PR-PS
PSA=PA+PS
AMJ=SQRT((((1.+PJ/PA)**GACI)-1.)*GI)
TJ=((TR+459.7)/(1.+G*(AMJ*AMJ)))
CJ=49.016*SQRT(TJ)
AMD=SQRT((((1.+PD/PSA)**GACI)-1.)*GI)
TD=((TR+459.7)/(1.+G*(AMD*AMD)))
CD=49.016*SQRT(TD)
PTC=PT+PM*CF
IF (PT.EQ.0.)PTC=0.
AMT=SQRT((((1.+PTC/PA)**GACI)-1.)*GI)
CT=CO
VJ=AMJ*CJ
VT=AMT*CT
ROC=GAM*PA*144./CO
ROD=GAM*(PS+PA)*144./CD
RD=2.013/12.
RI=0.
IF (IDX6.EQ.2)RI=.67/12.
AREF=RD*RD-RI*RI

```

C

```

C RD=INNER RADIUS OF THE DUCT
C FOR ANNULAR: INNER RADIUS OF OUTER DUCT
C RI=FOR ANNULAR: OUTER RADIUS OF INNER DUCT
C AREF=CROSS-SECTIONAL AREA OF THE DUCT/PI
C

```

```

RMC=100.*RE/12.
FACC=20.*ALOG10(RMP/RMC)
ARI=10.*ALOG10((1.+AMD)*(1.+AMD)*RD*RD*PI/ROD)
ARR=10.*ALOG10((1.-AMD)*(1.-AMD)*RD*RD*PI/ROD)
FACT=4.*RMC*RMC*SQRT((TA+460.)/(TD))/(((1.+AMD)**2)*AREF)
FACT=FACT*(1.+PS/PA)
FACT1=4.*PI*RMC*RMC/ROC
FACT=10.*ALOG10(FACT)
FACTT=10.*ALOG10(FACT1)-POWF
IF (IDX3.EQ.3)FACT=FACTT

```

C

```

C ***** TO READ PRESSURE & POWER DATA FROM FILES ***
C

```

C

```

LI=LMX+1
LR=LMX+2
LT=LR+1

```

C

```

C      LI=INCIDENT
C      LR=REFLECTED
C      LT=TRANSMITTED
C
      LIR=LR
      IF (IDX3.EQ.3.AND.IDX6.EQ.1) LIR=LI
      IF (IDX3.EQ.3.AND.IDX6.EQ.2) LIR=LT
      DO 200 I=1,LIR
      IF (IDX.EQ.1) IANG(I)=(I+L0-2)*10
      IF (I.EQ.LI) IANG(I)=360
      IF (I.EQ.LR) IANG(I)=180
      NP=IANG(I)+100
      IF (IDX6.EQ.2) GO TO 410
      IF (I.EQ.LI.AND.IDX3.EQ.3) NP=109
      IF (I.LT.LI) ENCODE(13,100,FNAME)NR,NP
      IF (I.EQ.LI.AND.IDX3.EQ.3) ENCODE(13,110,FNAME)NR,NP
      IF (I.GE.LI.AND.IDX3.NE.3) ENCODE(13,330,FNAME)NR,NP
100  FORMAT(2I3,'SFF.RDT')
110  FORMAT(2I3,'POW.RDT')
330  FORMAT(2I3,'SID.RDT')
      OPEN(UNIT=9,NAME=FNAME,STATUS='OLD')
      IF (I.EQ.LI.AND.IDX3.EQ.3) GO TO 140
      READ(9,300)(AM(I,J),J=1,IC)
C      AM = FAR-FIELD SPL (IF IDX3 = 3)
C      = FAR-FIELD AND INDUCT SPL (IF IDX3 NOT = 3)
      GO TO 130
140  CONTINUE
      DO 150 KDUM=1,15
      READ(9,300)(ADUM(J),J=1,IC)
      DO 160 KKD=7,15,4
      DO 170 J=1,IC
      IF (KDUM.EQ.7) AM(LI,J)=ADUM(J)
      IF (KDUM.EQ.11) AM(LR,J)=ADUM(J)
      IF (KDUM.EQ.15) AM(LT,J)=ADUM(J)
170  CONTINUE
160  CONTINUE
C
C      FOR IDX3=3      FOR IDX3=1 OR 2
C      ~~~~~
C      AM(LI,J)=INCIDENT POWER      INCIDENT SPL
C      AM(LR,J)=REFLECTED POWER      REFLECTED SPL
C      AM(LT,J)=TRANSMITTED POWER      (NOT INPUT)
C
150  CONTINUE
130  CONTINUE
      CLOSE(9)
      GO TO 310
410  CONTINUE

```

```

      IF(I.EQ.LI.AND.IDX3.EQ.3)NP=100
      IF(I.GT.LI.AND.IDX3.EQ.3)NP=300
      IF(I.LT.LI)ENCODE(13,320,FNAME)NR,NP
      IF(I.GE.LI.AND.IDX3.EQ.3)ENCODE(13,110,FNAME)NR,NP
      IF(I.EQ.LT.AND.IDX3.EQ.3)ENCODE(13,340,FNAME)NR,NP
      IF(I.GE.LI.AND.IDX3.NE.3)ENCODE(13,430,FNAME)NR,NP
320  FORMAT(2I3,'AFF.RDT')
430  FORMAT(2I3,'AID.RDT')
340  FORMAT(2I3,'POT.RDT')
      OPEN(UNIT=9,NAME=FNAME,STATUS='OLD')
      IF(I.GE.LI.AND.IDX3.EQ.3)GO TO 450
      READ(9,300)(AM(I,J),J=1,IC)
      GO TO 460
450  CONTINUE
      IF(I.EQ.LT)GO TO 370
      DO 380 NM=1,7
      READ(9,300)(AM(I,J),J=1,IC)
380  CONTINUE
      GO TO 390
370  CONTINUE
      DO 400 NM=1,8
      READ(9,300)(AM(I,J),J=1,IC)
400  CONTINUE
390  CONTINUE
460  CONTINUE
      CLOSE(9)
310  CONTINUE
200  CONTINUE
300  FORMAT(10F8.3)
C
      CALL HUMCAL(IC,IB,DF,PA,TA,AM,IANG,LMX,LO,IDX3,IDX4)
C  #####
C
      LMXS=LMX
C
      IF(IDX5.EQ.1)CALL FLIGHT(IB,RMP,VT,VJ,CO,CT,AMT,
C  #####
      *IANG,LMX,AM,DF)
C  #####
C
      IF(LMX.EQ.LMXS)GO TO 250
      DO 260 I=1,IB
      AM(LMX+1,I)=AM(LI,I)
      AM(LMX+2,I)=AM(LR,I)
      IF(IDX3.EQ.3)AM(LMX+3,I)=AM(LT,I)
260  CONTINUE
      LI=LMX+1
      LR=LI+1

```



```

        LT=LR+1
250  CONTINUE
        DO 270 K=1,LMX
        DO 270 I=1,IB
        AM(K,I)=AM(K,I)+FACC
270  CONTINUE
C
        IF(IDX1.GT.1)CALL OCTAVE(IDX1,IDX3,NFO,DF,IB,IC,AM,F,LT)
C
C      #####
C
        IF(IDX3.NE.2)CALL POWER(IB,RMC,RD,RI,LMX,IANG,AMD
C
C      #####
C      *,AM,TA,TD,PA,PS,IDX1,IDX2,IDX3,AM1,NFO)
C      #####
C
        NST=LMX
        IF(IDX2.EQ.2)CALL SMOOTHING(IC,IB,DF,AM,NST)
C
C      #####
C
        NST=6
        IF(IDX2.EQ.2)CALL SMOOTHING(IC,IB,DF,AM1,NST)
C
C      #####
C
        DO 290 I=1,IB
        IF(IDX3.EQ.3)AM(LI,I)=AM1(1,I)-POWF-ARI
        IF(IDX3.EQ.3)AM(LR,I)=AM1(2,I)-POWF-ARR
        AM(LT,I)=AM(LR,I)-AM(LI,I)
290  CONTINUE
        IF(IDX1.NE.1)GO TO 780
        DO 780 I=1,IB
        F(I)=(I-1)*DF
780  CONTINUE
C
        NP1=IDX2*100+IDX1*10
C
C      FIRST DIGIT OF NP1 REPRESENTS IDX2( 1=UNSMOOTHED,
C      2=SMOOTHED). SECOND DIGIT OF NP1 REPRESENTS IDX1
C      (1=NARROW BAND,2=1/3 OCTAVE,3=OCTAVE)
C
C      ***** PRINT & STORE STATEMENTS FOR INDUCT PRESSURE, *****
C      ***** POWER & REFLECTION COEFFICIENT SPECTRA *****
C
        WRITE(6,500)TITL1,TITL2
        WRITE(6,510)AMJ,AMT
        WRITE(6,660)
        WRITE(6,650)
650  FORMAT(10X,'FRQUENCY',2X,'INCIDENT',1X,'REFLECTED',
        *1X,'INCIDENT',1X,'REFLECTED',1X,'TRANSMITTED',1X,

```

```

      *'REFLECTION',/,23X,'SPL',7X,'SPL',6X,'POWER',5X,
      *'POWER',5X,'POWER',4X,'COEFFICIENT',/)
660  FORMAT(17X,'INDUCT PRESSURE, POWER AND REFLECTION
      * COEFFICIENT SPECTRA',/)
      WRITE(6,840)(F(I),(AM(K,I),K=LI,LR),(AM1(J,I),J=1,3),
      *AM(LT,I),I=1,NF,NSTF)
840  FORMAT(10X,F7.0,6F10.2)
C
      ENCODE(13,850,FNAME)NR,NP1
850  FORMAT(2I3,'PRW.ADT')
      OPEN(UNIT=9,NAME=FNAME,STATUS='NEW')
      DO 860 K=LI,LR
      WRITE(9,300)(AM(K,I),I=1,IB)
860  CONTINUE
      DO 870 J=1,3
      WRITE(9,300)(AM1(J,I),I=1,IB)
870  CONTINUE
      WRITE(9,300)(AM(LT,I),I=1,IB)
      CLOSE(9)
C
C      **** PRINT & STORE STATEMENTS FOR FARFIELD SPL ****
C      ***** AND POWER SPECTRA *****
C
      WRITE(6,500)TITL1,TITL2
      WRITE(6,510)AMJ,AMT
      WRITE(6,520)RMC
      WRITE(6,530)TITL3
      IF(LMX.EQ.13)WRITE(6,540)(IANG(J),J=1,LMX)
      IF(LMX.EQ.12)WRITE(6,800)(IANG(J),J=1,LMX)
      IF(LMX.EQ.11)WRITE(6,810)(IANG(J),J=1,LMX)
      IF(LMX.EQ.10)WRITE(6,730)(IANG(J),J=1,LMX)
500  FORMAT(1H1,/,25X,20A4,/,25X,20A4,/,25X,20A4,
      *,25X,20A4,/)
510  FORMAT(22X,'JET MACH NO, MJ =',F5.3,5X,'FREE JET
      * MACH NO =',F5.3,/)
520  FORMAT(20X,'SPL (dB) CORRECTED TO 100*EXIT DIAMETER,
      * RMC =',F7.3,' FT.',/)
530  FORMAT(/,20X,20A4,/,20X,20A4,/)
540  FORMAT(5X,'FREQUENCY',2X,'PWL',13I6//)
800  FORMAT(5X,'FREQUENCY',2X,'PWL',12I6//)
810  FORMAT(5X,'FREQUENCY',2X,'PWL',11I6//)
730  FORMAT(5X,'FREQUENCY',2X,'PWL',10I6//)
      IF(LMX.EQ.13)WRITE(6,550)(F(I),AM1(4,I),(AM(J,I),
      *J=1,LMX),I=1,NF,NSTF)
      IF(LMX.EQ.12)WRITE(6,820)(F(I),AM1(4,I),(AM(J,I),
      *J=1,LMX),I=1,NF,NSTF)
      IF(LMX.EQ.11)WRITE(6,830)(F(I),AM1(4,I),(AM(J,I),
      *J=1,LMX),I=1,NF,NSTF)

```

```

        IF(LMX.EQ.10)WRITE(6,740)(F(I),AM1(4,I),(AM(J,I),
        *J=1,LMX),I=1,NF,NSTF)
550  FORMAT(5X,F7.0,1X,14F6.1)
820  FORMAT(5X,F7.0,1X,13F6.1)
830  FORMAT(5X,F7.0,1X,12F6.1)
740  FORMAT(5X,F7.0,1X,11F6.1)
C
        ENCODE(13,560,FNAME)NR,NP1
560  FORMAT(2I3,'SPL.ADT')
        OPEN(UNIT=9,NAME=FNAME,STATUS='NEW')
        WRITE(9,300)(AM1(4,I),I=1,IB)
        DO 720 J=1,LMX
        WRITE(9,300)(AM(J,I),I=1,IB)
720  CONTINUE
        CLOSE(9)
C
        IF(IDX3.NE.3)GO TO 590
        DO 700 I=1,IB
        AM(LI,I)=AM(LI,I)+POWF+ARI
700  CONTINUE
590  CONTINUE
        DO 350 K=1,LMX
        DO 350 I=1,IB
        AM(K,I)=AM(K,I)-AM(LI,I)+FACT
350  CONTINUE
        DO 360 I=1,IB
        IF(IDX3.NE.3)AM(LT,I)=AM(LR,I)-AM(LI,I)
360  CONTINUE
C
C      ***** PRINT & STORE STATEMENTS FOR FARFIELD SPL & POWER*****
C      *****SPECTRA NORMALIZED TO INCIDENT PRESSURE FIELD*****
C
        WRITE(6,500)TITL1,TITL2
        WRITE(6,510)AMJ,AMT
        WRITE(6,610)
        WRITE(6,530)TITL3
        IF(LMX.EQ.13)WRITE(6,540)(IANG(J),J=1,LMX)
        IF(LMX.EQ.12)WRITE(6,800)(IANG(J),J=1,LMX)
        IF(LMX.EQ.11)WRITE(6,810)(IANG(J),J=1,LMX)
        IF(LMX.EQ.10)WRITE(6,730)(IANG(J),J=1,LMX)
610  FORMAT(33X,'SPL & POWER TRANSFER FUNCTIONS (dB) NORMALIZED',//
        *,35X,'WITH RESPECT TO INCIDENT PRESSURE FIELD',//)
        IF(LMX.EQ.13)WRITE(6,550)(F(I),AM1(5,I),(AM(J,I),J=1,LMX),
        *I=1,NF,NSTF)
        IF(LMX.EQ.12)WRITE(6,820)(F(I),AM1(5,I),(AM(J,I),J=1,LMX),
        *I=1,NF,NSTF)
        IF(LMX.EQ.11)WRITE(6,830)(F(I),AM1(5,I),(AM(J,I),J=1,LMX),
        *I=1,NF,NSTF)

```

```

      IF(LMX.EQ.10)WRITE(6,740)(F(I),AM1(5,I),(AM(J,I),J=1,LMX),
      *I=1,NF,NSTF)
C
      ENCODE(13,690,FNAME)NR,NP1
690  FORMAT(2I3,'TRI.ADT')
      OPEN(UNIT=9,NAME=FNAME,STATUS='NEW')
      WRITE(9,300)(AM1(5,I),I=1,IB)
      DO 180 J=1,LMX
      WRITE(9,300)(AM(J,I),I=1,IB)
180  CONTINUE
      CLOSE(9)
C
      DO 210 J=1,LMX
      DO 210 I=1,IB
      AM(J,I)=AM(J,I)+AM(LI,I)-FACT-AM1(3,I)+FACTT-POWF
210  CONTINUE
C
C      ***** PRINT & STORE STATEMENTS FOR FARFIELD SPL & POWER *****
C      ***** SPECTRA NORMALIZED TO TRANSMITTED PRESSURE FIELD***
C
      WRITE(6,500)TITL1,TITL2
      WRITE(6,510)AMJ,AMT
      WRITE(6,630)
      WRITE(6,530)TITL3
      IF(LMX.EQ.13)WRITE(6,540)(IANG(J),J=1,LMX)
      IF(LMX.EQ.12)WRITE(6,800)(IANG(J),J=1,LMX)
      IF(LMX.EQ.11)WRITE(6,810)(IANG(J),J=1,LMX)
      IF(LMX.EQ.10)WRITE(6,730)(IANG(J),J=1,LMX)
630  FORMAT(33X,'SPL & POWER TRANSFER FUNCTIONS (dB) NORMALIZED',//
      *,35X,'WITH RESPECT TO TRANSMITTED PRESSURE FIELD',//)
      IF(LMX.EQ.13)WRITE(6,550)(F(I),AM1(6,I),(AM(J,I),J=1,LMX),
      *I=1,NF,NSTF)
      IF(LMX.EQ.12)WRITE(6,820)(F(I),AM1(6,I),(AM(J,I),J=1,LMX),
      *I=1,NF,NSTF)
      IF(LMX.EQ.11)WRITE(6,830)(F(I),AM1(6,I),(AM(J,I),J=1,LMX),
      *I=1,NF,NSTF)
      IF(LMX.EQ.10)WRITE(6,740)(F(I),AM1(6,I),(AM(J,I),J=1,LMX),
      *I=1,NF,NSTF)
C
      ENCODE(13,190,FNAME)NR,NP1
190  FORMAT(2I3,'TRT.ADT')
      OPEN(UNIT=9,NAME=FNAME,STATUS='NEW')
      WRITE(9,300)(AM1(6,I),I=1,IB)
      DO 680 J=1,LMX
      WRITE(9,300)(AM(J,I),I=1,IB)
680  CONTINUE
      CLOSE(9)
C
      END

```

```

C      SUBROUTINE HUMCAL(IC,IB,DF,PA,TA,AM,IANG,LMX,LO,IDX3,IDX4)
C
C      *****
C
C      CORRECTS FOR HUMIDITY
C      CORRECTS FOR MICROPHONE POSITION TO A STANDARD POLAR RADIUS
C      CORRECTS THE EFFECT OF WIND SCREEN IF MOUNTED ON A MICROPHONE
C      CONVERTS TO ABSOLUTE LEVEL USING MIC/REF. MIC CALIBRATION
C
C      *****
C
C      DIMENSION IANG(16),HUMCOR(501),AM(16,501),DAMP(15),AMP(15)
C      *,WS(501),AW(501),FRES(501)
C
C      CHARACTER FNAME*13
C
C      LI=LMX+1
C      LR=LMX+2
C
C      READ(5,*)(AMP(I),I=1,LR)
C      -----
C      AMP(I)=ATTN DURING AVERAGING [A1]-ACTUAL AMPL
C
C      READ(5,*)REAL
C      -----
C      REAL=0. WHEN FUNCTION 12 NOT USED IN ZERO SETTING
C
C      DAMP(I)=(REF AMPL-ACTUAL AMPL)+(ATTN DURING AVERAGING [A1]-
C      ATTN OF REF SIGNAL DURING ZERO SETTING IN FCN 12 [A1] )
C      =REF AMPL(REAMP)-ATTN OF REF SIGNAL DURING ZERO
C      SETTING IN FCN 12 [A1] (REAL)+AMP(I)
C
C      NOTE:ATTN OF ACTUAL SIGNAL IN FCN 6 [A2] IS ALREADY ADDED.
C      AND (114-ATTN OF REF SIGNAL DURING ZERO SETTING IN FCN 6
C      [A2]) IS ALSO ADDED
C
C      DO 210 I=1,LR
C      REAMP=20.
C      IF(I.GE.LI)REAMP=0.
C      DAMP(I)=REAMP-REAL+AMP(I)
C      IF(IDX3.EQ.3.AND.I.GT.LMX)DAMP(I)=0.
210  CONTINUE
C      READ(5,*)RMP,RMS,IN1,IN2,RH
C      -----
C      RMP=STANDARD POLAR DISTANCE, FT.
C      RMS=SMALLER POLAR DISTANCE, FT.
C      IN1=LOWER LIMIT FOR RMS
C      IN2=UPPER LIMIT FOR RMS
C      RH=PERCENTAGE OF HUMIDITY
C

```

```

DO 200 I=1,IC
X=(I-1)*DF
IF(I.LE.31)FRES(I)=-5.33+.0318*X-.639E-04*X*X
*+.426E-07*X*X*X
IF(I.GT.31.AND.I.LE.51)FRES(I)=0.
IF(I.GT.51)FRES(I)=-.0876+.229E-03*X-.172E-06*X*X
*+.181E-10*(X**3)-.725E-15*(X**4)
200 CONTINUE
DS=2.5

C
C DS=INDUCT TRANSDUCER POSITION FROM EXIT, FT.
C

FACT1=20.*ALOG10(RMP/RMS)
PI=3.1415926
NRCAL=999
NPWIND=999
RD=2.013/12.
ENCODE(13,100,FNAME)NRCAL,NPWIND
100 FORMAT(2I3,'WNS.CAL')
OPEN(UNIT=9,NAME=FNAME,STATUS='OLD')
READ(9,300)(WS(I),I=1,IC)
C WS=WIND SCREEN CORRECTION
300 FORMAT(10F8.3)
CLOSE(9)
T01=273.16
P=PA/14.7
TF=TA
TC=(TA-32.)*5./9.
T=TC+T01
T1=T/293
PS=10.79586*(1.-T01/T)-5.02808*ALOG10(T/T01)+1.50474E-4*
1(1.-1/(10.**((8.29692*((T/T01)-1)))))+0.42873E-3*(10.**((4.76955*
2(1.-(T01/T)))-1.))-2.2195983
PS=10.**PS
H =PS/P*RH
FRO2=P*(24.+4.41E04*H*(0.05+H)/(0.391+H))
FRN2=P/SQRT(T1)*(9.+350.*H*EXP(-6.142*((1./T1)**.333-1.)))
DO 110 J=1,IC
CF=(J-1)*DF
AL=1.84E-11+2.1913E-4/T1*P*(2239.1/T)**2*EXP(-2239.1/T)
1/(FRO2+(CF**2/FRO2))
AL=AL+8.1619E-4/T1*P*(3352./T)**2*EXP(-3352./T)
1/(FRN2+(CF**2/FRN2))
AL=AL*SQRT(T1)*CF**2/P
HUMCOR(J)= AL*2647./1000.
110 CONTINUE
NRHAF=101
C NRHAF=RUN NO FOR HALF INCH MIC CAL W.R.T. REF MIC

```

```

DO 291 K2=1,LR
NP=IANG(K2)+100
IF(K2.GE.LI)NP=101
IF(K2.GE.LI.AND.IDX3.EQ.3)GO TO 510
ENCODE(13,500,FNAME)NRHAF,NP
500 FORMAT(2I3,'HAF.CAL')
OPEN(UNIT=9,NAME=FNAME,STATUS='OLD')
READ(9,300)(AW(I),I=1,IC)
C   AW=TRANSFER FUNCTION OF MIC/TRANSDUCER
CLOSE(9)
510 CONTINUE
DIST=RMP+DS
IF(IANG(K2).LE.IN1)DIST=RMS+DS
IF(IANG(K2).GT.IN2)DIST=RMS+DS
FACT=0.
IF(IANG(K2).LE.IN1)FACT=FACT1
IF(IANG(K2).GT.IN2)FACT=FACT1
DO 330 L=1,IC
IF(K2.LE.LMX)AM(K2,L)=AM(K2,L)+HUMCOR(L)*DIST-FACT+
*DAMP(K2)-AW(L)-FRES(L)
IF(K2.GT.LMX.AND.IDX3.NE.3)AM(K2,L)=AM(K2,L)+DAMP(K2)-
*FRES(L)-AW(L)
330 CONTINUE
IF(IDX4.EQ.2)GO TO 331
IF(IANG(K2).GT.IN1)GO TO 331
DO 332 L=1,IC
332 AM(K2,L)=AM(K2,L)+WS(L)
331 CONTINUE
291 CONTINUE
RETURN
END

```

```

C      SUBROUTINE FLIGHT(IB,RMP,VT,VJ,CO,CT,AMT,IANG,LMX,AM,DF)
C
C      *****
C
C      TRANSFORM NOISE DATA MEASURED IN A FREE JET FLIGHT
C
C      SIMULATION FACILITY TO THE IDEAL WIND-TUNNEL SIMULATION
C
C      *****
C
C      DIMENSION THEM(16),THET(16),KA(16),AM(16,501),AM1(13,501)
C      *,IANG(16)
C
C      RT=0.356
C      RM=RMP*0.305
C      R=RM
C
C      RT=FREE-JET NOZZLE RADIUS, M
C      RM=MEASUREMENT DISTANCE FROM NOZZLE EXIT PLANE
C      FOR FREE-JET DATA, M
C      R=EMISSION DISTANCE FROM SOURCE LOCATION FOR
C      IDEAL WIND-TUNNEL DATA, M
C
C      PI=3.1415926
C      RADD=180./PI
C      RBAR=R/RT
C      RMBAR=RM/RT
C      AOAT=CO/CT
C      VJAO=VJ/CO
C      AOMT=VT/CO
C      RHOR=AOAT*AOAT
C      VTAT=AMT
C      VJ=VJ*.305
C      VT=VT*.305
C      ACOS=-1./(AOAT+VTAT)
C      TANT=SQRT(1.-ACOS*ACOS)/ACOS
C      THETMX=RADD*ATAN(TANT)
C      IF(ACOS.LT.0.)THETMX=THETMX+180.
C      MTX=0
C      DO 200 K=1,LMX
C      KA(K)=0
200  CONTINUE
C      DO 100 K=1,LMX
C      THEM(K)=IANG(K)
C      THET(K)=IANG(K)
C
C      THEM(K)=MEASUREMENT ANGLES

```



```

C      THET(K)=INTERPOLATED ANGLES
C
      IF(THET(K).LE.THETMX)GO TO 100
      MTX=MTX+1
      KA(MTX)=K
100    CONTINUE
      LMX1=LMX
      IF(KA(1).NE.0)LMX1=KA(1)-1
      MTX=0
      DO 140 K=1,LMX
      KA(K)=0
140    CONTINUE
      NTM=LMX-1
      DO 120 K=1,LMX1
      CTHET=COS(THET(K)/RADD)
      STHET=SIN(THET(K)/RADD)
      COTPST=(CTHET+VTAT)/STHET
      COSTHO=(AOAT*CTHET)/(1.+VTAT*CTHET)
      SINTHO=SQRT(1.-COSTHO*COSTHO)
      COTTHO=COSTHO/SINTHO
      CF=-40.*ALOG10(1.+VTAT*CTHET)+10.*ALOG10(RHOR)
      XLBAR=COTPST
      ALBAR=XLBAR-COTTHO
      RROBAR=SQRT(RMBAR*RMBAR-ALBAR*ALBAR*SINTHO*SINTHO)-
      *ALBAR*COSTHO
      RRABAR=RROBAR+(1./SINTHO)*(((SINTHO/SQRT(((1.-AOMT
      **COSTHO)**2)*AOAT*AOAT-COSTHO*COSTHO))**3)*AOAT*AOAT)-1.)
      ACOS=(RMBAR*RMBAR+ALBAR*ALBAR-RROBAR*RROBAR)/(2.*ALBAR*RMBAR)
      TANT=SQRT(1.-ACOS*ACOS)/ACOS
      THEMI=RADD*ATAN(TANT)
      IF(ACOS.LT.0.)THEMI=THEMI+180.
      CR=10.*ALOG10(RROBAR*RRABAR/(RMBAR*RMBAR))
      IF(THEMI.LT.THEM(1).OR.THEMI.GT.THEM(LMX))GO TO 120
      DO 110 J=1,IB
      DO 160 I=1,NTM
      IF(THEMI.LE.THEM(I+1))GO TO 150
      GO TO 160
150    CONTINUE
      AM1(K,J)=AM(I,J)+((THEMI-THEM(I))/(THEM(I+1)-THEM(I)))*
      *(AM(I+1,J)-AM(I,J))
      GO TO 170
160    CONTINUE
170    CONTINUE
      IF(J.EQ.1)MTX=MTX+1
      KA(MTX)=K
      AM1(MTX,J)=AM1(K,J)+CF+CR
C      IF(AM1(K,J).LT.1.)AM1(K,J)=1.
110    CONTINUE
120    CONTINUE
      LMX1=KA(MTX)
      LMX2=KA(1)
      LMX=LMX1-LMX2+1

```

```
DO 180 K=1,LMX
  IANG(K)=IANG(LMX2-1+K)
DO 180 J=1,IB
  AM(K,J)=AM1(K,J)
180 CONTINUE
  RETURN
  END
```

```

C
SUBROUTINE OCTAVE(IDX1,IDX3,NFO,DF,IB,IC,AM,F,LT)
C
C *****
C
C OCTAVE AND ONE-THIRD OCTAVE CONVERSION OF SPECTRUM
C USING NARROW BAND DATA.
C
C *****
C
C DIMENSION AM(16,501),A1(501),FNL(40),F(501),NL(40),NL1(40)
C *,DL(40),FNH(40),NH(40),NH1(40),DH(40)
C
IF(IDX1.EQ.2)OTOF=2.**(1./6.)
IF(IDX1.EQ.3)OTOF=SQRT(2.)
DO 400 I=1,NFO
FNL(I)=F(I)/OTOF
ANL=FNH(I)/DF+1.
NL(I)=IFIX(ANL+.5)
NL1(I)=NL(I)+1
DL(I)=NL(I)-ANL+.5
FNH(I)=F(I)*OTOF
ANH=FNH(I)/DF+1.
NH(I)=IFIX(ANH+.5)
NH1(I)=NH(I)-1
DH(I)=ANH-NH(I)+.5
IF(NL(I).NE.NH(I))GO TO 400
DL(I)=DL(I)-.5
DH(I)=DH(I)-.5
400 CONTINUE
DO 410 K=1,LT
IF(IDX3.NE.3.AND.K.EQ.LT)GO TO 410
DO 110 I=1,IC
AM(K,I)=10.**(AM(K,I)/10.)
110 CONTINUE
DO 500 J=1,NFO
ML=NL1(J)
ML=NL(J)
MH1=NH1(J)
MH=NH(J)
A1(J)=AM(K,ML)*DL(J)+AM(K,MH)*DH(J)
IF(MH1.LT.ML1)GO TO 500
DO 510 I=ML1,MH1
A1(J)=A1(J)+AM(K,I)
510 CONTINUE
500 CONTINUE
DO 520 J=1,NFO
IF(AM(K,J).LE.0.)AM(K,J)=.001
AM(K,J)=10.*ALOG10(A1(J))
520 CONTINUE
410 CONTINUE
RETURN
END

```

```

C      SUBROUTINE POWER(IB,RMC,RD,RI,LMX,IANG,AMD,AM,TA,TD,PA,
*PS,IDX1,IDX2,IDX3,AM1,NFO)
C
C      *****
C
C      TO COMPUTE INDUCT AND FAR-FIELD POWER SPECTRA
C
C      AND POWER IMBALANCE SPECTRUM
C
C      *****
C
C      CHARACTER FNAME*13
C
C      DIMENSION AM(16,501),IANG(16),AM1(16,501),WTT(501)
C
      IF (IDX1.NE.1) IB=NFO
      LI=LMX+1
      LR=LI+1
      LT=LR+1
      GAM=1.402
      PI=3.1415926
      FAC=4.*PI*RMC*RMC
      FAD=PI*(RD*RD-RI*RI)
      FAD1=10.*ALOG10(FAD)
      ROA=GAM*PA*144./(49.0166*SQRT(TA+460.))
      ROD=GAM*(PS+PA)*144./(49.0166*SQRT(TD))
      FAD1=FAD1-10*ALOG10(ROD)
      FACT=10.*ALOG10(ROA)
      POWF=3.7396751
      DTHR=PI/18.
      SI=SIN(DTHR/2.)
      CO=COS(DTHR/2.)
      DO 150 I=1,IB
      AY=0.
      DO 160 K=1,LMX
      THR=IANG(K)*PI/180.
      IF (IANG(K).EQ.0) SR=(1.-CO)*FAC/2.
      IF (IANG(K).NE.0) SR=SI*SIN(THR)*FAC
      PW=10.**(AM(K,I)/10.)
      AY=AY+PW*SR
160  CONTINUE
      AM1(4,I)=10.*ALOG10(AY)-FACT+POWF
150  CONTINUE
      IF (IDX3.EQ.3) GO TO 400
      DO 180 I=1,IB
      WT1=(10.**(AM(LR,I)/10.))*(1.-AMD)*(1.-AMD)
      WT2=(10.**(AM(LI,I)/10.))*(1.+AMD)*(1.+AMD)
      WTT(I)=WT2-WT1
      AM1(1,I)=10.*ALOG10(WT2)+FAD1+POWF
      AM1(2,I)=10.*ALOG10(WT1)+FAD1+POWF

```

```

      AM1(5,I)=AM1(4,I)-AM1(1,I)
180  CONTINUE
      DO 320 I=1,IB
      NEZ=2
      IL=I
940  CONTINUE
      IF(WTT(I).GT.0.)GO TO 930
      IL=IL+(-1)**NEZ
      IF(IL.GE.IB)NEZ=1
      WTT(I)=WTT(IL)
      IF(IL.LE.1)WTT(I)=.0001
      GO TO 940
930  CONTINUE
      AM1(3,I)=10.*ALOG10(WTT(I))+FAD1+POWF
      AM1(6,I)=AM1(4,I)-AM1(3,I)
320  CONTINUE
      GO TO 410
400  CONTINUE
      DO 420 I=1,IB
      AM1(1,I)=AM(LI,I)
      AM1(2,I)=AM(LR,I)
      AM1(3,I)=AM(LT,I)
      AM1(5,I)=AM1(4,I)-AM1(1,I)
      AM1(6,I)=AM1(4,I)-AM1(3,I)
420  CONTINUE
410  CONTINUE
C
C      AM1(1,I)=INCIDENT POWER
C      AM1(2,I)=REFLECTED POWER
C      AM1(3,I)=TRANSMITTED POWER
C      AM1(4,I)=FAR FIELD POWER
C      AM1(5,I)=FAR FIELD NORMALIZED TO INCIDENT
C      AM1(6,I)=POWER IMBALANCE
C
      RETURN
      END

```

```

C      SUB ROUTINE SMOOTHING(IC,IB,DF,AM,NST)
C
C      *****
C      TO SMOOTH NUMERICALLY ANY SOUND PRESSURE LEVEL
C      SPECTRUM OR POWER SPECTRUM OR NORMALIZED
C      TRANSFER FUNCTION SPECTRUM
C      *****
C      DIMENSION AM(16,501),A(501),A1(501)
C
      JO=11
      KA=1
      PI=3.1415926
      IE=IB
      IO=IB-(JO-1)/2
      L1=1
      DO 100 JX=1,NST
      DO 110 I=1,IB
      A(I)=10**(AM(JX,I)/20.)
110    CONTINUE
      DO 225 N1=1,3
      DO 500 I=KA,IB
      IF(I.GT.IO)GO TO 520
      J=2*I-1
      IF(J.GE.JO)J=JO
      GO TO 530
520    J=(IB-I)*2+1
530    J1=(J-1)/2
      AJ=J-1
      J2=J-2
      J5=I-J1
      IF(I.EQ.1)GO TO 510
      IF(I.EQ.IB)GO TO 510
      A1(I)=0.
      DO 540 K=1,J2,2
      J3=I-J1+K
      J4=J3+1
      A1(I)=A1(I)+4.*A(J3)
      IF(K.EQ.J2)GO TO 550
      A1(I)=A1(I)+2.*A(J4)
550    IF(K.EQ.J2)A1(I)=A1(I)+A(J4)
      IF(K.EQ.1)A1(I)=A1(I)+A(J5)
540    CONTINUE
      A1(I)=A1(I)/(3.*AJ)
510    I1=IB-1
      IF(I.EQ.1)A1(KA)=(A(KA)+A(KA+1))/2.

```

```

      IF(I.EQ.IB)A1(IB)=(A(I1)+A(IB))/2.
500  CONTINUE
      DO 570 I=KA,IB
      A(I)=A1(I)
570  CONTINUE
225  CONTINUE
      DO 571 I=1,IB
571  AM(JX,I)=20.*ALOG10(A(I))
100  CONTINUE
      RETURN
      END

```

REFERENCES

1. Dean, P. D., Salikuddin, M., Ahuja, K. K., Plumblee, H. E., and Mungur, P., "Studies of the Acoustic Transmission Characteristics of Coaxial Nozzles with Inverted Velocity Profiles." NASA CR-159698, 1979.
2. Ahuja, K. K., Salikuddin, M., Burrin, R. H. and Plumblee, H. E. Jr., "A Study of the Acoustic Transmission Characteristics of Suppressor Nozzles." NASA CR-165144, 1980.
3. Salikuddin, M., Dean, P. D., Plumblee, H. E., Jr., and Ahuja, K. K., "An Impulse Test Technique with Application to Acoustic Measurements." *Journal of Sound and Vibration* (1980) 70 (4), 487-501.
4. Salikuddin, M., and Plumblee, H. E., Jr., "Low Frequency Sound Absorption of Orifice Plates, Perforated Plates, and Nozzles." AIAA Paper No. 80-0991, 1980.
5. Ahuja, K. K., Salikuddin, M., and Plumblee, H. E., Jr., "Characteristics of Internal and Jet Noise Radiation from a Multi-Lobe, Multi-Tube Suppressor Nozzle Tested Staticallly and Under Flight Conditions." AIAA Paper No. 80-1027, 1980.
6. Salikuddin, M., and Plumblee, H. E., Jr., "Internal Noise Radiation Characteristics of Baffles, Nozzles, Orifice Plates and Perforated Plates Used as Duct Terminations." Lockheed-Georgia Company Engineering Report LG80ER0204, 1980.
7. Levine, H. and Schwinger, J., "On the Radiation of Sound from an Unflanged Circular Pipe." *Physical Review*, Vol. 73, No. 4, pp. 383-406, 1948.
8. Favour, J. D., Lebrun, J. M., and Young, J. P., "Transient Waveform Control of Electromagnetic Test Equipment." *Shock and Vibration Bulletin* II, 1969.
9. Niedzwiecki, A. and Ribner, H. S., "Subjective Loudness of Minimized Sonic Boon Waveforms." *Journal of Acoustical Society of America*, 64 (6), 1978.
10. Singh, R., and Katra, T., "Development of an Impulse Technique for Measurement of Muffler Characteristics." *Journal of Sound and Vibration*, 56, 279-298, 1978.
11. Singh, R., and Katra, T., "On the Digital Generation of an Acoustic Excitation Impulse." *Journal of Sound and Vibration*, 58, 459-462, 1978.
12. Aoshima, N., "Computer-Generated Pulse Signal Applied for Sound Measurement." *Journal of Acoustical Society of America*, 69, 1484-1488, 1981.
13. Davies, J. C., McIntosh, J., and Mulholland, K. A., "The Generation of Short Duration Acoustic Signals." *Journal of Sound and Vibration*, 76, 77-82, 1981.

14. Ramakrishnan, R., Salikuddin, M., and Ahuja, K. K., "Generation of Desired Signals from Acoustic Drivers." (Submitted to *Journal of Sound and Vibration*), 1981.
15. Trimble, C. R., "What is Signal Averaging." *Hewlett-Packard Journal*, April 1968.
16. Doak, P. E., "Excitation, Transmission and Radiation of Sound from Sources in Hard-Walled Ducts of Finite Length (I): The Effects of Duct Cross-Section Geometry and Source Distribution Space-Time Pattern." *Journal of Sound and Vibration*, 31, 1-72, 1973.
17. Fahy, F. J., "A Technique for Measuring Sound Intensity With a Sound Level Meter." *Noise Control Engineering*, 9, 155-162, 1977.
18. Chung, J. Y., and Pope, J., "Practical Measurement of Acoustic Intensity - The Two-Microphone Cross-Spectral Method." Proceeding Internoise, 1978, (Unpublished).
19. Seybert, A. F., "Statistical Errors in Acoustic Intensity Measurements." *Journal of Sound and Vibration*, 75, (4) 519-526, 1981.
20. Thompson, J. K., and Tree, D. R., "Finite Difference Approximation Errors in Acoustic Intensity Measurements." *Journal of Sound and Vibration*, 75, 229-238, 1981.
21. Munro, D. H. and Ingard, K. U., "On Acoustic Intensity Measurements in the Presence of Mean Flow." *Journal of Acoustical Society of America*, 65, (6), 1979.
22. Doak, P. E., "Excitation, Transmission and Radiation of Sound from Source Distributions in Hard-Walled Ducts of Finite Length (II): The Effects of Duct Length." *Journal of Sound and Vibration*, 31, (2), 137-174, 1973.
23. Morse, P. M. and Ingard, K. U., "Theoretical Acoustics." *McGraw-Hill Book Company*.
24. Morse, P. M. and Feshbach, H., "Methods of Theoretical Physics," *McGraw-Hill Book Company, Inc.*
25. Weinberger, H. F., "A First Course in Partial Differential Equations With Complex Variables and Transform Methods." *Blaisdell Publishing Company*.
26. Zorumski, W. E., "Generalized Radiation Impedances and Reflection Coefficients of Circular and Annular Ducts," *The Journal of the Acoustical Society of America*, 54(6), 1973.
27. Abramowitz, M. and Stegun, I. A., "Handbook of Mathematical Functions With Formulas, Graphs, and Mathematical Tables." *National Bureau of Standards Applied Mathematics*, Series 55.

28. Candel, S. M., "Acoustic Conservation Principles and an Application to Plane and Modal Propagation in Nozzles and Diffusers." *Journal of Sound and Vibration*, 41(2), 207-232, 1975.
29. Salikuddin, M. and Zinn, B. T., "Adaption of the Impedance Tube Technique for the Measurement of Combustion Process Admittances." *Journal of Sound and Vibration*, 68, (1) 119-132, 1980.
30. Bell, W. A., "Experimental Determination of Three-Dimensional Liquid Rocket Nozzle Admittances." Ph.D. Thesis, Georgia Institute of Technology, 1972.
31. Pfahl, R. C., Jr., and Mitchel, B. J., "Nonlinear Regression Method for Simultaneous Property Measurement." *American Institute of Aeronautics and Astronautics Journal*, 8, 1980.
32. Marquardt, D. W., "An Algorithm for Least Square Estimation of Nonlinear Parameters." *Journal of the Society for Industrial and Applied Mathematics*, Vol II, 431, June 1963.
33. Cummings, A., and Eversman, W., "An Investigation of Acoustic Energy Loss in Radiation from Ducts to the Far field at Low Frequencies, Low Mach Numbers, and High Sound Pressure Levels." Aeroacoustics Research Report, LG80ER0154, Lockheed-Georgia Co., 1980.
34. Cummings, A., and Eversman, W., "Acoustic Power Dissipation on Radiation Through Duct Terminations - Theory." AIAA Paper 81-1979, 1981.
35. Bechert, D. W., "Sound Absorption Caused by Vorticity Shedding Demonstrated with a Jet Flow." *Journal of Sound and Vibration*, 70, (3), 389-405, 1980.
36. Howe, M. S., "The Dissipation of Sound at an Edge." *Journal of Sound and Vibration*, 70, (3) 407-411, 1980.
37. Howe, M. S., "Attenuation of Sound in a Low Mach Number Nozzle Flow." *Journal of Fluid Mechanics*, 91, (2), 202-229, 1979.
38. Salikuddin, M. and Ahuja, K. K., "Acoustic Power Dissipation on Radiation Through Duct Terminations - Experiments." AIAA paper 81-1978, 1981.
39. Heavens, S. N., "Visualization of the Acoustic Excitation of a Subsonic Jet." *Journal of Fluid Mechanics*, 100, 185-192, 1980.
40. Whiffen, M. C., and Ahuja, K. K., "An Improved Schlieren System and Some New Results on Acoustically Excited Jets." Accepted for Publication by *Journal of Sound and Vibration*.
41. Bechert, D., Michel, U., and Pfizenmaier, E., "Experiments on the Transmission of Sound Through Jets." (Synopsis published 1978 *American Institute of Aeronautics and Astronautics Journal*, 16, 873-874.) AIAA Paper 77-1278, 1977.
42. Ahuja, K. K., Tester, B. J., and Tanna, H. K., "The Free Jet as a Simulator of Forward Velocity Effects on Jet Noise," NASA CR-3056, 1978.

1. Report No. NASA CR-3656		2. Government Accession No.		3. Recipient's Catalog No.	
4. Title and Subtitle REFINEMENT AND APPLICATION OF ACOUSTIC IMPULSE TECHNIQUE TO STUDY NOZZLE TRANSMISSION CHARACTERISTICS				5. Report Date February 1983	
				6. Performing Organization Code	
7. Author(s) M. Salikuddin, W. H. Brown, R. Ramakrishnan, and H. K. Tanna				8. Performing Organization Report No. LG82ER0115	
9. Performing Organization Name and Address Lockheed-Georgia Company Marietta, Georgia 30063				10. Work Unit No.	
				11. Contract or Grant No. NAS3-20797	
12. Sponsoring Agency Name and Address National Aeronautics and Space Administration Washington, D. C. 20546				13. Type of Report and Period Covered Contractor Report	
				14. Sponsoring Agency Code 505-32-02 (E-1392)	
15. Supplementary Notes Final report. Project Manager, Eugene A. Krejsa, Fluid Mechanics and Acoustics Division, NASA Lewis Research Center, Cleveland, Ohio 44135.					
16. Abstract An improved acoustic impulse technique was developed and was used to study the transmission characteristics of duct/nozzle systems. To accomplish the above objective, various problems associated with the existing spark-discharge impulse technique were first studied. These included (1) the nonlinear behavior of high intensity pulses, (2) the contamination of the signal with flow noise, (3) low signal-to-noise ratio at high exhaust velocities, and (4) the inability to control or shape the signal generated by the source, specially when multiple spark points were used as the source. The first step to resolve these problems was the replacement of the spark-discharge source with electroacoustic driver(s). Following this, several processes to improve the impulse technique were studied and implemented. These included (1) synthesizing on acoustic impulse with acoustic driver(s) to control and shape the output signal, (2) time domain signal averaging to remove flow noise from the contaminated signal, (3) signal editing to remove unwanted portions of the time history, (4) spectral averaging, and (5) numerical smoothing. The acoustic power measurement technique was improved by taking multiple induct measurements and by a modal decomposition process to account for the contribution of higher order modes in the power computation. The improved acoustic impulse technique was then validated by comparing the results derived by an impedance tube method. The mechanism of acoustic power loss, that occurs when sound is transmitted through nozzle terminations, was investigated. Finally, the refined impulse technique was applied to obtain more accurate results for the acoustic transmission characteristics of a conical nozzle and a multi-lobe multi-tube supressor nozzle.					
17. Key Words (Suggested by Author(s)) Acoustic measurements; Refined impulse technique; Duct acoustics; Acoustic drivers; Signal synthesis; Signal averaging; Modal decomposition; Acoustic power loss; Power loss mechanism; Optical measurement of vortex structure; Modified impedance tube method; Conical nozzle; Daisy Lobe nozzle; Coannular duct-nozzle systems				18. Distribution Statement Unclassified - unlimited STAR Category 71	
19. Security Classif. (of this report) Unclassified		20. Security Classif. (of this page) Unclassified		21. No. of Pages 407	
				22. Price* A18	

* For sale by the National Technical Information Service, Springfield, Virginia 22161

NASA-Langley, 1983

☆U.S. GOVERNMENT PRINTING OFFICE: 1983 639 008 27

National Aeronautics and
Space Administration

Washington, D.C.
20546

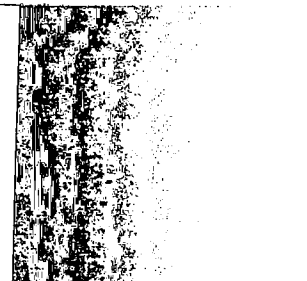
Official Business
Penalty for Private Use, \$300

SPECIAL FOURTH CLASS MAIL
BOOK

Postage and Fees Paid
National Aeronautics and
Space Administration
NASA-451



1 1 1U,H, 830112 S00903DS
DEPT OF THE AIR FORCE
AF WEAPONS LABORATORY
ATTN: TECHNICAL LIBRARY (SUL)
KIRTLAND AFB NM 87117



NASA

POSTMASTER:

If Undeliverable (Section 158
Postal Manual) Do Not Return